JOURNAL OF THE MYANMAR ACADEMY OF ARTS AND SCIENCE

Physics

Vol. XVII, No.2A, August 2019

Myanmar Academy of Arts and Science

Journal of the Myanmar Academy of Arts and Science

Vol. XVII, No. 2A

Contents

Physics

J. Myanmar Acad. Arts Sci. 2019 **Vol. XVII. No.2A**

STRUCTURAL, MORPHOLOGICAL AND MOTT-SCHOTTKY CAPACITANCE ANALYSIS OF PEROVSKITE TYPE $SrTiO_3$, $CaTiO_3$ AND $BaTiO_3$ THIN FILMS ON ITO GLASS*

Moht Moht Than[1]

Abstract

Phase-pure perovskite type $SrTiO_3$, $CaTiO_3$ and $BaTiO_3$ thin films are deposited on ITO coated glass substrate by using sol-gel process and spin-coating technique. The samples are studied by structural, morphological and electrical characteristics. The X-ray diffraction spectra of $SrTiO_3$, $CaTiO_3$ and $BaTiO_3$ thin films on ITO glass shows that the perovskite type cubic structures with preferred orientation along (110) plane. The surface morphological is investigated by scanning electron microscopy (SEM), which revealed the crystalline nature of the films. The lattice parameters, unit cell volume, crystallite size, dislocation density, strain and grain size are evaluated. Mott- Schottky capacitance analysis is adapted to determine the built-in voltage (V_{bi}) and doping density (N_A) of the perovskite thin film devices. The influence of the Schottky contact is studied for perovskite thin films devices, by using capacitance-voltage measurement at frequency 10 kH_z. Furthermore, the depletion region widths of the thin films devices are also evaluated.

Keyword: Perovskite type thin films, Sol-gel process, XRD, SEM, Mott-Schottky capacitance

Introduction

A thorough understanding of the device physics of perovskite-type solar cells is a crucial prerequisite for purposeful optimization of these devices and materials [Brabec C J et al 2011&2010, Clarke T M et al 2010,Blom P W M et al 2007, Deibel C et al 2010 and Glatthaar M et al 2007]. Stimulated by the study of capacitance/voltage (CV) measurements done on perovskite-type solar cells, there has been a recent debate about the correct band diagram of perovskite-type thin films solar cells and in particular about the relevance and magnitude of doping and contact barriers [Fabregat-Santiago F 2011 and Bisquert J et al 2011]. Mott-Schottky analysis is commonly used to determine the built-in voltage (V_{bi}) and doping density (N_A) of a semiconductor at Schottky and *p-n* junctions [Brabec C J et al 2011]. However, the method is not always straightforward. For example, when the analysis is applied to

---

[1] Dr, Lecturer, Department of Physics, University of Yangon

[*] Best Paper Award Winning Paper in Physics (2018)

organic solar cells the parameters are frequency dependent, making it difficult to extract the true values [Brabec C J et al 2010]. Furthermore, sources of capacitance other than the depletion capacitance distort the capacitance-voltage (CV) response, resulting in values of V_{bi} and N_A that are larger than the actual values.

Other types of solar technologies also exhibit capacitive responses related to contact phenomena as the depletion layer capacitance commonly exhibited by inorganic and organic photovoltaic devices [Fabregat-Santiago F 2011]. Voltage-modulation of the depletion layer width (w) allows extracting relevant parameters as the absorber acceptor defect density (N_A) and built-in potential (V_{bi}) by means of capacitance-voltage Mott-Schottky (MS) analysis [Bisquert J et al 2011]. These two parameters can be used to derive experimentally-supported PSCs device models, and also constitute key information of variations in materials properties induced by device processing modifications.

Experimental

Firstly, the glass slides coated with indium tin oxide (ITO) were cleaned by acetone, HCl and deionized water. Secondly, the perovskite type $SrTiO_3$, $CaTiO_3$ and $BaTiO_3$ powder were mixed with 2-methoxyethanol solution by using sol-gel method. And then these pastes were coated on ITO conducting glass by using spin coating technique and annealed at 100˚ C for 30 minutes. The structure of prepared films were characterized by X-ray diffraction (RigakuMultiflex, Japan) with Cu K_{α} source (λ =1.54056 Å). The scanning electron microscopies were performed to analyze the surface morphology of the films. Capacitance Voltage measurements were performed using a $G^{\underline{W}}$InSTEK (LCR-8110G) at frequency 10 kHz and various applied voltage.

Results and Discussion

The crystallinity of the films was investigated using X- ray diffraction. The detailed structural characterizations exhibited the perovskite-type with cubic structure for all samples. Figure (1) shows the diffraction peak of $SrTiO_3$, $CaTiO_3$ and $BaTiO_3$ thin films on ITO glass.

The average crystallite size measured in direction perpendicular to the surface of the sample was calculated using Scherrer formula as shown in equation 1, where B represents a width measured in radians at intensity equal to half of the maximum intensity, θ_B is Bragg angle and k is the shape factor of the average crystallite.

$$t = \frac{k\lambda}{B\cos\theta_B} \qquad (1)$$

Figure (2) shows the SEM micrograph of $SrTiO_3$, $CaTiO_3$ and $BaTiO_3$ thin films on ITO glass. From the SEM images, it can be seen that the particles are in spherical shape, fairly dense, crack-free and fine grain.

Mott-Schottky analysis probes the depletion capacitance at a Schottky or p-n junction which is determined by the width of the bias dependent depletion region. Hence the depletion capacitance “C” is also bias dependent and can be expressed as in equation 2, where, V is the applied bias voltage and V_{bi} is the built-in voltage.

$$\frac{1}{C^2} = \frac{2(V_{bi} - V)}{A^2 q\varepsilon_r\varepsilon_0 N_A} \qquad (2)$$

The structural properties of $SrTiO_3$, $CaTiO_3$ and $BaTiO_3$ thin films on ITO glass are listed in Table 1.

Table 1: The structural properties of $SrTiO_3$, $CaTiO_3$ and $BaTiO_3$ thin films on ITO glass

Samples	***Maximum peak***	***Lattice constant “a”(Å)***	***Unit cell volume “V” (nm)^3***	***Crystallite size “t” (nm)***	***Dislocation density “□” (m)$^{-2}$***	***Strain “□”***
$SrTiO_3$/ITO glass	(110)	3.8839	0.0586	36.4677	7.5194×10^{14}	9.5049×10^{-4}
$CaTiO_3$/ITO glass	(110)	3.8092	0.0553	30.4817	1.0763×10^{15}	1.1372×10^{-3}
$BaTiO_3$/ITO glass	(110)	4.0116	0.0646	31.1411	1.0312×10^{15}	1.1311×10^{-3}

Figure (3) depicts the characteristics $1/C^2$ versus V plots for $SrTiO_3$, $CaTiO_3$ and $BaTiO_3$ thin films on ITO glass at frequency range 10 kHz. The so-called Mott-Schottky plot of $1/C^2$ versus applied DC voltage yields a straight line, whose slope yield the doping density and whose extrapolated intersection with the voltage axis yields the built-in voltage. The doping density is given by equation 3.

$$N_A = -\frac{2}{q\varepsilon_s A^2}\left(\frac{d(C)^{-2}}{dV}\right)^{-1} \qquad (3)$$

The main parameters obtained from Mott-Schottky analysis for Perovskite-type thin film devices collected in Table 2.

Table 2: The main parameters obtained from Mott-Schottky analysis for Perovskite-type thin film devices

Samples	V_{bi} ***(V)***	N_A ***(cm)***^{3}	***W(cm)***
$SrTiO_3$/ITO glass	0.179	2.86×10^{16}	4.16×10^{-6}
$CaTiO_3$/ITO glass	0.370	5.03×10^{12}	5.71×10^{-4}
$BaTiO_3$/ITO glass	0.122	2.70×10^{14}	2.49×10^{-4}

Conclusion

Phase – pure perovskite type $SrTiO_3$,$CaTiO_3$ and $BaTiO_3$ thin films have been synthesized using sol-gel process and deposited on ITO coated glass substrate using spin-coating technique. The $SrTiO_3$/ITO glass, $CaTiO_3$/ITO glass and $BaTiO_3$/ITO glass, structures were studied by structural and microstructural characteristics. According to the XRD pattern, these films have perovskite type cubic structure. From the SEM investigation, the films crystallinity indicated that with large grain size. The average grain size was observed to be estimate of 0.79 μ m, 0.98 μ m and 0.75 μ m respectively.

Perovskite films thicknesses are 2.69 μ m for $SrTiO_3$/ITO glass, 10.66 μ m for $CaTiO_3$/ITO glass and 4.45 μ m for $BaTiO_3$/ITO glass respectively. The capacitance - voltage characteristics should be measured after applying reverse bias for several minutes at room temperature in order to obtain the true profile of shallow acceptors. Only under careful checking of the capacitance response, Mott-Schottky analysis can lead to meaningful and reliable parameter extraction to be properly used in device physical modeling.

Acknowledgements

I wish to express my sincere thanks to Professor Dr Khin Khin Win, Head of Department of Physics, Yangon University, for her kind permission to carry out this research.

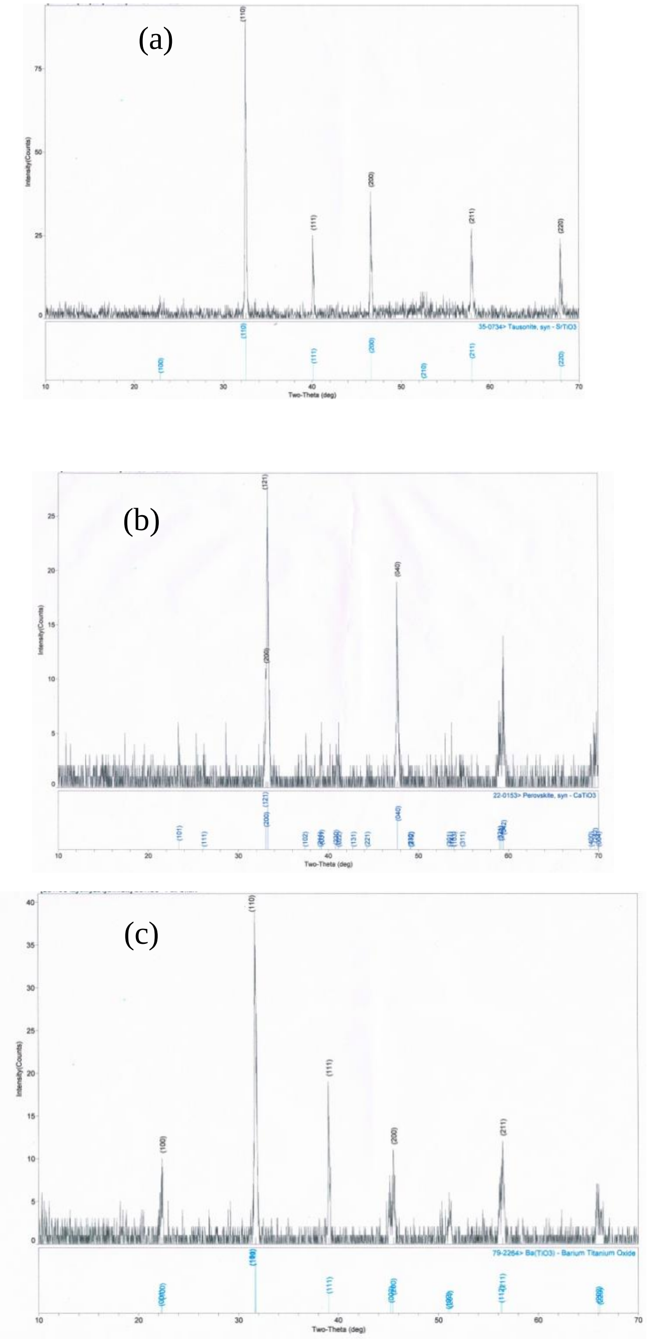

Figure 1: The diffraction peak of (a) $SrTiO_3$/ITO glass (b) $CaTiO_3$/ITO glass and (c) $BaTiO_3$/ITO glass thin fiml.

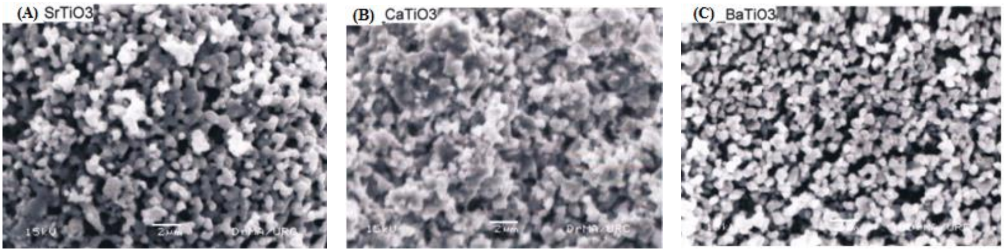

Figure 2: The scanning electron micrograph of (a) $SrTiO_3$/ITO glass (b) $CaTiO_3$/ITO glass (c) $BaTiO_3$/ITO glass thin film.

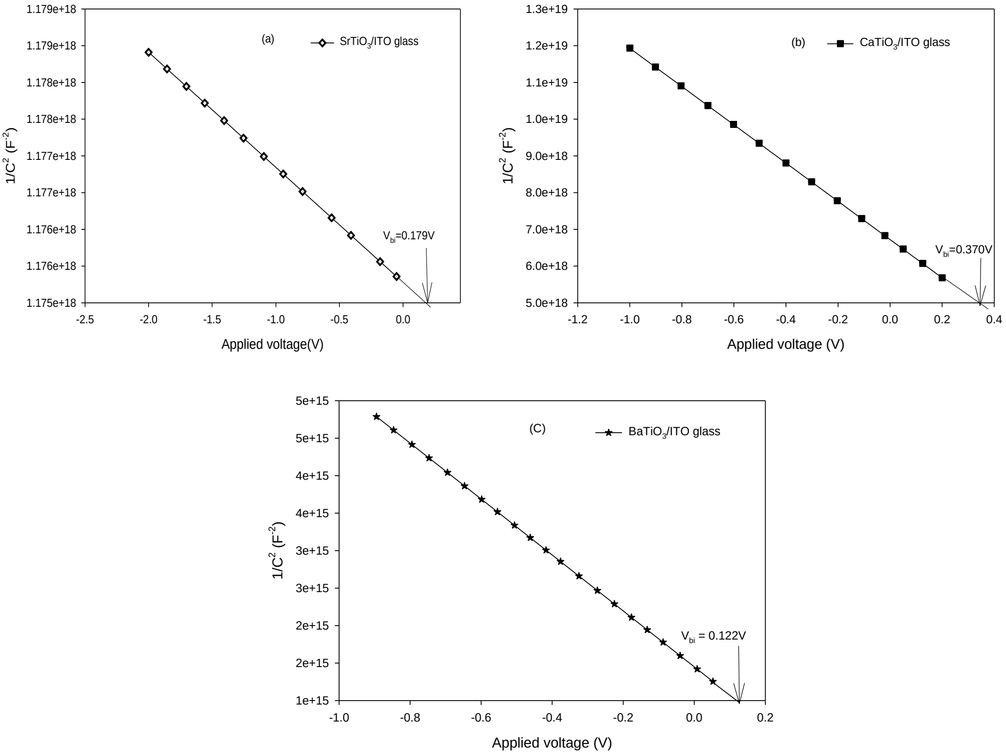

Figure 3: $1/C^2$ –V plots for Perovskite-type (a) $SrTiO_3$/ITO glass (b) $CaTiO_3$/ITO glass and (c) $BaTiO_3$/ITO glass thin film.

References

Brabec C J et al (2011); Chem Soc Rev 40, p 1185-1199

Brabec C J et al (2010); Adv Mater 22, p 3839-3856

Blom P W M et al (2007); Adv Mater 19, p 1551-1566

Bisquert J et al (2011); J Phys Chem Lett 2, p 1950-1964

Clarke T M et al (2010); Chem Rev 110, p 6736-6767

Deibel C et al (2010); Adv Mater 22, p 4097-4111

Deibel C et al (2010); Prog phys 73, p 401

Fabregat-Santiago F (2011); J Chem Phys 13, p 9083-9118

Glatthaar M et al (2007); Energy Matter Sol.Cell 91, p 390-393

J. Myanmar Acad. Arts Sci. 2019 **Vol. XVII. No.2A**

QUANTITATIVE ANALYSIS ON THE ELEMENTAL CONCENTRATIONS AND INTERMOLECULAR STRUCTURE OF SHAZAUNG-LET-PAT (*ALOE VERA* LINN.)

Ni Ni War[1], Kyi Thar Myint[2], & Khin Khin Win[3]

Abstract

The purpose of this research work was to study the elemental cocentrationand mode of chemical group between the possible vibrational frequencies in parts of *Aloe vera* plant by using Energy Dispersive X-ray Fluoresence (EDXRF), Fourier Transform Infra-Red (FTIR) and Ultraviolet and Vissible (UV-vis) Spectroscopy techniques. Hydrogel films composed of polyvinyl alcohol(PVA) and *Aloe vera*(AV) gel were prepared and characterized by different ratio of PVA/AV hydrogel films 1:1, 1:2and 1:3 variations in the *Aloe vera* content. From the the results obtained that *Aloe vera* improves the water absorption rate of the films. and average equilibrium water content is 84.67%. The morphological characterization of the film by Scanning Electron Microscopy (SEM) analysis.

Keywords: *Aloe vera*, PVA, EDXRF, FTIR ,UV and SEM

Introduction

Aloe is the genus plants that contains over 400 species. The widely known species is *Aloe vera* ,which is grown for its unusual shape as well as for medical purposes. *Aloe vera* plant has been known and used for its health, beauty, medicinal and skin care properties. *Aloe vera* gel play an important role in the treatment of tumars, diabetes, ulcer and cancer. Traditional herbal medicines are used for treatment of various illness, but sometimes they could turn out to be toxic because of the present of some heavy metals and other impurities apart from the pharmacological effect. The objective of the present study is to perform elemental concentration of *Aloe vera* analysis by (EDXRF). Elemental analysis of medicinal plants is also helpful for knowing the quantity of heavy toxic metals and quality of that medicinal plant. The medicinal plant depend on the presence of elements, therefore quantitative assessment of elemental concentration is important and essential to understand

---

[1] PhD Candidate, Lecturer, Department of Physics, University of Yangon

[2] Dr, Professor (Retd), Department of Physics, West Yangon University

[3] Dr., Professor & HOD, Department of Physics, University of Yangon

their nutritive and pharmacological value. The work also investigates the usefulness of (FTIR) analysis and UV-visspectroscopy technique for more aknowledge of constituents and chemical structure. Hydrogel films composed of polyvinyl alcohol (PVA) and *Aloe vera* (AV) gel were prepared and morphological of the film by SEM analysis. And also determine by characterization of the water absorption rate in films.

Materials and Methods

Collection and Identification

Shazaung-let-pat (*Aloe vera* Linn.) fresh plants belongs to the family aloaceae have been collected from Mawlamyine Township in Mon State. The classification and identification of *Aloe vera* plant was analysed by Botany Department, University of Yangon.

Preparation of *Aloe vera* Extracts

An *Aloe vera* leaf was obtained by surface sterilized with ethanol. The outer, green dermis of the leaf was peeled off using a sterile blade. Fillets were extensively washed with distilled water to remove the exudes from their surfaces. The fillets were homogeneized in a blender and then the homogenized mass was filtered. After that the flesh gelwas weighed and 25 g of this was added 50 ml of distilled water to it. This mixture was then boiled for 15 minutes. After cooling to room temperature. It was filtered. The green dermis of *Aloe vera* leaves and roots were dried at room temperature. The dried sample are crushed and grounded into powder by using grinding machine for homogeneous dense material. And then, these powdered sample were weighed with scientific balance to get about 5 grams. Then poured into a disc made of steel and pressed into pellet by using 3-ton weight of Hydraulic press. The diameter of each pellet is 1.2 cm.

Preparation of films

Solvent casting technique

3 ml of the 3% Polyvinyl Alcohol(PVA) solution and the *Aloe vera*(AV) gel extract was incorporated to the ratio of 1:1, 1:2, and 1:3 (v/v) respectively. PVA solutions were prepared varying the concentration for 3%

(v/v), dissolving PVA in distilled water under constant stirring for 2 hours at 70Ć. To prepare films, solution of PVA and *Aloe vera* (AV) were mixed for each concentration of PVA with magnetic stirrer during 30 min, to which relations ratio 1:1, 1:2, 1:3 (v/v) were varied then the mixtures were isolated at room temperature for 6 or 7 days to remove bubbles formed during the process. All films were made in triplicate for each ratio of PVA/AV used. Finally, dried mambranes are removed from petri dishes and labeled in Figure 5.

Characterizations of films

Water absorption of capacity

It is used to measure the capacity of the PVA/AV films and 1:1, 1:2, 1:3 films was measured by swelling the films in distilled water at room temperature. They were pre-weighed and then immersed in 15 ml distilled water. The films were withdrawn from the water every half hour upto 4 hour.The wet weight of the films were determined after first blotting with a filter followed by blowing with a stream of air to remove surface water and immediately weighing the films. Every time after noting the weight. The swelling ratio was calculated using the equation:

$$(\%)\ E_{sr} = ((\ W_s - W_d)/W_d) \times 100$$

Where, Esr is the water absorption (%) of the films. Wd and Ws are weight of the samples in the dry and swollen states respectively.

The equilibrium water content (EWC)

EWC was calculated from the following equation:

$$\%\ EWC = ((We-Wd)/\ We) \times 100$$

Where, We represents the weight of the swollen states at equilibrium.

Results and Discussion

EDXRF Analysis

The measurements of elements concentration in *Aloe vera* leaves, gel and root sample are shown in Table (1).From EDXRF analysis, the maximum concentrations of Calcium, Potassium, and Iron have been found in *Aloe vera* leaf is 76.300,14.648,2.069(%), in *Aloe vera* root is 70.343,10.973,0.975(%), and in *Aloe vera* gel is 75.350,6.722,17.100(%) respectively. Calcium, Potassium are macro elements present in high amount in leaf of *Aloe vera*. Calcium (Ca) is main component in bone growth and healful for regulating skeletal and cardiac muscle contractions. Potassium (K) is regulates water balance levels of acidity, blood pressure, muscles and nervous system, prevent diabetes. Iron (Fe) is the function to combine with protein and copper in making haemoglobin, the component of the blood that carries oxygen from the lungs to the tissue. An the other elements such as Mn, Cu, Zn, Sr, Rb found as minor elements and they detected as a very few weight percent. All organic compounds are mostly containing hydrocarbons. The element concentrations in EDXRF spectrum of *Aloe vera* gel, leaves and root are shown in Figure (6 to 8) and graph of Figure 9.

FTIR Analysis

The result from FTIR were shown twelve peak in absorbance wave number spectrum range from 4000 cm^{-1} to 400cm^{-1}. The FTIR spectra of the green dermis of *Aloe vera* leaf, gel and root in Figure (10 to 12). Astrong broad absorption band around 3450-3420 cm^{-1} found in all the samples may be due to the presence of hydrogen bounded N – H stretching, characteristic of amino acids group. The absorption band at 1750-1630 cm^{-1} is characteristic of C=O stretching indicates the presence of carbonyl groups. The absorption band at 1250-1240 cm^{-1} is due to the strecthing vibrations of C-O groups of esters and phenols. The strong absorption band at 1630-1620 cm^{-1} is due to C=C stretching which indicates the presence of vinyl ether and aloin compound. All constituent of chemical status in Aloe gel is greater than root and leaf. Since amino acids is the building blocks of protein, it’s considered to be the main functional group in tissue by human body. Phenolic compounds is medicinal herbs and to exert preventive activity against infectious and degenerative diseases.

Optical Analysis

The absorption spectrum of *Aloe vera* was obtained from UV-vis spectroscopy. The wavelength range of spectrum lie between 190 nm to

1100 nm. The UV-vis spectra of the green dermis of *Aloe vera* leaf, root and gel due to chemical status. These wavelengths corresponds to the presence of amino, aloin, phenolic compound and carbonyl groups were shown in Figure(13 to 15) and Table (3).

Film Forming

It was revealed that the *Aloe vera* plant extract do not form films. All the composite that involved polyvinyl alcohol (PVA) were able to form film. It was porve that PVA had film forming characteristics. The water absorption capacity of PVA/AV films decreased with increasing concentration of the plant extract.The EWC (equilibrium water content) of the films containing *Aloe vera* extract in PVA reduced gradually as the propotion of *Aloe vera* extract in the films increased. All the films reach their respective maximum water absorption within the 2 hours of introduction into the aqueous enviroment. From the results, it is possible to observe that the film containing 1:3 of PVA/AV film presented a quickly absorption of water along the first 30 min after immersion, reaching the equilibrium in approximated 120 min. The film with higher *Aloe vera* content exhibited a quickly absorption of water after immersion which was followed by a progressive and slower absorption of water, not reaching the equilibrium during the 24 hour of the test. The EWC of the sample 3, PVA/AV(1:3) film is (85.2%) higher than that of other films sample 2 and sample 3 are 84.2% and 84.8% respectively. These results clearly showed that the water absorption capacity of the films in Table (3) and Figure 17.

SEM Analysis

The SEM micrograph of the surface structure of *Aloe vera* hydrogel film sample 3 is shown in figure 18. This image confirms that the material is forming micro- size agglomerates. The surface structure of the hydrogel film image were taken of 1000 magnification at an operating voltage of 15 kV.

Figure 1: *Aloe vera* plants

Figure 2: The green dermis of *Aloe vera* leaves and gel

Figure 3: Collection of gel

Figure 4: Roots of *Aloe vera*

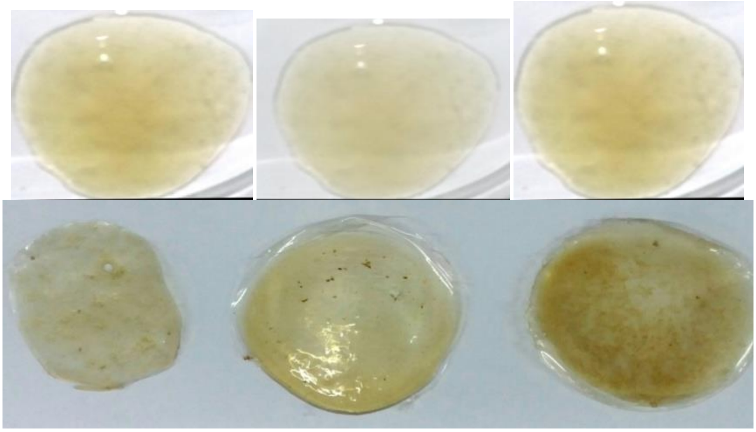

Figure 5: PVA/AV(1:1,1:2,1:3) films

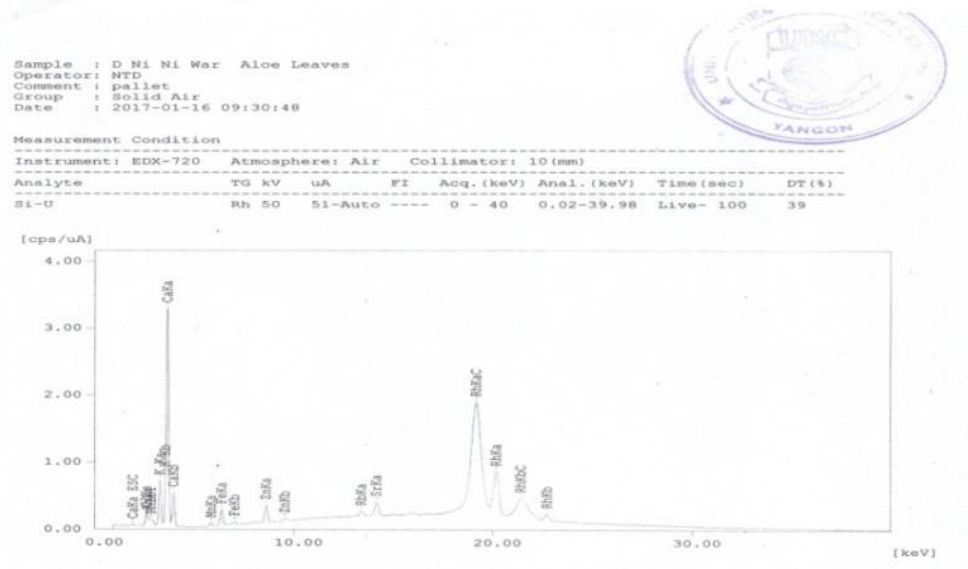

```
Sample   : D Ni Ni War  Aloe Leaves
Operator: NTD
Comment : pallet
Group   : Solid Air
Date    : 2017-01-16 09:30:48

Measurement Condition
------------------------------------------------------------------------------------
Instrument: EDX-720    Atmosphere: Air    Collimator: 10(mm)
------------------------------------------------------------------------------------
Analyte                TG kV   uA        FI    Acq.(keV) Anal.(keV)  Time(sec)   DT(%)
------------------------------------------------------------------------------------
Si-U                   Rh 50   51-Auto ----   0 - 40    0.02-39.98  Live- 100    39
```

Figure 6: EDXRF Spectrum of *Aloe vera* leaves

```
Sample   : D Ni Ni War Aloe gel
Operator: NTD
Comment : for not dried paper
Group   : solution_filter_air
Date    : 2017-01-16 09:20:59

Measurement Condition
------------------------------------------------------------------------------------
Instrument: EDX-720    Atmosphere: Air    Collimator: 10(mm)
------------------------------------------------------------------------------------
Analyte                TG kV   uA        FI    Acq.(keV) Anal.(keV)  Time(sec)   DT(%)
------------------------------------------------------------------------------------
Si - U                 Rh 50   625-Auto ----   0 - 40    0.02-39.98  Live- 100    39
```

Figure 7: EDXRF Spectrum of *Aloe vera* gel

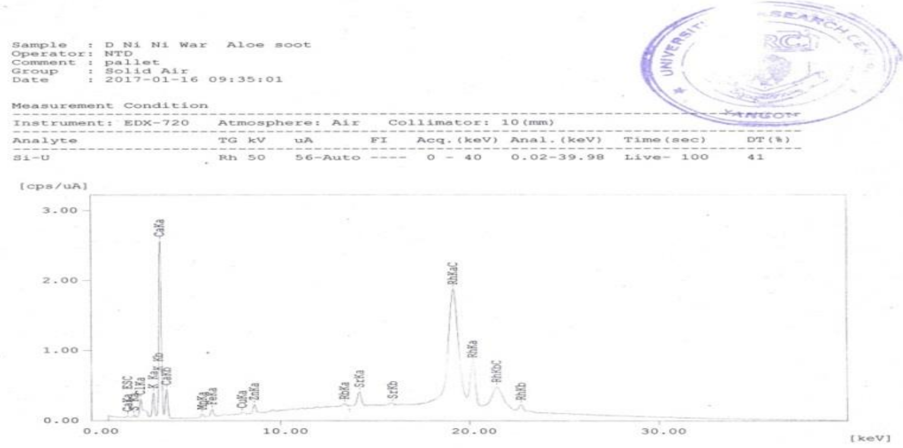

```
Sample   : D Ni Ni War  Aloe soot
Operator: NTD
Comment : pallet
Group    : Solid Air
Date     : 2017-01-16 09:35:01

Measurement Condition
---------------------------------------------------------------------------------------
Instrument: EDX-720    Atmosphere: Air    Collimator: 10(mm)
---------------------------------------------------------------------------------------
Analyte                TG kV    uA        FI    Acq.(keV) Anal.(keV)   Time(sec)     DT(%)
---------------------------------------------------------------------------------------
Si-U                   Rh 50    56-Auto ----   0 - 40    0.02-39.98   Live- 100     41
```

Figure 8: EDXRF Spectrum of *Aloe vera* root

Table 1: Elemental concentration in sample for various parts of *Aloe vera* (%)

Element	Average Elemental Concentration (W%) of three samples		
	Gel (%)	**Leaves (%)**	**Root (%)**
Ca	75.35	76.300	70.343
K	6.722	14.648	10.973
Fe	17.1	2.069	0.975
Mn	0.821	0.601	0.630
Cl	-	4.754	14.330
S	-	-	1.572
Cu	0.0032	-	0.152
Zn	0.0038	1.078	0.526
Sr	-	0.386	0.402
Rb	-	0.165	0.095

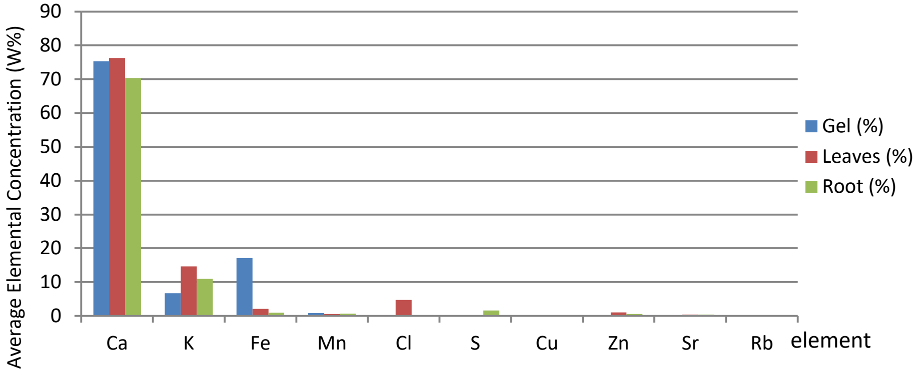

Figure 9: Element concentrations in *Aloe vera*leaves,gel and root

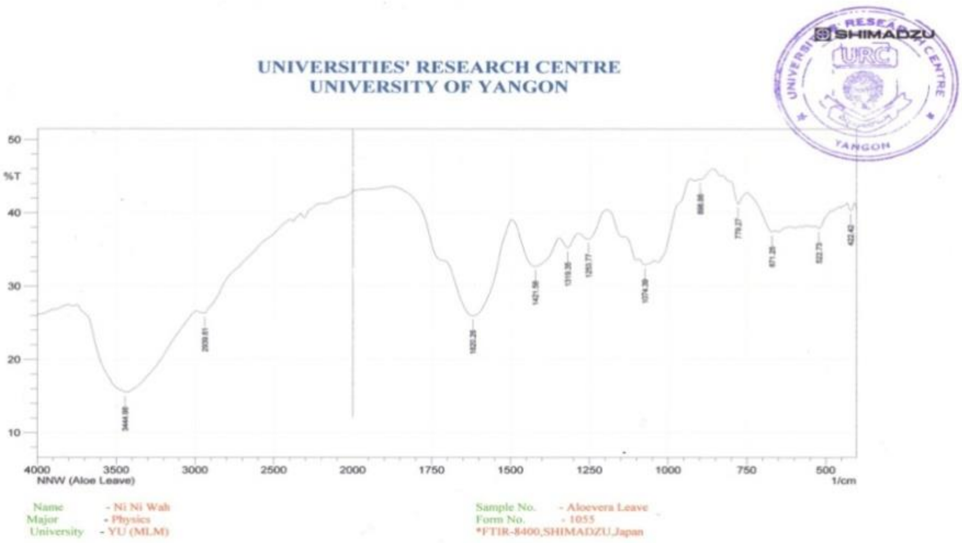

Figure 10: FTIR spectrum of *Aloe vera* leaves

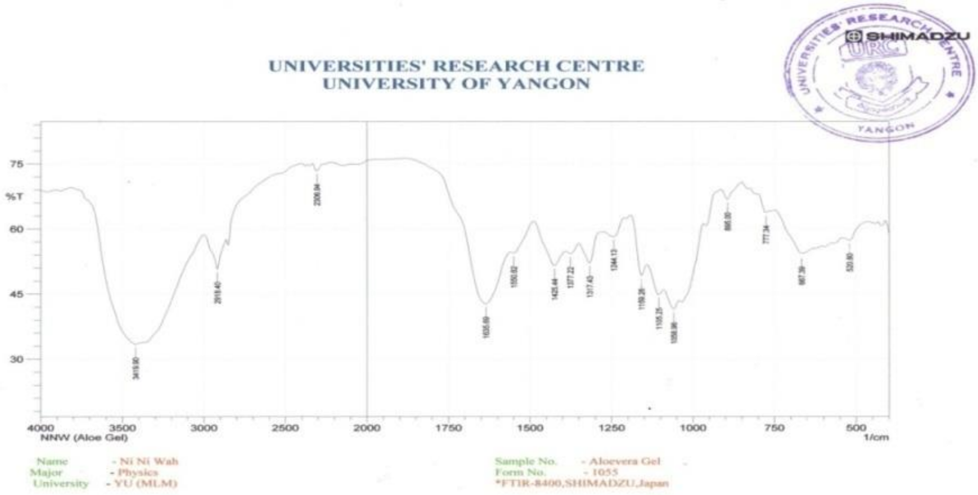

Figure 11: FTIR spectrum of *Aloe vera* gel

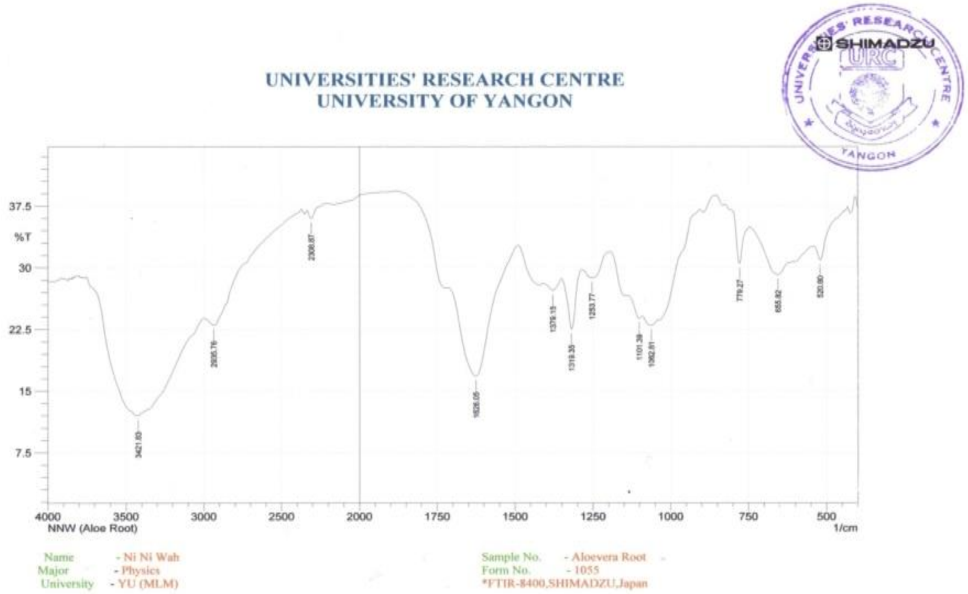

Figure 12: FTIR spectrum of *Aloe vera* root

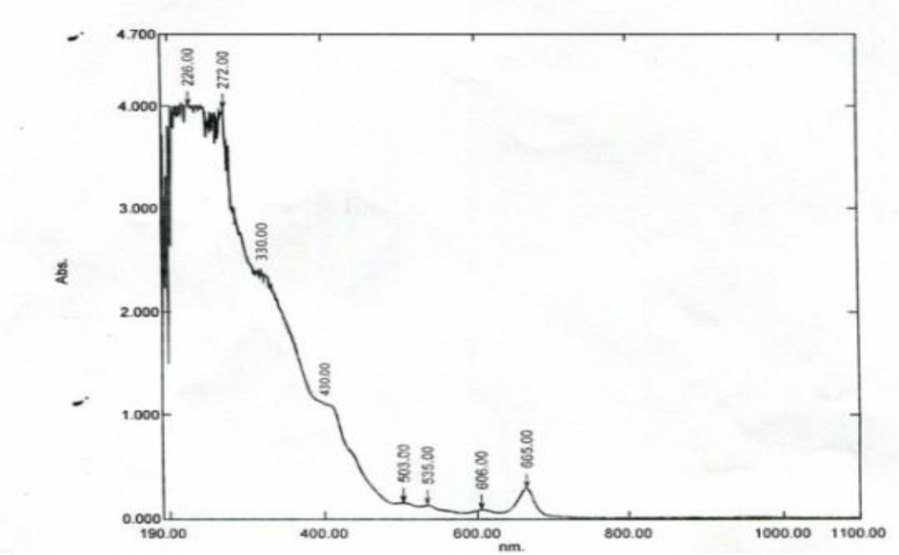

Figure 13: UV absorption spectrum of the *Aloe vera* leaves

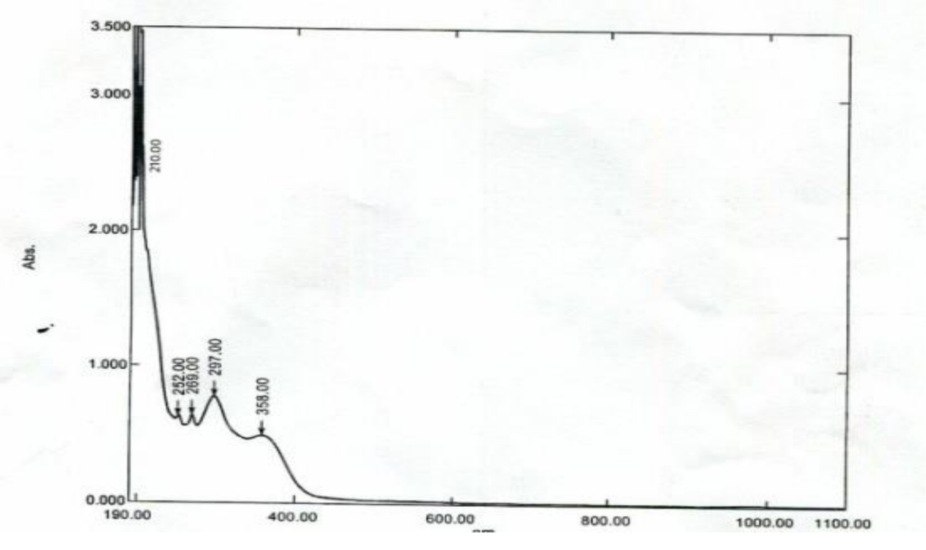

Figure 14: UV absorption spectrum of *Aloe vera*gel

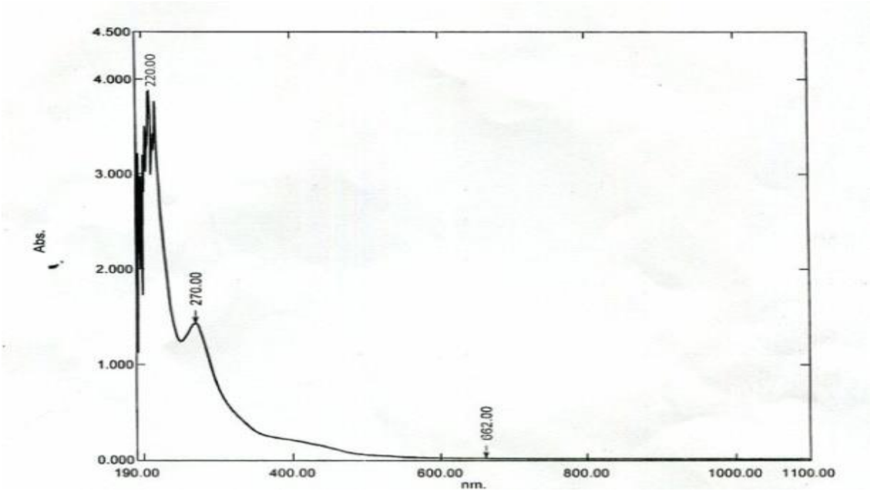

Figure 15: UV absorption spectrum of *Aloe vera* root

Table 2: UV spectral studies of *Aloe vera* samples

Sr No.	Chemical Status	Wavelength (nm)	leaf	gel	root
1	Aloin	272	Present	present	present
2	Phenolic compound	330	present	present	Absent
3	Carbonyl group	420	Absent	present	Absent
4	Amino group	220	Present	present	Present

Table 3: Water absorption capacity of *Aloe vera* film samples (swelling ratio)

Time (hours)	Sample 1(1:1)	Sample 2(1:2)	Sample 3(1:3)
0.5	278.95	305.26	368.42
1	368.42	373.68	405.26
1.5	431.58	447.37	505.26
2	531.58	557.80	573.68
2.5	500.00	547.37	563.16
3	494.74	536.84	552.63
3.5	489.74	536.84	552.63
4	487.74	536.84	552.63

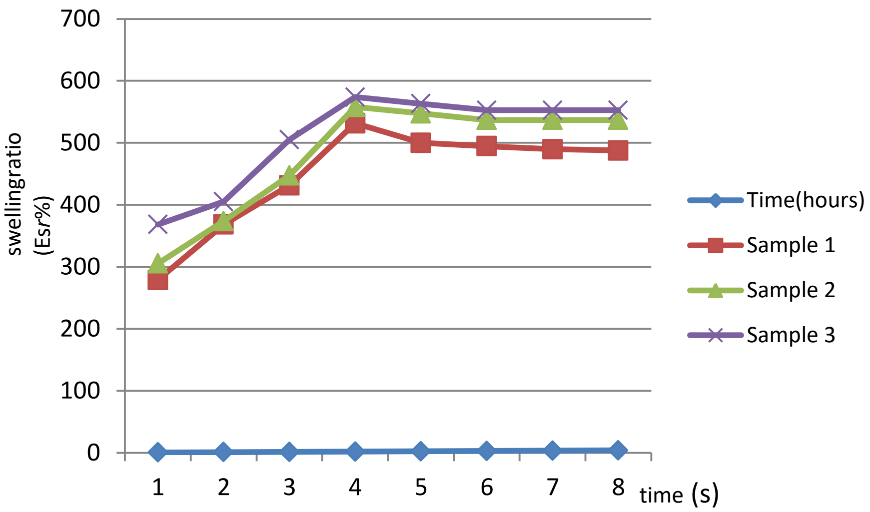

Figure 16: Water absorption capacity of *Aloe vera* film samples

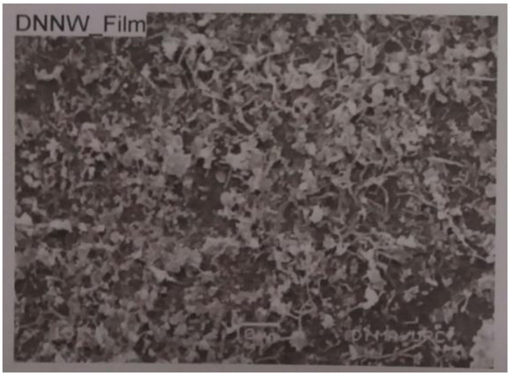

Figure 17: The SEM micrograph of the *Aloe vera* hydrogel (1:3)film

Conclusion

From the result showed the macro elements like Ca,K were found in maximum concentration and also found microelements like Fe, Mn, Cu, Zn in *Aloe vera* plant.The radiative elements to be Strontium contributed only a very few percentage (0.386% in leaves, 0.402% in root).The heavy and toxic metals which have not been detected in *Aloe vera* plant.From the FTIR and UV-vis analysis,it is found that all organic constituents of chemical statusis present in *Aloe vera* gel. The water absorption properties of the films are depend on the *Aloe vera* content. That increase on the *Aloe vera* content significantly improved due to the high water absorption properties of the films. The EWC of the sample 3, PVA/AV(1:3) film is (85.2%) higher than that of other films sample 1 and sample 2 are 84.2% and 84.8% respectively. However, all of the films have been found good swelling characteristics by reaching t heir maximum water absorption capacity within the second hour. The surface structure of the hydrogel film image confirms micro- size agglomerates. This study indicated that the *Aloe vera* hydrogel films may be suitable for applications that help wound healing and heat absorption as well as radiation burns.

Acknowledgements

I would like to express my sincere thanks to my Supervisor Professor Dr Khin Khin Win, Head of Department of Physics, University of Yangon, for her kind permission to carry out this work, then for her supervision, helpful advice and valuable suggestion.

I wish to show my sincere thanks to Professor Dr Aye Aye Thant, Department of Physics, University of Yangon, for her discussion and suggestion in experimental work.

I am also grateful to my Co-supervisor Dr Kyi Thar Myint, Professor (Retd), Department of Physics, West Yangon University for her valuable guidance.

References

Amdoun N, Zarrouk P, H, Juliemb C.M,(2003)" Ionics" 9, 47

Dassanayake, M. D. (1996). "A revised hand book to the Flora of Ceylon". (Vol.XIV). University of Peradeniya, Department of Agriculture, Peradeniya: Sri Lanka.

Glambattista, A.(2007) "College Physics " 2nd Edi (Boston ,McGraw Hill).

Gunasekaran, S., Lakshmi, S. and Hamaa, S., and Kavitha, (2000) "National Conference on Spectroscopy Physics"., 151 .

Katime, I, Katime, O y Katime, D, (2005) "Material Inteligents Hydrogels macromoleculars, algunasaplicacions biomedicas. Anales de la Real Sociedad Espafiola de Qulmica" pp 35-50.

J. Myanmar Acad. Arts Sci. 2019 **Vol. XVII. No.2A**

AUTOMATIC LIVER SEGMENTATION WITH FILTERING AND MORPHOLOGICAL METHODS

Thida Pyone[1], Aye Aye Thant [2]and Khin Khin Win[3]

Abstract

The main contribution of this paper is automatic liver segmentation which is the important step of liver benign or malignant classification. Morphological based automatic liver segmentation algorithm is proposed to get better classification results. Two popular image enhancing methods such as image filtering and morphological methods are used. It is required to remove texts in images by enhancing with image filtering method which extracts all connected liver components. In this research, automatic liver segmentation has been conducted to enhance liver image by image filtering and morphological operations such as image opening, dilation and filling holes. Liver region is segmented from the(512× 512) pixels abdominal CT liver images. This accuracy result is acceptable for liver segmentation.

Keywords: Computed Tomography (CT), Morphology, Segmentation.

Introduction

Imaging technology has seen a great development in spatial resolution and scan time, resulting in growing data volumes that the medical practitioner has to analyze. The internal structures hidden by the skin and bones can be sought in medical imaging. In medical images, liver detection and segmentation has been reported using Computed tomography (CT), Magnetic Resonance Imaging (MRI), Ultrasound (US) and Positron Emission Tomography (PET). By using these techniques reports are very reliable decisions for diagnosis. Computed Tomography(CT) is an invaluable tool for diagnosis and treatment planning in Medical imaging. This technique and process of creating visual representations of the interior of a body for clinical analysis of some organs or tissues (physiology). CT image modality can be widely used in liver diagnosis. Computed tomography (CT) is an imaging procedure that use of computer processed combinations of many x-rays measurements taken from different angles to produce cross-sectional (tomographic) images of specific areas of a scanned object, creating a series of detailed pictures, or scans, of areas inside the body without cutting. Image

---

[1.] PhD Candidate, Lecturer, Department of Physics, University of Yangon
[2.] Dr, Professor, Department of Physics, University of Yangon
[3.] Dr, Professor & HOD, Department of Physics, University of Yangon

segmentation is a technique for extraction and delineation of regions of interests (ROI) in images, are particularly interesting. The main goal of segmentation is to represent an image to be more meaningful and easier to analyze. Segmentation can be used diagnosis and study of anatomical structures or localization of pathologies such as cancer tumors. In many clinical applications, segmentation of the whole liver region from abdominal computed tomography (CT) image is the essential first step in the computer-aided diagnosis and process of partitioning an image. Although image segmentation is a well-studied area of image analysis, numerous problems have still in its application to medical images. It can be provided a more accurate anatomical information about the visualized structures. In this paper, liver region is segmented from the abdominal CT liver.

Related Works

Liver segmentation methods are generally divided into two main classes, semi-automatic and fully automatic methods, under each of these two categories, several methods, approaches, related issues and problems will be defined and explained. Many automatic liver segmentation methods have been proposed. They are intensity based approaches: The most common procedure is to apply threshold operators to discard regions with intensity outside the liver range, or to apply multi-model threshold. But the thresholds affect the result directly and hard to determine. Prior knowledge based approaches: The topological, distance and orientation relations are the most common used priori knowledge, used to exclude neighboring organs beside liver. They are always combined with other approaches. Statistical based approaches: A statistical model discrimination of the liver is established from quantities of data sets. And it is used to pre-process the images and obtained liver likelihood images for further process. Nevertheless, the model generation is time consuming and could not respond sensitively among different patients. In this study, the step of the algorithm adaptive morphological operations are performed including largest connected component selection, hole filling and morphological opening. Finally, morphological dilation is used to refine the segmentation results.

Materials and Methods

Image Acquisition

All CT liver images are collected from No (2) Military Hospital (500 Bedded), and Bahosi Hospital, Yangon (Myanmar). These are stored in database of images in JPEG formats and displayed as a gray scale images.

Image Enhancing

A gray scale image is a data matrix whose values represent intensities within some range. MATLAB stores a gray scale image as an individual matrix, with each element of the matrix corresponding to one image pixel. The basic segmentation, binarization is the process of converting a gray scale image to a binary image. Normally, low quality images are not effective and very difficult to measure. Therefore, there is a fundamental need of noise reduction from medical images. In medical image processing many methods are used for noise reduction. Each method can effectively working any one of the noise only not for all types of noises. Noise removal filters can produce the best results depends upon its parameter.

Morphological Operations

The morphological operators are based on set theoretic approach and are suitable for extracting shape information with the help of a structuring element, which may be viewed as a probe. Most elementary binary morphological operations are dilation, erosion and opening. Dilation and erosion are often used in combination for specific image preprocessing applications, such as filling holes or removing small objects. Dilation adds pixels to the boundaries of objects in an image, while erosion removes pixels on object boundaries. The methods of mathematical morphology make possible a large number of very powerful image analysis techniques and therefore morphological operators can be used to develop other image processing techniques. After image binarilization morphological operations were performed to remove the unwanted regions.

Opening

Opening is the process that includes erosion followed by dilation of the resulting image after the erosion process. Opening is defined by the following equation

$$A \circ B = (A \Theta B) \oplus B \text{ -} \tag{1}$$

Opening operators are generally used as filters that remove dots characteristic of pepper noise and to smooth the surface of shapes in images. These operators are generally applied in succession and the number of times they are depends on the structural element size and image structure.

Filling

Filling is used to fill the gaps, holes present in the binary image. Filling is defined by the following equation:

$$f(x,y) = \begin{cases} 1 - I(x,y) \quad if \quad f(x,y) \quad on \quad the \quad border \quad of \quad i \\ \qquad\qquad 0 \quad otherwise \end{cases} \tag{2}$$

This equation is filling operation where I =binary image, f = marker image

Erosion (Reduction)

Erosion is one of the fundamental morphological operators and is a process used to shrink the area of an object in the image. An erosion of A(image) by B(structuring element)is defined by

$$A \Theta B = \{a \mid B_a \subset A\} \tag{3}$$

Dilation (Increase)

Dilation is the complementary process to erosion. It is used to expand the images. If B has a center on the origin, as before, then the dilation of A by B can be understood as the locus of the points covered by B when the center of B moves inside A.

$$A \oplus B = \{a + b \mid a \in A, b \in B\} \tag{4}$$

Image Segmentation Procedure

This section presents two main parts: image enhancing and liver segmentation as shown in Figure1. Firstly, input CT scanned image is acquired by CT scanner and then this original CT image is converted to grayscale. The binarization process is the conversion from the grayscale image to binary image with level 0.4256 which level value is getting better binary images for all test data. The purpose of first part is to remove patient record text from the binary image by binary image filtering method which is to enhance liver portion. The binary image filtering method is used as a kind of cleanup or preprocessing operation to remove small “noise-like” patient record text according to the size of object having smaller objects. The next step of image enhancing is morphological opening process which eliminates some of the foreground bright pixels from the edges of regions of foreground pixels. Since opening process is an erosion followed by a dilation using the same structuring element (SE) for both operations, 5X5 SE whose all elements have one is used in this research. This process is separated the liver and other organs such as stomach, spleen, pancreas, etc. that support to obtain better result in the automatic segmentation process. The second part is the liver segmentation which includes image filtering, hole filling, morphological dilation and image masking. The image filtering process two times in both image enhancing and liver segmentation. The next step is hole filling process detects the boundary of a cell and want to obtain an object which is filled and covers the cell. And then the hole filled image is dilated with same SE of opening process. Actually, this dilated binary image is liver segmented image that is needed to convert grayscale image. Thus, the segmented binary image is processed by image masking which separates the binary liver image from its background, either to cause the liver grayscale image to stand out on its own or to place the grayscale image over another background. The main contributions of automatic liver segmentation has image enhancing with filtering methods and morphological operations such as opening, dilation with same SE whose all elements have value one 5X5 matrix.

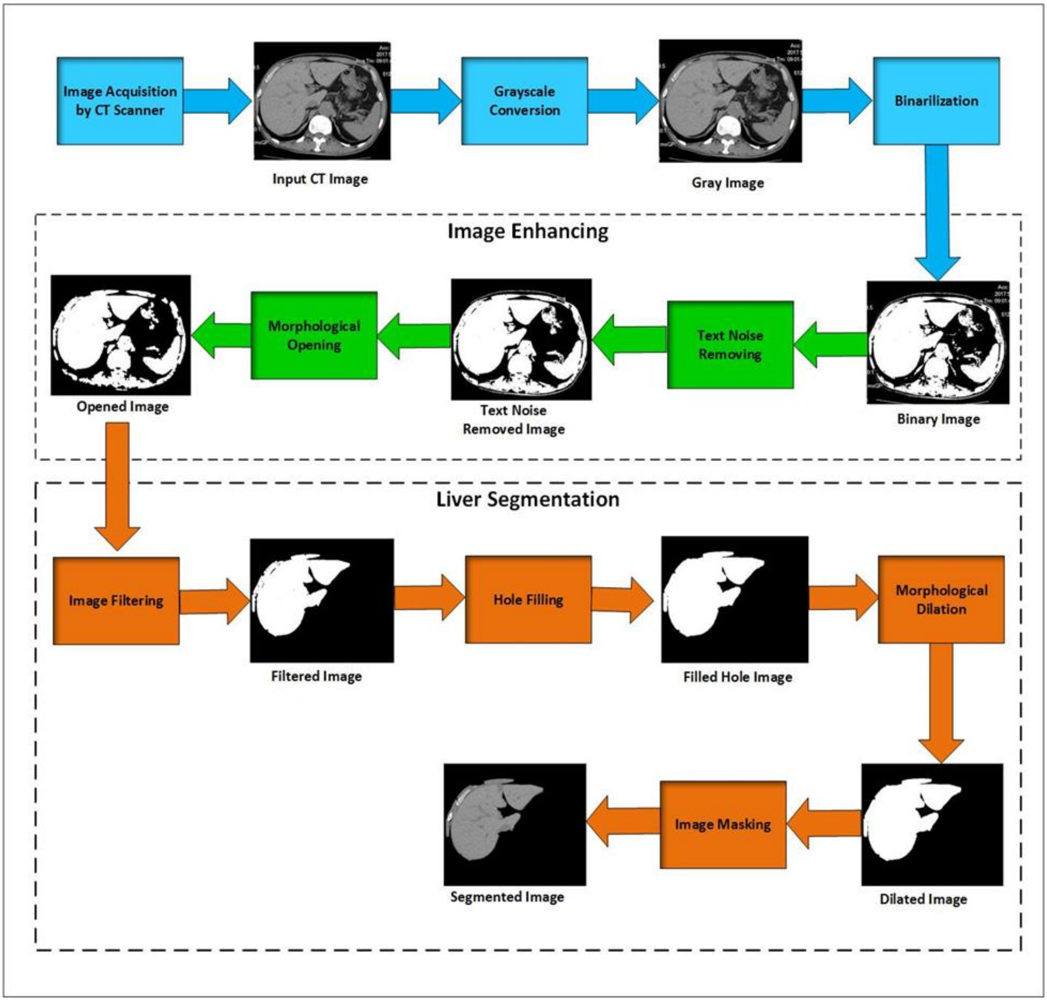

Figure 1: System design for Liver Segmentation

Results and Discussion

The tests of proposed technique are performed with respect to the liver region segmentation accuracy using 51Liver CT images of 30 different patients from the No (2) Military Hospital (500 Bedded), and Bahosi Hospital, Yangon (Myanmar). The images are of size 512×512 pixels. This paper describes the segmentation methods of CT liver images by using MATLAB R2018b. In order to check the accuracy of automated segmented from all liver region images is segmented manually by the radiologist and oncologist. Automatic liver segmentation is difficult because of the wide range of human variations in the shapes of the liver. The intensities of liver and near organs are same. So, the main problem of liver segmentation from CT images is related to low contrast between liver and nearby organs intensities.

Conclusion and Future Work

Medical image segmentation is difficult and challenging problem due to poor, contrast, complex nature of medical images and image segmentation methods. However, fully automatic methods are challenging tasks for several stages of development in a liver medical diagnosis. As good liver surface segmentation is the first important step to liver treatment planning. The results of this work are acceptable. In the future we will develop an algorithm for liver tumor extraction and liver tumor analysis and propose an algorithm for classification for the type of tumor.

Acknowledgement

I would like to express my gratitude to my Supervisor Professor Dr Khin Khin Win, Head of Department of Physics, University of Yangon for her kind permission to carry out this work, then for her supervision, helpful advice and valuable suggestion.

I wish to show my sincere thanks to my Co-supervisor Professor Dr Aye Aye Thant, Department of Physics, University of Yangon, for her discussion and suggestion in this work.

I would like to thank all the people who encourage and support me during the undertaking of this work.

References

M.A.A lagdar, M. E. Morsy and M. M. Elzalabany (2015), "Segmentation of Liver CT Images", Monsoura University, Egypt

N. H. Abdel-massieh, M. M. Hadhoud, K. A. Moustafa (2010), " A Fully Automatic and Efficient Technique for Liver Segmentation from Abdominal CT Images", Menoufia University.

R. C. Gonzalez and R. E. Woods, (2002), "Digital Image Processing*"*,2nd Edi, Upper Saddle River, NJ: Prentice-Hall

S. Senthilraja, Dr. P. Suresh, Dr. M. Suganthi (March-2014),"Noise Reduction in Computed Tomography", International Journal of Scientific & Engineering Research, Vol-5, Issue 3.

V. Thomasson, (2011), "Liver Tumor Segmentation Using Level Sets and Region Growing", Sweden.

J. Myanmar Acad. Arts Sci. 2019 **Vol. XVII. No.2A**

WALKING STICK WITH INTELLIGENT CONTROL SYSTEM

Khin Mar Win[1], Hla Htay Win[2] & Khin Khin Myo[3]

Abstract

Awalking stick with intelligent control system is designed and constructedfor the purpose to help the blind persons. The system is capable of avoiding any obstacle in the way for a blind person. The system operates by combination of the function of hardware and firmware. The hardware of the system consists of the ultrasonic motion sensor HC-SR04module, the light sensor (LDR), the water sensor module and buzzer. The ARDUINO MEGA 2560 development board is used to control all sensors' operationsand gives an output alert for each sensor to the blind person. Besides, the system is contributed by GPS (Global Positioning System) and GSM (Global System for Mobile communication). The control program is written in C programming language. Furthermore, someone can find out the position of that walking stick because of the GPS and GSM facility.

Keywords: ARDUINO MEGA 2560, ultrasonic motion sensor, water sensor, GPS, GSM, C programming language, blind person

Introduction

According to the World Health Organization (WHO) statistics, around 30 billion people are blind on the earth [Aras, (2012)]. This research proposes to design and develop a portable unit (stick) for the blind person for easy usage and navigation in public places. Blind stick is an innovative stick designed for visually disabled people for improved navigation. The generally available blind walking sticks are capable of finding obstacle that touches the stick physically. It is helpful to a blind person that allows sensing objects before stick touches them. A smart stick includes GPS tracking feature which will have SD memory card which used to store different locations and to find lost person along with other useful features [Gaurav, (2017)].

The constructed system proposed an advanced blind stick that allows visually challenged people to navigate with ease by using advanced technology. It uses ARDUINO MEGA 2560 based circuit to handle the entire system functioning. The system uses an ultrasonic sensor to sense and detect

---

[1] Dr, Lecturer, Department of Physics, Meiktila University

[2] Dr, Lecturer, Department of Physics, University of Yangon

[3] MRes Student, Department of Physics, University of Yangon

obstacles/objects that ahead using ultrasonic waves within certain range of the person. On sensing obstacles, the sensor passes data to the ARDUINO. The ARDUINO then processes this data and calculates if the obstacle is close enough. If the obstacle is not close to sensing stick, the sensor circuit will not give any response. If the obstacle is close to the sensing stick, the ARDUINO sends a signal to sound a buzzer.

Also, the system uses a shorting system to detect and check if there is water in front of the sensing stick. As soon as the water sensor is wet, that system signals the blind person by a beep pattern. Besides, the system also has a light sensing feature to give the blind person a sense of light. It signals the person if there is light or darkness so that he/she can know if it is night or would enter a very dark room/facility. In addition to the system has one more advanced feature integrated to help the blind person if they forget where they kept the blind stick. If the person looses the stick they can use the GPS system by calling the mobile phone and when the user called the mobile which will send the location of the stick. This system will send the message which can see the location of it at the Google map link thus the blind person able to find the lost stick. Thus, this system allows for obstacle detection as well as finding stick if misplaced by visually disabled person. The block diagram of the constructed system with GPS and GSM are shown in Figure (1).

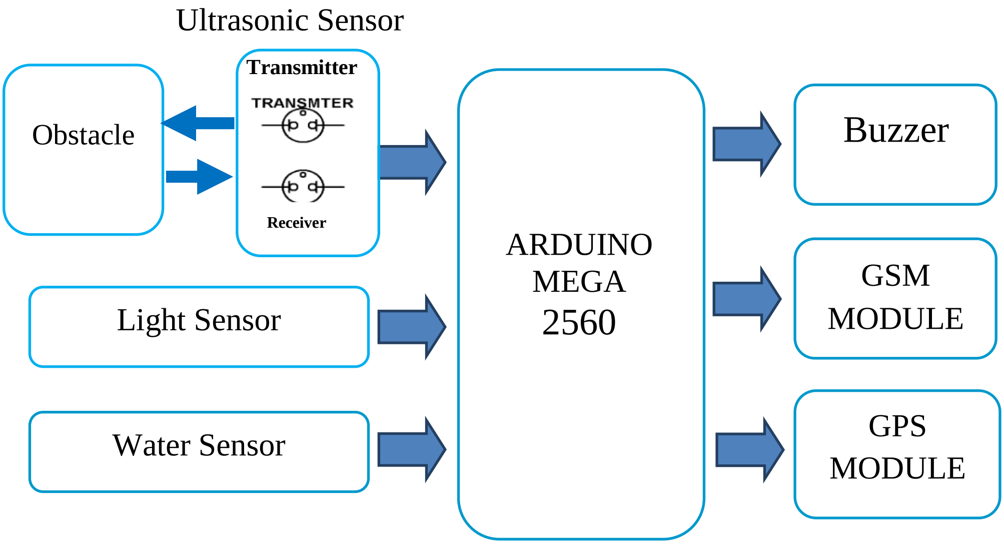

Figure 1: The block diagram of walking stick with intelligent control system

Methodology of the System

Design and Construction of the System

This circuit is based on ARDUINO MEGA 2560 which is quite compact and it is connected with the ultrasonic sensor, water sensor, GSM module and GPS module. The main objective is to help visually challenged people to navigate with ease using advance technology. In this constructed system, the circuit construction can be divided into two parts, the circuit work and programming. The circuit work is completed by fitting the components on the self-designed printed circuit board. The program is written in C programming language. The photograph of the ultrasonic sensor, water sensor, GSM module and GPS module are shown in Figure (2-4).

Circuit Design and Connection between ARDUINO and Sensor Units

The circuit is designed by computer aided software on the personal computer (PC). In this circuit diagram, the two analog pins of ARDUINO are used as input of two sensors and the digital pins of ARDUINO as output and input. The trigger (TX) pin of ultrasonic sensor is connected with digital output pin of ARDUINO (pin 10) and echo (RX) pin of sensor is joined with digital pin of ARDUINO (pin 11). A 5V pin of it is communicated with Vcc pin of sensor and GND pin is connected to GND pin of sensor. In this circuit, abuzzer is used as output for all sensors and an LED is used to indicate for farthest distance for motion sensor. The two resistors 330Ω are connected between each of LED, buzzer pin and GND pin of ARDUINO. The output pins of sensor are joined to digital output pin 12, 13 of ARDUINO. This sensor has the distance limitation, if the obstacle distance is less than 6cm the buzzer is ON state and during this condition the LED is OFF state. If the distance between sensor and obstacle is greater than 6cm the LED is ON state at this time the buzzer is OFF state.

The light sensor has two connectors; the first one is connected to 5V pin of ARDUINO. And then the analog input (pin A0) pin of ARDUINO is joined between the other pin of LDR and the resistor 330Ω. The digital (pin 7) of ARDUINO is used as output for sensor and it is connected with LED and resistor. The other remain side of each resistor are joined to GND. The GSM module is used for this sensor to send message to the user form stick. The five pins of GSM module are used for output which is TXD, RXD, GND, VCC and GND. When the GSM module is interfacing with ARDUINO, the transmit pins (RXD) and the receive pins (TXD) of GSM module and ARDUINO can be connected with each other in reverse manners. Because of the data of ARDUINIO transmit to GSM module and similarly transmitted data from GSM transmit pin (TXD) go to receive pin (RXD) receive pin of ARDUINO. This is a wired communication to send data from one device to another. There are many methods of wired communication but ARDUINO and GSM interfaced through two wire serial communication.

Serial communication means to send data bit by bit. There is one important to consider while using serial communication that is baud rate. Baud rate is the number of bits transfer per second from one device to another. So, the baud rate should check compatibility between two devices. Usually SIM900A GSM module support 9600 baud rates with Universal Asynchronous receiver and transmitter (UART) type serial communication. That is why the pin 9 and 8 of ARDUINO is defined as serial RXD receive and TXD transmit pins. The 5V power is applied to GSM's Vcc and ground pin of GSM module is joined to ground pin of ARDUINO. The next GND pin of GSM module is connected with GND pin of ARDUINO.

The operation of the sensor is if the dark shadow falls onto the Light Dependent Resistor (LDR) sensor, the indicator buzzer produces sound and after a few seconds a message ("Could you take me, it is so dark:") sends to the person at home. At the day time the LDR sensor does not show any sense. The objective of setting up the LDR sensor unit is to know day and night for the blind person especially for the night and this sensor help them to escape from the dangerous condition at night. In this sensor include four connectors which are analog (A_0), digital (D_0), GND and Vcc. Vcc pin is connected to the 5V power supply, GND pin is connected to the GND of ARDUINO, D0 pin is connected to a digital pin 6 and the A0 pin is connected to the analog output pin A1 of ARDUINO. The number of pin will base on the actual program code. After hardware connection, the control sketch is uploaded into the ARDUINO MEGA 2560 microcontroller by ARDUINO IDE. Using a USB cable, connect the ports from the ARDUINO MEGA 2560 to the computer and upload the program.

The GPS module has five connectors among them is used four pins for output. The RX pin and TX pin of module are connected with RX pin and TX pin of ARDUINO directly. The Vcc and GND pins are joined with ARDUINO. The PSS pin of GPS module is not used. The simulation of the circuit diagram on Trax Maker is shown in Figure (5). The circuit track lines of the both soldering side and components side of the stick is shown in Figure (6).

The buzzer is used as output in that sensor and the buzzer output is communicated to the digital output pin 5 of ARDUINO. If the water sensor gets wet, the buzzer is alarmed by a beep pattern and brush off the water on the sensor, the buzzer is not shown any more and it is restored to the initial state.

Etching PCB for Circuit Construction

The circuit is designed by using Trax Maker software to obtain a smart and efficient circuit work. Then it is printed on the paper and copied the printed circuit track-lines of carbon powders to the copper side of the circuit board by ironing. The ironing process last for 2 to 3 minutes until the printed paper firmly sticks to the copper side of the board. Then the board is immediately immersed in the water to remove the soaked papers.

After slowly and carefully removing the paper, the carbon track-lines of circuit lines are appeared on the board. Then the board is etched with a solution of ferric chloride which is the copper etching chemical. Slowly shaking in the ferric chloride solution removes the unwanted paper parts of the circuit board and obtains required circuit track-lines. This process took about 20 to 30 minutes, according to the concentration of the solution and the etching area of the circuit board. The larger the area of the board, the longer etching times it is taken.

After receiving the circuit track-lines, drill holes are made for component insertion. After drilling is finished, the board is washed with thinner for the carbon track-lines to obtain shiny copper track-lines. But the copper track-lines have to be cover with a petroleum based coating (polish) for protection of being copper-oxide. After finishing the circuit design work, the circuit is simulated several times until getting the optimum condition. This optimum circuit design is drove on the printed circuit board PCB and the circuit components is mounted at their places on this PCB. After soldering the circuit on the printed circuit board, check on soldering points for short circuit and orientation of the components. If everything is correct, the circuit is ready for test. The components side and soldering side of the printed circuit board is shown in Figure (7).

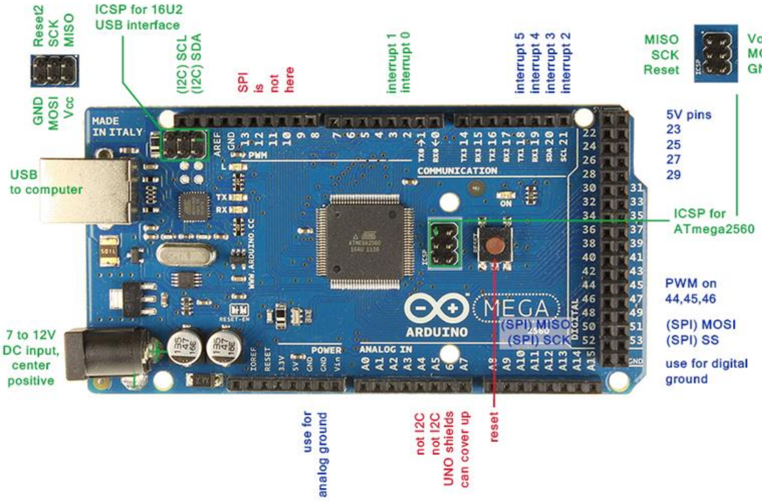

Figure 2: The pin configurations of ARDUINO MEGA 2560

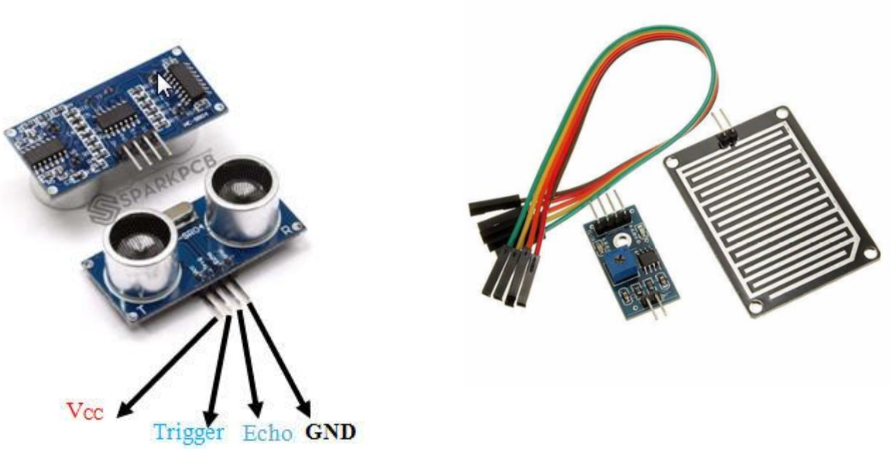

Figure 3: The photograph of Ultrasonic sensor and water sensor

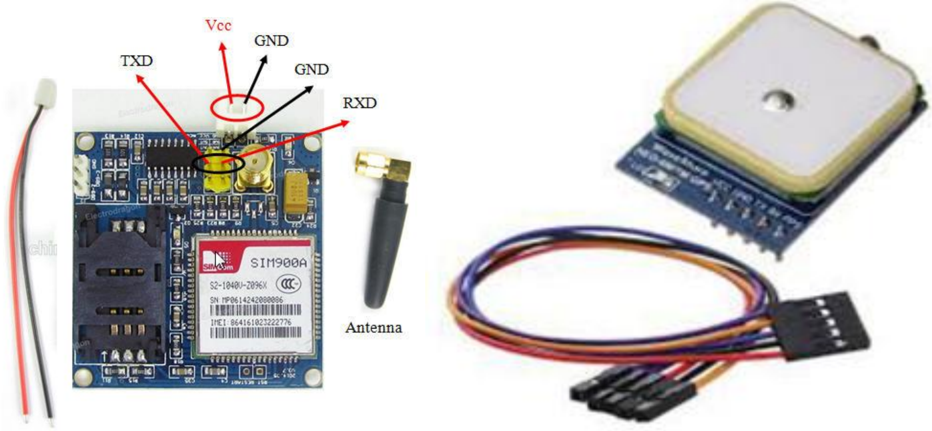

Figure 4: The photograph of GSM module and GPS module

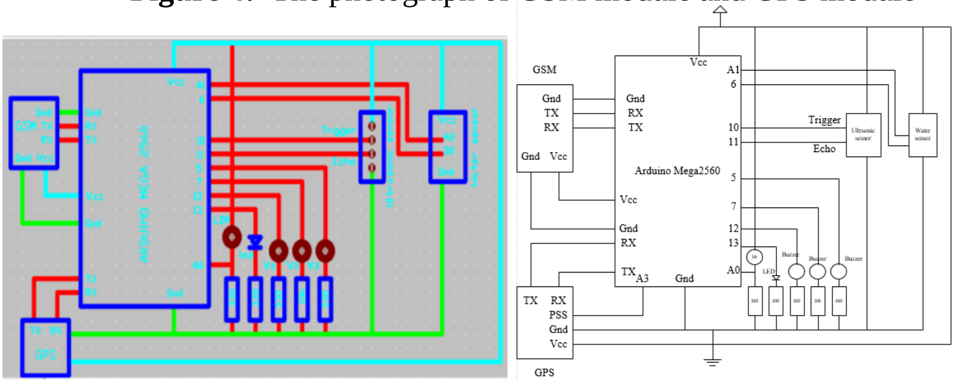

Figure 5: The simulation of the circuit on TraxMaker and complete circuit diagram of the whole system

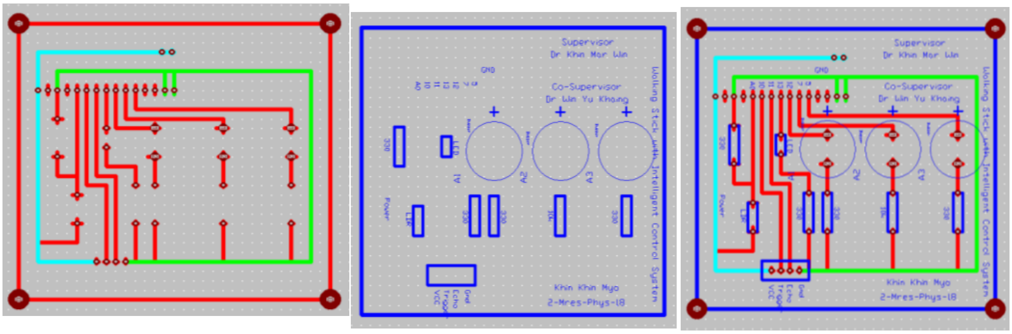

Figure 6: The circuit track line diagram of the blind stick in solder side, components side and both solder and components side

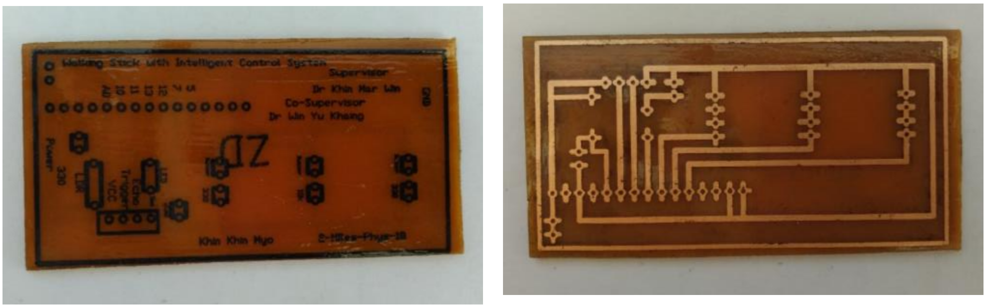

Figure 7: The components side and soldering side of the circuit board

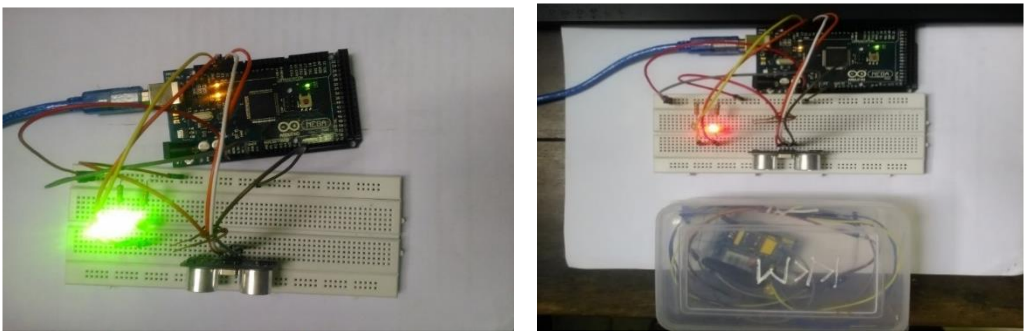

(a) (b)

Figure 8: The photograph of the motion sensor testing condition (a) for obstacle distance greater than 6 cm (b) for obstacle distance less than 6 cm

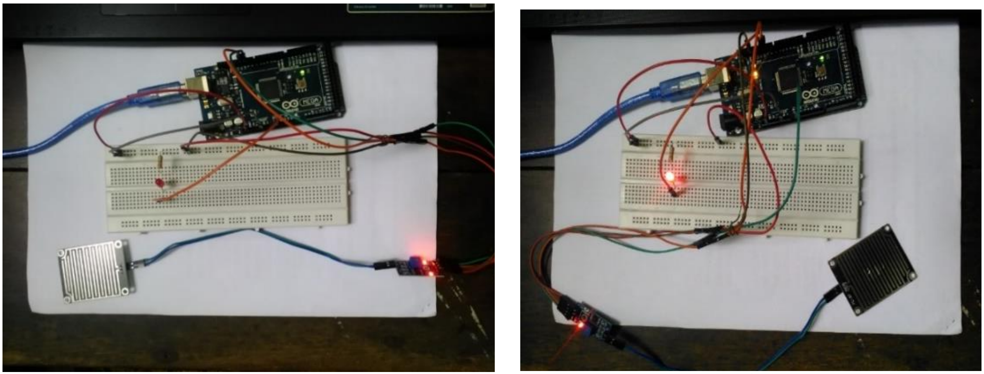

(a) (b)

Figure 9: The photograph of the circuit operation of water sensor (a) testing for the dry sensor and (b)testing for the water present on the sensor

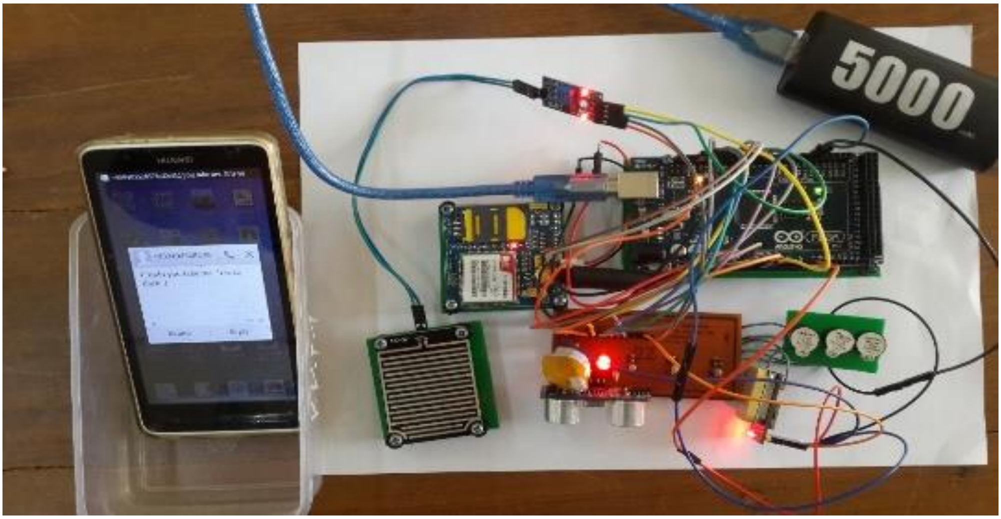

Figure 10: The photograph of the intelligent control system for walking stick

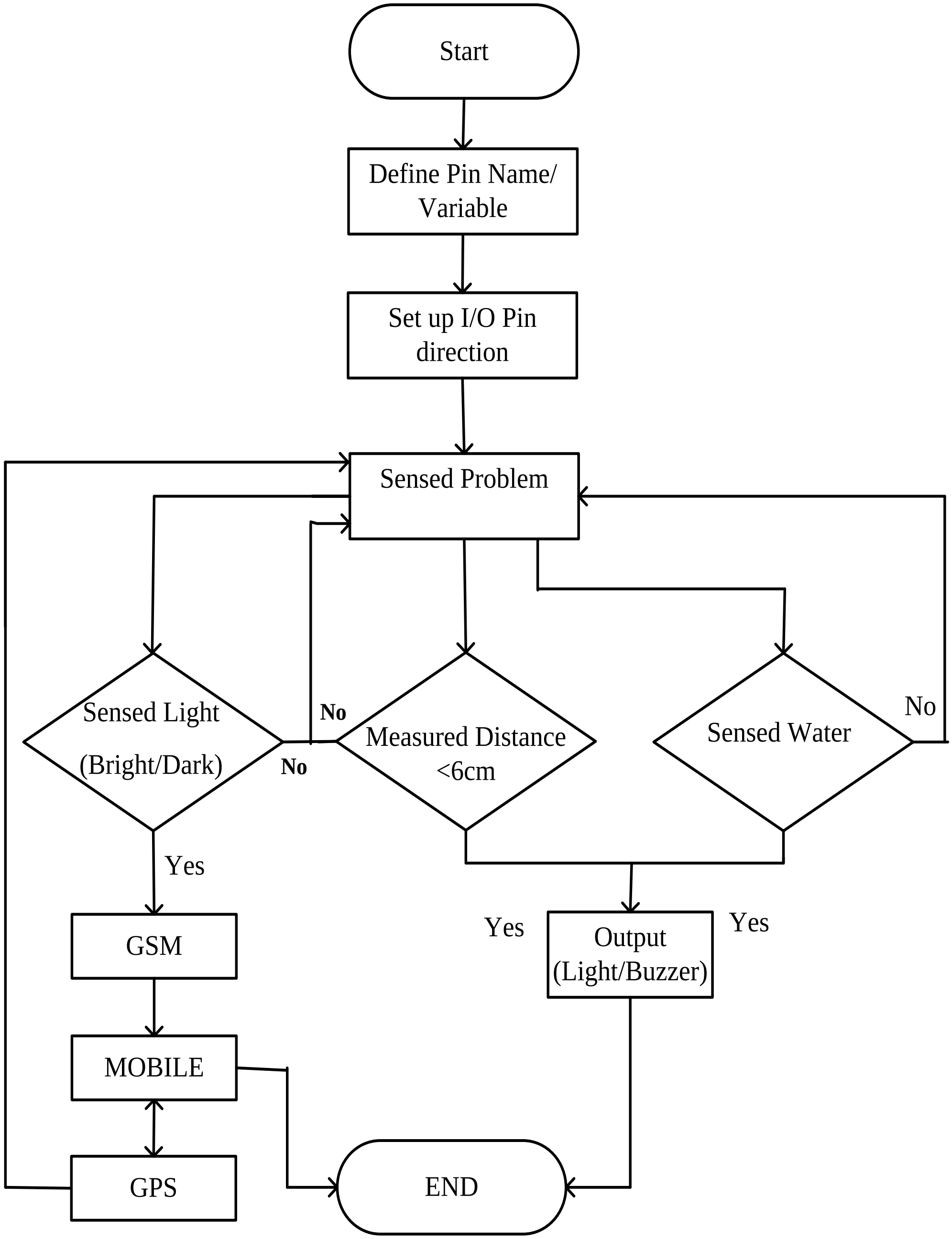

Figure 11: The flow diagram of the walking stick with intelligent control system

Discussion and Conclusion

Discussion

This research work gives the design of intelligent stick for blind person to detect any kind of obstacle by holding the stick. The stick is the most widely used travel aid for blind persons but it is not suitable for detecting potentially dangerous obstacles. The blind person can hear the sounds such as car horns but they cannot see any obstacles, which can be really dangerous. So, there is a great dependency for any type of movement or walking within area or out of the particular area, they use only their natural senses such as touch or sound for identification or walking. This walking stick for blind people has multiple sensors, with the help of which it has been possible to enhance more features to the walking stick.

Conclusion

Also, this research will aim to develop emergency trigger alert system along with design. It has an added functionality of GPS and GSM module that will enable immediate provision of help to the person in case of an emergency. The advantages of the system are the user can take easily everywhere, the system can be used both indoor and outdoor navigation. Blind person’s location can be tracked whenever needed which will ensure additional safety. Detects obstacles and alerts the blind person through sound alert. The blind person holding the stick will able to move from one place to another without others help. It would become a sufficient in future for all places with demonstrated success among the public to help blind person. The objective is to provide an aid to visually impair which will assist them everywhere they go.

Acknowledgement

The authors would like to acknowledge Professor Dr Khin Khin Win, Head of Department of Physics, University of Yangon, for her kind permission to carry out this work.

References

Aras M. S. M., Jamri M. S., Kassim A. M., Rashid M. Z. A., Yaacob M. R. *Design and development of obstacle detection and warning device for above abdomen level*, Proceedings of 12th International Conference on Control, Automation and Systems (ICCAS), 2012, pp. 410-13.

Bousbia-Salah M., A. Larbi, and M. Bedda, *An approach for the measurement of distance travelled by blind and visually impaired people,* 10th IEEE International Conference on Electronics, Circuits and Systems, Sharjah, United Arab Emiratses, pp. 1312-1315, 2003.

Dambhara, S. & Sakhara, A., 2011. *Smart stick for Blind*: *Obstacle Detection, Artificial vision and Real-time assistance via GPS*. International Journal of Computer Application (IJCA).

Deepika S., Divya B. E., Harshitha K., Komala B.K., & Shruthi P. C., Ambedkar, International Journal of Advance Electrical and Electronics Engineering (IJAEEE), ISSN (Print): 2278-8948, Volume-5 Issue-6 2016.

Gaurav S., Parminder K., Komal M., Hitesh V., *An Intelligent sensor based stick for Blind and Deaf*. Australian Journal of Basic and Applied Sciences, 11(8) Special 2017, Pages: 34-38.

Nusrat, S. A., 2010. *Send and Read SMS through a GSM Modem using AT Commands*. Retrieved August 5, 2017. www.codeproject.com/Articles/38705/Send-and-Read-SMS-through-a-GSM-Modem-using-AT-Com.

J. Myanmar Acad. Arts Sci. 2019 **Vol. XVII. No.2A**

GSM BASED AUTOMATIC GREENHOUSE CONTROLLED SYSTEM

Pyae Phyo Thwe[1], Hla Htay Win[2], Sandar Oo[3], Hnin Yu Wai[4]

Abstract

A scaled-down prototype of the GSM based Automatic Greenhouse Controlled system using Auduino board was build and tested. The automated greenhouse control system achieves monitoring and control of a greenhouse environment by using sensors and actuators which are under the control of a microcontroller. The codes for the controller were written in the Arduino programming language, debugged, complied and burnt into the microcontroller using the Arduino integrated development environment (IDE). The microcontroller ensures that the microclimatic parameters stay within pre-defined values as determined and set by the user. The climatic conditions of the greenhouse and state of actuators are transmitted to the remote monitoring station via a GSM (MODEM).

Keywords : GSM, IDE, Arduino board

Introduction

Myanmar is a country where the economy is dependent on agricultural produce. Myanmar weather conditions are characterized by having predominantly long rainy season, hot summers, and mild winters. Such climatic conditions put a great strain on the types of crops that could be successfully grown. A greenhouse is an exceptionally outlined homestead structure building to give a more controllable environment to better harvest generation, crop security, product seeding and transplanting.

The greenhouse automatic control system will fully automate the management of a greenhouse using the latest pervasive systems and technology. The proposed system controls and monitors light intensity, soil and air humidity using a controller and GSM modules. A temperature and humidity sensor, soil moisture sensor, gas sensor and light sensor which are automatically controlled are used in this project. The concern with a lot of consumer needs and demand for the agriculture products has stimulated

---

[1.] MRes Candidate, Department of Physics, University of Yangon

[2.] Dr, Lecturer, Department of Physics, University of Yangon

[3,4]Dr, Assistant Lecturer, Department of Physics, University of Yangon

awareness among the farmer that increases their products in the market by implementing advance technologies in this industry.

This project uses sensors and Global System for Mobile Communication (GSM) and short message service (SMS) to carry out data from the greenhouse with sensors directly alert the farmers to their mobile phone. Therefore, this makes controlling plants easier by directly sending alert notification messages to farmers using GSM and SMS technology. So, this project aims to design a smart greenhouse model controlled automatically by a GSM phone. Parameters like humidity, temperature, soil, gas in air and lightning will be controlled by microcontroller. Each of these parameters is measured by a sensor that is set at a specific range, if this sensor signals any change in that range, the system will take the appropriate action required, and the system sends a daily report to the user by SMS.

Figure 1 denotes that the main system identified the hazardous condition then GSM modem activated and send the message to another modem which is connected to computer system and computer system store the lots of SMS received and send and new SMS send to first GSM and after receiving SMS, main unit can starting the operation on greenhouse system.

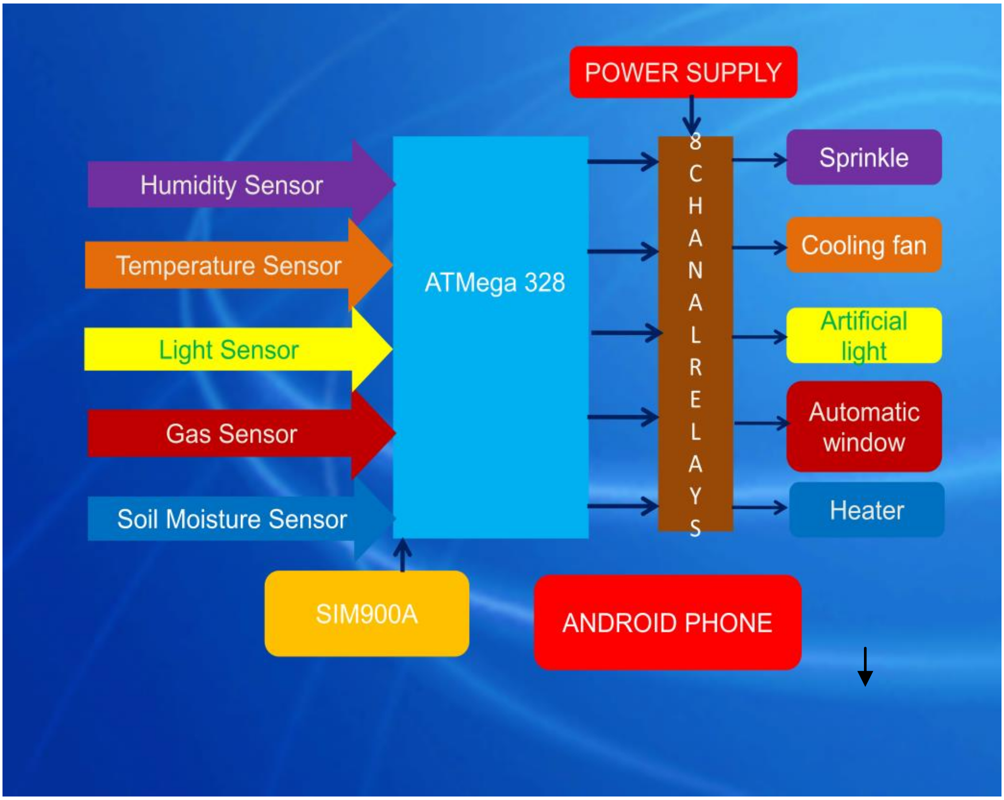

Figure 1: Block Diagram of Greenhouse

Construction of Circuit

This system below measures the values of temperature, humidity, light, and soil moistures in the greenhouse by sensors and sends the data that was measured to the ARDUINO The ARDUINO processes the data and controls the water heater, cooling fan, motor and light to maintain suitable conditions in the greenhouse.

If the values of temperature and humidity are greater than optimum, it opens the cooling fan to decrease the temperature and humidity in the greenhouse.

If the value of soil moisture is less than optimum, the value opens motor and sprinkle water pipe when it is greater, irrigation will be closed.

If the toxic gas has in greenhouse, the absorbed fan absorbs the unpleasant gas from this house and also the roof opens and ventilates the fresh air.

If value of light is less than the optimum, the artificial light turns on and closes after the period is finished and when the value is grater the lamp will be turned off. The GSM model sends SMS to the user about the value that system measures.

Circuit Explanation

This system consists of four inputs (temperature, humidity, soil sensor, gas sensor and LDR sensor) and six outputs (cooling fan, sprinkle fan, heater, and artificial light, automatic window) and PIC controller is as a main brain for this system because it controls the overall system in a greenhouse. Temperature sensor used to detect the temperature in a greenhouse. When the temperature sensor detects the high temperature, microcontroller will send the signal to the fan to stable the greenhouse condition. Then, when LDR sensor detects no light, microcontroller will be send the signal to the lamp and lamp will be on automatically. Water pump is used to supply water to the sprinkler and make sure the sprinkler watered the plants in a greenhouse. And also, gas sensor detects how many toxic in this room and then sends the data to the microcontroller. Absorbed fan and door system are used to absorb and waste the unwanted toxic air to the outside.

This ARDUINO controls circuit that will be connected to the soil sensor, humidity sensor, and temperature sensor. The ARDUINO UNO receives the value from sensor and analyses and then compares it with the threshold value stored in the ARDUINO memory, based on this value the ARDUINO takes the appropriate procedures, and also controls the output device based on these values; the ARDUINO sends the report by the GSM model to the owner’s phone. The flowchart diagram of the circuit is shown in Figure 2.

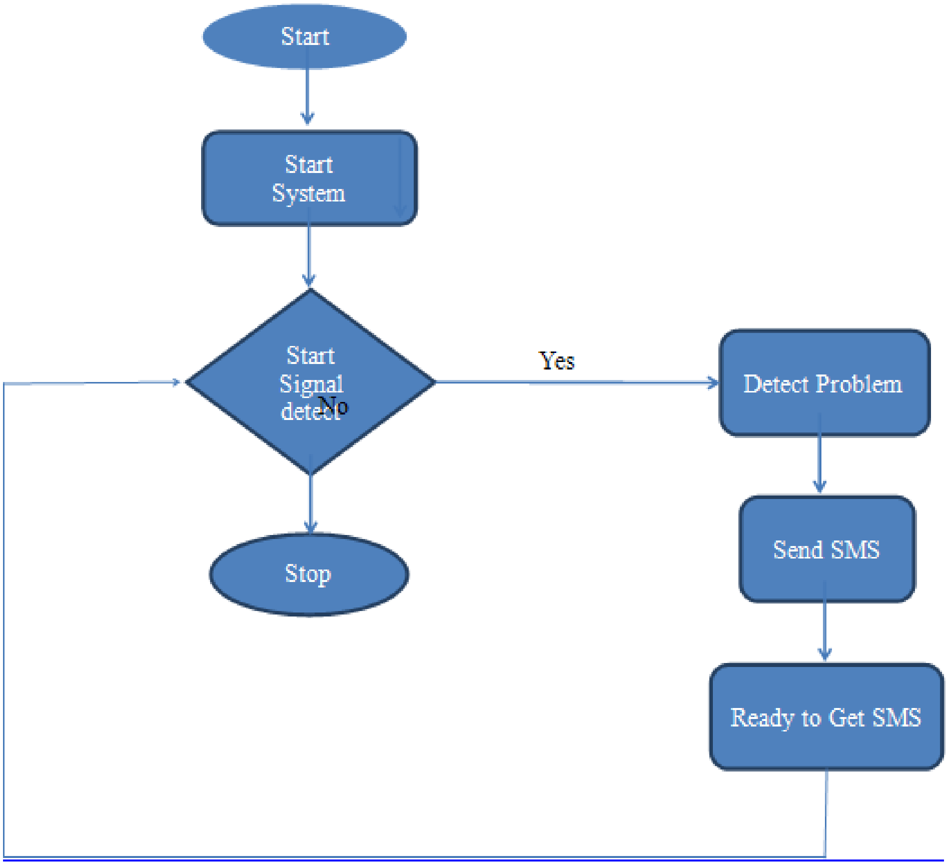

Figure 2: Flowchart diagram of Greenhouse Effects

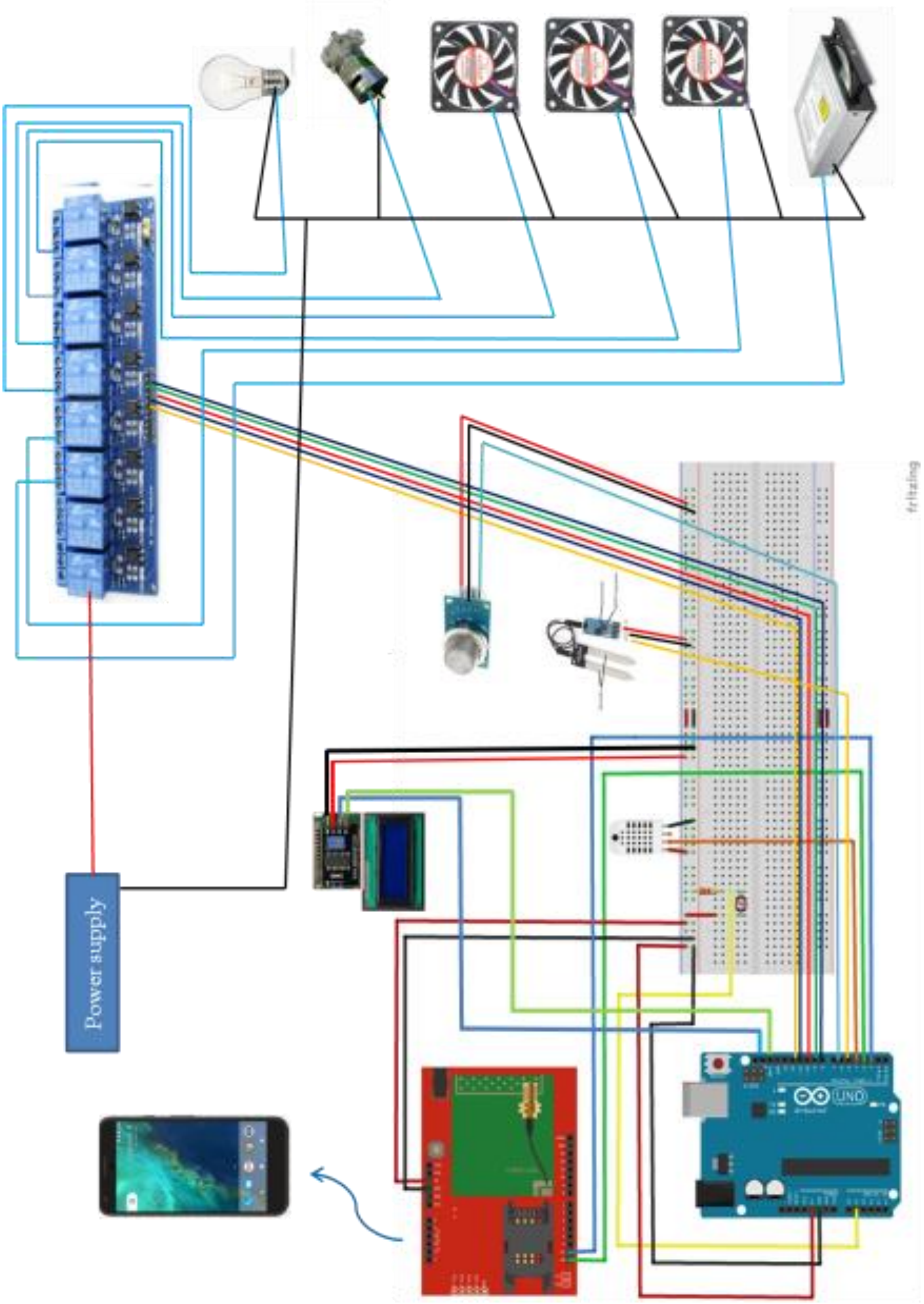
Power supply
fritzing
UNO

Figure 3: The whole system by using ARDUINO with GSM

Results and Discussion

Greenhouses controlling the temperature, humidity, light, water and that allow growing vegetables year round. It saves money, time, and effort.

It can provide a better environment to the plant to prevent it from damage and to increase its productivity. Some plants require a longer period of lighting than other plants; the smart greenhouse will provide the right amount of lighting. It can automatically control the amount of water needed for each plant. The photos of the Green house are shown in Figure 3 to Figure 7.

Advantages

- Increase fertility.
- Better productivity.
- Increase in quality of crop.
- Percentage of germination of seeds is high in green house

Disadvantages

- The tools are dealing with are very sensible, they need to be carefully and so the project may be a bit costly.
- Failure to supply the essential factors for optimum growth such as light, moisture, carbon dioxide and heat in amounts necessary for each individual crop and this problem faces greenhouses in general.
- Complete automation in terms of pest and insect detection and eradication cannot be achieved.
- Requires uninterrupted power supply.

Low Soil Moisture detected. Motor turned ON

Low Soil Moisture detected. Motor turned ON

Soil Moisture is Normal. Motor turned OFF

LIGHT LEVEL : 0%
VERY DARK
Lamp ON

Figure 4 : Photograph of front side of Greenhouse

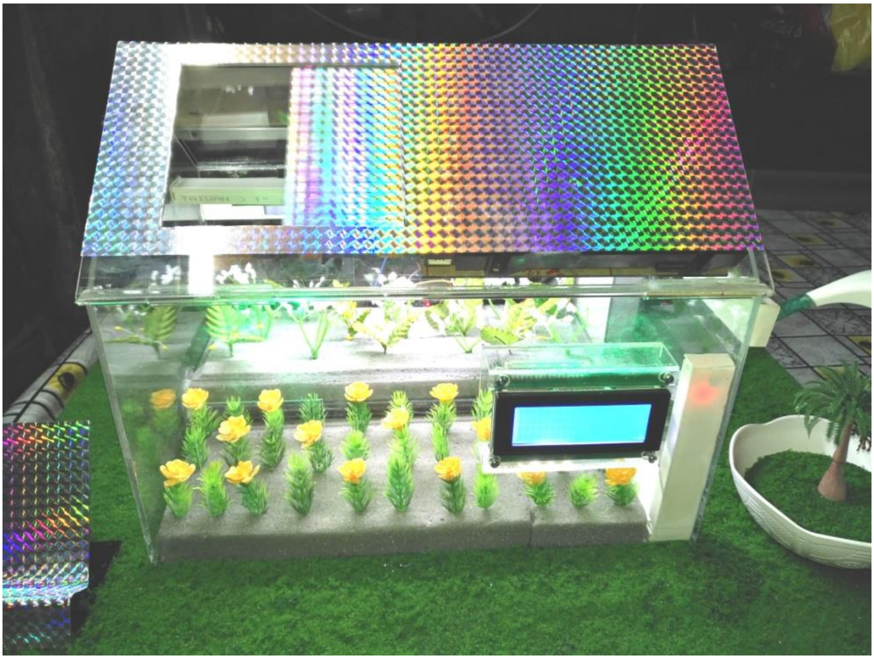

Figure 5: Photograph of Ventilated Door System of Greenhouse

Figure 6: Photograph of back side of Greenhouse

Figure 7: Photograph of Right Side of Greenhouse

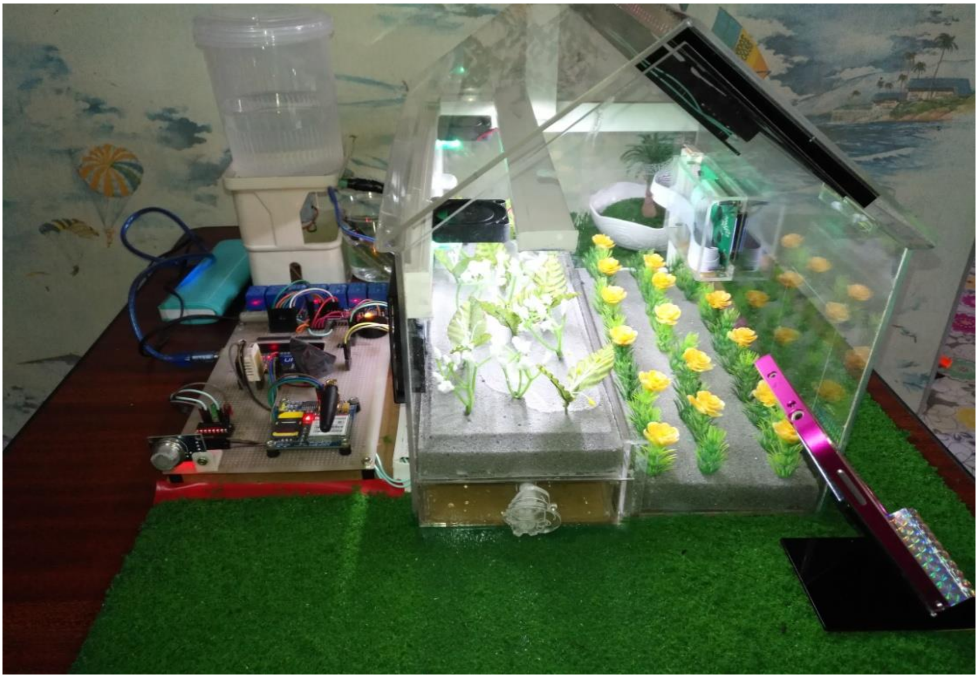

Figure 8: Photograph of Left Side of Greenhouse

Conclusion

This research offers a design of fully automated greenhouse management system. From the experiment it could be seen that it is fulfilling all requirements related greenhouse monitoring. The automatic greenhouse sensor design could help in increasing the productivity of plants.

As it has been mentioned earlier, not only providing automatic control over the devices like light, motor pump but also mechanism to alert owner regarding the parameter changes in the greenhouse so that early precaution steps can be taken. Thus this construction, productivity of cropping can be continuously increased so it can handle famine problem around the world. The greenhouse monitoring system using GSM is far better than the same system using the different technologies.

Future Work

This system can work more efficiently with present technology and may improve the existing technology in the field of wireless communication and with the wide improvement of GSM technology which can improve Short Message Service with the help of embedded technology anything may become possible and easy.

Acknowledgements

I would like to thank Professor Dr Khin Khin Win, Head of Department of Physics, University of Yangon for her encouragement to do this work.

I would like to express sincere thanks to Dr Aye Aye Thant, Professor, Department of Physics, University of Yangon, for her useful advice in the preparation of this research.

References

Banzi, M. (2009). Getting Started with Arduino, O'Reilly media Inc, 2nd Edition, California.

Duxiaoming, C. Y. (2009). "The realization of greenhouse controlling system based on wireless sensor network [j]," *journal of agricultural mechanization research*, 6, 141-144.

Chaudhary, D., Nayse, S., & Waghmare L. (2011). "Application of wireless sensor networks for greenhouse parameter control in precision agriculture," *international journal of wireless & mobile networks (ijwmn)* , 3, 140-149.

Quanminh, V. (2011). "*Automated Wireless Greenhouse Management System*", Master of Engineering in Electronics and Computer Systems, Massy University Press, Palmerston North, New Zealand.

Longmont, D. (2008). Gsm/gprs module. Linksprite technolgies, Gsm characteristics. Retrieved from the gsm server online website: http://gsmserver.com/articles/gsm charact.php

Prachi, K. & **B**halerao, V. (2009). Gsm based security system for examination paper. *International journal for engineering applicationsand technology*, 4, 62-65.

Mahmoud, S. & Ala'a, I. (2013). Greenhouse micro-climate monitoring system based on wireless sensor network with smart irrigation. *communication engineering*, 7(12),1072-1077.

Okunola. A. I. (2013). Glasshouse production of vegetable and ornamentals for agricultural production in nigeria. *World science research journals*, 1(3): 113-119.

J. Myanmar Acad. Arts Sci. 2019 **Vol. XVII. No.2A**

TO STUDY THE ROLE OF STRUCTURAL AND ELECTRICAL PROPERTIES OF ZnO/Cu_2O/ITO CORE-SHELL NANOSTRUCTURE SOLAR CELLS

Saw Shine Ko[1], Thida Win[2], Than Than Win[3] and Yin Maung Maung[4]

Abstract

In this work, Zinc Oxide Core layer films and Cu_2O Shell layers were synthesized by using both Chemical Bath Deposition techniques and Spin Coating Method. X-ray diffraction techniques were used to examine the lattice distortion, dislocation density and position parameters of deposited Core-Shell layers upon Indium Tin Oxide glass substrates. Scanning Electron Microscopy (SEM) study provides morphological of the sample surfaces. The photovoltaic properties of these Core-Shell nanostructure solar cells were investigated by current density-voltage characteristic. The power conversion efficiency (PCE) was influenced by the open-circuit voltage.

Keywords: X-ray diffraction, Scanning Electron Microscopy, Power conversion efficiency, Fill factor

Introduction

Core-Shell Nanostructure Solar Cells

In recent years, the optical properties of metallic Core-Shell nanostructure have received particular attention, since, the Core-Shell nanostructures can obtain many unique properties via the combination of different materials (Muehling O et al., 2009). The development of Core-Shell structured materials on a nanometer scale has been receiving extensive attention (Lee H B, 2006).

The shell can alter the charge, functionality and reactivity of the surface, or improve the stability and dispersive ability of the core material (Jing Z et al, 2003).

It is also believed that optical, catalytic or magnetic functions can be imparted to the core particles by the shell material. In general, the synthesis of core/shell structured thin films has the advantage of obtaining a new composite material having synergetic or complementary characteristics of the

---

[1,] Dr, Assistant Lecturer, Physics Department , University of Yangon

[2.] Physics Department, Mandalay University of Distance Education

[3.] Physics Department, University of Yangon composites. Many studies on the synthesis of composites i.e. TiO_2 (Bala H et al, 2007), $\gamma\, Fe_2\, O_3$ (Chou K. S. et al., 2007) and Ag coated with SiO_2 have been reported. The direct band gap increases with increasing in temperature. Annealing at higher temperature decreases the resistivity of Core-Shell structure (Agbo P.E et al., 2011). The study of semiconductor core-shell nanoparticles (NPs) has attracted increasing scientific and technological interest due to the ability to fine-tune their properties, (Caruso R A et al., 2001;Caruso F et al., 2001;Jiang Z et al., 2003;Sertchook H et al., 2003), the most extensive synthesis were focused on type-I core-shell NPs (Mokari T et al., 2003;Protiere M et al., 2007), in which a wide band gap material is coated onto the core of a narrow band gap material. There have been relatively rare reports concerning the preparation of reverse type I core-shell NPs(Zhong X et al., 2005) in which a narrow band gap material is over grown on the core of a wide band gap material and unique characteristic must be observed. Indium tin oxide, widely used in solar cells and optoelectronic devices,(Liu Q et al., 2005) is a direct wide band gap and photostable (Sirimanne P M et al., 2000) material (~3.6 eV) (Levi S A et al., 2001;Kim W T et al., 1986). A type II core-shell that facilitates charge separation, a key step for the formation of the photocurrent, and the large band gap semiconductors (e.g., ZnO and ZnSe), which on their own neither of can be an efficient light absorber, by working together they can absorb a much broad spectrum of light as through the type II core-shell has a much lower band gap than any of the components. Therefore, an array of type II core-shell nanowires in particular, can make an efficient solar cell (Zhang Y et al., 2007).

Experimental procedure

Preparation of ITO/ZnO/Cu_2O core-shell thin film

For the preparation of Cu_2O shell layer deposited onto Zinc oxide core layer, Cuprous oxide and 2-methoxyethanol were chosen as the starting materials. 50g of Cu_2O powder were weighted by digital balance. To reduce the particle size, Cu_2O powder was ground by an agate motor for 5hours. After that, Cu_2O fine powder was applied by ball milling method. The milling interval was set for 6 hours. Sample was milled in a grinding bowl (volume of 50g) and grinding ball (20 balls, 5mm diameter dimension) at 250 rpm in ambient temperature. To get the uniform and lightest particles, all mesh-sieves are cleaned and assembled them in the ascending order of sieve number (100mesh sieve, 250 mesh sieve and 400 mesh sieve) and sieving with 3 times. After 30 min, it was carefully weight of last sieve with its retained powder. Cuprous oxide Shell layer thin films were prepared by the sol-gel spin coating method. First, the copper precursor solution was prepared using Cu_2O powder, 2-methoxyethanol as the solute, solvent and solution stabilizer respectively. Cuprous oxide (3.5g) was first added in amount of 3ml 2-methoxyethanol solution. After 30 min of stirring with 300 rpm at room temperature the hot plate temperature was ramped up to 60℃ to 80℃ ranges to obtain a homogenous solution. After the process for preparation sol-solution, all the Cu_2O paste were coated onto the ITO/ZnO substrates at a speed of 3000 rpm 30s and at the end of above process coated films were annealed at 150 ℃ for 3h placed on the hot plate and provided each of them and finally provided post annealing temperature 300℃ and 400 ℃ at muffle furnaces.

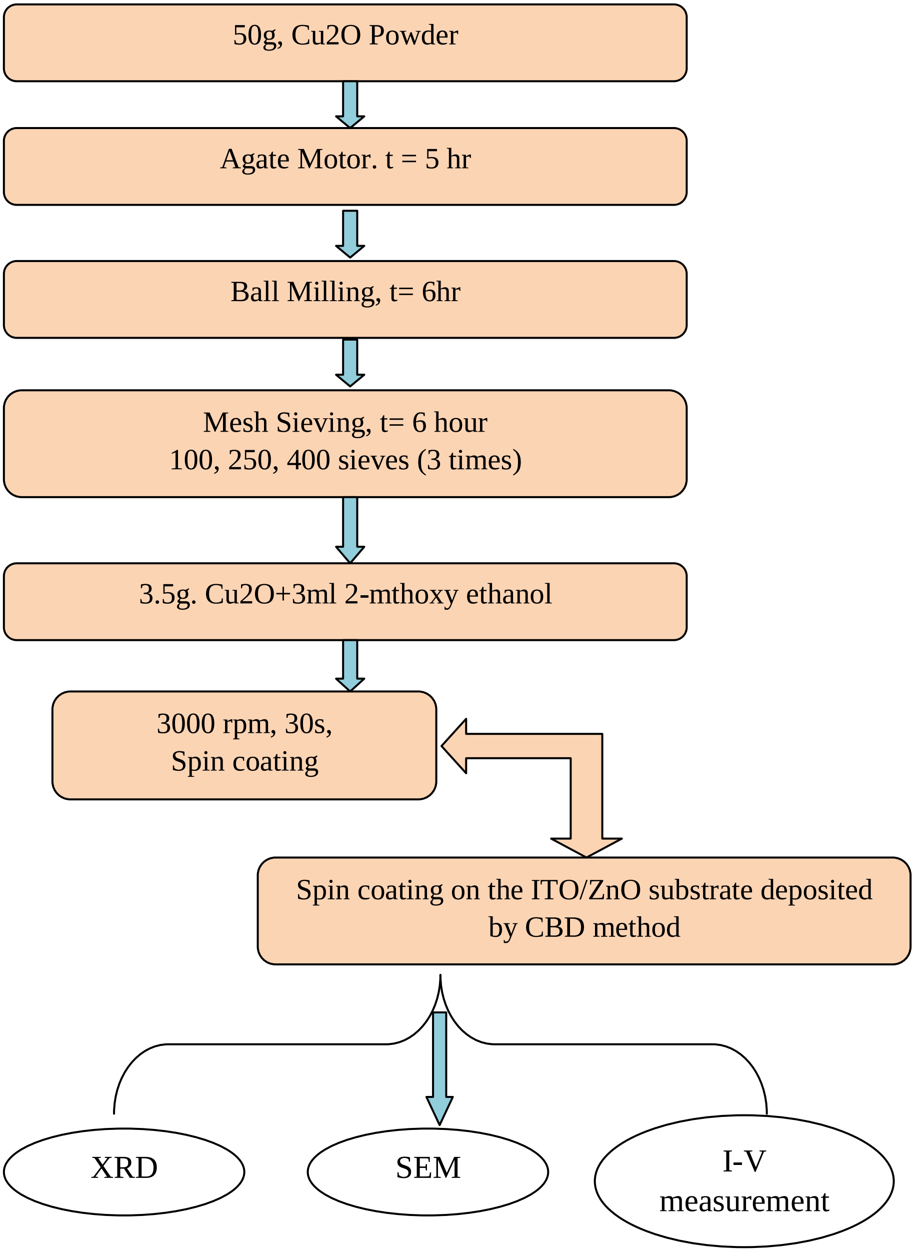

Figure 1.1: Flow chart for preparation of ITO/ZnO/Cu_2O Core-Shell layers deposited with different method on ITO glass substrate with different annealing temperature

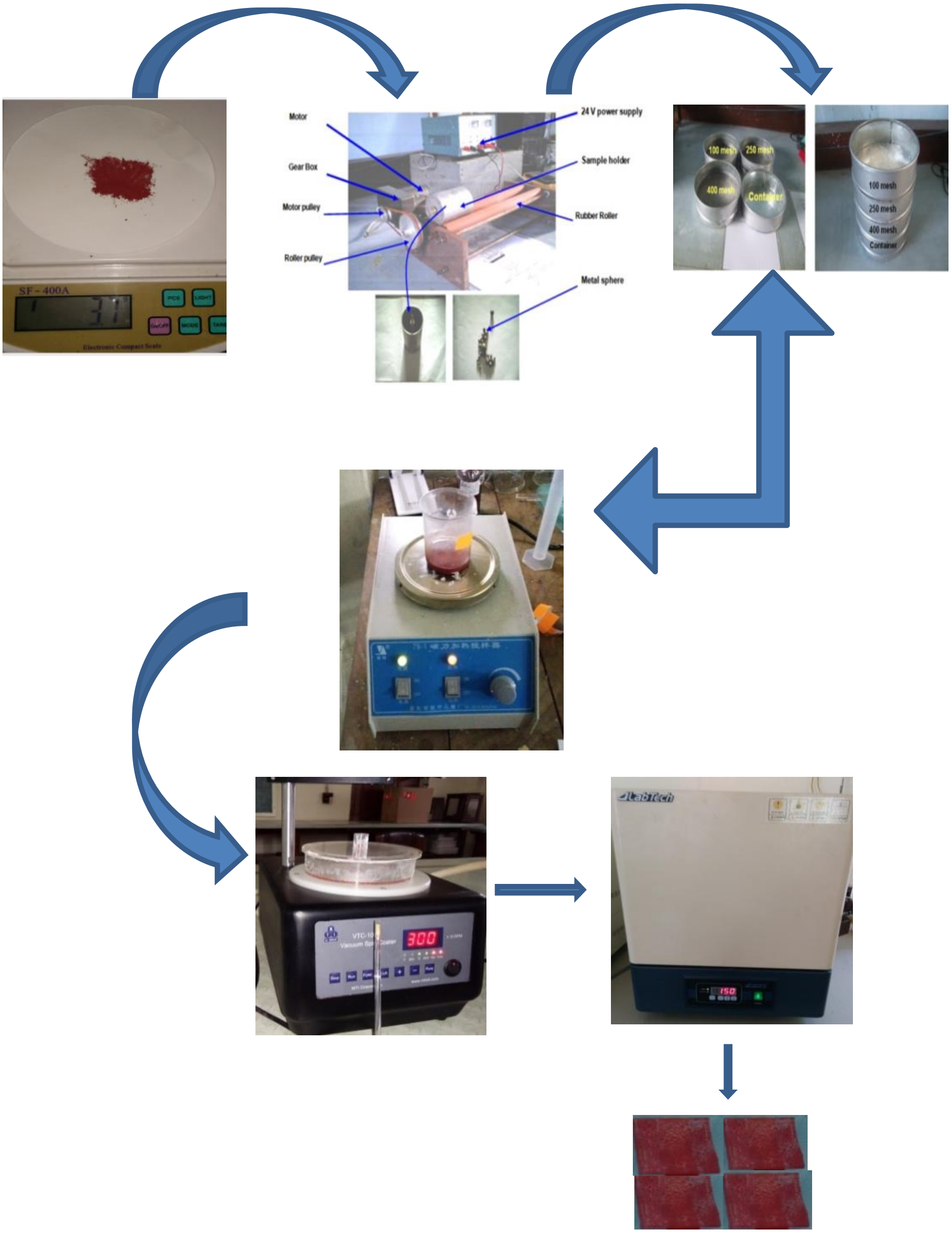

Figure 1.2: The photo depicted to the step by step preparation of Cu_2O Shell thin film onto ZnO/ITO substrate by spin coating technique

Results and Discussion

XRD analysis

X-ray diffraction (XRD) is the most well-known family of techniques to investigate structural properties of a material. Traditionally, XRD is employed on thick or powdered materials because of its penetration depth and thus its ability to reveal internal structural properties are often investigated by surface characterization techniques (e.g., atomic force microscopy), approximating the internal structure as being similar to the surface structure changes have been seen in organic ultra-thin films (Xu Z et al., 2009;Campoy Quiles M et al., 2008;Widjonarko N E et al., 2014;Mauger S A et al., 2013).

$$D = \frac{K\lambda}{\beta_{h\,k\,l}\ \mathrm{Cos}\,\theta} \qquad (1)$$

Where $\beta_{h\,k\,l}$ is the integral half width, K is a constant equal to 0.90, λ is the wavelength of the incident X-ray using source of CuKα (λ = 1.54056Å), D is the crystallite size, and θ is the Bragg angle.

Structural analysis of the Cuprous oxide shell layer thin films deposited onto the ITO/ZnO Core thin films annealed at 300°C and 400°C were carried out by using CuKα radiation source of wavelength (λ = 1.54056 Å) and the diffraction patterns of films were recorded by varying diffraction angle (2θ) in the range 10° - 70°. From figure (2.1) showed the X-ray diffraction patterns of Cuprous oxide Shell thin layer films deposited on the ITO/ZnO Core thin layers. The X-ray diffraction patterns of Cuprous Oxide thin films elaborated with sample I show high intensity of picks observed peaks matched with characteristic peaks of the Cuprite, Cu_2O (ICDD 01-077-7719) at 2θ= 36.536°, 42.424° and 61.620° corresponds to the (1 1 1), (2 0 0) and (2 2 0) diffraction planes and some small peaks assigned to (1 0 0), (0 02), (1 0 2), (110), (1 0 3) and (1 1 2) observed at 2θ = 31.783°, 34.490°, 47.693°,56.540°, 63.093° and 68.109° were perfectly matched with the characteristic peaks of Zinc Oxide wurtzite structure, ZnO, (ICDD# 01-075-0576).

At sample II, Figure (2.2) showed the X-ray diffraction patterns of cuprous oxide Shell thin layer films deposited on the ZnO/ITO Core thin layers. The X-ray diffraction patterns of Cuprous Oxide thin films elaborated with sample II show high intensity of picks observed peaks matched with characteristic peaks of the Cuprite, Cu_2O (ICDD 01-077-7719) at 2θ = 36.480°, 42.315°and 61.412° corresponds to the (1 1 1), (2 0 0) and (2 2 0) diffraction planes and some small peaks assigned to (1 0 0), (0 0 2), (1 0 2), (1 1 0), (1 0 3) and (1 1 2) observed at 2θ = 31.871°,34.575°, 47.750°, 56.777°, 63.139° and 68.201° were perfectly matched with the characteristic peaks of Zinc Oxide wurtzite structure ,ZnO, (ICDD# 01-075-0576).

The crystallite size of dominant plane (1 1 1) at different annealing temperature were found to be 20.18 nm and 32.25 nm respectively. Improved in crystallinity quality with rising annealing temperature. As a result, oxygen defect are favorable to the merging process to form the larger grains size while increasing the annealing temperature and their treated time. According to the above XRD analysis, the observable peak were good agreement with standard ICDD data reference file (card no 01-077-7719 and 01-075-0576).No unidentifiable peaks were not found in observable spectrum.

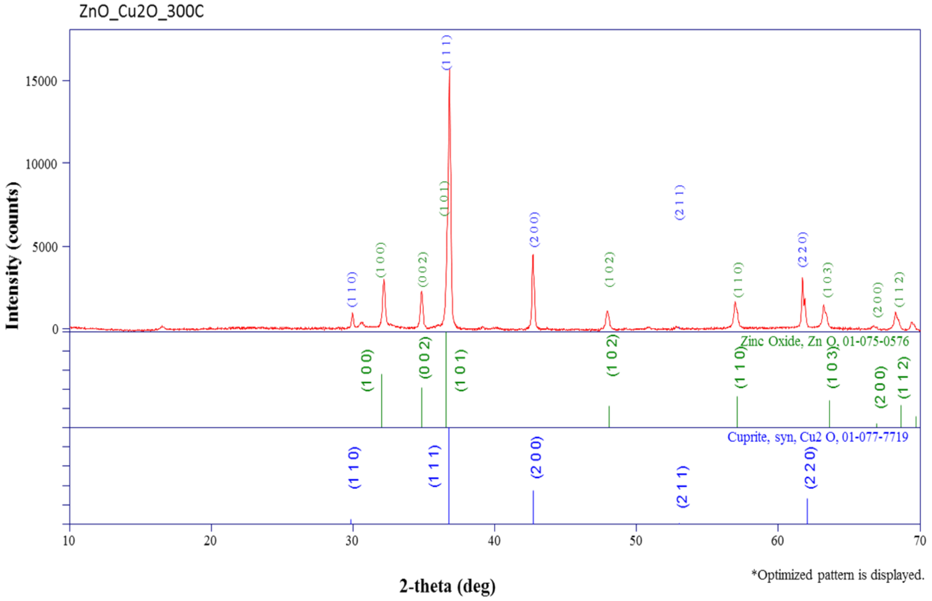

Figure 2.1: X-ray diffraction pattern of ITO/ZnO/Cu_2O Core-Shell thin film annealed at 300℃

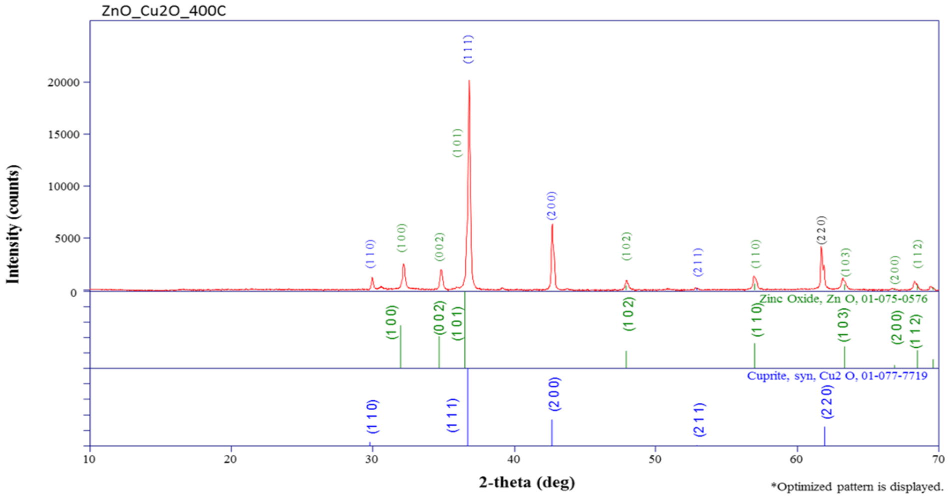

Figure 2.2: X-ray diffraction pattern of ITO/ZnO/Cu_2O Core-Shell thin film annealed at 400°C

Table 1.1: The comparison of Standard 2θ and Observed 2θ value for ITO/ZnO/Cu_2O core-shell thin film annealed at 300°C

(h k l)	Crystal structure	Observed (2θ) (deg)	Standard (2θ) (deg)
(1 0 0)	Hexagonal	31.783	31.941
(0 0 2)	Hexagonal	34.490	34.589
(1 1 1)	Cubic	36.536	36.476
(2 0 0)	Cubic	42.424	42.307
(1 0 2)	Hexagonal	47.693	47.709
(1 1 0)	Hexagonal	56.540	56.770
(2 2 0)	Cubic	61.620	61.374
(1 0 3)	Hexagonal	63.093	63.026
(1 1 2)	Hexagonal	68.109	68.121

Table 1.2: FWHM and Crystallite size value for ITO/ZnO/Cu_2O thin film annealed at 300^{o}C

(h k l)	FWHM (deg)	Crystallite size(nm)
(1 0 0)	0.251	31.61
(0 0 2)	0.292	27.17
(1 1 1)	0.393	20.18
(2 0 0)	0.287	27.64
(1 0 2)	0.588	13.49
(1 1 0)	0.209	37.96
(2 2 0)	0.342	23.20
(1 0 3)	0.643	12.34
(1 1 2)	0.351	22.60

Table 2.1: The comparison of Standard 2θ and Observed 2θ value for ITO/ZnO/Cu_2O thin film annealed at 400^{o}C

(h k l)	Crystal structure	h k l	Observed (2θ) deg	Standard (2θ) deg
(1 0 0)	Hexagonal	(1 0 0)	31.871	31.941
(0 0 2)	Hexagonal	(0 0 2)	34.575	34.589
(1 1 1)	Cubic	(1 1 1)	36.480	36.476
(2 0 0)	Cubic	(2 0 0)	42.315	42.307
(1 0 2)	Hexagonal	(1 0 2)	47.750	47.709
(1 1 0)	Hexagonal	(1 1 0)	56.777	56.770
(2 2 0)	Cubic	(2 2 0)	61.412	61.374
(1 0 3)	Hexagonal	(1 0 3)	63.139	63.026
(1 1 2)	Hexagonal	(1 1 2)	68.201	68.121

Table 2.2: FWHM and Crystallite size value for ITO/ZnO/Cu_2O thin film annealed at 400°C

(h k l)	Observed (d) (Å)	Standard (d) (Å)
(1 0 0)	0.534	14.85
(0 0 2)	0.164	48.38
(1 1 1)	0.246	32.25
(2 0 0)	0.305	26.01
(1 0 2)	0.427	18.58
(1 1 0)	0.630	12.59
(2 2 0)	0.365	21.73
(1 0 3)	0.306	25.93
(1 1 2)	0.295	26.89

SEM analysis

The surface morphology and chemical composition of the ITO/ZnO/Cu_2O Core-Shell thin films were analyzed using a Scanning Electron Microscope coupled with an Energy dispersive X-ray analysis. Bar code size was formed to be 5μ m with magnification of 15 kV × 4400 and EHT 3.00 kV. Both of the samples consist of randomly distributed grains with a smaller size and shape and with limited porosity. The average grain size of this film for sample I was 1.53 μ m. Fig 3.2 shows that at lower concentration of dopant, the numbers of Cu_2O shell distributed on ZnO core thin layer. The average grain size of 400°C ITO/ZnO/Cu_2O core shell thin film was 1.74 μ m.

Table 3.1: Deposited films, average grain size for ITO/ZnO/Cu_2O Core-Shell films annealed at different temperature.

Annealing temperature	Deposited film	Average Grain Size(μm)
300 ℃	ITO/ZnO/Cu_2O	1.53
400 ℃	ITO/ZnO/Cu_2O	1.74

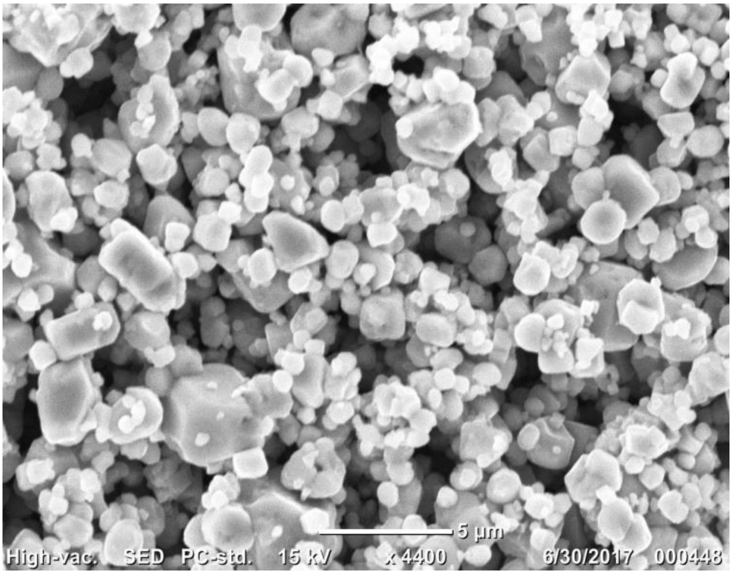

Figure 3.1: SEM analysis image for ITO/ZnO/Cu_2O Core-Shell film annealed at 300°C.

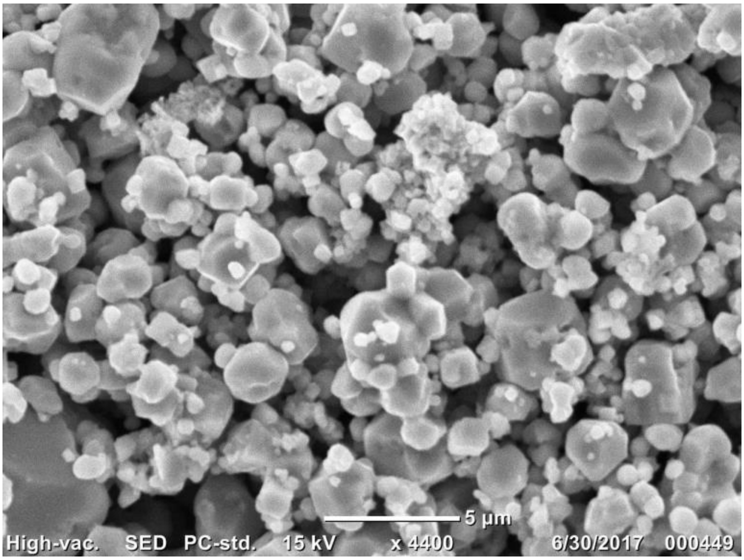

Figure 3.2: X-ray diffraction pattern of ITO/ZnO/Cu_2O Core-Shell film annealed at 400℃

Current - voltage analysis

The current–voltage measurement of the ITO/ZnO/Cu_2O core-shell thin films has been measured at room temperature in the dark and under illumination (Halogen lamp 100W). Dark current-voltage (dark I-V) measurement are commonly used to analyze the electrical characteristic of solar cells, providing an effective way to determine fundamental performance parameters without the need for a solar simulator. I-V characteristics of ITO/ZnO/Cu_2O core-shell thin film are measured in the region of -5V to +5V by using Cu-electrode. Ln I-V characteristics obey the linear relationship and I_s was obtained by extrapolating the variation line in which I_s = exp (intercept) relation is used. The forward applied voltage ranges, the ideality factor (η), zero bias barrier height (ϕ_{bo}) are measured by the following equation:

$$I_s = A\,R^*\,T^2\, exp^{\frac{-q\,\phi_{bo}}{kT}} \qquad \text{--------(2)}$$

$$\frac{1}{n} = \left(1 - \frac{\partial\phi_{bo}}{\partial V_f}\right) \qquad \text{--------(3)}$$

I_s = Saturation current

A = diode area

R^* = Richardson constant (8.16 A $k^{-2}\,cm^{-2}$)

q = electron charge (1.6×10^{-19} C)

ϕ_{bo}= Zero biased barrier height

$k = Boltzmann\ constant$ (1.38×10^{-23}) JK^{-1}

$n =$ Ideality factor

V_f = forward voltage

I-V characteristics of ITO/ZnO/Cu_2O Core-Shell thin layer films at various annealing temperature under illumination condition. These figure demonstrates V_{oc} -I_{sc} characteristics of Core-shell ZnO/Cu_2O/ITO thin layer films at different annealing temperature under illumination condition. Measurement for I-V curves, open circuit voltage (V_{oc}) and short-circuit current (I_{sc}) are carried out using a FLUKE meter, PSN-305_D 30 A Dual voltage source, Lux meter (AS-803) series, and Digital multimeter (UT-120) series. A halogen lamp is used as the source of monochromatic light.

Measurements under illumination with 1000 Lux are performed to estimate the power-conversion efficiency (PCE) and fill factor (FF) of the device under test. It is observed that the value of fill factor for ITO/ZnO/Cu_2O Core-Shell thin layer films annealed at different temperature was 0.80 for ITO/ZnO/Cu_2O Core-Shell thin layer annealed at 300ºC and 0.55 for ITO/ZnO/Cu_2O Core-Shell thin layer annealed at 400ºC.

The conversion efficiency is the percentage of power converted from absorbed light to electrical energy and collected, when photovoltaic cell is connected to an electrical circuit. The value of the open-circuit voltage, short circuit current, fill factor, and conversion efficiency at various annealing temperature are collect in Table (3.2).

Table 3.1: Ideality factor, Barrier height, and Saturation current density values for ITO/ZnO/Cu_2O core shell nanostructure solar cells at different annealing temperature.

Annealing Temperature(℃)	Ideality factor(n)	Barrier height potential(ϕ_{bo}) eV	Saturation current(µA)
ITO/ZnO/Cu_2O300℃	1.48	0.33	8.57×10^{-7}
ITO/ZnO/Cu_2O400℃	1.42	0.29	2.91×10^{-7}
[Nadir Habubi F et al., 2015]	1.71	0.69	6.14×10^{-6}

Table 3.2: Photovoltaic measurement for ITO/ZnO/Cu_2O Core-Shell films deposited on ITO thin films under illumination conditions.

Sample	V_{oc} **(mV)**	I_{sc} **(μA)**	**Fill factor (%)**	**PCE(%)**
ITO/ZnO/Cu_2O(300℃)	344.80	7.27	0.80	1.34
ITO/ZnO/Cu_2O(400℃)	315.00	13.2	0.55	1.53
FTO/ZnO/CuO/Al(Thowra Abd Elradi Daldowm et al.,2015)	221.00	2.858(mA)	0.99	6.24

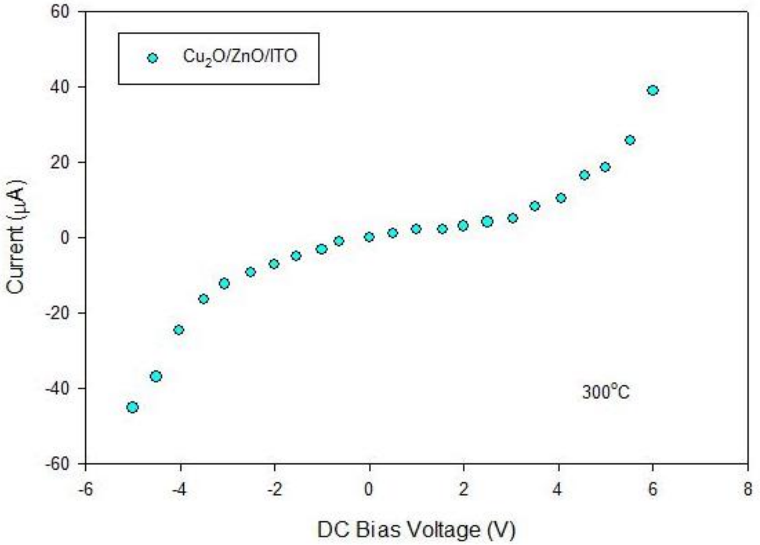

Figure 5: I-V characteristic of dark condition ITO/ZnO/Cu$_2$O Core-Shell thin film annealed at 300ºC

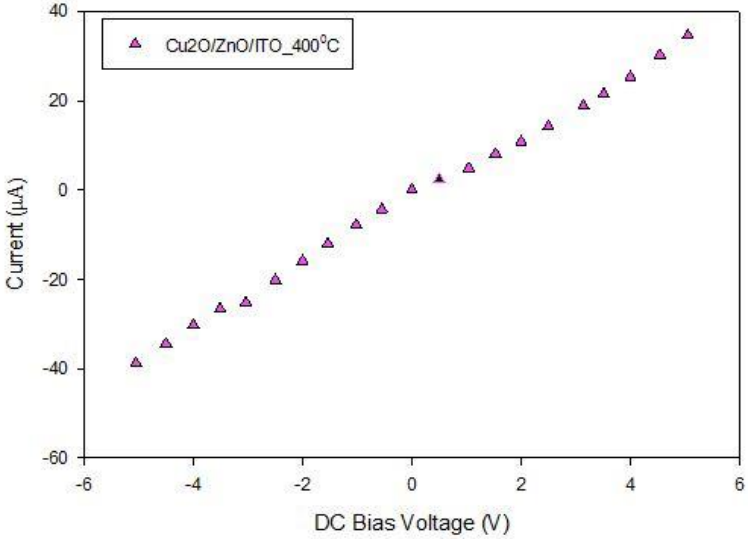

Figure 6: I-V characteristic of dark condition ITO/ZnO/Cu$_2$O Core-Shell thin film annealed at 400ºC

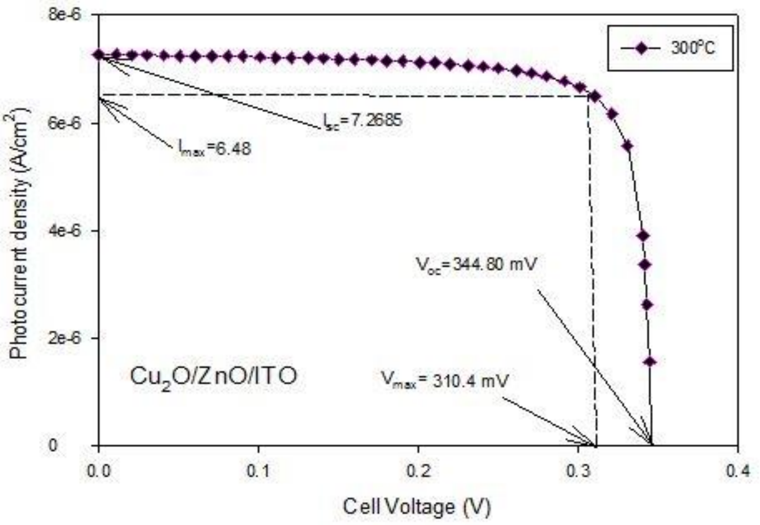

Figure 7: I-V characteristic under illumination condition ITO/ZnO/Cu_2O core shell film annealed at 300ºC

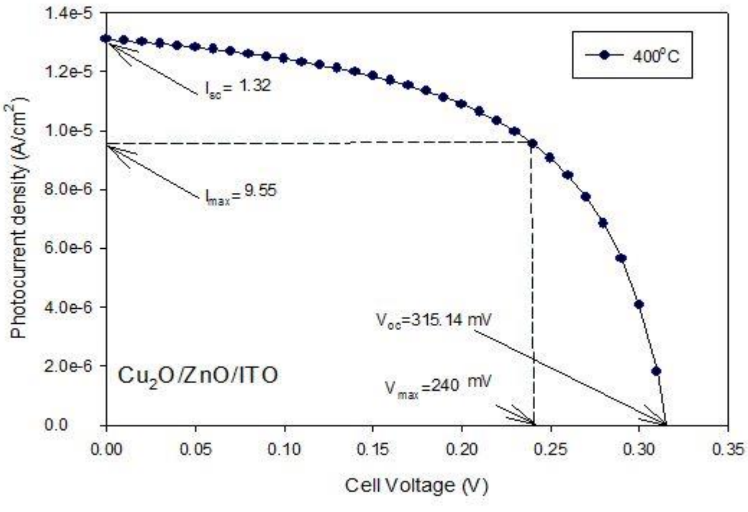

Figure 8: I-V characteristic under illumination condition ITO/ZnO/Cu_2O core shell film annealed at 400ºC

Conclusion

In this research, the fabrication and characterization of a device application of ITO/ZnO/Cu_2O core-shell nanostructure solar cells has been investigated. XRD analysis showed that the core-shell thin film is crystallized in the hexagonal phase. The average crystallite size calculated for deposited ITO/ZnO/Cu_2O Core-Shell thin layer films annealed at 300℃ and 400 ℃ were 20.21 nm and 32.28 nm. The electrical parameters such as ideality factor (n) and potential barrier (ϕ_{bo}) are formed to be strongly temperature dependent. The ideality factor of ITO/ZnO/Cu_2O core-shell thin films decreases while the corresponding barrier potential height decreasing with an increasing temperature. The ideality factor is an important parameter for device performance. All the core-shell thin films showed a clear rectifying behavior in the current-voltage characteristic at room temperature. The ideality factor was 1.48-1.42 at the lower voltage region in forward bias. From the I-V measurement under the illumination condition, the value of fill factor for ITO/ZnO/Cu_2O Core-Shell thin layer films annealed at different temperature was 0.80 for ITO/ZnO/Cu_2O Core-Shell thin layer annealed at 300ºC and 0.55 for ITO/ZnO/Cu_2O Core-Shell thin layer annealed at 400ºC. So, it can be concluded that the fabricated ITO/ZnO/Cu_2O core-shell thin film solar cells is quite suitable for photovoltaic applications.

Acknowledgement

Special thanks to Professor Dr Khin Khin Win, Head of Department of Physics, University of Yangon, for her kind permission.

I am greatly indebted to Professor Dr Aye Aye Thant, Department of Physics, University of Yangon, for her encouragement.

I am also deeply grateful to Dr Yin Maung Maung , Associate Professor , Department of Physics, University of Yangon, for her valuable advice in my experimental work.

Special thanks to Supervisor Dr Thida Win, Lecturer, Department of Physics, University of Yangon, for her valuable advice and supervision throughout in this research.

References

Avinash Dive S., Deepak., et al,(2015), "Growth structural optical and electrical properties of ZnO thin films Deposited by chemical bath deposition technique",8,189.

Basol .B.M., et al,(1985),"Effects of heat treatment on the composition and semiconductivity of electrochemically deposited CdSe films",58,601.

Cao.B &Cal .W., et al,(2008),"ZnO nanorods to nanoplates chemical bath deposition growth and surface related emission",112,680..

Danahher W.J., et al,(1978),Nature 271,139.

Fulop G.F., et al, (1985),"Mater.Sci", 15,197.

Guozhi Jia,Yunfeng Weng, Jianghong Yao et al.,(2010),"Growth mechanism of ZnO nano-structure using chemical bath deposition",6,303.

Jhon Harper, Xin-dong Wang., et al.,(2010),"I-V,C-V and AC Impedance Techniques and characterization of Photovoltaic cells",2044.

Kroger F.A., et al, (1978), "J.Electrochem.Sci", 125, 2082.

Mandal S.K., et al,(2006), "Thin solid films", 515, 2535.

Malevu T.D& Ocaya R.O.,et al,(2015),"Effect of Annealing temperature on structural, Morphology and optical properties of ZnO nano-needles prepared by Zinc-Air cell system Method",10,1752.

Nanda Shaki & Gupta P.S., et al,(2010),"Structural and optical properties of Sol-gel prepared ZnO Thin film",2,19.

Nadir F.Habubi, Abdulazeez O.Mousa, Noor A, Nema,(2015),"Fabrication and characterization of ZnO/P-Si Heterojunction Solar cell",18,118.

Ortega .J., et al, (1989), "J Electrochem.Soc", 136, 3388.

Panicker M.P.R ., et al, (1978), "J.Electrochem .Soc", 125, 568.

Prabakaran Kandasamy & Amalraj Lourdusamy.,(2014),"Studies on zinc oxide thin films by chemical spray pyrolysis technique",9,261.

Widjonarko, N.E., et al, (2014), “Impact of hole transport layer surface properties on the morphology of a polymer fullerene bulk heterojunctions,” 4, 1301879.

Wolden, C.A., & Kurtin, J., (2011), “J. Vac. Sci. Technology,” 29, 30801.

White, B., & Yin, M., (2006), “The structural and optical properties of Cu2O films electrodeposited on different substrates,” 20,44.

Xu, H., & Wang,W., (2006), "Shape evolution and size controllable synthesis of Cu2O octahedral and their morphology dependent photo catalytic properties," 110, 13829.

Xin Xin Ma & Gang Wang., (2007), "characteristics of copper oxide films deposited by PBII& D ," 201, 6712.

Xu, Z., & Yang, L.M., (2009), "Vertical phase separation in poly (2-hexylthiphene) fullerene derivation blends and its advantages for inverted structure solar cells," 19, 1227-1234.

Yang, H., & Wang, J., (2011), "Layer structured ZnO nanowire arrays with dominant surface and acceptor related emissions," 65, 1351-1354.

Zhou, Y.C., & Switzer, J.A., (1998), "Galvan static electrodeposited microstructure of cuprous (I) oxide films," 2,22.

Zhu, J., & Yu, C. M, (2010), "Nanodome solar cells with efficient light management and self-cleaning nano let," 10, 1979-1984.

Zaboborski, et al, (2010), "Effect of ionic liquid and surfactants on zinc oxide nanoparticles activity in cross linking of acrylonitrile butadiene elastomers," 116, 155-164.

Zhang, Y., & Wang, L.W., (2007), "Quantum coaxial cables for solar energy harvesting Nano letters," 7, 1264-1269.

J. Myanmar Acad. Arts Sci. 2019 **Vol. XVII. No.2A**

SCANNING ELECTRON MICROSCOPY AND CURRENT-VOLTAGE CHARACTERISTICS OF $CaMn(CO_3)_2$ /n-Si THIN FILM

May Sandar Win[*]

Abstract

Mn(20mol%) doped $CaCO_3$ ceramic was first prepared by solid-state reaction method at 1000°C for 1 h. The prepared $Ca_{0.80}Mn_{0.20}(CO_3)_2$ was deposited on n-Si substrate by using thermal diffusion technique at 400°C for 1 h. Surface morphology of the $Ca_{0.80}Mn_{0.20}(CO_3)_2$/ n-Si film was investigated by Scanning Electron Microscope. Surface morphology, grain shape, grain size and diffusion layer thickness of the film were studied in this work. In addition, current-voltage characteristics of $Ca_{0.80}Mn_{0.20}$ $(CO_3)_2$/ n-Si thin film were investigated in dark and four different illuminations of light source. Output currents were observed in the bias voltages of (-5 V - +5 V) with the step voltage of 0.2 V. Light sensitivity and output currents of the film were reported in this work.

Keywords: $Ca_{0.80}Mn_{0.20}(CO_3)_2$/n-Si film, Surface morphology, SEM, Thermal diffusion, Current-voltage characteristics

Introduction

Ceramics, an artifact made of hard brittle material are produced from nonmetallic minerals by firing at high temperatures. Atomic and molecular nature of ceramic materials, resulting characteristics of performances are using industrial applications. In addition to the well-known physical properties of ceramic materials in hardness, compressive strength, brittleness there is the property of electric resistivity. Categories of advanced ceramic materials are employed in a wide variety of electric, optical, and magnetic applications. Advance ceramics also have important uses in electronics, aerospace, biomedical, construction, and nuclear industries.

Carbonates are among the most widely distributed minerals in the Earth's crust. The crystal structure of many carbonate minerals reflects the trigonal symmetry of the carbonate ion, which is composed of a carbon atom centrally located in an equilateral triangle of oxygen atoms. This anion group

---

[*] Dr, Assistant Lecturer, Department of Physics, University of Yangon

usually occurs in combination with calcium, sodium, uranium, iron, aluminum, manganese, barium, zinc, copper, lead, or the rare-earth elements.

Advanced Ceramic materials are not only nonmetallic, inorganic compounds and primarily compounds of oxygen, but also compounds of carbon, nitrogen, boron, and silicon which include the manufacture of earthenware, porcelain, bricks, and some kinds of tile and stoneware. Advanced Ceramics generally display the properties of hardness, refractoriness, high melting point, low conductivity and brittleness. Advanced industrial materials, owing and modifications in their structures, serve as electrical conductors. Resistivity and conductivity of insulator (ceramic), semiconductor and conductor are shown in Fig 1.

Scanning Electron Microscope (SEM) is one of the most versatile instruments available for the examination and analysis of the microstructural characteristics of solid objects. In the present work, sample preparation, surface morphology and diffusion layer thickness of $Ca_{0.80}Mn_{0.20}(CO_3)_2$ / n-Si thin film was reported by scanning electron microscopy.

"Kutnohorite" is the chemical formula of Calcium Manganese Carbonate, $CaMn(CO_3)_2$. It is a dolomite, $CaMg(CO_3)_2$ group mineral of naturally occurring species. The Manganese analogue of dolomite, it forms a chemical substitution (solid-solution) series with that mineral, in which Magnesium replaces Manganese in the crystal structure. It is probably intermediate in the discontinuous (at normal temperatures) solid-solution series between Calcite ($CaCO_3$) and rhodochrosite ($MnCO_3$). In the present work, current-voltage characteristics of $Ca_{0.80}Mn_{0.20}(CO_3)_2$/n-Si thin film were investigated in dark and four different illuminations of light source.

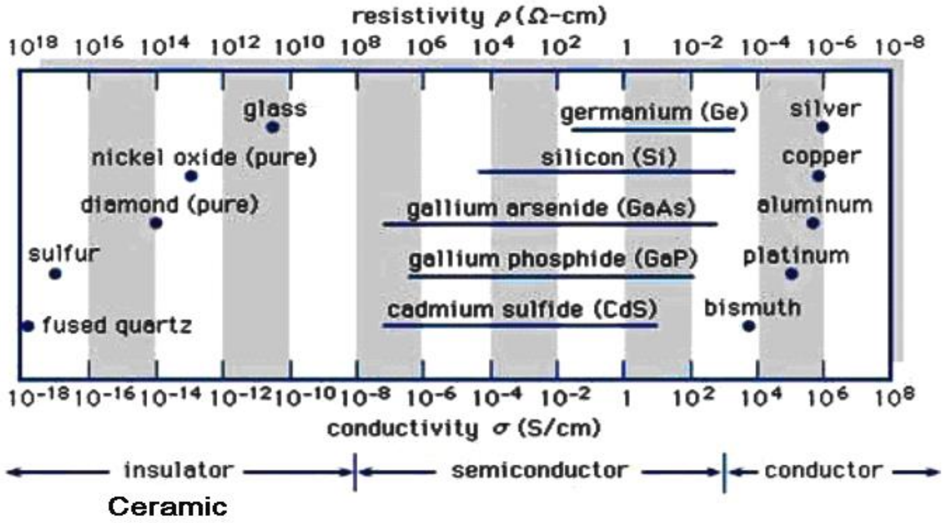

Figure 1: Resistivity of insulator, semiconductor and conductor

Experiment

Preparation of $Ca_{0.80}Mn_{0.20}(CO_3)_2$ Ceramics

For the intention sample $Ca_{0.80}Mn_{0.20}(CO_3)_2$ ceramic, raw materials of $CaCO_3$ and MnO_2 have been chosen as the starting materials. The starting materials $CaCO_3$ and MnO_2 were then mixed by the stiochiometric formula with desirable composition. These homogeneous powders were annealed at 1000 °C for 1 h. Then, sintered $Ca_{0.80}Mn_{0.20}(CO_3)_2$ powder was grounded by agate motor for 10 h to be homogeneous. 1 g of the powder and 2-methoxythanol are mixed. Obtained mixture is stirred and boiled at 100°C to get the sol state. Finally, the solution was cooled down at room temperature and was coated on cleaned n-Si substrate by spin coating method.

The sample was heat treated at 1000°C for 1 h in vacuum chamber. FOTEK MT-20 temperature controller was used to control the desire temperature and K-type thermocouple (1300°C) was used as the temperature sensor.

N-Si (100) wafer dimension of (0.5 cm x 0.5 cm) was used as the substrate. The substrate was cleaned using standard wafer cleaning process.

N-type silicon substrate was etched in HF:H_2O (1:5) for 10 min, and immerse in deionized water for 10 minutes. And then, the substrate was immersed in acetone and methyl alcohol for 10 min and was rinsed in deionized water for 10 min. Next, the substrate was dried at room temperature. Finally, cleaned substrate was kept in an oven at 80°C for 10 min to dry. After cleaning process, the precursor solution was coated onto substrate by spin-coating technique. Later, coated-layer was dried at room temperature. $Ca_{0.80}Mn_{0.20}(CO_3)_2$ /n-Si material was deposited at 400°C for 1 h in thin film fabrication chamber. Experimental arrangement of thin film deposition system is shown in Fig 2.

Figure 2: Photograph of experimental arrangement of sample preparation system

Scanning Electron Microscopic (SEM) Measurement

In the present work, surface morphology and diffusion layer thickness of $Ca_{0.80}Mn_{0.20}(CO_3)_2$ /n-Si thin film were investigated by JEOL JSM-5610LV Scanning Electron Microscope (SEM) with the accelerating voltage of 15 kV and the beam current of 50 mA to study the grain shape, grain size and film quality as a function of annealing temperature. Photograph of JEOL JSM-5610LV Scanning Electron Microscope is shown in Fig 3.

Figure 3: Photograph of JEOL JSM-5610LV Scanning Electron Microscope (Japan: Kyoto)

I-V Characteristic Measurement

Light sensitive effect of $Ca_{0.80}Mn_{0.20}(CO_3)_2$/n-Si thin film has been investigated in dark condition (0 lux) and four different illumination conditions using (60 W) electric bulb light source. The light intensity sensor of Si-photodiode (LIGHTMETER 2330LX, SEW) was placed near the sample with parallel position to record constant intensity of light source throughout the measurement. I-V (Current – voltage) characteristics of the film in dark and in illumination conditions were also measured between the bias voltages of -5 V and +5 V with the step voltage of 0.2 V. In this measurement, DT-830B and FUKE FK9208X were used as the digital ammeter and voltmeter. Photograph of the experimental arrangement of I-V characteristic measurement is shown in Fig 4.

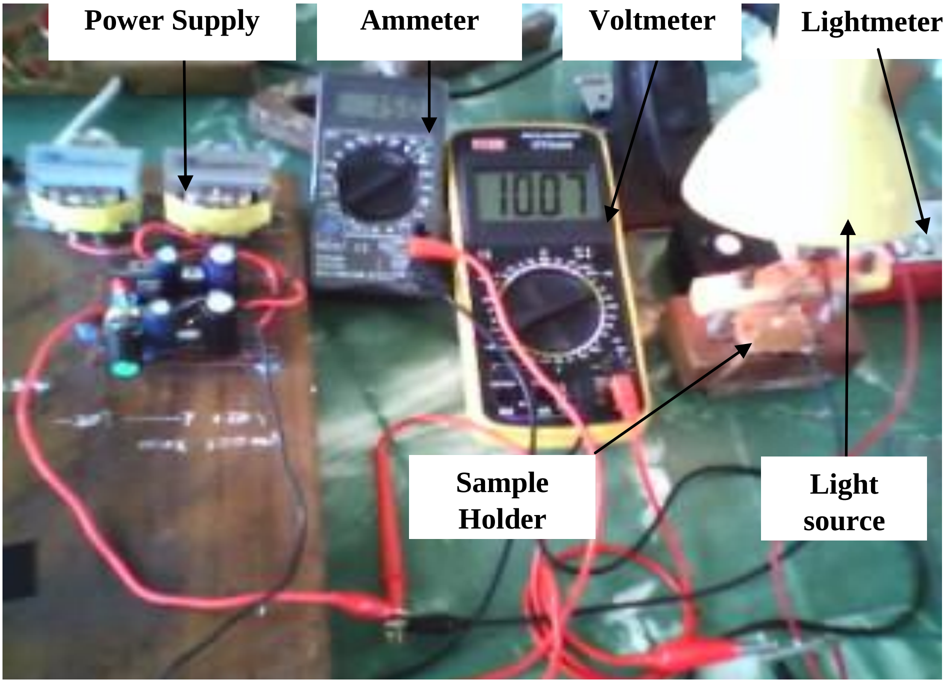

Figure 4:Photograph of the experimental arrangement of I-V characteristic measurement

Results and Discussions

SEM micrograph of $Ca_{0.80}Mn_{0.20}(CO_3)_2$ /n-Si thin film at the deposition temperature of 400°C for 1 h is shown in Fig 5 and the diffusion layer thickness of $Ca_{0.80}Mn_{0.20}(CO_3)_2$ on n-Si substrate is also shown in Fig 6.

As shown in recorded SEM micrograph, grain shapes of the samples are found to snow-like patterns. Grain sizes of the sample of micrograph are about 0.2 μ m to 0.5 μ m. In this micrograph, some holes are found but it is crack free layer.

As shown in observed diffusion layer thickness of the $Ca_{0.80}Mn_{0.20}$ $(CO_3)_2$ on n-Si substrate, it is found that (1) the layer boundary of the sample and substrate is mostly homogeneous and (2) the diffusion layer of the $Ca_{0.80}Mn_{0.20}(CO_3)_2$ sample on n-Si substrate is about 31.5 μ m.

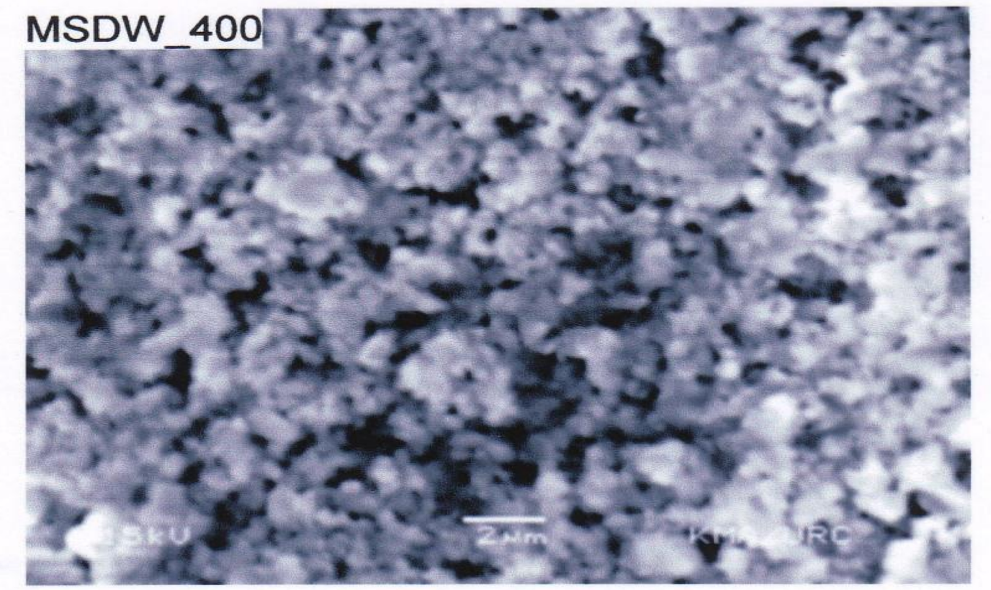

Figure 5: SEM micrograph of the $Ca_{0.80}Mn_{0.20}(CO_3)_2$ /n-Si thin film

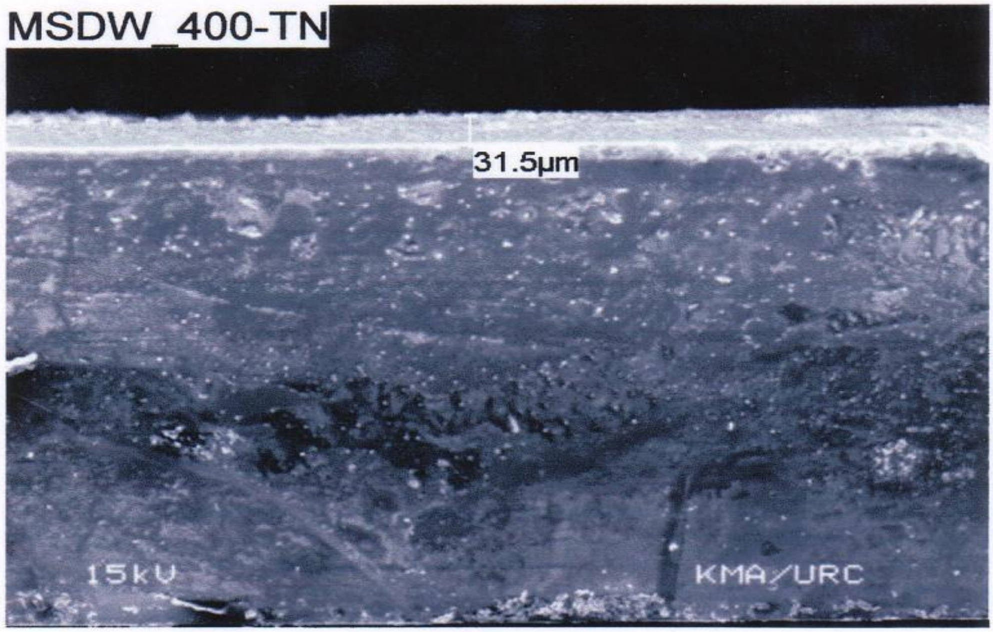

Figure 6: Diffusion layer thickness of the $Ca_{0.80}Mn_{0.20}(CO_3)_2$ on n-Si thin film

Current-Voltage Characteristics of $Ca_{0.80}Mn_{0.20}(CO_3)_2$/n-Si Thin Film

Current-voltage measurements of $Ca_{0.80}Mn_{0.20}(CO_3)_2$/n-Si thin film in the bias voltages of (-5 V - +5 V) under the different illumination conditions were investigated to study the photosensitive effect of the sample. Copper are used as electrodes for the top and bottom regions. I-V characteristic curves of the $Ca_{0.80}Mn_{0.20}(CO_3)_2$/n-Si thin film under dark (0 lux), ambient (390 lux), 1000 lux, 1500 lux and 2000 lux using (60W) electric bulb are shown in Fig 7(a) – (e).

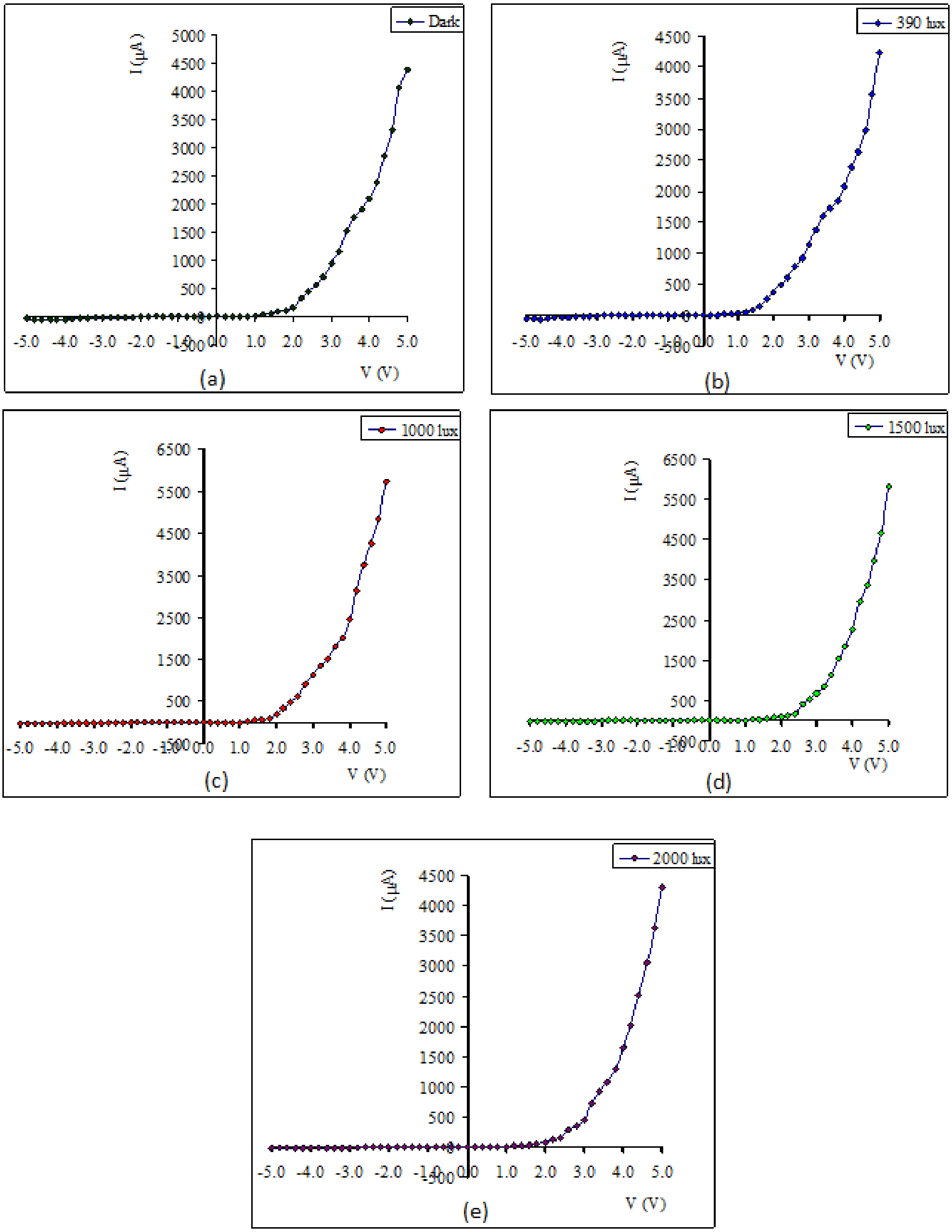

Figure 7: Current-voltage characteristic curves of $Ca_{0.80}Mn_{0.20}(CO_3)_2$/n-Si thin film under (a) dark (0 lux), (b) 390 lux (ambient), (c) 1000 lux, (d) 1500 lux and (e) 2000 lux illuminations

Current-voltage characteristic curves of the $Ca_{0.80}Mn_{0.20}(CO_3)_2$/n-Si thin film like as the junction diode characteristics. The output current of the film in the reverse saturation region (third quadrant) is found to linear. In the forward region (first quadrant), the output current is found to exponentially increase with increasing bias voltage. At (0 V) bias, the output current is (0 A) that shows the junction diode characteristic. Furthermore, comparison of the output currents as a function of (0 – 5 V) bias voltages in different illumination conditions is shown in Fig 8. Maximum output currents of the $Ca_{0.80}Mn_{0.20}(CO_3)_2$/n-Si thin film at +5 V in different illumination conditions are listed in Table 1. As presented in Table 1, the maximum output current of the film is 5810 μ A in 1500 lux illumination. The sample is a light sensitive device.

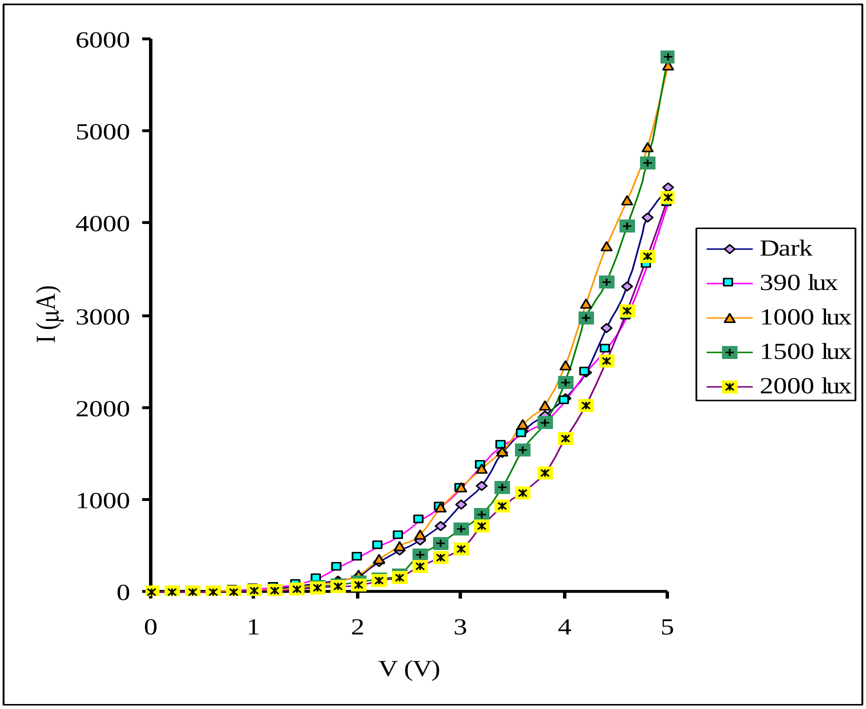

Figure 8: Comparison of the I-V characteristic curves of $Ca_{0.80}Mn_{0.20}(CO_3)_2$/ n-Si thin film in dark and in different illumination conditions

Table 1: Maximum output currents of $Ca_{0.80}Mn_{0.20}(CO_3)_2$/n-Si thin film in different illuminations

Sr No	Illumination (lux)	I_{max} (□A)
1	0 (dark)	4390
2	390	4230
3	1000	5720
4	1500	5810
5	2000	4290

Conclusion

Mn (20 mol%) doped Calcium Carbonate, $CaCO_3$ thin film was deposited on n-Si substrate by using thermal diffusion method at 400°C for 1 h in vacuum chamber. Surface analysis of the sample was investigated by SEM at room temperature. According to SEM micrographs, grain shapes of the samples are found to snow-like pattern. Grain sizes of the sample are about 0.2 μm to 0.5 μm. Some holes are found in SEM micrographs but it is crack free layer. Homogeneously layer was found to be deposited on n-Si substrate with 31.5 μm in thickness.

I-V characteristics of the film were reported under dark and different illuminations. From the I-V characteristic curve, it is shown that the film has the junction diode characteristic. The output currents in reverse saturation region and forward region were investigated. The maximum output currents were compared for the different illuminations. The maximum output current is found to be 5810μA for 1500 lux illumination condition. According to experimental results, the sample is found to be light sensitive.

Acknowledgement

The authors are grateful to Dr Khin Khin Win, Professor and Head of the Department of Physics, University of Yangon for her kind permission to carry out this work.

References

Bhattacharva P (1995) "Semiconductor Optoelectronic Devices" (New Delhi: Prentic-Hall)

Engler P et al 1988 The Rigaku Journal 5 (2) 3

Moulson A J & Herbert J M (1997) "Electroceramics Materials, Properties & Applications" (London: Chapman & Hall)

Pillai S O (2006) "Solid State Physics" (New Delhi: New Age)

Tsuchiya T & et al (2006) Sci Lett 231 11

Xiu X et al (2007) Journal of Materials Science and Technology 23 (4) 509

Yoo J et al (2005) Journal of the Korean Physical Society 47 576

Xu Y (1991) “Ferroelectric Materials and Their Applications” (Amsterdam: North-Holland)

2001 “Vacuum Technique and Thin Film Deposition” (California: California Institute of Technology)

2011 Encyclopedia Britannica Library CD-ROM Catalogue

J. Myanmar Acad. Arts Sci. 2019 **Vol. XVII. No.2A**

REVERSE MOVING CONTROL SYSTEM BY USING BLUETOOTH MODULE

Sandar Oo[1], Myo Yu Yu Thin [2], Me Me Aung [3], Zaw Zaw Aung [4]

Abstract

The "Reverse Moving Control System" is mainly implemented by using Arduino UNO microcontroller board and ultrasonic sensor (HC-SR04). The peripheral components are liquid crystal display (LCD), light emitting diodes (LEDs), piezo buzzer and Bluetooth wireless module (HC-06). The ultrasonic sensor transmits and receives the signals from the obstacles near the automobile. The signal is then sent to the UNO board which is the main controller of the whole system. The distance between the automobile and the obstacle is calculated by Arduino IDE software. The output data is sent to piezo buzzer, LCD and LEDs. Bluetooth module is used to control the moving of automobile in back and forth direction. It is a connection module between automobile and android mobile phone. This device intends to protect the automobiles from accidents during parking. It can also be modified as a backup camera in modern cars.

Keywords: Ultrasonic sensor, Bluetooth module, Arduino UNO, LCD, buzzer, LEDs

Introduction

Nowadays, the population in every country is kept on increasing. The higher the population, the higher the demand of food and shelter we need. To improve the standard of living, new modern constructions are built in downtown area. So, the car owners need to face some problems such as lack of parking space, rode condition, traffic congestion, traffic management by police and so on. Among them, the lack of parking space or small parking area is one of the problems to solve. Cities usually mandate that all new residential and commercial buildings have a certain amount of parking. Thus, the parking alarm system is necessary to prevent the automobile from the dangerous conditions.

The main purpose of this research is to design a parking alarm of automobile while parking on crowded and narrow streets. Without a parking sensor, collisions and accidents can happen because the driver cannot see well

---

[1] Dr, Lecturer, Department of Physics, University of Yangon.

[2] MRes Candidate, Department of Physics, University of Yangon.

[3] Dr, Assistant Lecturer, Department of Physics, University of Yangon

[4] Dr, Lecturer, Department of Physics, University of Yangon.

the back or corner of the car. This device can allow the driver to park safely in every small space without having to worry about the circumstances. The system is designed in order to alert the driver of various packed cars and other obstacles. If the parking sensor installed in front and at the rare of the car, it is like having X-ray vision where it is needed, especially when the cars are being parked in a limited space between two cars. This system can fully detect moving or unmoving objects near the car and it gives off alerting beeps to warn the driver to apply the brake. It also has a good safety measure against hitting objects when reversing out of the garage. Nobody is needed to watch out for the car while it is in and out of the parking area.

Arduino is an open-source project that created microcontroller based kits for building digital devices and interactive objects that can sense and control physical devices. The projects are based on designs, produced by several electric components, using various microcontrollers. These systems provide sets of digital and analog input/output (I/O) pins that can interface to various expansion boards termed shield and other circuits. The boards feature serial communication interfaces, including Universal Serial Bus (USB) for loading programs for personal computers.

An ultrasonic sensor is a device that can measure the distance to an object by using sound waves. It measures distance by sending out a sound wave at a specific frequency and listening for that sound wave to bounce back. By recording the elapsed time between the sound wave being generated and the sound wave bouncing back, it is possible to calculate the distance between the sonar sensor and the object. Ultrasonic sensor also known as transceivers when they both send and receive work on a principle similar to radar or sonar which evaluate attributes of a target by interpreting the echoes from radio or sound waves respectively.

In this way, the car parking circuit is quite easy and used commonly available components such as Arduino Uno microcontroller, ultrasonic sensor (HC-SR04), liquid crystal display (LCD), light emitting diode (LEDs), piezo buzzer and other electrical components. This research is going to develop a Bluetooth controlled robot car. A Bluetooth module (HC-06) is used to drive the automobile by using an android based application. So, the user can control the automobile from a distance without touching the automobile. The block diagram of the constructed system is shown in Figure 1.

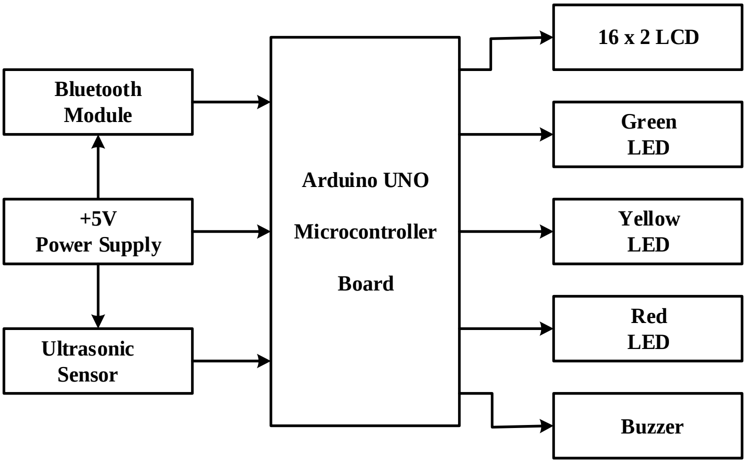

Figure 1: Block Diagram of the Constructed System

Theoretical Background

Arduino Uno Microcontroller Board

Arduino is an open-source platform used for building electronics projects. Arduino consists of both a physical programmable circuit board as a microcontroller and a piece of software, or IDE (Integrated Development Environment) that runs on the computer, used to write and upload computer code to the physical board. The Arduino platform has become quite popular with people just starting out with electronics and for good reason. Unlike most previous programmable circuit boards, the Arduino does not need a separate piece of hardware which is called a programmer in order to load new code into the board by using a USB cable simply. Additionally, the Arduino IDE uses a simplified version of C and C++, making it easier to learn to program. Finally, Arduino provides a standard form factor that breaks out the functions of the microcontroller into a more accessible package [Yahya Tawil, 2016]. Figure 2 shows the Arduino UNO SMD R3 Microcontroller Board.

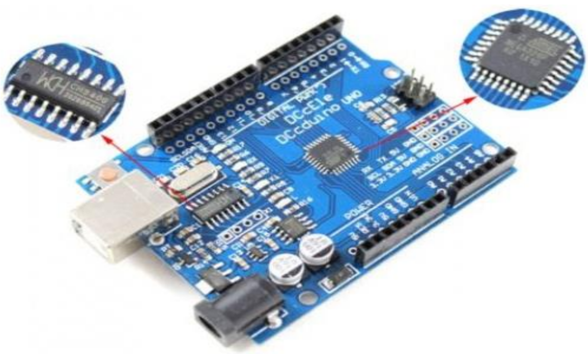

Figure 2: Arduino UNO SMD R3 Microcontroller Board

Ultrasonic Sensor (HC-SR04)

HC-SR04 ultrasonic sensor is commonly used with both microcontroller and microprocessor platforms like Arduino, PIC, Raspberry Pie etc. HC-SR04 ultrasonic sensor consists of a transmitter, a receiver and a control module. It is a sensor that works on principle similar to radar or sonar. Therefore, ultrasonic sensor can be used to measure distance. It generates high frequency sound and calculates the time interval between the sending of signal and the receiving of echo. The sensor head emits an ultrasonic wave and receives the wave reflected back from the target. Ultrasonic Sensors measure the distance to the target by measuring the time between the emission and reception. Figure 3 shows working principle of Ultrasonic Sensor and frequency (directivity) and influence of the ground is shown in Figure 4 [Marian, P.2013].

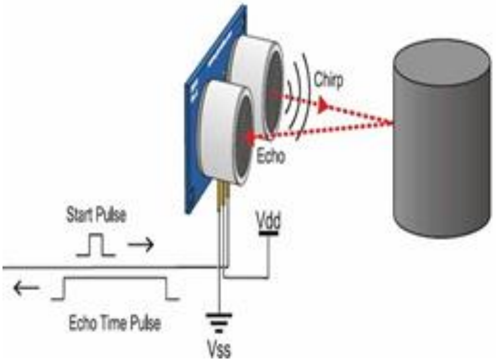

Figure 3: Working Principle of Ultrasonic Sensor

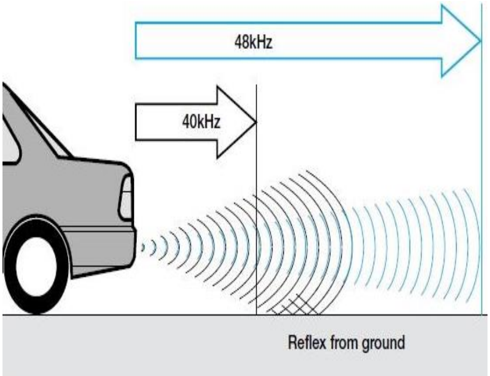

Figure4: Frequency and influence of the Ground

Bluetooth Wireless Module (HC-06)

The HC-06 is a class two slave Bluetooth module designed for transparent wireless serial communication. Once it is paired to a master Bluetooth device such as PC, smart phones and tablets, its operation becomes transparent to the user. All data received through the serial input is immediately transmitted over the air. When the module receives wireless data, it is sent through the serial interface exactly at it is received. No user code specific to the Bluetooth module is needed at all in the user microcontroller program. It uses the UART protocol to make it easy to send and receive data wirelessly. This Bluetooth module has 4 pins: RX, TX, GND and +5V [Stan, 2014].

Construction and Operation of the Whole System

The "Reverse Moving Control System" is mainly developed into three parts:

(i) Interfacing the peripheral components

(ii) Circuit description

(iii) Circuit operation

The circuit construction of the whole system is drawn by Visio software and shown in Figure 4. The detail facts are described in the following sections. Figure 5 shows the flow diagram of the whole system.

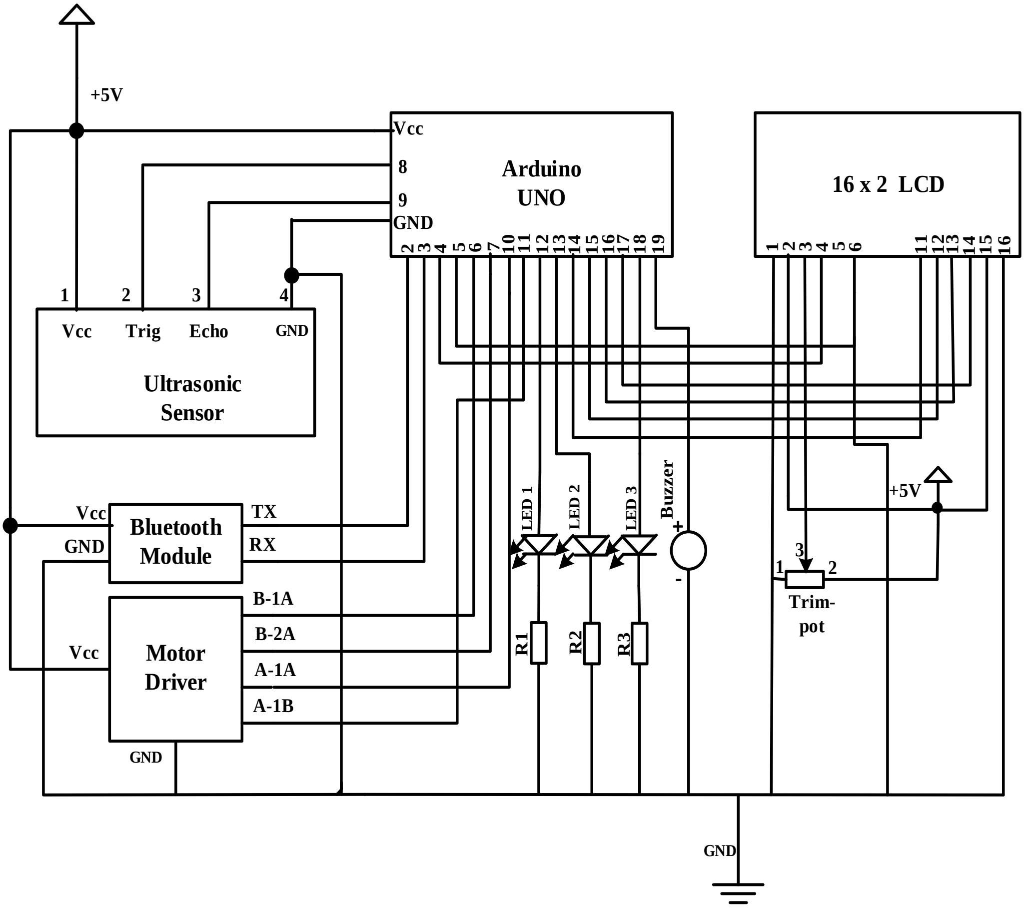

Figure 4: Complete circuit diagram of the whole System

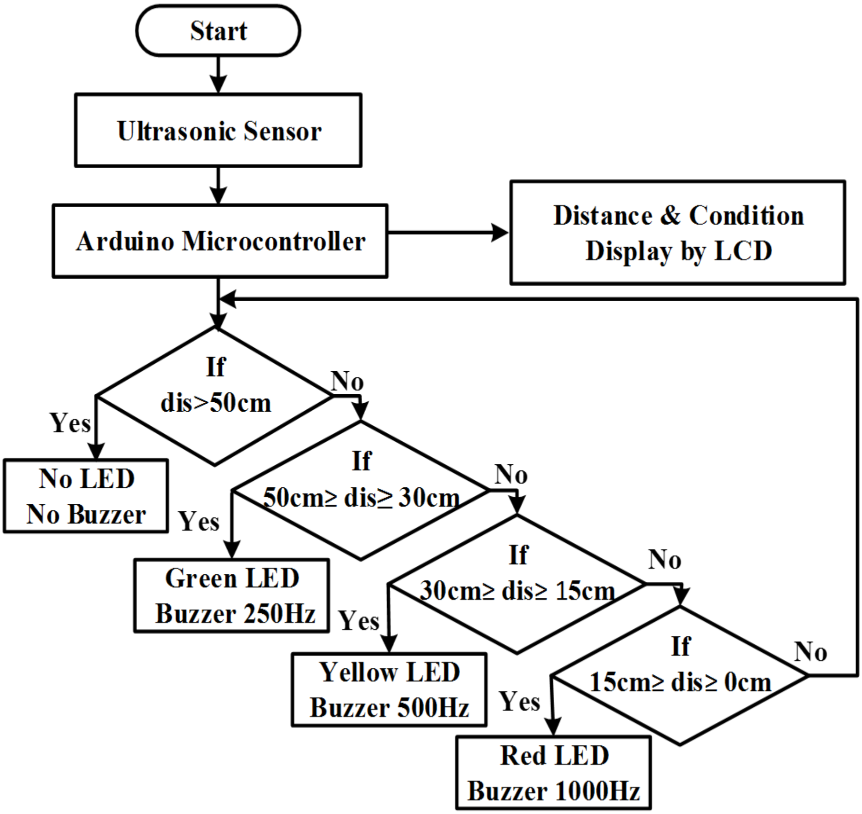

Figure 5: Flow diagram of the whole System

Interfacing the Peripheral Components

Bluetooth-controlled automobile moves according to button touched in the android Bluetooth mobile application. To run this system, Bluetooth RC controller application is installed into the android mobile phone. Then, select desired Bluetooth device and configure keys. Any Bluetooth controller application that supports or sends data can be used. The user gives the command to Bluetooth module through the mobile phone. The Bluetooth module receives this command and transmits to Arduino UNO.

Then, Arduino receives the signal and sends command to the input of the motor driver. The output of the driver is connected to the motor wheels. This automobile has two DC motors at its front sides and two ordinary wheels at its rear sides. Only the front side motors are used for driving the car in forward and backward direction. When the user touches forward button in Bluetooth controller application, the automobile starts moving in forward direction and moving continues forward until next command comes. When the user touches backward button in Bluetooth controller application, the automobile starts moving in reverse direction and moving continues reverse until next command comes. The motor driver is connected to Arduino to run the automobile.

Circuit Description

In this research, the program is written in Arduino C programming language. It is simulated by using Arduino software (IDE), liquid crystal library and software serial library for Bluetooth module. The Arduino UNO SMD (Surface Mount Device) R3 is a clone Arduino, unlike the other UNO boards; the driver of uploading code CH341SER is needed. Arduino UNO is used compatible with CH340G UART to USB converter. After completing this process, the driver is successfully installed and Arduino UNO R3 is ready to upload the program. Then, connecting Uno microcontroller USB via into computer and choose board and port. Finally, it will compile and upload the program conveniently. After finishing this process, the hardware components are constructed on the circuit board.

LCD display is mainly used to show the distance between the car and the obstacles. The output system also includes LEDs and buzzer. Green, Yellow and red LEDs are used to alert the three different conditions of automobile and the crushing distance. The buzzer is used to give alarm the driver in these three stages.

Circuit Operation

The automobile parking alarm controller system consists of ultrasonic sensor, LCD, piezo buzzer and LEDs. The ultrasonic sensor is placed at the rear side of the car. It emits acoustic pulses with a control unit measuring and returns interval of each reflected signal which is sent to the Arduino UNO board. This board plays as the main control unit of the circuit and calculates the object distances and shows the result on LCD display. It is controlled by a particular program. The sensor also gives the correct idea of the space available for parking. When the automobile reaches the three limits; 50cm, 30cm and 15cm, green, yellow and red LEDs glow. Different colors of LEDs are used for different types of distance. At the same time, the buzzer produces different sounds when the automobile approaches any object. The sound gets shaper when the distance between the automobile and the target lessens.

Results Discussion

In this research, the circuit construction is very compact and creative. The constructed system is controlled by using android mobile phone instead of using other method like buttons, gesture, etc. The touch button in android phone is needed to drive the automobile in forward-backward direction and stop. The operations are quite simple to test the program in real world. There are four conditions for reverse moving control system:

(i) Out of range (greater than 50cm)
(ii) Green LED glowing condition (between 50cm and 30cm)
(iii) Yellow LED glowing condition (between 30cm and 15cm)
(iv) Red LED glowing condition (less than 15cm)

Out of Range (greater than 50cm): If the automobile doesn’t reach the limited range (50cm), there is no LED light and buzzer sound. Only the correct distance value in centimeter is shown on the first line of LCD and the driver cannot get any alarm. Since the automobile is in safety condition, no message is shown on second line of LCD display. Figure 6 shows the photograph of automobile in out of range condition.

Green LED Glowing Condition: If the automobile keeps on reversing and it reaches the distance between 50cm and 30cm, the green LED glows. The buzzer produces tone with a frequency. The first line of LCD shows the value of distance between the automobile and obstacles. The driver sees the short message “Can Reverse” on the second line of LCD. Figure 7 shows the first condition of automobile with green LED light.

Yellow LED Glowing Condition: When the automobile is at the distance between 30cm and 15cm, the yellow LED glows for the second condition. The buzzer sound gets sharper than the first condition. The LCD shows the current distance and the character words “Little Reverse.” Figure 8 shows the second condition of automobile with yellow LED light. At that time, the driver must take care the distance between the automobile and obstacles.

Red LED Glowing Condition: Once the red LED is glowing, the automobile is reaching the distance 15cm and less. The LCD shows a message "Cannot Reverse" to warn the driver. At that time, the driver must apply the brake as there is no more space to reverse. The buzzer produces the sharpest sound to alert the driver. Figure 9 shows the third condition of automobile with red LED light.

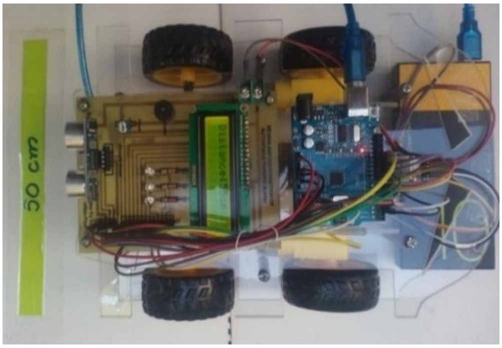

Figure 6: "Out of Range" Condition

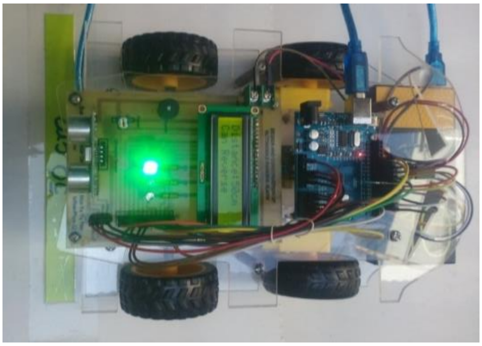

Figure 7: "Can Reverse" condition

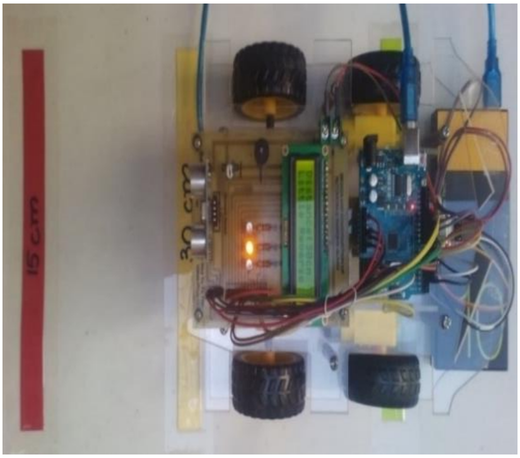

Figure 8: "Little Reverse" condition

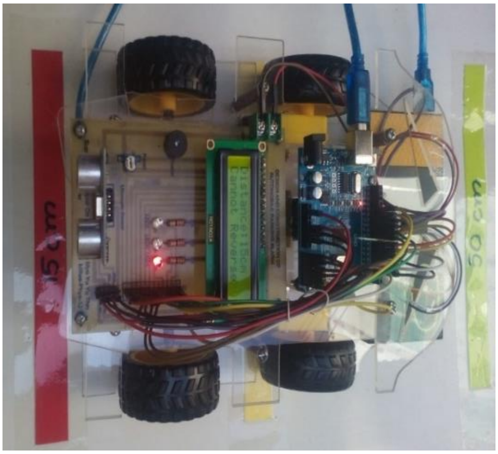

Figure 9: "Cannot Reverse" condition

Conclusion

The “Reverse Moving Control System” is successfully analyzed in real world by a simple design of automobile. This device operates like a backup camera in modern car. The driver can control the automobile very well when using this device. Even a wire fence can be detected if it is close to the automobile. It is not expensive at all. The using of Arduino UNO R3 is cheaper than other UNO board. It is the brain of the whole system. By the use of microcontroller, the system is reliable, accurate and easy to upload the program. The whole system operates automatically and simultaneously. Thus, all the measurements can be taken from time to time. It is a very interesting project for hobbyists and students for fun as well as learning. Nowadays, the modern and luxury automobiles are increasing year by year so such kind of device is necessary to protect the driver and automobile from accident.

Acknowledgements

I am very grateful to Professor Dr Khin Khin Win, Head of Department of Physics, University of Yangon, for her kind permission to do this work.

I wish to thank Dr Aye Aye Thant, Professor, Department of Physics, University of Yangon, for her encouragement to do this work.

References

Ben, (2011). Introduction of Arduino, Spark Fun Electronics.

Brock, J.D., Bruce, R.F., & Reiser, S.L. (2009). *Using Arduino for introductory programming courses*. J. Comput. Sci. Coll., 25(2), 129-130.

Jessie, W. (2017). Ultrasonic Technical Information.

Ken Wilson, D. (2017). The Benefits of Every Parking Sensor when Parking and Reversing, Travel-guide of Street dictionary.

Marian, P. (2013). Ultrasonic Sensor Circuit.

Saddam, (2016). Bluetooth Controlled Toy Car Using Arduino.

Stan, (2014). HC-06 Bluetooth Module Datasheet and Configuration with Arduino.

Wheat, D. (2011). Arduino Internals.

Yahya Tawil, (2016). Understanding Arduino Uno Hardware Design.

J. Myanmar Acad. Arts Sci. 2019 **Vol. XVII. No.2A**

CALL AND SEND MESSAGES BY USING GSM MODULE

Hla Htay Win[1], Pyae Phyo Thwe[2], Mar Mar Swe[3], Me Me Aung[4]

Abstract

This research focuses on the construction and control of GSM module with Arduino Mega by using AT commands which are the instructions used to control a modem. The construction of circuit comprises 8-bit microcontroller ATMega-328P, GSM module (SIM 900A), 16x2 liquid crystal display, 4x4 keypad, GSM SIM card and power supply. GSM module is used to communicate with the mobile phone network for calling and messaging purpose. The system used in this research can act as a simple mobile phone using Arduino Mega. GSM module is used as an interface between Arduino and any other mobile phones to make the connections for this system. C++ programming language is used for the codes to operate the whole system. A program code is loaded into the ROM of ATMega-328P microcontroller and runs the commands. The system can make the calls and send the messages to any phone number.

Keywords: AT commands, GSM module (SIM 900A), ROM, Arduino Mega, ATMega-328P,

Introduction

GSM stands for Global System for Mobile communications. This is a global standard to use GSM modules inside the cellular phones for connecting with any mobile network around the world. In certain applications, the microcontroller-based systems must be connected with the GSM network which will enable a user to control the system by sending messages or making a call. The systems can also send messages to the user to alert or inform about the status of the system running.

For all of such cases, a separate GSM module is used rather than using the mobile phone. The advantage of using a GSM communication with a system or device is that the user can control the system wirelessly no matter how far it is as long as both the user and the device are in a cellular coverage area, compared to any other wireless communication.

The Arduino can communicate with the other devices using its digital I/O, serial port, I2C port, SPI port and etc.

[1,3] Dr, Lecturer, Department of Physics, University of Yangon

[2.] MRes Candidate, Department of Physics, University of Yangon

[4.] Dr, Assistant Lecturer, Department of Physics, University of Yangon

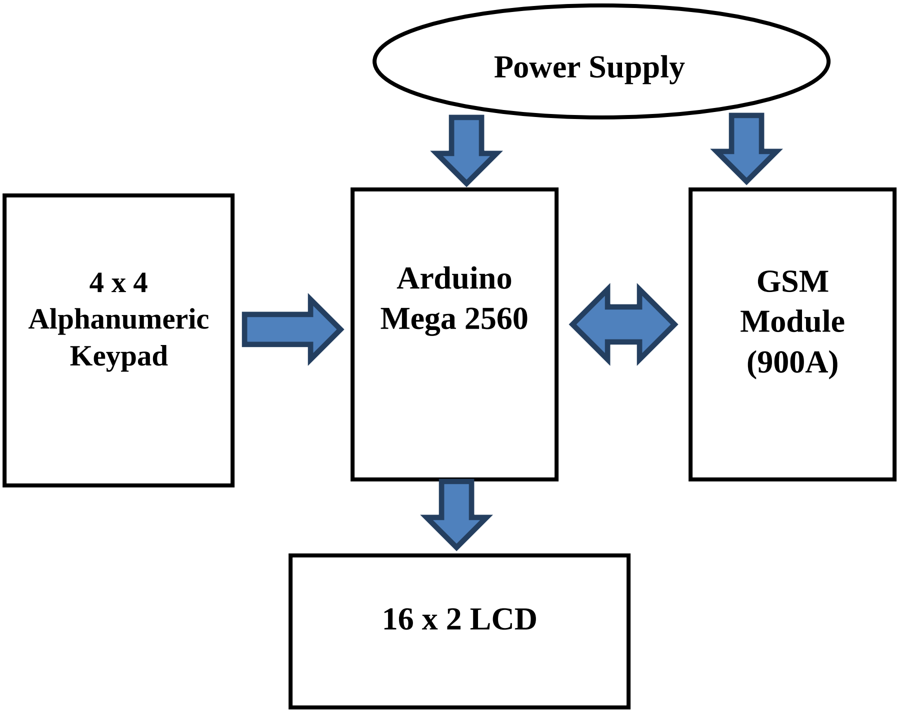

Figure 1: Block diagram of the call and send messages by GSM module

GSM module is used as an interface between Arduino and any other mobile phones to make the connections for this system. A GSM Module is basically a GSM Modern (like SIM 900A) connected to a printed circuit board (PCB) with different types of output taken from the board. The block diagram of calling and sending messages by GSM module is shown in Figure 1.

Function of Components in The Circuit

In this research, Arduino Mega 2560 is used to control the features of whole system and interface all the components in the system. GSM module is used to communicate with the mobile phone network for calling and messaging purpose. A 4x4 alphanumeric keypad is used for taking all kind of inputs including entering mobile number, typing messages, making a call and sending SMS. All of the features will be performed by using alphanumeric keypad. Alphanumeric is a method to enter the numbers and alphabets both by using the same keypad. The 2x16 LCD is used to show the messages, instructions and alerts.

Circuit Diagram and Construction of the Circuit

Insert the SIM card by locking it to GSM module, connect the adapter to GSM module and turn it ON. Circuit Diagram of the system for interfacing GSM SIM900A and Arduino is shown in Figure 2. The following pins of 16x2 LCD: RS, EN, D4, D5, D6 and D7 are connected with pin number 24, 25, 26, 27, 28 and 29 of Arduino respectively. RX and TX pins of GSM module are directly connected to pins of Arduino: D0 and D1 respectively.

The 4x4 keypad Row pins: R1, R2, R3 and R4 are directly linked to pin number 11, 10, 9, 8 of Arduino and Colum pins of keypad: C1, C2, C3 and C4 are linked with pin number 7, 6, 5, 4 of Arduino. The flowchart diagram of the circuit can be seen in Figure 3.

Operation of the Circuit

When the system received the +5V power supply voltage, it will be searching for the network. If the system is ready to use, Call → C and SMS → B will be displayed on the LCD. And pressing 'B' from keypad will lead to 'Initializing SMS', and if 'Enter No and Press 'D' is performed, after that 'Enter Rept No:' will appear successively on the LCD screen. The user needs to press the key 'D' after typing the phone number through keypad. As soon as 'Enter your SMS' will appear, the text can be pressed and the user has to press the key 'D'. After pressing the 'D', 'Sending SMS' will appear while GSM module is working and 'SMS sent' will be displayed after sending the message. The phone of recipient will receive the message. This system will be back to the ready state by showing Call → C and SMS → B again on LCD screen after performing the messaging command.

When the user presses the key 'C', 'After Enter No.', 'Press C to Call' and then, 'Enter Number' will appear. In this time, the user can press the phone numbers, and key 'C'. Then, the user can receive a call ringing on the phone screen. After the system had done performing the command, it will be waiting for the next command. The photo of the whole circuit is shown in Figure 4.

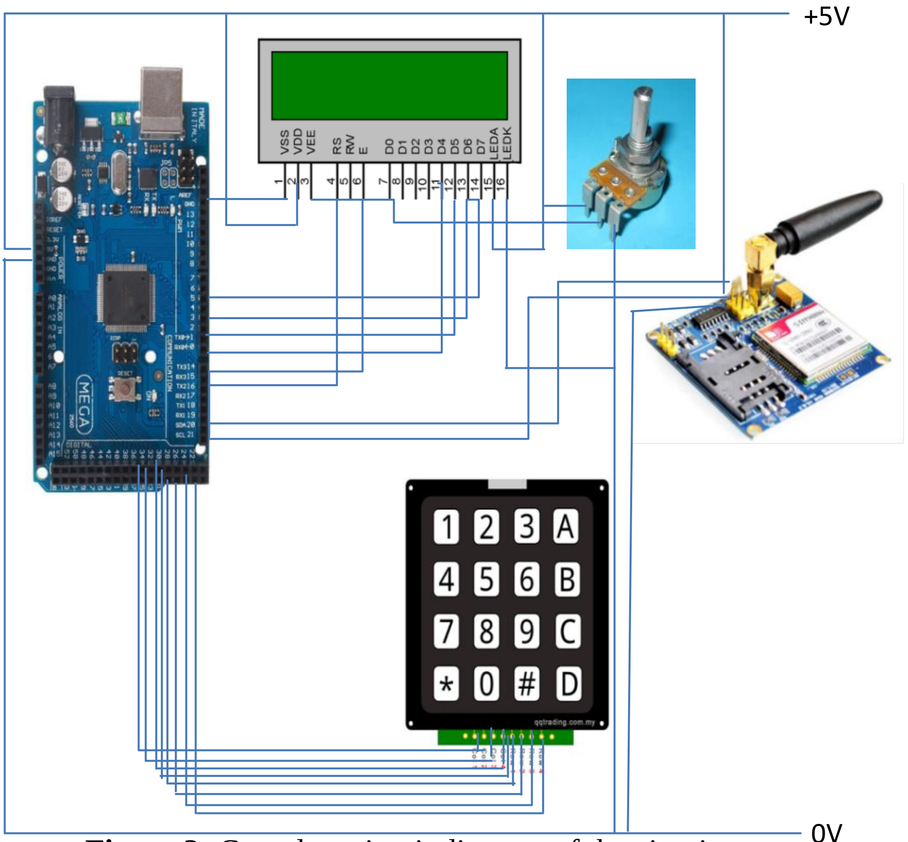

Figure 2: Complete circuit diagram of the circuit

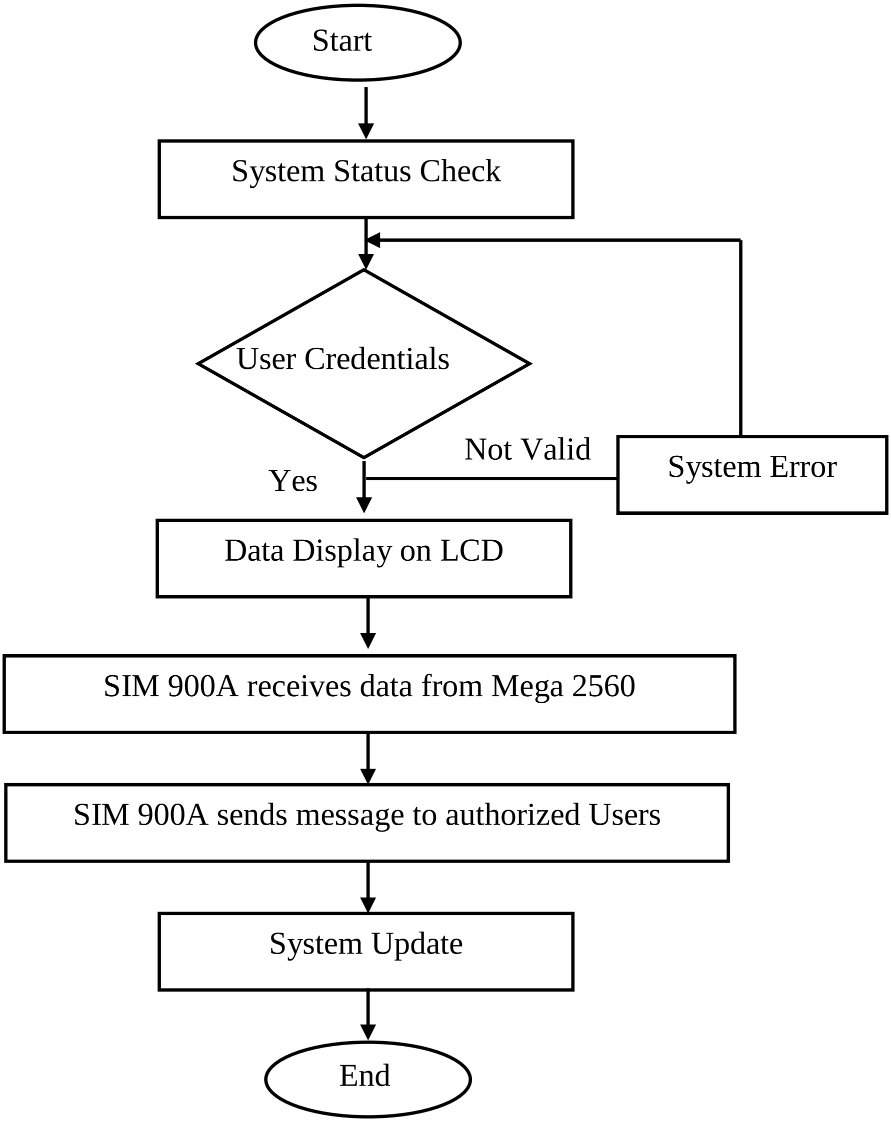

Figure 3: Flowchart diagram of the circuit

Results and Discussion

GSM technology is used to communicate with mobile phones. GSM stands for Global System for Mobile communication. The module supports communications in 900MHz band and power requirement is 5-12V inputs but 5V supply is used for this circuit. Therefore, it is feed 5V and 1A power supply. The GSM shield accepts the card in the mini-SIM format (25mm long and 15mm wide). After the key 'B' from keypad is pressed to send a SMS, the phone number of recipient and text message to be sent can be written from keypad and shown on serial monitor or LCD screen. The phone number of recipient and text message can be edited on serial monitor and LCD screen. When GSM phone receives a message, the text and the number will be shown on phone screen. When the key 'C' is pressed, the phone will be ringing, and the user can see the incoming call on the phone screen. This circuit is tested only for sending messages and making phone calls. This research can be extended by adding receiving messages and phone calls functions for further study. The photo of calling and sending messages using GSM module is shown in Figure 5 and 6.

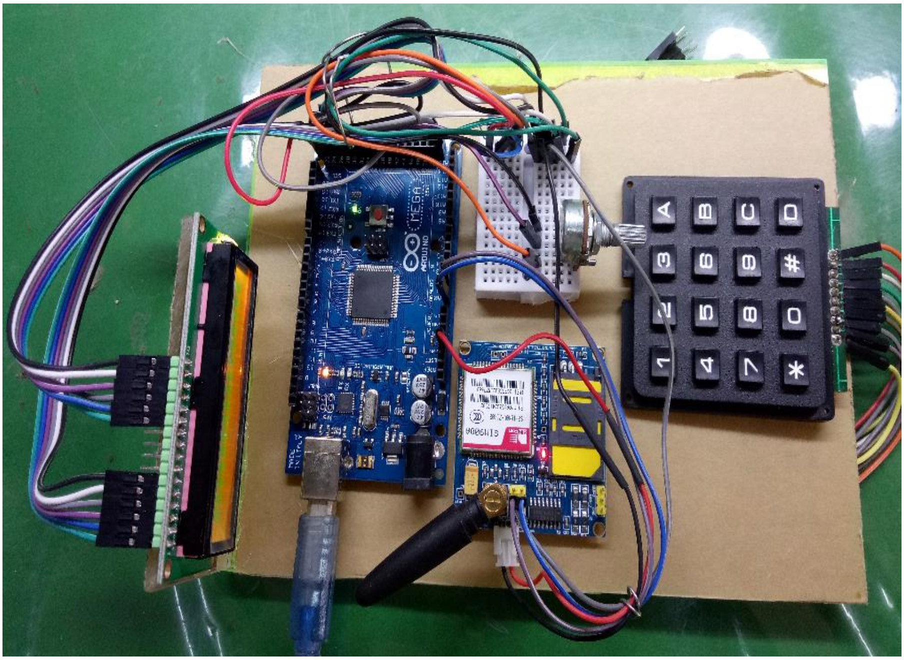

Figure 4: Photo of the call and send messages circuit using GSM Module

Conclusion and Future Work

This circuit was costly and not compacted but it is easy to use for everyone. This device allows only commendable SIM card number. This research makes sure for the researcher to get a great deal of knowledge about GSM technology. The system can be used to connect, making a phone call and sending messages. The advantage of using a GSM communication with a system or device is that the user can control the system wirelessly no matter how far it is as long as both the user and the device are in a cellular coverage area, compared to any other wireless communication. This is a flexible way to control and explore the services of the mobile. AT commands are used in the system. This system is tested only one-sided communication, for calling and messaging from GSM modem which is connected to the Arduino to any kind of mobile network.

Figure 5: Photo of the calling the phone using GSM module

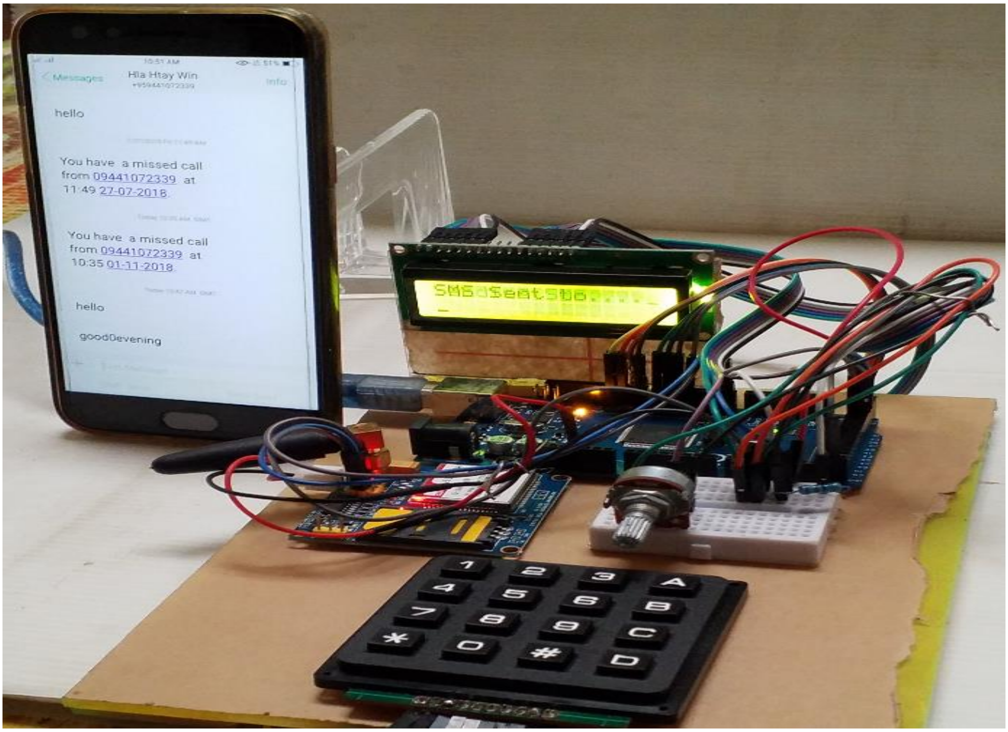

hello

You have a missed call from 09441072339 at 11:49 27-07-2018.

You have a missed call from 09441072339 at 10:35 01-11-2018.

hello

good0evening

Figure 6: photo of the sending the message using GSM module

The system presented in this research is the first step which made to realize the design of a cell phone by exploring various material, shapes and some functions. The application can be upgraded by adding new functionalities such as receiving text messages, receiving phone calls, rejecting an incoming call, including a phone book and a caller ID, and showing the time.

Acknowledgements

I would like to thank Professor Dr Khin Khin Win, Head of Department of Physics, University of Yangon for her encouragement to do this work.

I would like to express sincere thanks to Dr Aye Aye Thant, Professor, Department of Physics, University of Yangon, for her useful advice in the preparation of this research.

References

Banzi, M. (2009). Getting Started with Arduino, O'Reilly media Inc, 2nd Edition, California.

Duxiaoming, C. Y. (2009). "The realization of greenhouse controlling system based on wireless sensor network [j]," *journal of agricultural mechanization research*, 6, 141-144.

Longmont, D. (2008). Gsm/gprs module. Linksprite technolgies, Gsm characteristics. Retrieved from the gsm server online website: http://gsmserver.com/articles/gsm charact.php

Prachi, K. & Bhalerao, V. (2009). Gsm based security system for examination paper. *International journal for engineering applicationsand technology*, 4, 62-65.

Purdum ,J. (2012). Beginning C for Arduino: Learn C Programming for Arduino, Ed. Michelle L., Apress media, California.

Rahali, A., Guerbaoui, M., Ed-dahhak, A., Elafou, Y., Tannouche, A., Lachhab, A., & Bouchikhi, B. (2011). Development of data acquisition and greenhouse control system based on gsm. *International journal of engineering, science and technology*, 3(8), 297-306.

J. Myanmar Acad. Arts Sci. 2019 **Vol. XVII. No.2A**

HEART BEAT AND BODY TEMPERATURE MEASUREMENT WITH HEART BEAT AND TEMPERATURE SENSORS

Me Me Aung[1], Sandar Oo[2], Hla Htay Win[2], Thandar Aung[1]

Abstract

The main purpose of this research work is intended to measure the blood pressure and body temperature of human body. The Arduino microcontroller Uno board, heart beat sensor, Temperature sensor (LM-35) and 20x4 Liquid Crystal Display are responsible for reliable operation. Heart beat sensor senses the blood pressure and temperature sensor senses the temperature of the body for human. The obtainable data from the sensors are sent to the Arduino microcontroller. Arduino microcontroller Uno board is used as main control circuit of this system. The software code for the proposed system is written by using C programming Language. The output is on the Liquid Crystal Display and serial plotter. Blood pressure and body temperature are very important for human body. The developed device is shown acceptable outcomes when compared with other measuring devices.

Keywords: Arduino Uno, Heart Beat Sensor, Temperature sensor (LM-35), 16 x 2 Liquid Crystal Display, C programming language.

Introduction

Health monitoring is important to be checked regularly in order to make sure our body constantly remains in healthy and excellent condition. The heart rate is a basic health sign, beneficial in both medical measurements and home health care. Heart rate simply indicates the soundness of our heart. Heart rate varies according to the demand of muscles to absorb oxygen and excrete carbon dioxide changes such thing happen during exercise or sleep. Normally the heart rate which is calculated for a resting person is about to 70 bpm for adult males and 75 bpm for adult females. A heart rate monitor is simply a device that takes a sample of heartbeats and calculates the heart beats per minute and the information can easily track the current heart condition. Body temperature is also a general indication of body condition. Normal human body temperature is (98.6°F ± 0.7°F) and it varies activity of the

---

[1] Dr, Assistant Lecturer, Department of Physics, University of Yangon

[2] Lecturer, Department of Physics, University of Yangon

person as well as place of measurement. Since heart rate and body temperature are the most vital notable indexes of the human health, an affordable device to measure such indexes will be helpful for human health. In general, medical equipment is expensive. In emergency situation, time should not be wasted. Sometimes continuous assessment is also necessary. Therefore, an automated system for continuous measuring of heart rate and body temperature is very much essential. Heartbeat Sensor is an electronic device that is used to measure the heart rate. The normal body temperature is about 37°C or 98.6°F.

In this paper, a machine is designed and constructed. Different mechanical hardware are constructed and tested repeatedly, until an operation prototype is achieved. A machine design consists of an Arduino Uno, buzzer, LM35 temperature sensor, LCD display, pulse sensor and PC. Temperature can be measured by using different types of sensors. The temperature sensor produces analog output voltage which is proportional to the temperature. The temperature sensor requires analog to digital (A/D) converter so that the analog output voltage can be converted to digital form. The output of the temperature sensor is connected to the Arduino Uno. The Arduino Uno processes this data and displays it in LCD. This paper describes the design of a very low-cost remote patient monitoring system which measures heart rate and body temperature of a patient. This device is needed during emergency period or for saving time of both patient and doctor.

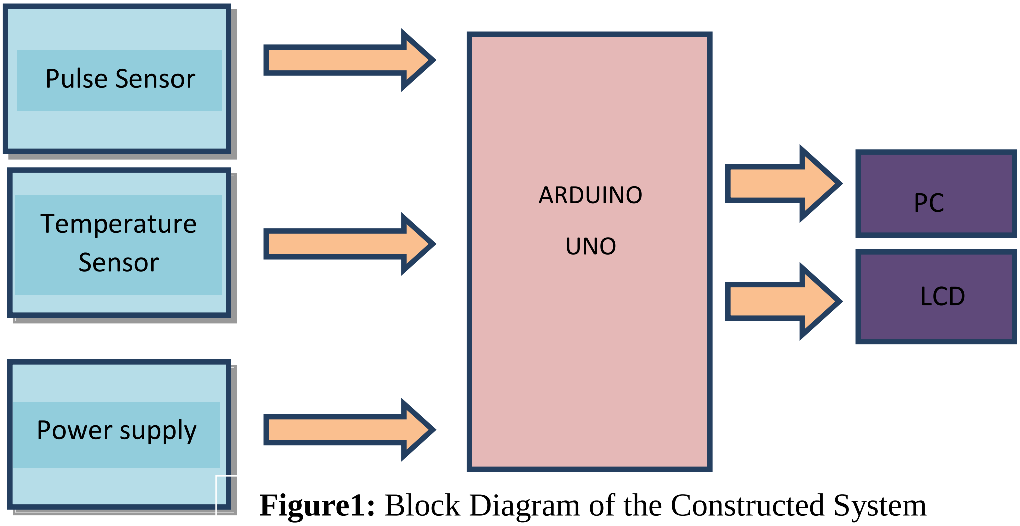

Figure1: Block Diagram of the Constructed System

Theoretical Background

Arduino Uno Microcontroller Board

Figure 2: Arduino UNO board

The Arduino is a microcontroller board based on the ATmega8. It has 14 digital -input/output pins (of which 6 can be used as PWM outputs), 6 analog inputs, a16 MHz ceramic resonator, a USB connection, a power jack, an ICSP header, and a reset button. It contains everything needed to support the microcontroller; simply connect it to a computer with a USB cable or power it with a AC-to-DC adapter or battery to get started. "Uno" means one in Italian and is named to mark the upcoming release of Arduino 1.0. The Uno and version1.0 will be the reference versions of Arduino, moving forward. The Uno is the latest in a series of USB Arduino boards, and the reference model for the Arduino platform.

IC LM35 Temperature Sensor

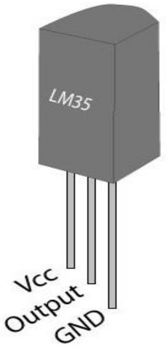

Figure 3: Pin diagram of IC LM35

The LM35 is a popular and inexpensive temperature sensor. It provides an output voltage of 10.0mV for each degree Centigrade of temperature from a reference voltage. The output of this device can be fed to A/D Converter; any microcontroller can be interfaced with any A/D Converter for reading and displaying the output of LM35. The circuit should be designed, so that output should be at 0V when the temperature is 0 degrees Centigrade and would rise to 1000mV or 1.0V at 100 degrees Centigrade. To get the temperature value accurately, output voltage must be multiplied with 100.

The LM35 series are precision integrated-circuit temperature devices with an output voltage linearly proportional to the Centigrade temperature. The LM35 device has an advantage over linear temperature sensors calibrated in Kelvin, as the user is not required to subtract a large constant voltage from the output to obtain convenient Centigrade scaling. The LM35 device does not require any external calibration or trimming to provide typical accuracies of ±1⁄ 4°C at room temperature and ±3⁄ 4°Cover a full 5°C to 150°C temperature range. Lower cost is assured by trimming and calibration at the water level. The low-output impedance, linear output, and precise inherent calibration of the LM35 device makes interfacing to readout or control circuitry especially easy. The device is used with single power 2 Applications supplies, or with plus and minus supplies. As the LM35 device draws only 60 μ A from the supply, it has very low self-heating of less than 0.1°C in still air. The LM35 device is rated to operate over a−55°C to 150°C temperature range, while the LM35C device is rated for a−40°C to 110°C range (−10° with improved accuracy). The LM35-series devices are available packaged in hermetic TO transistor packages, while the LM35C, LM35CA, and LM35D devices are available in the plastic TO-92 transistor package.

Liquid Crystal Display (LCD)

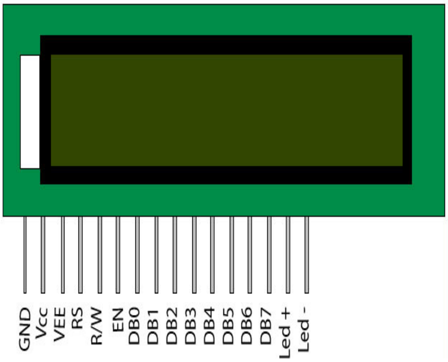

Figure 4: pin diagram of 16x2 LCD

LCD (Liquid Crystal Display) screen is an electronic display module and find a wide range of applications. A 16x2 LCD display is very basic module and is very commonly used in various devices and circuits. These modules are preferred over seven segments and other multi segment LEDs. The reasons being: LCDs are economical; easily programmable; have no limitation of displaying special & even custom characters (unlike in seven segments), animations and so on. A 16x2 LCD means it can display 16 characters per line and there are 2 such lines. In this LCD each character is displayed in 5x7 pixel matrix. This LCD has two registers, namely, Command and Data. The command register stores the command instructions given to the LCD. A command is an instruction given to LCD to do a predefined task like initializing it, clearing its screen, setting the cursor position, controlling display etc. The data register stores the data to be displayed on the LCD. The data is the ASCII value of the character to be displayed on the LCD.

Pulse sensor

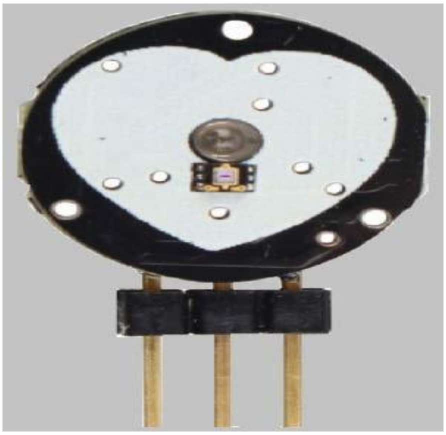

Figure 5: Pulse sensor

Figure 6: Image of visible greenlight sensor

Pulse sensor has three pin and connection of it with Arduino is very easy. Connection is made through 5V supply provided by Arduino, the ground pin of the pulse sensor is connected to the ground of the Arduino and the signal pin to the A0 of Arduino. There are several types of LED with a different wavelength that is suitable to detect the heart rate. The difference of the signal produce in between visible light and IR is demonstrated. The wavelength of the visible greenlight PPG ranging from 495–570 nm is normally being used due to the reason that it had shown to have a minimal influence from motion artefacts. The visible greenlight of 550 nm wavelength is used as shown in Figure (6). IR is an invisible light that cannot be seen directly by human eyes. It has a longer wavelength than visible light which is around 700 nm-1 mm, and it frequencies is lower than a visible light. IR is also commonly used to record the arterial heart rate directly from the skin.

Where nnn is an integer between 1 and 999. The body temperature of the patients and heart beat pulses per minute are displayed on the LCD display. After that, pulse sensor connected to Arduino Uno board, positive pin to +5V, negative pin to GND and S to A0 pin. Potentiometer connected to GND, V0 and Vcc of LCD. Potentiometer is connected to pin3 of LCD (contrast adjust pin). And then, Arduino Uno Board join to computer via USB Cable. Temperature sensor is used to measure the body temperature. Heartbeat sensor is used to measure the function of heart by blood flow through Finger. The output of each sensor is interfaced with Analog to Digital circuit (ADC) pins of microcontroller.

Construction of the Circuit

The components are solder on the printed circuit board as design of the drawings on the printed circuit. There is only one circuit to make soldering components. Components and jumpers were inserted and soldered in the following procedure;

1. The wire jumper connections
2. Resistors
3. Switch and LED
4. LM 35
5. pulse sensor Arduino
6. buzzer
7. Potentiometer 10K

Instead of soldering the Arduino Uno directly on the board. And then, temperature sensor and pulse sensor are connected to the Uno board. Pins D_4, D_5, D_6, D_7 of LCD are joined to Arduino Uno pins D_2, D_3, D_4, D_5, D_6, D_7. LM 35 is an analog temperature sensor which outputs an analog signal. Arduino Uno has an analog pin, LM 35 analog output pin connected to analog input pins A0 of Arduino. The LCD screen is display the temperature in Celsius. Pulse sensor connected to Arduino pin. The calculated heart rate is displayed on an LCD in beats- per- minute in the following,

Rate = nnn bpm

Where nnn is an integer between 1 and 999. The body temperature of the patients and heart beat pulses per minute are displayed on the LCD display. After that, pulse sensor connected to Arduino Uno board, positive pin to +5V, negative pin to GND and S to A0 pin. Potentiometer connected to GND, V0 and Vcc of LCD. Potentiometer is connected to pin3 of LCD (contrast adjust pin). And then, Arduino Uno Board join to computer via USB Cable. Temperature sensor is used to measure the body temperature. Heartbeat sensor is used to measure the function of heart by blood flow through Finger. The output of each sensor is interfaced with Analog to Digital circuit (ADC) pins of microcontroller.

Operation of the circuit

Heartbeat Measurement

The circuit operation of Arduino Uno based heartrate monitor system is constructed. Upload the code to Arduino Uno and power on the system. Firstly, any finger (except the Thumb) attach the pulse sensor, it can be detect the pulse easily. Then the pulse sensor is measure the change in volume of blood, which occurs when every time heart pump, blood in the body. This change in the light intensity through that organ. The Arduino is converted this change into the heart beat per minute (BPM). While the sensor is collecting the data, sit down and relax, do not shake the wire as it might result in a faulty values. The heart rate reading for visible greenlight and IR respectively. It indicates that both of the signals are simultaneous and given a similar heart rate value but visible greenlight show smoother output signal of heart rate. After the result is displayed on the LCD and PC monitor.

Temperature Measurement

LM35 is an analog temperature sensor which outputs an analog signal. Microcontrollers don’t accept analog signals as their input directly. Thus, need to convent analog output signal to digital before feeding to a microcontroller’s input. For this reason, use an ADC. Modern day boards like Arduino and most modern day microcontroller come with inbuilt ADC. Arduino Uno has an in built 10-bit ADC (6 channel). Make use of this in built ADC, there are 6 analog input pins numbered from A0 to A5. Connect analog out of LM35 to any of these analog input pins of Arduino. When the power is turned on, a LED on PCB start glowing, indicating that circuit is working properly. A temperature sensor LM 35 which gives us room temperature in °C. That temperature is displayed on the LCD.

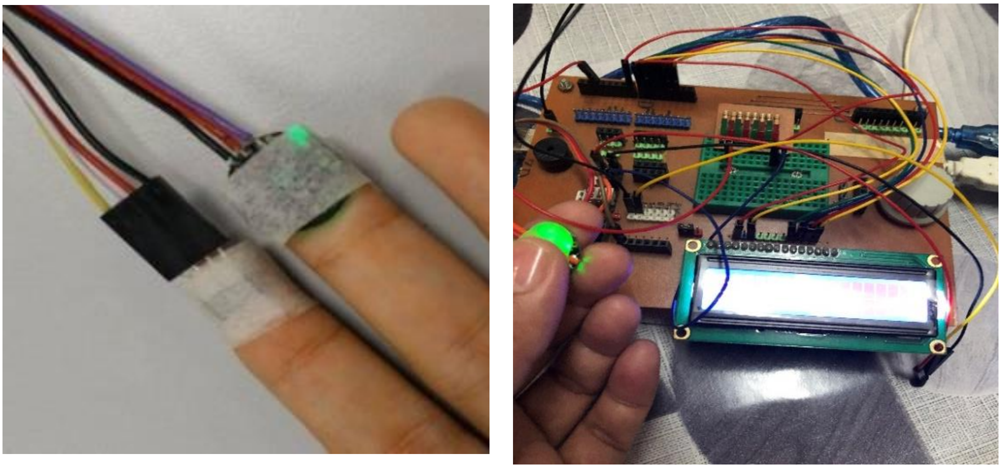

Figure 7: pulse rate Output display on LCD

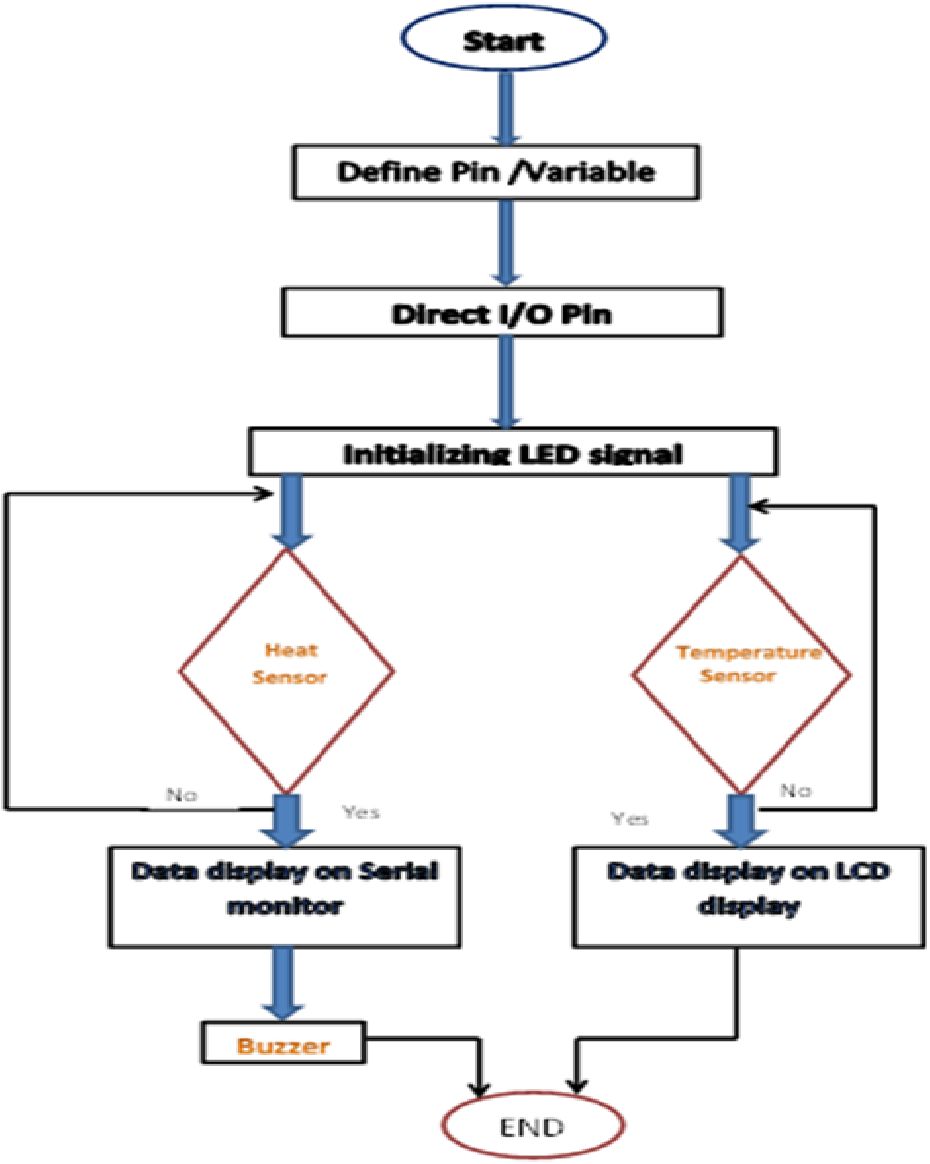

Figure 8: Flow diagram of the whole System

Result and Discussions

Once the circuit has built, codes have been uploaded into the Arduino Uno then the project is ready for testing. The heart rate was obtained using the pulse sensor to determine the accuracy of the project's circuit. The circuit is supplied by 3.3V power. For accurate reading as much as possible, the finger needs to be placed close to sensor. The output result as an ECG in the monitor. The results were outputted via the Serial Monitor as shown in Figure 9 below.

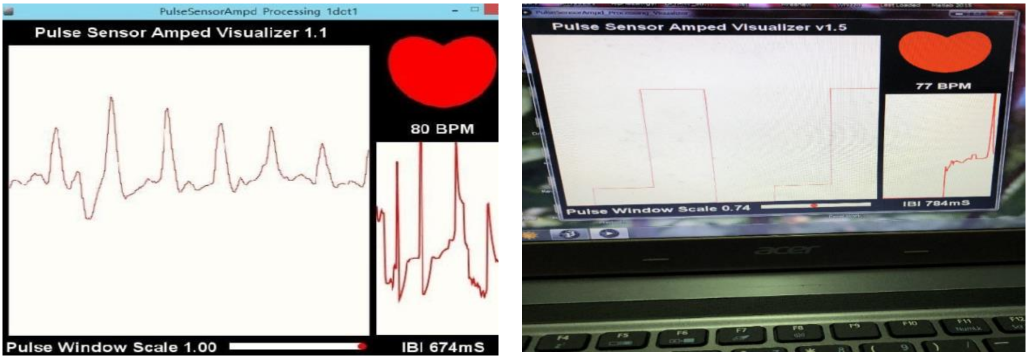

Figure 9: Pulse rate output display on PC monitor

Body temperature was obtained by interaction between the fingertip and the LM35. First we measured the temperature using thermometer then we measured it again using LM35 to compare the results. At the time of testing, measured temperature was almost 27°C and Figure 10 showed the body temperature measured by sensor and displayed in the LCD continuously.

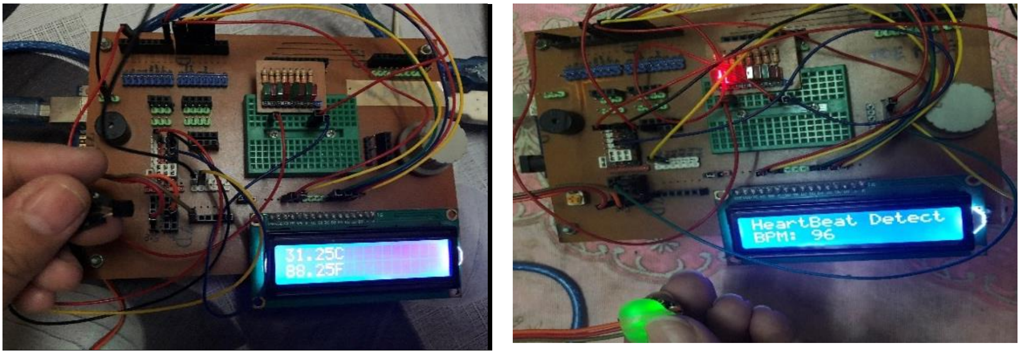

Figure 10: Sensor placement while taking the reading

Conclusions

The pulse rate sensor senses the hart beat and the result is displayed on serial monitor as spectrums. The output spectrums look like ECG spectrums. To show these spectrums, the Pulse Sensor Amped Visualizer 1.1 application need to installed in PC. The display screen contains two windows. The display spectrums of each windows are not different from each other. The measured heart rate is displayed on the screen by BPM unit. The body temperature is measured by temperature sensor LM35. The output voltage (mV) is sent to the AT mega 328 microcontroller input. These analog inputs are converted digital signal and gave the measure data in °F and °C. The result is not much different with the other thermometer results.

Table 1:The constructed system is designed and constructed for medical purpose.

Construct (°C)	Thermometer (°C)
29.30	30
31.25	31
33.32	32
34.67	33

Acknowledgement

I am very grateful to Professor Dr Khin Khin Win, Head of Department of Physics, University of Yangon, for her kind permission to do this work.

I wish to thank Dr Aye Aye Thant, Professor, Department of Physics, University of Yangon, for her encouragement to do this work.

References

J. Lee, K. Matsumura, K. I. Yamakoshi, P. Rolfe, S. Tanaka and T. Yamakoshi. (2013). "Comparison between red, green and blue light reflection photoplethysmography for heart rate monitoring during motion". *In Engineering in Medicine and Biology Society (EMBC)*, 1724-1727. IEEE.

K. Parsons. (2014). The Effects of Hot, Moderate, and Cold Environments on Human Health, Comfort, and Performance. in Human thermal environments Crc Press.

M. N. I. Khan, D. F. Noor, M. J. H. Pantho, T. S., Parveen, F. Abtahi, and M. I. H. Bhuiyan. (2013). "A low cost optical sensor based heart rate monitoring system," *In International Conference on Informatics, Electronics and Vision (ICIEV)*.

Miah, M. A. Raihan, S. Basak, M. R. Huda and A. Roy. (2013). "Low cost computer based heart rate monitoring system using fingertip and microphone port," *In International Conference on Informatics, Electronics and Vision (ICIEV),* 1-4. IEEE.

R. A. Ramlee, M. Azlishah, B. Othman, M. Ikhwan, and B. Abdul. (2014). "Low Cost Heart Rate Monitoring Device Using Bluetooth," *In Information and Communication Technology (ICoICT),* 2, 42-46. IEEE.

W. H. M. Saad, N. A. A. Salam, T. K. Leong and S. N. A. Bahrom. (2014). "Verification of Heart Rate Monitor Using PPG Pulse Sensor". *International Journal of Applied Engineering Research (IJAER).* Vol. 9, 24369-24378.

Y. Maeda, M. Sekine, T. Tamura, A. Moriya, T. Suzuki and K. Kameyama. (2008). "Comparison of reflected green light and infrared photoplethysmography". *In Engineering in Medicine and Biology*.

J. Myanmar Acad. Arts Sci. 2019 **Vol. XVII. No.2A**

LAMPPOST CLIMBING ROBOT UTILIZING ARDUINO DEVELOPMENT BOARD

Poe Zarli Maung[1], Mar Mar Swe[2], Hla Htay Win[3], Khin Mar Win[4]

Abstract

Design and construction of a model of Lamppost Climbing Robot is implemented by using the locally avaivable components. The system design consists of two stepper motors, two ULN 2003 ICs, limited switches, 4-key remote transmitter and receiver and Arduino Nano development board. The Arduino Nano board utilizes ATMega328 microcontroller. A program sketch was created with Arduino IDE software to operate the system. The robot consists of two parts – motor unit and controller unit. The circuits and motors are mounted on each unit. The system is very useful and can be applied to send tools or objects in dangerous places, instead of human.

Keywords: ARDUINO NANO, Remote Control, Stepper Morts, Ball Barings and Springs

Introduction

The term robot comes from a Czech word, robota, meaning “forced labor”. A robot is a machine designed to execute one or more tasks automatically with speed and precision. People have been interested in building machines to do work for them for a long time. But it takes time and money to build such a machine. Leonardo da Vinci designed a man-shaped machine to look like a knight in 1464. But it was controlled with ropes and wheels. The most successful robot design was build in 20th century and they did not look like people. They were designed to use. George Devol made the first of these, the Unimate, in 1954, with one arm and one hand. They are used to lifting, transporting and stacking pieces of metal that were too hot or heavy for people. The engineers could program the machine to operate.

A robot is an integration of mechanics, electronics and software. There are many different reasons for using a robot but the major reason for most applications is to eliminate a human operator. The most obvious reason is to save labor and reduce cost in production sites. The other reason is safety concern, a robot can handle dangerous materials, such as radioactive

---

[1] MRes Candidate, Department of Physics, University of Yangon

[2,3] Dr, Lecturer, Department of Physics, University of Yangon

[4] Dr, Lecturer, Department of Physics, Meiktila University

materials, thermal radiation devices, defusing a bomb, climbing high towers or poles, sending underground caves and investigating a toxic area, which are not suitable to a human being. Therefore, various kinds of robots are invented for various fields; production sites, military use, scientific experimental use and even for personal helper.

In this thesis, a climbing robot is designed and constructed. Different mechanical hardware are constructed and tested repeatedly, until an operating prototype is achieved. The climbing robot design consists of an Arduino Nano development board, two stepper motors, two stepper motor driver ICs, a 4-key remote transmitter and receiver module, and two lithium ion batteries. The primary purpose of the device is to carry accessories vertically around a lamppost. It is hard working for electric power service workers to climb a lamppost personally. If they are on the top, and some accessories are currently required, the climbing robot is a solution for them. That's why the climbing robot is researched and developed in this thesis report.

In the prototype model, only a few light weight accessories are able to transport vertically. Design and development is infinity, it can be upgraded with powerful motor and can be integrated with sensors to be autonomous, such as changing the bulb of a lamppost automatically instead of human worker.

Construction of the Circuit

The components are soldered on the printed circuit board as design of the drawings on the printed circuit. There is only one circuit to make soldering components. Components and jumpers were inserted and soldered in the following procedure;

1. The wire jumper connections
2. Resistors
3. Switch and LEDs
4. IC socket, and male connector pins
5. Female socket for 4-key remote receiver
6. The green terminal

The resistors, and jumpers, are inserted in their positions and soldered carefully. It is shown in Figure 1. The soldering side was illustrated in Figure 2.

Instead of soldering the Arduino Nano directly on the board, female connector pins are inserted from the component side. Then the pins are soldered carefully from the soldering side. There are two groups of five male connecter pins on the upper side of the circuit. The pins are differentiated with color; the blue is for the stepper motor signal pins and the red for common power pin of the stepper motor. On each group, two stepper motor wire terminal can be fitted on each position. There are two 16-pin IC bases required to solder in their position. But in the moment, only one of the 16-pin dual inline package is available, therefore, two 8-pin dual inline sockets are inserted on the right side of the socket position as shown in Figure 3. There are two blue LEDs on each side of the circuit to indicate the climbing robot operating function. The two 560 Ω resistors are used to limit the current for LEDs. There is a green terminal on the far right of the circuit. It is used to connect with a dc power source. Between the Arduino Nano and the power input, a double pole double throw toggle switch is inserted and soldered for power switching. The last part on the circuit is 4-key remote receiver module and it is also not directly soldered on the circuit. Instead, a 7-pin female header is inserted and soldered on the lower edge of the circuit.

It has not extra power regulator circuits in pcb design, since the Arduino Nano consists of 5 V and 3.3 V on board regulators.

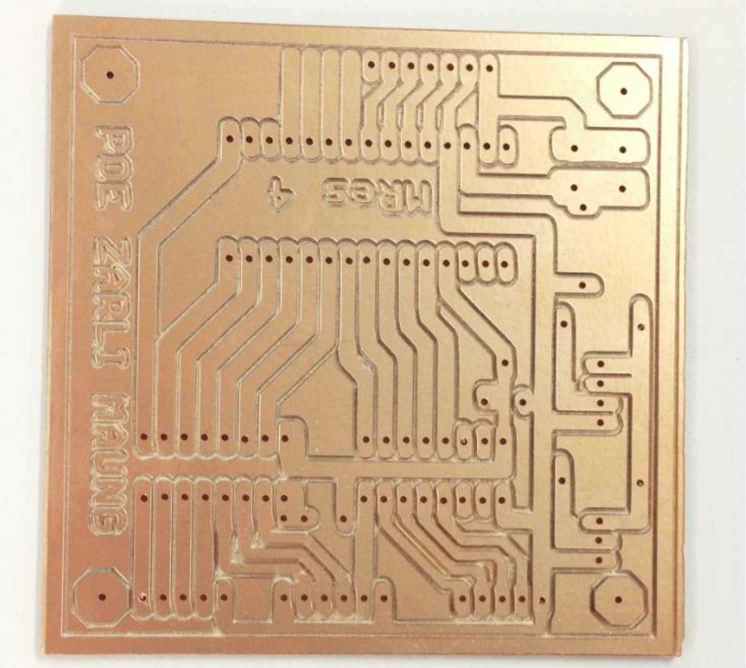

Figure 1: The Result Photo of Printed Circuit Board

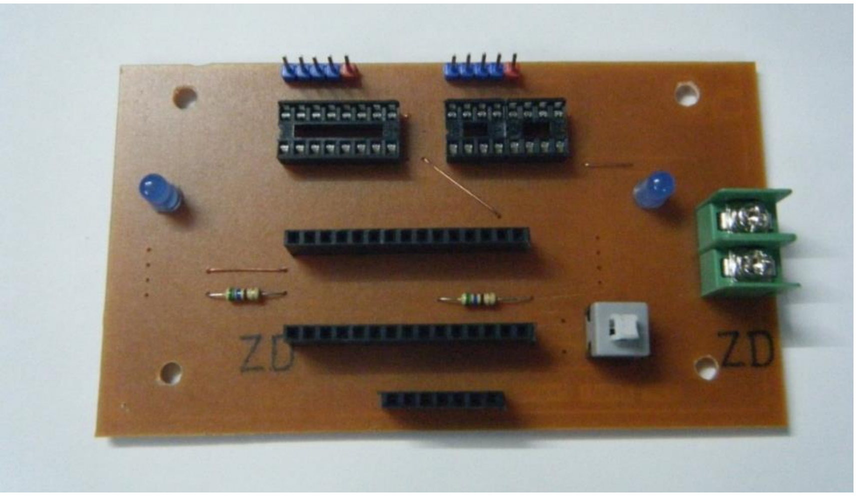

Figure 2: The Components Side of Circuit Board after Soldering

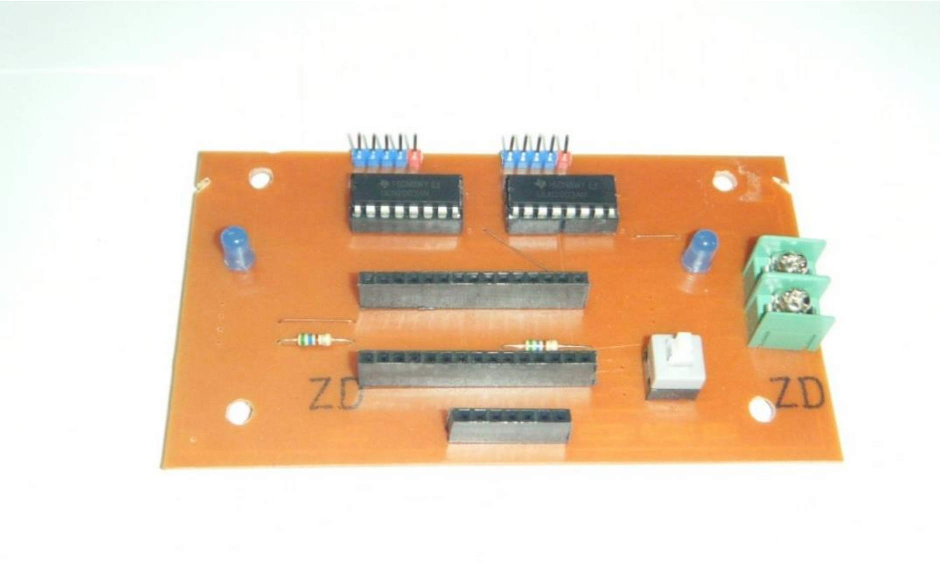

Figure 3: Control Circuit Board Preparation for Control Unit Assembly

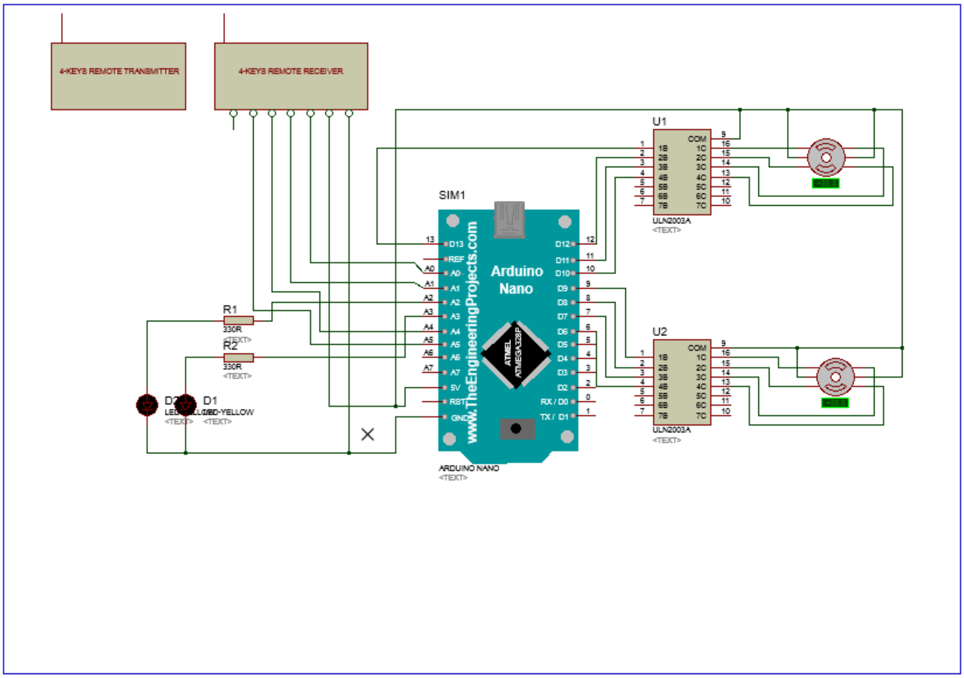

Figure 4: Complete Circuit Diagram of Lamppost Climbing Robot on Proteus Stimulation Software

Assembly of the whole Circuit

The circuit after soldering was tested for soldering shorts between the IC pins and isolated track lines on the board. Some of the soldering shorts are removed by using soldering gun and solder sucker. The circuit design in isolation routine, it was perfectly designed and drawn. Therefore, no more extra wires are connected on the back of the circuit board.

For the hardware assembly of climbing robot, there are a total of four cutting pcb boards. Each pair are attached together and become two units; controller side and motor side. The controller side consists of circuit board and battery unit. The motor side consists of two unipolar stepper motors.

The assembly of controller side was attaching control circuit and battery holder board with 4 mm bolts on each corner. Between the two boards, some spacers and baring wheels are added as shown in the Figure 5. Before inserting the battery and components on the circuit, two battery wires are inserted and screwed on the green terminal as shown in Figure 6. Then the Arduino Nano and remote receiver are inserted in their positions as shown in Figure 7.

Another part to assemble is the motor unit. The motor unit consists of two motor holder plates and a unipolar stepper motor is attached on each plate. The rotor pole of stepper motor is 3 mm and two (50 mm diameter) wheels are attached on each side. The wheels consist of high efficiency rubber tires, with slipping protect on each wheel. The wheel is extruded about 5mm from the motor holder board. Similarly, four baring wheels are inserted in parallel with two stepper motor wheels. But the baring wheels are used only to support smooth climb up/down function. Therefore, the corner of the motor holder board will not jam on the way climbing up or down. There are four pulling springs on each corner of the motor unit. The purpose of the springs is to pull each unit facing against the lamppost. The force of the springs must be balance with the stepper motor. If the springs is stronger than the stepper motor torque, the movement of climbing robot will not achieve. Therefore, it is important. If the stress of springs is very weak, the two facing unit cannot hold the position and will fall back.

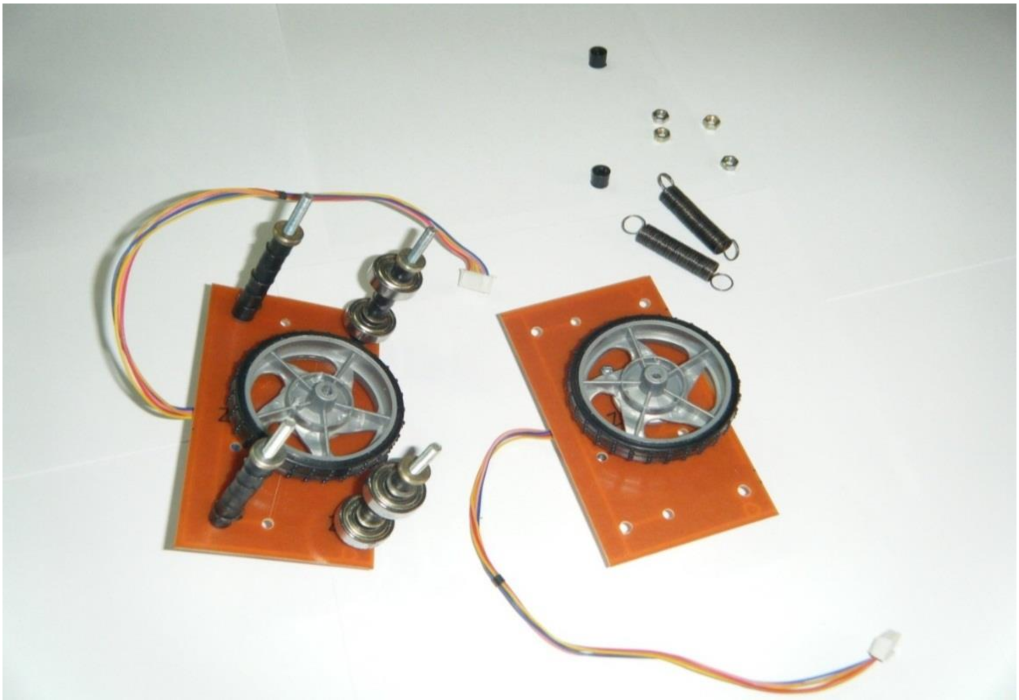

Figure 5: The 50mm Wheels are Attached on Each Stepper Motor

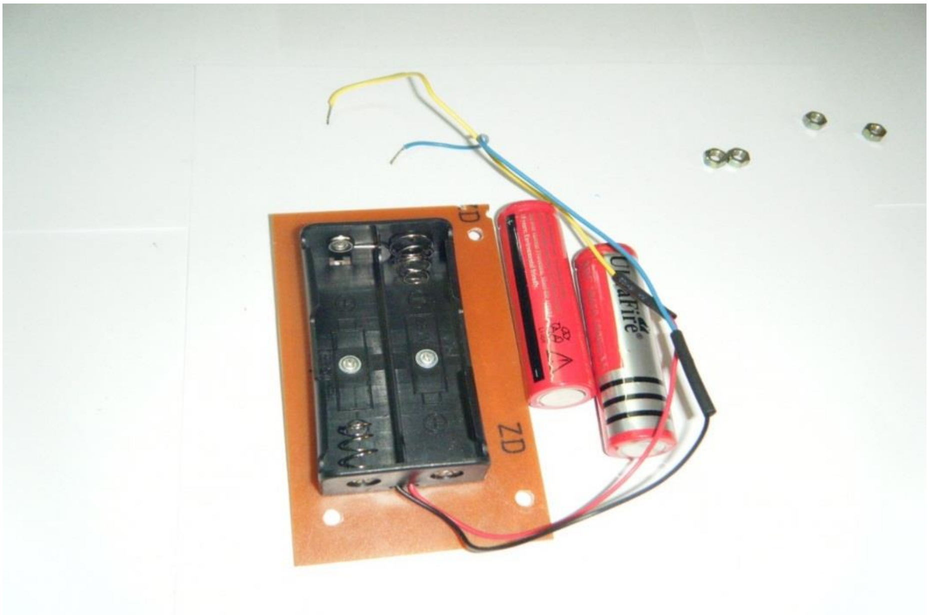

Figure 6: Battery Unit Plate Preparation for Control Unit Assembly

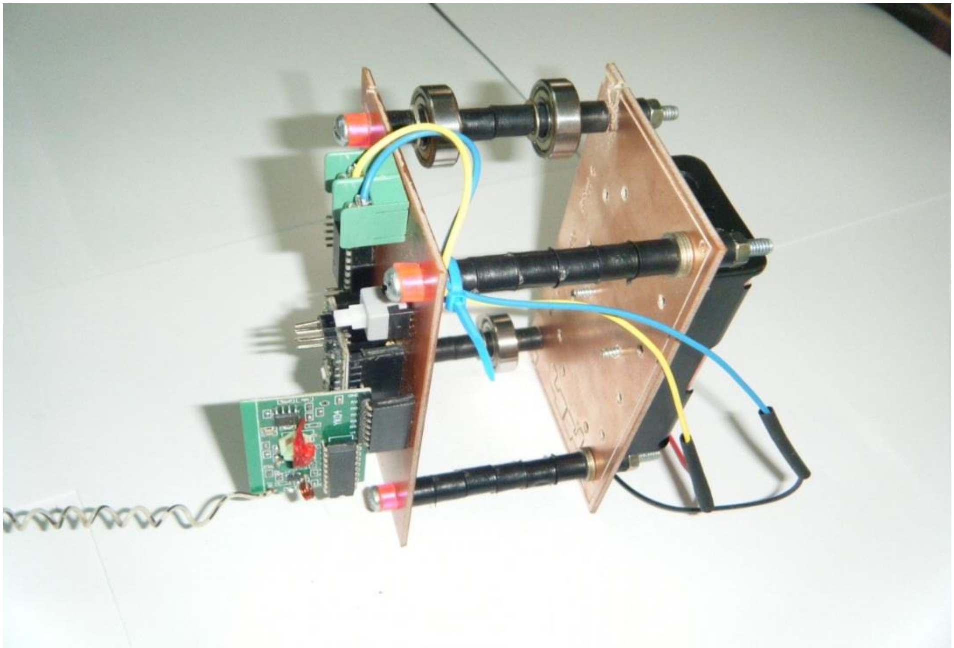

Figure 7: Complete Photo of Control Unit

Flowchart

The initial step to create the program sketch is drawing an outline flow diagram and it is usually known as flowchart diagram. The flowchart illustrate, programming flow with blocks and labels. In regular statements, it is illustrated with rectangular shape text boxes. In decision making process, it is illustrated with diamond shape text boxes. The flowchart of the lamppost climbing robot operating system is illustrated in Figure 8.

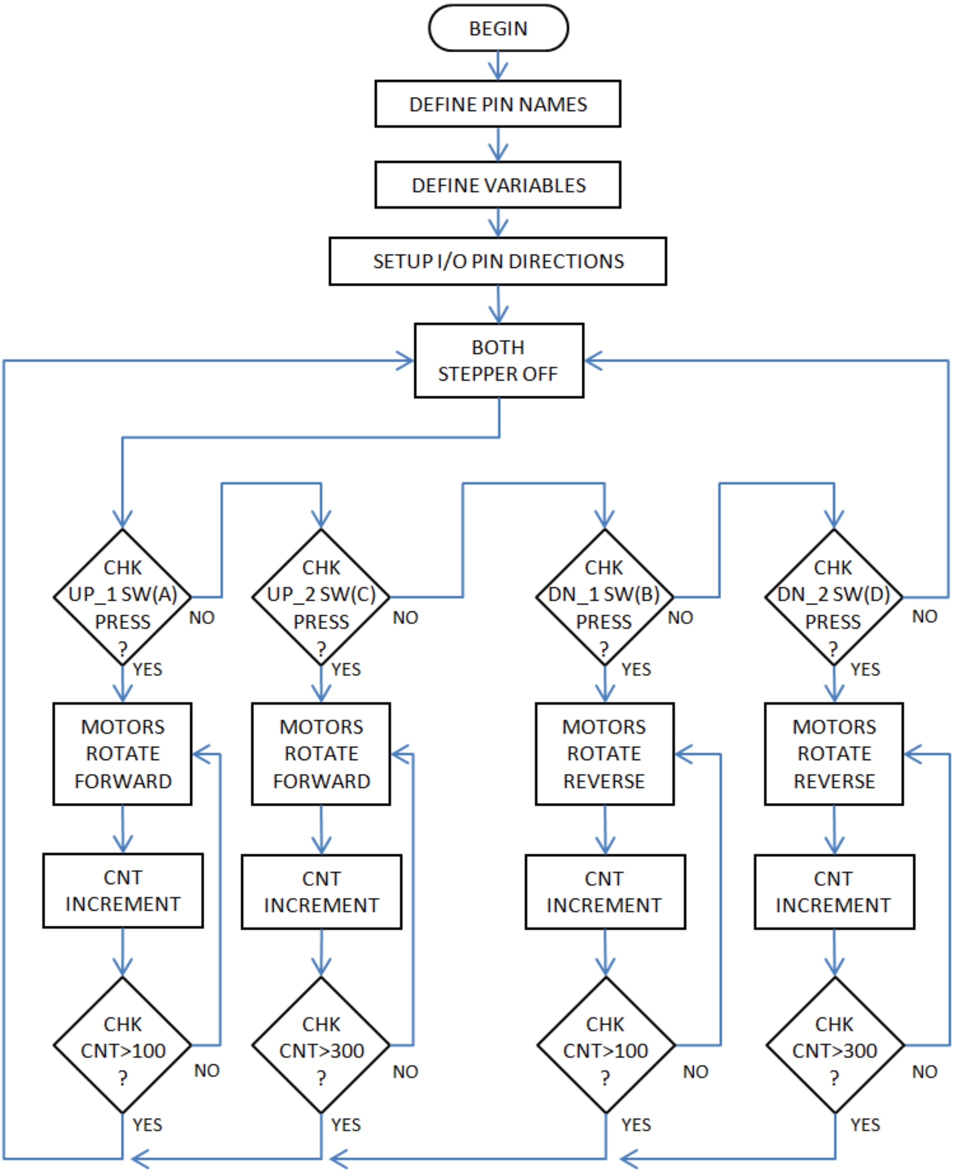

Figure 8: Flowchart Diagram of Lamppost Climbing Robot Control System

Result and Discussion

Research field in flying and climbing robots have been very popular and attractive for many decades, since there are numerous applications that cannot be performed directly by human operators because of difficulties in accessing the operating positions in a proper and safe manner. Some flying devices can move vertically around the wall or a tree, but it is not safe to close with the wall or tree since they are bulky and the propellers can be crush into the wall or tree. But for a climbing robot, it is safe and easy to go over the wall or tree without crushing. But the height and load is limited.

In this research work, a lamppost climbing robot is designed and constructed. It is intended to save the lives of electricians who often climb the lampposts and risk their lives on duty. Instead of checking or repairing personally at the top of a lamp post, a climbing robot can be used safely. The design of the lamppost climbing robot consists of three stepper motors, limit switches, control switches, stepper motor driver circuits and an Arduino development board, utilizing ATMega328. The ATMega328 is an 8-bit microcontroller and it was chosen for numerous pins numbers, 32 kbyte of program memory and easy to develop a prototype developing experiments, which is well suit to the lamppost climbing robot.

The system design consists of two different experimental fields; hardware construction and software creating. The hardware consists of mechanical moving parts and they are used to climb the lamppost. But the hardware mechanisms cannot operate without a microcontroller. The microcontroller is loaded with a program sketch created with Arduino IDE software.

The system design construction can be used in many different practical applications other than climbing lamppost. The system can be used in, inspecting, cleaning, changing bulbs and connecting and cutting the wires over the top of lamppost. The prototype of climbing robots is intended to replacing human operators in the accomplishment of essential safety critical tasks in hazardous environments such as firefighting scenes, petrochemical plants, and nuclear reactors or even in emergency rescue teams.

Conclusion

The lamppost climbing robot control system is designed and constructed. It is constructed on a self-designed printed circuit board. The printed circuit was made by using CNC pcb isolation routing method. Circuit construction and error corrections were made before connecting the Arduino Nano and remote receiver circuit. The microcontroller was loaded with a program code, which is created and tested with Proteus virtual simulator software. After completing the debugging the program is compiled and uploaded into the memory ROM of ATMega328. Then the coding was tested with the constructed prototype circuit board. The results were illustrated with photos in circuit operation title. In the results and observations on actually climbing on a lamppost, there are some difficulties and problems. The speeds of climbing up and down are not equal for both without load and with loads. The climbing down operation is smooth and faster than climbing up operation. Some changes were made for the spring's tensions. Adding springs tension make more difficult to move along the lamppost. Reducing the spring's tension cannot hold the position. For a better and really applicable lamppost climbing robot design, many more developments are required to research. Anyway it is very first prototype of climbing robot and further enhancements and developments may achieve a great help to those electrical powering repair men and telecommunication workers.

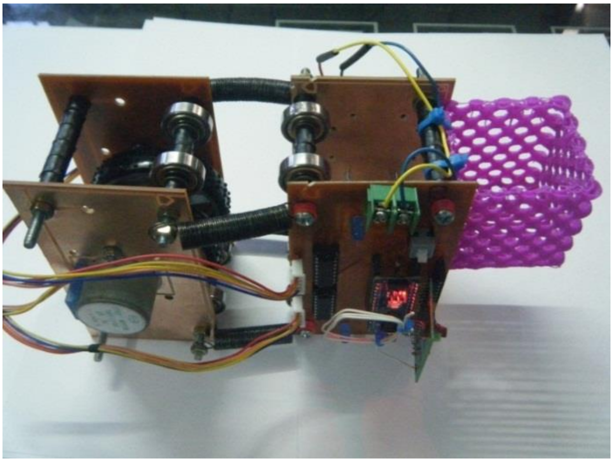

Figure 8: The Climbing Robot Itself Ready to Test

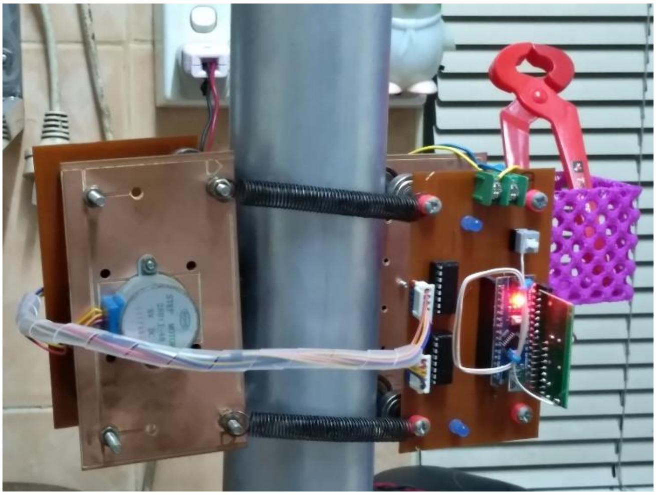

Figure 9 : The Controller Circuit Side of Climbing Robot Attached on the Lamppost

Acknowledgements

I would like to thank Professor Dr Khin Khin Win, Head of Department of Physics, University of Yangon for her permission to do this work.

I would like to express sincere thanks to Dr Aye Aye Thant, Professor, Department of Physics, University of Yangon, for her useful advice in the preparation of this research.

I greatly indebted to my Supervisor, Dr Hla Htay Win, Lecturer, Department of Physics, University of Yangon, for her valuable guidance and encouragements throughout the process of this thesis.

I would like to express gratitude to my Co-supervisor, Dr Mar Mar Swe, Lecturer, Department of Physics, University of Yangon, for her valuable guidance throughout the process of this thesis.

I am also very grateful to all my teachers of the Department of Physics, University of Yangon, for their kind understanding.

References

Brian Evans, (2011). Beginning Arduino Programming: Springer Science + Business Media, LLC., 233 Spring Street, 6th floor, Nework, NY 10013.

Floyd, T. L. (2007). *Electronic Devices*, 7th ed, New Jersey : Prentice- Hall International Inc.

Husain, A.M (2016). Air Quality Monitoring: The Use of Arduino and Android; Journal of Modern Science and Technology, Vol.4.No.1.Pp.86-96

Michael Mc Roberts,(2013). Beginning Arduino: Springer Science + Business Media, LLC., 233 Spring Street, 6th floor, Nework, NY 10013.

J. Myanmar Acad. Arts Sci. 2019 **Vol. XVII. No.2A**

THE INVESTIGATION OF ELEMENTAL CONTENT IN WATER SAMPLES COLLECTED FROM YANGON REGION USING EDXRF AND AAS METHODS

Khin Nyein Chan[1], Shwe Nan Htet[2], Cho Cho Aung[3]

Abstract

Energy Dispersive X-Ray Fluorescence Method for elemental concentration quantitatively and toxic and heavy elemental concentration were investigation by using Atomic Absorption Spectroscopy. The natural water samples were collected from artesian well in the eastern district of Yangon Region. The elemental concentrations were compared with the permissible standard levels and pH values were determined by using digital pH meter. The elemental contents were observed in the range as follows: Mn (0-0.394) ppm, Fe (0.028-0.236) ppm, Cu (0.031-0.076) ppm, Zn (0.025-0.505) ppm, As (0-0.002) ppm, Pb (0.047-0.080) ppm. Then, the comparison with World Health Organization guideline values were used. The concentration of the observed elements except Lead (Pb) were found to be within the acceptable levels. According to the pH value results, the artesian water from Thingangyun Township and Tamwe Township can be used as drinking water.

Keywords: EDXRF method, AAS method, pH method.

Introduction

Earth is known as the “Blue Planet” because 71 percent of the Earth’s surface is covered with water. Water also exists below land surface and as water vapour in the air. Water is a finite source. Water on the Earth occurs in three forms: vapour; clouds, mist and steam, fluid; rain, in streams, lakes, dams, wetlands and the sea, solid; ice in glaciers, hail, snow and frost. Water is found in many different forms and in many different places. There are spring water, purified water, mineral water, artesian water, tap water, well water and sparkling water and so on. Artesian water is special and is not simply from an underground spring but this title of “artesian” contains specific parameters about how deeply set the water source is. It has the chance of being ‘more pure’ than basic spring water since it comes from a deeper source and has to travel through deeper levels of natural filtering through

---

[1] Dr, Assistant Lecturer, Department of Physics, University of Yangon
[2] Dr, Lecturer, Department of Physics, University of Yangon
[3] Dr, Associate Professor, Department of Physics, University of Yangon

Earth. To be an artesian well the water in the aquifer must be under enough pressure to force it up the well to a level that is higher than the top of the aquifer. Artesian water comes from an artesian well that is deep in the earth. In the present study, artesian water samples were analyzed by EDXRF techniques and especially to find out the toxic and heavy elemental concentration by using AAS techniques. After the elemental concentrations were compared with the permissible standard levels and pH values.

Experimental Details

Sample Collection

The water samples were collected from specific places in eastern district of Yangon Region. Map of places of sample collection in Eastern District of Yangon Region is shown in Figure (1). The places were chosen because they were crowded area in respective site and mainly used artesian water in those places. Seven artesian water samples were collected in this work. The collected water samples from respective artesian well (at least 100 ft depth) were immediately stored in separate air tight narrow cleaned 1 Litre bottle.

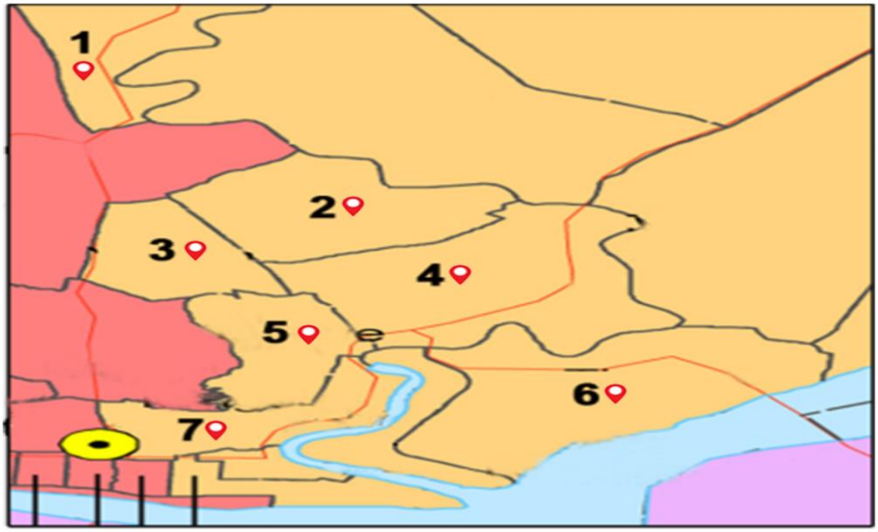

Figure 1: Map of Places of Sample Collection

1 = Thiri Kan Thar Street, North Okkalapa Township
2 = Kyaw Thu Street, South Okkalapa Township
3 = Yan Shin Street, Yankin Township
4 = Pyi Thar Yar Street, Thingangyun Township
5 = Ar Thaw Ka Street, Tamwe Township
6 = Aung Thu Kha Street, Thaketa Township
7 = Mya Yar Kone Street, Mingalartaungnyunt Township

Sample Preparation and Measurement

Artesian water samples were filtered with filter paper. The elemental concentration in liquid, filter paper was used for experimental purposes. The filter paper was cut into a circular with 30 mm (3cm) diameter and then the water sample of (0.1 ml) was dropped on that paper using pipette. And then it was completely left dried in room temperature and carefully and separately stored. After that these papers were analyzed by EDX-720 spectrometer.

Water samples are poured into 100ml beaker and 1ml of nitric acid is added. For the determination of trace and matrix elements in water samples, sample are not filtered, but acidified with acid to pH<2. Prepared samples for measuring with AA-900H Spectrometer.

Results and Discussion

Elemental contents, analyzed by EDX-720 spectrometer, in seven artesian water samples collected from specific places in Eastern district of Yangon Region were expressed in Table (1). The comparison of elemental concentration in each of artesian water samples were expressed in Figure (2). The results obtained by EDXRF technique can be seen that the contents of heavy toxic elements such as nickel (Ni), arsenic (As), cadmium (Cd), mercury (Hg) and lead (Pb) were not included. So, the rest of work should be performed with using of AAS technique. Table (2) shows the elemental concentration of Seven Artesian Water samples by AA-900H Spectrometer. Comparison of Iron, Copper, Zinc, Arsenic and Lead Concentration of artesian water samples by AAS are shown in Figure 3,4,5,6,7 and 8 respectively.

The pH values of samples from different regions were shown in Table 3. The results indicate that the data show the relative concentration of toxic elements contained in the sample of analysis. The concentrations of arsenic were detected in the range from 0.001 ppm to 0.002 ppm. This value is lower than the guideline value of 0.01 ppm. The concentrations of lead were detected in the range from 0.047 ppm to 0.080 ppm. This value is slightly greater than the guideline value of 0.015 ppm.

Table 1: Elemental Concentration of Seven Artesian Water Samples by EDX-720 Spectrometer

Sample No.	**Elemental Concentration (ppm) of Artesian Water Samples**									
	S	**K**	**Ca**	**Mn**	**Fe**	**Co**	**Cu**	**Gd**	**Tb**	Tm
S-1	ND	44.975	75.992	9.316	14.214	8.138	12.000	ND	ND	ND
S-2	44.139	ND	70.355	ND	13.526	ND	11.775	25.606	ND	ND
S-3	ND	ND	69.627	ND	16.062	ND	10.677	ND	ND	ND
S-4	46.925	ND	59.562	6.434	15.075	ND	9.320	ND	ND	ND
S-5	ND	33.358	68.538	ND	14.675	ND	9.362	22.395	25.449	ND
S-6	ND	ND	80.092	9.812	15.115	ND	8.081	29.449	ND	14.290
S-7	ND	ND	73.512	ND	7.326	ND	10.738	23.689	40.453	ND

ND = Not Detected

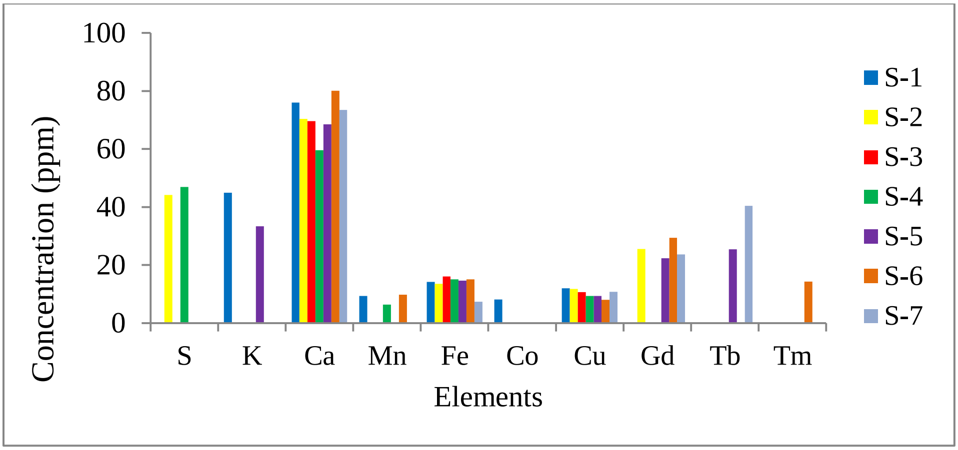

Figure 2: Comparison of elemental concentration in seven artesian water samples by EDX-720 spectrometer

Table 2: Elemental Concentration of Seven Artesian Water Samples by AA-900H Spectrometer

Sample No.	**Elemental Concentration (ppm) of Artesian Water Samples**						
	Mn	**Fe**	**Cu**	**Zn**	**As**	**Cd**	**Pb**
S-1	ND	0.124	0.039	0.033	ND	ND	0.052
S-2	0.085	0.236	0.031	0.047	0.002	ND	0.051
S-3	0.057	0.086	0.046	0.040	0.002	ND	0.069
S-4	0.198	0.028	0.076	0.505	0.002	ND	0.047
S-5	0.078	0.083	0.040	0.041	0.001	ND	0.080
S-6	0.394	0.110	0.036	0.029	0.002	ND	0.073
S-7	ND	0.130	0.038	0.025	ND	ND	0.075

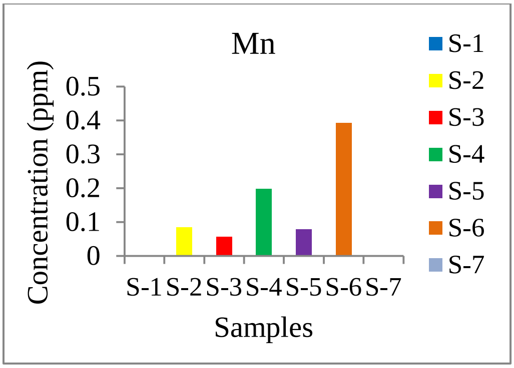

Figure 3: Comparison of Manganese (Mn) concentration of artesian water samples by AAS

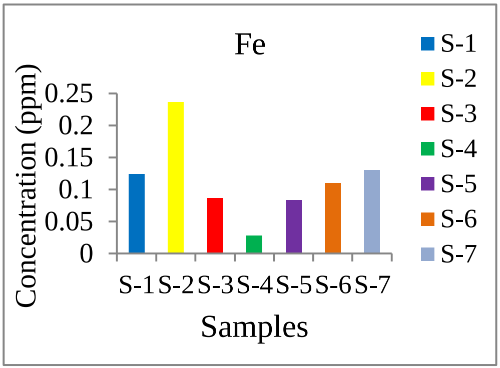

Figure 4: Comparison of Iron (Fe) concentration of artesian water samples by AAS

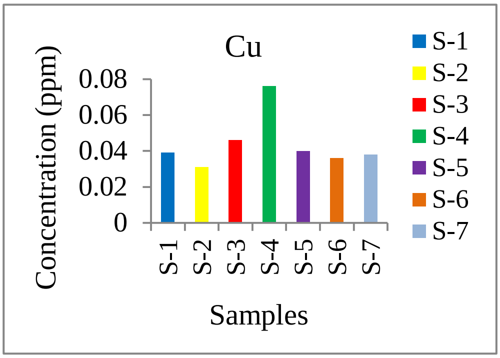

Figure 5: Comparison of Copper (Cu) concentration of artesian water samples by AAS

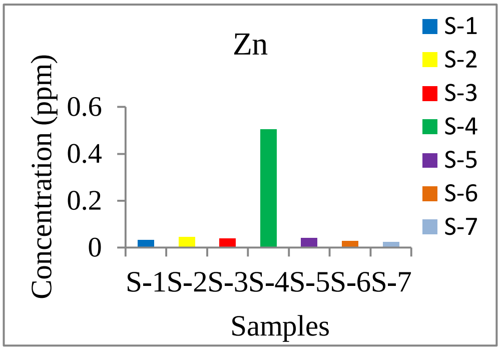

Figure 6: Comparison of Zinc (Zn) concentration of artesian water samples by AAS

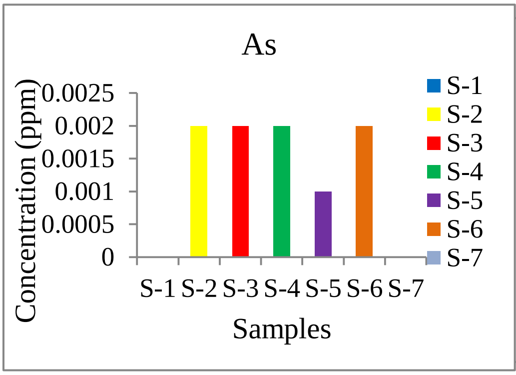

Figure 7: Comparison of Arsenic (As) concentration of artesian water samples by AAS

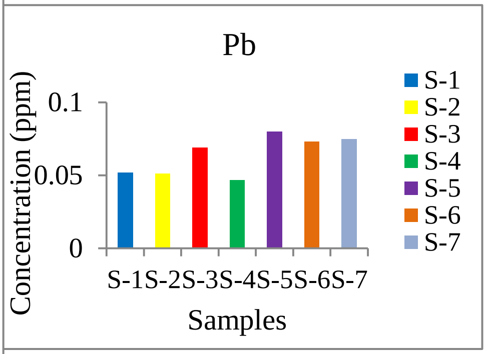

Figure 8: Comparison of Lead (Pb) concentration of artesian water samples by AAS

Table 3: pH Values of Samples from Different Regions

Artesian Water Samples	pH value
Sample -1 (North Okkalapa Township)	6.5
Sample -2 (South Okkalapa Township)	6.7
Sample -3 (Yankin Township)	6.4
Sample -4 (Thingangyun Township)	6.9
Sample -5 (Tamwe Township)	6.9
Sample -6 (Thaketa Township)	6.2
Sample -7 (Mingalartaungnyunt Township)	6.8

Conclusion

Seven artesian water samples collected from North Okkalapa, South Okkalapa, Yankin, Thingangyun, Tamwe, Thaketa and Mingalartaungnyunt were analyzed using Shimadzu EDX-720 spectrometer and Perkin Elmer AA-900H spectrometer at the Universities' Research Centre (URC) in University of Yangon. The results of this study indicate that Arsenic and Lead concentration exists in all artesian water samples. The concentration of toxic element Arsenic (As) is lower than the guideline values of World Health Organization standard (As-0.01 ppm). The concentrations of Lead (Pb) in all samples were above World Health Organization guideline value (Pb-0.015 ppm). The concentration of toxic element Cadmium (Cd) was not found in all samples. The normal range for pH in surface water systems is 6.5 to 8.5 and for ground water systems is 6 to 8.5. The results of pH values measurement indicate that pH values of artesian water samples lie in the range of 6.2 to 6.9. From the pH values results, the artesian water from Thingangyun Township and Tamwe Township can be used as drinking water although the elemental concentration of Lead is slightly greater than (WHO) guideline value.

Acknowledgements

I am highly grateful thanks Professor Dr Khin Khin Win, Head of Department of Physics, University of Yangon for her permission to do and her encouragement throughout this paper.

I also would like to thank Professor Dr Aye Aye Thant, Department of Physics, University of Yangon for her allowing me to do the paper.

References

Bernhard, W. (1976). *Atomic Absorption Spectroscopy*. New York: Oxford University.

Dr. C. Nagamani (2015). *Physical-chemical Analysis of Water Samples*. International Journal of Scientific & Engineering Research, Vol.6, Issue 1, 2015 pp. 2149-2155. ISSN: 2229-5518.

Dziunikowsi, B. (1989). *Energy Dispersive X-Ray Fluorescence Analysis*. Warszawa: PWN-Polish Scientific.

Gupta, K.C., Shweta, C., & Jyoti, S. (2015). *Purification of Drinking Water with the Application of Natural Extracts*. Journal of Global Biosciences, Vol.4, SI 1, 2015 pp. 1861-1866. ISSN: 2320-1355.

Nick, S. (2015). *Analysis of Major Elements in Drinking Water Using FAST Flame Sample Automation for Increased Sample Throughput*. Waltham: Perkin Elmer, Inc.

Perkin Elmer Instrument Manual, 2015. *Pin AAcle 900 AA Spectrometers*. Waltham: Perkin Elmer, Inc.

Shimadzu EDX Series Manual, 2013. *EDX-720/800HS* Spectrometers. Tokyo: Shimadzu Corporation. Printed in Japan 3655-03332-15ANS.

Taqveem, A.K. (2011). *Trace Elements in the Drinking Water and Their Possible Health Effects in Aligarch City, India*. Journal of Water Resource and Protection, 2011, 3, 522-530.

World Health Organization (2017). *Guidelines for Drinking Water Quality, 4th Edition, Incorporating the First Addendum*. ISBN: 978-92-4-154995-0.

J. Myanmar Acad. Arts Sci. 2019 **Vol. XVII. No.2A**

COMPARATIVE STUDIES ON PURE MIXING AND MILLING-MIXING OF Y_2O_3-ZrO_2/HAp BIOCOMPOSITE

Zaw Linn Htun[1], Nurazreena Ahmad[2], Aye Aye Thant[3] & Ahmad-Fauzi[4]

Abstract

The milling-mixing Y_2O_3-ZrO_2/HAp biocomposites have been investigated compared to the pure mixing ones to distinguish the effects of those two methods. The milling method reduced appreciably the particles size of the powders and resulting to better homogeneity and enhanced sinterability. The better densification process of HAp with ZrO_2 favored to improve physical and mechanical properties of the biocomposite. The crystallized size of the milling-mixing samples was found to be 38.5 nm while pure mixing composite had a size of 46.2 nm. The former samples showed higher density than the latter ones in whole sintering temperature range (1050°C - 1250°C). Fine grains formation was also found in the milling-mixing samples. The highest flexural strength of 46.21 MPa and fracture toughness of 1.16 $MPa.m^{1/2}$ were achieved by milling-mixing samples. The formation of apatite layer on the surfaces of Y_2O_3-ZrO_2/HAp biocomposite samples also indicated the biocompatibility and potential bone forming ability.

Keywords: biocomposite, flexural strength, fracture toughness, hydroxyapatite, zirconia.

Introduction

HAp is chemically similar to the inorganic mineral component of bone and teeth[1,2] and possesses exceptional biocompatibility and unique bioactivity[3]. Although HAp offers high biocompatibility, relatively low density, high compressive strength and high hardness, application of HAp as a load bearing implant is limited because of its brittleness and relatively low mechanical properties. Hence, there is a necessity of reinforcement to HAp without hampering its biocompatibility[4]. For these reasons, the biocomposites of HAp and ZrO_2 was conducted in this work in order to combine the biocompatibility of HAp and the high strength and toughness of ZrO_2 using

---

[1] Assistant Lecturer, Department of Physics, University of Yangon

[2] Lecturer, School of Materials and Mineral Resources Engineering, Universiti Sains Malaysia

[3] Professor, Department of Physics, University of Yangon

[4] Professor, School of Materials and Mineral Resources Engineering, Universiti Sains Malaysia

both pure mixing and milling mixing methods. The ZrO_2 has been found to retain high mechanical strength and toughness without degrading the biocompatibility of HAp when incorporated as a second phase[5,6]. HAp-ZrO_2 biocomposites have shown the improved strength and toughness as compared to monolithic HAp itself[7]. However, the reaction between ZrO_2 and HAp will enhance the decomposition of HAp and leads to inhibit densification of the composite resulted in low mechanical properties. Again, the presence of ZrO_2 in the system decreases the decomposition temperature of HAp into tri-calcium phosphate (TCP; α- or β-)[8]. Therefore, CaF_2 was added into the biocomposite to improve sinterability and to retain the HAp phase. Based on these backgrounds, the current study was performed to fabricate HAp and Y_2O_3-ZrO_2 biocomposites through the incorporation of CaF_2 by air sintering at temperatures ranging from 1050 °C to 1250 °C. The effect of the added-CaF_2 on sintering behavior of Y_2O_3-ZrO_2/HAp was also investigated.

Materials and Methods

2.1. Materials fabrication

As starting materials, 95wt% of high-purity HAp (Fluka) and 5wt% of Y_2O_3-ZrO_2 (Goodfellow) powders were used to fabricate (ZrO_2/HAp) biocomposites with the addition of 1wt% CaF_2 (Merck KGaA, Germany) powders, designated as Mix_H-5YZ-1CF and Mill-Mix_H-5YZ-1CF respectively. The samples were produced by both pure mixing and milling-mixing with zirconia ball milling. In pure mixing, the composition of Y_2O_3-ZrO_2 and HAp were added in ball milled with only 10 zirconia balls to aid mixing. For the case of milling-mixing system, the powders were wet mixed and milled with ball-to-powder weight ratio of 4:1 in ball milling for 24 hours in order to obtain a homogeneous and agglomerate-free powder mixture. Deionized water was used as a mixing media. After mixing, the mixture was dried in an oven at 100 °C for 24 h. Dry aggregates were lightly ground into fine powders using agate mortar and sieved through a 250 µm screen. A 55 mm × 10 mm die was used to form rectangular bar shape sample and a uniaxial pressure of 90 MPa was employed to compact. Sintering was conducted in air atmosphere at five different temperatures (1050, 1100, 1150, 1200 and 1250 °C) using *LENTON* muffle furnace. The schedule of sintering includes soaking time of 5 h with heating and cooling rate of 5 °C/min.

2.2. Characterization and Mechanical Test

Using Archimedes method, the density and apparent porosity of the sintered specimens were measured. The samples were subsequently ground using SiC paper, followed by polishing using 1 µm, 0.3 µm and 0.05 µm alumina powders. After etching at a temperature 100 °C below its sintering temperature for 2 h, their microstructures were analyzed by Zeiss Supra 35VP Field Emission Scanning Electron Microscope (FESEM). The specimens were also characterized by XRD Bruker DX 8 for the phase formed. The scan started from 20° to 80° 2θ, using copper (Kα Cu) with wavelength of 1.5406 nm as X-ray source.

For the flexural strength, 3-point bending test was conducted using INSTRON 3366 universal testing machine with a crosshead speed of 0.5 mm/min, and outer span length of 40 mm. Microhardness of the specimens was measured by Vickers microhardness tester. A diamond indenter with 1 Kgf load was used to test the samples, and loading time of 12 seconds was applied. Indentation fracture in ceramic materials was suggested as a simple technique to determine fracture toughness value[9]. Based on this knowledge, fracture toughness measurement was determined by applying 3 Kgf load to make significant crack from the indent tips.

Results and Discussion

3.1. Phase Identification

From Fig: 1(a) and 1(b), the samples were found to contain β-TCP phase, which suggest that decomposition of HAp into β-TCP had occurred at both temperatures investigated in both pure mixing and milling-mixing of Y_2O_3-ZrO_2/HAp composites. The diffraction peaks of the samples sintered at different temperatures matches with the reference patterns of HAp at 25.87°, 31.97°, 32.28° and 33.16° (JCPDS card number 4-0506) and β-TCP at 27.78°, 31.01°, 31.05° and 34.35° (JCPDS card number 7-6561). Peaks at 30.17°, 50.17°, 50.58° and 60.04° matched with the peaks from tetragonal ZrO_2 (JCPDS card number 9-1974). When the temperature is higher, the transformation to β-TCP is increased and small amount of $CaZrO_3$ was also found, especially in pure mixing samples (Fig: 1b). The peaks at 31.60°, 45.30°, 56.29° and 75.03° (JCPDS card number 6-2992) confirm the presence of $CaZrO_3$. The formation of $CaZrO_3$ would indicate that HAp reacts with the Y_2O_3-ZrO_2 whilst the presence of 1wt% CaF_2 would not be able to prevent the reaction, as was suggested by Firmandika Harda[10]. Thus, 1wt% CaF_2 can be considered as being relatively low to prevent secondary reaction.

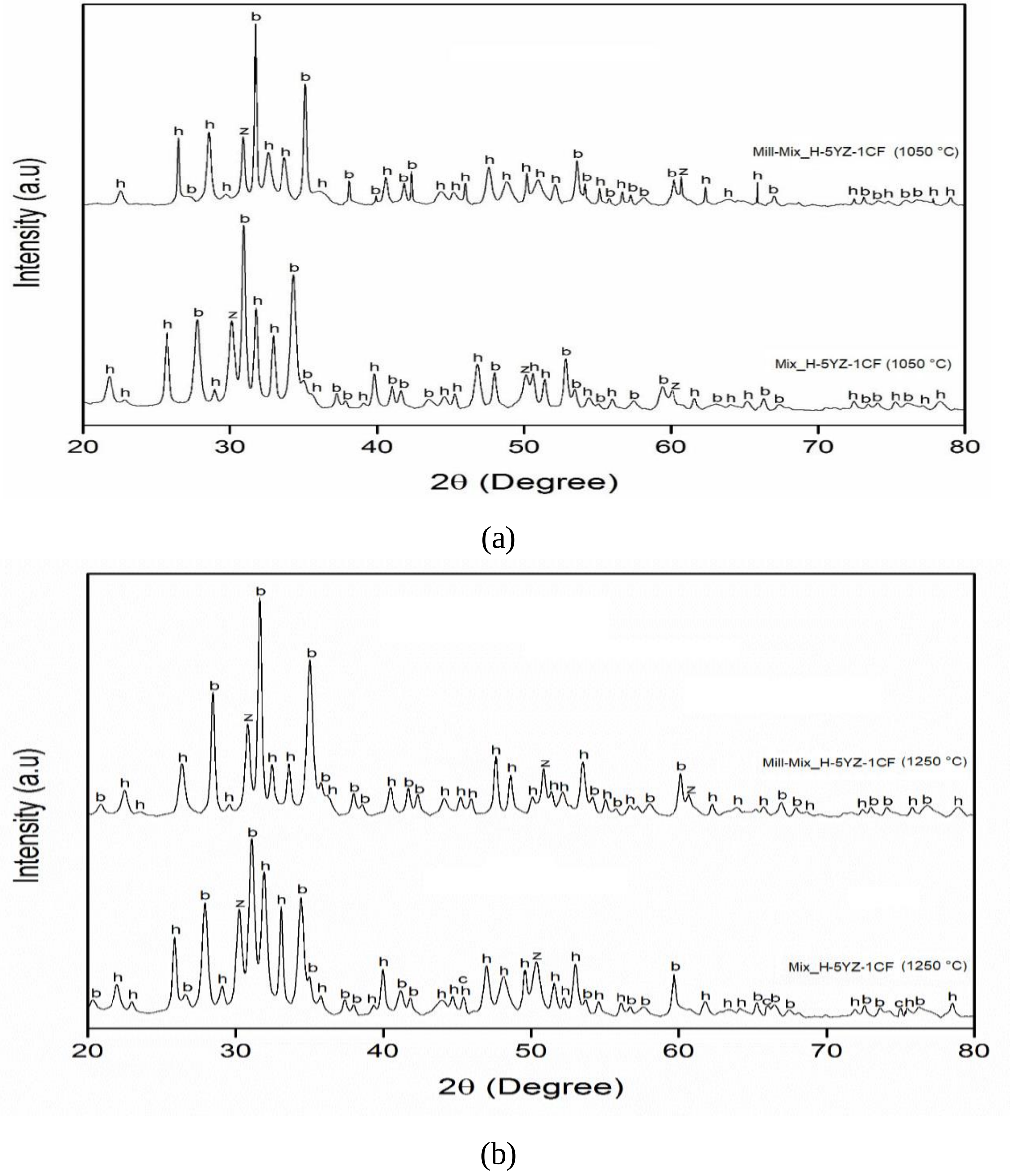

(a)

(b)

Figure 1: XRD patterns of Mix_H-5YZ-1CF and Mill-Mix_H-5YZ-1CF samples at (a) 1050°C and (b) 1250°C Key: h = HAp, b = β -TCP, z = ZrO_2 (tetragonal), c = $CaZrO_3$

3.2. Crystallite Size Determination

From Fig: 1(a), it reveals that the diffraction peaks of Mill-Mix_H-5YZ-1CF samples shifted to higher 2θ values and it can be known that the crystallite size of these samples becomes smaller than that of pure Mix_H-5YZ-1CF samples. For instance, the strongest peak shifts from the original 2θ position at 30.92° to 31.73°. Crystallite size calculated from the corresponded peak was found to be 38.5 nm for Mill-Mix_H-5YZ-1CF composite, while Mix_H-5YZ-1CF composite has a size of 46.2 nm. This could be resulted from the milling of the powders. The milling system reduces appreciably the particles size of the powders and resulting to better homogeneity and enhanced sinterability, and better densification process of HAp with ZrO_2.

3.3. Particle Size Determination

The particle size distribution curves for Mix_H-5YZ-1CF and Mill-Mix_H-5YZ-1CF samples are shown in Fig: 2 and it was found that the average particle size of pure Mix_H-5YZ-1CF sample is about 8.51 µm (Fig: 2(a)) and that of Mill-Mix_H-5YZ-1C sample was about 5.36 µm (Fig: 2(b)). Based on this results, it could be realized that the particle size reduction was obtained by milling-mixing procedure.

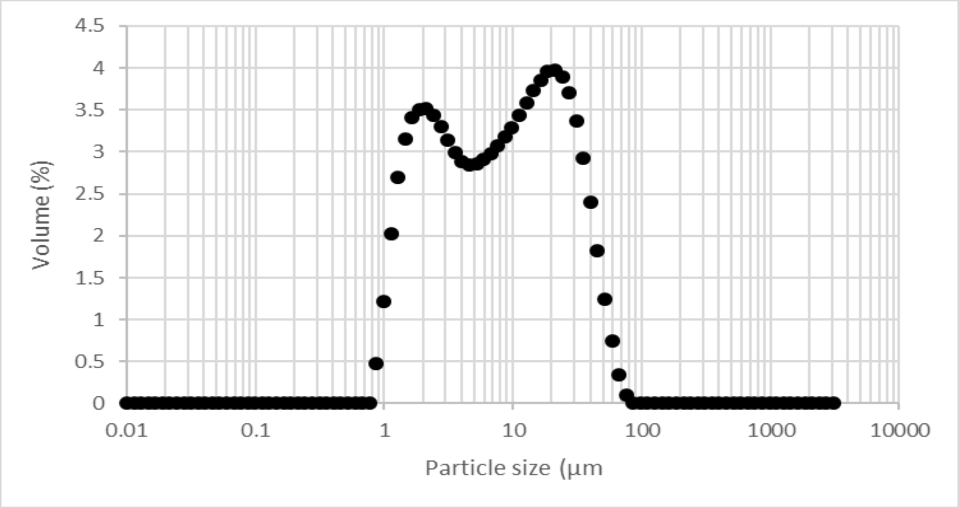

(a)

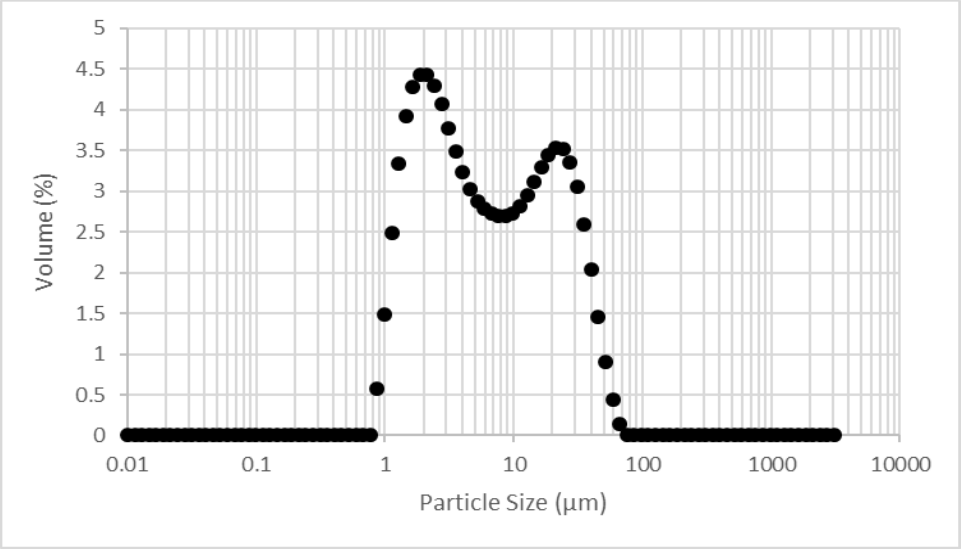

(b)

Figure 2: Particle size distribution curves for (a) Mix_H-5YZ-1CF and (b) Mill-Mix_H-5YZ-1CF samples

3.4. Evaluation of Physical Properties

3.4.1 Bulk Densities

From the graph (Fig: 3), it can be observed that the increase in density values with consistency displayed at all temperatures for Mill-Mix_H-5YZ-1CF samples as compared to Mix_H-5YZ-1CF samples. The optimum density of 2.95 gcm^{-3} was reached at the temperature of 1250°C for these samples in the temperature range while the density at 1200°C was the highest for pure Mix_H-5YZ-1CF samples. At the highest temperature, 1250°C, it was unable to enhance the density of pure Mix_H-5YZ-1CF samples. In the whole sintering temperature range (1050°C - 1250°C), the densities of Mill-Mix_H-5YZ-1CF samples are noticeably higher than that of pure Mix_H-5YZ-1CF samples. This enhancement in density is because of better homogeneity as well as the particle size reduction by zirconia ball milling in 24 hours with ball-to-powder weight ratio of 4:1.

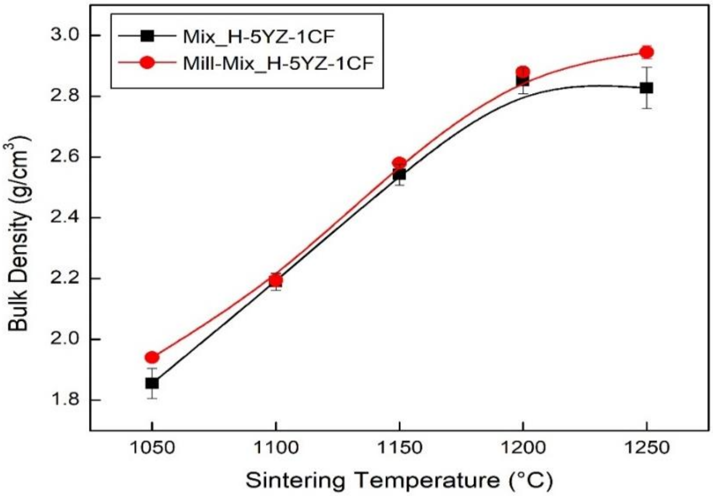

Figure 3: Bulk densities of Mix_H-5YZ-1CF and Mill-Mix_H-5YZ-1CF samples as a function of sintering temperature

3.4.2 Apparent Porosities

Fig: 4 presents the apparent porosities of Mix_H-5YZ-1CF and Mill-Mix_H-5YZ-1CF samples at various temperatures with soaking of 5 hours. It can be observed from the graph that the apparent porosities of Mill-Mix_H-5YZ-1CF samples are apparently lower than that of Mix_H-5YZ-1CF samples for all sintering temperatures. This result shows high consistency to the above density values, i.e., the higher the sintering temperature is, the lower the porosity and the greater the density will be. However, the minimum porosity in the firing range does slightly differ from the bulk density results.

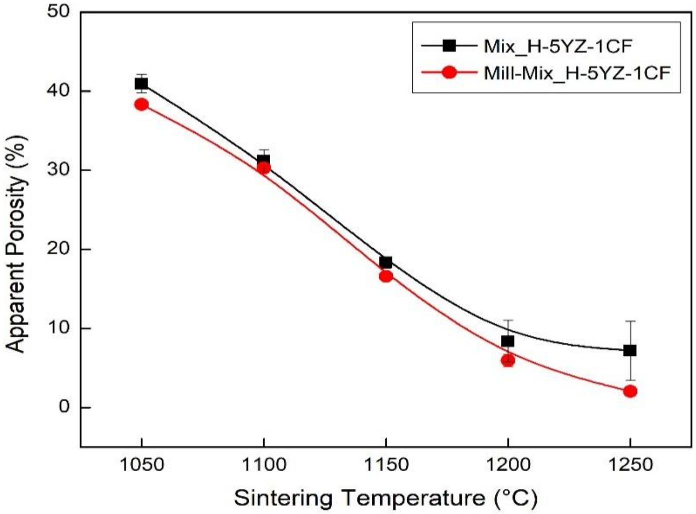

Figure 4: Apparent porosities of Mix_H-5YZ-1CF and Mill-Mix_H-5YZ-1CF samples as a function of sintering temperature

3.5. Evaluation of Strength and Toughness

The flexural strength of Mix_H-5YZ-1CF and Mill-Mix_H-5YZ-1CF samples after sintering at various temperatures for 5 hours are presented in Fig: 5. For the Mill-Mix_H-5YZ-1CF samples, the optimum strength of 46.21 MPa was achieved at the sintering temperature, 1150°C, and this value is apparently higher than that of pure Mix_H-5YZ-1CF samples which have the optimum value of 34.71 MPa at 1200°C. Therefore, a better strength was obtained by the milling-mixing method as expected.

The fracture toughness (K_{IC}) of Mix_H-5YZ-1CF and Mill-Mix_H-5YZ-1CF samples are also presented in Fig: 6. From the graph, the optimum toughness values for Mill-Mix_H-5YZ-1CF samples occurred at 1250°C. The maximum K_{IC} values, in the range of ~ 0.54 to 1.16 MPa.m$^{1/2}$, was obtained by the Mill-Mix_H-5YZ-1CF sample, while pure Mix_H-5YZ-1CF samples were giving values, in the range of ~ 0.47 to 1.08 MPa.m$^{1/2}$. Although the toughness values of both biocomposites were not much different from each other's, better toughness was found in milling-mixing composites.

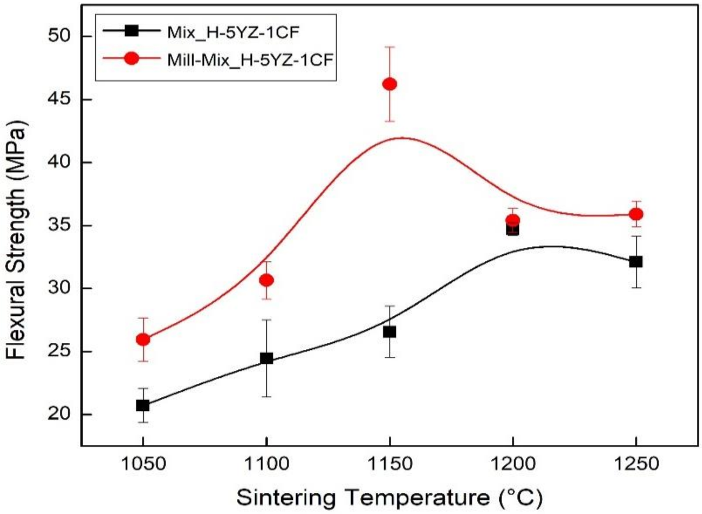

Figure 5: The flexural strength of Mix_H-5YZ-1CF and Mill-Mix_H-5YZ-1CF samples after sintering at various temperatures for 5 hours

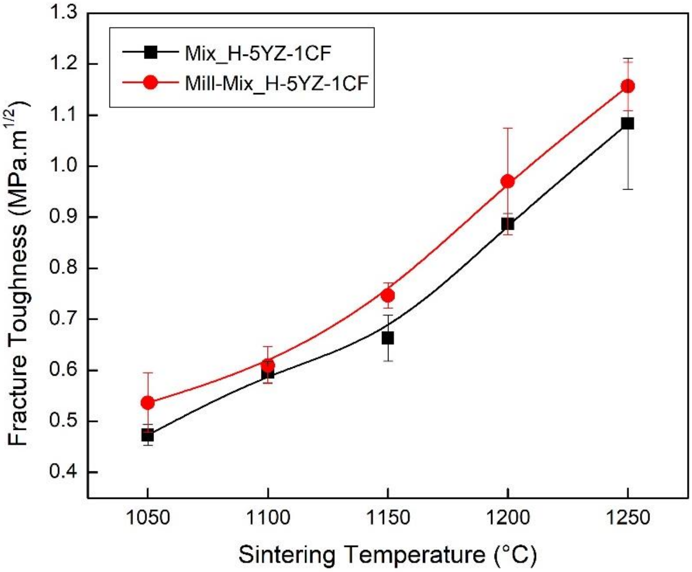

Figure 6: The fracture toughness of Mix_H-5YZ-1CF and Mill-Mix_H-5YZ-1CF samples after sintering at various temperatures for 5 hours

3.6. Microstructural observation

The SEM images of pure mixing and the milling-mixing samples are shown in Fig: 7 and Fig: 8. It can be observed from the images that excessive grain coarsening occurred at highest sintering temperature of 1250°C and also some large pores were observed in Fig: 7(b) for Mix_H-5YZ-1CF samples. It affected the densification process and thereafter results in the deterioration of mechanical properties of the biocomposite. Vasconcelos[11] reported similar effect on mechanical properties. On the contrary, uniformly distribution of ZrO_2 phase with uniform fine grains were observed in the SEM images of Mill-Mix_H-5YZ-1CF samples at 1250°C as shown in Fig: 8(b). Based on this observation, Mill-Mix_H-5YZ-1CF samples showed better densification and fine grains as compared to pure Mix_H-5YZ-1CF samples. This also confirmed the particle size reduction in milling-mixing procedure.

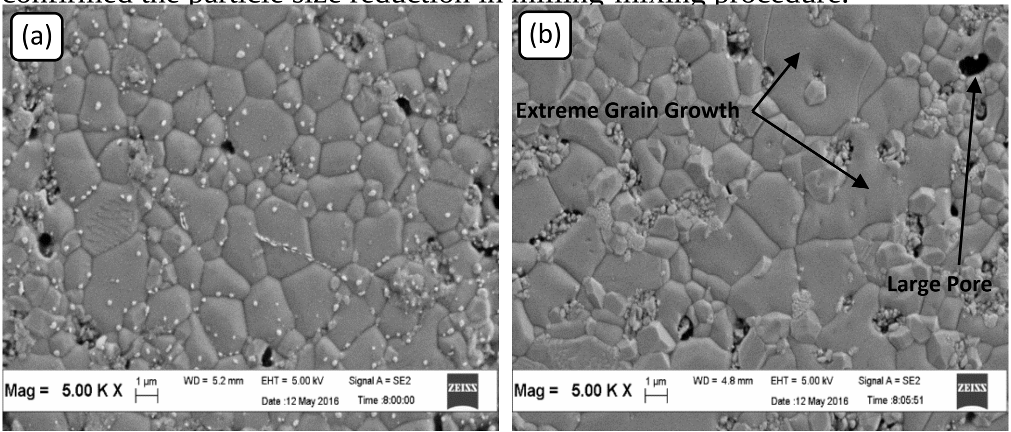

Figure: 7: SEM images of Mix_H-5YZ-1CF samples sintered at (a) 1200°C and (b) 1250°C

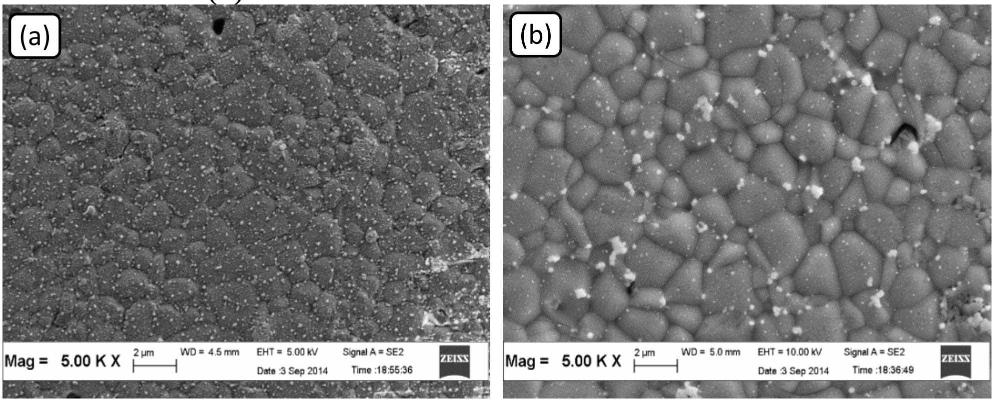

Figure 8: SEM images of Mill-Mix_H-5YZ-1CF samples sintered at (a) 1200°C and (b) 1250°C

3.7. Evaluation of Bioactivity in SBF

Fig: 9(a) and 9(b) shows 5000X and 20,000X magnifications SEM images of the Mill-Mix_H-5YZ-1CF samples sintered at 1250°C after soaking in SBF for 7 days. The magnified image shown in Fig: 9(b) clearly shows that spherical-like apatite particles has grown on the sample surface after 7 days. These apatite particles can be considered as the aggregates of small crystals as also reported by Yokogawa & Nagata (2005)[12]. Therefore, it can be said from these findings that Y_2O_3-ZrO_2/HAp composites show the bone-bonding ability and can be considered to be useful as an implant.

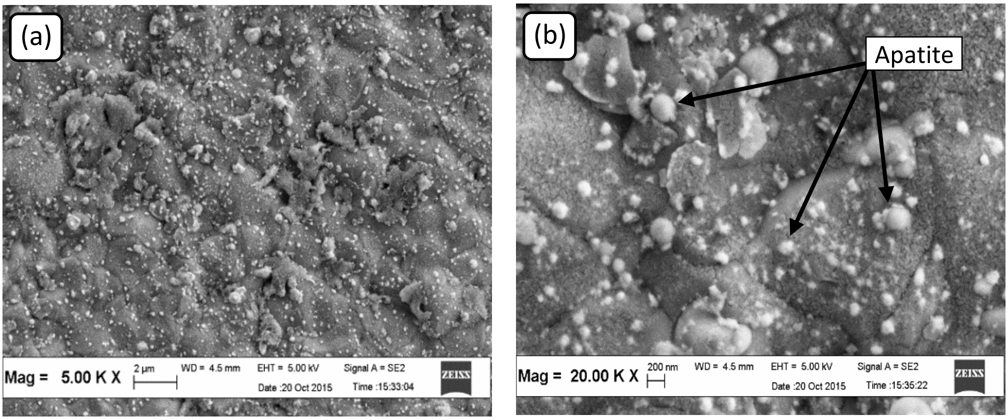

Figure 9: SEM images of the surfaces of Mill-Mix_H-5YZ-1CF sample sintered at 1250 °C at (a) 5000X and (b) 20,000X magnification after soaking in SBF for 7 days

Conclusion

Particles size reduction of the powders, better homogeneity and enhanced sinterability were achieved by the milling-mixing method. The better densification process of HAp with ZrO_2 was found to be improved physical and mechanical properties of the biocomposite. The smaller crystallized size of 38.5 nm was also observed in the milling-mixing samples, and fine grains formation as well. The highest flexural strength of 46.21 MPa and fracture toughness of 1.16 MPa.$m^{1/2}$ were also achieved by milling-mixing samples. The apatite formation was also found on Y_2O_3-ZrO_2/HAp biocomposite samples surface through bioactivity test, showing potential bone forming ability.

Acknowledgements

We are greatly indebted to Professor Dr. Khin Khin Win, Head of Department of Physics, University of Yangon for her kind permission.

The authors would like to thank AUN/SEED-Net for providing the research grant to conduct this project under Collaborative Research Program (CR) (304/PBAHAN/ 6050293/A119).

References

Adolfsson E, Shen Z. Densification of Zirconia–Hydroxyapatite Ceramics Without Phase Changes. In: Key Engineering Materials. 2006. p. 1141–4.

Balani K, Lahiri D, Keshri AK, Bakshi SR, Tercero JE, Agarwal A. The nano-scratch behavior of biocompatible hydroxyapatite reinforced with aluminum oxide and carbon nanotubes. JOM J Miner Met Mater Soc. 2009;61(9):63–6.

EVans AG, Charles EA. Fracture toughness determinations by indentation. J Am Ceram Soc. 1976;59(7–8):371–2.

Harda F. Zirconia Reinforced Hydroxyapatite Biocomposite for Strength and Toughness Improvement. Universiti Sains Malaysia (USM); 2008.

Hench LL, Wilson J. An Introduction to Bioceramics. Singapore: World Scientific; 1993. 386 p.

Jarcho M, Kay JF, Gumaer KI, Doremus RH, Drobeck HP. Tissue, cellular and subcellular events at a bone-ceramic hydroxylapatite interface. J Bioeng. 1977 Jan;1(2): 79–92.

Li J, Liao H, Hermansson L. Sintering of partially-stabilized zirconia and partially-stabilized zirconia—hydroxyapatite composites by hot isostatic pressing and pressureless sintering. Biomaterials. 1996 Sep;17(18):1787–90.

Nayak AK. Hydroxyapatite synthesis methodologies: An overview. Int J ChemTech Res. 2010;2(2):903–7.

Silva V V., Lameiras FS, Domingues RZ. Microstructural and mechanical study of zirconia-hydroxyapatite (ZH) composite ceramics for biomedical applications. Compos Sci Technol. 2001 Feb;61(2):301–10.

Vasconcelos C. New Challenges in the Sintering of HA/ZrO2 Composites. Sinter Ceram - New Emerg Tech. 2012 Mar 2;2:179–202.

Yokogawa Y, Nagata F. Hydrothermal Synthesis of Hydroxyapatite – Polymer Composite Materials. In: In Review in International Conference on the Properties of Water and Steam in Kyoto. 2005. p. 373–6.

Zhang J, Iwasa M, Kotobuki N, Tanaka T, Hirose M, Ohgushi H, et al. Fabrication of Hydroxyapatite?Zirconia Composites for Orthopedic Applications. J Am Ceram Soc. 2006 Nov;89(11):3348–55.

J. Myanmar Acad. Arts Sci. 2019 **Vol. XVII. No.2A**

CHARACTERIZATION AND OPTICAL PROPERTIES OF THE COLEUS BLUMEI EXTRACT AS DYE SENSITIZED SOLAR CELLS (DSSC)

Khine Myint Zu[1], Swe Swe Thein[2], Yin Maung Maung[3]
and Than Than Win[4]

Abstract

The natural dyes used in this research were poinsettia leaves *(Coleus Blumei).*The absorbance and energy levels of dyes solutions were characterized using UV-Vis spectrophotometer and cyclic voltammetry. From UV-Vis absorption spectrum and , it was known that combination of anthocyanin and chlorophyll with ethanol was the broader region of the visible light spectrum in the range of 400 to 700 nm compared to extracted with methanol. All dyes were measured under the different solvents and temperatures to estimate the energy of the highest occupied molecular orbital (HOMO) and the energy of lowest unoccupied molecular orbital (LUMO). Optical band gap was measured from the absorption spectrum of each dye sensitizer. Fourier transform inferred (FTIR) was used to characterize the dye active components from 4000 to 500 cm^{-1}. From FTIR results, the coleus blumei match with AMANO LIPASE (C_{11} H_9 N_3 Na O_2) compound corresponding to the carboxylic acidic group in dye solutions were observed.

Keywords: Coleus Blumei leaves, Optical Band gap energy, UV-Vis, Cyclic Voltammetry, FTIR

Introduction

Energy technology is one of the most important technologies, since the demand for energy is growing day by day. In recent year, dye–sensitized solar cells (DSSCs) have been developed as the third generation of solar cells. [Hassan K. Tajudeen etal, 2017]. DSSC is the basically a photo electrochemical devices used for the conservation of solar energy into electrical energy. [Muhamad IK et al 2015]. The sensitizing dye, as a part of photoelectrode plays a key role in absorbing, sunlight and transforming solar energy into electrical energy.[Hassan K. Tajudeen et al 2017]. Therefore, the cell performance is mainly dependent on the type of dyes used as sensitizer[NT

---

[1] PhD candidate, Department of Physics, University of Yangon

[2] Lecturer, Department of Physics, University of Yangon

[3] Associate Professor, Department of Physics, University of Yangon

[4] Associate Professor, Department of Physics, Mandalay University of Distance Education

Mary Rosana 2014].Natural dye has several advantages over rare metal complexes because ease of extraction with minimal chemical procedure, large absorption coefficients, low cost, non toxicity, environmentally friendly, easily biodegradable and wide availability. [NT Mary Rosana 2014]. Natural dye can easily extract from flowers, leaves, seeds and fruits.

In this research work, natural dyes were extracted from two different colors of leaves in coleus blumei (Family Lamiacae) (Kawzaw Ywet Hla). Natural dyes were extracted by using two different solvent methanol and ethanol solutions. These were characterized by UV-Vis absorption spectroscopy to observe the absorption spectra. FTIR spectral analysis was used to determine the functional group in the natural dye. Cyclic voltammetry method was used to investigate the HOMO and LUMO energies and estimate the band gap energies of natural dye.

Extraction of dye solution

The anthocyanin extraction of the mixture two different colors of coleus blumei leaves were made following procedures. Purple and pink coleus blumei leaves were washed with distilled water and kept them some time in room temperature to remove the surface water. 5g of leaves were weight and crushed adding 150 ml of 70% ethanol (w/v %) and stored overnight in the refrigerator at 4° C. On the following day, the extraction was mixed thoroughly by using a magnetic stirrer for two hours at 25°C, 45°C and 65°C. The extractions were filtered using 110 mm filter paper to remove solid residues. Subsequently, the extract was centrifuged at 4000 rpm using a Denley BS 400 (UK) centrifuge machine for 5 minutes to separate all residues. Similar procedures were applied by taking same amount solvents for rest extracting solutions.

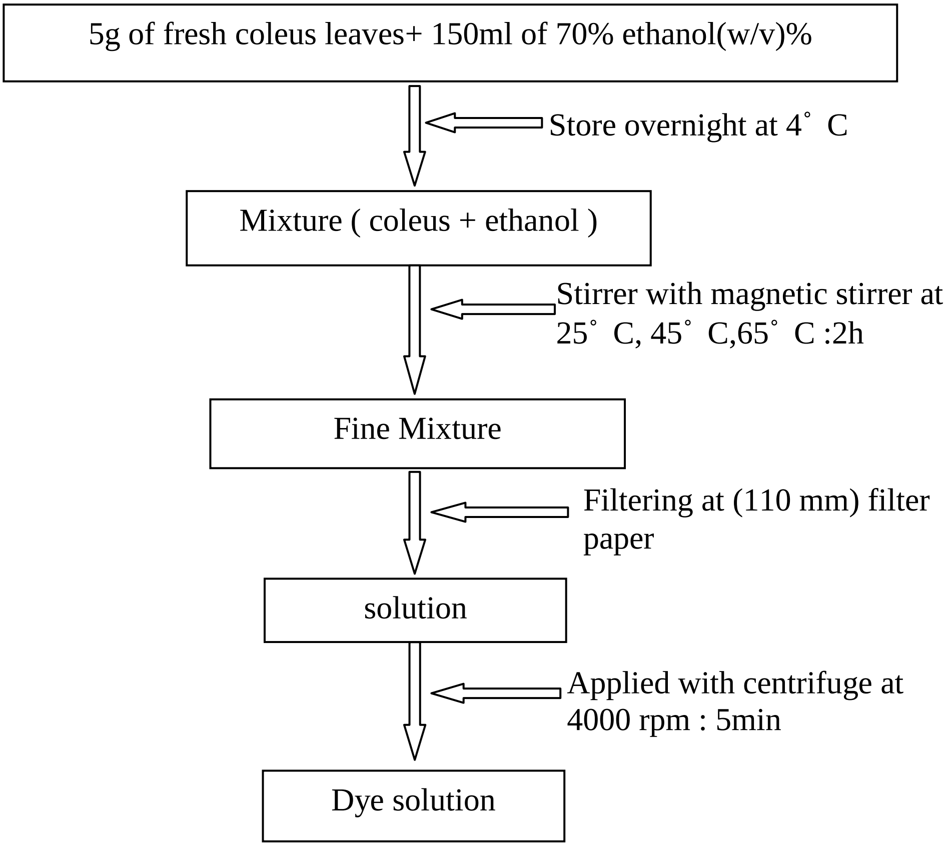

Figure 1: Block diagram of extraction of dye solution by using ethanol solvent.

Results and Discussion

UV-Analysis

UV-Vis absorption spectra analysis of poinsettia (Coleus Blumei) dye solution. Fig 2 found that the absorption peaks of dye solution of mixed Pink & Purple (Coleus Blumei) dye with ethanol 150 ml at 25˚C, 45˚C and 65˚C are 440nm (anthocyanin) and 665 nm (chlorophyll) and Fig 4 mixed Pink and Purple (Coleus Blumei) dye with methanol 150 ml at different temperatures are the same values (440 nm and 665 nm). And also the absorption peaks of dye solution at 25˚C, 45˚C and 65˚C are 400-700nm in the visible range. So the absorption peaks of these solutions at different temperatures are in UV range. The energy band gaps (E_g) of these samples at different temperatures were calculated by using Tauc Method equation and The relation between energy (hν) and $(\alpha h\nu)^2$ for Mixed (pink & purple) Coleus dye with ethanol 150 ml at 25˚C,45˚C,65˚C, 2h are shown in Fig 3 (a,b,c) and while that of mixed (pink & purple) Coleus dye with methanol 150 ml at 25˚C, 45˚C and 65˚C , 2h are shown in Fig 5 (a,b,c).

Tauc Method ,

$$(\alpha h\nu) = A(h\nu - \qquad (1)$$

Where, α = absorption coefficient (α = 2.303 A/ thickness)

E_g = Energy Bandgap of the material
n = order of transition (1/2,3/2,2,3)

The measured and calculated values of UV-vis for Coleus Blumei dyes at 25 ˚C, 45 ˚C and 65 ˚C with two solvents were described in Table 1(a) to (b).

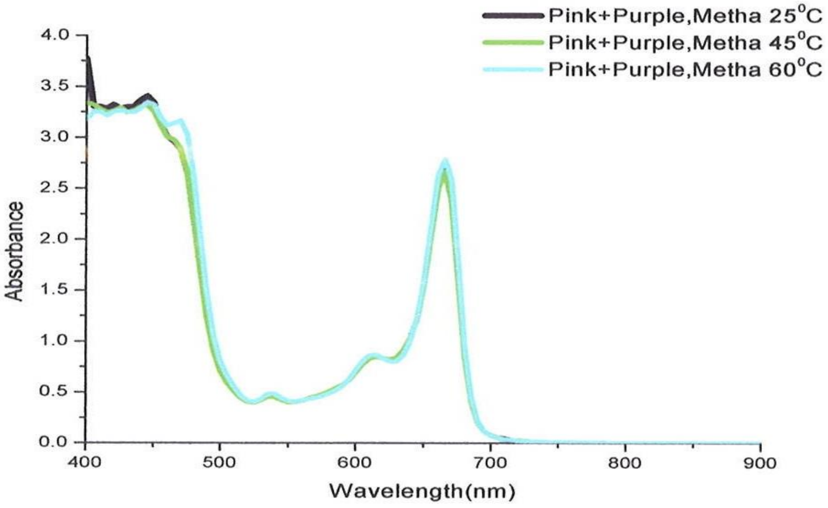

Figure 2: The absorption spectra of Mixed (Pink &Purple) Coleus at 25˚C, 45˚C and 65˚C, 2h

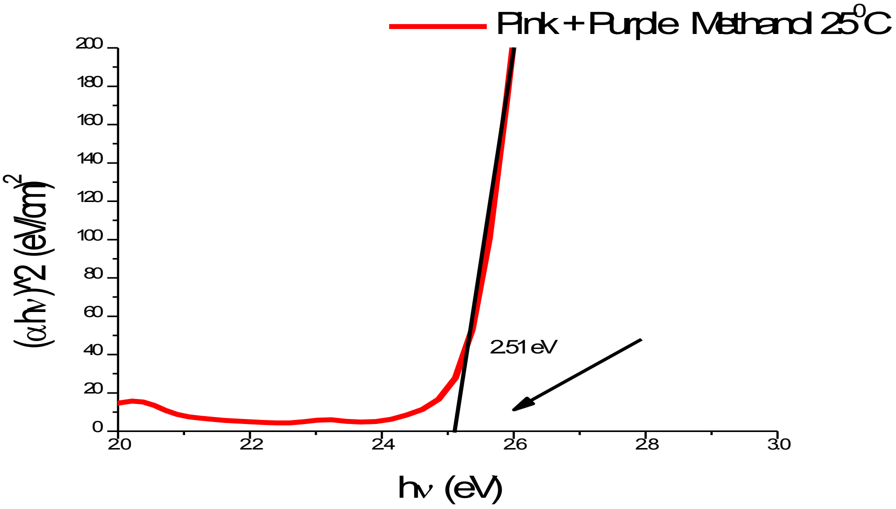

Figure 3: (a) The Cyclic Volammetry curve for Mixed Coleus (pink + purple) at 25 ˚C, 2h

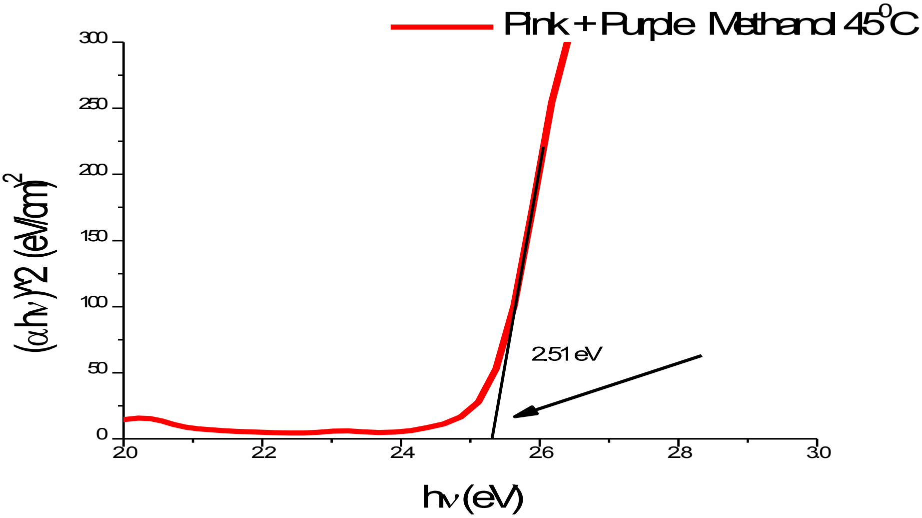

Figure 3: (b) The Cyclic Volammetry curve for Mixed Coleus (pink + purple) at 45 ˚C, 2h

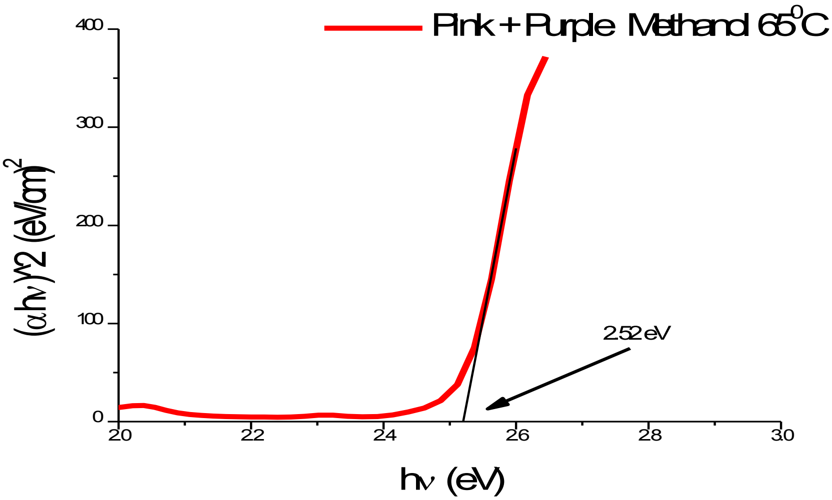

Figure 3: (c) The Cyclic Volammetry curve for Mixed Coleus (pink + purple) at 65 ˚C, 2h

Table 1: (a) pH level s and Energy levels for Purple Coleus with Methanol at 25 ˚C, 45 ˚C and 65^{0}C, 2h

Temperature (°C)	pH level	Wavelength (nm)	Energy Band gap (E_g)(eV)
25	6.60	490	2.52
45	6.34	492	2.51
65	7.70	490	2.52

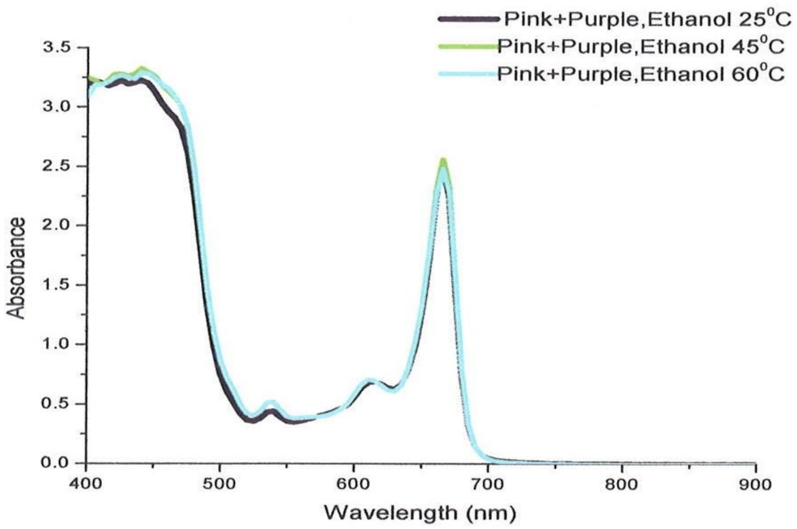

Figure 4: The absorption spectra of Mixed (Pink &Purple) Coleus at 25 ˚ C, 45 ˚ C and 65 ˚ C, 2h

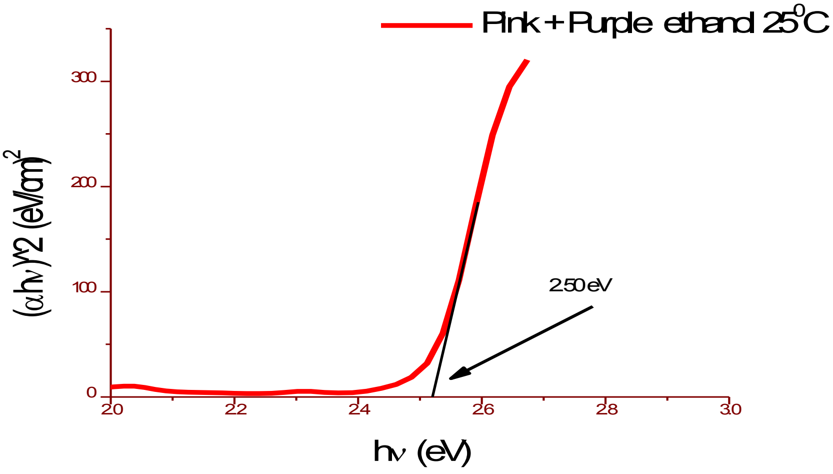

Figure 5: (a) The Cyclic Volammetry curve for Mixed Coleus (pink + purple) at 65 ˚ C, 2h

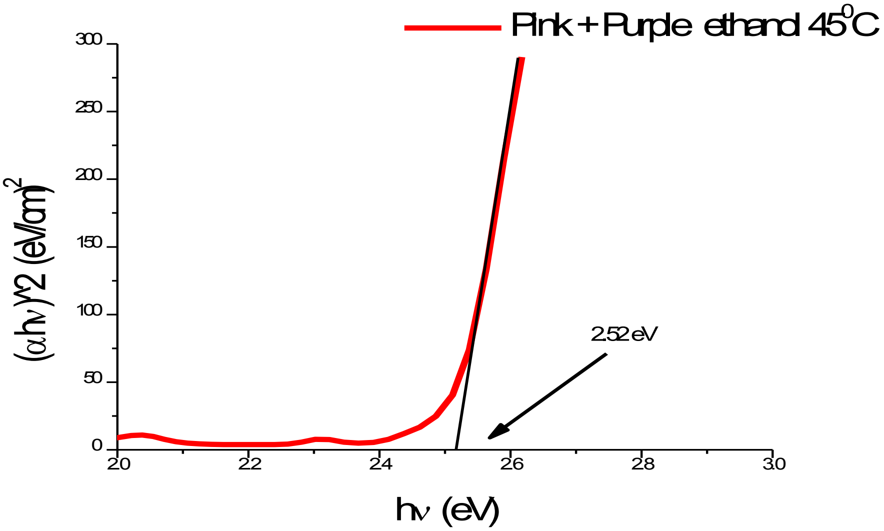

Figure 5: (b) The Cyclic Volammetry curve for Mixed Coleus (pink + purple) at 65 ˚C, 2h

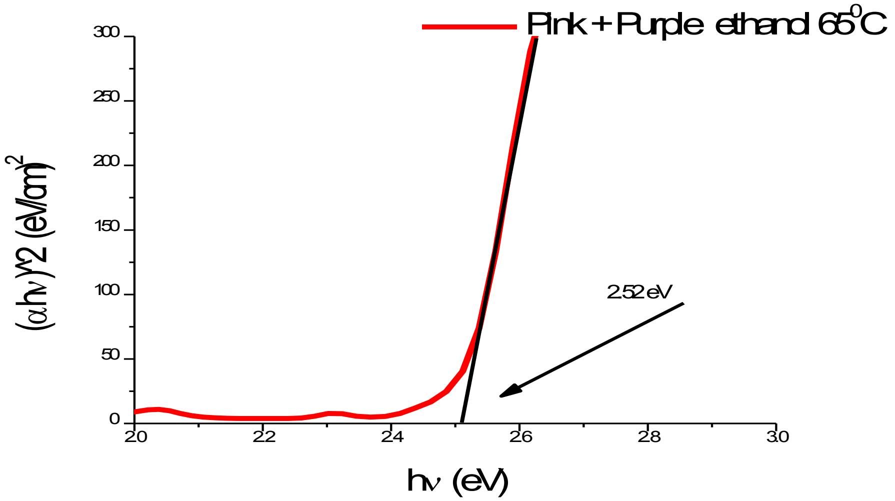

Figure 5: (c) The Cyclic Volammetry curve for Mixed Coleus (pink + purple) at 65 ˚C, 2h

Table 1: (b) pH levels and Energy levels for mixed (Pink &Purple) Coleus with Ethanol at 25°C, 45°Cand 65°C, 2h

Temperature (˚C)	**pH level**	**Wavelength (nm)**	**Energy Band gap (E_g)(eV)**
25	6.56	494	2.50
45	6.37	490	2.52
65	7.03	490	2.52

Electrochemical Properties of Natural Dye Extract

Cyclic voltammetry (CV) is very suitable method for wide range of applications. Moreover, in some area of research, cyclic voltammetry is one of the useful methods to characterize the organic material and estimate the energy band diagram. HOMO and LUMO are types of molecular orbitals. HOMO is “highest occupied molecular orbital” and LUMO is “lowest unoccupied molecular orbital”. The energy difference between HOMO and LUMO are called HOMO-LUMO gap. The difference these two orbitals can be used to predict the strength and stability of transition material complexes, as well as the colors they produce in solution.[8,13]

Electrochemical cyclic voltammetry (CV) was performed to determine the HOMO and the LUMO energy levels of the natural dyes. Fig 6 (a-c) showed the cyclic voltammograms of Pink & Purple Coleus Blumei by using methanol solvent and Fig 7 (a-c) by using ethanok solvent. In this research, the energy levels were calculated using the following equations and the calculated values were shown in Table 2(a) to 2(b).

$$E_{LUMO} = -[E^{onset} + 4.4]\ \text{eV} \qquad (2)$$

$$E_{HOMO} = E_{LUMO} + E_g \qquad (3)$$

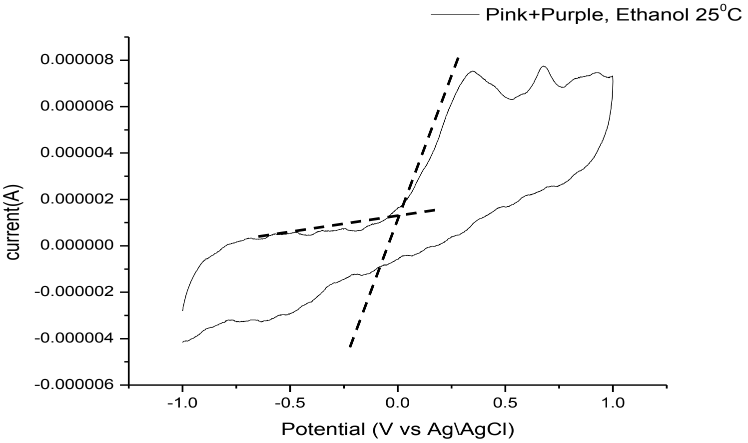

Figure 6: (a) The Cyclic Volammetry curve for (Pink + Purple) Coleus at 25˚C, 2h

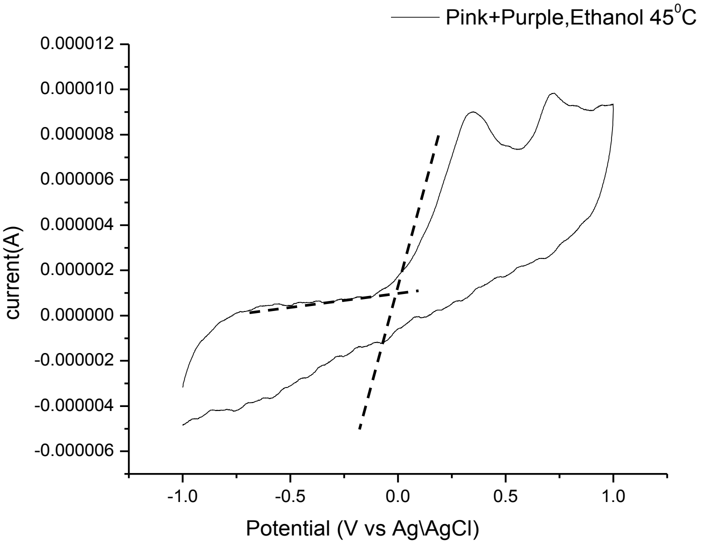

Figure 6: (b) The Cyclic Volammetry curve for (Pink + Purple) Coleus at 45˚C, 2h

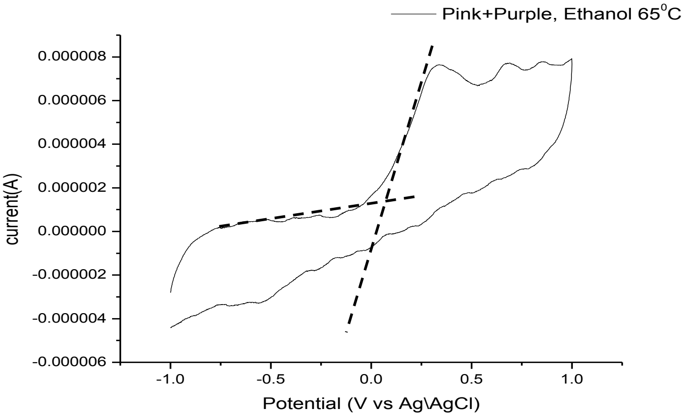

Figure 6: (c) The Cyclic Volammetry curve for (Pink + Purple) Coleus at 65˚C, 2h

Table 2: (a) Energy levels (HOMO and LUMO) for Mixed Coleus (Pink+Purple) with Ethanol at 25˚C, 45 ˚C and 65 ˚C, 2h

Temperature (˚C)	LUMO(eV)	HOMO(eV)
25	-4.36	-1.86
45	-4.34	-1.82
65	-4.32	-1.8

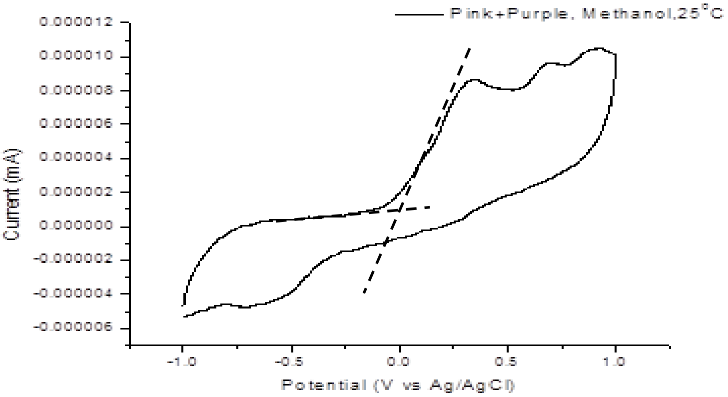

Figure 7: (a) The Cyclic Volammetry curve for (Pink + Purple) Coleus at 25˚C, 2h

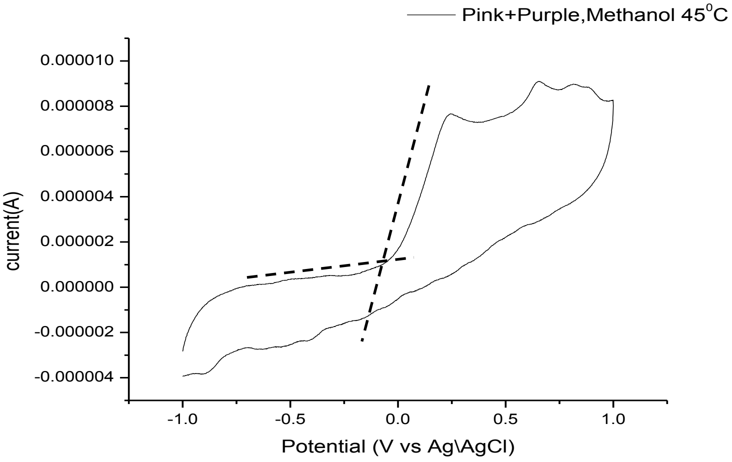

Figure 7: (b) The Cyclic Volammetry curve for (Pink + Purple)Coleus at 25 ˚C, 2h

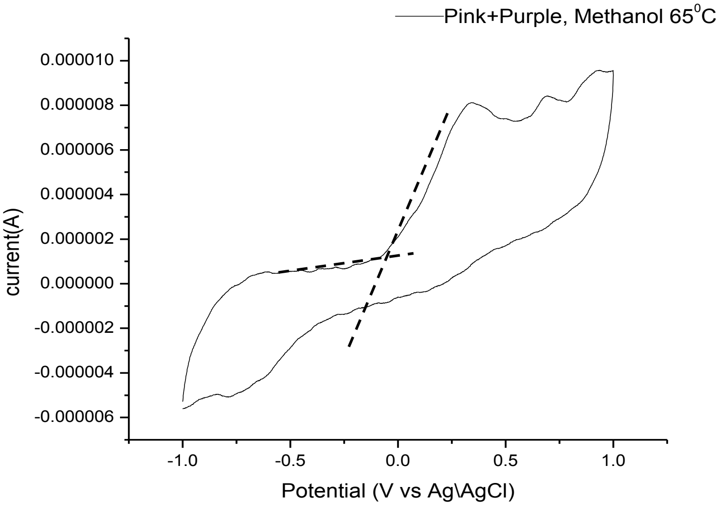

Figure 7: (c) The Cyclic Volammetry curve for (Pink + Purple) Coleus at 25 ˚C, 2h

Table 2: (b) Energy levels (HOMO and LUMO) for Mixed Coleus (Pink + Purple) with Methanol at 25˚C, 45 ˚C and 65 ˚C, 2h

Temperature (˚C)	LUMO(eV)	HOMO(eV)
25	-4.36	-1.85
45	-4.35	-1.84
65	-4.38	-1.86

FTIR Analysis

Fourier Transform-Infrared Spectroscopy (FTIR) is a technique used to identify organic (and in some cases inorganic) materials. This technique measures the absorption of infrared radiation by the sample material versus wavelength. The infrared absorption bands identify molecular components and structures. When a material is irradiated with infrared radiation, absorbed IR radiation usually excites molecules into a higher vibrational state. The wavelength of light absorbed by a particular molecule is a function of the energy difference between the at-rest and excited vibrational states. The wavelengths that are absorbed by the sample are characteristic of its molecular structure.[1,7,5]

Fig 8 (a) showed the FTIR spectrum of (pink + purple) coleus with methanol solvent, (b) showed the FTIR spectrum of (pink + purple) coleus with ethanol solvent. Table 3(a) showed chemical bond, chemical compound and frequencies range of pink coleus leaves by using methanol solvent, (b) showed chemical bond, chemical compound and frequencies range of pink coleus leaves by using methanol solvent.

All of dye solutions were displayed the sharp peaks frequencies range (3300 cm^{-1} - 2500cm^{-1}) indicated the presence of C-H (Alkanes) and O-H (carboxylic acids), (1640 cm^{-1}-1580 cm^{-1}) indicated the presence of N-H(Amines) and (1320 cm^{-1}-1000 cm^{-1}) indicated the presence of C-O (carboxylic acids) respectively. Therefore all dyes were corresponded to the presence of carboxylic acids groups. In additional, typical bond corresponding to C-N groups were observed. The results obtained from this research were similar as AMANO LIPASE Compound ($C_{11} H_9 N_3 Na O_2$) in FTIR library file.

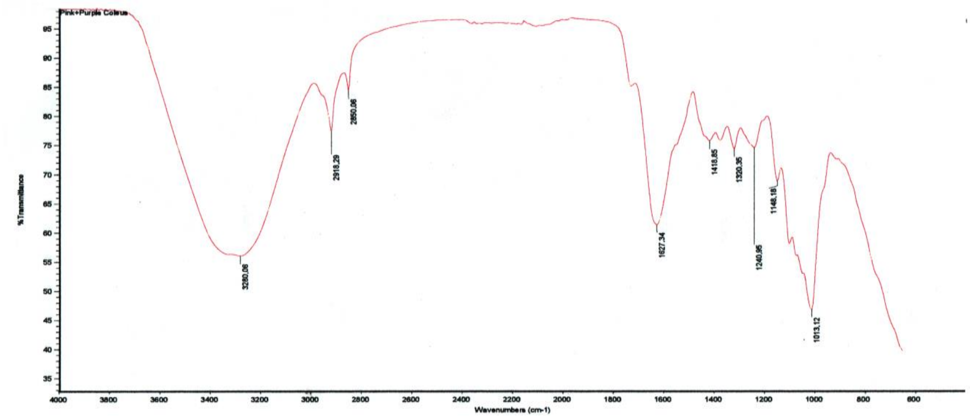

Figure 8: (a) FTIR spectrum of (Pink + Purple) Coleus leaves by using methanol solvent

Table 3: (a) Chemical Bonds, compound types & frequencies in (Pink + Purple) Coleus leaves by using methanol solvent

Bond	**Compound type**	**Frequency range(cm^{-1})**
C-H	Alkynes	3280.47 (strong, strength)
O-H	Carboxylic acid	2918.29, 2850.06 (broad, stretch)
N-H	Amines	1627.34 (bend)
C-H	Alkanes	1418.85(medium, stretch)
C-O	Alcohols, Ethers, Carboxylic acid, Esters	1013.12 (strong, stretch)

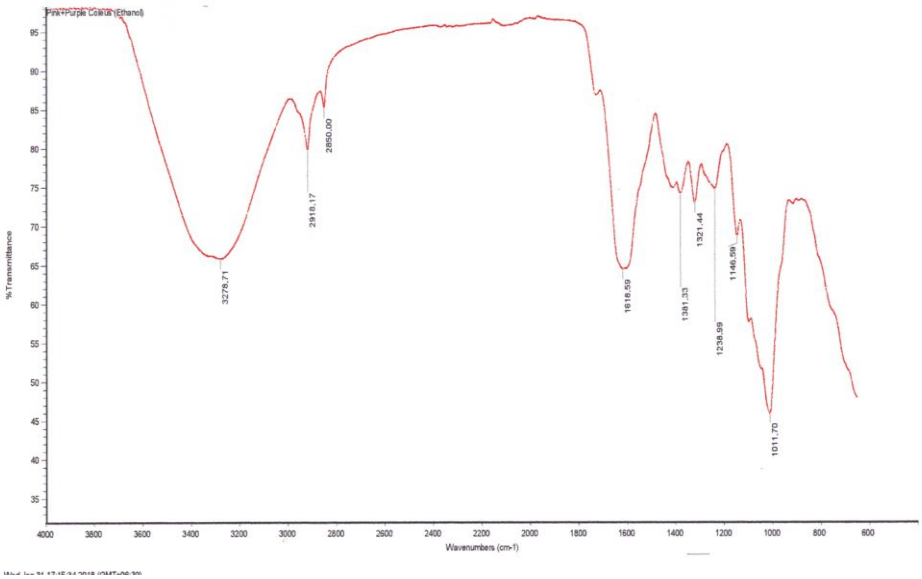

Figure 8: (b) FTIR spectrum of (Pink + Purple)Coleus leaves by using ethanol solvent

Table 3: (b) Chemical Bonds, compound types & frequencies in (Pink + Purple)Coleus leaves by using ethanol solvent

Bond	Compound type	Frequency range(cm^{-1})
C-H	Alkynes	3278.71 (strong, strength)
O-H	Carboxylic acid	2918.74, 2850.19 (broad, stretch)
N-H	Amines	1618.59 (bend)
C-H	Alkanes	1381.33(medium, stretch)
C-O	Alcohols, Ethers, Carboxylic acid, Esters	1011.70(strong, stretch)

Conclusion

The mixture of two colors of Coleus Blumei natural dyes were studied for photovoltaic applications. The maximum band gap energy was found 2.52 eV for (pink + purple) Coleus with ethanol as well as methanol solvents at 45 °C. Cyclic Voltammetry measurements were performed for these dye sensitizers to estimate their energy levels. According to the results, the largest value of LUMO was determined – 4.36 eV for (Pink+purple) Coleus with ethanol at 25 °C and – 4.38 eV with methanol at 65 °C. All types of dye solutions were pH levels round about 6, 7 and over, all of these solutions were acidic properties. The results of FTIR showed these dye solutions were AMANO LIPASE Compound which contained Carboxylic acids group. This study leads to the conclusion that dye extracted from Coleus Blumei leaves can be used as sensitizer for DSSC.

Acknowledgements

I am greatly indebted to Professor Dr Khin Khin Win, Head of Department of Physics, University of Yangon, for her kind permission.

I would also like to thank Professor Dr Aye Aye Thant, Department of Physics, University of Yangon, for her valuable advice in the preparation of this paper.

References

Arman Yusoff, N.T.R.N Kumara, Andery Lim, Piyarsiri Ekanayake and Kushan U. Tennakoon, " Impects of Temperature on the Stability of Tropical Plant Pigments as Sensitizers for Dye Sensitized Solar Cells " Journal of Biophysics, (2014), Vol.2014.

Asmaa Soheil Najm, Abu Bakar Mohamad and Norasikin A. Ludin, "The Extraction and Absorption Study of Natural Dye from Areca catechu for Dye Sensitized Solar Cell Application." International Workshop on Nanotechnology for Young Scientists, (2016),Vol.4 , pp 1-6.

Hassan K. Tajudeen etal, " Synthesis of Dye-Sensitized Solar Cells Using Chromophores from West African Plants" International journal of Science & Engineering Research, (2017) Vol.8, pp 631-635.

Hnin Ei Maung, Me Me Theint, Nyein Wint Lwin and Than Zaw Oo, " Optical Absorption and Absorption of Natural Dye Extracts on TiO_2 Scaffolds: Comparison between Green Leaf- and Red Fruit-Extracts" Journal of Material Science and Engineering, (2017), pp 166-170.

Jayaprada Rao Chunduri and Hetwi R. Shah, "FTIR Phytochemical Fingerpinting and Antioxidant Anlyses of Selected Indoor Non-Flowing Indoor Plants and Their Industrial Importance", International journal of Current Pharmaceutical Research, (2016), Vol.8, pp 37-43.

Kasim Uthman Isah, Umar Ahmadu, Adamu Idris and Isah Kimpa, " Betalain pigment as natural photosensitizers for dye-sensitized solar cells: the effect of dye pH on the photoelectric parameters". Mater Renew Sustain Energy, (2015), Vol.39, pp 1-5.

Lucia LEONAT and Gabriela SBARCEA, "Cyclic Voltammetry for Energy Levels Estimation of Organic Materials", (2013), Vol.75, pp 111-118.

Mohammed IK, Kasim Uthman ISAH, Yabagi JA , Taufiq S, "The Effect on Extracting Solvents using Natural Dye Extracts from Hyphaene hebaica for Dye-sensitized Solar Cells", Materials Science and Engineering, , (2015), Vol.5.

N.T Mary Rosana, Joshua Amarnth, K.L. Vicent Joseph, A Suresh, S. Anandan, G Saritha "Natural Sensitizers for Dye Sensitized Solar Cell Application", International Journal of Scientific & Engineering Research, (2014) Vol.5.

J. Myanmar Acad. Arts Sci. 2019 **Vol. XVII. No.2A**

PREPARATION AND OPTICAL PROPERTIES OF SOME NATURAL DYES (IXORA COCCINEA &TRADESCANTIA SPATHACEA)

Aye Mya Khaing[1], Khaing Nway Win[2], Yin Maung Maung[3],
Than Than Win[4]

Abstract

PoneNaYeik petal (**IxoraCoccinea**) and TainPyarTaungNyo leaf (**TradescantiaSpathacea**) dyes were extracted with acidified solvent, ethanol to study the effects of solvent type on the extraction. UV-vis spectrometer can analyze the optical properties of these natural extract dyes. Characterization results showed high absorbance values 0.5494, 0.5845 and 0.3994 at 450 nm for PoneNaYeik dye. The sharp absorbance values in this study were 1.5244, 1.0997, 1.3577 at 435 nm and 0.9136, 0.6518, 0.7981 at 665 nm for TainPyarTaungNyo. The electrochemical properties of these dyes were observed by cyclic voltammetry (CV). These were indicative of the extract can be used as dye sensitized solar cells. Fourier Transmission Infrared Spectroscopy (FTIR) indicated the structural properties of these dyes.

Keywords: Natural dyes, optical absorption, electrochemical properties, FTIR

Introduction

DSSC has been increasingly used because it provides high energy conversion efficiency. [Nurezyanic S et al 2017]. This type of cells exhibits potential for future photovoltaic applications because of its simple fabrication process, low manufacturing cost, low environmental impact, and flexibility. [R. Syafinar et al 2015] Natural dye solar cells are a sub category of organic solar cells. Natural dyes are relatively easy to obtain and extract from plants, fruits, flowers, and leaves, reducing the cost manufacturing of DSSC, as opposed to the production of synthetic dyes. [Zularif Z et al 2015] [Michael Grätzel 2003]

The natural dyes used in this study were obtained from petals of red colored IxoraCoccinea (coded as “PNY”), species- I. coccinea, family-

---

[1] PhD candidate, Department of Physics, University of Yangon, Myanmar

[2] Lecturer, Department of Physics, University of Yangon, Myanmar

[3] Associate Professor, Department of Physics, University of Yangon, Myanmar

[4] Associate Professor, Department of Physics, Mandalay University of Distance Education, Myanmar

Rubiaceae and leaves of Tradescantia Spathacea (coded as “TPTN”), species- T. spathacea, family- Commilinaceae by using ethanol solvent. These plants were found in various places of Myanmar. In this investigation, the samples were collected from Yangon region. The effect on temperature and band gap and molecular energy levels of extracting dyes were investigated systematically by UV-vis spectroscopy and cyclic voltammetry methods. FTIR spectral analysis was used to determine the functional group in the natural dye.

Experimental Procedure

Preparation of Dyes

25g of petals of Ixora Coccinea and 25g leaves of Tradescantia Spathacea, each of one was ground and mixed with 150 mL of 70% ethanol and then stored overnight in the refrigerator at 4°C. On the following day, the extracted samples were stirred using magnetic stirrer at 25°C, 45°C and 65°C for two hours. The procedure continued with the filtration of the samples to remove large residue. Subsequently, the extracts were centrifuged at 4000 rpm using a Denley BS400 (UK) centrifuge machine for five minutes to separate any remaining residues. After that the extracts were placed in a 45–50°C water bath to dissolve more pigments into the extracting solvent.

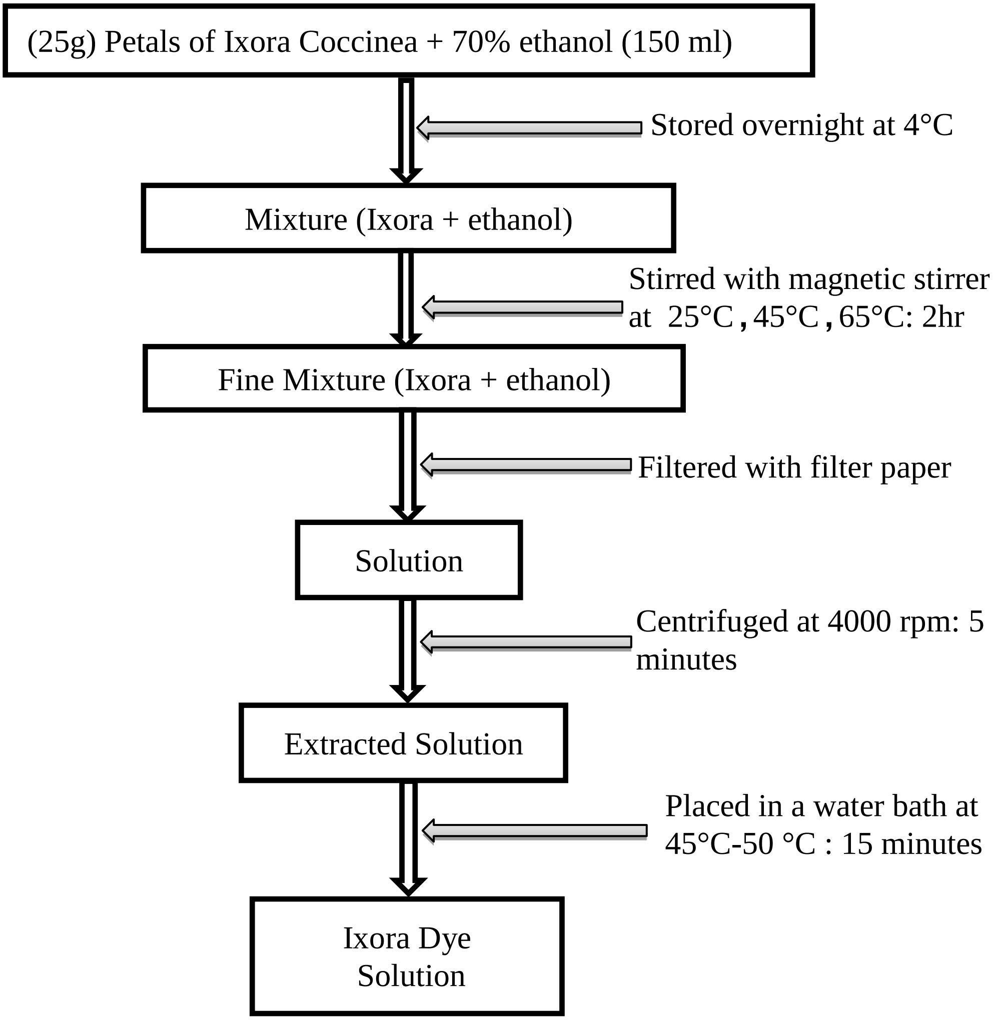

Figure 1: Flow chart of Ixora Coccinea dye extraction

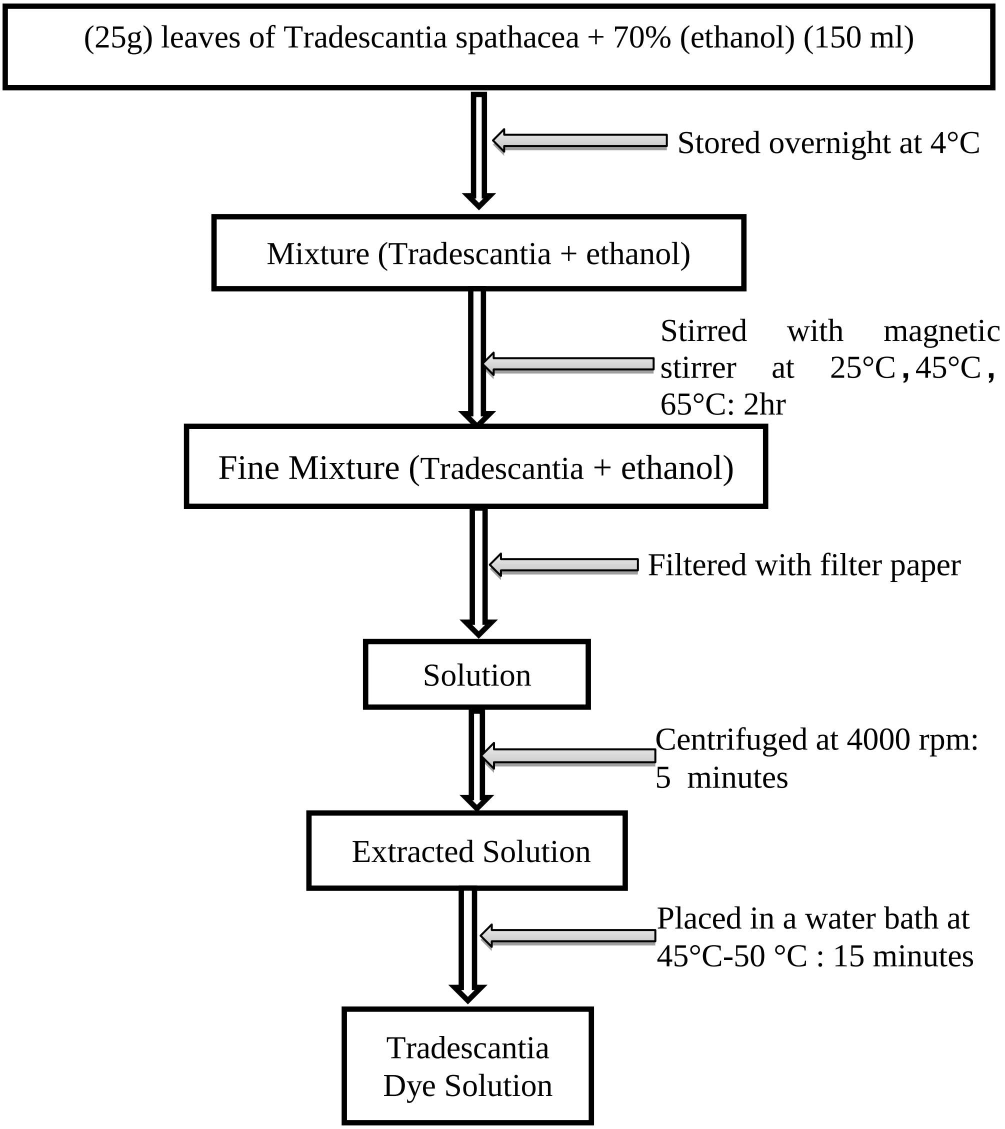

Figure 2: Flow chart of Tradescantia spathacea dye extraction

Characterization

The presence of anthocyanin and chlorophyll pigments in these natural dyes was determined by measuring their absorbance spectra using UV-Vis spectrophotometer (Shimadzu UV-1800, Japan). UV-vis spectroscopy can be used to measure the absorbance of ultra violet or visible light by organic dyes in the range of 400 nm to 700 nm. The functional groups of the sensitizers were determined via Fourier transform infrared spectroscopy (FTIR) (Perkin Elmer Spectrum 400 FT-IR).

Cyclic voltammetry Measurement

Cyclic voltammetry is a very suitable method for a wide range of applications and it is one of the standard techniques used for characterization. [Lucia L et al 2013] It is accomplished with a three electrode arrangement such as a glassy carbon working electrode, platinum counter electrode, and Ag/AgCl reference electrode at a scan rate of 50 mV/s. [P.Petovra et al 2013]

Results and Discussion

Figure 3 showed the optical absorption spectra of PoneNaYeik dye with different growing temperature, 25°C, 45°C and 65°C for the same concentration. It was found that the maximum absorption peaks were found at 450 nm dye solution of PoneNaYeik at 25 °C, 45 °C and 65 °C.

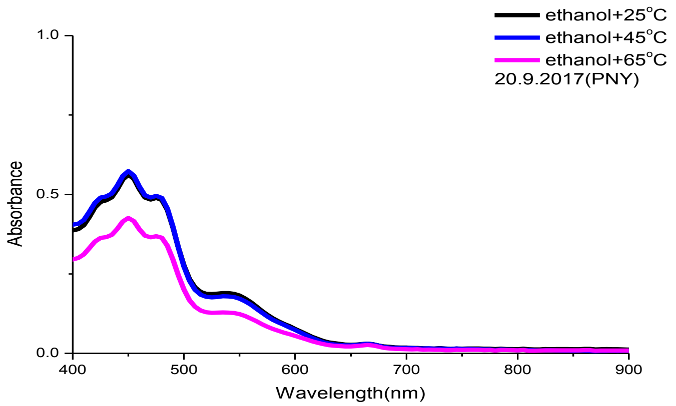

Figure 3: Optical absorption spectra of ***Ixora Coccinea*** (PoneNaYeik) dye extract in solvent ethanol (25°C, 45°C, 65°C)

Figure 4 described the optical absorption spectra of Tain Pyar Taung Nyo dye at 25 °C, 45 °C and 65 °C for the same concentration. The sharp absorbance values were 1.5244, 1.0997, 1.3577 at 435 nm and 0.9136, 0.6518, 0.7981 at 665 nm for Tain Pyar Taung Nyo dye.

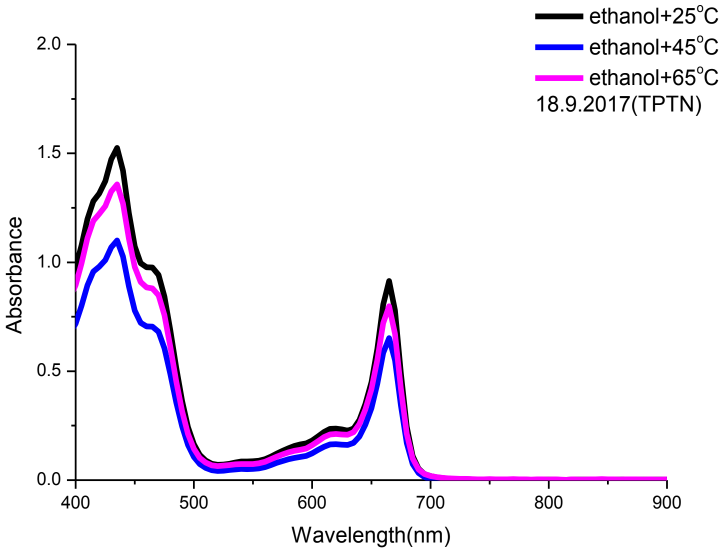

Figure 4: Optical absorption spectra of ***Tradescantia Spathacea*** (Tain Pyar Taung Nyo) dye extract in solvent ethanol (25^{o}C, 45^{o}C, 65^{o}C)

Optical Properties the energy band gaps (E_g) of these samples at different temperatures were calculated by the following equation.

$$E_g = \frac{hc}{\lambda}$$

where $h =$ Planck's constant $= 6.626 \times 10^{-34}$ Js, $c =$ velocity of light $= 3 \times 10^{8} ms^{-1}$ and $\lambda =$ wavelength

Electrochemical Properties

Electrochemical cyclic voltammetry (CV) was performed to determine the HOMO and the LUMO energy levels of the natural dyes. [P. Petrova et al 2013] Figure 5 (a-c) showed the cyclic voltammograms of Ixora Coccinea (PoneNaYeik) dye. Figure 6 (a-c) showed the cyclic voltammograms of Tradescantia Spathacea (Tain Pyar Taung Nyo) dye. The electrons from the lowest unoccupied molecular orbital (LUMO) and the highest occupied molecular orbital (HOMO) levels were determined from the following equations. [T.JAbodunrin et al 2015] [Changqing Ye et al 2012]

$$E_{Lumo} = -\left[E^{onset} + 4.4\right]eV$$

$$E_{Homo} = E_{Lumo} + E_g$$

The reduction onset potential E^{onset} is determined from the intersection of the two tangents drawn at the rising current and baseline of the CV traves. The optical band gap energies E_g were determined from the UV-Vis absorption spectra. The electrochemical energy levels and optical band gap energies of these dyes are listed in table 1 and 2.

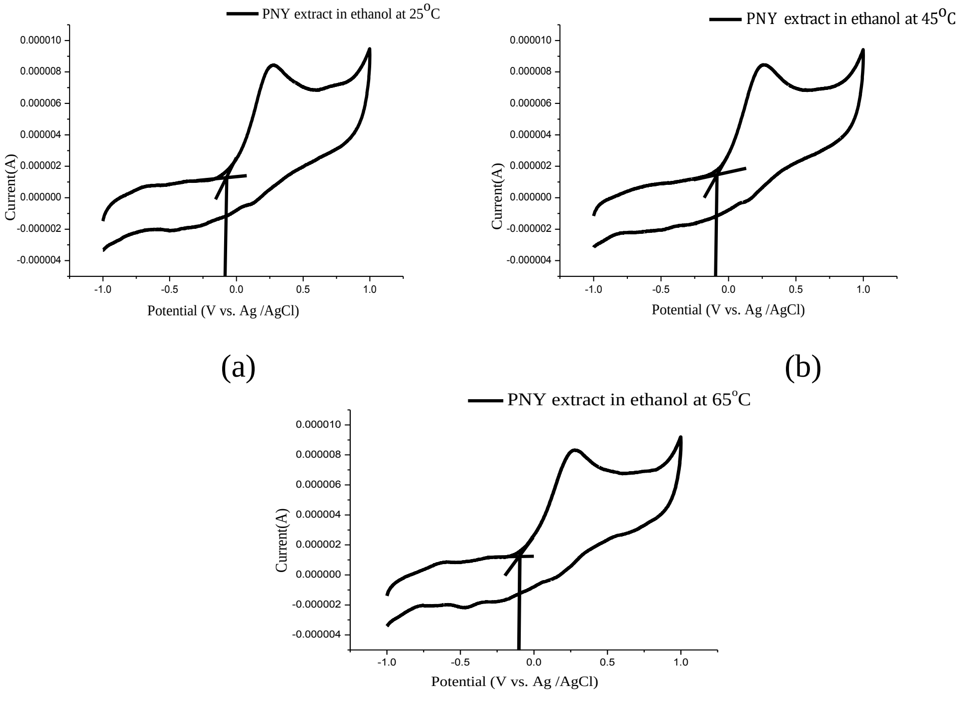

(a) (b)

(c)

Figure 5: (a) The Cyclic Voltammetry curve for Ixora Coccinea at 25 °C, 2h
(b) The Cyclic Voltammetry curve for Ixora Coccinea at 45 °C, 2h
(c) The Cyclic Voltammetry curve for Ixora Coccinea at 65 °C, 2h

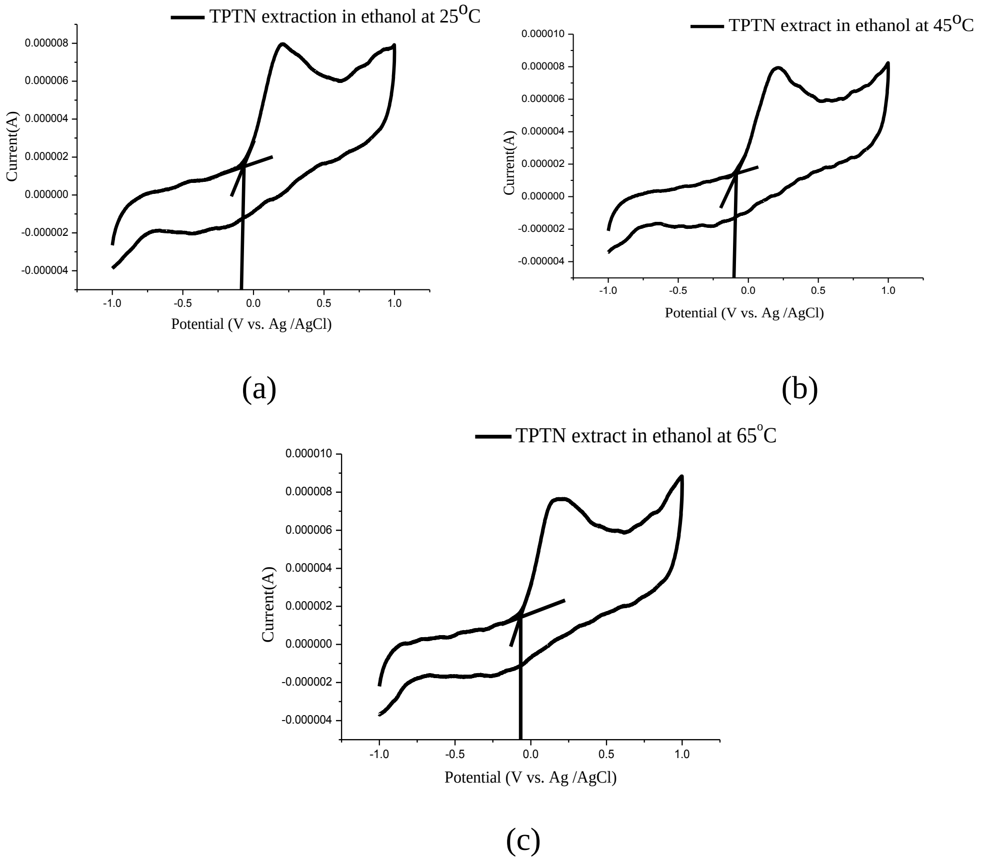

Figure 6. (a) The Cyclic Voltammetry curve for Tradescantia Spathacea at 25 °C, 2h
(b) The Cyclic Voltammetry curve for Tradescantia Spathacea at 45 °C, 2h
(c) The Cyclic Voltammetry curve for Tradescantia Spathacea at 65 °C, 2h

Table 1: Energy levels & Band gap energies for IxoraCoccinea (PoneNaYeik) at 25 °C, 45 °C and 65 °C, 2h

Temperature (℃)	Band Gap Energies (eV)	LUMO (eV)	HOMO (eV)
25	2.445	-4.484	-2.039
45	2.459	-4.496	-2.037
65	2.474	-4.496	-2.022

Table 2 : Energy levels & Band gap energies for Tradescantia Spathacea (TainPyarTaungNyo) at 25°C, 45°C and 65°C, 2h

Temperature (℃)	**Band Gap Energies (eV)**	**LUMO (eV)**	**HOMO (eV)**
25	2.533	-4.316	-1.783
45	2.538	-4.298	-1.760
65	2.533	-4.333	-1.800

FTIR Analysis

FTIR spectroscopic results of IxoraCoccinea with ethanol studied in Figure 7 revealed the presence of various chemical constituents in the extract of with various peaks values corresponding with 3371.68, 2933.83, 1732.13, 1612.54, 1523.82, 1442.80, 1363.72, 1251.84, 1064.74, 819.77, 767.69 and 609.53cm^{-1} stretching frequency when it was compared with the standard. The IR stretching frequencies at 3371.68 cm^{-1} could be due to the Alcohol O-H stretching frequency. The band at 2933.83 cm^{-1} was due to Alkane C-H stretching. A peak at 1732.13 cm^{-1}assigned Aldehyde C=O stretching. The bands at 1612.54 and 1523.82 cm^{-1}were due to Aromatic and Alkene C=C stretching. The IR stretching frequencies at 1251.84 and 1064.74cm^{-1} were due to Carboxylic acids, Ester C-O stretching and Anhydrides O-C stretching. A peak at 1442.80, 1363.72,819.77, 767.69 and 609.53cm^{-1} confirmed the presence of Sulphur compounds such as Esters S-OR and Sulphate S=O. [Asmaa Soheil Najm et al 2016] [Kasim Uthman Isah et al 2015] [Jayaprada Rao Chunduri et al 2016]

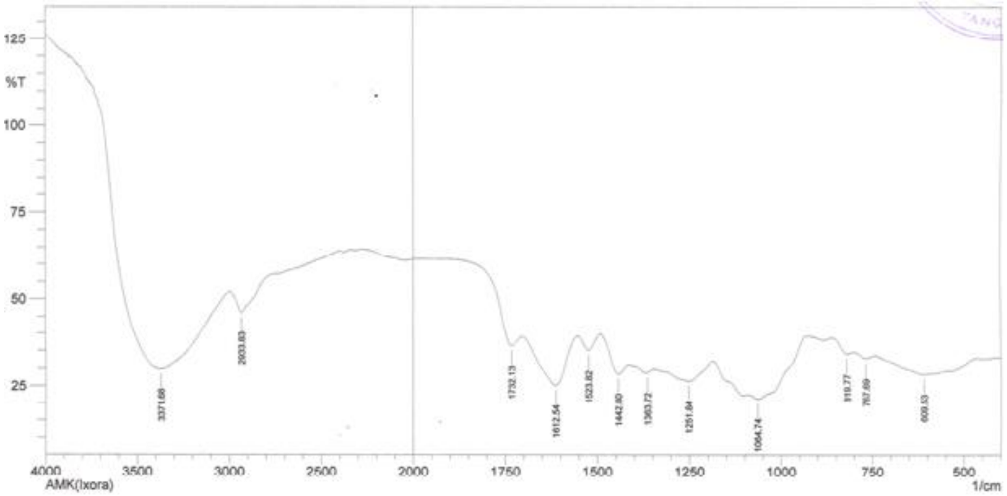

Figure 7: FTIR spectrum of IxoraCoccinea extracted from ethanol solvent

In the case of Tradescantia Spathacea with ethanol FTIR spectrum-Figure 8, the intense bands occurred at 2999.41, 2883.68, 2306.94, 1604.83, 1433.16, 1145.75, 1084.03, 966.37, 829.42, 763.84 and 694.40 cm^{-1}stretching frequency. 2999.41 and 2883.68 cm^{-1} stretching frequencies indicated the presence of Alkane C-H stretching and Carboxylic Acids O-H stretching. The bands at 2306.94 cm^{-1} was due to Phosphine P-H stretching and Silane Si-H stretching. The IR stretching frequencies at 1604.83, 1084.03,966.37, 829.42, 763.84 and 694.40 cm^{-1}could be due to the Nitrogen Compound Amines NH_2, C-N, NH_2 & N-Hand Amine Oxide (N-O) aliphatic stretching. The bands at 1433.16 and 1084.03cm^{-1}indicated the presence of Sulphur compound Sulphate S=O and Tricarbonyl C=S stretching. The peaks at 1145.75 and 966.37cm^{-1} were due to Phosphorous compound Phosphine oxide P=O, P-H and Phosphate P=O stretching. A peak at 1084.03cm^{-1} confirmed the presence of Silicon compound Silane Si-OR stretching frequency. [Asmaa Soheil Najm et al 2016] [Kasim Uthman Isah et al 2015] [Jayaprada Rao Chunduri et al 2016]

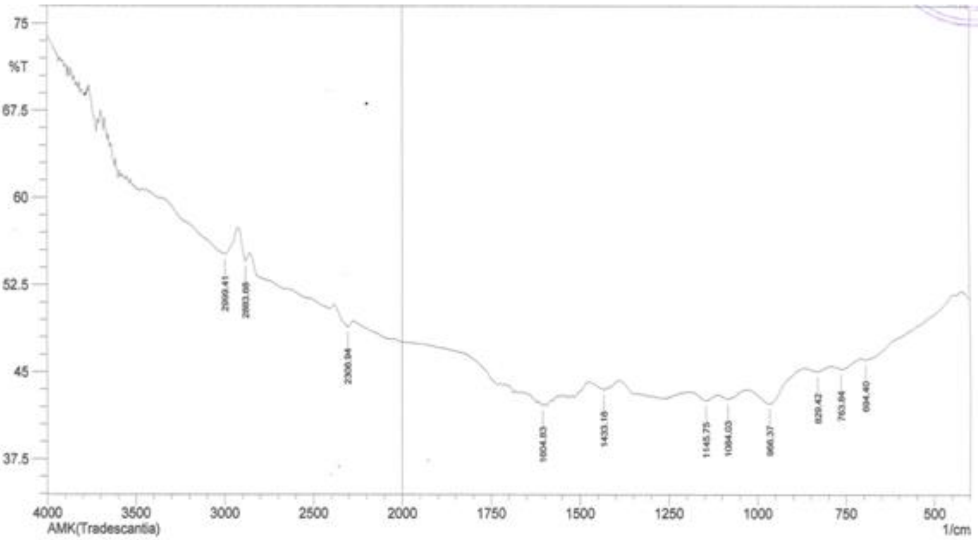

Figure 8: FTIR spectrum of Tradescantia Spathacea extracted from ethanol solvent

Conclusion

The natural dyes extracted from petal of ***IxoraCoccinea*** (Pone Na Yeik) and leaf of ***Tradescantia Spathacea*** (Tain Pyar Taung Nyo) were used to build dye-sensitized solar cells. They were characterized by UV-vis spectrophotometer. The absorption spectrum from UV-vis can give to calculate the maximum energy band gap. The results from this work for Ixora Coccinea dye are 2.445 eV at 25°C, 2.459 eV at 45°C and 2.474 eV at 65°C. In Tradescantis Spathacea dye, the results are 2.533 eV at 25°C, 2.538 eV at 45°C and 2.533 eV at 65°C. The energy band gaps of all these dyes are nearly to 2.5 eV for organic dyes. So the dyes extracted in this research work may be applied in use for a part of dye sensitized solar cells. According to the results of Cyclic Voltammetry measurements, the largest value of LUMO was found -4.496 at 45°C and 65 ^{o}C for IxoraCoccinea dye while -4.333 at 65 ^{o}C for Tradescantis Spathacea dye. The results of FTIR showed IxoraCoccinea dye and Tradescantis Spathacea dye solution were AMANO LIPASE Compound which contained Carboxylic acidic group. So the dye extracted in this research work may be applied in use for a part of dye sensitized solar cells.

Acknowledgements

I would like to express my sincere thanks to Professor Dr Khin Khin Win, Head of Department of Physics, University of Yangon, for her kind permission to carry out this work.

I am also greatly thankful to Professor Dr Aye Aye Thant, Department of Physics, University of Yangon, for her valuable advice in the preparation of this paper.

References

Asmaa Soheil Najm, Abu Bakar Mohamad and Norasikin A. Ludin, "The Extraction and Absorption Study of Natural Dye from Arecacatechu for Dye Sensitized Solar Cell Application." International Workshop on Nanotechnology for Young Scientists, (2016), Vol.4, pp 1-6.

A. Yusoff, N. T. R. N. Kumara, A. Lim, P. Ekanayake, K. U. Tennakoon, (2014), "Impacts of temperature on the stability of tropical plant pigments as sensitizers for dye sensitized solar cells". Journal of Biophysics, vol.2014, 8 pages.

Changqing Ye, Mingzhu Li, JiaLuoLinfengChan, Zhengming Tang, Jian Pei, Lei Jiang, Yanlin Song, and Daoben Zhu, "Photo-induced amplification of readout contrast in nanoscale data storage". Electronic supplementary Information (ESI), Journal of Materials Chemistry, (2012), Vol. 22, pp 4115-4536.

Hosseinnezhad.M, S. Moradian and K. Gharanjig, "Natural Dyes Extracted from Black Carrot and Bramble for Dye-Sensitized Solar Cells" Progress Journal, (2015), Vol.8, pp 153-162.

Hnin Ei Maung, Me Me Theint, Nyein Wint Lwin and Than Zaw Oo, "Optical Absorption and Absorption of Natural Dye Extracts onTiO2 Scaffolds: Comparison between Green Leaf-and Red Fruit-Extracts" Journal of Material Science and Engineering, (2017), pp 166-170.

Jayaprada Rao Chunduri and Hetwi R. Shah, "FTIR Phytochemical Fingerpinting and Antioxidant Anlyses of Selected Indoor Non-Flowing Indoor Plants and Their Industrial Importance", International journal of Current Pharmaceutical Research, (2016), Vol.8, pp 37-43.

Kasim Uthman Isah, Umar Ahmadu, Adamu Idris and Isah Kimpa, "Betalain pigment as natural photosensitizers for dye-sensitized solar cells: the effect of dye pH on the photoelectric parameters". Mater Renew Sustain Energy, (2015), Vol.39, pp 1-5.

Lucia Leonat, Gabriela Sbarcea, (2013), "Cyclic Voltammetry for Energy Levels Estimation of Organic Materials". U.P.B. Sci. Bull, Series B, vol.75, pp. 111-118.

Michael Grätzel, (2003), "Dye-sensitized solar cells". Journal of Photochemistry and Photobiology, vol. 4 (2003), pp. 145–153.

Nurezyanic Safie, Norasikin Ahmad ludin. Norul Hisham Hamid. Suhaila Sepeai. Mohd Asri Mat Teridi. MohdAdib Ibrahim. Kamaruzzaman Sopian. Hironori Arakawa, (2017), "Energy levels of natural sensitizers extracted from rengas (Gluta spp.) and mengkulang (Heritieraelata) wood for dye-sensitized solar cells". Master Renew Sustain Energy, (2017) 6:5, 9 pages.

P.Petovra, P. Ivanvo, Y. Marcheva, and R.Tomova, "Estimation of energy levels of new Iridium cyclometalated complexs via cyclic voltammetry." Bulgarian Chemical Communication, (2013), Vol-45, pp 159-164.

R. Syafinar, N. Gomesh, M. Irwanto, M. Fareq, Y.M. Irwan, (2015), "Chlorophyll Pigments as Nature Based Dye for Dye-Sensitized Solar Cell (DSSC)". Energy Procedia, vol. 79 (2015), pp. 896 – 902.

T.J Abodunrin, O. obafemi, A.O. Boyo , and T Adebayo, "The Effect of Electrolyte on Dye Sensitized Solar Cells Using Natural Dye from Mango (M. indica L.) Leaf as Sensitizer" Advance in Material Physics and Chemistry, (2015), Vol.5, pp 205-213.

Zularif Zolkepli, Andery Lim, Piyasiri Ekanayake, Kushan Tennakoon, (2015), "Efficiency Enhancement of Cocktail Dye of Ixoracoccinea and Tradescantiaspathacea in DSSCs". Journal of Biophysics, vol. 2015, 8 pages.

J. Myanmar Acad. Arts Sci. 2019 **Vol. XVII. No.2A**

TOXIC ELEMENT CONCENTRATION IN SOIL FROM GOLD MINE

Khaing Yi Mon Shein[1] , Win Win Khaing[2],
Shwe Nan Htet[3] and Cho Cho Aung[4]

Abstract

Toxic element concentration in soil samples from 3m, 6m, 9m and 12m depths of gold mine at Satekalay village and Chaytawyar village, Shwegyin Township, Bago Division were investigated by using Energy Dispersive X-ray Fluorescent (EDXRF) method. Iron and silicon were found as major elements whereas potassium and titanium were found as second major elements. Other elements such as calcium, vanadium, chromium, manganese, copper, zinc, arsenic, rubidium, strontium, yttrium, zirconium and barium were found as minor elements in all the soil samples. The toxic elements such as cadmium and lead were measured by using Atomic Absorption Spectroscopy (AAS) method.

Key words: soil samples, Energy Dispersive X-Ray Fluorescent (EDXRF) method, elemental concentration, Atomic Absorption Spectroscopy (AAS) method, trace elements concentration

Introduction

In soils, some of the chemical elements occur as the components of minerals may be toxic. The chemical elements such as metals cannot break down, but their characteristics may change so that they can be easily taken up by plants or animals. Soil is clean when the concentration of elements contained in it is equal to the background concentration. The background concentration is the total element concentration obtained from soils that had not been affected by human activity.

Knowledge of elemental concentration in soil is very important for assessing the purity and quality of the soil in an environment. Energy Dispersive X-Ray Fluorescence (EDXRF) provides a rapid and nondestructive method for the analysis of elements in a sample. It is a very powerful technique for measuring the concentration of elements in a sample. In EDXRF, the intensities of the characteristic X-rays are measured to determine

---

[1] PhD Candidate, Department of Physics, University of Yangon

[2] Dr, Assistant Lecturer, Department of Physics, University of Yangon

[3] Dr, Lecturer, Department of Physics, University of Yangon

[4] Dr, Associate Professor, Department of Physics, University of Yangon

the elemental concentration of a sample. Atomic absorption spectrometry (AAS) is an analytical technique that measures the concentrations of certain elements in a sample. Atomic absorption is so sensitive that it can measure down to parts per million or milligram per litre in a sample.

The elemental concentrations of soil samples were measured by using the Energy Dispersive X-Ray Spectrometer and the trace concentrations of toxic elements in soil samples were measured by using the Atomic Absorption Spectrometer (AAnalyst-800). The measurement results were compared with the maximum permissible level recommended by the World Health Organization (WHO). The elemental concentrations of soil sample were determined in weight percent (W%) and the trace element concentrations were determined in milligram per litre (mg/L).

Experimental Work

The soils samples were collected from four different depths (3 m, 6 m, 9 m and 12 m) of gold mine at (1) Satekalay Village, Shwegyin Township, Bago Division, (2) Mine-1, Chaytawyar Village, Shwegyin Township, Bago Division and (3) Mine-2 Chaytawyar Village, Shwegyin Township, Bago Division. The collected soil samples were listed in the Table 1.

Table 1: The soil samples from four different depths of gold mines

No	G 1 (Satekalay)	G 2 (Mine 1,Chaytawyar)	G 3 (Mine 2,Chaytawyar)	Depths of the gold mine (m)
1	S 1	S 1	S 1	3
2	S 2	S 2	S 2	6
3	S 3	S 3	S 3	9
4	S 4	S 4	S 4	12

G1= gold mine at Satekalay Village , G 2= gold mine at Mine-1, Chaytawyar Village

G 3= gold mine at Mine-2, Chaytawyar Village

S 1= soil sample at 3 m , S 2= soil sample at 6 m

S 3= soil sample at 9 m , S 4= soil sample at 12 m

At first, the collected soil samples were dried in air and all the rocks were removed from the soil. Each sample was ground into fine powder by using the grinding machine. Then, the powder samples were filtered through 250 μ m sieve to obtain the same grain size. For the EDXRF measurement, the powder samples were poured into a mould which is made of steel and pressed into a pellet. The powders can be pressed into pellets, either hydraulically or manually. By pressing, the powder sample would be compacted and homogeneous and thus the more exact and better result could be obtained. The determination of elemental concentration was performed by using EDX-720 Spectrometer.

For the AAS measurement, 1g of soil sample was accurately weighted by using the scientific balance and placed into 100 ml beaker. The sample was digested with 5 ml of 10% hydrochloric acid (HCl) at a temperature of (250-300 °C). After a digestion time of 5 hours, the beaker was cooled to room temperature and filtered the sample. And then the clear solution volume was made up to 100 mL for each sample using the distilled water. The determination of trace element concentration was performed by using AAnalyst-800 Spectrometer.

Results and Discussion

The results of the elemental concentrations in the soil samples were shown in Table 2 and the respective graph was shown in Figure 1. According to Table 2, it was found that iron and silicon were the major elements and potassium and titanium were found as second major elements. Other elements such as calcium, vanadium, chromium, manganese, copper, zinc, arsenic, rubidium, strontium, yttrium, zirconium and barium were found as very few amount in all samples. The toxic elements such as cadmium and lead were not detected in weight percent level.

Table 2: Measurements of Elemental Concentrations in soil samples from from gold mines at Shwegyin Township, Bago Division (W%)

Sample	Si	K	Ca	Ti	V	Cr	Mn	Fe	Cu	Zn	As	Rb	Sr	Y	Zr	Ba
G 1 (S 1)	43.29	8.17	ND	3.43	ND	ND	0.66	43.41	0.13	0.16	ND	ND	0.08	0.10	0.57	ND
(S 2)	53.83	9.46	ND	4.64	0.17	ND	0.51	29.82	0.11	0.14	ND	0.15	0.10	0.08	1.01	ND
(S 3)	39.97	9.05	3.66	2.68	ND	ND	0.81	42.91	0.11	0.17	ND	0.01	0.16	0.08	0.37	ND
(S 4)	42.99	7.86	9.64	2.55	0.12	ND	0.68	35.24	0.08	0.11	ND	0.01	0.33	ND	0.38	ND
G 2 (S 1)	40.44	7.31	ND	3.18	ND	0.14	0.08	46.77	0.11	ND	0.06	ND	0.08	0.06	0.42	1.35
(S 2)	44.25	10.84	ND	3.36	ND	0.16	0..05	39.16	0.10	ND	0.12	ND	0.05	0.05	0.44	1.43
(S 3)	43.58	12.75	ND	3.74	0.25	ND	0.12	39.04	0.11	ND	ND	ND	0.10	0.06	0.30	ND
(S 4)	45.09	12.61	ND	3.86	0.15	0.10	0.14	37.52	0.11	ND	ND	ND	0.09	0.06	0.26	ND
G 3 (S 1)	35.42	10.11	ND	4.18	0.22	0.31	0.16	48.94	ND	ND	ND	ND	ND	0.11	0.67	ND
(S 2)	31.13	8.12	ND	5.05	0.21	0.12	0.12	54.32	ND	ND	ND	ND	0.08	0.09	0.77	ND
(S 3)	31.78	11.22	ND	2.41	0.27	0.26	0.03	52.82	0.20	0.10	0.72	ND	ND	0.07	0.13	ND
(S 4)	29.54	4.94	ND	2.58	0.16	ND	0.14	62.16	ND	ND	ND	ND	ND	ND	0.47	ND

ND = not detected

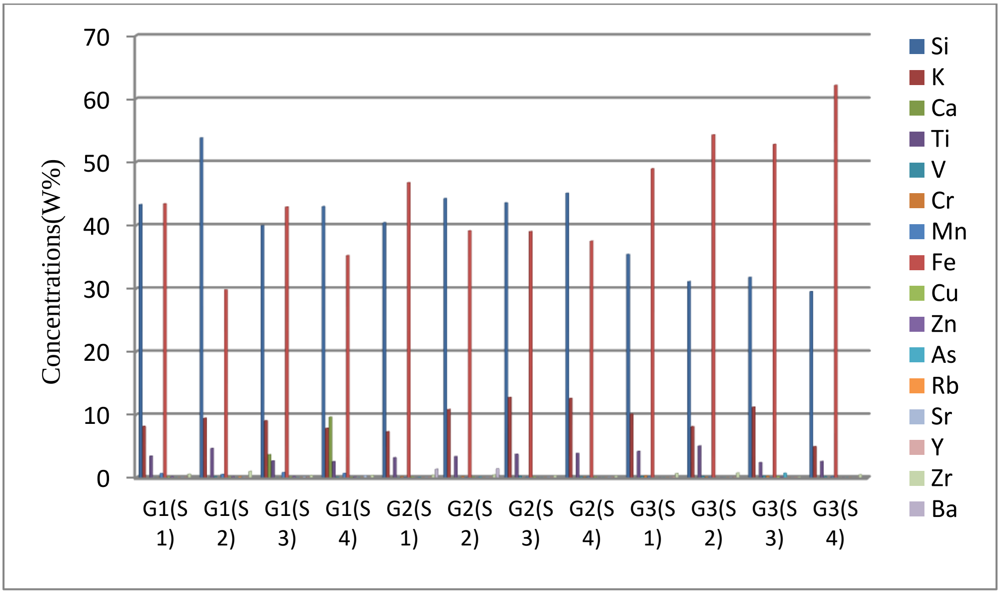

Figure 1: The elemental concentrations in the soil samples from gold mines at Shwegyin Township, Bago Division

The results of the trace elements concentration of soil samples at Shwegyin Township, Bago Division were shown in Table 3 and the respective graph was shown in Figure 2. According to Table 3, it was found that cadmium and lead were found as very few amount in all samples of the gold mines and the concentrations were randomly with the depth. The trace concentrations of all the elements were much less than the maximum permissible level.

Maximum permissible level for cadmium = 3 mg/L

Maximum permissible level for lead = 100 mg/L

Table 3: The measure results of trace elements concentration in the soil samples from gold mines at Shwegyin Township, Bago Division (mg/L)

Sample	Cd	Pb
G1(S 1)	0.035	0.289
(S 2)	0.042	0.267
(S 3)	0.041	0.298
(S 4)	0.044	0.262
G2(S 1)	0.045	0.015
(S 2)	0.044	0.074
(S 3)	0.055	0.024
(S 4)	0.040	0.045
G3(S 1)	0.061	0.019
(S 2)	0.021	0.025
(S 3)	0.865	0
(S 4)	0.042	0

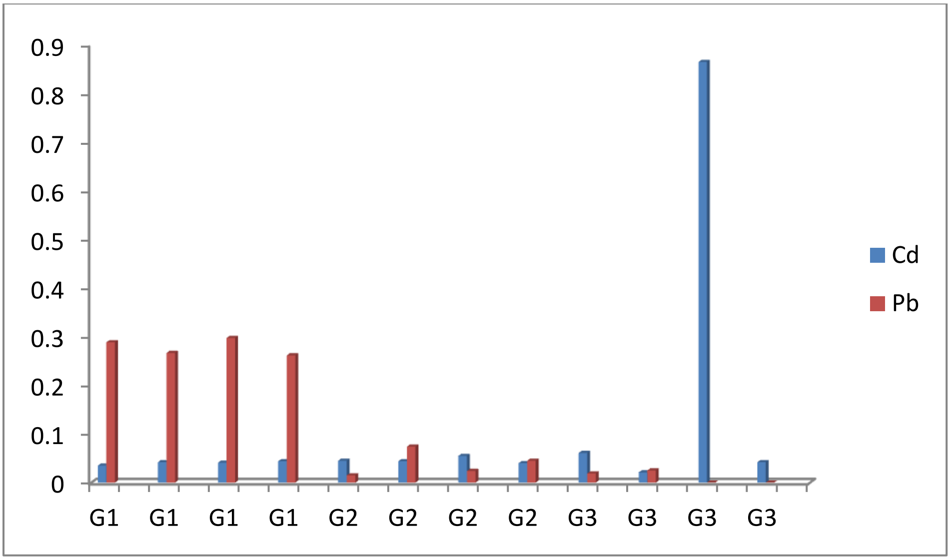

Figure 2: The trace elements concentration in the soil samples from gold mines at Shwegyin Township, Bago Division

Conclusion

From the EDXRF measurement, it was found that iron and silicon were the major elements and potassium and titanium were found as second major elements in all samples of all of the gold mine. Heavy elements such as copper and arsenic were detected but very few amount in comparison with iron and silicon. The other toxic elements such as cadmium and lead were not detected in weight percent level.

From the AAS measurement, it was found that the toxic elements cadmium and lead were detected but very few amount in all of the soil sample. The trace concentrations of all the soil samples were less than the maximum permissible level. From the point of view of AAS measurement, all of the gold mines cannot be affected by the toxic elements, cadmium and lead.

Therefore, it was found that the trace concentrations of toxic elements, cadmium and lead in the collected soil samples were less than the maximum permissible level. So that it can be concluded that the research gold mines were safe from the side effects of toxic elements such as cadmium and lead for the health of human beings who live near the gold mine and miners who work at the gold mine.

Acknowledgements

I would like to thank Professor Dr Khin Khin Win, Head of Department of Physics, University of Yangon for her kind permission to carry out this research.

I would like to express my sincere thanks to Professor Dr Aye Aye Thant, Department of Physics, University of Yangon, for her advice and help.

References

Antoaneta Ene, Claudia Stihi, I.V. Popescu, Anca Gheboianu, Alina Bosneaga, I. Bancuta (2009) Comparative studies on heavy metal content of soils using AAS and EDXRF atomic spectrometric techniques

AN-XRF-003, Rev B1, “EDXRF of Light Elements in Water”

Joshua O. Olowoyo, Anthony I.Odiwe, Nquobile M.Mkolo, Linda Macheka (2013) Investigating the Concentrations of Different Elements in Soil and Plant Composition from a Mining Area

K. KODOM,1 K. PREKO,1 AND D. BOAMAH2, (2012), X-ray Fluorescence (XRF) Analysis of Soil Heavy Metal Pollution from an Industrial Area in Kumasi, Ghana

K.N. Yua,*, Z.L.L. Yeunga, L.Y.L. Leea, M.J. Stokesa, R.C.W. Kwokb, (2002) Determination of multi-element profiles of soil using energy dispersive X-rayfluorescence (EDXRF)

http://liskeard.cornwall.sch.uk/images/Liskeard-Sixth-Form/Atomic-Absorption-Spectrometry.pdf

J. Myanmar Acad. Arts Sci. 2019 **Vol. XVII. No.2A**

PREPARATION AND CHARACTERIZATION OF ACTIVATED CARBON DERIVED FROM RICE HUSK BIOMASS

Thinzar Lwin[1], Than Than Win[2], Mar Lar Wai[3], Yin Maung Maung[4]

Abstract

Rice husk was washed with distilled water to remove the contaminants present in the rice husk. The wet rice husk was dried at room temperature. The most important properties that provide information about the fuel were proximate such as moisture, ash content, volatile and fixed carbon contents. The fixed carbon content of rice husk biochar (RHB) was measured to be 10.3 mf wt%. The experiment was carried out to study the characterization of the rice husk ash. The rice husk biomass was heated at 300˚ C for 1h in muffle furnace and grounded into the uniform powder. Then, the carbonized material obtained was socked in 1M KOH, in 1:1 ratio for 24 h and followed physical activation at 300°C for 2h in muffle furnace. The structure characterization of activated carbon rice husk biochar (AC-RHB) was identified by X-ray diffraction (XRD) technique. The carbon C was observed by Energy Dispersive X-ray spectroscopy (EDXRF). The porous nature of AC-RHB was studied by scanning electron microscopy (SEM). The carbon C, O, and Si were observed by Energy Dispersive X-ray spectroscopy (EDX). The Fourier transform infrared spectroscopy (FTIR) analysis showed the presence of a variety of functional groups of AC-RHB.

Keywords – Rice husk biomass, Activated Carbon, XRD, EDXRF, SEM-EDX, FTIR.

Introduction

The biomass can be considered as the most easily available and useful bio-material in the current days. Because of the renewable nature, the biomass is widely used for various purposes such as direct source of heat generation, as the feedstock for thermochemical and biological conversion to produce useful fuels or chemicals. [Monoj Bardalai. et al (2016)] Biomass materials agricultural from residues such as straw, bagasse and groundnut shell, coffee husk and rice husk as well as residues from forest-related activities such as wood chips, sawdust and bark having high energy potential. [McKendriya P

---

[1] Department of Physics, University of Yangon,
[2] Department of Physics, Mandalay University of Distance Education, Myanmar
[3] Department of Physics, University of Yangon, Myanmar
[4] Department of Physics, University of Yangon, Myanmar

(2002), Bidayatul Armynah, et al (2018)] These biomass wastes are one of the main assets for renewable energy. Consequently, there are numerous prominent technologies to transform biomass into energy. [Lim. J.S., et al (2012), A. Anchan Paethanom, et al (2012)] In general agro residues normally have the following compositions on moisture and ash free basis: 50% carbon, 6% hydrogen and 44% oxygen. The moisture content varies over wide range from oven dry to about 90% on wet basis and ash content varies from 0.5 to 22%. [Zhao. R., et al (2015), Purakayastha, T.J., et a; (2016)] The term activated carbon is basically referred as carbonaceous materials [Cuhadaroglu D, et al (2008)], with high porosity [Hayashi J, et al. (2000), Yacob AR, et al. (2008) 2-6], high physicochemical stability [Zhu Z, et al (2008)7-1]. Activated carbon is also called as activated charcoal or activated coal [Hiremath MN, et al (2012)] and sometime called as solid sponge. [Zanzi R, et al. (2001)] Activated carbon usually prepared from organic matter that contain of highly carbon, so agricultural waste was interesting choice because of its low cost and it was a source of renewable energy. [A. Buasri, et al (2013), J.C. Moreno-Pirajan, et al (2010), Y. Sudaryanto, et al (2006)] In the presence investigation, rice husk biomass was characterized for proximate analysis viz. Moisture(M), Ash (A), Volatile Matter (VM) and Fixed Carbon (FC). The activated carbon was prepared from rice husk biochar and this AC-biochar was characterized by XRD. Energy Dispersive X-ray Fluoresces (EDXRF) was employed to examine the elemental concentration of biochar. The rice husk biochar samples were also analyzed by Scanning Electron Microscope (SEM) equipped with an energy dispersion X-ray Spectroscopy (EDX) and FTIR for identification of pore size and functional groups.

Experimental

Preparation of Activated Carbon

Rice husk washed with distilled water to remove the impurities such as dust then the wet rice husk was dried at room temperature. Rice husk sample were weighed and then placed into furnace, temperature at 300˚ C for 1 h, and the sample were weighed. The rice husk ash sample was grounded and sieved to the average particle size. Then, 5.6 g of KOH was added to 100 mL of distilled water. The mixture of KOH solution was then stirred. After that, the rice husk sample were soaked in this KOH solution for 24 h. Then the impregnated activated carbon is heated at 300° C for 2 h.

Characterization Methods

The rice husk biomass (RHB) was subjected to carbonization at 300° C for 1 h. The rice husk biomass and biochar samples were characterized for proximate (Moisture, Volatile Matter, Ash Content and Fixed Carbon). Moisture Content was determined according to MOC63U Moisture Analyzer. Moisture content was also obtained by the sample was placed in the oven at 105° C for 2h. Then the sample was cooled in desiccator and reweighed again. The moisture was less than 10 mf wt%. For volatile matter sample was heated at 900° C for 30 min; this mass loss is attributed to volatile matter. For ash content the sample was heated at 700° C for a minimum 5h. The difference between the initial and final weight of the sample represents the ash content. The weight of the original sample, subtracted byits moisture content, ash content and volatile matter content (as determined by the aforementioned proximate analysis) corresponds to the stable carbon fraction of that sample and hence, his fraction is termed ‘fixed carbon or fixed-C fraction’. Figure 1. shows the schematic diagram for preparation of activated carbon from rice husk biomass.

$$M\text{oisture Content} = \frac{\text{initial mass} - \text{moisture mass}}{\text{initial mass}} \text{ x } 100 \qquad (1)$$

$$\text{Volatile Matter} = \frac{\text{moisture mass} - \text{Volatile mass}}{\text{initial mass}} \text{ x } 100 \qquad (2)$$

$$\text{Ash Content} = \frac{\text{Ash Mass}}{\text{Initial mass}} \text{ x } 100 \qquad (3)$$

$$\text{Fixed Carbon Content} = 100 - [\text{Moisture} + \text{Volatile} + \text{Ash}] \qquad (4)$$

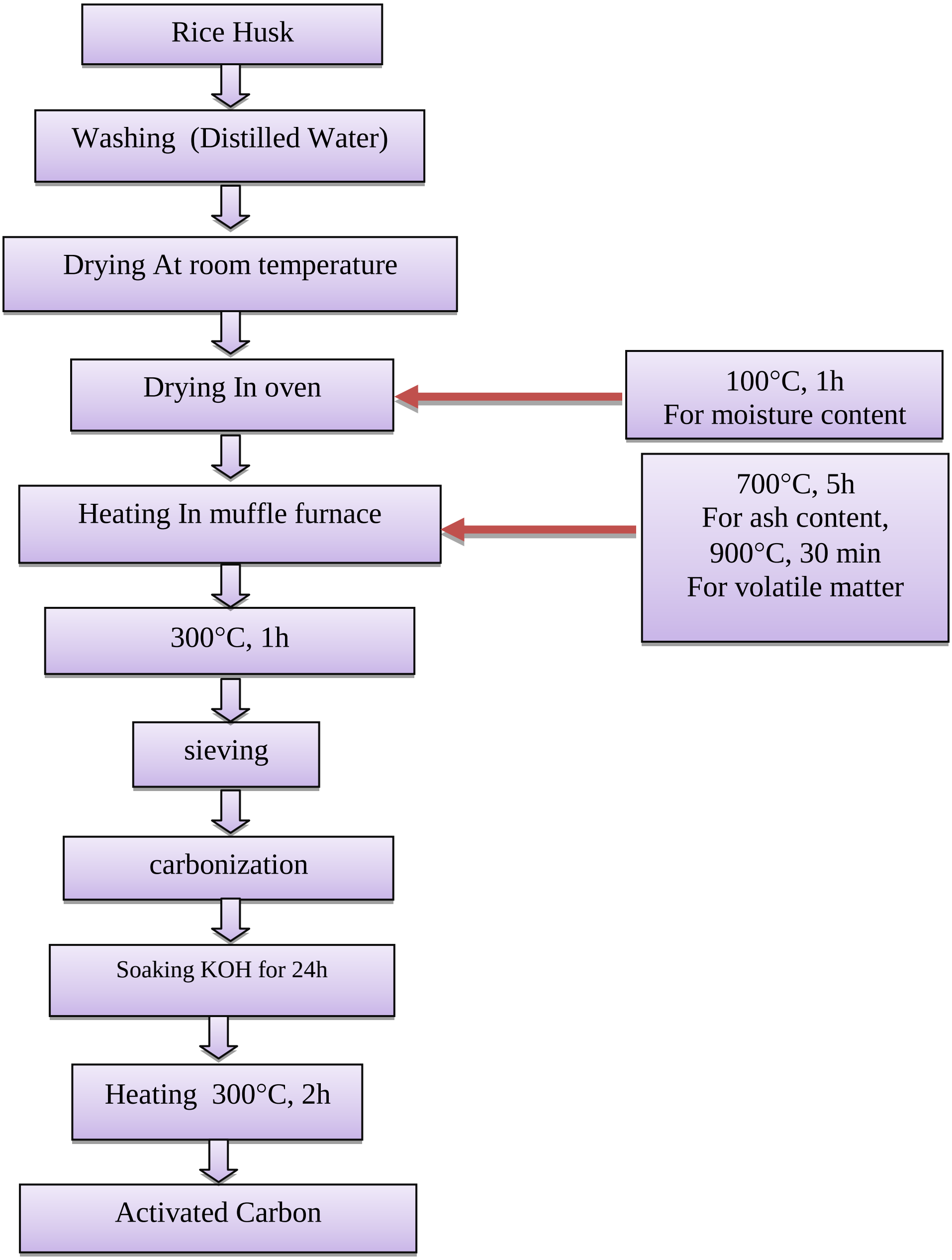

Figure 1: Schematic diagram for the preparation of activated carbon (AC) from rice husk biomass

Results and discussion

Proximate Analysis

The results of the proximate analysis of rice husk are also presented in moisture-free weight percentage, mf wt %. Table.1 shows the properties of the raw rice husk. From proximate analysis, it is observed that rice husk contains its moisture was less than 10 mf wt %, a large percentage of volatile matter, 72.7 mf wt %, a moderate percentage of ash content, 17 mf wt %, and a small percentage of fixed carbon content 10.3 mf wt %. Generally, a raw biomass has high volatile matter content where 80 - 90 % of biomass is combusted in the form of volatiles. Since most of the energy is stored in the volatiles, volatile matters are highly reactive, which makes the combustion process more difficult to be controlled. [Smith, J.L., et al (2010)] Hence, low content of volatile matter is desirable because it is an indication that the combustion process is easier to be controlled. The result suggested that the fixed carbon content was affected by the higher ash content of RHB, which inhibited the formation of aromatic carbon during the thermochemical conversion process. [Angin, D., et al (2014)] It is a common consensus that high ash content is likely to cause fouling at the current collector in DCFC. In addition, a fixed carbon is one of the important elements that determine the quality of biomass as a fuel cell. From these results were neither bad nor good. Hence, further study it requires to reduce the volatile matter and to more produce fixed carbon.

Table 1: Characterization of rice husk biochar

Proximate analysis result of rice husk biochar (wt% dry basis)			
Moisture content	**Volatile matter content**	**Ash content**	**Fixed Carbon Content**
9.54	72.7	17	10.3

X-ray Diffraction (XRD) Analysis

The impregnated activated carbon is heated at 300˚ C for 2 h. The XRD spectrum for activated carbon rice husk biochar (AC-RHB) sample was shown in Figure 2. The XRD pattern for AC-RHB showed the amorphous nature although, it has some local crystalline structure with high conjugated aromatic elements. From the result, XRD patterns revealed the absence of any ordered crystalline structure and the broad band localized between (20° and 60°) 2θ corresponded to the contribution from both amorphous carbon and silica.

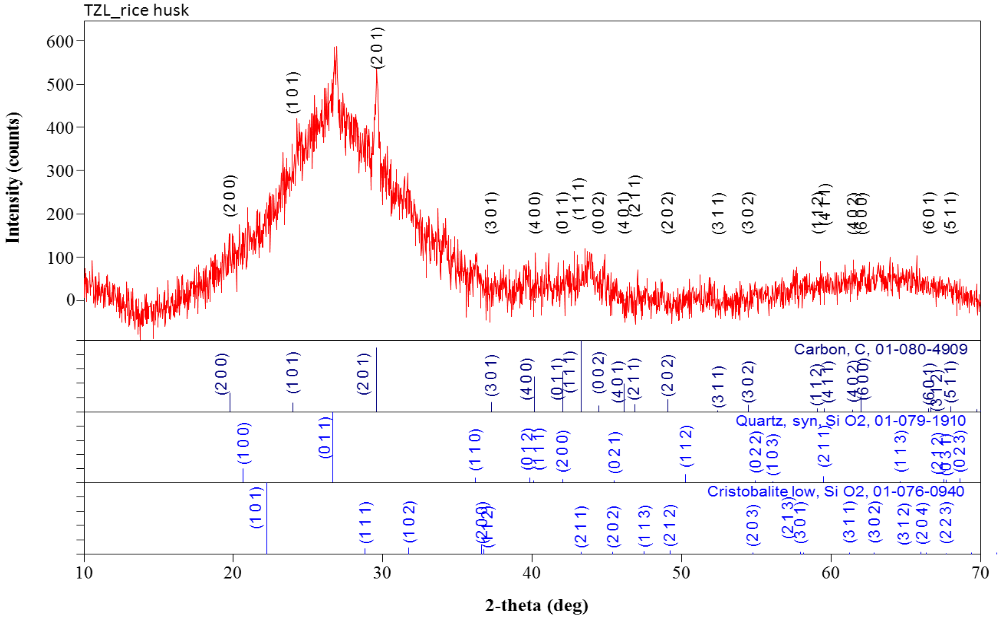

Figure 2: XRD spectrum of AC-RHB at 300˚ C

Energy Dispersive X-ray Fluorescence (EDXRF) Analysis

Table.2 indicates that elemental concentration in AC-RHB at 300˚ C for 1 h. Eleven elements namely C, K, Si, Ca, S, Fe, Cr, Cu, Mn, Ti and Ni were quantified in the rice husk biochar sample by EDXRF technique. Carbon (C) was found to be present as the major element, whereas K, Si, Ca, S, Fe, Cr, Cu, Mn, Ti and Ni were present as minor element. From the result, AC-

RHB contains 98.464 % of Carbon (C). Therefore, AC-RHB was quantified by EDXRF.

Table 2: Elemental Analysis of rice husk biochar

Elemental Analysis of AC-RHB												
Sr No.	**Element**	**C**	**K**	**Si**	**Ca**	**S**	**Fe**	**Cr**	**Cu**	**Mn**	**Ti**	**Ni**
1.	Content Weight %	98.464	1.226	0.224	0.016	0.016	0.08	0.02	0.01	0.01	0.01	0.01

Scanning Electron Microscopy (SEM-EDX) Analysis

The microstructural properties of AC-RHB were observed by SEM analysis. Scanning electron micrographs for external morphology (SEM-EDX) analysis of AC-RHB at 300˚ C for 1 h were shown in Figure 3. At 300˚ C, the pores of about 5μm diameter were found on some region. From SEM micrograph, it was found that AC-RHB had irregular, rough and highly porous. The energy dispersion X-ray spectroscopy (EDX) corresponding to AC-RHB at 300˚ C for 1 h indicated that the AC-RHB has more minals C, O and Si. The elemental constitution of AC-RHB at 300˚ C with two major peak and one minor peak were found to have weight percentage of 71.81 of Carbon, 25.68 of oxygen and 2.51 of Silica. The RHB have atomic percentage of 74.32 of Carbon, 24.33 of Oxygen and 1.35 of Silica. It contains low fractions and absent of various elements such as Cl, K, S, Zn and Mg. This is important to study the influence of these impurities on the DCFC performance because the accumulated ashes would affect the life time of DCFC fuel source, high Carbon (C) content and low Sulphur content were required.

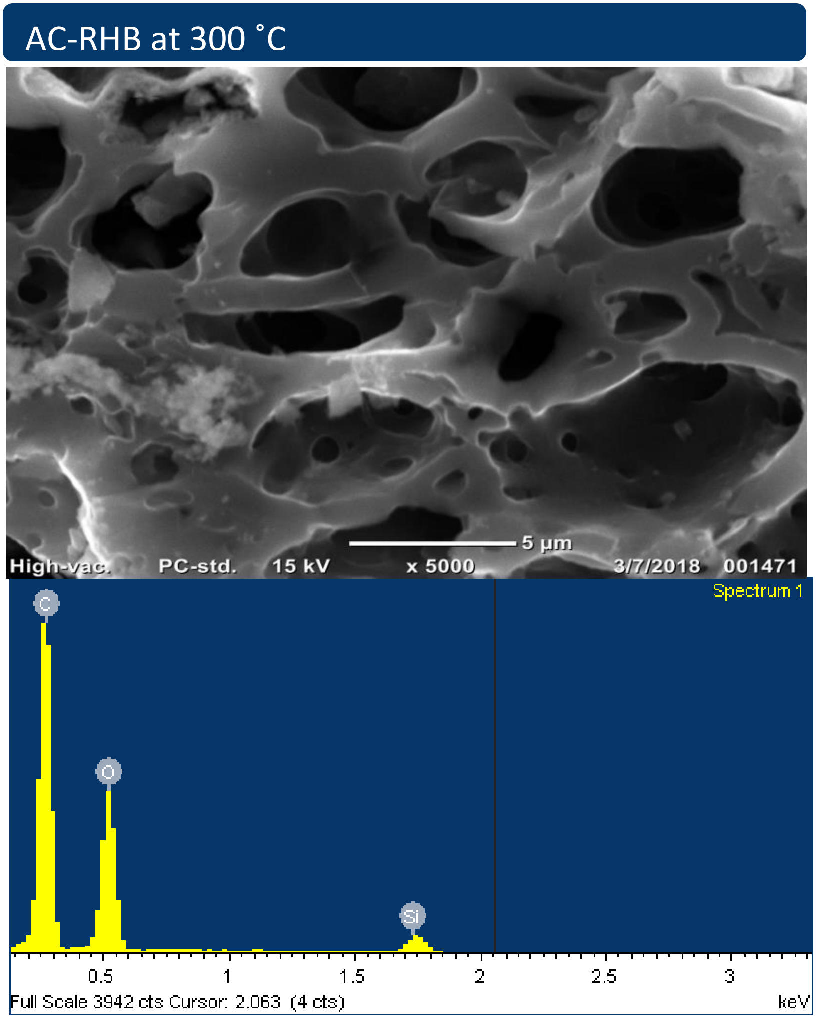

Element	**Weight%**	**Atomic%**
C	71.81	74.32
O	25.68	24.33
Si	2.51	1.35
Totals	**100.00**	

Figure 3: SEM and EDX spectrom of AC-RHB at 300˚ C

Fourier Transform Infrared Spectroscopy (FTIR) Analysis

FTIR result for 300° C of AC-RHB was shown in Figure 4. The first peak at 3231.01cm^{-1} represents the compounds with alcohol and phenolic groups having O-H stretching. The second peak that was located at 1559.37cm^{-1} indicates C=C stretching vibration consists of aromatic groups in lignins. The next peak that was located at 1361.02 cm^{-1} indicates presence of alkanes group having C-H stretching. Additionally, the peak at 1006.89 cm^{-1} corresponding to C-O stretch of alcohols, carboxylic acids, ester and ethers groups. The presence of functional groups such as the alcohol and aromatics groups, carboxylic acids, ester and ethers groups suggest that this AC-RHB could be affected in DCFC.

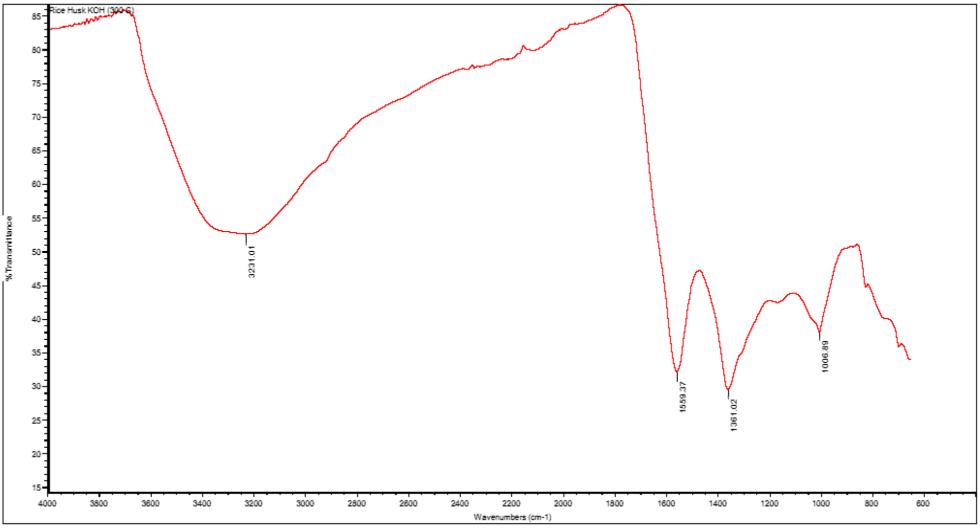

Figure 4: FTIR spectrum of AC-RHB at 300° C

Table 3: FTIR Analysis of AC-RHB

Sr No.	Chimical bond	300□C Peak position (cm^{-1})
1.	O-H Stretch	3231.01
2.	C=C Stretch	1559.37
3.	C-H Stretch	1361.02

4.	C-O Stretch	1006.89

Conclusion

In this work, biochar was successfully produced from rice husk using KOH treatment for activated carbon. The structural characterization of activated carbon rice husk biochar (AC-RHB) by X-ray Diffraction (XRD) technique revealed the presence of Carbon mainly and traces of SiO_2 were found. The treated RHB was quantified by EDXRF spectrometer. Carbon (C) was found that the highest concentration of about 98.464% in the AC-RHB. According to (SEM) analysis, AC-RHB which shows plane cleavage surface and irregular pores are observed. These results are good agreement with FTIR result. According to these results, AC- RHB (300^oC) is quite potential candidate for direct carbon fuel cell (DCFC) application.

Acknowledgements

This research was done at Physics Department in University of Yangon. The authors would like to thank Professor Dr Khin Khin Win, Head of Department of Physics, University of Yangon, for kind permission to carry out this work. They also gratefully thank to Professor Dr Aye Aye Thant, Professor, Department of Physics, University of Yangon, for her helpful permission to carry out this work.

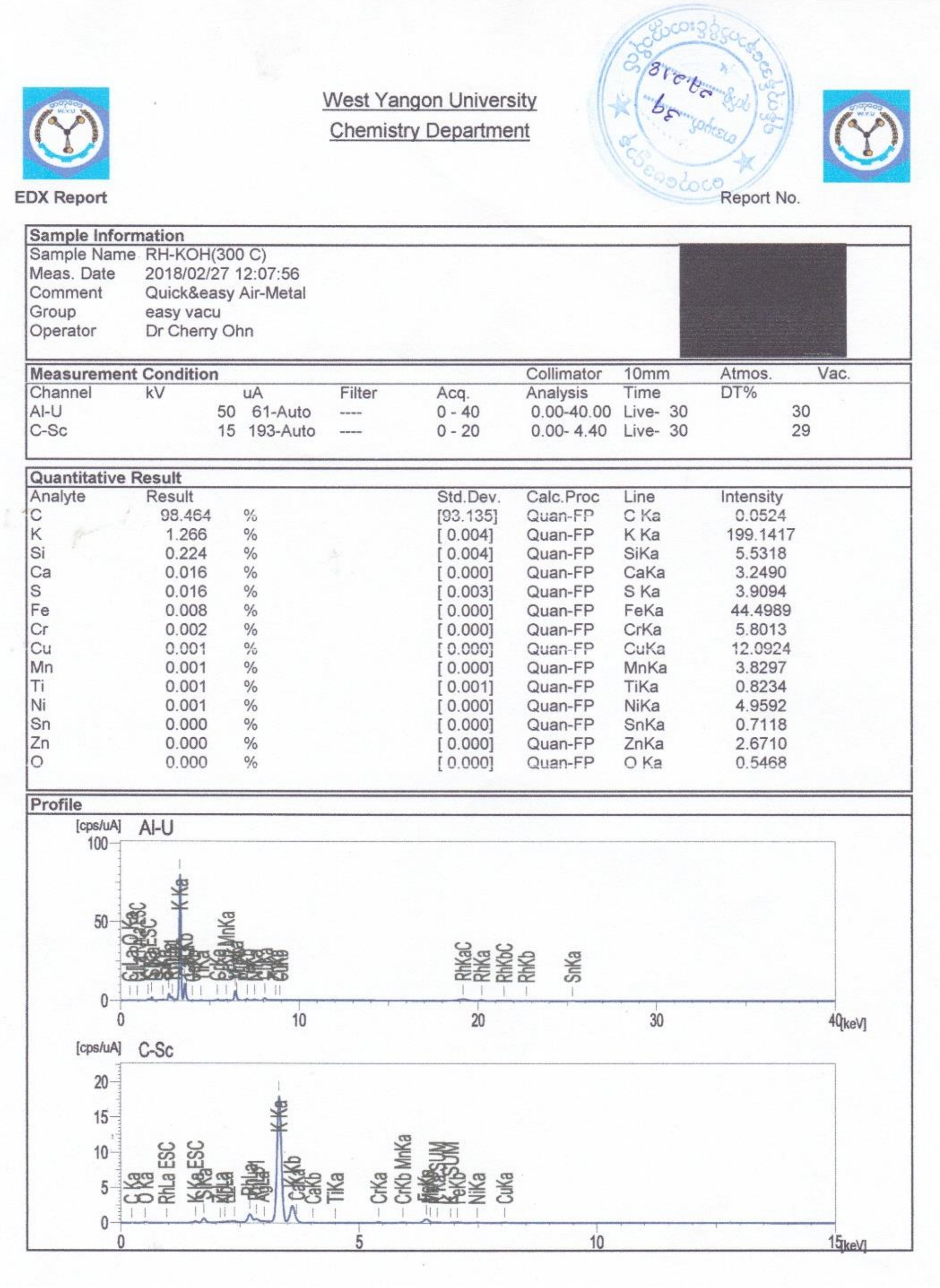

West Yangon University

Chemistry Department

၈.၃.၁၈

၃၄

EDX Report

Report No.

Sample Information

Sample Name	RH-KOH(300 C)
Meas. Date	2018/02/27 12:07:56
Comment	Quick&easy Air-Metal
Group	easy vacu
Operator	Dr Cherry Ohn

[redacted]

Measurement Condition

Collimator 10mm Atmos. Vac.

Channel	kV	uA	Filter	Acq.	Analysis	Time	DT%
Al-U	50	61-Auto	----	0 - 40	0.00-40.00	Live- 30	30
C-Sc	15	193-Auto	----	0 - 20	0.00- 4.40	Live- 30	29

Quantitative Result

Analyte	Result		Std.Dev.	Calc.Proc	Line	Intensity
C	98.464	%	[93.135]	Quan-FP	C Ka	0.0524
K	1.266	%	[0.004]	Quan-FP	K Ka	199.1417
Si	0.224	%	[0.004]	Quan-FP	SiKa	5.5318
Ca	0.016	%	[0.000]	Quan-FP	CaKa	3.2490
S	0.016	%	[0.003]	Quan-FP	S Ka	3.9094
Fe	0.008	%	[0.000]	Quan-FP	FeKa	44.4989
Cr	0.002	%	[0.000]	Quan-FP	CrKa	5.8013
Cu	0.001	%	[0.000]	Quan-FP	CuKa	12.0924
Mn	0.001	%	[0.000]	Quan-FP	MnKa	3.8297
Ti	0.001	%	[0.001]	Quan-FP	TiKa	0.8234
Ni	0.001	%	[0.000]	Quan-FP	NiKa	4.9592
Sn	0.000	%	[0.000]	Quan-FP	SnKa	0.7118
Zn	0.000	%	[0.000]	Quan-FP	ZnKa	2.6710
O	0.000	%	[0.000]	Quan-FP	O Ka	0.5468

Profile

References

A. Buasri, N. Chaiyut, V.Loryuenyong, E. Phakdeepataraphan, S. Watpathomsub, V. Kunakemakorn, ‘Synthesis of Activated Carbon Using Agricultural Wastes from Biodiesel Production’, Vol.7, No.1, p.106-110, 2013

Anchan Paethanom, Kunio Yoshikawa, “Influence of Pyrolysis Temperature on Rice Husk Char Characteristics and its Tar Adsorption Capability”, Energies, 5, p.4941-4951; doi: 10.3390/en 5124941, 2012

Angin, D.; Sensoz, S. Effect of pyrolysis temperature on chemical and surface properties of biochar of rapeseed (Brassica napus L.). Int J. Phytoremed., 16, p.684-693, 2014.

Bidayatul Armynah, Atika, Zuryati Diafar, Wahyu H Piarah, Dahlang Tahir, “Analysis of Chemical and Physical Properties of Biochar from Rice Husk Biomass”, IOP Conf Series: Journal of Physics: Conf. Series 979 012038, 2018.

Cuhadaroglu D, Uygun OA, ‘Production and characterization of activated carbon from a bituminous coal by chemical activation. Afr J Biotechnol; 7(20):3703-10, 2008.

Hayashi J, Kazehaya A, Muroyama K, Watkinson AP, “Preparation of activated carbon from lignin by chemical activation. Carbon; p.38:1873-8, 2000.

Hiremath MN, Shivayogimath CB, Shivalingappa SN. “Preparation and characterization of granular activated carbon from corn cob by KOH activation.”, Int J Res Chem Environ; 2(3): p.84-7, 2012.

J.C. Moreno-Pirajan, L. Giraldo, ‘Study of activated carbons by pyrolysis of cassava peel in the presence of chloride zinc’, J. Anal. Appl. Pyrolysis, 87(2), p. 288-290, 2010.

Lim, J.S.; Manan, A.A; Alwi, S.R.W.; Hashim H “A review on utilization of biomass from rice industry as a source of renewable energy”. Renew.Sustain. Energy Rev., 16, p.3084-3094, 2012

Mc Kendriya P (2002) J. “Bioresource Technology”, 1 83-37

Monoj Bardalai, Eimbendra Kumar Mahanta, “Characterization of Rice Husk Throgh X-Ray Diffraction, Scanning Electron Microscope and Fourier Transformed Analysis”, International conference ‘Innovative Trends in Science, Engineering and Management, p.470-477, 2016.

Purakayastha, T.J.; Das, K.C.; Gaskin, J.; Harris, K.; Smith, J.L.; Kumari, S.Effect of pyrolysis temperatures on stability and priming effects of C_3 and C_4 biochars applied to two different soils. Soil Tillage Res. 155, p.107-115. 2016,

Smith, J.L.; Collins, H.P.; Bailey, V.L. The effect of young biochar on soil respiration. Soil Biol. Biochem., 42, p.2345-2347, 2010.

Yacob AR, Majid ZA, Dasril RSD, Indian V. Comparison of various sources of high surface area carbon prepared by different types of activation. Malays J anal Sci; 12(1): 264-71, 2008.

Y. Sudaryanto, S.B. Hartono, W. Irawaty, H. Hindarso, S. Ismadji, ‘High surface area activated carbon prepared from cassava peel by chemical activation’, Bioresour. Technol., 97(5), p.734-739, 2006.

Zanzi R, Bai X, Capdevila P, Bjornbom E. “Pyrolysis of biomass in presence of steam for preparation of activated carbon, liquid and gaseous products. In: Proceedings of the 6th world congress on chemical engineering, Melbourne, Austilla;. P.1-8, 2001.

Zhao, R.; Coles, N.; Wu, J. Carbon mineralization following additions of fresh and aged biochar to an infertile soil. Catena, 125, p.183-189, 2015

Zhu Z, Li A, Xia M, Wan J, Zhang Q, “Preparation and characterization of polymer based spherical activated carbons. Chin J Polym Sci; 26(5): p.645-51, 2008.

J. Myanmar Acad. Arts Sci. 2019 **Vol. XVII. No.2A**

INDOOR RADON CONCENTRATION MEASUREMENTS OF THE NARANI HALL (SOUTH) IN MEIKTILA UNIVERSITY BY USING SOLID STATE NUCLEAR TRACK DETECTORS

Aye Aye Soe[1], Tin Tin Phyo Lwin[2], Shwe Nan Htet[3] and Cho Cho Aung[4]

Abstract

A study of indoor radon concentration has been carried out in the three rooms of Narani Hall (south) in Meiktila University Campus, Meiktila Township, Mandalay Region in Myanmar, using LR-115 Type II Solid State Nuclear Track Detectors (SSNTDs). Three small pieces of LR-115 ($1\text{cm} \times 1cm$) detectors each was attached on the ceiling 9 ft from the floor of the room.According to the present measurements, it was found that, the value of concentration of radon ranges from 25.12 ± 3.39 Bq m^{-3} to 53.63 ± 11.76 Bq m^{-3} with an average value of 35.75 ± 6.98 Bq m^{-3}. The annual effective dose ranges from 0.43 ± 0.044 m Sv yr^{-1} to 0.92 ± 0.074 m Sv yr^{-1} with an average value of 0.61 ± 0.045 m Sv yr^{-1}.

Keywords: Indoor radon concentration, radon concentration ranges, annual effective dose ranges

Introduction

Radon is a natural radioactive gas, released from the normal decay of the elements uranium, thorium, and radium in rocks and soil, without odour, colour or taste and is an α emitter that decays with a half-life of 3.82 days**.** Radon is an unstable radionuclide that disintegrates through short lived decay products called radon daughters and radon progenies. The short lived progeny, which decay emitting heavily ionizing radiation called alpha particles. Indoor radon concentrations are almost always higher than outdoor concentrations. Radon levels are generally highest in cellars and basements because these areas are nearest to the source and are usually poorly ventilated**.** The detection and radon concentration measurements are one of the most important procedures in environmental protection. In the present study indoor radon concentration in Narani Hall (south) at Meiktila University were measured. Figure (1) shows Radioactive decay scheme of radon ^{222}Rn. In this radon

---

[1] Dr, Assistant Lecturer, Department of Physics, University of Yangon

[2] Assistant Lecturer, Department of Physics, University of Yangon

[3] Lecturer, Department of Physics, University of Yangon

[4] Associate Professor, Department of Physics, University of Yangon

concentration measurements, one type of solid state nuclear track detectors (SSNTDs), LR-115 type II was used. The principle of this technique is based on the production of track in the detector due to alpha particles emitted from radon and its progeny.

After exposure, the tracks are made visible by chemical etching and counted manually under the optical microscope. From the alpha track detection, we carried out alpha track densities, the radon concentrations and annual effective doses. The plastic track detector LR-115 Type II used in this work is a cellulose nitrate red dyed film, manufactured by Kodak Pathe France, LR-115 is a solid state nuclear track detector (SSNTD) based on cellulose nitrate and has been commonly used for measurement of concentration of radon gas and / or radon progeny. The sensitive surface for alpha particle, red dyed, is of 10μm thickness of cellulose nitrate (CN) layer on a colorless inert backing material and the base is 100μm polyester. The composition of LR-115 Type II ($C_6H_8O_9N_2$) is shown in fig (2). Its advantage is that after suitable etching, the tracks appear as colorless holes against a red background. Obviously, only one side of this film is sensitive, and this must determined before used. Etched tracks show up as bright holes in a dark red background, and are very clearly visible under a low power microscope of magnification.

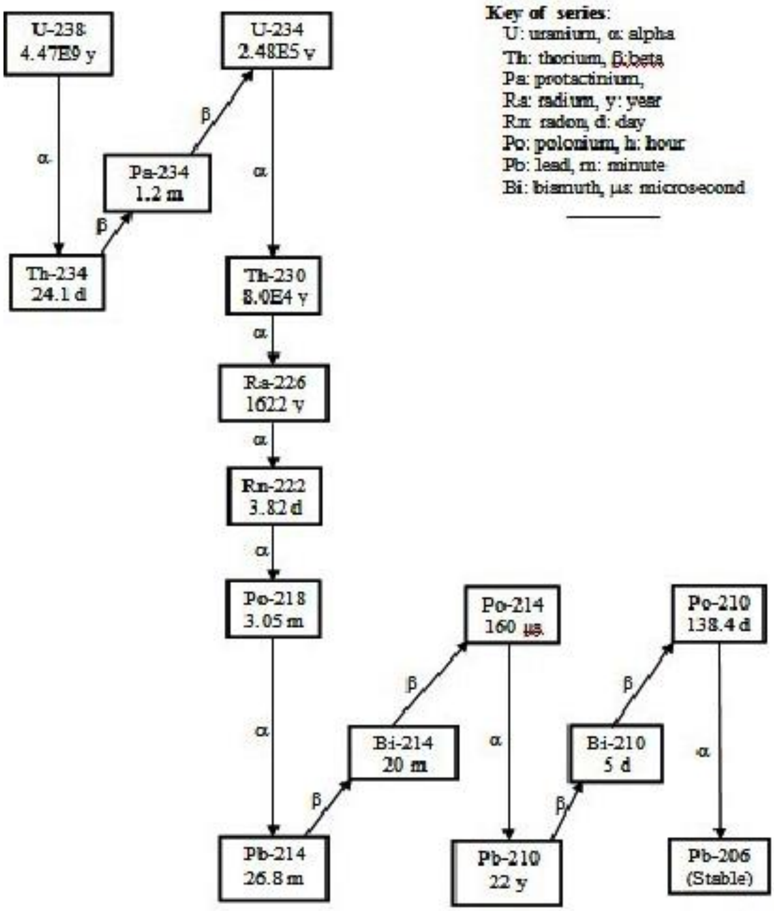

Figure 1: Radioactive decay scheme of uranium ^{238}U

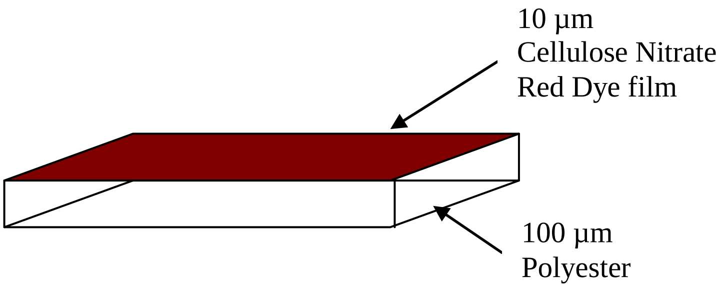

Figure 2: The Structure of the Solid State Nuclear Track Detector LR -115 Type II Cellulose Nitrate film

Experimental Details

In this work, large sheets of LR-115 having 24 cm^2 was cut into small pieces of size 1 cm × 1 cm. There small pieces of LR-115 detectors were attached on the ceiling at 9 ft height from the floor. One of the detector sample (S1) was attached at the ground floor, another one sample (S2) was attached at the first floor and the last one sample (S3) was attached at the second floor of Narani Hall (South) in Meiktila Uniuersity Campus. The photograph of Narani Hall at Meiktila University is shown in Fig (3). The installed places of sample (1) (Ground floor of Narani Hall at Meiktila University) is shown in Fig (4). The install places of sample (2) (First floor of Nartani Hall at Meiktila University) is shown in Fig (5). The installed places of sample (3) (second floor of Narani Hall at Meiktila University) is shown in fig (6). These samples were exposed to radon in air to collect α- tracks on 100 days. At the end of exposure time, these samples were etched with 2.5N NaOH solution. Chemical etching was carried out in a thermostatically controlled bath at temperature 60 ± 1℃ for 90 minutes as etching duration. The etching process of detector is shown in figure(7).After etching process, the samples were removed and washed under running tap water to remove the etching residue from the etch pits. And then the samples were dried on the filter paper. After drying, the number of tracks was determined using optical microscope and the track densities, radon concentration and annual effective doses were calculated.

Figure 3: The photograph of Narani Hall at Meiktila University

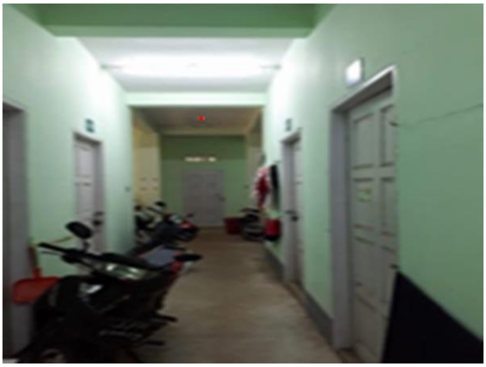

Figure 4: The installed places of sample (1) Ground floor of Narani Hall at Meiktila University

Figure 5: The installed places of sample(2) First floor of Narani Hall at Meiktila University

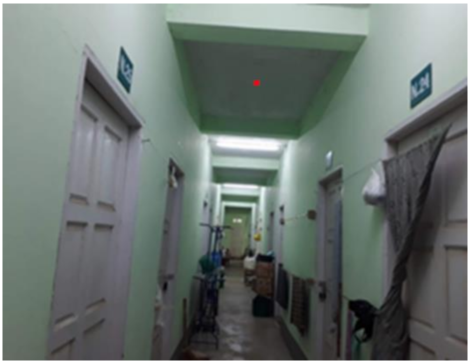

Figure 6: The installed places of sample(3) Second floor of Narani Hall at Meiktila University

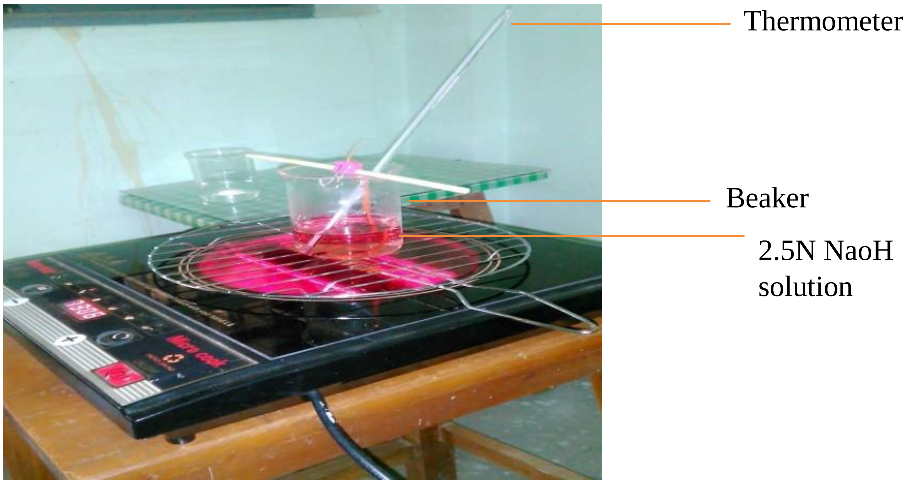

Figure 7: Etching Process of Detectors

After chemical etching, the etched tracks produced by alpha particles were observed and counted using biological microscope model Optima G-205 at Botany Department in Meiktila University. The mostly used method of track counting employs an optical microscope is as shown in Figure (8). According to the observation views of the screen of microscope, alpha tracks were counted to reduce the statistical errors. The photographs of alpha tracks in LR-115 detectors are shown in figure (9) to figure (11).

In this work, alpha tracks were counted for different fifty views and the track densities were calculated by using equation:

$$\text{Track Density(track cm}^{-2}\text{)day}^{-1}\text{)} = \frac{Number\ of\ Net\ Tracks}{\text{Area of counted view} \times \text{Exposure time}} \quad (1)$$

$$\text{Radon(Bqm}^{-3}\text{)} = \frac{\text{Track Density}}{\text{Calibration Factor}} \quad (2)$$

$$\text{Annual Effective Dose} = \text{Radon Concentration} \times 0.0172\ \text{mSvyr}^{-1} \quad (3)$$

Figure 8: OPTIMA G-205 Biological Microscope

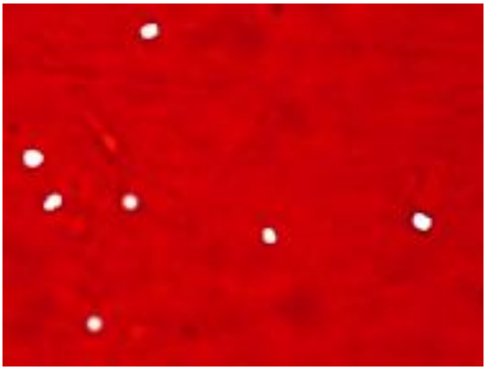

Figure 9: Photograph of Alpha tracks in LR - 115 Detector for Sample(S1)

Figure 10: Photograph of Alpha tracks in LR -115 Detector for Sample (S2)

Figure 11: Photograph of Alpha tracks in LR-115 Detector for Sample (S3)

Results and Discussion

From the experimental work, the estimate of radon concentrations and the annual effective doses were carried out. Average number of alpha tracks and track densities of each sample were calculated by using equation(1). By using calibration factor 0.05016 track cm^{-2} day^{-1} = 1 Bqm^{-3}, radon concentrations can be calculated from equation (2). And then the annual effective doses were calculated by using equation(3).The average number of tracks and track densities were mentioned in Table (1). The radon concentrations and annual effective doses were mentioned in Table (2) and Table (3).The graphs of alpha track densities, radon concentrations and annual effective doses from three different places are shown in Fig (12) to Fig(14). The comparison graph of ICRP Level and Samples in annual effective doses are shown in Fig (15).

Table 1: The Alpha Track Densities (track cm^{-2} day^{-1}) for three different floors

Sr. No.	Name of Samples	Average number of Alpha Tracks	Alpha Track Densities (track cm^{-2} day^{-1})
1	S1	0.76 ± 0.19	2.69 ± 0.22
2	S2	0.46 ± 0.12	1.43 ± 0.15
3	S3	0.42 ± 0.09	1.26 ± 0.13

Table 2: The radon concentrations (Bq m^{-3}) for three different floors

Sr. No.	Name of Samples	Radon concentrations (Bq m^{-3})
1	S1	53.63 ± 11.76
2	S2	28.51 ± 5.78
3	S3	25.12 ± 3.39

Table 3: The Annual Effective Doses (m Sv yr^{-1}) for three different floors

Sr. No.	Name of Samples	Annual Effective Doses (m Sv yr^{-1})
1	S1	0.92 ± 0.07
2	S2	0.49 ± 0.05
3	S3	0.43 ±0.04

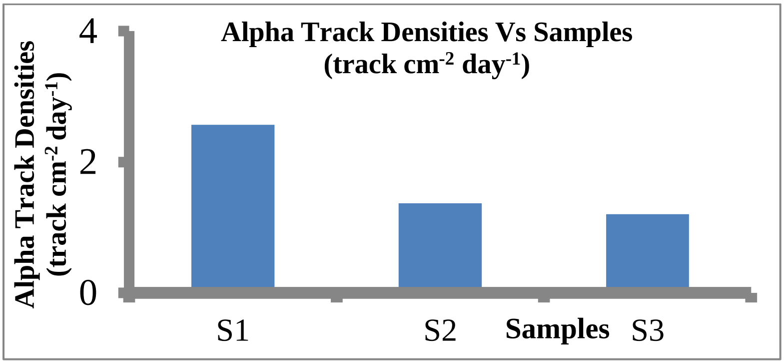

Figure 12: Comparison graph of alpha track densities for three different floors

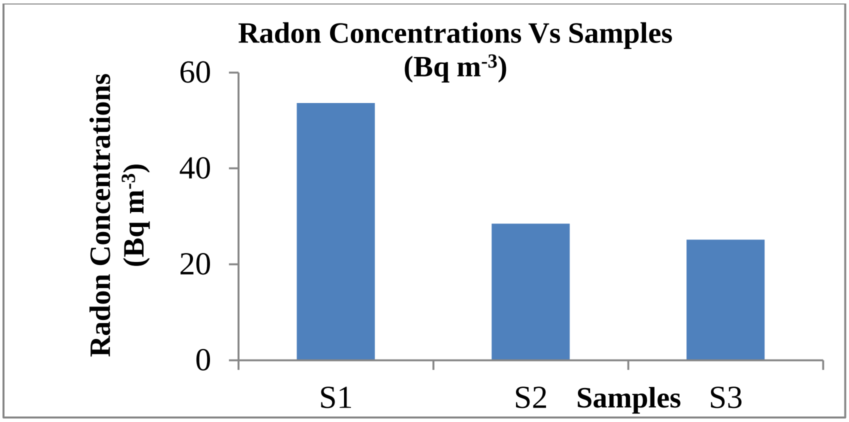

Figure 13: Comparison graph of radon concentrations for three different floors

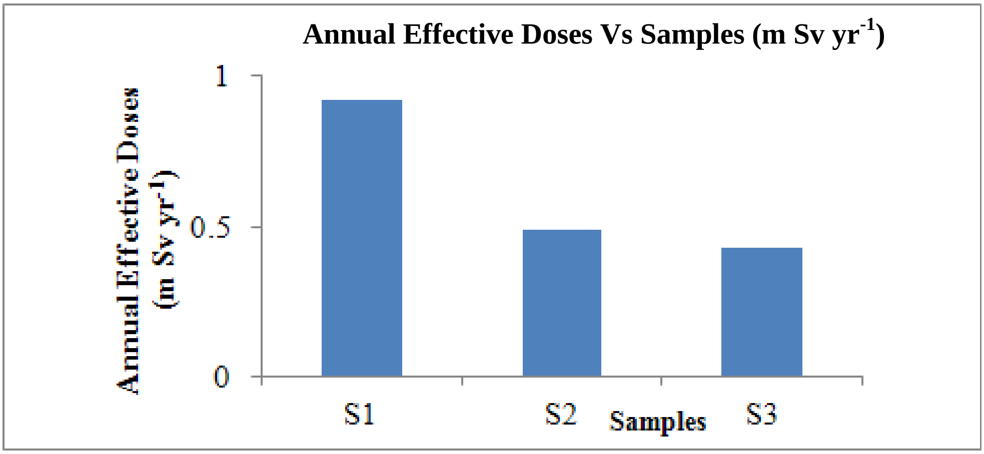

Figure 14: Comparison graph of annual effective doses for three different floors

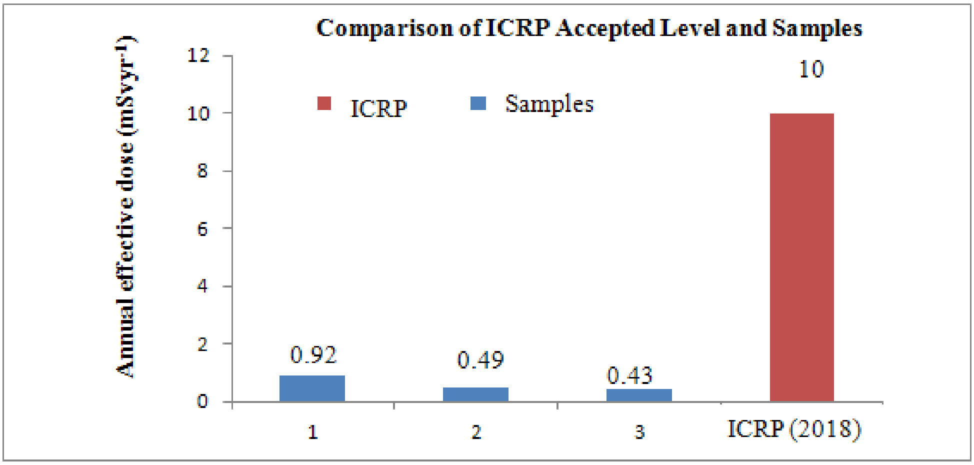

Figure 15: Radioactive decay scheme of radon ^{222}Rn

Conclusion

Radon is the biggest contributor to natural radiation in the environment and causes long term health concern. Therefore, the measurement of radon concentration is needed for environmental purpose. The results of indoor radon concentration measured with LR-115 type II were presented in this work. The results have been found lower than that of ICRP limited level. From this observation, radon will not accumulate in this building due to rich ventilation. Because, a ventilation rate is inversely proportional to the radon level. Finally, it is proved that concentration of radon crowded areas are generally safe in terms of health risks.

Acknowledgements

I am highly grateful thanks to Professor Dr Khin Khin Win, Head of Department of Physics, University of Yangon for her permission to do and her encouragement throughout this paper.

I also would like to thank Professor Dr Aye Aye Thant, Department of Physics, University of Yangon for her allowing me to do the paper.

References

http://www.epa.gov/radiation/radionuclides/radon.html

http://www.chemicalelements.com/…/rn.html

http://www.who.int/ionizing-radiation/env/Radon-Info-sheet.pdf

http://www.impactjournals.us

http://www.water.epa.gov

http://www.en,wikipedia.org/wiki/SSNTD

http://www.epa.gov/radiation/understand/alpha.html

http://barc.ernet.in/publications/…/200506-2.pdf

http://www.djs.si/proc/port 2000/655A.htm

http://www.barc.gov.in:

Tsoulfanidis Nicholas, (1995) "Measurement and Detection of Radiation", (London: Taylor & Francis).

http://www.radon leaders.org/…/…

J. Myanmar Acad. Arts Sci. 2019 **Vol. XVII. No.2A**

A STUDY ON ELEMENTAL AND RADON CONCENTRATION IN RAW MATERIALS OF LIGHTWEIGHT CONCRETE BRICK AND ORDINARY BRICK

Myat Thanda Mon[1] and Shwe Nan Htet[2]

Abstract

In the present work, raw materials samples (lime, gypsum, aluminum powder, cement, river sand, terracotta and a mixture of terracotta and black clay) of lightweight concrete brick and ordinary brick were collected from concrete and brick factories in Yangon. The elemental contents and radon concentration of raw materials from lightweight concrete brick and ordinary brick were determined by EDXRF method and passive cup method respectively. Toxic elements such as Hg, Pb, Cd and As concentration in weight percent level were not observed in raw materials of lightweight concrete brick and ordinary brick in EDXRF measurement. From the radon measurement of seven samples, a mixture of terracotta and black clay showed the maximum value of average alpha track_67.82 ± 1.68, alpha track density_93.98 ± 2.54 tracks $cm^{-2}day^{-1}$ and radon concentration_4699 ± 127.08 Bqm^{-3} respectively, whereas the value of radon concentration of aluminum powder was comparable with background value. The values of radon concentration from lime, gypsum, aluminum powder and cement for building materials were below ICRP recommended permissible level of 200-600 Bqm^{-3} but river sand, terracotta and a mixture of terracotta and black clay samples were above permissible level. The annual effective dose of lime, gypsum, aluminum powder, cement and river sand samples were less than recommended level 50m Sv/y. The results showed that cement, gypsum (plaster of paris), lime and aluminum powder could be used as raw material for manufacture of building materials. They were radiological safe as compared to limit ICRP and did not pose any radiological risk

Keywords: elemental analysis, EDXRF method, toxic elements, LR-115 Type II plastic track detectors, passive cup technique

Introduction

The raw materials which are used in production of lightweight concrete brick and ordinary brick are containing various amounts of natural

---

[1] PhD Candidate, Department of Physics, University of Yangon

[2] Lecturer, Department of Physics, University of Yangon

radioactive elements. Determination of population exposure to radiation from raw materials is great importance since people spend about 80% of their life inside the buildings. Natural radionuclides in building materials may cause both external exposure caused by their direct gamma radiation and internal exposure from radon gas˙ Radon is present outdoors and is normally found at very low levels in outdoor air and in surface water, such as rivers and lakes. It can be found at higher levels in the air in houses and other buildings, as well as in water from underground sources, such as private well water. Radon gas that moves from under the ground can migrate into indoor spaces, such as basements and crawl spaces. Once inside an enclosed space, such as a home, radon can accumulate. The main source of indoor radon is its immediate parent radium-226 in the ground of the site and in the building materials˙ Radon concentrations in soil gas within a few meters of the surface of the ground are clearly important in determining radon rates of entry into pore spaces and subsequently into the atmosphere and it depends on the radium concentration in the bedrock and on the permeability of the soil.

Experimental Procedure

The raw material samples were dried in a temperature controlled furnace (oven) at a temperature 80 ± 0.1°C for 6 hours to ensure that moisture was completely removed. Then the samples were crushed to a fine powder and sieved through a small mesh size 250µm to remove the larger grains size and render them more homogenous. After sample preparation, all the samples were analyzed using an EDXRF, model Shimadzu EDX-720 at Universities' Research Center. The method of the fundamental parameter (FP) was used for the spectrum analysis. About 100 g of each sample was placed in a plastic can of dimensions of 11 cm in height and 8 cm in diameter. A piece of LR-115 detector of size 1.5 cm × 1.5 cm was fixed on the top of inner surface of the can, in such a way, that it was sensitive surface always facing the sample. The can was sealed air tight with adhesive tape and kept for exposure of 90 days as shown in Figure 1. After that, the detectors were removed from the sample cup, collected and chemically etched in a 2.5N NaOH solution at (60 ± 0.1) °C for a period of 90 min. The resulting alpha tracks were counted under an optical microscope of magnification 10X. The track density of each sample was calculated by using the track density equation:

$$\text{Average Track Density} = \frac{Net\ Tracks}{Microscopic\ Area \times Exposure\ Time}$$

To get the values of radon concentration, calibration factor must be used. The resulting track density was then converted into Bqm^{-3} by appropriate calibration factor of 0.02 tracks cm^{-2} day^{-1}. The annual effective doses from raw materials samples were calculated following International Commission on Radiological protection Publication where $1Bqm^{3}$= 0.0172 $mSvyr^{-1}$.

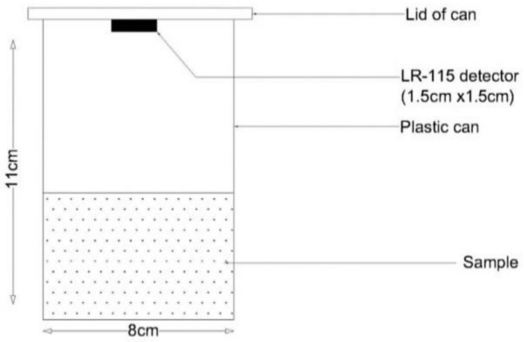

Figure 1: The schematic diagram of can technique

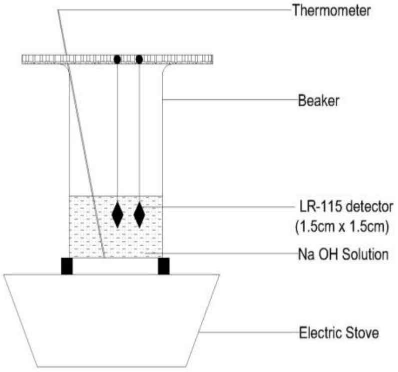

Figure 2: Schematic diagram of etching system

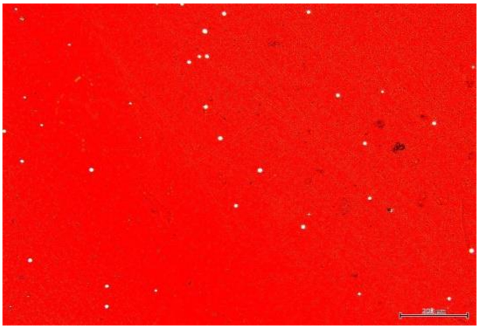

Figure 3: (a) Photomicrograph of Alpha Tracks in LR115 for River Sand sample at total magnification of 10X

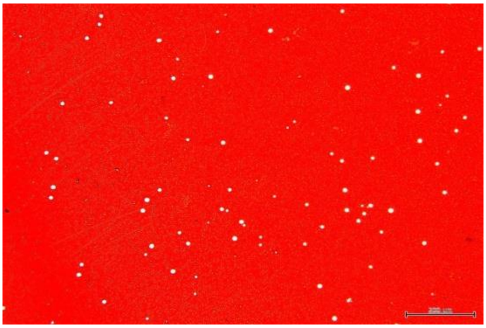

Figure 3: (b) Photomicrograph of Alpha Tracks in LR115 for Terracotta sample at total magnification of 10X

Table 1: Concentrations of elements in raw material samples of lightweight concrete brick and ordinary brick

Element	**Sample1 (lime)**	**Sample 2 (Gypsum)**	**Sample 3 (Aluminum powder)**	**Sample 4 (cement)**	**Sample 5 (River sand)**	**Sample 6 (Terracotta)**	**Sample 7 (terracotta + black clay)**
Si	ND	ND	ND	61.846	6.454	51.768	43.43
Fe	0.21	0.306	3.856	19.228	5.978	37.257	35.562
Ca	99.336	68.9	1.163	7.186	83.331	ND	9.103
K	ND	0.494	ND	9.272	1.986	6.642	7.077
Ti	ND	ND	ND	1.357	0.368	3.234	3.413
Zr	ND	ND	ND	ND	ND	0.401	0.381
Cr	ND	ND	0.146	0.414	ND	0.169	0.237
Mn	ND	ND	ND	0.32	0.05	0.204	0.225
Sr	0.21	0.19	ND	0.237	0.178	0.067	0.13
Zn	ND	ND	0.082	ND	0.025	0.087	0.116
Ni	ND	ND	ND	ND	ND	0.119	0.11
V	ND	ND	ND	ND	ND	ND	0.099
Y	ND	ND	ND	ND	ND	0.053	0.071
Rb	ND	ND	ND	0.139	ND	ND	0.047
S	ND	30.078	1.798	ND	1.595	ND	ND
Cu	0.031	0.032	0.057	ND	0.036	ND	ND
Al	ND	ND	92.651	ND	ND	ND	ND
W	ND	ND	0.176	ND	ND	ND	ND
Ga	ND	ND	0.071	ND	ND	ND	ND

ND= non- detected

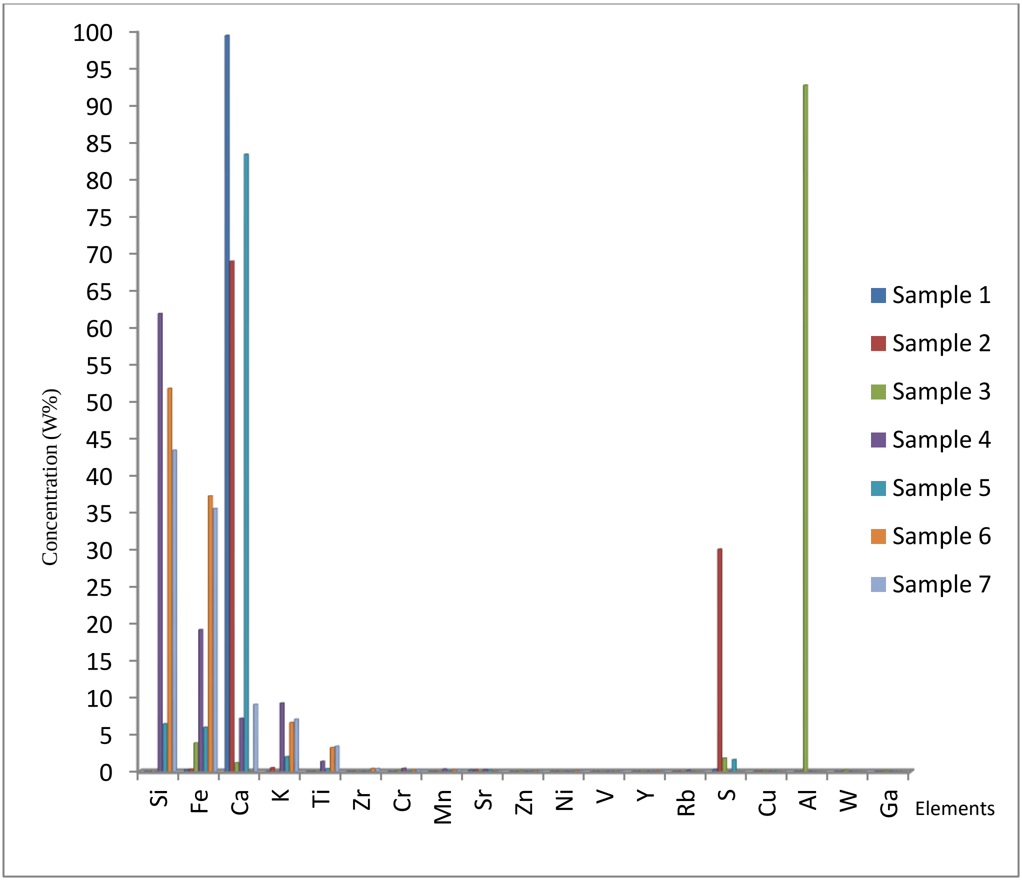

Figure 4: Concentration (W%) of elements contained in raw materials of lightweight concrete brick and ordinary brick

Table 2: Average alpha tracks, track density and radon concentration from raw materials samples of Lightweight concrete brick and ordinary brick

No	Samples	Alpha Track Density (tracks cm^{-2}day^{-1})	Radon Concentration (Bqm^{-3})	Annual effective dose (mSv/y)
1	Lime (S1)	3.45 ± 0.51	73 ± 25.49	2.97 ± 0.44
2	Gypsum (S2)	1.50 ± 0.42	75 ± 20.72	1.29 ± 0.36
3	Aluminum Powder (S3)	0.54 ± 0.40	27 ± 19.79	0.46 ± 0.34
4	Cement (S4)	7.36 ± 0.59	368 ± 29.67	6.33 ± 0.51
5	River Sand (S5)	39.10 ± 1.29	1955 ± 64.45	33.62 ± 1.11
6	Terracotta (S6)	66.12 ± 1.75	3306 ± 87.64	56.86 ± 1.51
7	Terracotta + Black Clay (S7)	93.98 ± 2.54	4699 ± 127.09	80.82 ± 2.19

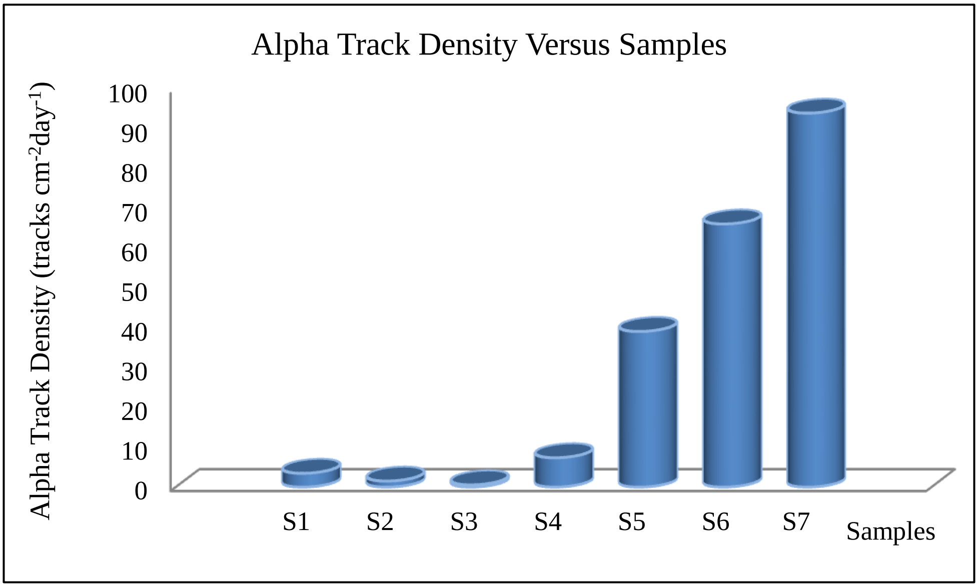

Figure 5: The average alpha track density of raw materials samples of lightweight concrete brick and ordinary brick

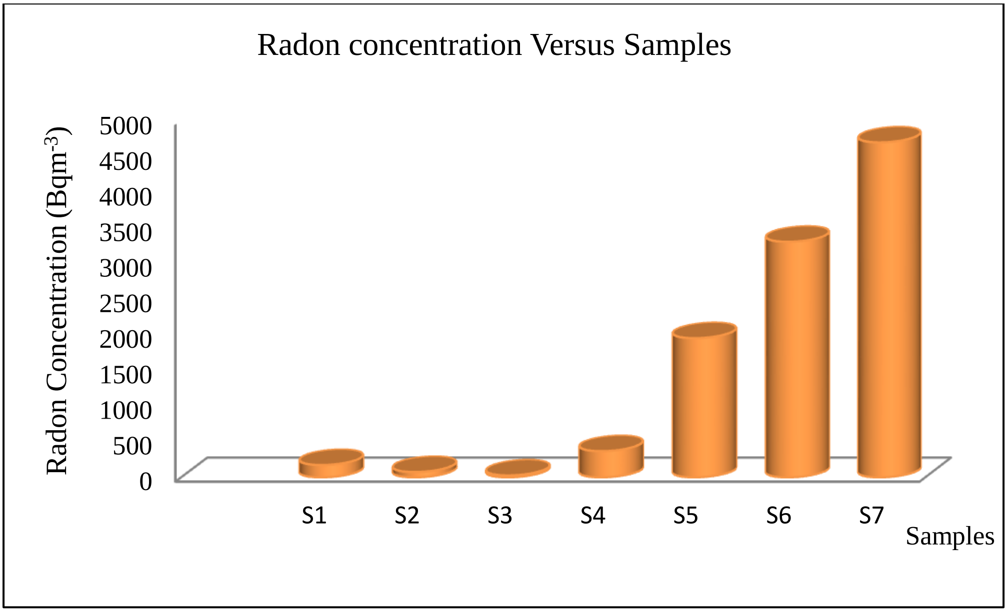

Figure 6: The radon concentration of raw materials samples of lightweight concrete brick and ordinary brick

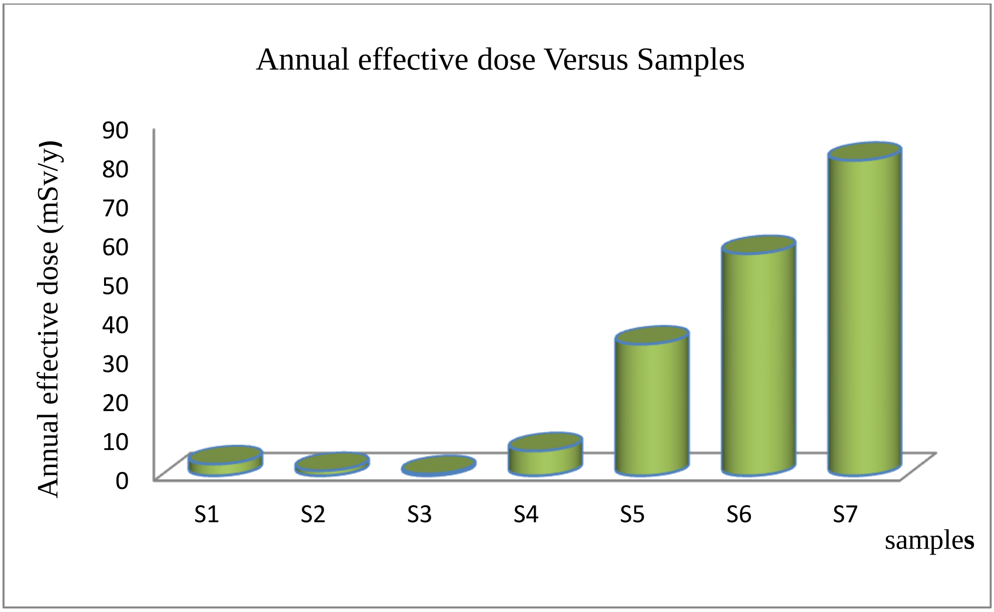

Figure 7: Annual effective dose for raw materials samples of lightweight concrete brick and ordinary brick

Results and Discussion

The elemental concentrations of raw materials of lightweight concrete brick and ordinary brick were measured by using Energy Dispersive X-ray Fluorescence method. The contents of elements in raw materials are shown in table 1 and the results are shown in figure 4. According to the measurement data of raw materials samples of lightweight concrete bricks using EDX-720, the results showed that Ca was found in sample 1 (lime), sample 2 (Gypsm, p-o-p) and sample 5 (river sand) as major elements. The result showed that Si was found higher amount and Fe is second large as major element and Zr, Cr, Mn, Zn and Ni were found in raw materials samples of ordinary brick as minor constituents. By using LR-115 detector, the calculated values of average alpha track from raw material samples varied from 1.76 ± 0.16 to 67.82 ± 1.68 and the values of alpha track density varied from 0.54 ± 0.40 to 93.98 ± 2.54 tracks cm^{-2} day^{-1}, based upon these values, radon concentration had been calculated. The values of radon concentration varied from 27 ± 19.79 Bqm^{-3} to 4699 ± 127.09 Bqm^{-3}. From the Table 2, it was observed that the values of radon concentration from lime, gypsum, aluminum powder and cement for building materials were below the recommended permissible level of 200-600 Bqm^{-3} by ICRP -103, 2007 but the radon concentration of river sand, terracotta and a mixture of terracotta and black clay samples were above permissible level. The highest value of annual effective dose of terracotta and a mixture of terracotta and black clay samples were above permissible level. Since the annual effective dose of lime, gypsum, aluminum, cement and river sand samples were less than recommended level 50m Sv/y, there was no health hazard for people.

Conclusion

Toxic elements such as Hg, Pb, and Cd and As concentration in weight percent level were not observed in raw materials of lightweight concrete and ordinary brick in EDXRF measurement but Sr concentration was found in poor weight percent level of raw materials of light weight concrete brick. Based on seven samples examined, a mixture of terracotta and black clay showed the maximum value of average alpha track, alpha track density and radon concentration 67.82 ± 1.68, 93.98 ± 2.54 tracks cm^{-2}day^{-1} and 4699 ±

127.09 Bqm^{-3} respectively, whereas the value of radon concentration of aluminum powder was comparable with background value. The highest value of annual effective dose of terracotta and a mixture of terracotta and black clay samples were above permissible level. The annual effective dose of lime, gypsum, aluminum powder, cement and river sand samples were less than recommended level 50m Sv/y. It depends on the radioactive content of the materials, emanation factor and diffusion coefficient of radon in that material, porosity and density of the material. Although the radon concentration of river sand sample used in lightweight concrete brick was above permissible level, it was much less than raw materials samples of ordinary brick. So lightweight concrete brick could be used safety for building constructions.

Acknowledgements

I would like to thank Professor Dr Khin Khin Win, Head of Department of Physics, University of Yangon for her kind permission to carry out this research.

I am greatly indebted to Professor Dr Aye Aye Thant, Department of Physics, University of Yangon for her encouragement.

References

Anjos R.M.,Ayub JJ.Cid A.S., Cardoso R.and Laceuda T. (2011). External gamma ray dose rate and radon concentration in indoor radon environments covered with Brazillian granites. Journal of Environmental Radioactivity (102), 1055-1061

Amrani, D., Tahtat, M.,(2001). Natural radioactivity in Algerian building materials. Appl. Radiat. Isot. 54, 687-689.

ICRP, (1993),Protection against radon-222 at home and at work. ICRP Publication 65.Ann. ICRP 23

ICRP, (2007). The 2007 Recommendations of the international Commission on Radiological Protection. ICRP Publication 103.Ann. ICRP 37 (2-4)

J.K. Otton, L.C.S. Gundersen and R Schumann,(1993).The Geology of Radon.

WWW.elsevier.com/locate/radmeas

J. Myanmar Acad. Arts Sci. 2019 **Vol. XVII. No.2A**

DETERMINATION OF ELEMENTAL CONCENTRATION AND GAMMA ATTENUATION COEFFICIENT OF CONCRETE BLOCK

Nyein Myat Thu[1], Shwe Nan Htet[2]

Abstract

The present work is performed to find out the elemental concentration and gamma attenuation coefficients of Autoclaved Aerated Concrete (AAC) block by using EDXRF method (EDX-720) and gamma spectroscopy method using NaI(Tl) detector for Cs-137 gamma source. The various thicknesses of AAC block samples are used as attenuator for gamma ray intensity in this work. Toxic elements and radioactive nuclides are not detected by EDXRF method. It is highly attenuated to radiation shielding. So, these results will be helpful in the development of radiation shielding technology.

Keywords: Elemental analysis, EDXRF method, AAC concrete block, NaI(Tl) scintillation detector, ^{137}Cs gamma source

Introduction

Autoclaved aerated concrete was invented in the mid-1920s by the Swedish architect and inventor John Axel Eriksson. Autoclaved Aerated Concrete, AAC is an economical, sustainable, lightweight solid block that provides thermal and acoustic insulation and is also fire and termite resistance. AAC is good for heat isolation, fire protection, and seismic resistance especially for high tower buildings. The prominent advantage of aerated concrete is its lightweight. AAC products include blocks, wall panels, floor and roof panels, cladding panels and lintels. The ingredients for manufacturing Autoclaved Aerated Concrete block are fly ash or sand 60~70%, limestone powder 15~20%, cement 8~10%, gypsum 2% and aluminum powder 0.074%. Human beings are continuously exposed to background radiation from the sun and cosmic rays in the atmosphere, naturally occurring radioactive materials within Earth, their bodies, houses and food. So Human safety and structural material that may be compromised from radiation exposure are vital concerns in nuclear technology. As technology is developed day by day, the gamma rays are used in many fields,

---

[1.] PhD Candidate, Department of Physics, University of Yangon
[2.] Lecturer, Department of Physics, University of Yangon

like medicine, food preservation, surgery, industry, research, agriculture etc. it has now become necessary to provide shielding to reduce exposure to gamma radiation. For safety of people, selection of attenuating materials, attenuation coefficient becomes most important. Radiation shielding usually consist of barriers of lead, concrete or water. There are many materials, which can be used for radiation shielding, but there are many situations in radiation protection. Nowadays, autoclaved aerated concrete are used widely. Attenuation coefficient describes the extent to which the radiant of a beam is reduced as it passes through a specific material. The attenuation of gamma radiation can be then described by the following equation.

$$I = I_o.e^{-\mu x}$$

where I is intensity after attenuation, I_o is incident intensity, μ is the linear attenuation coefficient (cm^{-1}), and physical thickness of absorber (cm).

Experimental Procedure

AAC block sample was ground with grinding machine to get powder samples and the samples were at least 5 grams weighed with scientific balance and pressed into pellet with 5 tons of hydraulic press, SPECAC, Cambridge Electric Industries. The diameter of pellet is 2.5cm. After sample preparation, the samples were analyzed by EDXRF (Shimadzu EDX-720) system at Universities' Research Center (URC). And the samples were prepared with square shape of AAC block samples (10 cm × 10 cm) with increasing thicknesses ranging from 1.4cm to 24.1cm. The block diagram of experimental setup is shown in Figure 1. The source to detector distance is 35cm. For energy calibration, the intensities of the standard gamma sources measurement were carried out firstly to reduce the background radiation. After calibration, the incident beam intensity (I_o) of gamma source of cesium (^{137}Cs) was measured firstly and the attenuated beam intensities (I) of each sample were measured one by one with ten different thickness samples. Each sample was placed 7cm from the gamma ray detector. The spectra of gamma ray energies of these samples were counted at a fixed time period of 900 seconds using MCA measure software with gain level 1 and offset 1. The counts under the peak spectrum area were got from the data table and the gamma ray intensities I_o and I of ^{137}Cs source for different attenuators were obtained.

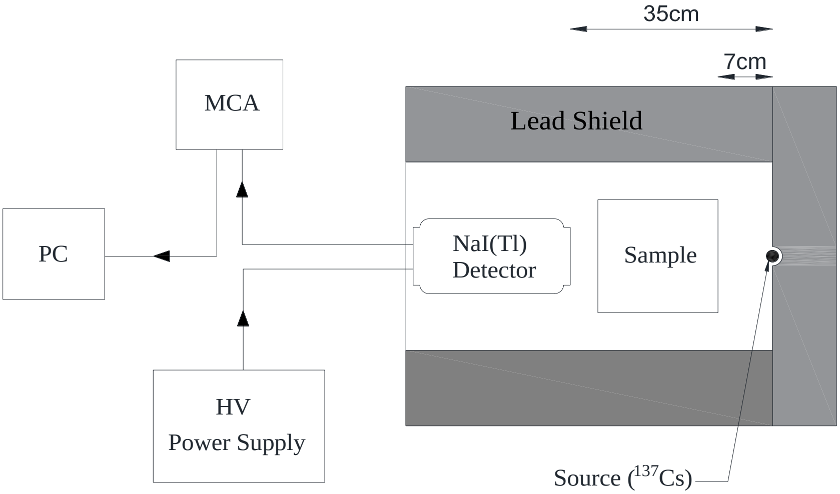

Figure 1: Block diagram of Experimental Set up

Table 1: Elemental Concentration in AAC Block Sample

Element	Wt %
Ca	60.884
Si	25.697
Fe	8.951
K	1.306
Ba	1.021
S	0.856
Ti	0.787
Cr	0.119
Mn	ND
Sr	0.081
Zn	0.186
Cu	0.075
Zr	0.037

ND = non-detected

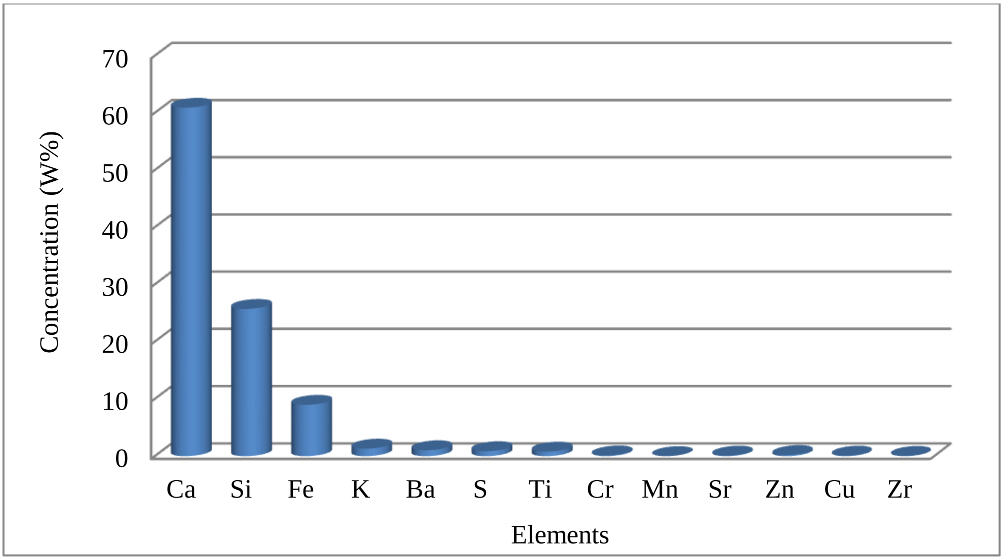

Figure 2: Elemental Concentrations in AAC Block Sample

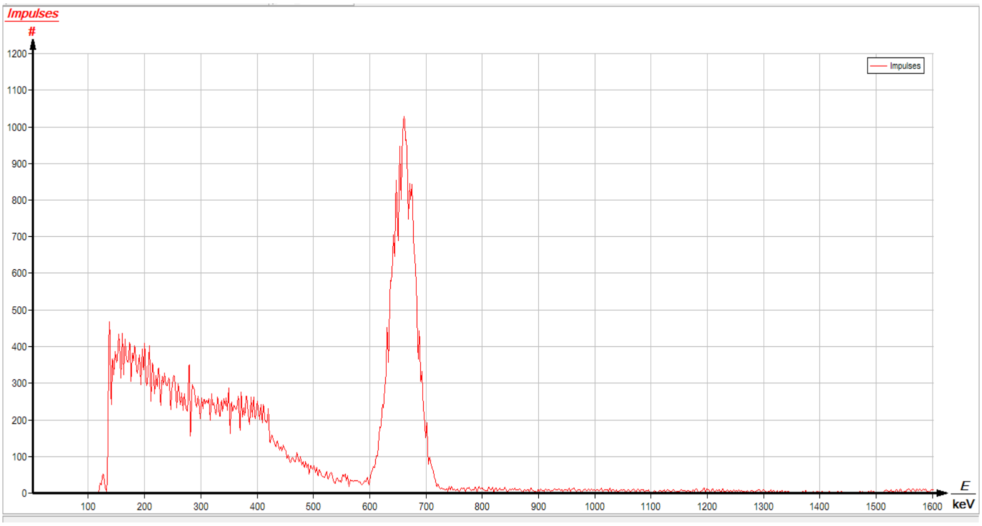

Figure 3: The recorded spectrum of AAC block sample for ^{137}Cs source without absorber

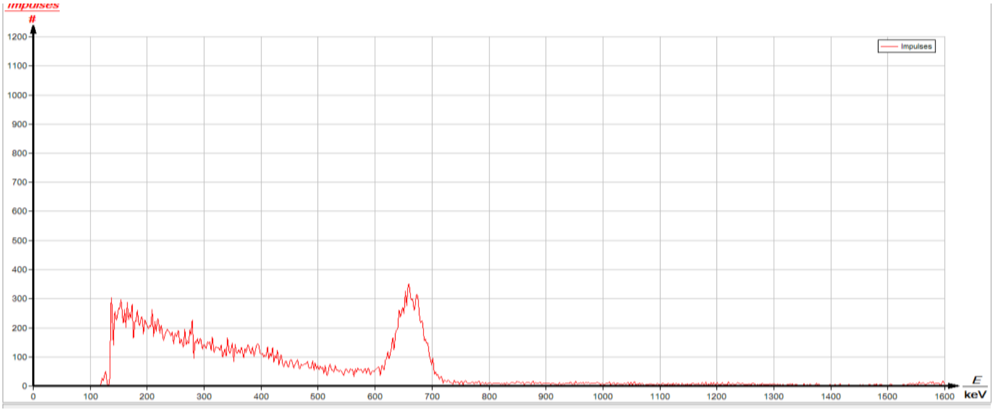

Figure 4: The recorded spectrum of AAC block sample for ^{137}Cs source with absorber thickness 24.1cm

Table 2: Attenuation coefficients of AAC block sample with different thicknesses by using ^{137}Cs source

Thickness		$I_o \pm \sqrt{I_o}$	$I \pm \sqrt{I}$	–ln	μ	μ_m
(cm)	(gcm^{-2})	(Cmin^{-1})	(Cmin^{-1})	(I/I_o)	(cm^{-1})	(cm^{2}g^{-1})
1.4	1.21	1537.6 ± 39.21	1448.27±38.06	0.06	0.0427	0.0584
3.8	2.83		1300.67±36.06	0.16	0.0440	0.0592
6.4	4.51		1154.07±33.97	0.29	0.0438	0.0636
8.9	6.93		1054.87±32.48	0.37	0.0423	0.0554
11.4	7.16		994.93±31.54	0.43	0.0382	0.0608
14	10.98		832.53±28.85	0.62	0.0438	0.0549
16.5	12.14		790±28.11	0.67	0.0404	0.0581
19.1	13.51		701.53±26.49	0.78	0.0411	0.0596
21.6	14.5		647.87±25.45	0.87	0.0400	0.0629
24.1	15.85		567.73±23.83	0.99	0.0413	0.0628

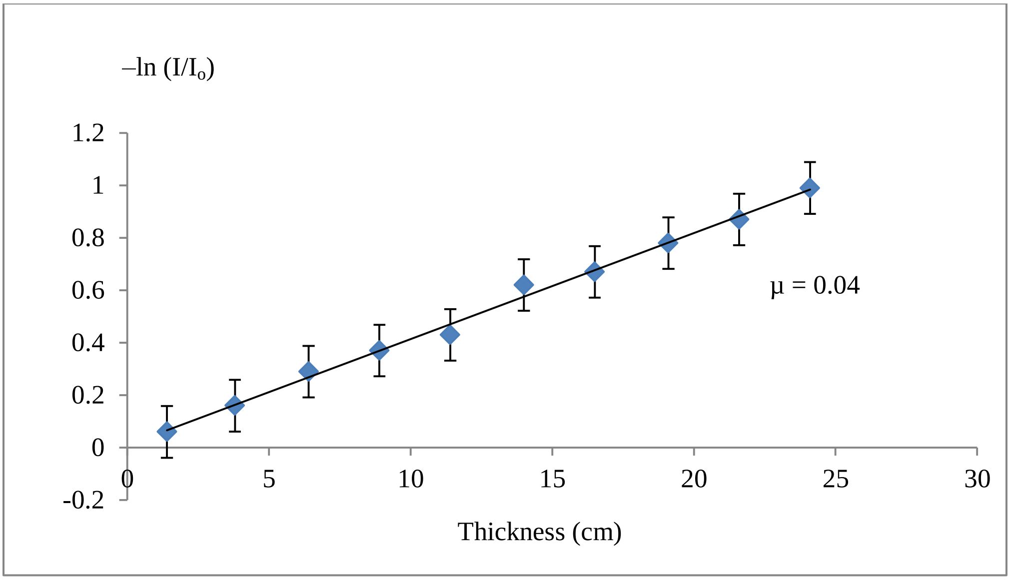

Figure 5: –ln (I/I_o) versus different thicknesses (cm) of AAC block sample of ^{137}Cs source

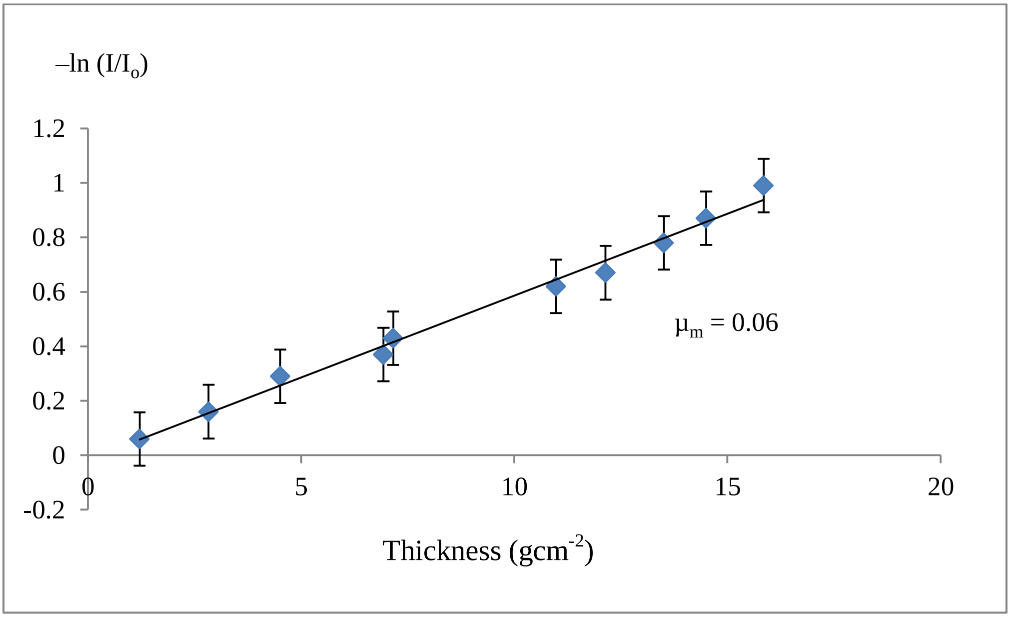

Figure 6: –ln (I/I_o) versus different thicknesses (gcm^{-2}) of AAC block sample of ^{137}Cs source

Results and Discussion

The elemental concentration in AAC block sample was shown in Table 1 and Figure 2 showed the graph of elemental concentration in AAC block sample. According to the measurement data of AAC block sample using EDX-720, calcium was found as major element contained in this sample 60.884 weight%. Silicon was found as second major element with 25.697weight%. Iron was also found as third major element contained in this sample 8.951%. Potassium, barium, sulphur, titanium, chromium, manganese, strontium, zinc, copper and zirconium were found as minor elements. The recorded spectrum of AAC block sample for ^{137}Cs source without absorber was shown in Figure 3 and that of spectrum with absorber thickness 24.1cm was shown in Figure 4. The graph of –ln (I/I_o) versus different thicknesses of AAC block sample of ^{137}Cs source was shown in Figure 5. From the graph, the slope gave the value of linear attenuation coefficient (μ). Figure 6 showed the graph of –ln (I/I_0) versus different thicknesses (gcm^{-2}) of AAC block sample of ^{137}Cs source. The slope of this graph gave the value of mass attenuation coefficient (μ_m).

Conclusion

From the results of elemental analysis in AAC block sample, it was concluded that toxic elements such as fluorine, lead, cadmium, and arsenic were not observed obviously in weight percent level in the present study. And also radioactive nuclides thorium (Th) and uranium (U) were not detected by EDXRF method. Gamma attenuation coefficients of AAC block sample with different thicknesses were measured by gamma detection system. All the values of mass attenuation coefficient are nearly equal for ten sample thickness. Thus, attenuation coefficients do not depend on sample thickness. The attenuation coefficient of AAC is slightly less than aluminium (Al) but there are no toxic elements. So, AAC block can be used as radiation shielding material for both internal and external construction in desirable and these results will be helpful in the development of radiation shielding technology.

Acknowledgements

I would like to thank Professor Dr Khin Khin Win, Head of Department of Physics, University of Yangon, for her kind permission and encouragement to carry out this work.

I would like to thank Professor Dr Aye Aye Thant, Department of Physics, University of Yangon for her encouragement.

References

American University in Bulgaria. Retrieved 27 March (2016)"Gamma Spectroscopy with a Scintillation Detector and Multichannel Analyzer".

EDXRF Technology, Shimadzu's New Integrated HPLC Bioethano Analyzer Offers Round-the-Clock QC Testing at Bioethanol Production Plants

Hebel, (2010) The History of A A Cat the Wayback Machine

Hubbell, J. H.; Seltzer, S. M. Retrieved September (2007)"Tables of X-Ray Mass Attenuation Coefficients and Mass Energy-Absorption Coefficients". National Institute of Standards and Technology (NIST).

Nicholas Tsoulfanidis, From the book of measurement and detection of radiation

J. Myanmar Acad. Arts Sci. 2019 **Vol. XVII. No.2A**

SILVER MODIFIED TITANIUM DIOXIDE THIN FILMS FOR EFFICIENT PHOTODEGRADATION OF METHYL ORANGE

May Thu Aung[1], Aye Aye Thant[2] and Pho Kaung[3]

Abstract

Silver-modified titanium dioxide thin films have been prepared via a two-step dipping method. Optimization of the photocatalyst's performance as a function of dipping time, irradiation time and concentration of dipping solution was performed. The optimum concentration of silver nitrate was found to be 0.001 M. UV-irradiation process of the films were examined for their catalytic activity towards photodegradation of methyl orange (MO). The modified materials presented enhanced photocatalytic efficiency and managed to decompose the organic pollutant. Its pollutant rate was faster than that of undoped original films (TiO_2). The increase in Ag^+ ion concentration in the dipping solution resulted a decrease in the film's photocatalytic efficiency due to a shading of available semiconductor surface by the silver layer. Moreover, the lower the average particle size, the higher is the photodegradation percentage. UV analysis indicate the decomposition of M.O.

Keywords: titanium dioxide, thin films, photocatalyst, photodegradation

Introduction

Titanium dioxide heterogeneous photocatalysis has been the subject of numerous investigations in recent years as it is an attractive technique for the complete destruction of undesirable contaminants (pollutants) in both liquid and gaseous phases by using solar or artifical light illumination. TiO_2 photocatalysis are oriented towards the photocatalyst immobilization in the form of a thin film. Titania photocatalysis with advantages, such as low operation temperature, low cost, significantly low energy consumption, have led the relevant applications to the stage of commercialization. A proficient way to enhance photocatalytic reaction rate is addition of transition metals to semiconductor. This research work aimed to develop a new composite, immobilized photocatalyst consisting of silver particles photochemically deposited on rough and high surface area nano crystalline TiO_2 films with

---

[1] Dr, Assistant Lecturer, Department of Physics, University of Yangon.

[2] Dr, Professor, Department of Physics, University of Yangon.

[3] Dr, Rector, Department of Physics, University of Yangon.

increased efficiency. The photodegradation of the well known organic azo-dye methyl orange (MO), a typical pollutant in the textile industry, was investigated as a model compound under near UV irradiation.

Experimental Procedure

Preparation of Titania Film

TiO_2 thin film was prepared on optically transparent microscopy glass substrates using doctor-blade method. The schematic diagram of preparation is shown in Figure 1. 10ml of vinegar (or dilute acetic acid) and 6g of titanium dioxide were mixed and stirred with a glass rod for 5 min. the glass slide was fastened with a tape to a table as shown in Figure 1 in order to get the film thickness to be that of the scotch tape. Then, 3-5 drops of the TiO_2 solution were dropped on the glass slide. In order to deposit a uniform thin layer across the unmasked portion of the slide, a glass rod was rolled on the slide Before removing the tape, the slide had been allowed to dry for a few minutes. Finally, TiO_2 thin films were annealed in an oven at 450°C for 15 min.

Preparation of silver deposition on Titania Film

A simple single dip method was used to deposit silver on the titanium dioxide thin film. Firstly, an aqueous solution of silver nitrate ($AgNO_3$) 0.001M was prepared by using distilled water. Then the films were dipped in that solution for 3s. After dipping, the films were illuminated by UV light for 2 hours. The illumination process made the films to be darken due to the presence of silver compound. Finally, the modified catalyst films were immediately tested for the photodegradation of MO.

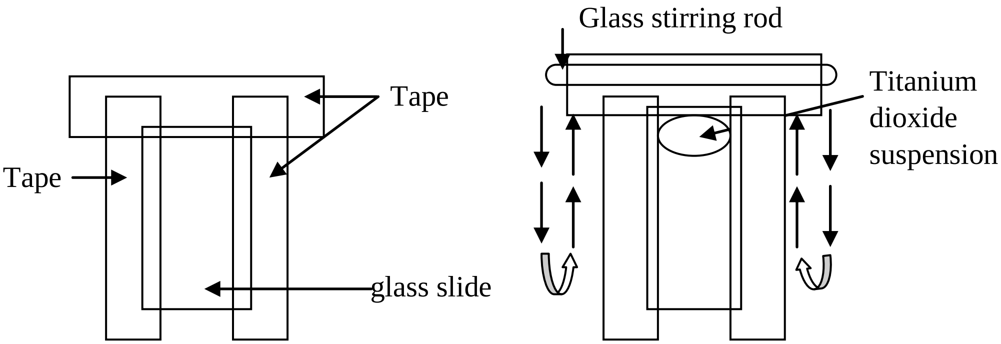

(a) Preparation before coating (b) Procedure of TiO_2 coating

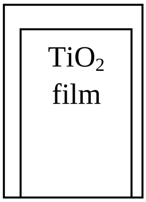

(c) Thin Film after coating

Figure 1: Schematic diagrams of preparation of TiO_2 film by doctor- blade method

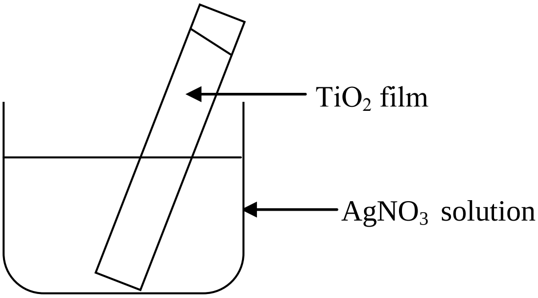

Figure 2: Schematic diagram of Silver deposition on TiO_2 thin film

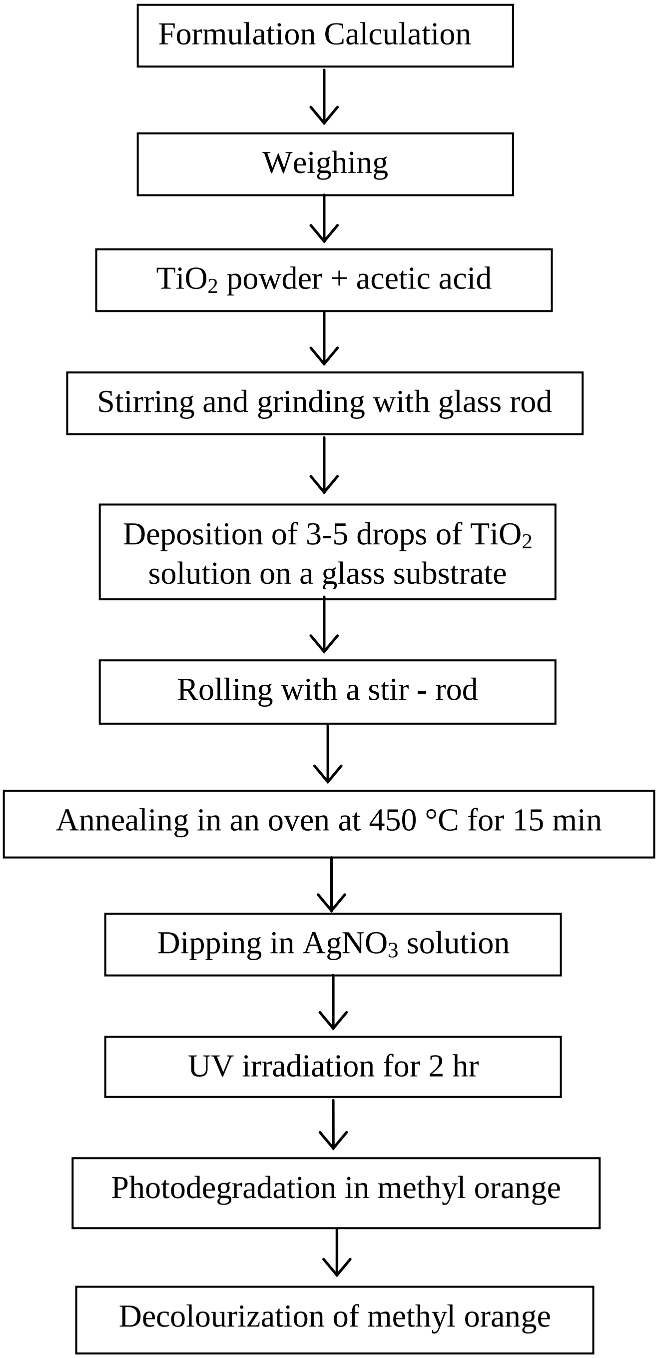

Figure 3: Block diagram for the preparation of Silver-modified Titanium dioxide thin films for efficient photodegradation

Result and Discussion

XRD Analysis of Titanium dioxide Thin Film

The XRD spectra of Ag/TiO_2 film and TiO_2 films were presented in Figure 4. According to the X-ray diffraction, well-organized crystal structure of titania particles were observed in the films. There are three phases in TiO_2: Anatase, Rutile and Brookite. In the present work, the XRD spectrum confirms that the anatase reflections are dominating where a small amount of rutile is also present. The reflections (101, 004, 200, 211, 204, 213, 116) represent anatase phase while the reflections (110, 101, 111, 210, 211, 220, 310, 112, 221) represent rutile phase. The tetragonal structure of TiO_2 was identified by using the International Centre for Diffraction Data (ICDD) file number 21-1272 (for anatase) and 21-1276 (for rutile) in Figure 4 Brookite phase is not present in TiO_2 film. It may be due to the synthesis parameters in the formation of the film.

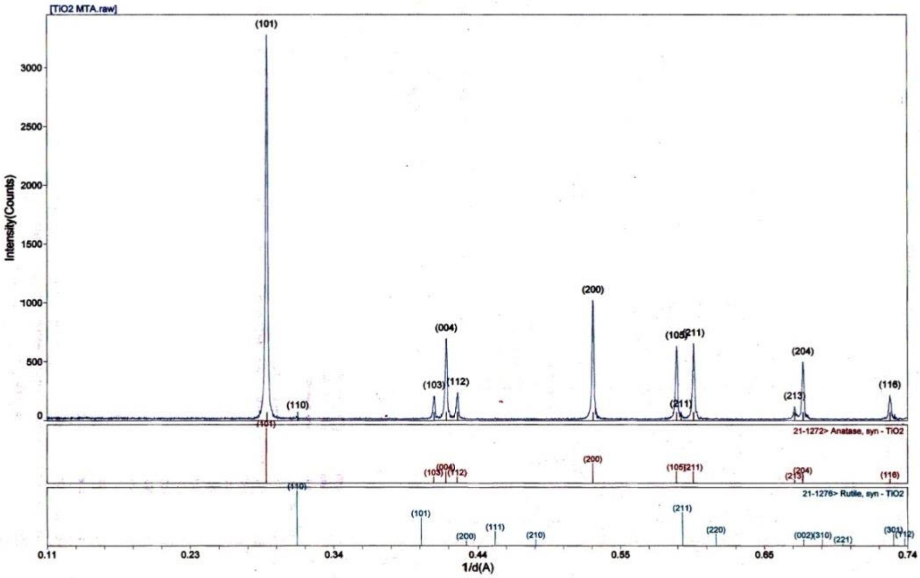

Figure 4: XRD spectrum of TiO_2 with reference patterns (Anatase 21-1272 and Rutile 21-1276)

XRD Analysis of Silver-modified Titanium Dioxide Thin Film

The XRD spectrum of silver-modified titanium dioxide thin film is shown in Figure 5. The XRD result showed that only small amount of silver percentage was observed in silver modified Titanium dioxide film. The face-centered cubic structure of Ag was identified by using the International Centre for Diffraction Data (ICDD) file number (41-1402). This observation proved to be extremely efficient for the photodegradation of methyl orange. It is also confirmed that silver oxide particles were not crystallized on TiO_2 surface as shown in Figure 5. This is probably due to the fact that the majority of the silver particles were only deposited on the surface of the TiO_2 film but not incorporated into the TiO_2 matrix.

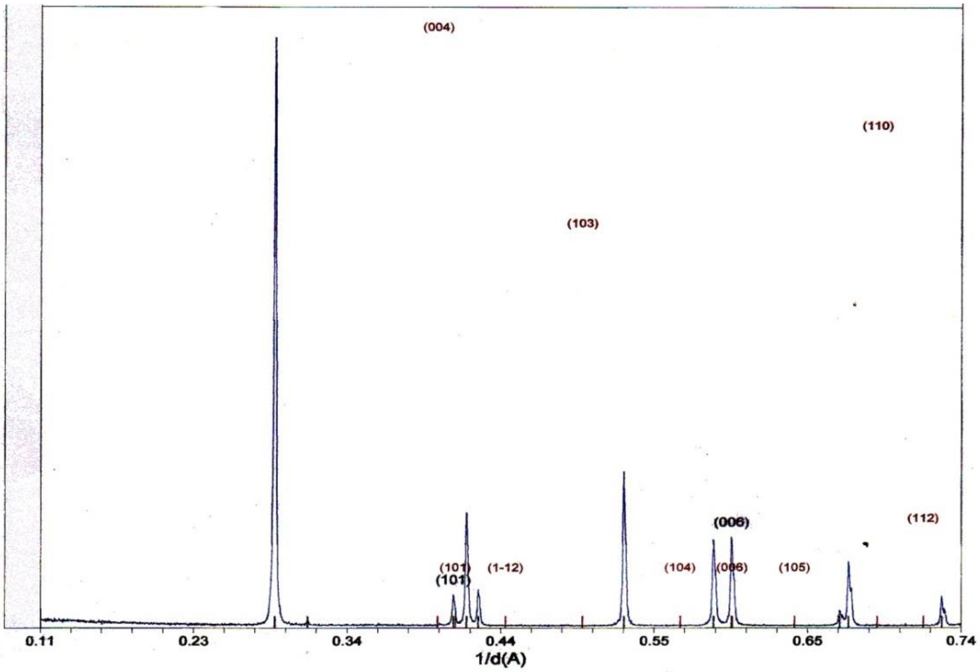

Figure 5: XRD spectrum of Ag/TiO_2

Photocatalyst Surface Properties

The morphology of the silver lager deposited on the titania surface plays a crucial role in catalytic efficiency. The surface morphology of the Ag/TiO_2 films for 0.1 M $AgNO_3$ and 0.001 M $AgNO_3$ were characterized by Scanning Electron Microscope (SEM) and shown in Figure 6 and 7 respectively. Both microstructures present a porous, sponge like network of high roughness and complexity in general. Moreover, there is no crack in the film showing that the viscosity of the solution is optimum. The film deposited from the lower concentration of the Ag^+ solution exhibits surface characteristic of higher roughness in comparison with those resulting from higher concentration. This might be one reason for the higher photocatalytic behavior in the film with 0.001 M Ag^+.

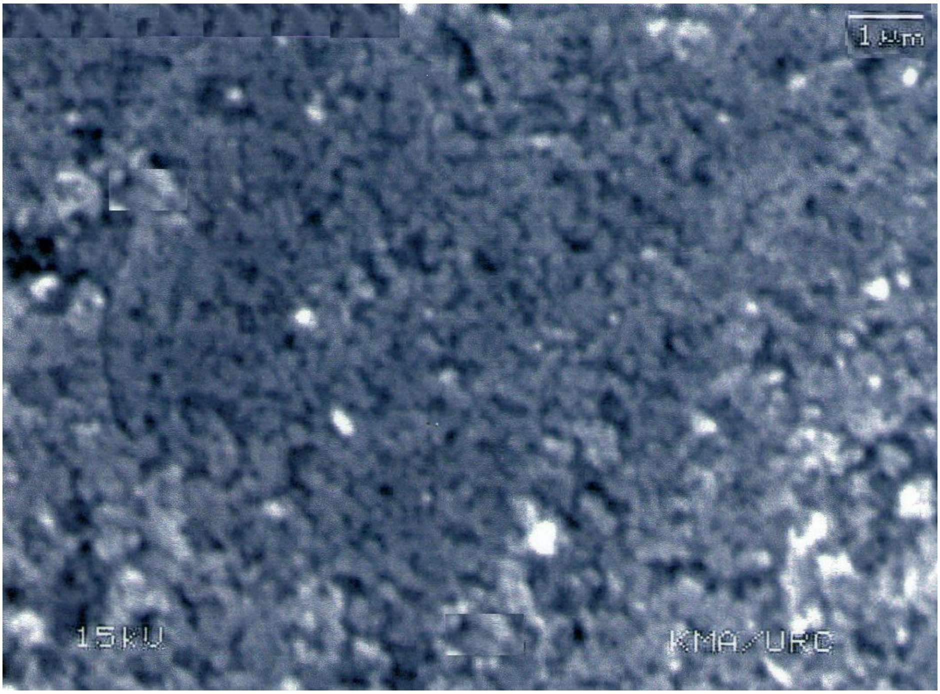

Figure 6:SEM picture of silver-modified TiO_2 film: dipping in 0.1 M $AgNO_3$

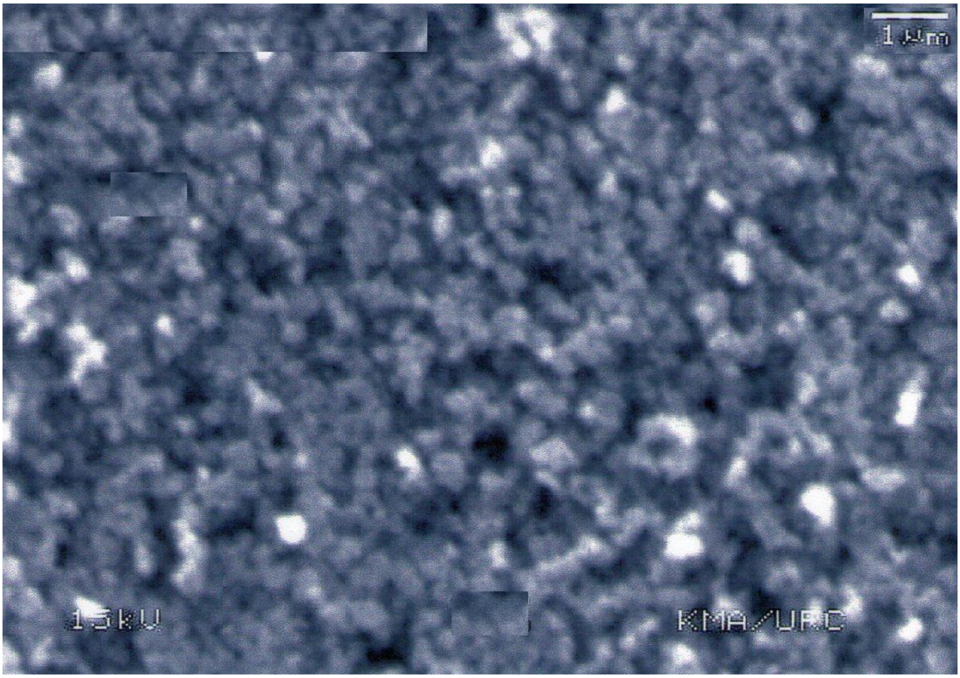

Figure 7: SEM picture of silver-modified TiO_2 film: dipping in 0.001 M $AgNO_3$

Photocatalytic Activity

The experiments on photocatalysis was done with an aqueous solution of methyl orange to evaluate the films activity. The phtocatalytic activity was evaluated as the percentage of pollutant disappearance. The mixture solution of UV irradiated TiO_2 with and without $AgNO_3$ and MO was prepared prior the absorbance measurement. After degradation of MO, the photocatalyst TiO2 was filtered out to obtain the clear solution of degraded MO. Then, The absorbance of MO solutions before and after degradation were measured at different degradation times. Measurements were carried out using Shimadzu UV - 1800 spectrophotometer in the photon energy range of wavelength 190 nm to 600 nm and with aid of quartz cells. The percentage of degradation was calculated from the following equation (1).

$$\text{Degradation \%} = \left(1 - \frac{A_t}{A_0}\right) \times 100 \qquad (1)$$

Where, A_t is the absorbance after time t and A_0 is the dye initial concentration before degradation. The photocatalytic efficiency of TiO_2 with different reaction time for the MO decomposition is illustrated in Figure 8 and presented in Table 1. A maximum degradation (58%) was observed for the reaction time of 2 hours. It was also found that the percentage of decolorization and photodegradation increase with the increase in reaction time. Again, a maximum degradation (65%) was observed for $AgNO_3$ (0.1M) modified TiO_2, shown in Figure 9 and presented in Table 2. The photodegradation efficiency of photocatalyst TiO_2 is lower than that of Ag modified TiO_2. Therefore, it is concluded that the presence of Ag do enhance the degradation percentage. To confirm this finding, the experiment was repeated for $AgNO_3$ concentration (0.001M) and the results are shown in Figure 10 and presented in Table 3. A high maximum degradation of (82%) was found for $AgNO_3$ (0.001M) modified TiO_2.The results show that the decrease in concentration of $AgNO_3$ can increase the photocatalytic efficiency. In order to observe the effect of Ag concentration on photocatalytic behavior, the measurement were conducted at 2 min reaction time for different concentration of $AgNO_3$ which shown in Figure 11 and presented in Table 4. A maximum (96%) was observed for the TiO_2 film immersed in 0.001 M $AgNO_3$ solution. Further increase in the Ag concentration results a considerable decrease in efficiency. All the result confirm the dependence of degradation on the reaction time. Further more these observation also show that the TiO_2 photocatalyst modified with less amount of Ag do enhance the photocatalytic efficiency via the decomposition of organic pollutant.

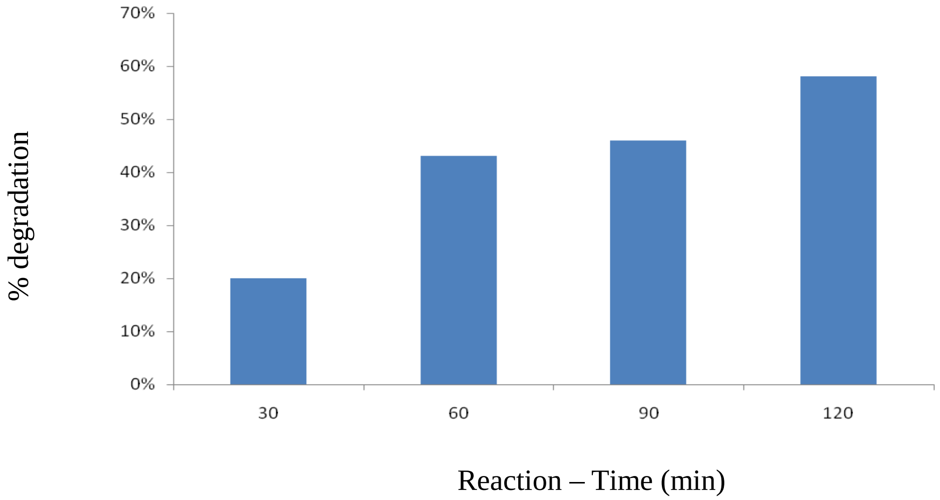

Figure 8: % degradation of methyl orange by TiO_2 film with reaction time 2 hours .

Table 1: Variation in % degradation of methyl orange via TiO_2 film with reaction time 2 hours.

Time (minute)	**%degradation**	**Absorbance**
30	20%	1.517
60	43%	1.079
90	46%	1.032
120	58%	0.800

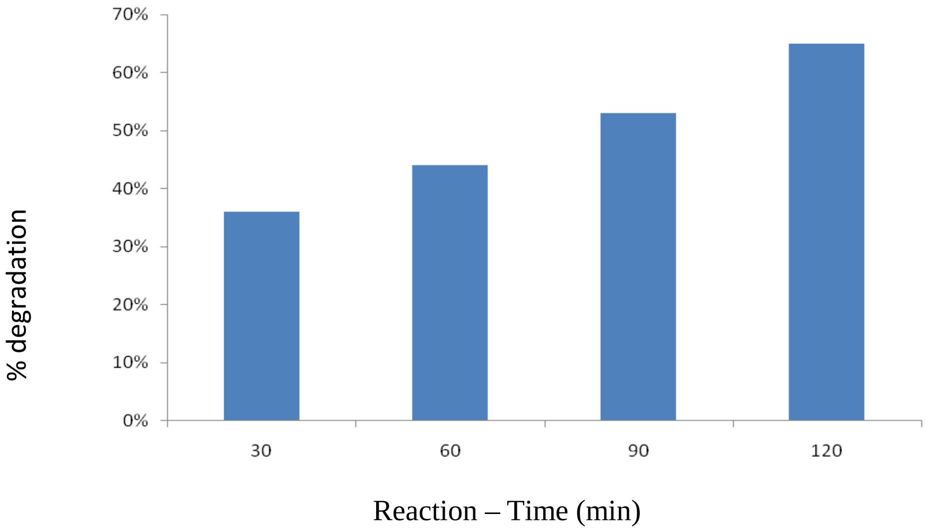

Figure 9: % degradation of methyl orange by Ag / TiO_2 film after dipping for 3s in 0.1 M of silver solution with reaction time 2 hours .

Table 2: Variation in % degradation of methyl orange via Ag / TiO_2 film after dipping for 3s in 0.1 M of silver solution with reaction time 2 hours.

Time (minute)	**%degradation**	**Absorbance**
30	36%	0.605
60	44%	0.535
90	53%	0.454
120	65%	0.341

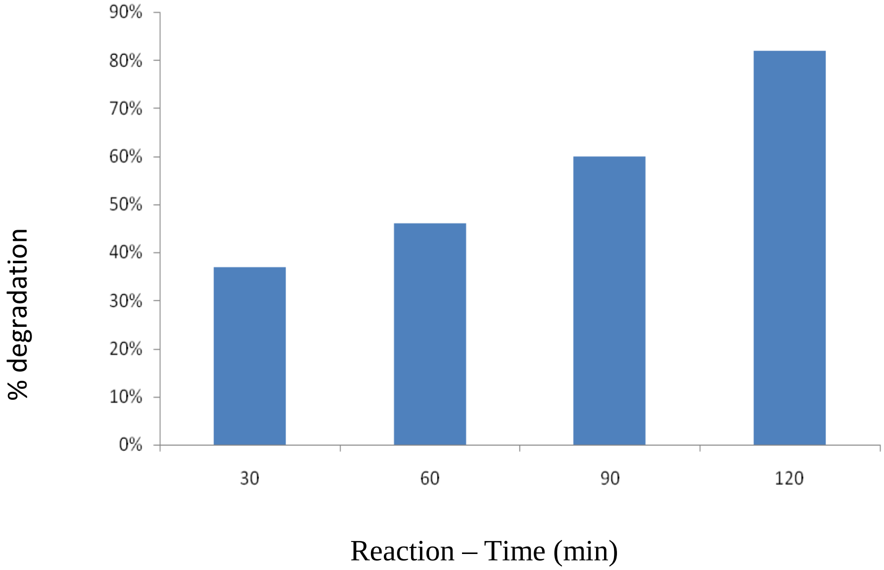

Figure 10: % degradation of methyl orange by Ag / TiO_2 film after dipping for 3s in 0.001 M of silver solution with reaction time 2 hours .

Table 3: **Variation in % degradation of methyl orange via Ag / TiO_2 film after dipping for 3s in 0.001 M of silver solution with reaction time 2 hours.**

Time (minute)	**%degradation**	**Absorbance**
30	37%	0.600
60	46%	0.512
90	60%	0.380
120	82%	0.163

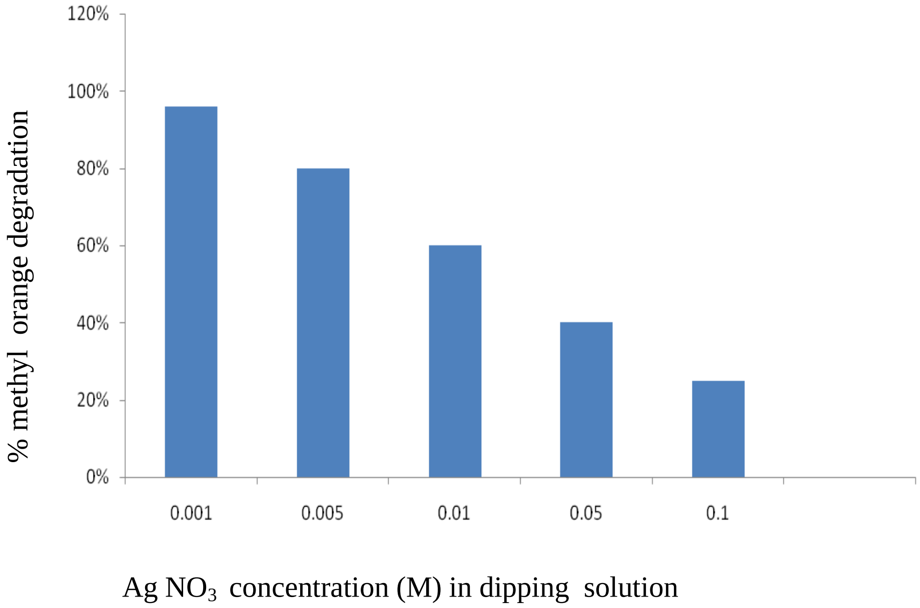

Figure 11: Photocatalytic activity of Ag / TiO_2 films as a function of the Ag NO_3 dipping solution.

Table 4: Variation in % degradation of methyl orange by Ag / TiO_2 as a function of Ag NO_3 dipping solution.

Ag NO_3 Concentration (M)	**%degradation**	**Absorbance**
0.1	25%	17.800
0.05	40%	14.250
0.01	60%	9.500
0.005	80%	4.750
0.001	96%	0.950

Figure 12: Photo of degradation of methyl orange by Ag/TiO_2– film after dipping for 3s in 0.001 M of silver solution during 2 hours.

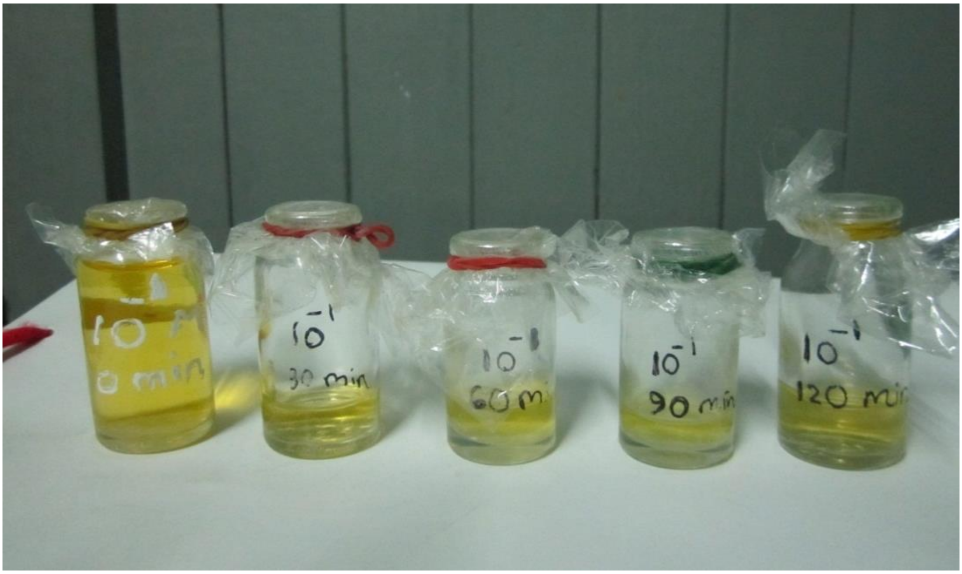

Figure 13: Photo of degradation of methyl orange by Ag/TiO_2– film after dipping for 3s in 0.1 M of silver solution during 2 hours.

Conclusion

Titanium dioxide films developed on the glass slides were modified by silver deposition and successfully tested for the photocatalytic degradation of the pollutant methyl orange. According to the SEM results, the film deposited from the lower concentration of the Ag^+ solution exhibits surface characteristic of higher roughness in comparison with those resulting from higher concentration. This might be one reason for the higher photocatalytic behavior in the film with 0.001 M Ag^+. According to the XRD analysis the silver oxide particle were not crystallize on TiO_2 surface. According to the UV analysis, it was also found that the percentage of decolorization and photodegradation increase with the increase in reaction time due to photocatalytic activity observations. Moreover, the photodegradation efficiency of photocatalyst TiO_2 is lower than that of Ag modified TiO_2. Therefore, it is concluded that the presence of Ag do enhance the degradation percentage. Besides, the results show that the decrease in concentration of $AgNO_3$ can increase the photocatalytic efficiency. Finally, all the observations in this work pointed out that TiO_2 photocatalyst modified with less amount of Ag do enhance the photocatalytic efficiency via the decomposition of organic pollutant. Therefore, it is concluded that the characterization of silver and titania surface is essential for the research of water pollution.

Acknowledgements

I would like to acknowledge to Professor Dr Khin Khin Win, Head of Department of Physics, University of Yangon, for giving me the chance to participate in this event. My thanks go to Professor Dr Aye Aye Thant for her encouragement of this work.

References

Arabatzis Z.M (2003) "Applied Catalysis B: Environment 42, 187-201" (Greece: 153 10 Aghia Paraskevi, Attikis, Athens.)

Fujishima A (1999) "TiO_2 Photocatalysis, Fundamentals and Applications" (Tokyo : Bkc Inc.,)

International Journal of Physical Sciences (2007) vol. 2(3), pp 073-081 (Physics Department, Faculty of science, Aswan, South Valley University, 81528 Aswan, Egypt).

John V B (1992) "Introduction to Engineering Materials" (London: Macmillan)

Linsebigler A.L, Lu G, Yates J.T 1995 Chem. Rev. 95, 735

Rancourt J D (1996) "Optical Thin Films" (New York: Optical Engineering)

J. Myanmar Acad. Arts Sci. 2019 **Vol. XVII. No.2A**

STRUCTURAL STUDIES OF SB DOPED SNO$_2$ THIN FILMS DEVICES

Toe Toe Wai[1] and Moht Moht Than[2]

Abstract

A series of Sb-doped samples, SnO$_2$ with doping levels 2mo 4 mol%, 4 mol%, 6 mol%, 8 mol% have been prepared by sol-gel and spiin coating methods. The structural properties of samples were characterized by X-ray Diffraction (XRD) analysis. The microstructural and morphology properties were examined by Scanning Electro microscopy (SEM).The optical properties of the samples were investigated by UV-Vis spectroscopy. According to UV-Vis spectroscopy, the band gap of SnO$_2$:Sb varied from 3.2 eV to 3.7 eV with variation of Sb dopant concentration .According to the result, it was observed that the structural studies of Sb doped thin films devices were successfully fabricated.

Keywords: sol-gel process, spin coating, X-ray, SEM, SnO$_2$, Sb

Introduction

Tin Oxide (SnO2),an important n-type semiconductor with a wide band gap (Eg=3.6eV),exhibits excellent optical, electrical and chemical properties and high thermal stability. Research has shown that the semiconductor SnO2 material has potential applicability in gas sensors, glass electrodes, secondary lithium batteries, solar cells, transistors and catalysts. In recent years, doped SnO2 and SnO2- based materials, such as Sb-doped SnO2, Mn-doped SnO2 so on, have been extensively studied due to their special optical and electrical properties of these materials also depend on the sizes and shapes of particles. During the past few years, these materials have been prepared by many techniques such as sol-gel, simple thermal evaporation, hydrothermal method, and other method.

In this paper, we present our success in the synthesis of SnO2 and SnO2-Sb nanoparticles by sol-gel method with Sb dopant concentration changed from 2 to 8 mol % and some characteristics of the material.

---

[1] Dr, Assistant Lecturer, Department of Physics, University of Yangon

[2] Dr, Lecturer, Department of Physics, University of Yangon

Experimental procedure

Sb (2 mol %, 4 mol %, 6 mol %, 8 mol %) doped SnO_2 thin films are synthesized by solid state method, using high purity (99.9% reagent grade) SnO_2 and Sb powders. These powders were weight on the basis of stoichiometric composition. The resultant stoichiometric composition of the SnO_2 (1-x) Sb(x) (x=0.01, 0.02, 0.04, 0.06 and 0.08) powders were ground by agate motor to obtain the homogeneity. The mixed powder were annealed at 500ºC for 1 hr. each mixture of Sn(1-x) Sb(x) mixed with 2-mothoxyethanol ($CH_3OCH_2CH_2OH$) solution and then heated up to 100ºC with indirect heat treatment for 1hr. Finally, homogeneous pre cursor solutions or coating solutions are obtained. The glass substrate are cleaned by standard cleaning method. The resulting pre cursor solution are deposited on glass substrates by spin coating, deposited thin films are heat treated at 600ºC for 1hr. X ray diffraction analysis was used as the major tool for identification of phase of prepared thin films. The morphology of the films was observed with scanning electron microscopy. The optical properties of the samples were investigated by UV-Vis spectroscopy.

Results and Discussion

X-ray diffraction patterns of Sb(2 mol%, 4mol%, 6mol%, 8mol%) doped SnO_2 films are shown in Fig.1 (a~d) showing the polycrystalline of the samples. Matching of the observed and standard (h k l) planes confirms that the deposited films have a primitive tetragonal structure. On the other hand, the preferred orientation was found to be along the (110) plan for all the films. However, the doped films showed lattice constants a and c for the tetragonal phase structure are determined by the relation.

$$\frac{1}{d^2} = \left(\frac{h^2}{a^2} + \frac{k^2}{a^2}\right) + \left(\frac{l^2}{c^2}\right) \qquad (1)$$

where d and (hkl) are the interplanar distance and Miller indices, respectively. The lattice constant a and c were calculated and are given in table 1. The calculated lattice constants and unit cell volume matched well with the standard JCPDS data card.

In order to determine the variation of crystallite size with doping, the size of the crystallites oriented along the (110) plane was calculated using Scherrer's formula.

$$D = \frac{0.9\lambda}{B\,cos\theta} \tag{2}$$

Where B,θ, and λ are the broadening of the diffraction line measured at half its maximum intensity in radians, the diffraction angle, and the x-ray wavelength, respectively. The calculated values of crystallite size are given in Table 1. It can be seen that the crystallite size decreases with increasing doping.

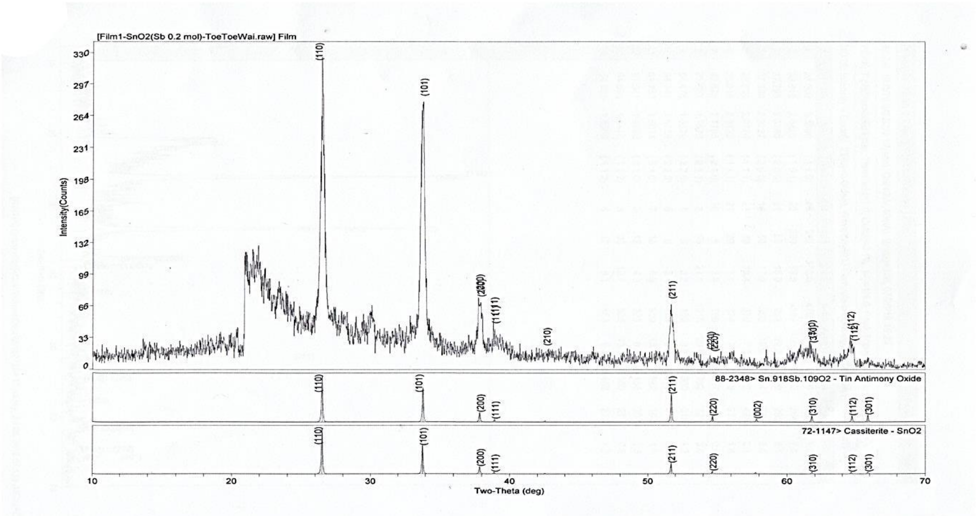

Figure 1: (a) XRD patterns obtained for Sb(2 mol% SnO_2) doped

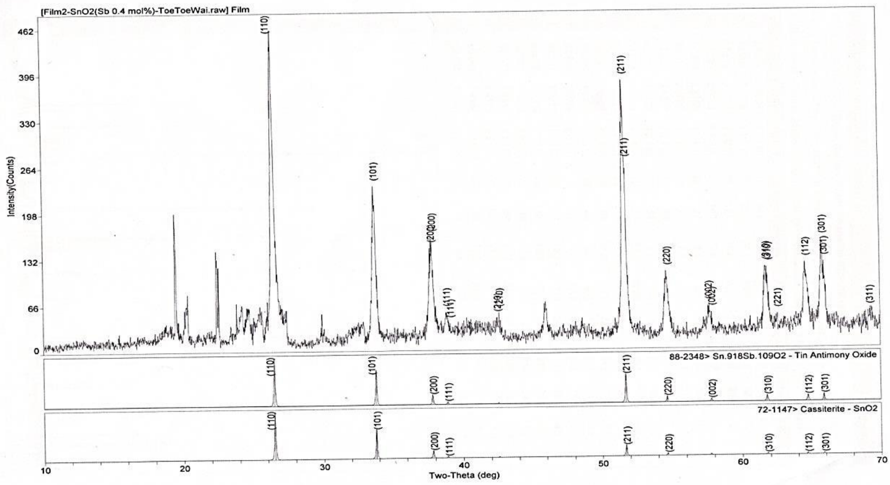

Figure 1: (b) XRD patterns obtained for Sb(4 mol% SnO_2)

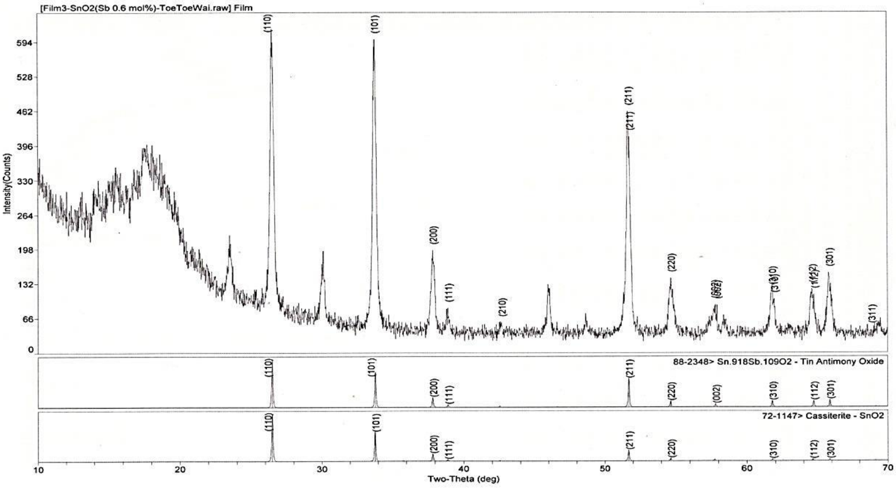

Figure 1: (c) XRD patterns obtained for Sb(6 mol% SnO_2)

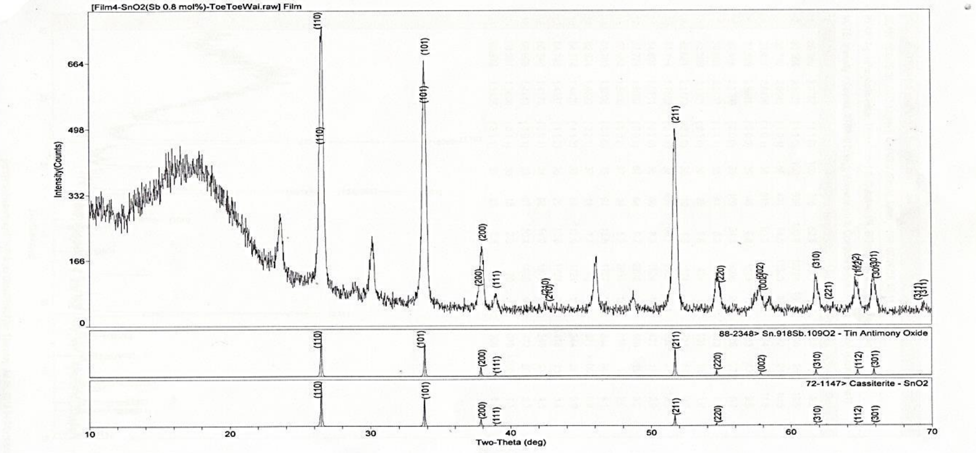

Figure 1: (d) XRD patterns obtained for Sb (8 mol% SnO_2)

Table 1: Structure parameters of SnO_2: Sb thin films

Samples	a (nm)	c (nm)	c/a	D (nm)	V $(nm)^3$
SnO2: 2% Sb	4.7512×10^{-1}	3.1929×10^{-1}	0.672	28.5403	0.0720
SnO2: 4% Sb	4.7512×10^{-1}	3.1806×10^{-1}	0.669	24.9108	0.0717
SnO2: 6% Sb	4.7489×10^{-1}	3.1880×10^{-1}	0.671	24.7980	0.0718
SnO2: 8% Sb	4.7636×10^{-1}	3.1876×10^{-1}	0.669	24.6090	0.0723

The surface morphology of the Sb-doped SnO_2 films is shown in fig.2 (a~d). In this SEM image, the spherical size SnO_2 nanoparticles with nearly uniform size from the SEM image we observed that the particles were agglomerated. The agglomeration affects dopants on the size of the particles. The size of the particles was estimated to the around 0.3-0.4 um using SEM.

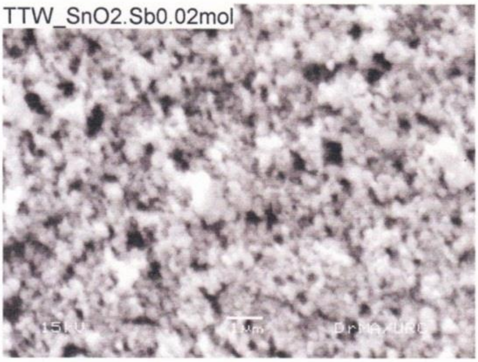

Figure 2: (a). SEM photo graph of Sb (2 mol% SnO_2)

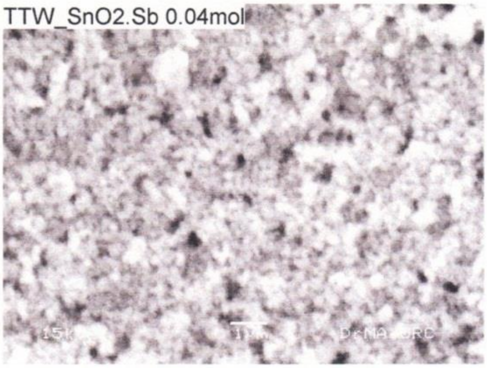

Figure 2: (b). SEM photo graph of Sb (4 mol% SnO_2)

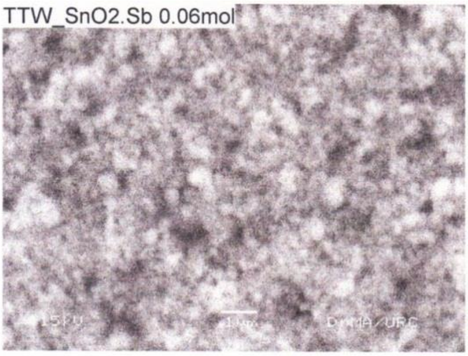

Figure 2: (c). SEM photo graph of Sb (6 mol% SnO_2)

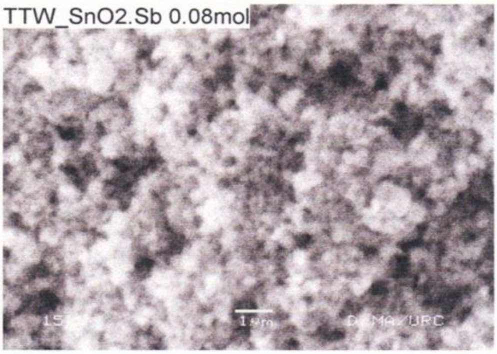

Figure 2:(d) SEM photo graph of Sb (8 mol% SnO_2)

Table 2: The particle size of SnO_2: Sb powders

Sample	**Size of particles (μm)**
SnO_2 : 2% Sb	0.398
SnO_2 : 4% Sb	0.327
SnO_2 : 6% Sb	0.320
SnO_2 : 8% Sb	0.285

UV-Vis violet radiation (UV) is the part of the electromagnetic radiation spectrum below visible light. The measurement of the band gap of material is important in the semiconductor, nanomaterial and solar industries. This note demonstrated how the bandgap of a material can be demonstrated from its UV absorption spectrum. Figure3(a-d)illustrated the absorption spectra for Sb: SnO_2films. The energy bandgap of the thin films were calculated by the equation E = hc/λ.

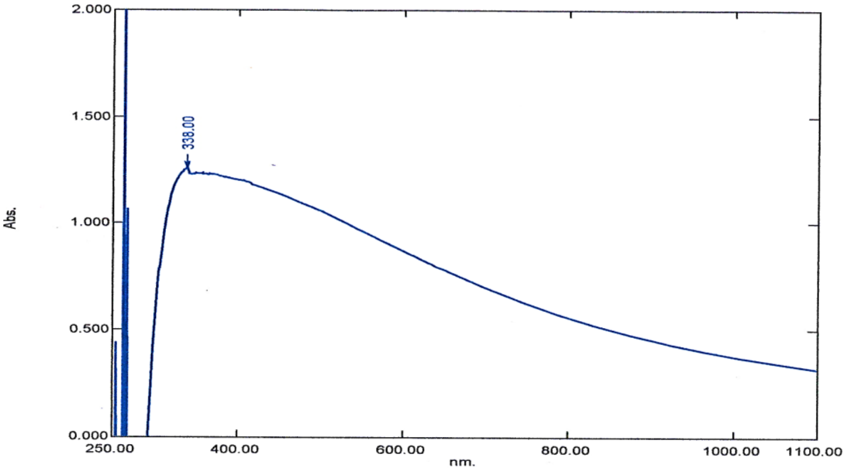

Figure 3: (a) Sb:SnO_2 2 mol% (Absorbance)

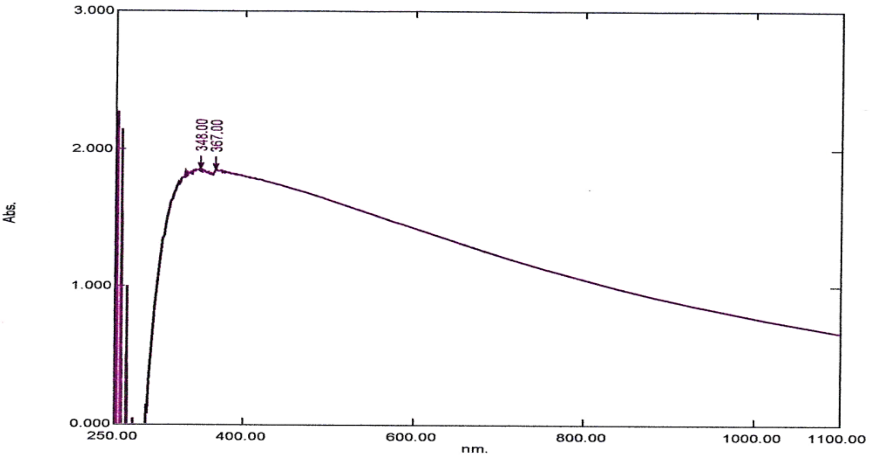

Figure 3: (b) Sb:SnO_2 4 mol% (Absorbance)

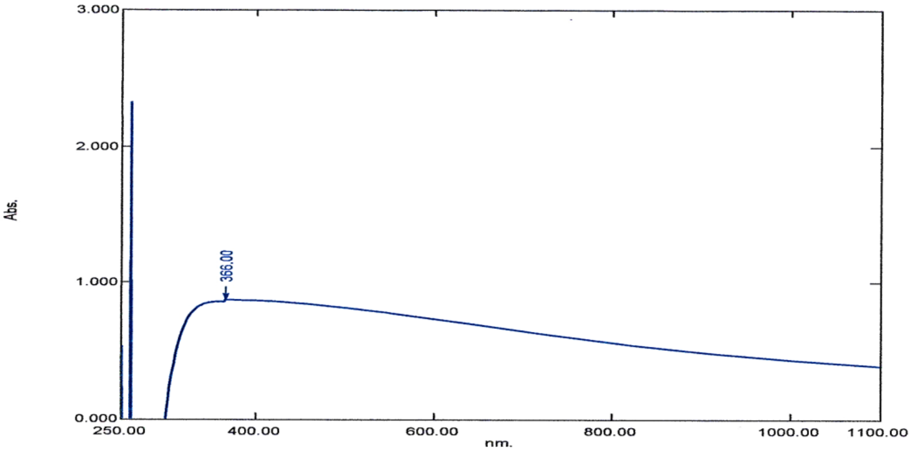

Figure 3: (c) Sb:SnO_2 6 mol% (Absorbance)

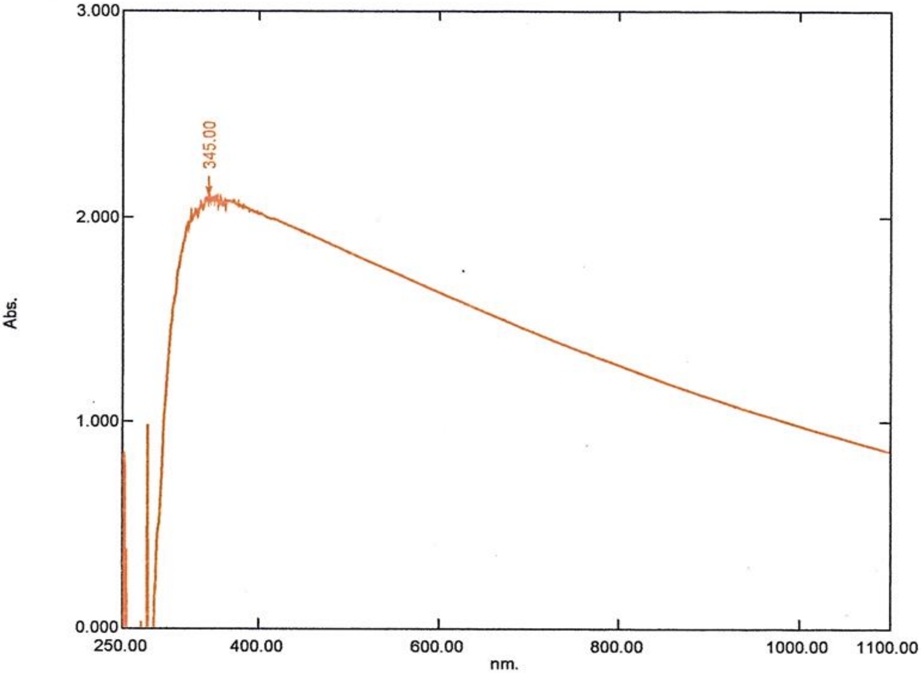

Figure 3: (d) Sb:SnO_2 8 mol% (Absorbance)

Table 3: The optical Bandgap of SnO_2 :Sb Thin Flims

Specimen	Optical Band Gap (eV)
SnO_2 : 2% Sb	3.67
SnO_2 : 4% Sb	3.37
SnO_2 : 6% Sb	3.34
SnO_2 : 8% Sb	3.23

Conclusions

SnO2:Sb transparent films deposited on g;lass substrates by sol-gel and spin coating techniques were successfully obtained.SnO2:Sb dopant films with different molar ratios were synthesized using sol-gel technique. The XRD result was indicated the tetragonal structure formation with (110) preferred orientation. The crystallite size of SnO2:Sb samples with molar ratios are 28.540nm, 24.9108nm, 24.7980nm, and 24.6090nm. According to SEM micrographs, the grains distributions were found to be highly dense. Some grains were agglomerated on some region, some grains were separated by pores. According to the UV-Vis measurements, the energy band gaps of SnO2:Sb films were found to be 3.67eV, 3.37eV, 3.34eV and 3.23eV respectively. The results showed that SnO2:Sb films exhibited a promising application for solar cell fabrication with all tested species.

Acknowledgement

I am highly grateful thanks Professor Dr Khin Khin Win, Head of Department of Physics, University of Yangon for her permission to do and her encouragement throughout this paper. I also would like to thank Professor Dr Aye Aye Thant, Department of Physics, University of Yangon for her allowing me to do the paper.

References

Badway W.A et al (1988) “Thin Solid Films” 158, 277.

Barsan N et al (2003); “J. Phys: condens. Matter” 15, R 813.

Landfredi A.J.C et al (2009); “J. Appl. Phys” 105, 023708.

Matt N.F et al (1971) “Electric Processes in Non Crystalline Materials (Oxford Clarendan)

Serin T et al (2006); “J.Non-Cryst.Solid” 352, 209.

Terrier C et al (1997). “Thin Solid Films” 295,95.

Yildiz A et al (2008); “J. Non-Cryst. Solid” 354, 4944.

Zhang G et al (2000); “Sens. Actuators B:Chem” 69, 144.

J. Myanmar Acad. Arts Sci. 2019 **Vol. XVII. No.2A**

STUDY ON STRUCTURAL, MICROSTRUCTURAL, OPTICAL AND ELECTRICAL PROPERTIES OF LITHIUM COBALT OXIDE AND LITHIUM NICKEL OXIDE FOR THE APPLICATIONS OF SOLID OXIDE FUEL CELLS

Moe Min Min Aye[1], Tun Aye[2], Htet Naing Lwin[3] & Win Kyaw[4]

Abstract

Solid Oxide Fuel Cell (SOFC) is an electrochemical device that converts the energy of a chemical reaction directly into electrical energy. SOFC materials of Lithium Cobalt Oxide ($LiCoO_2$) and Lithium Nickel Oxide ($LiNiO_2$) were prepared by solid-state reaction method. Structural, microstructural, optical and electrical properties were studied by XRD, SEM, UV-VIS-NIR and electrical conductivity measurement. XRD patterns reveal that the samples analogous to hexagonal structure. The crystallite sizes of the samples were also estimated by using the most intense peaks and obtained as 77.14 nm for $LiCoO_2$and 21.40 nm for $LiNiO_2$ respectively. SEM micrographs indicated that the grain shape of the samples was block shape with clear grain boundary. The energy band gaps E_g were estimated by using the $(\alpha h\upsilon)^2$ vs. $h\upsilon$ graphs and obtained as 2.69 eV for $LiCoO_2$ and 0.52 eV for $LiNiO_2$. The samples exhibited as the superionic conductors and their activation energies were obtained as 0.4363 eV for $LiCoO_2$ and 0.4370 eV for $LiNiO_2$.

Keywords**:** SOFC, $LiCoO_2$, $LiNiO_2$, XRD, SEM, UV-VIS-NIR, electrical conductivity

Introduction

Solid Oxide Fuel Cell (SOFC) is an electrochemical device that converts the energy of a chemical reaction directly into electrical energy. In materials science, fast ion conductors are solids in which ions are highly mobile [Azurdia, (2006)]. These materials are important in the area of solid-state ionic, and are also known as solid electrolytes and superionic conductors. They are mainly useful in batteries and various sensors. Fast ion conductors

---

[1] Dr, Lecturer, Department of Physics, University of Yangon

[2] PhD Candidate, Assistant Lecturer, Department of Physics, Pathein University

[3] PhD Candidate, Assistant Lecturer, Department of Physics, University of Yangon

[4] Dr, Associate Professor, Department of Physics, Pyay University

are used primarily in solid oxide fuel cells. As solid electrolytes they allow the movement of ions without the need for a liquid or soft membrane separating the electrodes [Arico, (2005)].

Lithium transition-metal oxides are functional intercalation compounds for their applications in rechargeable lithium-ion batteries. They have been widely studied in search of structural stability and improved electrochemical performance. $LiCoO_2$-based lithium-ion batteries are highly successful commercial products used for powering consumer devices such as laptop computers, video cameras, and cellular phones [Julin, (2003)]. This work deals with the preparation of $LiCoO_2$ and $LiNiO_2$ using solid-state reaction method and their structural, microstructural, optical and electrical characteristics were studied by XRD, SEM, UV-VIS-NIR and temperature dependent electrical resistance measurements.

Experimental Details

Preparation of the Samples

Lithium Cobalt Oxide ($LiCoO_2$) and Lithium Nickel Oxide ($LiNiO_2$) were prepared by solid state reaction method. The starting materials of Analytical Reagent (AR) grade Lithium Carbonate (Li_2CO_3), Cobalt Oxide (CoO) and Nickel Oxide (NiO) were weighed with molar ratio. The weighed powders were mixed and ground by an agate mortar for 3 h to be homogeneous and to obtain fine powder. The fine powder was annealed at 450°C for 8 h and followed by 800°C for 15 h to be crystalline phase. Flow diagram of the sample preparation procedure of $LiCoO_2$ and $LiNiO_2$ is shown in Figure 1. Photographs showing the sample preparation processes are shown in Figures 2(a – i).

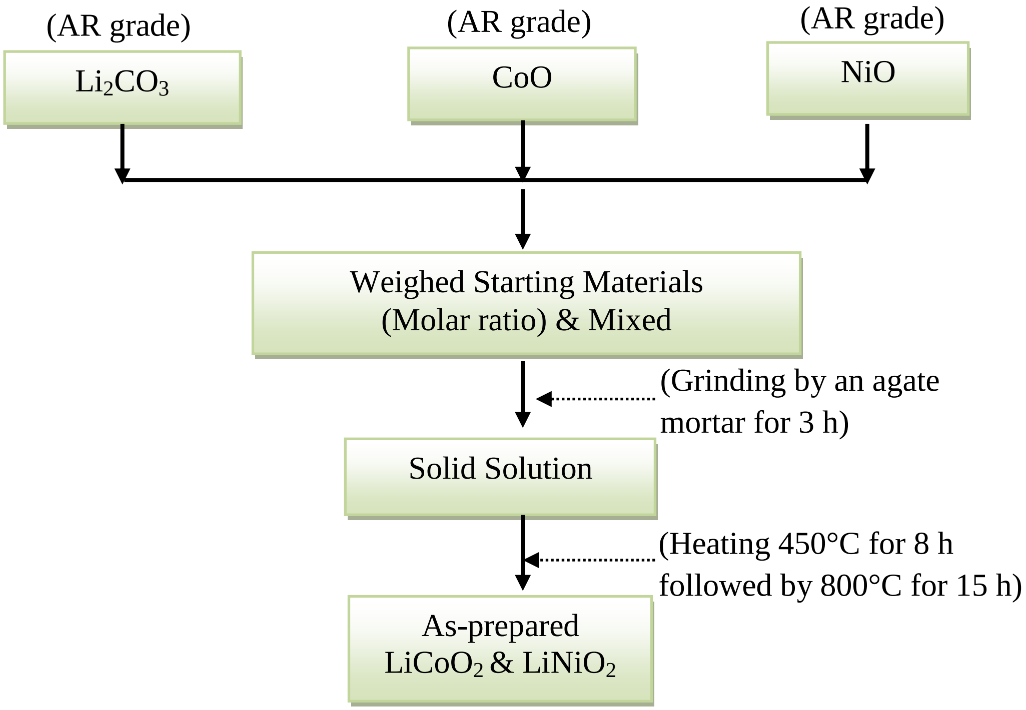

Figure 1: Flow diagram of the sample preparation procedure of $LiCoO_2$ and $LiNiO_2$ samples

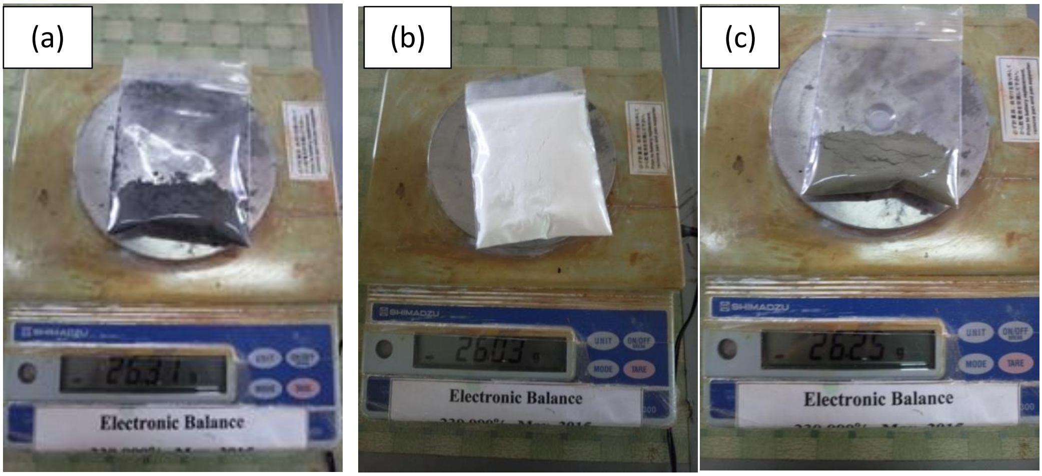

Figure 2: Photographs of the weighing of (a) CoO, (b) Li_2CO_3 and (c) NiO starting materials

Figure 2:(d) Photograph of the weighed Li_2CO_3, CoO and NiO

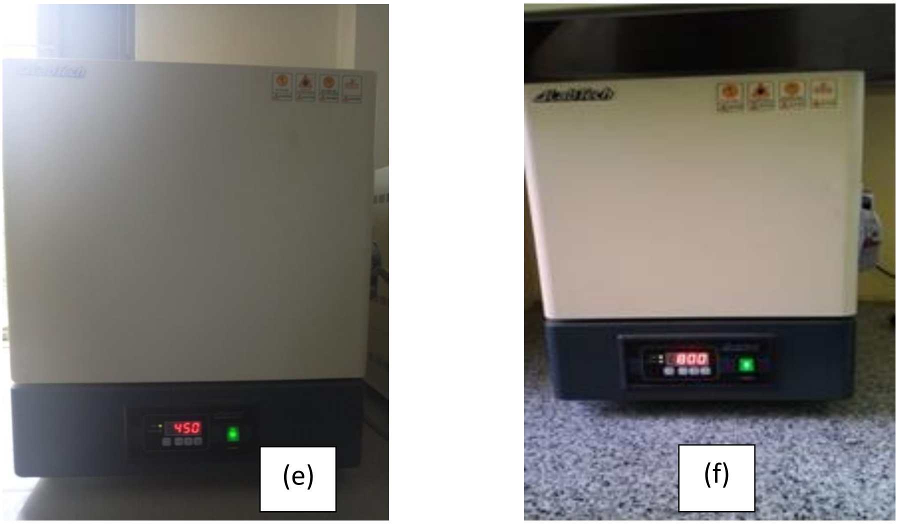

Figure 2: Photographs of the JLabTech electric oven (e) at 450°C and (f) at 800°C

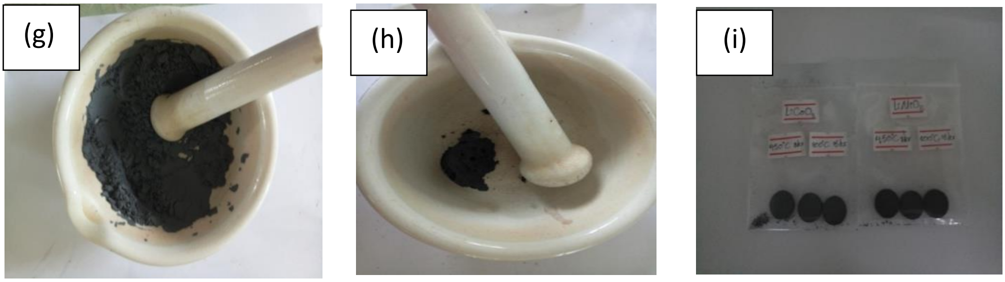

Figure 2: Photographs of the (g) grinding of $LiCoO_2$, (h) $LiNiO_2$ and (i) pellets of $LiCoO_2$ and $LiNiO_2$

XRD, SEM and UV-VIS-NIR Measurements

Powder XRD patterns of the samples were observed by Rigaku MiniFlex 600 X-Ray Diffractometer [Department of Physics, University of Yangon]. Microstructural properties of the powder samples were investigated by using JCM-6000Plus Scanning Electron Microscope (SEM) [Department of Physics, West Yangon University] with the accelerating voltage of 15 kV and 7000 times of photo magnification. UV-VIS-NIR (Ultraviolet-Visible-Near Infrared) transmission spectra were collected on PC-controlled SHIMADZU (UV-1800) UV-VIS-NIR Spectrophotometer in the wavelength range of 200 nm – 900 nm.

Temperature Dependent Electrical Resistance Measurement

The $LiCoO_2$ and $LiNiO_2$ samples were made into pellets by SPECAC hydraulic pellet-maker using 5 ton (~70 MPa). Thicknesses and area of the samples were 2.50 mm and 1.14×10^{-4} m^2. The electrical resistances were observed by using FLUKE 180 digital multi-meter in the temperature range of 303 K – 673 K. DELTA A SERIES DTA-4896 and K-type thermocouple were used as the temperature controller and temperature sensor. Photograph of the experimental setup of temperature dependent electrical resistance measurement is shown in Figure 3.

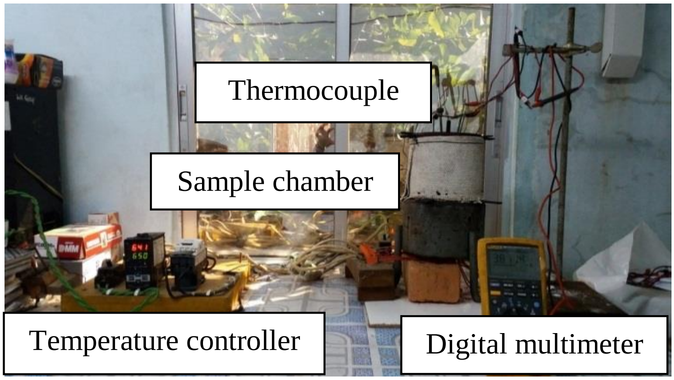

Figure 3: Photograph of the experimental setup of temperature dependent electrical resistance measurement

Results and Discussion

XRD Study

XRD patterns of the sample are shown in Figures 4(a) and (b). The observed XRD lines were identified by using standard JCPDS data library files of

(i) Lithium Cobalt Oxide, $LiCoO_2$, 00-062-0420 for Lithium Cobalt Oxide ($LiCoO_2$) sample and

(ii) Lithium Nickel Oxide, $LiNiO_2$, 00-062-0468 for Lithium Nickel Oxide ($LiNiO_2$) sample.

XRD patterns show the formation of single phase hexagonal structure with dominant peak corresponding to (003) reflection in $LiCoO_2$ sample and (104) reflection in $LiNiO_2$ sample indicating that the crystallites are preferentially oriented along these planes. The observed lattice parameters of the samples are tabulated in Table 1. Tao, H. et. al. (2010) has reported that the lattice parameters of the $LiCo_{0.25}Ni_{0.75}O_2$ sample are $a = b = 2.90$ Å and $c = 14.29$ Å respectively. The obtained lattice parameters in the present study are acceptable compared with the results of Tao, H. et. al. (2011). The crystallite sizes of the samples were estimated by using the Scherrer formula, $D = \frac{0.9\lambda}{B\cos\theta}$, where D is the crystallite size (nm), λ is the wavelength of incident X-ray (Å), θ is the diffraction angle of the peak under consideration at FWHM (°) and B is the observed FWHM (radians). The obtained crystallite sizes of samples are 77.14 nm for $LiCoO_2$ and 21.40 nm for $LiNiO_2$ respectively.

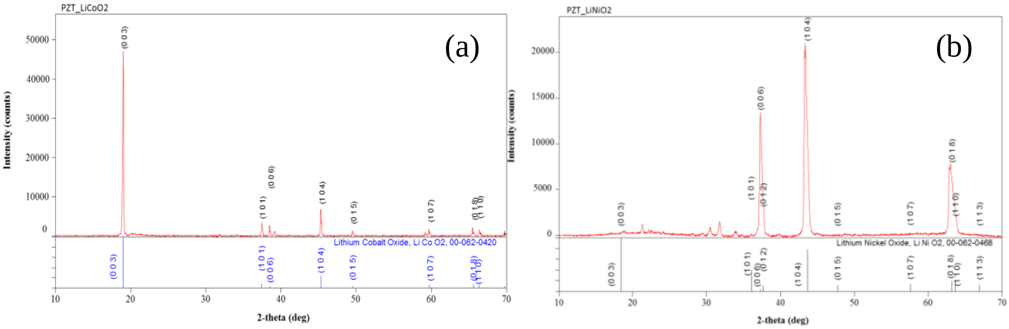

Figure 4: XRD patterns of (a) $LiCoO_2$ and (b) $LiNiO_2$

Microstructural Analysis

Grain size and pore structure have a major effect on the properties in polycrystalline materials. SEM micrographs of $LiCoO_2$ and $LiNiO_2$ are shown in Figures 5(a) and (b). The image reveals that the grain shape of the samples was block shapes with clear grain boundary.

Table 1: The lattice parameters and crystallite sizes of the $LiCoO_2$ and $LiNiO_2$ samples

Sample	Obs. *a*=*b*, *c*(Å)	*D* (nm)
$LiCoO_2$	$a=b$ = 2.8137 c = 13.9911	77.14
$LiNiO_2$	$a=b$ = 2.9186 c = 14.4427	21.40

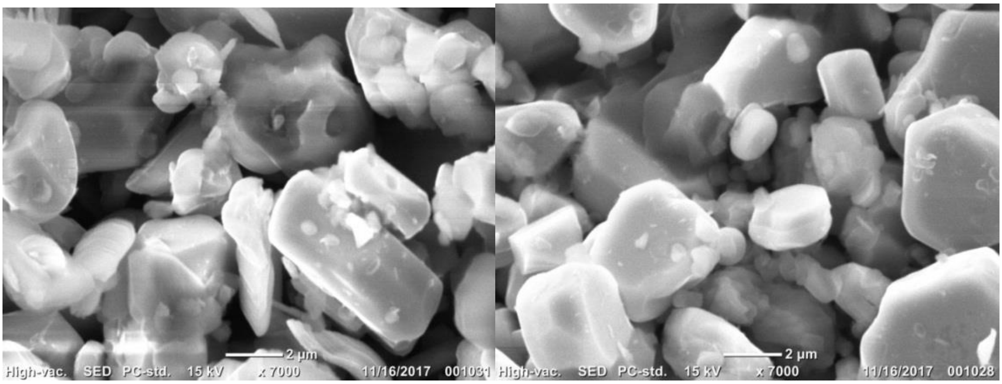

(a) (b)

Figure 5: SEM micrograph of (a) $LiCoO_2$ and (b) $LiNIO_2$

The grain sizes of the samples are obtained as in the ranges of 0.80 – 5.80 µm for $LiCoO_2$ and 0.50 – 4.20 µm for $LiNiO_2$. Some pores appeared in the observed micrographs due to the decomposition of the starting materials. These pores are important role for the movements of ionic materials and it follows the increase in ionic conductivity.

UV-VIS-NIR Spectroscopic Analysis

The effects of Co and Ni on the $LiCoO_2$ and $LiNiO_2$ samples on the optical transmission and energy band gaps were examined by UV-VIS-NIR (Ultraviolet-Visible-Near Infrared) transmission spectra. Photons, depending on their energy, interact with matter in a variety of ways. In the present work, only the effect of UV-VIS-NIR (190 nm –1100 nm) corresponding to the energy (wavelength) region was studied. UV-VIS-NIR transmission and absorption spectra of the samples are shown in Figures 6(a) and (b) for $LiCoO_2$ and Figures 7(a) and (b) for $LiNiO_2$ respectively. The intense absorption bands were found in the wavelength ranges of about 250 nm – 1100 nm for $LiCoO_2$ and 234 nm –1100 nm for $LiNiO_2$. It was generally found that the transmission regions of the VIS and NIR light were slightly decreased with the wavelength.

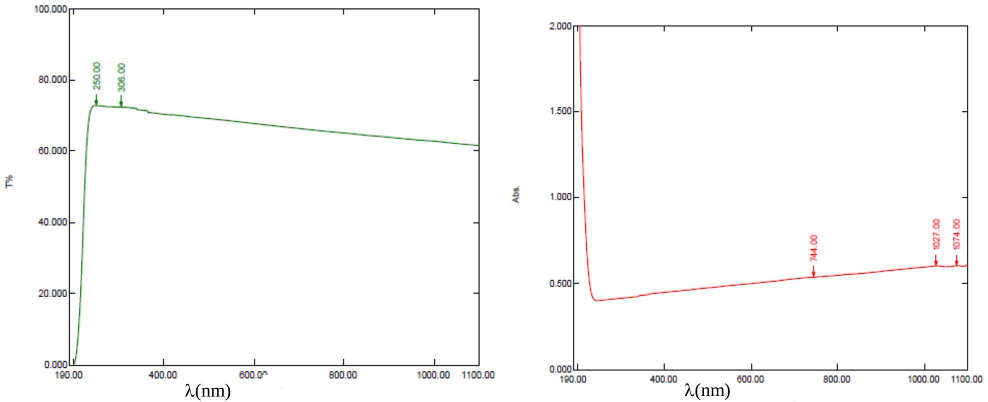

(a) (b)

Figure 6: UV-VIS-NIR (a) transmission and (b) absorption spectra of $LiCoO_2$

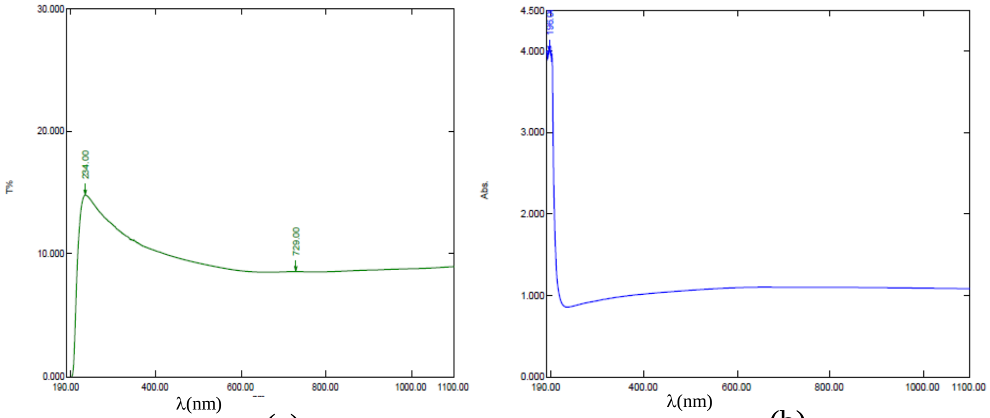

(a) (b)

Figure 7: UV-VIS-NIR (a) transmission and (b) absorption spectra of $LiNiO_2$

It can be deduced that the transmission of UV-VIS-NIR light of Co and Ni effects on the optical transparent in UV than the VIS and NIR regions. The energy band gaps E_g of the samples were determined by using optical percentage transmission with the corresponding wavelength data. To determine the energy band gap, the graph of $(\alpha h\upsilon)^2$ vs. $h\upsilon$ was plotted. The intercept of the horizontal line at $\alpha = 0$ gives the value of energy band gap.

The plots of $(\alpha h\upsilon)^2$ vs. $h\upsilon$ of the samples are shown in Figures 8(a) and (b). The energy band gaps are obtained as 2.69 eV for $LiCoO_2$ and 0.52 eV for $LiNiO_2$ respectively. Liu., et. al. (2015) has reported the energy band gap value of $LiCoO_2$ is 2.70 eV. Also, Chan., et. al. (2011) has reported that the energy band gap value of $LiNiO_2$ is 0.50 eV. It was found that the obtained energy band gaps are found to be agreed with the results of Liu., et. al. (2015) and Chan., et. al. (2011).

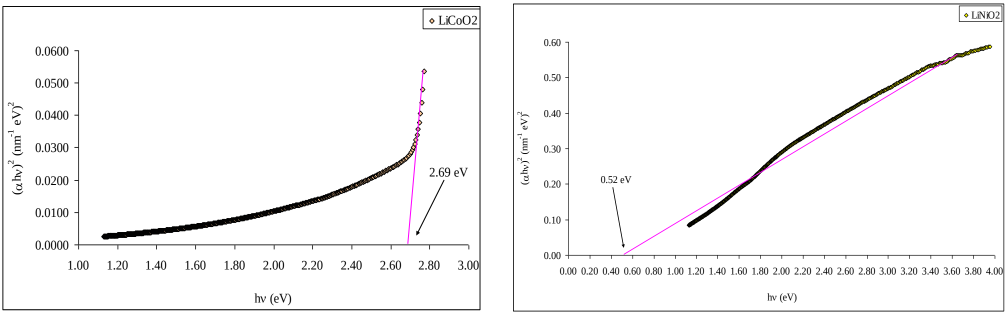

(a) (b)

Figure 8: Plots of the $(\alpha h\upsilon)^2$ vs. $h\upsilon$ graphs of (a) $LiCoO_2$ and (b) $LiNiO_2$

Temperature Dependent Electrical Conductivity Study

Electrical conductivity of the solid oxide materials obeys Arrhenius's expression, $\sigma = \sigma_0 \exp(\frac{-E_a}{kT})$ where, σ_0 is the pre-exponential factor, E_a is activation energy (eV), k is Boltzmann's constant and T is absolute temperature (K). Arrhenius's plots of the samples are shown in Figures 9(a) and (b) respectively. The graph shows that the increase in temperature leads to increase in conductivity, which is the normal behaviour of superionic materials and it obeys the well known Arrhenius relation. The higher values of temperature for the samples help the trapped charges to be librated and participate in the conduction process which results increase in conductivity. According to the conduction mechanism in ceramics, the decrease in resistivity could also be related to the increase in the drift mobility of the thermally activated electrons. The activation energies were evaluated by using the slopes of the ln σ vs 1000/T relationship. The obtained activation energies of the samples were obtained as 0.4363 eV for $LiCoO_2$ and 0.4370 eV for $LiNiO_2$.

From the experimental results, the samples exhibited as superionic conductors because their electrical conductivity were 1.04×10^{-3} S m^{-1} at 423 K (superionic phase temperature T_{SI}) for $LiCoO_2$ and 1.13×10^{-3} S m^{-1} at 403 K for $LiNiO_2$. Since the solid material has the electrical conductivity $\sigma \sim 1 \times 10^{-3}$ S m^{-1} called the superionic conductor. A few solids conduct electricity better by ion motion than by electron motion. These unusual materials are technologically important in making batteries. All batteries have two electrodes separated by an electrolyte, which is a material that conducts ions better than electrons.

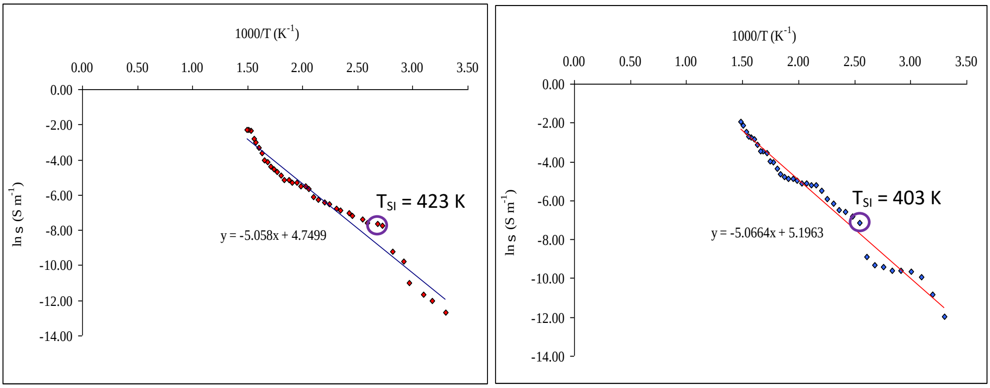

(a) (b)

Figure 9: Arrhenius plots of the temperature dependent electrical conductivity of (a) $LiCoO_2$ and (b) $LiNiO_2$

Conclusion

Solid oxide materials of $LiCoO_2$ and $LiNiO_2$ were successfully prepared by solid state reaction method and their structural, microstructural, optical and electrical conductivity were studied in this work. XRD patterns reveal that the investigated samples analogous to hexagonal structure. The crystallite sizes of the samples were obtained as 77.14 nm for $LiCoO_2$and 21.40 nm for $LiNiO_2$ respectively. From the SEM micrographs, the image reveals that the grain shape of the samples was block shape with clear grain boundary. Some pores appeared in the observed micrographs due to the de-carbonation of the starting materials. From the observed UV-VIS-NIR transmission spectra, the samples demonstrated that less than 100% transmittance of throughout the UV-VIS-NIR region. The energy band gaps E_g were obtained as 2.69 eV for $LiCoO_2$ and 0.52 eV for $LiNiO_2$. The obtained energy band gap values indicated that the samples were semiconducting materials. Temperature dependent electrical resistance measurements showed that the samples exhibited as the superionic conductors. The activation energies were obtained as 0.4363 eV for $LiCoO_2$ and 0.4370 eV for $LiNiO_2$. According to experimental results, the samples can be applied as the solid oxide fuel cell materials because they are semiconducting materials and/or superionic conductors with the activation energies lower than 1 eV.

Acknowledgements

The authors would like to acknowledge Professor Dr Khin Khin Win, Head of Department of Physics, University of Yangon, for her valuable suggestion and comments for this work.

References

Arico, A. S., Bruce, P., Scrosati, B., Tarascon, J. M. & Shalkwijk, W. (2005). Nanostructured materials for advanced energy conversion and storage devices. *Nature*, 4, 366 – 377.

Azurdia, J., Marchal, J. & Laine, R. M. (2006). Synthesis and Characterization of Mixed-Metal Oxide Nanopowders along the CoO_x-Al_2O_3 Tie Lie Using Liquid Feed Flame Spray-Pyrolysis. *Journal of American Ceramic Society*, 89(9), 2749 – 2756.

Chen, H., Freeman, C. L. & Harding, J. H. (2011). Charge disproportion ation in $LiNiO_2$? – A Density Functional Theory Study, *Physical Review B*. 84(8), 16 – 28.

Julin, C. (2003). Local structure and electrochemistry of lithium cobalt oxides and their doped compounds. *Solid State Ionic*, 157, 57 – 71.

Liu, H. L., Ou-Yang, T. Y., Tsai, H. H., Lin, P. A., Jeng, H. T., Shu, G. J. & Chou, F. C. (2015). Electronic structure and lattice dynamics of Li_xCoO_2 single crystals. *New Journal of Physics*, 17(10),1 – 8.

Tao, H., Feng, Z., Liu, H., Kan, X. & Chen, P. (2011). Reality and Future of Rechargeable Lithium Batteries. *The Open Materials Science Journal*, 5(2), 204 – 214.

J. Myanmar Acad. Arts Sci. 2019 **Vol. XVII. No.2A**

STRUCTURAL ANALYSIS, MICROSTRUCTURAL INVESTIGATION AND ENERGY BAND GAP DETERMINATION OF ZINC OXIDE AND MAGNESIUM TITANATE MIXED COMPOSITE

July Oo[1], Myo Nyunt[1], Aye Aye Lwin[2], Cho Cho Aung[3] & Win Kyaw[4]

Abstract

Mixed composite materials of Zinc Oxide and Magnesium Titanate ($ZnO:MgTiO_3$) with the compositions of (20%:80%, 40%:60%, 60%:40% and 80%:20%) were prepared by using solid state reaction method. The samples were characterized by powder X-Ray Diffraction (XRD), Scanning Electron Microscopy (SEM) and Ultra-Violet-Visible-Near Infrared (UV-VIS-NIR) spectroscopy to analyze the structural, microstructural and optical properties of the samples. The crystalline phase formation and the structural properties were analyzed from the observed XRD patterns. Microstructural properties of grain shape and sizes were investigated by SEM. The energy band gaps E_g were determined from the Tauc plot of $(\alpha h\upsilon)^2$ vs. $h\upsilon$ graphs. It was found that the energy band gap decreased with increase in ZnO composition.

Keywords: Mixed composite, $ZnO:MgTiO_3$, XRD, SEM, UV-VIS-NIR, energy band gaps

Introduction

In recent years, TiO_2 has been well known as a semiconductor with photocatalytic activities and has a great potential for applications such as environmental purification. TiO_2 is mainly applied as pigments, adsorbents, catalyst supports, filters, coatings, photoconductors, and dielectric materials. The performance of the material (TiO_2) affected by the size of the particles. Thus particle size plays a great role [Ruhela, (2013)]. Zinc oxide (ZnO) has a relatively large energy band gap (~ 3.3 eV) at room temperature. The band gap of zinc oxide may be increased to nearly 3 – 4 eV by alloying it with

---

[1] Dr, Department of Physics, University of Yangon

[2] Dr, Lecturer, Department of Physics, Bago University

[3] Dr, Associate Professor, Department of Physics, University of Yangon

[4] Dr, Associate Professor, Department of Physics, Pyay University

magnesium oxide. Zinc oxide is commonly used in laser diodes and light emitting diodes (LED). Some optoelectronic applications of ZnO overlap with that of GaN, which has a similar band gap (~ 3.4 eV at room temperature). Now different compositions of materials ($MgTiO_3$ with ZnO) are analyzed by X-ray diffraction (XRD) and comparative study will be observed with the obtained XRD pattern [Azurdia, (2006); Ferri, (2009)]. Magnesium titanate ($MgTiO_3$) has potential applications such as high frequency capacitors, chip capacitors, and temperature compensating capacitors, resonators, filters, antennas for communication, radar and direct broadcasting satellite [Tao, (2011); Wang, (2010)]. In this work, mixed composite materials of ZnO:$MgTiO_3$ were prepared by solid state reaction method and their structural, microstructural and optical properties were reported by XRD, SEM and UV-VIS-NIR spectroscopic measurements.

Materials and Method

Sample Preparation

Mixed composite materials of zinc oxide and magnesium titanate (ZnO:$MgTiO_3$) with the compositions of 20%:80%, 40%:60%, 60%:40% and 80%:20% were prepared from the starting materials of Zinc Oxide (ZnO), Magnesium Oxide (MgO) and Titanium Dioxide (TiO_2). Starting materials of Analytical Reagent (AR) grade those oxide materials were weighed with desired compositions and the weighed powders were mixed each other. The mixed materials were heated at 800°C for 5 h in JLabTech electric oven. The heated composite samples were ground by an agate mortar for 1 h to obtain fine powder. Flow diagram of the sample preparation procedure is shown in Figure 1. Photographs of the sample preparation processes are shown in Figures 2(a – d) respectively.

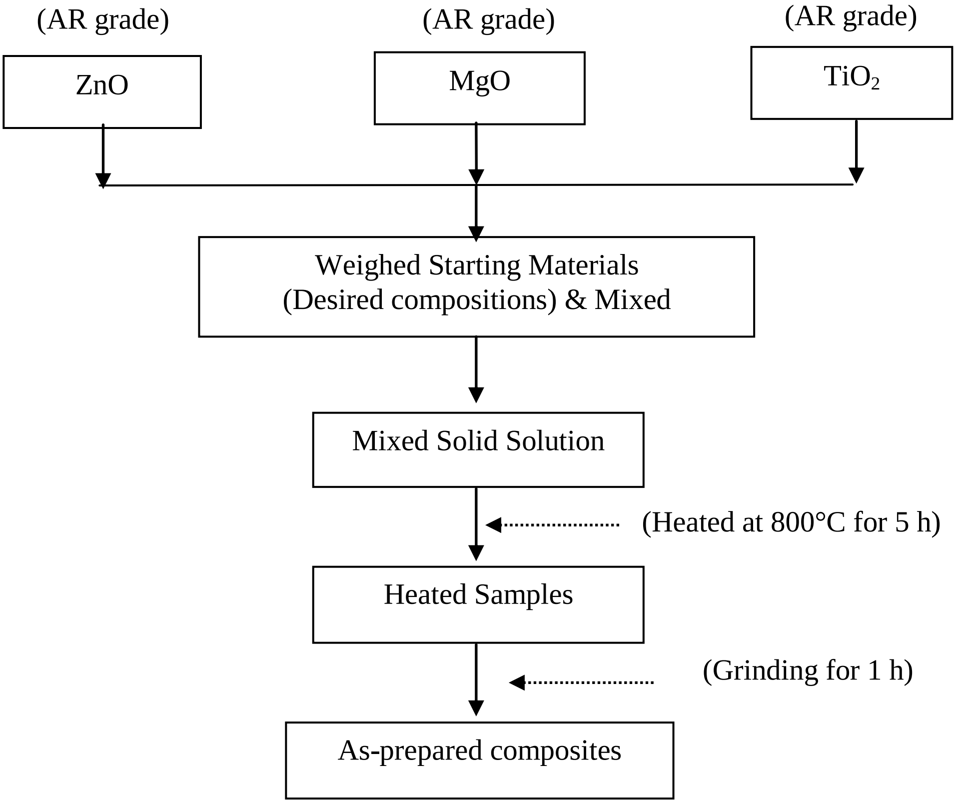

Figure 1: Flow diagram of the sample preparation procedure

Figure 2: Photographs of the weighed starting materials of (AR) grade (a) ZnO, (b) TiO_2 and (c) MgO powders for the preparation of 80%:20%, 60%:40%, 40%:60% and 20%:80% ZnO:$MgTiO_3$ composite materials

Figure 2: (d) Photograph of the as-prepared (80%:20%, 60%:40%, 40%:60% and 20%:80%) ZnO:$MgTiO_3$ composite materials

XRD, SEM and UV-VIS-NIR Measurements

The XRD spectra of the ZnO:$MgTiO_3$ were observed by Rigaku MiniFlex 600 X-Ray Diffractometer [Department of Physics, University of Yangon] using the CuK_α radiation with wavelength of 1.54056 Å. The microstructural properties were investigated by using JEOL JCM-6000Plus Scanning Electron Microscope (SEM) [Department of Physics, West Yangon University] with the accelerating voltage of 15 kV and 7000 times of photo magnification. UV-VIS-NIR (Ultraviolet-Visible-Near Infrared) transmission spectra were collected on PC-controlled SHIMADZU UV-1800 Spectrophotometer [AMTT, Co. Ltd., Yangon] in the wavelength range of 190 nm – 1100 nm.

Results and Discussion

XRD Analysis

Powder X-ray diffraction patterns of the samples are shown in Figure 3(a – d). To assign the observed XRD lines, the lines were identified by using the Joint Committee on Powder Diffraction Standards (JCPDS) data library files of (i) Cat. No. 01-079-0831> Magnesium Titanium Oxide – $MgTiO_3$ and (ii) Cat. No. 01-080-0074 Zinc Oxide – ZnO for the samples. Most of the observed XRD lines were assigned by the standard JCPDS data library files but some of the lines were not assigned due to the dual-phase of composite materials of ZnO:$MgTiO_3$.

XRD patterns show that the samples analogous to the hexagonal structure. The lattice parameters of the samples are evaluated by the equation: $\frac{1}{d^2}=\frac{4}{3}\left(\frac{h^2+hk+k^2}{a^2}\right)+\frac{l^2}{c^2}$, where *d* is the interplanar spacing (Å), *a* and *c* are the lattice parameters (Å) of the unit cell, (*hkl*) are the Miller indices. The obtained lattice parameters of the samples are tabulated in Table 1. The diffraction lines appear in the diffraction angle range of about 23° – 32° are not assigned with the JCPDS data library files because these lines may be attributed to the heat treatment effect of the ZnO and $MgTiO_3$ samples. They are new compound formation from the ZnO and $MgTiO_3$ samples due to thermal agitation.

The Scherrer formula for the calculation of crystallite size (grain diameter), D, of the sample is $D = k\lambda/\beta \cos\theta$, where, D is the crystallite size (nm) , k is a constant varies with crystallite shape but usually nearly equal to 0.94, λ is the wavelength of source radiation (Å)and β is full-width at half maximum (FWHM) of the peak (radian) and θ is Bragg's angle (Å). The crystallite sizes are listed in Table 1.

SEM Analysis

Microstructural properties of the solid samples can be analyzed by using Scanning Electron Microscope. SEM micrographs of the samples are shown in Figures 4(a – d). As shown in micrographs, the image reveals that the grain shape of the samples was spherical with the poor boundary. Some of the grains are agglomerated particles. The obtained grain sizes of the samples are tabulated in Table 2.

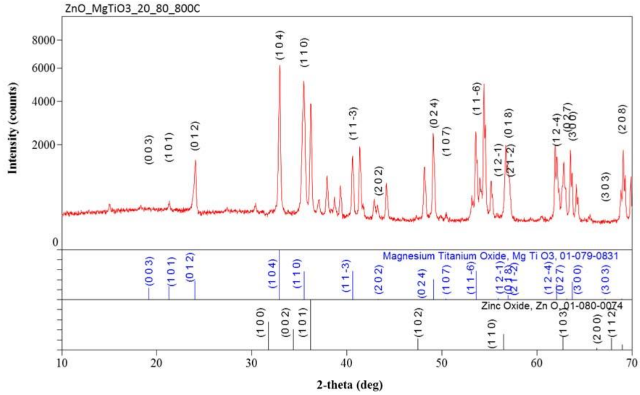

(a)

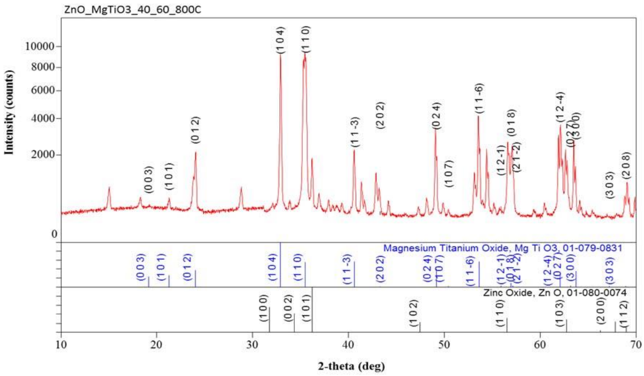

(b)

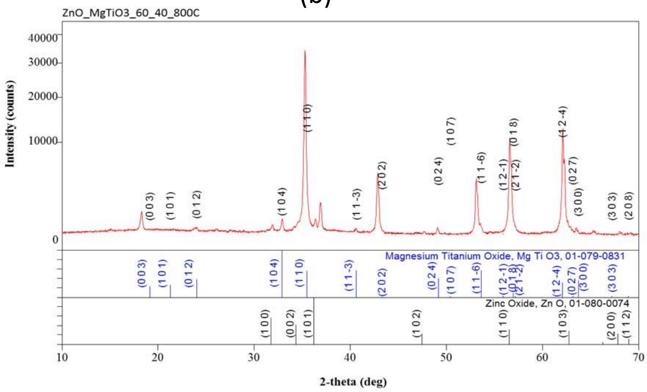

(c)

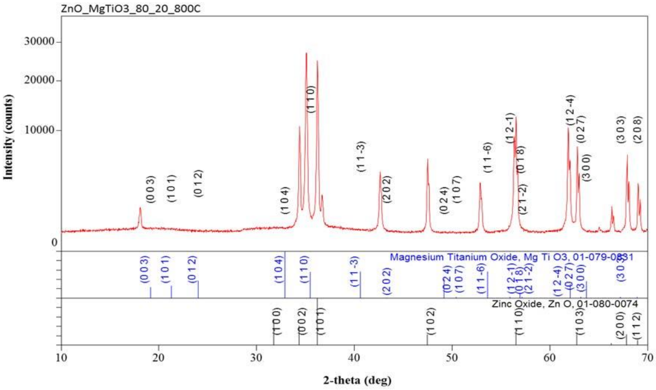

(d)

Figure 3: XRD patterns of the mixed composite materials of ZnO:$MgTiO_3$ with the compositions of (a) (20%:80%), (b) (40%:60%), (c) (60%:40%) and (d) (80%:20%)

Table 1: The lattice parameters and crystallite sizes of the samples

Sample (ZnO:$MgTiO_3$)	***a* = *b* (Å)**	***c* (Å)**	***D* (nm)**
(20%:80%)	3.2503	5.2158	20.71
(40%:60%)	3.2211	5.1617	72.51
(60%:40%)	3.2463	5.1491	48.27
(80%:20%)	3.2504	5.2069	59.59

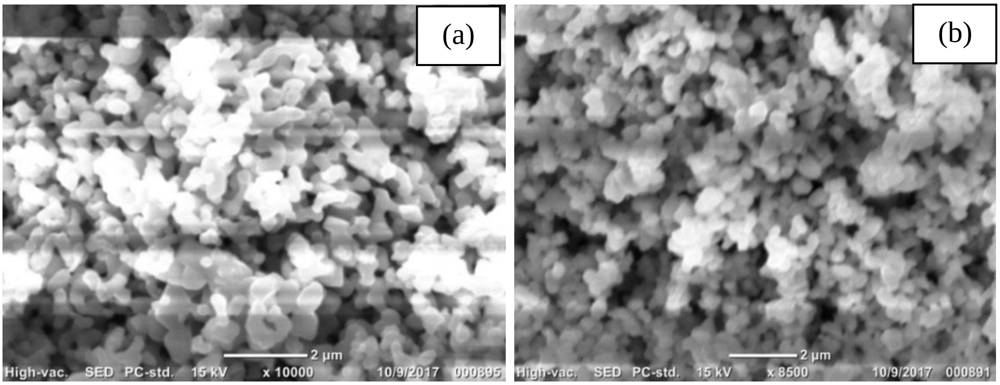

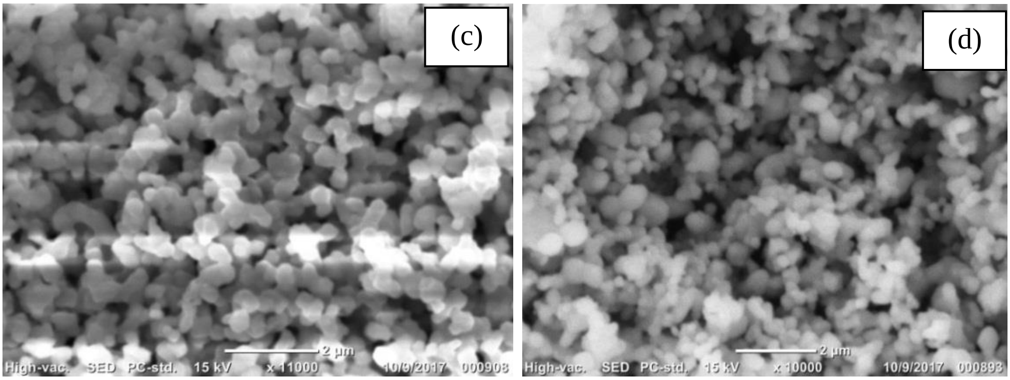

Figure 4: SEM micrographs of the mixed composite materials of ZnO:$MgTiO_3$ with the compositions of (a) (20%:80%), (b) (40%:60%), (c) (60%:40%) and (d) (80%:20%)

Table 2: The grain sizes of ZnO:$MgTiO_3$ mixed composites

Sample (ZnO:$MgTiO_3$)	**Grain size (μm)**
(20%:80%)	0.18 – 0.50
(40%:60%)	0.20 – 0.50
(60%:40%)	0.22 – 0.45
(80%:20%)	0.18 – 0.72

UV-VIS-NIR Study

The collected UV-VIS-NIR transmission spectra of "T%" vs. "λ" of the ZnO:$MgTiO_3$ with the compositions of 20%:80%, 40%:60%, 60%:40% and 80%:20% samples are shown in Figures 5(a – d). As depicted in figures, the samples demonstrate that less than 100% transmittance of throughout the Ultraviolet-Visible-Near Infrared region.

The energy band gaps E_g of all the samples have been examined with the help of optical absorption and percentage transmission data using the graph of $(\alpha h\nu)^2$ versus hν. The theory of optical transmission gives the relationship between the absorption coefficient "α" and the photon energy "hν' has a relation; $\alpha = - \ln(1/T)$. From the optical transmission spectrum, the measured transmittance "T" was used to calculate the absorption coefficient "α". To estimate the energy band gap for all the samples, the graph of $(\alpha h\nu)^2$ versus hν has been plotted. The interception of the line at $\alpha = 0$ in $(\alpha h\nu)^2$ versus hν graph gives the value of energy band gap of the material.

The plots of $(\alpha h\nu)^2$ versus hν of the samples are shown in Figures 6 (a –e). The obtained energy band gaps are listed in Table 3. The variation in band gap may be attributed to the variation of structural parameter (lattice constants) with ZnO semiconducting materials effects on $MgTiO_3$. Ferri, et. al. (2009) was reported that the E_g of $MgTiO_3$ prepared at 700°C was 4.05 eV. In this work the obtained E_g decreased with the increase in concentration of ZnO.

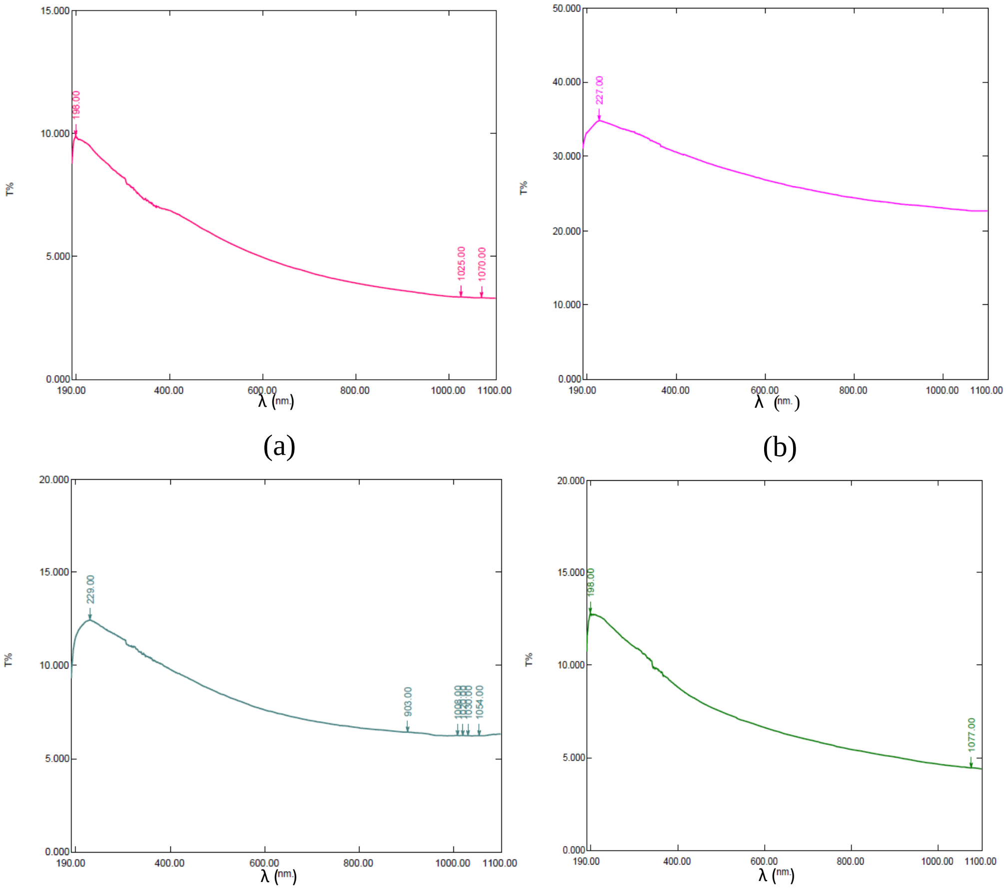

(a) (b)

(c) (d)

Figure 5: UV-VIS-NIR transmission spectra of $ZnO:MgTiO_3$ with the compositions of (a) (20%:80%), (b) (40%:60%), (c) (60%:40%) and (d) (80%:20%)

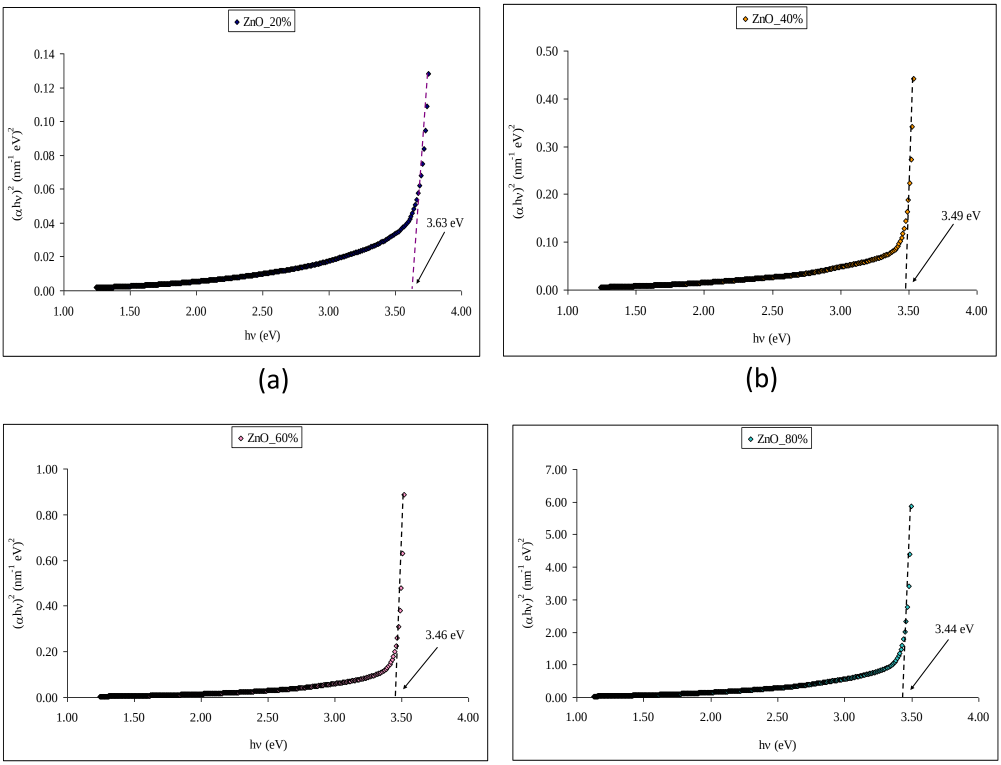

(a) (b)

(c) (d)

Figure 6: Plots of $(\alpha h\nu)^2$ vs. hν of the ZnO:$MgTiO_3$ samples with the compositions of (a) (20%:80%), (b) (40%:60%), (c) (60%:40%) and (d) (80%:20%)

Table 3: The energy band gaps of ZnO:$MgTiO_3$ mixed composites

Sample (ZnO:$MgTiO_3$)	**E_g (eV)**
(20%:80%)	3.63
(40%:60%)	3.49
(60%:40%)	3.46
(80%:20%)	3.44

Conclusion

Zinc oxide and magnesium titanate (ZnO:$MgTiO_3$) mixed composite materials were prepared by solid state reaction method. XRD patterns show that the samples analogous to the hexagonal structure. SEM micrographs showed that the grain shape of the samples was spherical with the poor boundary. Some of the grains were agglomerated particles. The samples demonstrate that less than 100% transmittance of throughout the Ultraviolet-Visible-Near Infrared region. The energy band gaps E_g decreased with the increase in concentration of ZnO from 20% to 80%.

Acknowledgement

The authors would like to acknowledge Professor Dr Khin Khin Win, Head Department of Physics, University of Yangon, for her valuable discussions and comments on this work.

References

Azurdia, J., Marchal, J. and Laine, R. M. (2006). Synthesis and Characterization of Mixed-Metal Oxide Nanopowders along the CoO_x-Al_2O_3 Tie Lie Using Liquid Feed Flame Spray-Pyrolysis, *Journal of American Ceramic Society*, 89(9), pp. 2749 – 2756.

Ferri, E. V. A. (2009). Photoluminescence behavior in $MgTiO_3$ powders with vacancy/distorted clusters and octahedral tilting, *Materials Chemistry and Physics*, 117, pp. 192 – 198.

Ruhela, S. and Srivastava, S. K. (2013). Study of XRD Patterns of Mixed Composite of $MgTiO_3$ and ZnO, *International Journal of Innovative Research in Science, Engineering and Technology*, 2(5), pp. 1320 – 1322.

Tao, H., Feng, Z., Liu, H., Kan, X. and Chen, P. (2011). "Reality and Future of Rechargeable Lithium Batteries", *The Open Materials Science Journal*, 5(2), pp. 204 – 214.

Wang, G., Liu, H., Liu, J., Qiao, S., Lu, G. M., Munroe, P. and Ahn, H. (2010). Mesoporous $LiFePO_4$/C Nanocomposite Cathode Materials for High Power Lithium Ion Batteries with Superior Performance, *Advanced Materials*, 22, pp. 4944 – 4948.

J. Myanmar Acad. Arts Sci. 2019 **Vol. XVII. No.2A**

STRUCTURAL, MICROSTRUCTURAL AND OPTICAL CHARACTERIZATION OF DEPOSITED CUPROUS OXIDE (Cu_2O) THIN FILM

Amy Aung[1], Hnin Yu Wai[2], Khin Lay Thwe[3], Soe Soe Han[4]

Abstract

Cuprous Oxide (Cu_2O) thin film has been grown onto indium tin oxide (ITO) coated glass substrate by spin coating technique using different additives, namely, polyethylene glycol and ethylene glycol. It was found that the organic additives added had a significant influence on the formation of Cu_2O films and lead to different microstructures and optical properties. The films were characterized by X-ray diffraction (XRD), Scanning Electron Microscopy (SEM) and Ultraviolet-Visible Spectroscopy (UV-Vis). The Cu_2O thin films were used as electron collection layer in the application of solar cells.

***Keywords*:** Cuprous Oxide, Thin Film, ITO, Spin Coating

Introduction

Copper oxide thin films are semiconductor which is used as an active layer in various types of solar cells and a passive layer in solar selective surfaces. Copper forms two well-known oxides; Cu_2O and CuO. Cuprous oxide is very attractive as a photovoltaic material because of its high absorption coefficient in visible regions, non-toxicity and low cost to produce. Cuprous oxide (Cu_2O) is an interesting p-type semiconductor with direct energy band gap of 1.5 eV - 2.2 eV. Cu_2O forms a cubic crystal structure with a lattice parameter of 4.27 Ǻ and this material is a promising material in solar energy applications.

Cu_2O thin films can be prepared by various methods like electrodeposition, vacuum evaporation, plasma evaporation, chemical vapor deposition, thermal oxidation, anodic oxidation, spray pyrolysis, r.f. magnetron sputtering, reactive evaporation, sol-gel method, chemical deposition methods and spin coating process. Among these, spin coating is

---

[1] Dr, Assistant Lecturer, Department of Physics, University of Yangon

[2] Assistant Lecturer, Department of Physics, University of Yangon

[3] Lecturer, Department of Physics, University of Yangon

[4] Lecturer, Department of Physics, University of Yangon

the simplest, low cost production and convenient technique to investigate the behavior of Cu_2O thin film under different additives.

Spin coating is one of the most common techniques for applying thin films to substrates. The use of spin coating in organic electronics and nanotechnology is widespread and has built upon many of the techniques used in other semiconductor industries. It also has some differences due to the relatively thin films and high uniformity required for effective device preparation, as well as the need for self-assembly and organization to occur during the casting process. Cu_2O thin film was deposited onto indium tin oxide (ITO) coated glass using spin coating technique with two different polymer additives such as polyethylene glycol and ethylene glycol because of it is a soft bottom-up approach to achieve a good control over film composition and microstructure.

Investigations had shown that additive polyethylene glycol; effectively improve the Cu_2O properties under relatively low temperature. To prepare Cu_2O thin film onto indium tin oxide (ITO) coated glass substrate for solar cell application by means of spin coating technique ad to investigate the behavior of Cu_2O thin films under different additives. The as-prepared films were annealed at 250˚ C in order to get single phase Cu_2O films.

The annealing temperature of 300˚ C is the optimum annealing temperature to prepare the single phase Cu_2O films. If annealing temperature is increased to 350˚ C, other phases exist such as Cu or CuO comes into existence. However, spin coating method became a favorite technique due to simple equipment involved and cheaper compared to other techniques.

Using the spin coating technique to form Cu_2O films on ITO substrates and conduct a detailed microstructures and optical investigation of Cu_2O films.

Materials and Method

Cu_2O thin films are characterized to investigate their microstructures and optical properties. The crystallinity and the phase composition of as-prepared films on indium tin oxide (ITO) substrates were examined with X-Ray diffractometer (XRD). The size of the particles and morphology of

Cu_2O films were studied by Scanning Electron Microscopy (SEM). Optical transmission and absorption spectra were measured for Cu_2O films grown on glass substrates using Shimadzu UV-Vis spectrophotometer (UV-1800).

Preparation of substrates

Indium tin oxide (ITO) coated glass was used as substrates. To prepare Cu_2O thin films by using spin coating technique on ITO glass slides with dimension (1cm x 1cm x 0.1cm) were used as the substrates. To get a high quality of thin film, the ITO glass substrates were soaked in acetone for a few minutes and rinsed in deionized water. The glass was taken out and dried in air at room temperature and baked the glasses about 15 minutes at 200°C to ensure good adhesion at the surface. Baking creates an ultra-thin layer of Cu_2O on the substrate surface, which proved to be an excellent solution to the problem of poor adherence for some of the materials.

Preparation of copper oxide solution

In this process, the starting materials used were copper (II) acetate, isopropyl alcohol and diethanolamine (DEA, $C_4H_{11}NO_2$) solution and mixed polyethylene glycol and ethylene glycol. 0.5 molar concentration of solution was formed by dissolving 0.5 gram copper acetate powder in 9 ml isopropyl alcohol and 0.5 ml diethanolamine which act as precursor, solvent and complexing agent respectively. There were three set of samples; (a) sample 1 (sample without any additive), (b) sample 2 (sample with polyethylene glycol), (c) sample 3 (sample with ethylene glycol). Small amount of polyethylene glycol and ethylene were added into the solution and the copper oxide solutions were continuously stirred for 24 hours using magnetic bar. The solutions were filtered using 10~15μm filter prior to spin coating process.

Preparation of copper oxide thin films deposition by spin coating method

Films were prepared by depositing the solution at room temperature by spin coating technique onto the substrates. The compound solutions were spread onto the substrates with spinning speed at 3000 rpm for 40 seconds. Immediately after coating process, the samples were dried for 5 minutes at

200°C for each layer to evaporate the solvent. The process was repeated to produce three layers of coating. After the drying of the last layer, samples were annealed for 1 hour at 300 °C. The flow diagram of sample preparation of Cu_2O thin films is shown in Figure 1. Figure 2 shows the photograph of sample preparation sequence for Cu_2O thin films using spin coating technique.

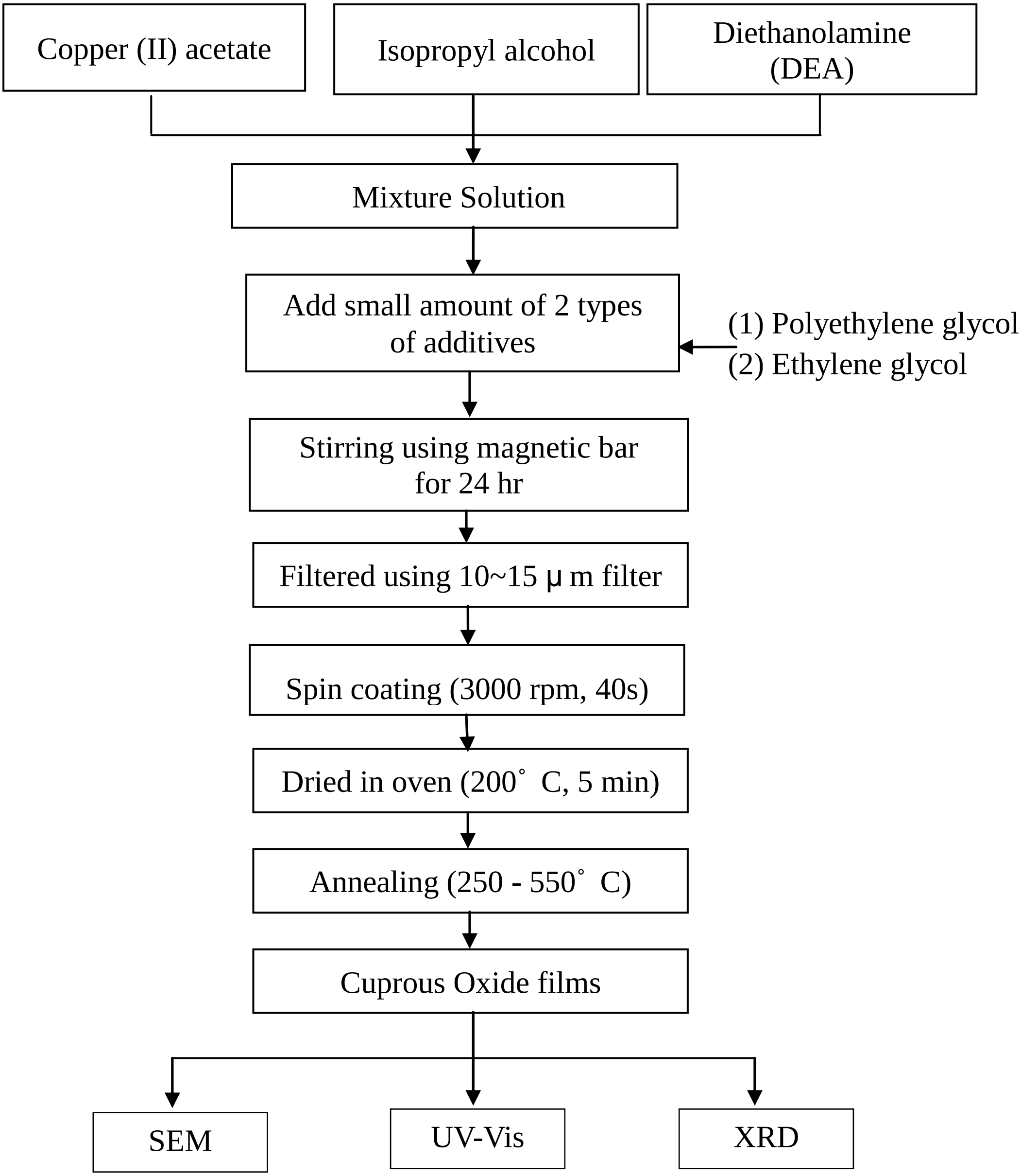

Figure 1: Flow diagram of sample preparation

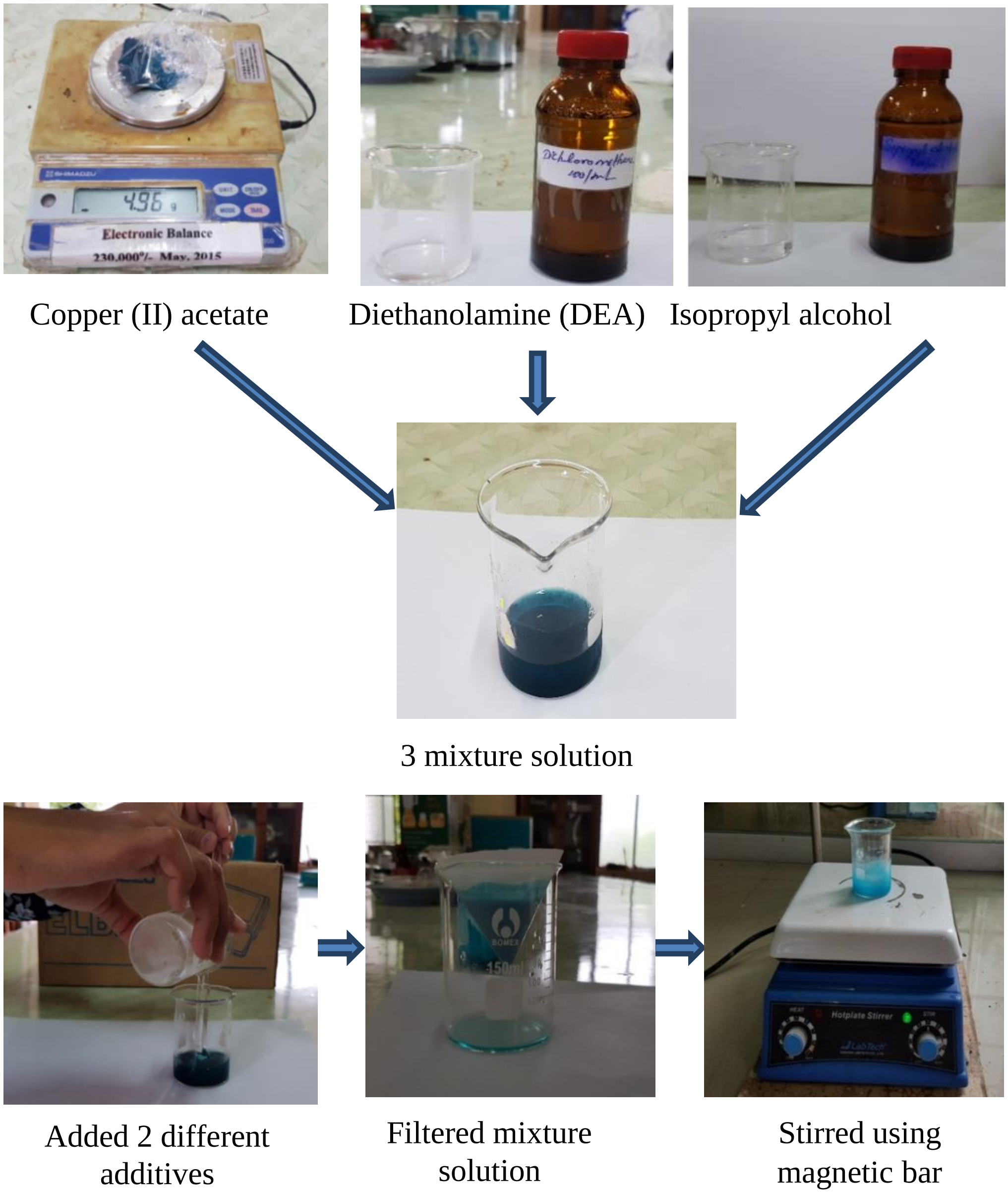
Copper (II) acetate
Diethanolamine (DEA)
Isopropyl alcohol
3 mixture solution
Added 2 different additives
Filtered mixture solution
Stirred using magnetic bar

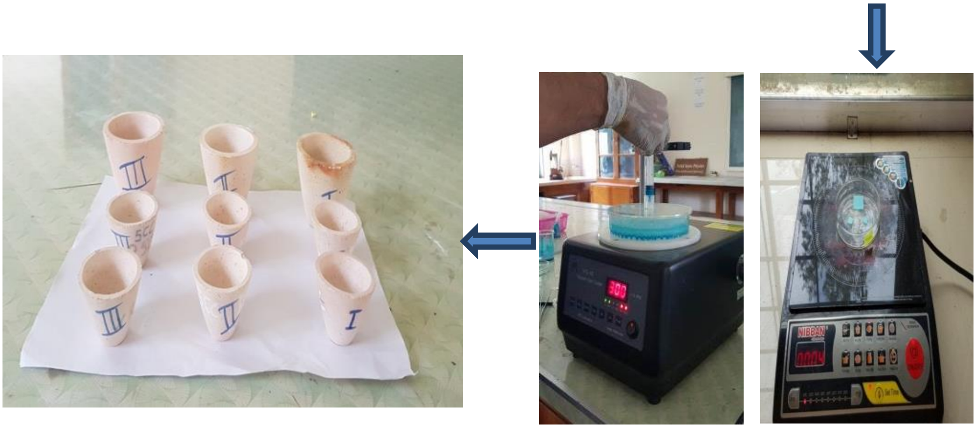

Annealed the samples Spin coating and heat treated

Figure 2: The photograph of sample preparation sequence for Cu_2O thin films using spin coating technique

Result and Discussion

XRD Analysis

The XRD patterns of obtained samples with different additives are shown in Figure 3 (a), (b) and (c). All diffraction peaks can be indexed to the cubic phase of Cu_2O crystals a match well with standard data. No other phases such as CuO or Cu are found in XRD patters confirming that all the samples exist as main Cu_2O phase. The single phase of Cu_2O films can be prepared at temperature of 300 °C and time of annealing of 1 hour. When the temperature is lower or the time is shorter, it is hard to reduce cupric acetate to cuprous oxide completely, whereas if the temperature is too high or the reaction time is too long, it is easy to get copper rather than cuprous oxide.

The film deposited onto ITO glass, two diffraction peaks are observed and identified as Cu_2O (111) and (200) directions. The strongest peaks in the XRD spectrum represent the crystal direction of Cu_2O (111). The lattice parameter for the films is the same and it is in agreement with the standard value of a 4.27Å. An average value of the crystallite size at the (111) plane can be obtained by applying the Debye-Scherer’s equation

$$D = \frac{0.9\lambda}{\beta \mathrm{Cos}\theta}$$

Where D is the crystallite size, λ is 1.5406Å for $\mathrm{CuK}_{\alpha 2}$, β is the full width at half maximum (FWHM) of the peak in radian and θ is the Bragg angle indicated the calculated grain size of the Cu_2O diffraction peak. ITO glass used is a polycrystalline isotropic material with no preferred orientation. The Cu_2O film deposited on this substrate shows (111) preferential orientation, which may suggest that the fastest growth direction of Cu_2O is along the (111) direction. Table 1 summarized XRD analysis results of Cu_2O samples on ITO glass substrates at (111) plane.

Table 1: The energy gap, grain size and crystallite size of Cu_2O thin films

Samples	**Energy Gap (eV)**	**Grain Size (□m)**	**2□ (deg.)**	**Crystallite size (nm)**	**FWHM peak (deg.)**	**Plane (*hkl*)**
1	2.06	122	35.51	32.69	0.24	(111)
2	2.17	97	35.39	20.02	0.39	(111)
3	1.49	106	35.40	45.68	0.19	(111)

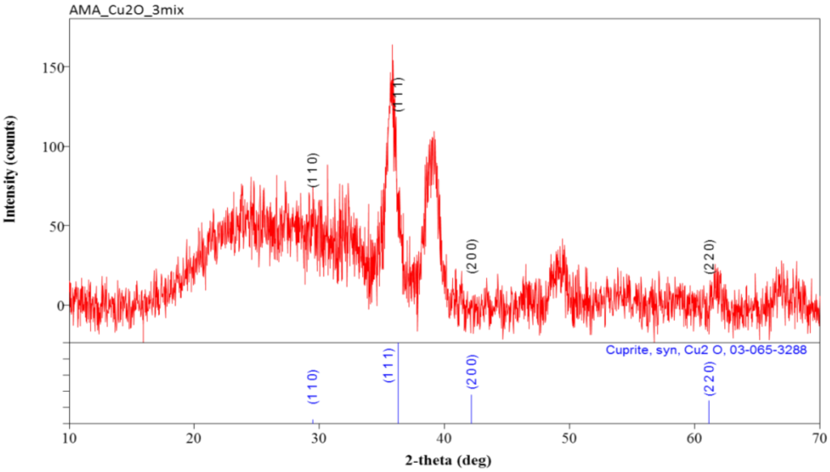

(a) sample 1

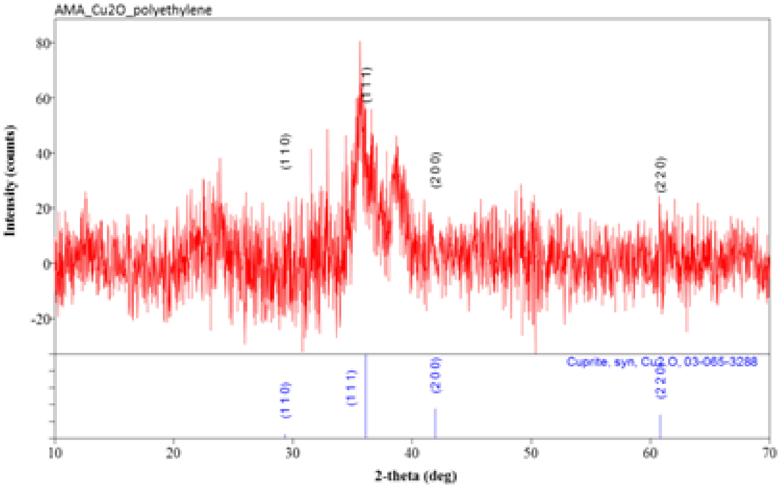

(b) sample 2

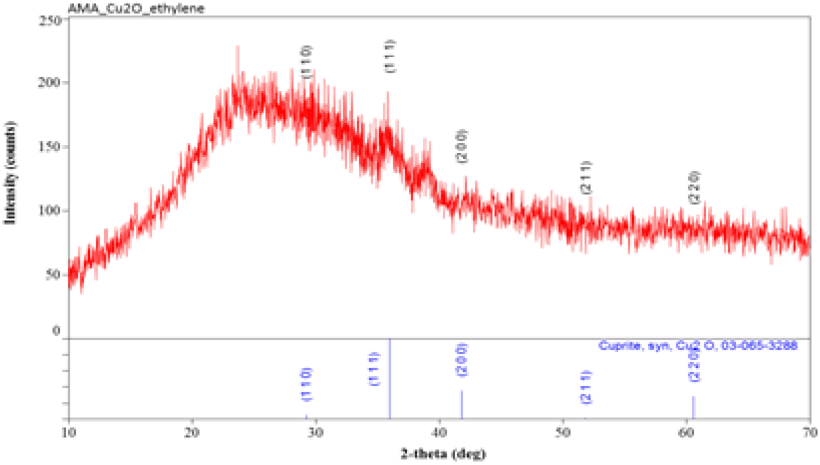

(c) sample 3

Figure 3: XRD patterns of Cu_2O thin film annealed at 300 °C for 1 hour (a) sample 1 (b) sample 2 and (c) sample 3

Film Morphology

Figure 4 shows the surface morphology of three set of samples. It is showed that the surface morphology depends on the addition of additive and the films grown on ITO substrates are uniform. The average grain sizes of the Cu_2O films for the samples are shown in Table 1. After adding polyethylene glycol, the grain size reduces from 122 µm to 97 µm. It shows that the addition of polyethylene glycol increases the viscosity of the solution due to chain length effects. The addition of ethylene glycol has been widely used in the polyol synthesis of metal and metal oxide due to its strong reducing ability and relatively high boiling point (~197˚ C). The Cu_2O samples grains were irregular shape.

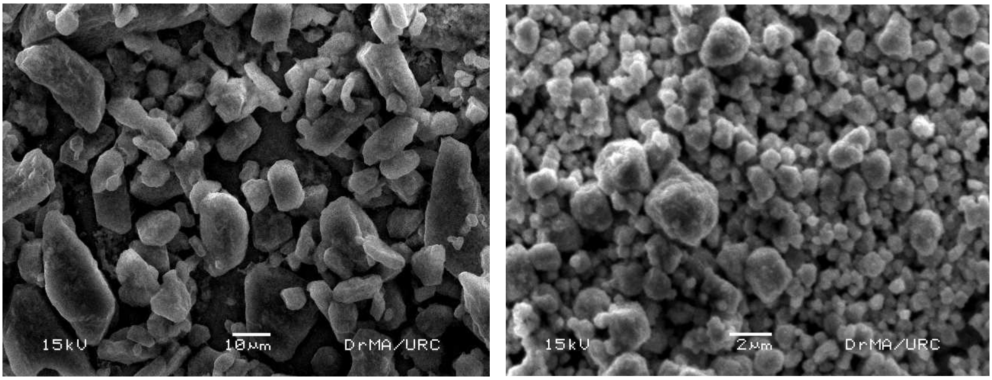

(a) sample 1 (b) sample 2

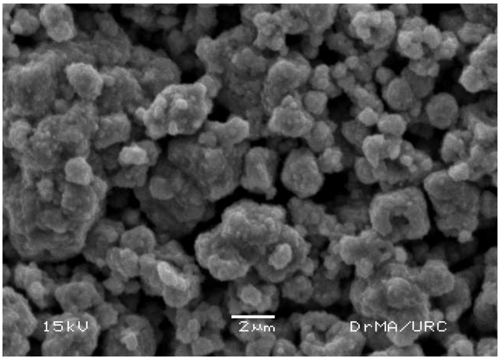

(c) sample 3

Figure 4: SEM images of Cu_2O Thin film at 250°C with different additives (a) sample 1 (b) sample 2 and (c) sample 3

Optical properties

The UV-Vis spectra of different Cu_2O samples are shown in Figure 5 (a), (b) and (c). The absorbance of sample may be influenced by grain size, shape and coverage of sample. There is a possibility of increasing of absorbance contribute by scattering at grain size. The highest absorbance obtained for sample 2 (with polyethylene glycol addition) is due to it had the thickest film and smaller grain size. The film of sample 2 is more compact compared to other samples. The addition of polyethylene glycol will produce cracking free films with high optical absorbance. The polyethylene glycol additive can avoid the particle aggregation occurring in the solution, the sample 2 with polyethylene glycol has finer crystalline grain (97 µm) and thus decreases scattering at crystalline boundary. The absorption coefficient α , of the Cu2O film is related to the photon energy $h\upsilon$.

$$(\alpha h\upsilon)^2 = (h\upsilon - E_g)^{1/2}$$

Where $h\gamma$ is the photon energy and E_g is the optical energy gap. These energy gaps are calculate from the intercept of straight line on the photon energy ($h\upsilon$) of the $(\alpha h\upsilon)^2$ vs ($h\upsilon$) plot and the value listed in Table 1. The energy gap for these films was found to be in the range of 1.49 -2.17 eV and was found to be influence by film thickness and also the optical absorbance. The addition of polyethylene glycol produced the thickest film with higher energy gap and high optical absorbance.

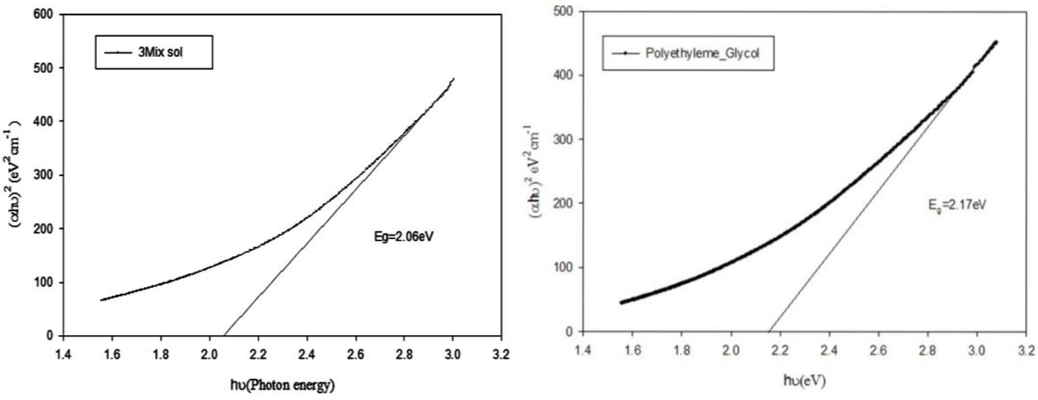

(a) sample 1 (b) sample 2

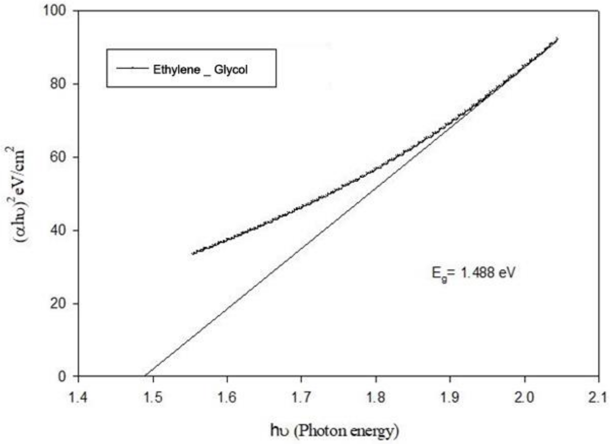

(c) sample 3

Figure 5: Plots of $(\alpha h\upsilon)^2$ vs $(h\upsilon)$ to determine the energy of the optical absorption coefficient for Cu_2O films deposited onto ITO samples with different additives(a) sample 1 (b) sample 2 and (c) sample 3

Conclusion

Cu_2O thin film has been successfully grown on ITO substrates by spin coating with different additives and annealed at 300°C. Various properties of Cu_2O thin films have been characterized. The addition of polyethylene glycol to the parent solution can be enhance various properties of the films, such as decreasing grain size but increasing optical absorbance and energy gap of films. Based on the grain size of film prepared by polyethylene glycol has smallest grain of about 97μm with irregular shape. The highest optical absorbance film was obtained by the addition of polyethylene glycol. The energy band gap for these films was found to be in the range of 1.5 – 2.2 eV which is in a good agreement with the value of optical band gap for Cu_2O. The results indicate that the Cu_2O thin film prepared by spin coating technique can be used for solar cell. Then, the samples were characterized by means of XRD, SEM and UV-Vis measurement.

Acknowledgements

I would like to express profound thanks to Professor Dr Khin Khin Win, Head of Department of Physics, University of Yangon for her kind permission and supporting this work.

I also thanks to Professor Dr Aye Aye Thant, Department of Physics, University of Yangon for her helpful advice to carry out this work.

References

Halin D.S.C, K.R. Ahmad, Kamarudin Hussin, I.A. Talib, A.R. Daud, M.A.A. Hamid and A.V. Sandu, (2015), "Applied Mechanics and Materials", Volume 754-755, pp 1141-1145.

Halin D.S.C, I.A. Talib, M.A.A. Hamid, A.R. Daud, (2008), "Solid State Science and Technology", Volume 16 (1), pp 232-237.

Halin D.S.C, Haiza Haroon, I.A. Talib, A.R. Daud and M.A.A. Hamid, (2013), "Advanced Materials Research", ISSN: 1662-8985,Volume 626, pp 849-852.

Halin D.S.C, I.A. Talib, A.R. Daud and M.A.A. Hamid, (2014), "International Journal of Photonenergy", Article ID 352156, pp 6.

H. Hashim, S.S. Shariffudin, P.S.M. Saad and H.A.M. Ridah, (2015), "IOP Conference Series: Materials Science and Engineering", Volume 99, pp 012-032.

J. Myanmar Acad. Arts Sci. 2019 **Vol. XVII. No.2A**

STRUCTURAL AND VIBRATIONAL INVESTIGATION OF K^+(1 MOL%) DOPED $LiNH_4SO_4$ SINGLE CRYSTAL

Hnin Yu Wai,[1] Thin Thin Kyu[1], Myat Wutyi Han[1] and Amy Aung[1]

Abstract

Crystals of K^+ (1mol%) doped Lithium Ammonium Sulphate, $LiNH_4SO_4$, were grown by slow evaporation method of room temperature. Starting materials of Lithium Sulphate, Li_2SO_4 and Ammonium Sulphate, $(NH_4)_2SO_4$ with the addition of (1mol%). Potassium Sulphate K_2SO_4 were used to grow and synthesis the crystals. Structural investigation of the crystal will be reported by XRD method. Lattice parameters of the crystal were also examined. FTIR transmission spectrum of the crystal will be collected by pc controlled FTIR-8400 /SHIMADZU spectrometer between the wavenumber range of 400 cm^{-1} and 4000 cm^{-1} region.

Keywords: slow evaporation method, K^+/ $LiNH_4SO_4$, XRD, FTIR

Introduction

Several Li-based binary sulphates of the type $LiASO_4$ (where A = Na, K, Rb, NH_4, Cs) have been found to exhibit temperature induced phase transition characters. Under ambient conditions, $LiNH_4SO_4$ crystallizes in the hexagonal system under the space group $P31c$ $(C_{3v}^{4})$with six formula units per unit cell but two formula unit per unit cell of $LiNH_4SO_4$. Hence, the compound has 22 atoms in the unit cell. The sulphur atoms of the sixsulphate ions are located on three sets of three-fold-axes with one of the S-O bonds of the sulphate ions lying on the axis. The three pairs of the sulphate ions have different bond lengths and bond angles, since their immediate neighbours are different. One pair of SO_4 has only lithium neighbours, while the remaining two pairs are closely coordinated by ammonium. Consequently, one pair is elongated and another is compressed along the three-fold axis, while the third one is nearly regular.

Techniques using electromagnetic radiation are among the most fruitful of these. The very short wavelengths of X-rays are instrumental even

---

[1] Dr, Assistant Lecturer, Department of Physics, University of Yangon

essential in examining the atomic Lattice that define crystalline solids. Wavelengths from the ultraviolet through the visible and infrared to the millimeter range have enormous power to examine all aspects of solids.

Infrared spectroscopy is a versatile analytical technique. The most popular way of obtaining infrared spectra is to pass the infrared beam directly through the sample, known as the transmission technique. Transmission method is the oldest and most basic infrared method. The method is based upon the absorption of infrared radiation at specific wavelengths as if passes' through a sample. The advantage of this technique is the transmission spectra have signal-to-noise ratio. It is relatively easy to obtain spectra from solids, liquids and gases. Potassium Bromide (KBr) pellets are used to obtain the infrared spectra of solids, and are particularly well suited to powder samples. The most commonly used alkali halide is Potassium bromide (KBr), which is completely transparent in the middle IR region. KBr is an inert, infrared transparent material, and acts as a support and a diluent for the sample.[1,2,3]Due to the vast application of practical work, the present study deal with structural and vibrational analysis of $K^+/LiNH_4SO_4$ crystal was investigated by X-Ray Diffraction XRD method and FTIR spectroscopy.

Experimental Result

Growth of K^+(1 mol%) doped $LiNH_4SO_4$ Crystal

Crystals of K^+(1 mol%) doped Lithium Ammonium Sulphate, $LiNH_4SO_4$ were grown by slow evaporation method from aqueous solutions at room temperature (29°C). Starting materials of Lithium Sulphate, Li_2SO_4 and Ammonium Sulphate, $(NH_4)_2SO_4$ with equimolar ratio were used to grow and synthesis the crystals. (1 mol%) Potassium Sulphate, K_2SO_4 was used as the dopant material. Transparent and homogeneous crystals were selected for measurements. Preparation process of K^+ (1 mol%) Doped $LiNH_4SO_4$ single crystalis shown in figure 1.

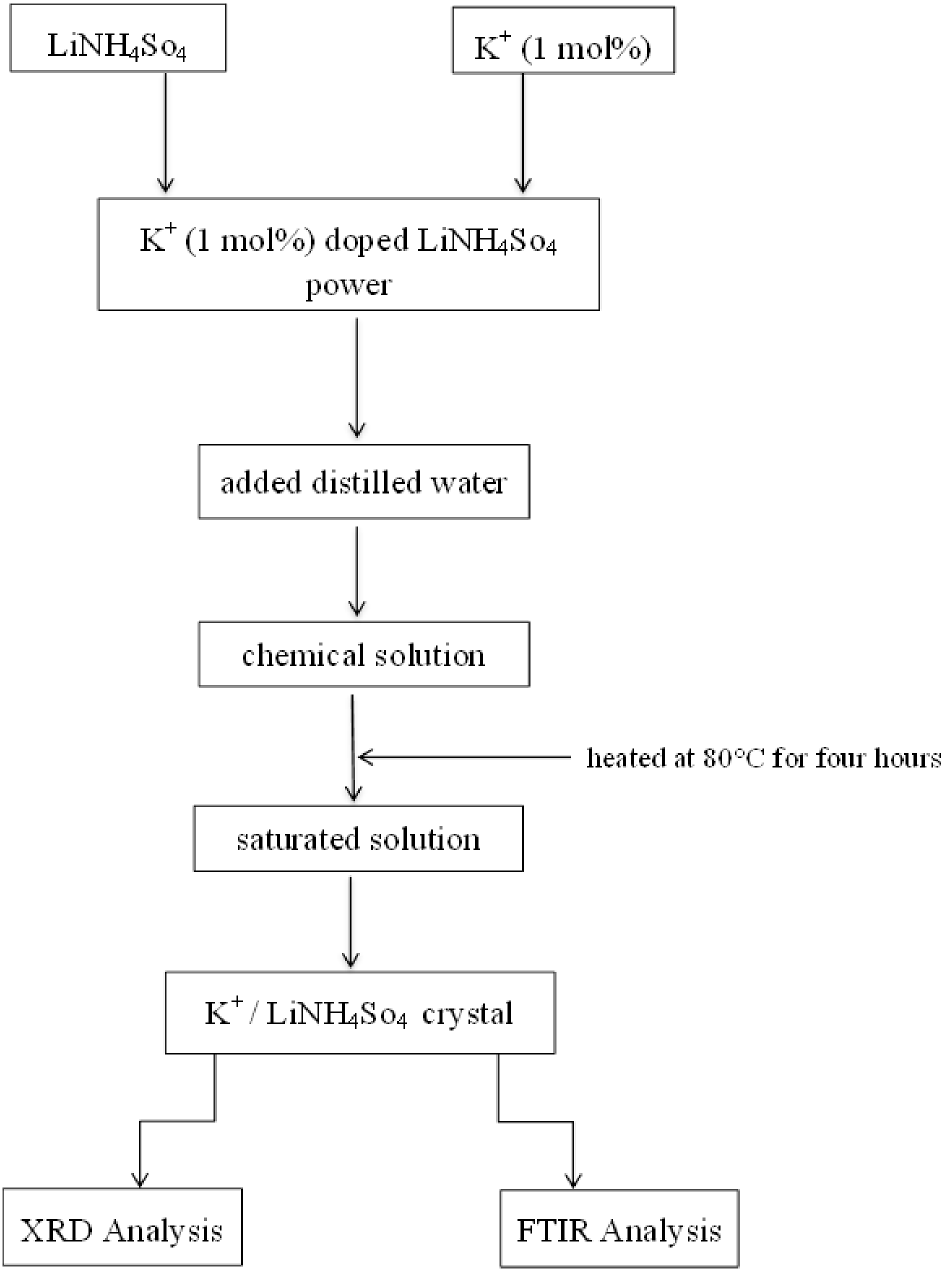

Figure 1: Preparation process of K^+ (1 mol%) Doped $LiNH_4SO_4$ single crystal

At room temperature, $K^+/LiNH_4SO_4$ crystal is colourless. Photograph showing the as-grown $K^+/LiNH_4S0_4$ crystal (duration of growth is two months) is shown in Figure 2.

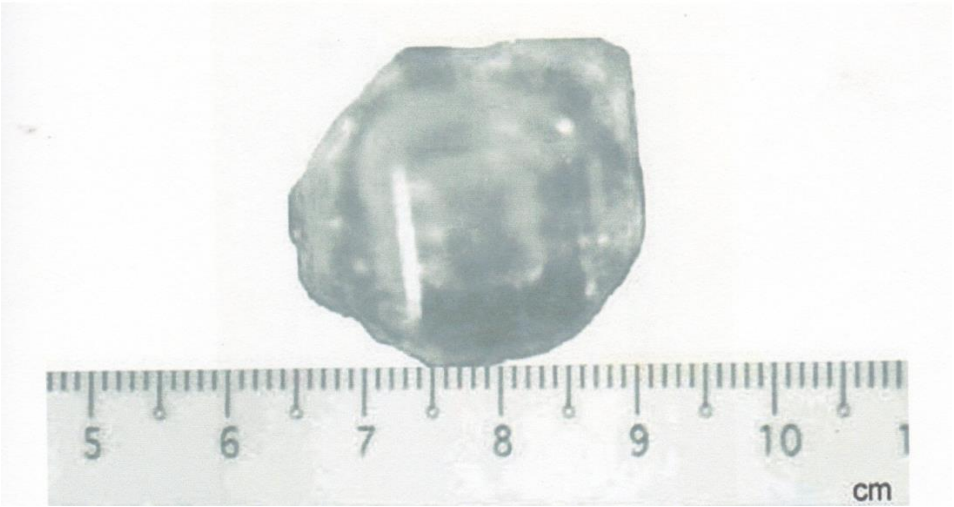

Figure 2: Photograph showing the as-grown crystal of K^+(1mol%) doped $LiNH_4SO_4$

X-Ray Diffraction Measurement

X-ray diffractometry was mainly used for identification and qualification of crystals by their diffraction patterns. The X-ray diffraction measurements were carried out by using RIGAKU MULTIFLEX X-ray powder diffractometer at URC, University of Yangon. Photograph showing the RIGAKU MULTIFLEX X-ray powder diffractometer is shown in Fig 3. The X-ray diffractometry consists of three basic parts: a source of radiation, consisting of (1) X-ray tube and high voltage generator, (2) the detector and counting equipment, and (3) the diffractometer.

The powder sample of $K^+/LiNH_4SO_4$ crystal was placed at the center of the goniometer. The samples were scanned through an angle 2θ from 10° to 70°. The surface of the sample was radiated by X-ray beam from Cu fine focus tube. The applied voltage and current were maintained at 40 kV and 40 mA. The diffracted X-ray beams entered the detector and then recorded.

The recording scan speed was 4º/min. Each diffracted ray is recorded as a peak. The peak heights are roughly proportional to the X-rays intensity. The diffraction patterns of specimens were identified by using Material Data Inc. data book. The initial "d" spacing was determined using a second derivative peak search algorithm, followed by careful editing of the raw data to improve the position accuracy and to resolve ambiguous lines. The "d" values were determined using the Cu K_α radiation with wavelength of 1.54056Å. The lattice parameters can be examined by using the following equation.

$$\frac{1}{d^2}=\frac{4}{3}\left(\frac{h^2+hk+k^2}{a^2}\right)+\frac{l^2}{c^2}$$

where d is interplanar spacing (Å), *a*, *b* and *c* are lattice parameters (Å) of the unitcell, *(h k l)*are Miller indices, θ is diffraction angle (◦) and λ is wavelength of incident X-ray (Å).The experimental conditions were as follows:

Tube Voltage : 40 kV. 40 mA
Target : Cu
Filter : Ni
Wavelength : 1.54056 Å ($\mathrm{CuK_u}$-radiation)
Scan Speed : 4º/min
20 range : 10° - 70°

Figure 3: Photograph of the RIGAKU MULTIFLEX X-ray Difractometer

FTIR Spectroscopic Measurement

In the present work, FTIR transmission spectrum of K^+(1 mol%) doped $LiNH_4SO_4$ crystal with Potassium Bromide, KBr pellet method was observed by SHIMADZU FTIR-8400 Spectrophotometer to investigate the vibrational characteristics of the SO_4^{2-} molecules in the crystalline environments of Li-NH_4 and K. Experimental conditions were as follows:

Measurement mode : %T
Wavenumber range : 400 cm^{-1} - 4000 cm^{-I}
Number of scan : 60 s
Apodization function : Happ-Genzel
Resolution : 4 cm^{-1}
Method : KBr disc

Photograph of the SHIMADZU FTIR-8400 Spectrophotometer is shown in Figure4.

Figure 4: Photograph of the SHIMADZU FT IR-8400 Spectrophotometer

Results and Discussion

Powder XRD Analysis

Powder XRD pattern of K^+(1mol%) doped $LiNH_4SO_4$ crystal is shown in Figure5. As shown in XRD pattern, the collected diffraction lines are identified by using JCPDS data files. The observed diffraction peaks and corresponding diffraction angles (2θ), atomic spacings (d), Miller indices (hkl) and peak height of the sample are tabulated in Table 1. Most of the diffraction lines are well assigned by JCPDS. However, some of the diffraction lines for 2θ such as 21.30°, 30.28° and 30.58° are not assigned with JCPDS because the ratio of the starting materials and the standard file of $Li(NH_4)_{0.97}K_{0.03}SO_4$ are not precisely equal to those of candidate sample of $K^+/LiNH_4SO_4$. Furthermore, it shows the dopant effects of K_2SO_4 on $LiNH_4SO_4$ crystal.

According to XRD pattern, $K^+/LiNH_4SO_4$ crystal belongs to hexagonal structure at room temperature. Lattice parameters of the crystal are calculated by using the equation of $\frac{1}{d^2}=\frac{4}{3}(\frac{h^2+hk+k^2}{a^2})+\frac{l^2}{c^2}$. Lattice parameters of the crystalre a=b=11.19Å and c=9.40Årespectively.

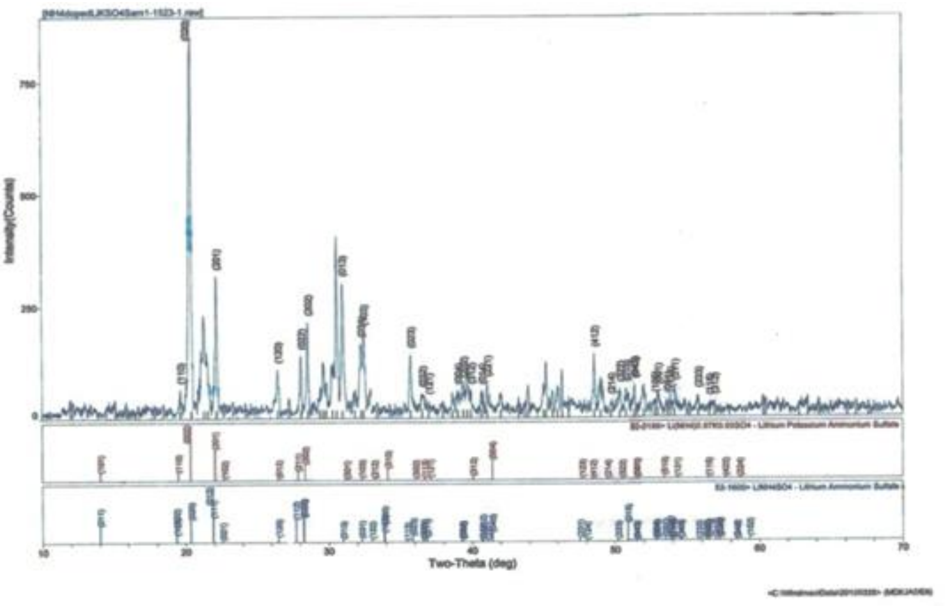

Fig 5.1 XRD pattern of K^+(1 mol%) $LiNH_4SO_4$ crystal

Figure 5: XRD pattern of K+(1mol%) $LINH_4SO_4$ crystal

Table 1 XRD data of K^+(1 mol%) $LiNH_4SO_4$ crystal

Line No	2θ (°)	(*hkl*)	*d* (Å)	Peak height (%)
1	19.66	(110)	4.51	6.60
2	20.43	(020)	4.34	100.00
3	22.18	(201)	4.00	36.00
4	26.46	(120)	3.37	11.90
5	28.10	(022)	3.17	15.60
6	28.58	(202)	3.12	24.90
7	30.98	(013)	2.88	34.30
8	32.28	(031)	2.77	17.60
9	32.46	(103)	2.76	20.90
10	35.74	(023)	2.51	14.80

FTIR Spectroscopic Analysis

According to vibrational analysis of SO_4^{2-} or NH_4^+ using factor group theory, which obeys the (tetrahedral) T_d-symmetry and it has four types of fundamental modes of vibrations. These four modes are (1) v_1-mode (symmetric-stretching), v_2-mode (bending), v_3-mode (dipole) and v_4-mode (polarization) respectively. Also H_2O molecule obeys (2-fold vertical rotation) C_{2v}-symmetry and it has three types of fundamental modes of vibrations, namely; (1) v_1-mode (symmetric-stretching),v_2-mode (bending) and v_3-mode (asymmetric-stretching). Moreover, vibrational frequencies of (1) metal compound molecules (e.g., ZnO, $A1_2O_3$,...)lies under 400 cm^{-1}, (2) inorganic compound molecules (e.g., $P0_4^{3-}$, $S04^{2-}$,…) lies between 400 cm^{-1} and 1500 cm^{-1} and (3) organic compound molecules (e.g., NH_4^+, H_20,...) lies over 1500 cm^{-1} region. Sometime, most of the vibrational frequencies of molecules are appeared in the boundary region of about 400 cm^{-1}, 1500 cm^{-1}, etc.

FTIR transmission spectrum of K^+(1 mol%) doped $LiNH_4SO_4$ crystal is shown in Figure6. As shown in figure, the recorded wavenumbers (absorption lines or resonance lines of molecules with the frequencies of incident infrared beam) and their corresponding vibrational characteristics of molecules in crystalline environments of Li - NH_4 - K are compared to those of $LiNH_4SO_4$ crystal. These are tabulated in Table 2.

In the observed FTIR spectrum, fourteen absorption lines are found in the wavenumber range of 400 cm^{-1} - 4000 cm^{-1}. These lines are represented by the vibrational characteristics of sulphate (SO_4^{2-}), ammonium (NH_4^+), water (H_2O), carbon dioxide (CO_2) and ($S0_4^{2-}$-NH_4^+-SO_4^{2-}) molecular network respectively.

The lines at 982 cm^{-1}, 432 cm^{-1}, 1079 cm^{-1} / 1151 cm^{-1}, and 625 cm^{-1} are indicated by four fundamental vibrational modes (v_1-mode, v_2-mode, v_3-mode andv_4-mode) of $S0_4^{2-}$.

The lines at 1431 cm^{-1} and 1470 $cm^{-1}$are indicated by v_4-mode of NH_4^+. Others three fundamental modes (v_1-mode, v_2-mode and v_3-mode) are not found because these lines are normally appeared in the high frequency region.

The line at 723 cm^{-1} is represented by the librational rocking vibration of (SO_4^{2-} -NH_4^+-SO_4^{2-}) molecular network.

The band observed in the high wavenumbers region of 2000cm^{-1} - 4000cm^{-1} are vibrational characteristics of organic molecules: i.e., CO_2 and H_2O, etc. The lines at 2056 cm^{-1}, 2127cm^{-1} and 2245 cm^{-1} are represented by the bending vibrations of CO_2. The lines of 3214 cm^{-1}, 1676 cm^{-1} and 3413 cm^{-1} are attributed by three fundamental modes (v_1-mode, v_2-mode and v_3-mode) of H_2O. These lines are often appeared in the FTIR transmission spectrum of KBr pellet method.

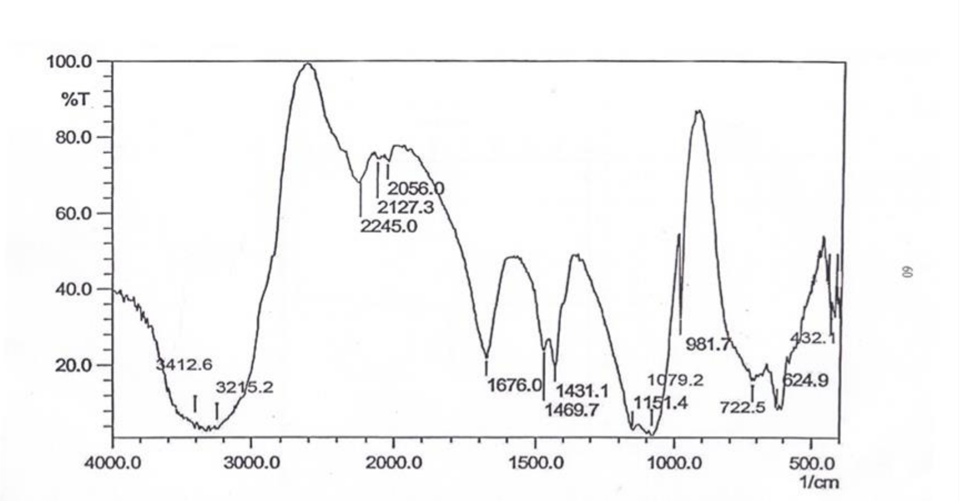

Figure 6: FTIR transmission spectrum of K$^+$(1mol%) doped $LiNH_4SO_4$

Table 2: Wavenumbers and corresponding vibrational mode assignments of K^+(1 mol%) doped $LiNH_4SO_4$ crystal

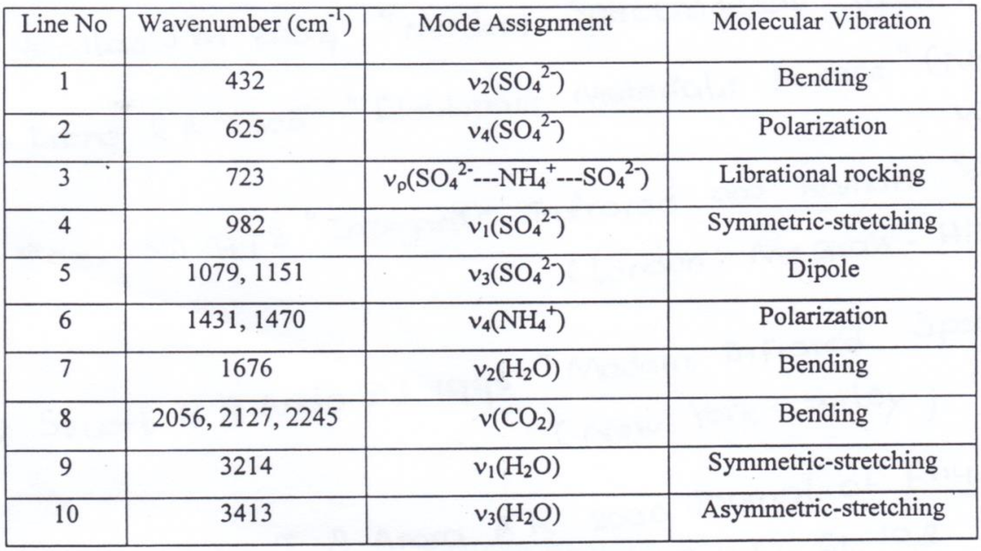

Line No	Wavenumber (cm^{-1})	Mode Assignment	Molecular Vibration
1	432	$\nu_2(SO_4^{2-})$	Bending
2	625	$\nu_4(SO_4^{2-})$	Polarization
3	723	$\nu_\rho(SO_4^{2-}\text{---}NH_4^+\text{---}SO_4^{2-})$	Librational rocking
4	982	$\nu_1(SO_4^{2-})$	Symmetric-stretching
5	1079, 1151	$\nu_3(SO_4^{2-})$	Dipole
6	1431, 1470	$\nu_4(NH_4^+)$	Polarization
7	1676	$\nu_2(H_2O)$	Bending
8	2056, 2127, 2245	$\nu(CO_2)$	Bending
9	3214	$\nu_1(H_2O)$	Symmetric-stretching
10	3413	$\nu_3(H_2O)$	Asymmetric-stretching

Conclusion

Crystals of K^+(1 mol%) doped Lithium Ammonium Sulphate $LiNH_4SO_4$ were grown by slow evaporation method from aqueous solutions at room temperature. The as grown crystal was characterized by powder X-ray diffraction (XRD) to investigate the structural properties of the sample. According to XRD pattern, the crystal belongs to hexagonal structure and lattice parameters of the crystal are a=b=11.19Å and c=9.40Å. From the recorded FTIR spectrum, fourteen absorption lines are observed and precisely assigned by using molecular vibration theory. The absorption lines at 982cm^{-1}, 432cm^{-1}, 1079 cm^{-1} / 1151 cm^{-1} and 625 cm^{-1} are indicated by four fundamental modes of SO_4^{2-}. The lines at 1431 cm^{-1} and 1470 cm^{-1} are indicated by γ_4-mode of NH_4^+. All others absorption lines are represented by the CO_2 and H_2O due to KBr pellet method. Thus crystal of K^+ (1 mol%) doped $LiNH_4SO_4$ can be considered as the solid electrolyte material.

Acknowledgements

I would like to express my sincere thanks to my Professor Dr Khin Khin Win, Head of Department of Physics, University of Yangon, for her kind permission to carry out this work, then for her supervision, helpful advice and valuable suggestion.

I wish to show my sincere thanks to Professor Dr Aye Aye Thant, Department of Physics, University of Yangon, for her discussion and suggestion in experimental work.

References

Aung Myat Kyaw, Thandar Min, Win Kyaw, Pho Kaung and Sein Htoon, (2005). Journal of the Myanmar Academy of Arts and Science 3 (3) 43

Cullity B. D. (1978) "Elements of X-ray; Diffraction" (Reading: Wesley)

Gaulitz G &Vo-Dinh T. (2003) "Handbook of Spectroscopy" (New York: Wiley)

Hollas J. M. (2004) "Modern Spectroscopy" (New York: Wiley)

Irene E. A. (2005) " Electronic Materials Science" (New York: Wiley)

Ross S. D. (1972) "Inorganic Infrared and Raman Spectra" (London: McGraw-Hill)

Stuart B & Ando D. J. (1996) "Modern Infrared Spectroscopy" (New York: Wiley)

Sakuntala T& Arora A. K. (2000) " Journal of Physics & chemical Solids 61 103

J. Myanmar Acad. Arts Sci. 2019 **Vol. XVII. No.2A**

CHARACTERIZATION OF MUD OF MUD VOLCANO IN MINBU (NAGA BWET TAUNG) AS GEOPOLYMER RAW MATERIAL

Khin Moe War[1],Yu Mar lar Lwin[2], Me Me Soe[3]

Abstract

The mud of mud volcano sample was collected from an eruption site named "Naga Bwet Taung", Minbu, Magway Region for characterization.X-ray fluorescence (XRF) was used to measure the chemical composition of mud of mud volcano and fly ash. Structure properties of mud and fly ash were examined by X-ray diffraction(XRD).XRD Analysis showed that the major constituents of mud are SiO_2 which are higher than those in fly ash. Scanning Electron Microscopy (SEM) was used to observe the microstructure and shape of the mud to compare fly ash. Fourier Transform Infrared Spectroscopy (FTIR) was performed to determine the bonding between the particles in mud and fly ash. The crystalline sizes were also calculated. In brief, the contents in mud of mud volcano is similar to that of fly ash which is commercial product and it was shown that the mud of mud volcano has potential as a raw material in geopolymer system due to characteristic of mud which is comparable to the fly ash.

Keywords: geopolymer, XRF, XRD,FTIR,SEM

Introduction

Myanmar has a few active volcanoes related to the mud volcanoes in Indonesia. There are three active and extinct volcanoes in Myanmar. List of active and extinct volcanoes in Myanmar are shown in Table (1) and Fig (1).

Mud volcanoes are formed from methane gases trapped deep below the ground being forced to the surface. In some instances, the pressure will push though the water table and mix the clay or mud in the surrounding areas to create a "volcano" such as the ones found in Minbu. It is situated on the western shore of the Irrawaddy near the oil-fields of Yenangyaung. Locally, the mud volcanoes of Minbu are known as Naga Bwet Taung which is loosely translates to something about Dragons breath.

---

[1] Dr, Assistant Lecturer, Department of Physics, University of Yangon

[2] Assistant Lecturer, Department of Physics, University of Yangon

[3] Assistant Lecturer, Department of Physics, University of Yangon

Unlike regular volcanoes, there is no heating involved and in fact, the mud is cool to the touch. The landscape is in Minbu looks like the surface of the moon with multiple vents bubbling out of ever-growing creators in the ground. Fig (2)

Fly ash is the fine solid particulated residue driven out of the boiler with the flue gases in coal-fired power plants. During the combustion of coal, the products formed are fly ash, bottom ash and gases or vapours.Most of the fly ash particles are glassy oramorphous. Fly ash is the fine part of the ash which is entrained in the flue gases, whereas the bottom ash is the residue consisting of coarser discrete or fused particles heavy enough to drop out of the combustion zone onto the bottom of the furnace. Fig (3). The vapour and gases from the volatilized fraction of the carbonaceous material which are partly discharged into the atmosphere and partly condense onto the surface of the fly ash particles.Some of the carbon particles do not burn and thus the fly ashes also contain unburned carbon or carry over carbon particles. The efficiency level of the coal burning power plant is also reflected in the quality of fly ash it produces. Thus, better plant efficiency means getting a better fly ash for use in concrete mixes.

The properties of fly ash are extremely variable and depend upon several factors, such as the type and origin of coal(bituminous, sub-bituminous and lignite coals), degree of coal pulverization, flame temperature, oxidation conditions and pretreatment during or to burning for SO, removal, method of collection and storage of fly ash. Fly ash is categorized into Class N, F, C and S. Class F and C pozzolans refer to fly ash derived from the burning of different coals. Class F refers to fly ash derived from burning anthracite or bituminous coal. Class C refers to ashes derived from burning lignite or sub-bituminous coal and contains less than 50 percent as oxides of silica (SiO_2), alumina(Al_2O_3) and iron (Fe_2O_2). In this study, Class C fly ash is used as a comparison process of mud of mud volcano (Naga Bwet Taung) .

About 500 million tonnes of coal combustion residue(ash) is produced annually by thermal power plants all over the world. The efficient use of coal ash as structural fill in embankments and dykes as an admixture in cement and concrete as sub-base and base course of roads as back fill for retaining structures, as till for land reclamation, etc. has transformed the costly liability of its disposal into an economic and environmentally safe proposition. Fly ash also find use as raw material in the manufacture of cement and for the production of sintered lightweight fly ash aggregates and bricks.

Table 1: The active and extinct volcanoes in Myanmar

Name	Elevation		Location	Last eruption
	meters	Feet		
Lower Chindwin	385	1263	Along the lower Chindwin River in central Myanmar	Holocene
Mount Popa	1518	4980	At the northern end of the BagoYoma Hills range	442 BC
Singu Plateau	507	1663	In north-central Myanmar, north of the city of Myanmar	Holocene

Figure 1: Map of volcanoes in Myanmar

Figure 2: Mud volcanoes in Minbu(Naga Bwet Taung)

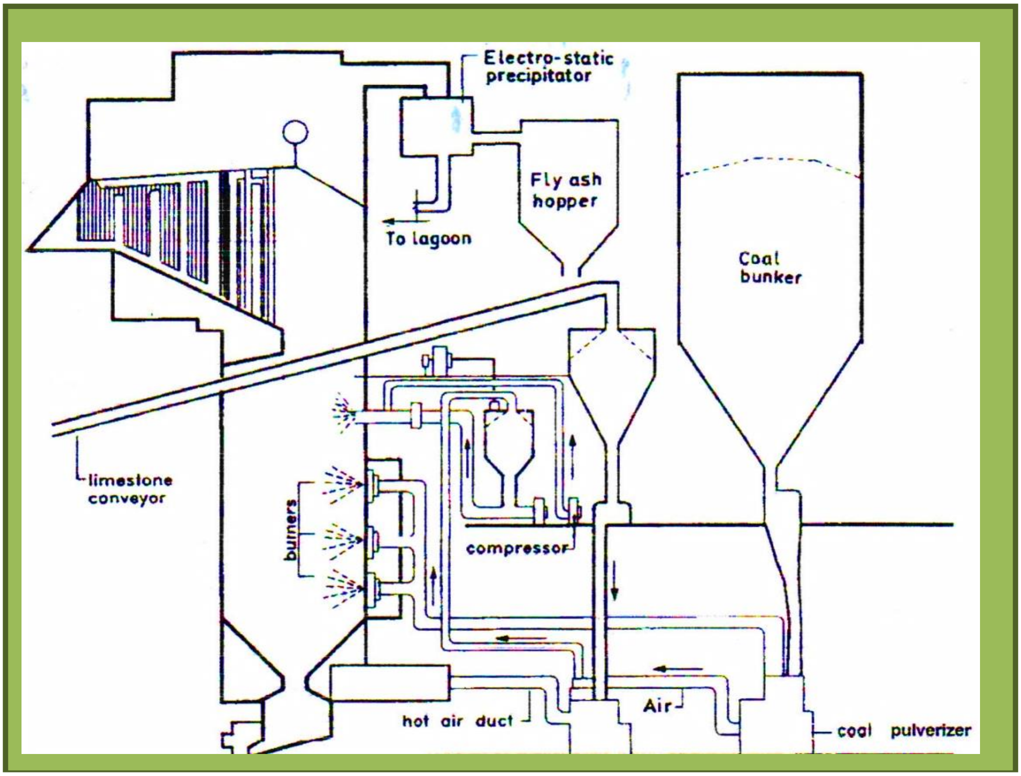

Figure 3 : Schematic diagram showing fossil fuel furnace, anti- pollution additive equipment and fly ash collection system

Experimental Procedure

Sample collecttion

The mud volcano sample was collected from the eruption sites called the Naga Bwet Taung mud volcano which is situated in Minbu, Magway Region. And, the fly ash sample was collected from the Tee Gyit coal industry, Shan State. Fig(4)

Figure 4: The raw mud (liquid)

Sample Preparation

The mud was transferred into sealed container. It was medium gray in colour. Firstly, the mud in the container was dried through direct sunlight under atmospheric pressure for three or four day and ground by agate mortar to obtain the powder form for testing purpose. Fig (5,6,and7)

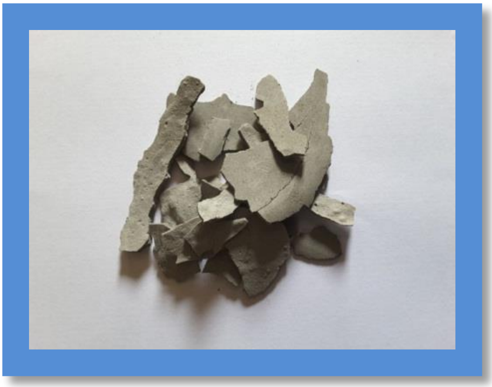

Figure 5: The dried mud of mud volcano after burning in direct sun light

Figure 6: Agate mortar

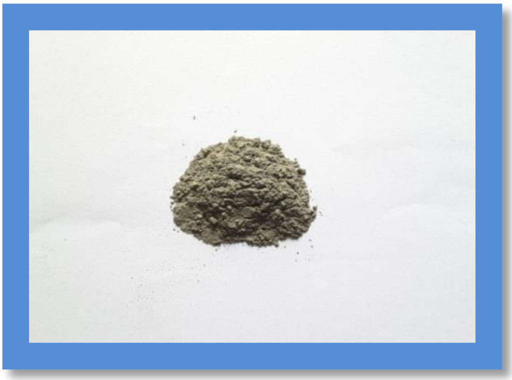

Figure 7 : The obtained mud powder after grinding

Sieve Analysis

For obtaining the unnecessary materials and uniform size of mud, sieve analysis by using mesh size of (100X100) microns pan was done. A small quantity of mud was placed in the pan and did the analysis twice to get the pure and uniform size of mud. Fig (8) and Fig (9). Moreover, the block diagram of experimental methods of raw mud is shown in Fig (10).

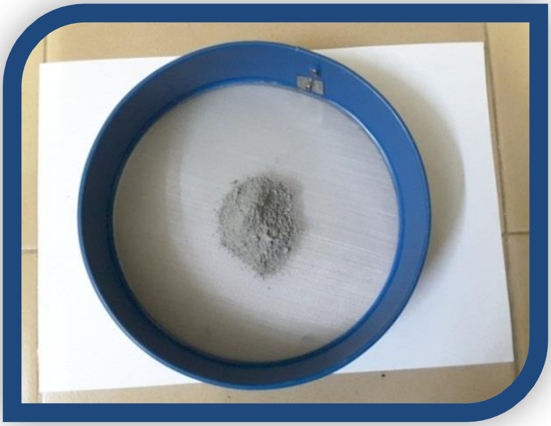

Figure 8 : Sieve analysis of mud of mud volcano using with mesh

Figure 9 : The pure and uniform size of mud

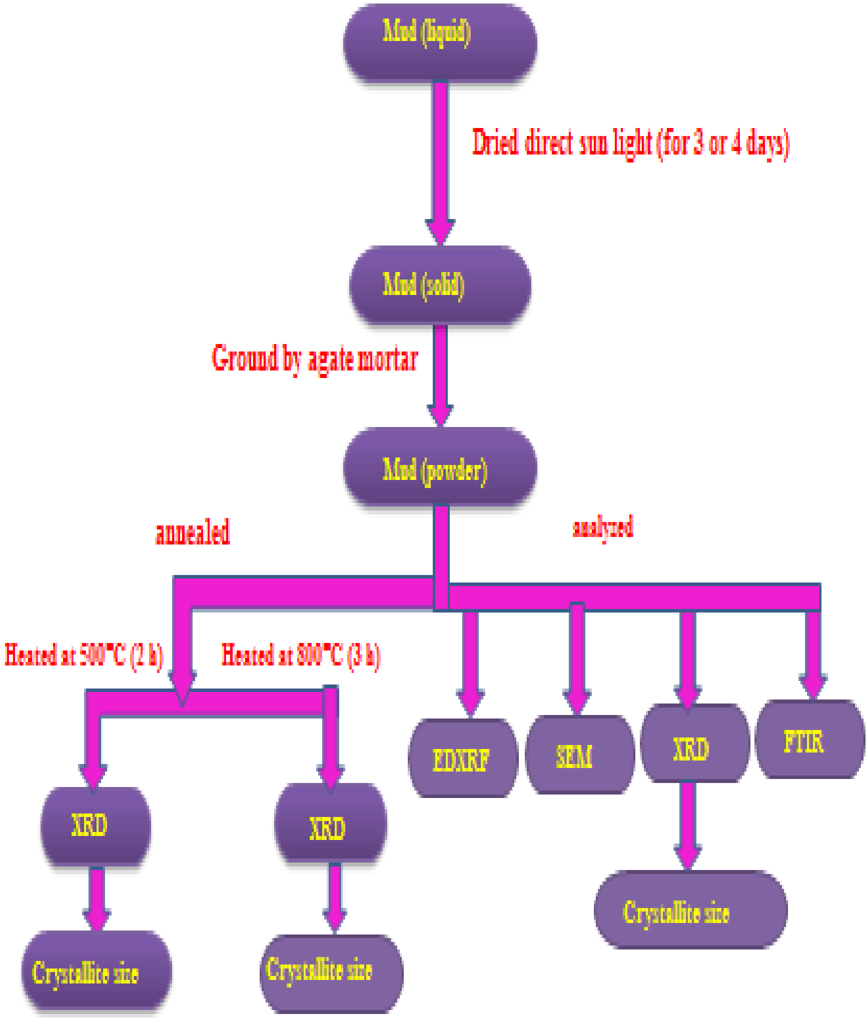

Figure 10: The block diagram of experimental methods of mud

Laboratory Methods

The block diagram of experimental methods of mud was shown in Fig (10).The mud and fly ash were collected and analyzed for different parameters by EDXRF, XRD, SEM and FTIR methods at Universities of Research Centre (URC), Yangon. Fig (11) (a),(11) (b) and (11)(c).

Figure11: (a) Shinmadzu EDX-700 X-ray spectrometer

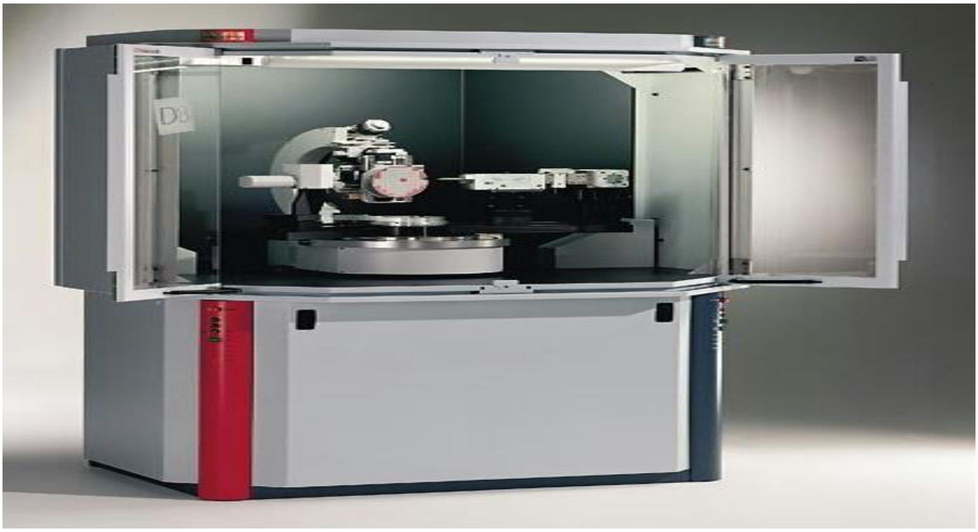

Figure 11: (b): XRD spectrometer

Figure11: (c) SEM (JSM-5610) spectrometer

Results and Discussion

In this present work, the chemical composition of mud and fly ash is shown in table (2) and fig (12) by EDXRF method. The EDXRF results showed that the chemical compositions of mud and fly ash and they had the major constituents of Si (75.98%) and (68.98%) . It was found that the concentration of Si in mud was higher than that of fly ash. It was showed that the mud was suitable to replace as a raw material for production of cement.

Table 2: The major chemical concentration of the mud compared to fly ash.

Elememts	Mud of mud volcano (Naga BwetTaung) %	Fly ash Tee Gyit coal industry, Shan State. %
Si	75.98	68.98
Ca	1.54	2.243
Ti	1.42	1.706
Fe	16.29	18.791
K	4.88	5.687
Mn	0.298	0.313
Zr	0.122	0.152

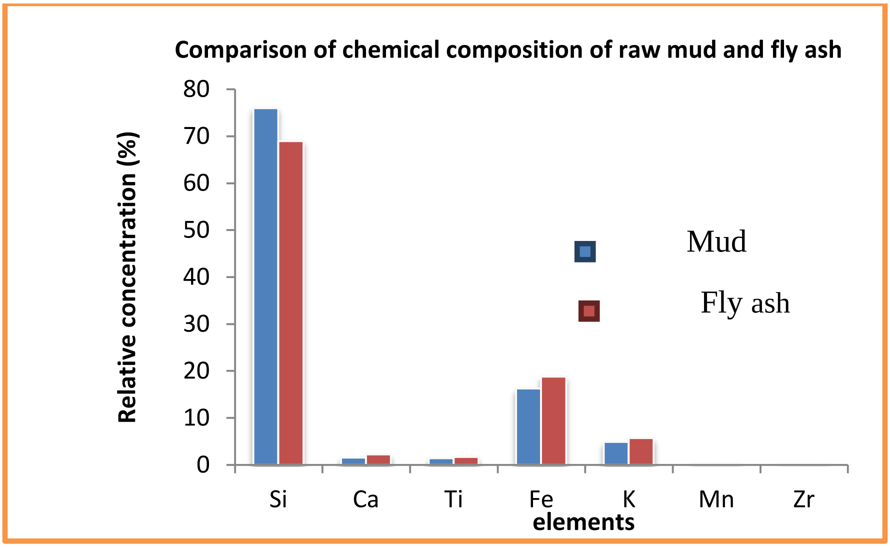

Figure 12: Comparison of concentrations of raw mud and fly ash

SEM investigation of raw mud and fly ash

The morphology of the mud and fly ash were examined by using SEM (JSM-5610) with accelerating voltage 15 kV and photo magnification 1000. SEM analyzed of the mud compared to fly ash is shown in Fig 13 (a) and (b). As seen in Fig 13(a), the particles of mud were plate-like structure and as seen in Fig 13(b), the particles of fly ash were spherically-shaped.

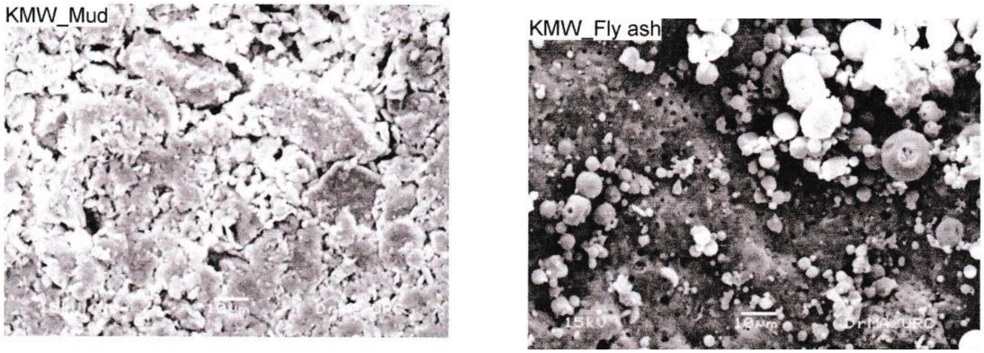

(a) (b)

Figure 13 : (a) SEM of raw mud of mud volcano (b) SEM of mud of mud volcano

X-ray Diffraction analysis

X-Ray diffraction (XRD) patterns for the mud compared with fly ash are shown in Figure 10. Both starting materials exhibit a peak at 2 thetha where 2 thetha = 20º - 32º, which is characteristic of structurally disordered compounds, and the peak at 2 thetha = 27° of mud shows slightly towards higher than fly ash due to higher composition of SiO_2 in mud compared to fly ash.(fig 14(a) and (b))

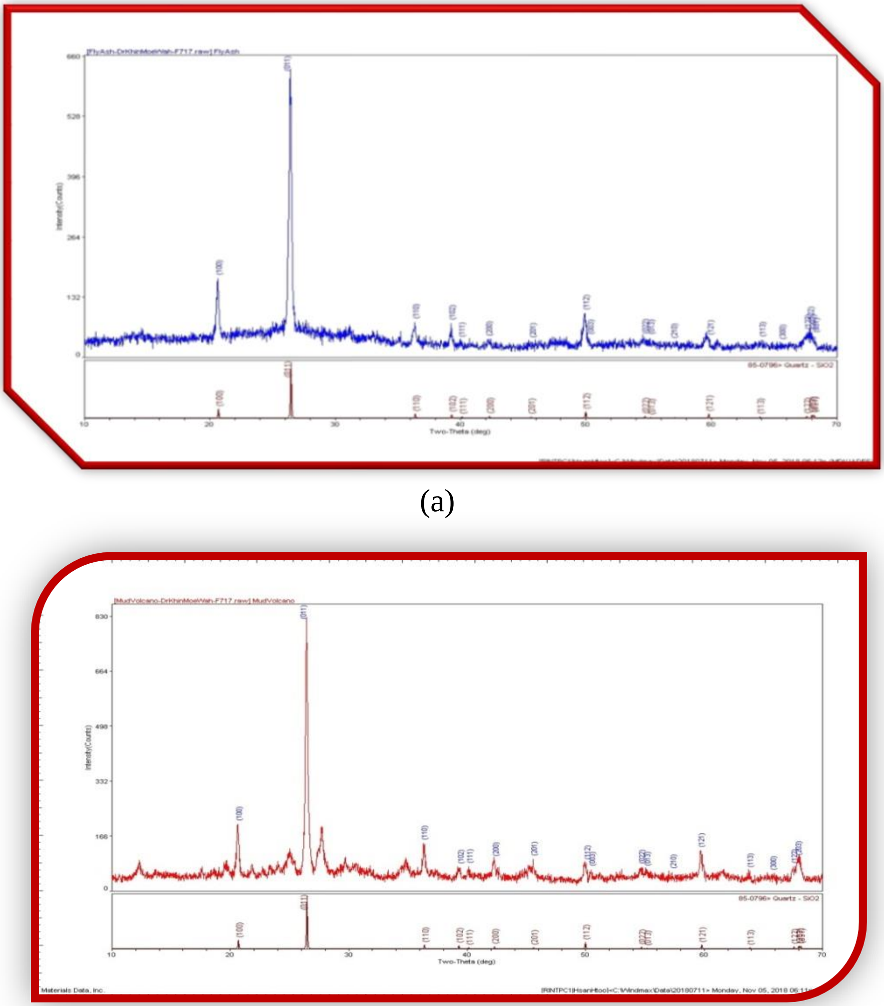

(a)

(b)

Figure14: (a): X-ray Diffraction pattern of fly ash (b) X-ray Diffraction pattern of mud

Fourier Transform Infrared Spectroscopy (FTIR)

Infracted spectra of mud fly ash were recorded at room temperature in the range from 400cm^{-1} to 4000 cm^{-1} using FTIR (8400, SHIMSDZU, Japan). The FTIR spectra of mud and fly ash were reported in Fig 15(a) and (b). The transmission band of the range from 423 cm^{-1} to 450 cm^{-1} is due to overlapping bending modes of Si-O-Si and 440cm^{-1} to 550 cm^{-1} is due to deformation vibrational modes of Si-O-Si, indicating the presence of Si in mud. Between the band 3570 cm^{-1} and 3200 cm^{-1} was assigned to the stretching vibration of O-H and H-OH groups from the weakly-bound water molecules which were absorbed on the surface of the mud.

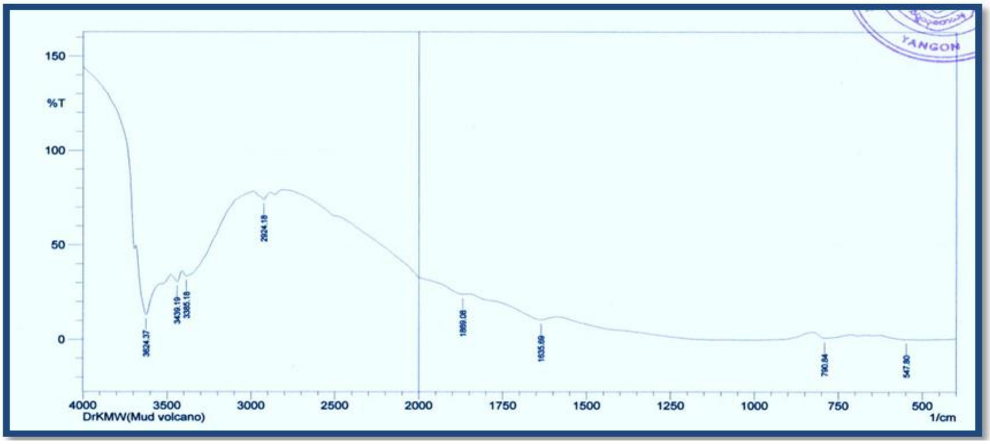

Figure 15: (a) FTIR spectrum of mud of mud volcano

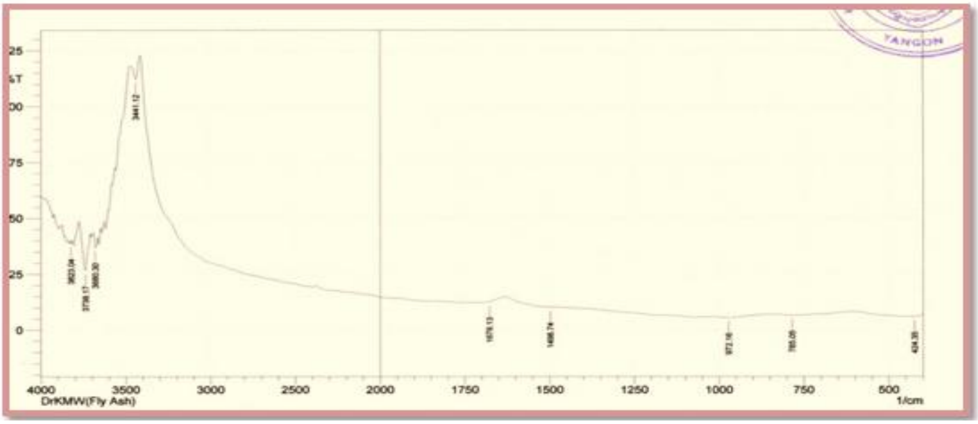

Figure 15: (b) FTIR spectrum of fly Ash

Investigation of crystalline size of raw mud and fly ash

The crystalline size of mud and fly ash can be calculated by Scherre's equation.

The equation of crystalline size is

$$D = \frac{0.9\,\lambda}{\beta\ \cos\theta}$$

Where, D is the crystallite size, β is the full width half maximum (FWHM) of the peak in radian, and θ is the diffraction peak position. The calculated value of crystallite sizes are shown in table (3).

Table 3: The calculated value of crystallite sizes of raw mud and fly ash

Samples	β	θ	cos θ	**D(nm)**
Raw Mud	0.227	13.210	0.9735	359.48
Fly Ash	0.229	13.201	0.9735	356.33

XRD analysis of the annealed mud at 500° and 800°C

The mud samples were annealed at 500°C and 800°C for 3 h and analyzed by XRD method to know the compound and to calculate the crystalline size. The XRD spectrums of the annealed mud were shown in fig 16 (a) and (b).It was found that the the peak at 2 thetha = 27° of mud is higher than fly ash due to higher composition of SiO_2 in mud compared to fly ash.The crystal sizes of the annealed mud were calculated by Scherre's equation.

The comparison of crystallite sizes of ordinary mud, the annealed mud and fly ash shown in Table (4).It was evaluated that the crystalline size of ordinary mud and fly ash were nearly equal but that of the annealed mud (800°C) was larger than any other samples and the annealed mud (500°C) was smaller the crystalline size of all samples. The lesser crystalline size was more suitable for replacing the fly ash. Therefore, The annealed temperature less than and equal 500 °C was the best to use. The data was shown in Table (5).

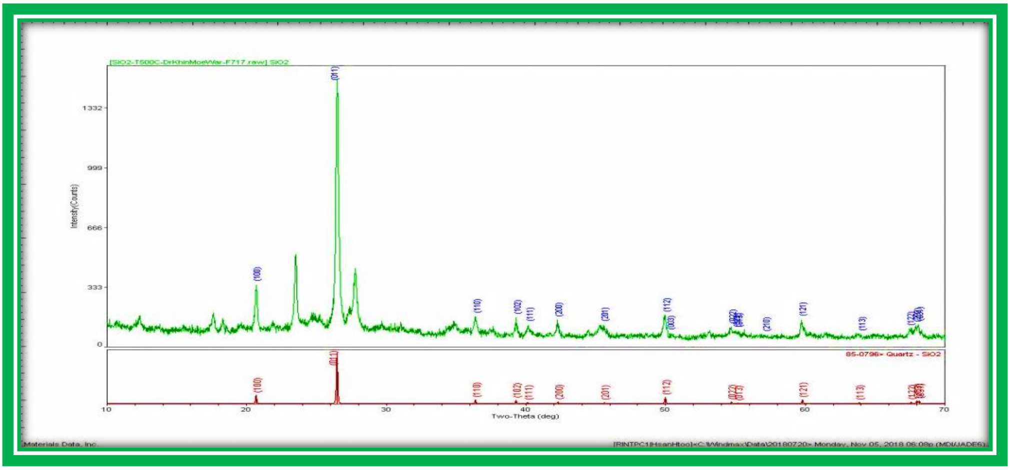

Figure16 : (a) XRD spectrum of mud at 500°C for 3 h

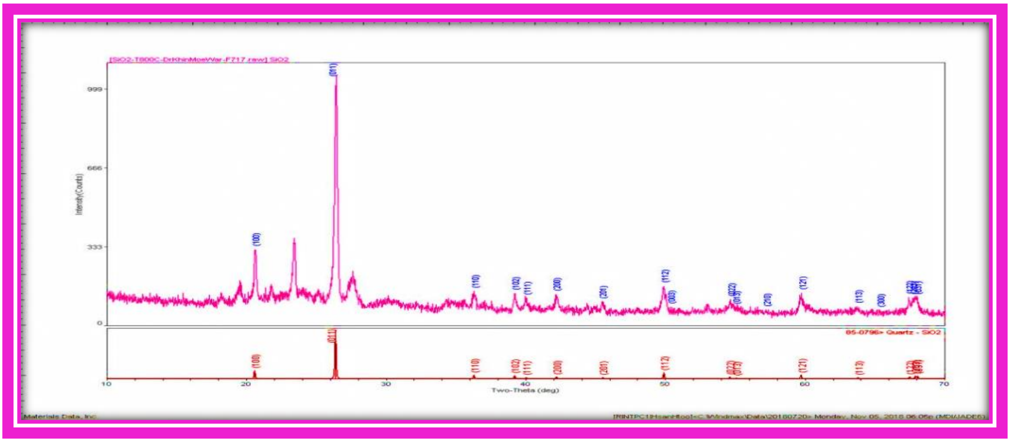

Figure16 : (b) XRD spectrum of mud at 800°C for 3 h

Table 4: The calculated values of crystallite sizes in annealed mud (500°C and 800°C)

Samples	**Temperature(°C)**	β	θ	cos θ	**D(nm)**
Mud	500	0.234	13.248	0.9733	348.77
	800	0.222	13.209	0.9735	367.566

Table 5: The comparison of crystallite sizes of raw mud, the annealed mud and fly ash

Samples	**β**	**θ**	**cos θ**	**D(nm)**
Raw mud	0.227	13.210	0.9735	359.48
Annealed mud (500°C)	0.234	13.248	0.9733	348.77
Annealed mud (800°C)	0.222	13.209	0.9735	367.566
Fly ash	0.229	13.201	0.9735	356.33

Conclusion

Analysis was carried out to explore the characteristic of mud of mud volcano as the potential benefits of the unstoppable mud flow. The EDXRF results showed that the chemical compositions of mud and fly ash and they had the major constituents of Si (75.98%) and (68.98%). It was found that mud contained higher amount silicon which is suitable to use as a raw material for production of cement. SEM analyzed the microstructure of the particles of mud and fly ash. The particles of mud were plate-like structure and the particles of fly ash were spherically-shaped and they all were different sizes. XRD analysis showed the mud was slightly towards higher than fly ash due to higher composition of SiO_2 in mud compared to fly ash. The crystalline size of ordinary mud and fly ash were nearly equal but that of the annealed mud (800°C) was larger than any other samples and the annealed mud

(500°C) was smaller the crystalline size of all samples. The lesser crystalline size was more suitable for replacing the fly ash. Therefore, The annealed temperature less than and equal 500 °C was the best to use. The FTIR peaks indicated the existence of Si-O-Si and H/OH bonding in original mud. Finding from this study shows that the mud of mud volcano has potential as a raw material in geopolymer system due to characteristic of mud which is comparable to the fly ash. Research will continue replacing the cement by mud for various methods and will continue to study how to relate the properties of compressive strength, will investigate the radon measurement.

Acknowledgements

I would like to thank Professor Dr Khin Khin Win, Head of Department of Physics, University of Yangon for her kind permission to carry out this research.

I also would like to thank Dr Aye Aye Thant, Professor, Department of Physics, University of Yangon, for her allowing me to do this work.

References

A. D. Buck, (1988). Evaluation of the Frost Resistance of Concrete Using Critical Dilation. Cement, Concretes and Aggregates, 10: pp. 48-50.

A. Palomo, A. M., M. T. Blanco, F. Puertas. (1992). Physical, chemical and mechanical characterization of geopolymers.

Cheng, T.-W. (2003). Fire resistant geopolymer produced by waste serpentine cutting. Paper presented at the Proceedings of the 7th International Symposium on East Asian ResourcesRecycling Technology, Taiwan.

Deacon GB, Phillips RJ (1980) Relationships between the carbonoxygen stretching frequencies of carboxylato complexes and the type of carboxylate coordination. Coord Chem Rev 33:227–250

J. Myanmar Acad. Arts Sci. 2019 **Vol. XVII. No.2A**

SYNTHESIS AND CHARACTERIZATION OF STRONTIUM STANNATE TITANATE THIN FILMS

May Kalayar Kyaing[1], Toe Toe Wai[2] , Saw Moh Moh Oo[3]
and Moht Moht Than[4]

Abstract

Strontium stannate titanate, $Sr(Sn_xTi_{1-x})O_3$ thin films on silicon substrates were successfully prepared by spin coating technique. The crystallographic properties of the films were analyzed by X-ray diffractometer and a cubic perovskite structure was found in all samples. The surface morphologies of the films were investigated using scanning electron microscope (SEM) and it was observed that fine grains with different sizes distributed the whole surface of the films. The dielectric constants as a function of applied electric field were calculated from capacitance-voltage measurements at the frequency range of 1 kHz to 100 kHz using LCR meter and the transition behavior was studied depend upon tin content.

Keywords: $Sr(Sn_xTi_{1-x})O_3$ thin films, SEM, XRD, dielectric constants

Introduction

Strontium titanate ($SrTiO_3$) with a cubic perovskite structure has been investigated intensively due to its unique dielectric and ferroelectric properties which are of great interest in the technological applications such as capacitors, actuators, and nonvolatile random-access memory devices. Strontium titanate (ST) has been of particular importance from the perspective of fundamental solid state physics, as well as in technological applications. Because of its good dielectric properties, it has become very usable in devices in integrated microelectronics and in memory storage. Also, the $SrTiO_3$ has gained additional practical importance as the most widely used substrate for depositing high–Tc superconducting films. As experiments on semitransparent samples are becoming more common, it is important to know the substrate dielectric function in order to correctly analyze the optical measurements performed on film plus the substrate system.

---

[1] Assistant Lecturer, Department of Physics, University of Yangon

[2] Assistant Lecturer, Department of Physics, University of Yangon

[3] Assistant Lecturer, Department of Physics, University of Yangon

[4] Lecturer, Department of Physics, University of Yangon

Doping is often used to change the dielectric properties of the strontium titanate that arise as a result of the incorporation of different cations is essential. It has been well documented that a small number of impurity ions can change the properties of this interesting system. The variation in the lattice parameters of tin doped strontium titanate thin films with change in dopant concentration may be attributed to the change in ionic radius. The ionic radii of Sr^{2+}, Ti^{4+} and Sn^{4+} are 1.12, 0.68 and 0.69 Å respectively. Hence the ionic radius of Sn^{4+} is approximately equal to that of Ti^{4+} and hence tin can be easily diffused into the lattice and may substitute on B site atom in ABO_3 perovskite structure. The increased value of lattice parameters indicates that tin ion substitutes the B site of ABO_3 structure.

In the present research, the influence of doping by the Sn ions on the dielectric properties of the SST thin films were examined by a frequency range of 1kHz to100kHz. The fabrication of high quality SST thin films with a high dielectric constant and low loss tangent is very important technological issue for practical frequency agile device and optical waveguide applications. In particular, non-linear dielectric and optical properties are suitable for application in the area of dynamic random access memory (DRAM) and optical waveguide applications. They are also used for frequency agile devices such as radio frequency (RF) switches, phase shifters, filters, delay lines, antennas and tunable microwave device applications.

Experimental Details

Tin doped strontium titanate, $Sr(Sn_xTi_{1-x})O_3$ thin films coated over silicon substrates with various dopant concentrations of (x= 0.1 to 0.3) were prepared by sol-gel method. Coating of solution onto the substrates was performed by spin coating at 3000 rpm for 30 sec. Coated layers were dried in order to remove the solvent. The three different films were annealed at 700˚C for 1 hr in a furnace to obtain crystallization. Scanning electron microscopy (SEM) were used to examine the surface grain morphologies of the strontium stannate titanate (SST) thin films. The phase and crystallinity of the films were characterized by X-ray diffraction (XRD) analysis with Cu-$K_{\propto 1}$ radiation. The dielectric constants as a function of applied electric field were calculated from capacitance-voltage measurements at the frequency range of 1 kHz to 100 kHz using LCR meter.

Results and Discussion

X-ray diffraction (XRD) analysis

X-ray diffraction pattern of tin doped strontium titanate thin films coated onto silicon substrates with various dopant concentrations are shown in Fig 1 (a-c). The characteristics peaks in the XRD patterns confirmed the presence of SST material and also indicated that all the films are well crystallized and cubic perovskite structure. The lattice parameters were slightly increased with the increasing of tin content. The variation in the lattice parameters of tin doped ST thin films with change in dopant concentration may be attributed to the change in ionic radius. The XRD patterns showed that the increased dopant concentration leads to decrease in intensity of diffraction peaks with preferred orientation at (110) planes. The crystallite size was calculated using Scherrer's formula,

$$D = \frac{0.9\lambda}{\beta\cos\theta}$$

The peak positions (2θ), intensity, full width half maximum, lattice parameters and crystallite sizes of all the films are listed in Table 1.

Morphology and Compositional analysis

The surface morphologies of the tin doped strontium titanate thin films were evaluated using SEM as shown in Fig 2 (a-c). These results showed a well-developed grain size and dense microstructure in all samples. Grain sizes of the samples are 0.45 μm, 0.67μm and 0.825 μm respectively. The average grain size increases with the increasing of tin content. The effect of doping on grain size is usually interpreted in terms of dopant solubility and distribution of doping ions between the surface and interior parts of the grain.

Dielectric Properties

The dielectric constants of strontium stannate titanate thin films were calculated from capacitance-voltage measurements at the frequency range of 1 kHz to 100 kHz. The dielectric constant varies with the applied voltage. The dielectric constant and dielectric loss of the films as function of applied voltage, Sn content and frequency are shown in Fig 3 (a-d). The maximum value of dielectric constant was occurred at the 10% tin doped strontium titanate thin film measured in a frequency range of 1 kHz. The dielectric constants of the films decrease with the increasing of dopant concentration and the results are listed in Table 2.

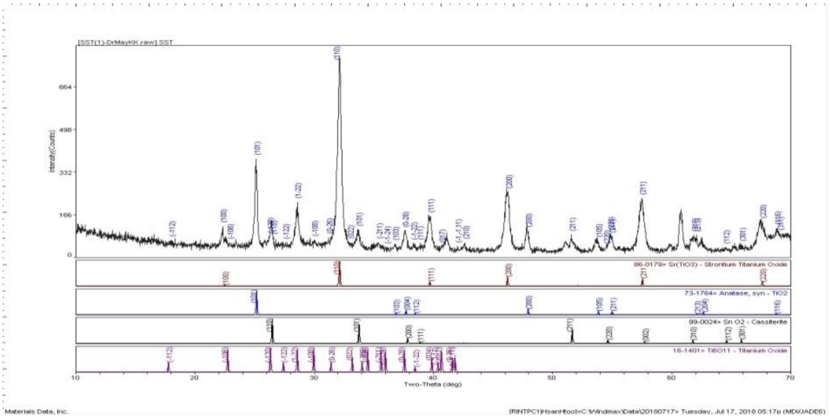

Figure1: (a) X-ray diffraction of 10% tin doped ST thin film

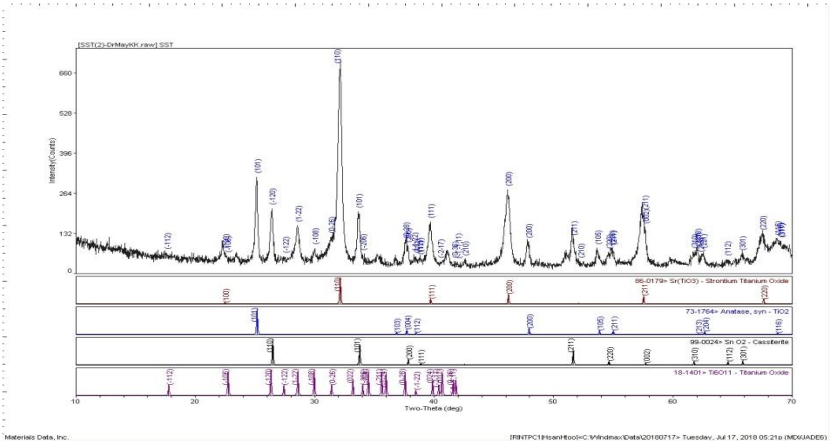

Figure 1: (b) X-ray diffraction of 20% tin doped ST thin film

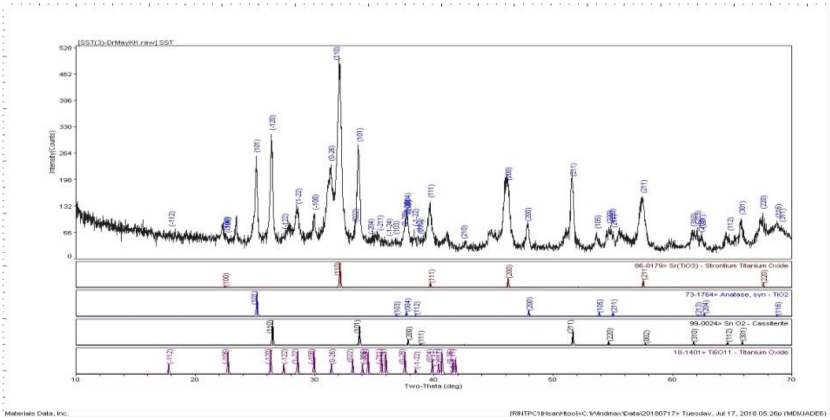

Figure 1: (c) X-ray diffraction of 30% tin doped ST thin film

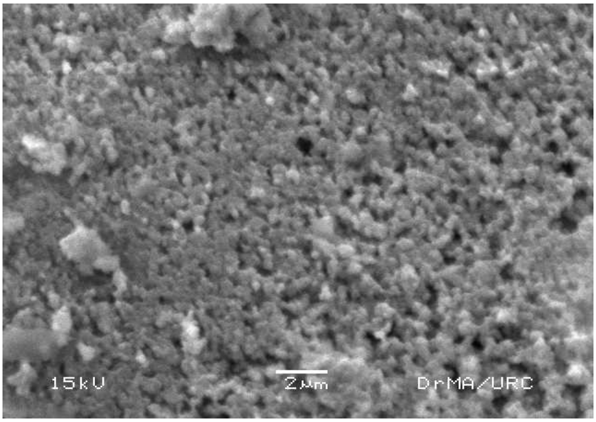

Figure 2: (a) SEM image of 10% tin doped ST thin film

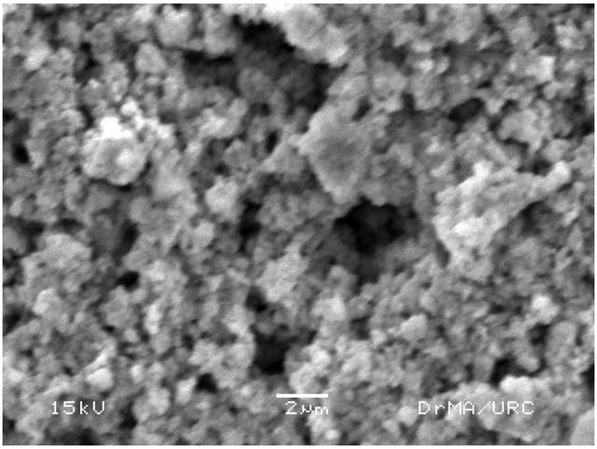

Figure 2: (b) SEM image of 20% tin doped ST thin film

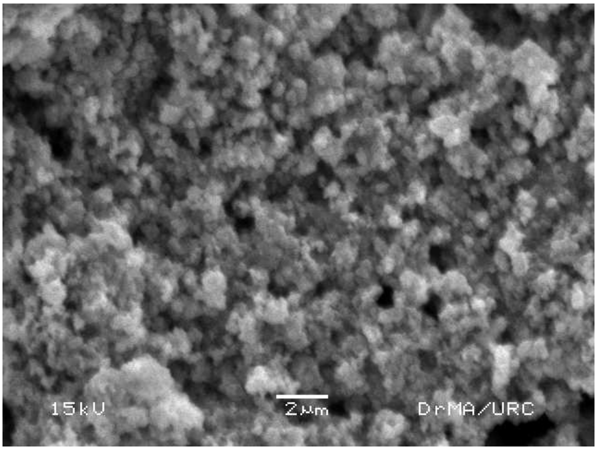

Figure 2: (c) SEM image of 30% tin doped ST thin film

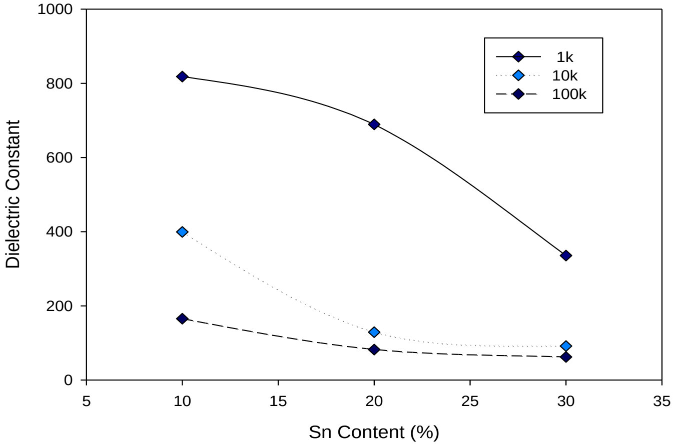

Figure 3: (a) The dielectric constant of three SST thin films as a function of tin content

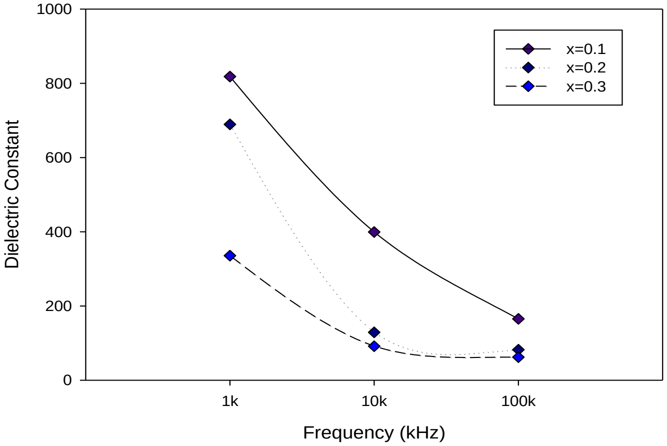

Figure 3: (b) The dielectric constant of three SST thin films as a function of frequency

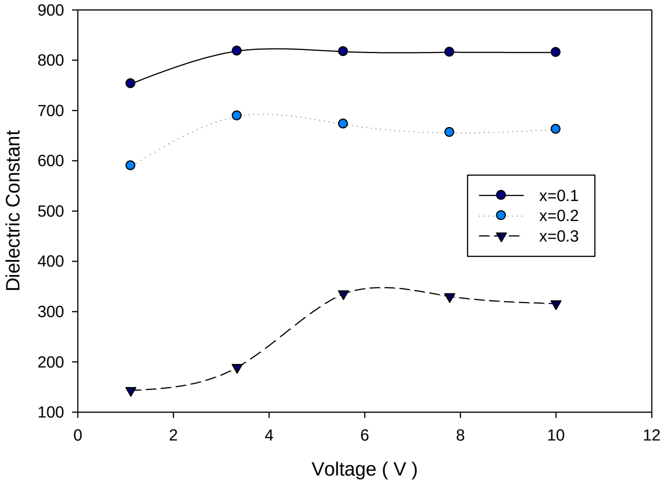

Figure 3: (c) The dielectric constant of three SST thin films as a function of applied voltage

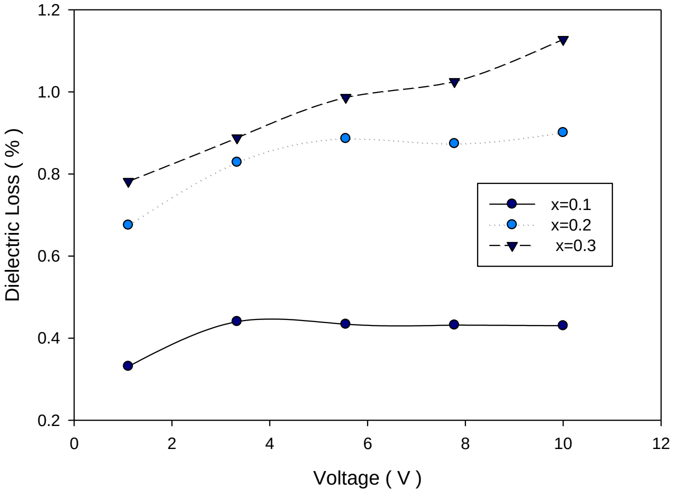

Figure 3: (d) The dielectric loss of three SST thin films as a function of applied voltage

Table 1: The peak positions (2□), intensity, full width half maximum (FWHM), lattice parameters (a) and crystallite sizes (D) of SST thin films

Thin Films	Peak positions (2□)	Intensity (cps)	FWHM	a (nm)	D(nm)
10% tin doped ST	32.135	724	0.368	3.935	22.467
20% tin doped ST	32.139	662	0.412	3.936	20.068
30% tin doped ST	32.074	463	0.392	3.943	21.088

Table 2: The values dielectric constant and dielectric loss of SST thin films

Thin Films	Dielectric constant	Dielectric loss (%)
10% tin doped ST	818.1279	0.4403
20% tin doped ST	689.1494	0.7891
30% tin doped ST	335.4931	0.9839

Conclusion

Strontium stannate titanate, SST thin films coated on silicon substrates with various dopant concentrations were prepared by sol-gel method. XRD patterns indicated that all the films are well crystallized and cubic perovskite structure. The lattice parameters were slightly increased with the increasing of tin content. SEM micrographs confirmed the crack free and uniform surface of the film. Grain sizes of the samples are in the range from 0.45μm to 0.825μm. The dielectric constant and dielectric loss of the films changed with different concentrations of tin. The maximum value of dielectric constant was occurred at the 10% tin doped strontium titanate thin film measured in a frequency range of 1 kHz. The polarization of the material is directly proportional to the dielectric constant of the material. Therefore, it is believed that tin doped strontium titanate thin films having high dielectric properties are good candidate materials for memory device applications.

Acknowledgements

The authors sincerely thank Professor Dr Khin Khin Win, Head of Department of Physics, University of Yangon, for her kind permission to carry out this research. We are grateful to Professor Dr Aye Aye Thant, Department of Physics, University of Yangon, for her permission to this paper.

References

Eswaramoorthi, V. and Victor Williams, R., (2015) "Structural and Electrical behavior of Tin Doped $Ba_{0.6}Sr_{0.4}TiO_3$ Thin Films," *International Journal of Development Research*, 5, 5725 – 5732

F. M. Pontes et al., (2000), "High dielectric constant of $SrTiO_3$ thin films prepared by chemical process," *Journal of Material Science*, 35, 4783 - 4787

Jae-Yeol Hwang et al., (2006) " Dielectric Properties of Artificially Textured $(Ba_{0.5}Sr_{0.5})TiO_3$ Thin Film Prepared by Pulsed Laser Deposition," *Journal of the Korean Physical Society*," 49, 447- 696

Malic, B. et al., (2007) "Processing and dielectric characterization of $Ba_{0.3}Sr_{0.7}TiO_3$ Thin Films" *Journal of the European Ceramic Society*, 27, 2945-2948

Mascot, M., Fasquelle, D. and Carru, J. C. (2011), "Very high tunability of $BaSn_xTi_{1-x}O_3$ ferroelectric thin films deposited by sol-gel," *Functional Materials Letters*, 4, 49-52

T. Bongkran and W. Khiawwangthong, (2008) " The Preparation of Barium Stannate Titanate Ceramics via Solid State Reaction Method," *Advanced Materials Research*, 57, 181-184

Xiaoyong Wei and Xi Yao, (2007) "Preparation, structure and dielectric property of barium stannate titanate ceramics," *Materials Science and Engineering B*, 137, 184-188

J. Myanmar Acad. Arts Sci. 2019 **Vol. XVII. No.2A**

MICROSTRUCTURE AND STRUCTURAL PROPERTIES OF (Cu, Al, In) DOPED SnO_2 THIN FILMS DEPOSITED BY SPIN COATING METHOD

Ohn Mar Swe[1]and Moht Moht Than[2]

Abstract

The effect of Cu,Al and In doping on the microstructural and structural properties of the SnO_2 thin films were studied. The undoped, Cu, Al and In (5 mol%) dopedSnO^2 thin films were deposited on glass substrates by sol-gel and spin coating technique. The microstructure properties of the samples were investigated by X-ray diffraction (XRD) method. It was determined that the samples formed at polycrystalline structure in tetragonal phase and structure was not changed by doping materials. The surface morphology of the samples were investigated by scanning electron microscopy (SEM). The lattice parameters, unit cell volume, crystallite size and grain size were determined.

Keywords: Tetragonal type thin films, Sol-gel process, XRD, SEM

Introduction

Tin dioxide (SnO_2) has been intensively investigated because of its rich physical properties and large applications in commercial devices. The SnO_2 with a wide-band-gap(Eg=3.6-4.0eV) is one of the excellent semiconductors which can be applied to solid state gas sensors, sensing arrays, solar cells, photovoltaic cells, organic light emitting diodes, touch sensitive screens and thin film transistors.[Bagheri Mohaghegi M M ef al (2008), Bagheri Mohagheghi MM et al 2008,Khan AF et al (2010),Khan Af et al 2010,Moharrami F et al (2012]. The SnO_2 thin films can be fabricated by a number of techniques such as chemical vapour deposition (CVD), metalorganic deposition, rf sputtering, sol-gel dip coating, spin coating and spray pyrolysis. [Maekava T et al (2001) , Yin LT et al (2000), Yin LT et al (2000), Ouerfelli J et al (2008).] It was clearly established spin coating that structural, electronic transport and optical properties of SnO_2 films are very sensitive to preparation method, deposition conditions, dopant atoms and amount of dopant atoms.

---

[1] Dr , Lecturer, Department of Physics, University of Yangon.

[2] Dr, Lecturer, Department of Physics, University of Yangon

Experimental

The glass substrates were ultrasonically cleaned by keeping in ethanol and in the distilled water, for ten minutes, respectively. Then the glass substrates were dried. Then the glass substrates were dried. The films were deposited on the glass substrates by spin coating technique. In order to prepare the coating solution, firstly, Cu,Al and In (5 mol%) doped SnO_2 powder mixed by conventional stoichiometric composition. The mixture powder is ground by agate mortor to obtain the homogeneous and uniform grain size of powder. This powder is heat treated at 500° C for 1 hr. The crystalline powder, were mixed with 2-methoxgethanol solution by using sol-gel method. And then these pastes were coated on glass substrates and annealed at 400°C for 1 hr, respectively.

Results and Discussion

The XRD patterns of undoped and Cu, Al, In doped SnO_2 films are shown in Fig.1(a~d). The films deposited showed four peaks namely (110), (101),(200) and (211). Since all the peaks are sharp it is evident that the films deposited are polycrystalline in nature and the positions of X-ray diffraction peaks fit well with the tetragonal structure of SnO_2 (JCPDS Card tin oxide, 72-1147), As seen from fig 1 (a~d), the preferred orientation is (101) plane for undoped SnO_2 film. The addition of Cu, Al and In atoms do not affect the preferred orientation along (101) plane and crystal structure. The dopants form extra peaks in the XRD pattern of doped SnO_2 films because dopant atoms do not incorporated homogeneously into the tin oxide matrix.

The lattice constants a and c for the tetragonal phase structure are determined by the relation

$$\frac{1}{d^2} = \left(\frac{h^2}{a^2} + \frac{k^2}{a^2}\right) + \left(\frac{l^2}{c^2}\right)$$

where d and (hkl) are the interplanar distance and Miller indices, respectively. The calculated lattice constants a, c and c/a vlues are given in Table (1).

Table 1: Lattice parameters and crystallite size values of SnO_2 films prepared for various dopant atoms.

Doping Atom	a ($\dot{A}$)	b ($\dot{A}$)	c/a	D (nm)	V $(nm)^3$
Undoped	4.7630	3.1903	0.67	31.6339	0.0725
Cu	4.7467	3.1911	0.67	31.6887	0.0719
AI	4.7629	3.1913	0.67	31.0877	0.0721
In	4.7548	3.1893	0.67	28.7258	0.0721

Fig(2). (a) to (d) SEM micrograph of undoped, Cu, Al and In (5mol%) doped thin film. from the SEM images, it can be seen that the particles are in fairly dense, and crack-free. The estimated grain size are listed in Table(2).

Table 2: The values of SnO_2 films prepared for various dopant atoms.

Doping Atom	Grain Size (m)
Undoped	0.6818×10^{-6}
Cu	0.5740×10^{-6}
Al	0.5545×10^{-6}
In	0.6060×10^{-6}

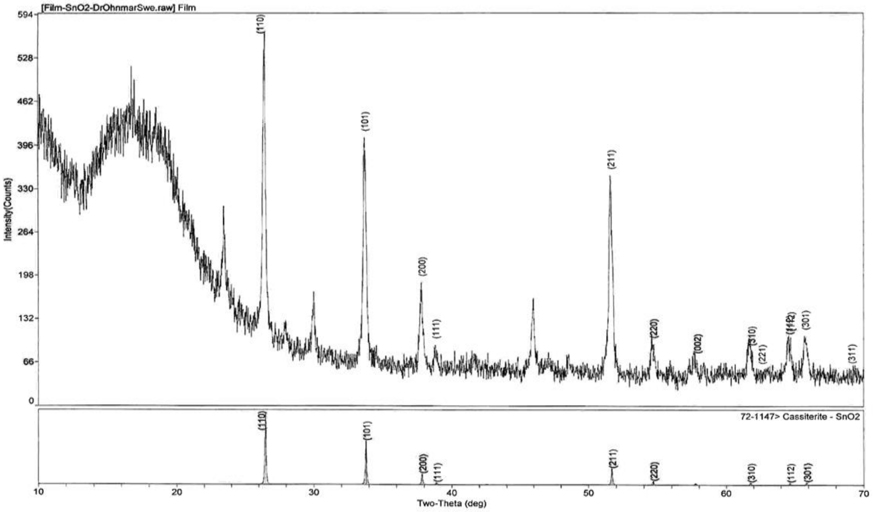

Figure 1:(a). The diffraction peak of undopedSnO_2 film

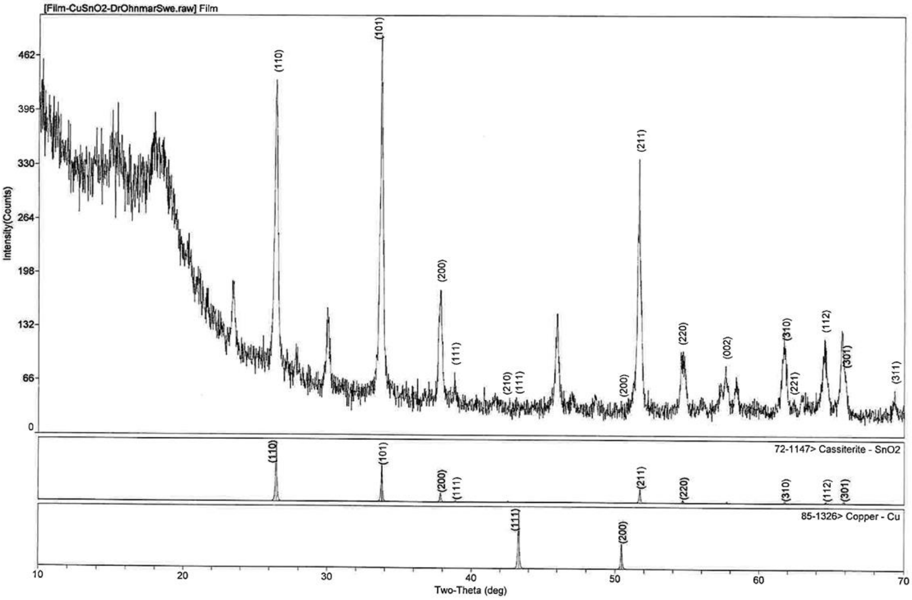

Figure 1:(b). The diffraction peak of Cu doped SnO_2 film

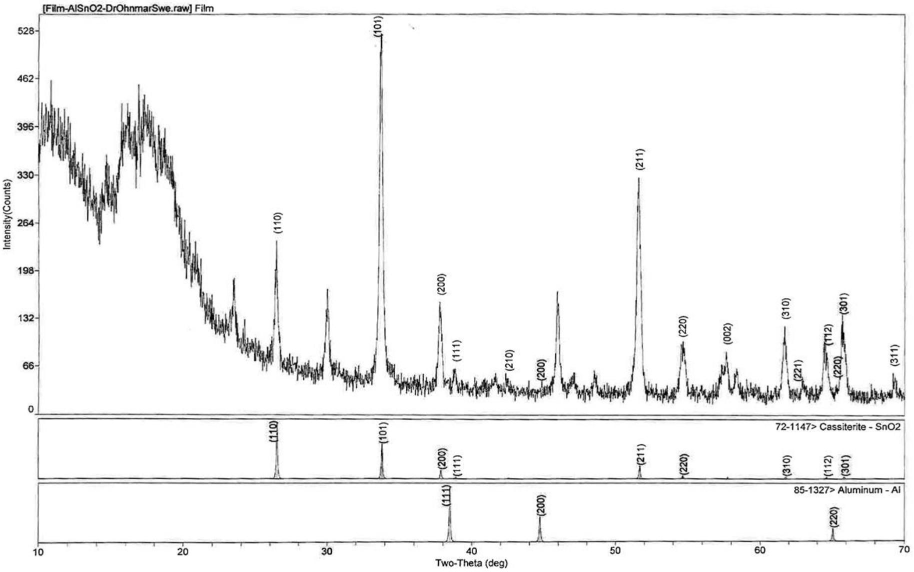

Figure 1: (c). The diffraction peak of Al doped SnO_2 film

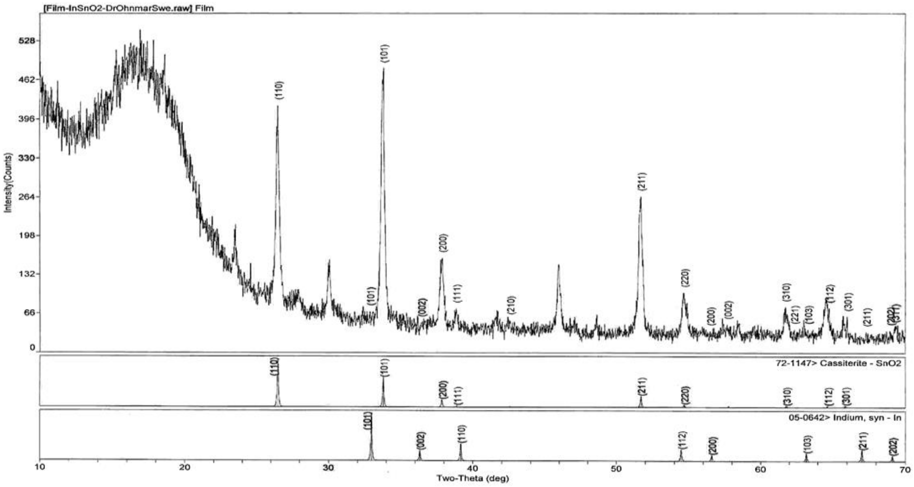

Figure 1: (d). The diffraction peak of In doped SnO_2 film

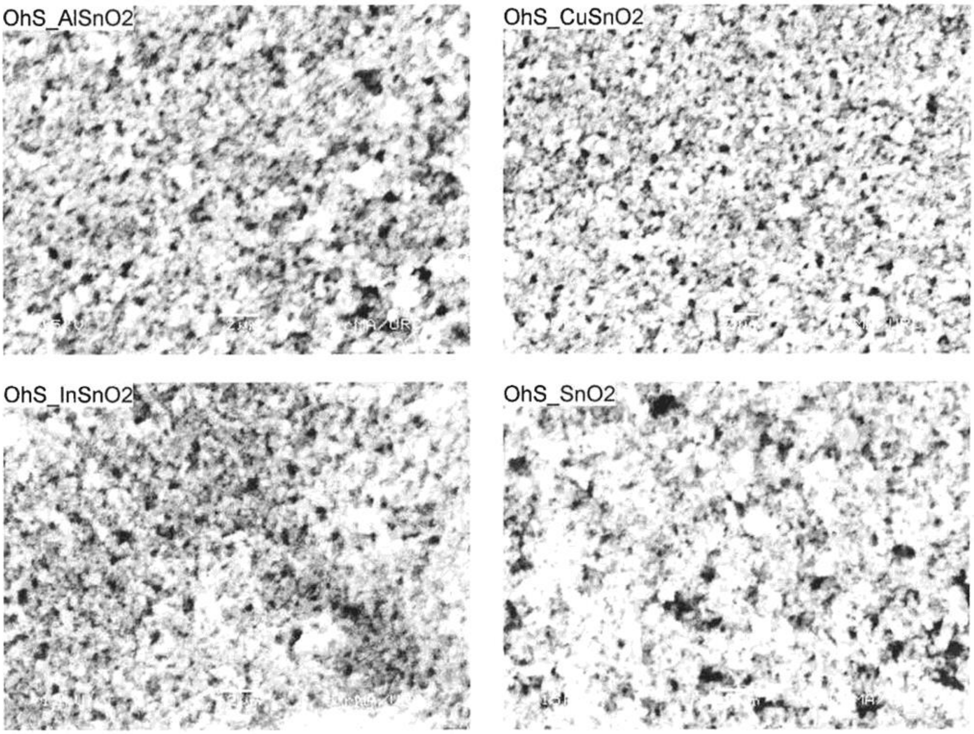

Figure2: The Scanning electron micrograph of undoped, Cu, Al, In doped SnO_2 film

Conclusion

In this study it was concluded that the kind of dopant atoms dit not change the structure of undoped and Cu, Al and In doped SnO_2 films grown by spin coating technique. The orientation of the films was along the (101) plane. The films were polycrystalline in nature and had tetragonal structure. The ratio of lattice parameters (c/a) was found as 0.67. The crystallite size of the films calculated from XRD depending on the kind of dopant atoms.

Acknowledgements

I wish to express my sincere thanks to Professor Dr Khin Khin Win, Head of Department of Physics, University of Yangon, for her kind permission to carry out this research.

References

Agashe C et al (2009); Solar Energy Materials and Solar Cells 93, P 1256-1253

Bagheri Mohaghegi M M ef al (2008) Physica B 403, P2431-2437

Khan AF et al (2010); Applied Surface Science 256, P2252-2258,

Kikuchi N et al (2002); Vacuum, 66 P 365-371

Moharrami F et al (2012); Solid films, 520, P -6503-6509

Maekava T et al (2001); Sensors and Actuators, B 80, P 51-58

Ouerfelli J et al (2008); Materals Chemistry and Physics, 112, P 198-201

Rani S et al (2007; Sensors and Actuators, B 122, P204-210

Yin LT et al (2000); Sensors and Actuators, B 71, P 106-111)

J. Myanmar Acad. Arts Sci. 2019 **Vol. XVII. No.2A**

RADON DETERMINATION FOR BASEMENT OF BUILDING BY USING SOLID STATE NUCLEAR TRACK DETECTOR

Shwe Nan Htet[1], and Cho Cho Aung[2]

Abstract

Determination of radon in basement of building was carried out by using LR 115 Type II solid state nuclear track detector with exposure period of 100 days during rainy season, winter and summer. The detectors were placed about 2.4 m from the floor at the five concrete tiles in the basement of selected building. After exposure, the detectors were etched in a NaOH solution of 2.5 N at temperature of 60°C for 90 min. Optical microscope NIKON ECLIPSE 50i was used to count the number of tracks on the detector. It was observed that track density of samples ranged from 7.80 ± 0.49 to 16.51 ± 0.91 C/cm^2 day^{-1} in rainy reason, 5.48 ± 0.33 to 8.79 ± 0.54 C/cm^2 day^{-1} in winter and 6.88 ± 0.41 to 14.73 ± 0.74 C/cm^2 day^{-1} in summer. Radon concentration values were found to vary from 155 ± 9.73 to 329 ± 18.14 Bqm^{-3} with a mean value of 239.4 ± 12.35 Bqm^{-3} in rainy season, 109 ± 6.51 to 175 ± 10.71 Bqm^{-3} with a mean value of 139.6 ± 8.79 Bqm^{-3} in winter and 137 ± 8.25 to 294 ± 14.72 Bqm^{-3} with a mean value of 181.80 ± 10.60 Bqm^{-3} in summer. The overall radon concentration varied from 109 ± 6.51 to 329 ± 18.14 Bqm^{-3} with an average of 186.80 ± 10.58 Bqm^{-3} and the annual effective dose varied from 1.88 ± 0.11 to 5.66 ± 0.31 mSv/yr with the average value of 3.22 ± 0.18 mSv/yr in basement of selected tower for rainy season, winter and summer. The value of radon concentration and the annual effective dose in basement of selected building for rainy season, winter and summer were within the reference levels (200–600 Bqm^{-3} and 3–10 mSv/y) of International Commission of Radiological Protection (ICRP).

Keywords: Radon concentration, Annual effective dose, LR-115 type II SSNTDs

Introduction

Radon is a chemical element with symbol Rn and atomic number 86. It is a radioactive, colorless, odorless, tasteless, noble gas, occurring naturally as a decay product of radium-226, which is found in uranium ores, phosphate rock, shale, igneous and metamorphic rocks such as granite, gneiss, and schist, and in common rocks such as limestone. Its most stable isotope, ^{222}Rn, has a

---

[1] Dr, Lecturer, Department of Physics, University of Yangon

[2] Associate Professor, Department of Physics, University of Yangon

half-life of 3.8 days. Radon gas produced by natural sources can be accumulated in buildings, especially in confined areas such as basements or lowest levels of homes. The concentration of radon in buildings depends on house construction type, soil characteristics, ventilation rate, wind direction, atmospheric pressure, humidity, temperature and even the life style of people. Radon concentration inside the buildings varies from season to season, and from month to month and from day to day until between day and night.

Experimental Procedure

Data Collection

LR 115 Type II solid state nuclear track detector, SSNTD (1.5cm ×1.5cm) was hang with the string at the five concrete tiles in the basement of selected building for summer, rainy season and winter through 100 days illustrated in Figure 1. The height of detectors was kept about 2.4 m from the floor.

Figure 1: Sample at concrete tiles inside the basement of selected building near Kamayut Township

Etching of Detectors

The etching process of radon exposed detectors was performed at Nuclear Laboratory, Department of Physics, University of Yangon. 10 g of NaOH granular was firstly weighed with filter paper using weight balance and 100 ml of measuring cylinder was filled 100ml of distilled water. Both of them were put into the 250 ml glass beaker and stirred with glass rod until NaOH granular were completely dissolved in distilled water. The beaker with 2.5 N NaOH solution was heated on a stove with temperature controller. When the temperature reached at 60°C, the radon exposed LR- 115 detector was put into the beaker for 90 minutes. During etching, the temperature was kept constant with accuracy of ± 1°C and without stirring. After etching, the detector was washed under the running water until the surface of the detector became cleaned from etchant. Finally, the detectors were taken out and dried with filter paper.

Track Counting and Track Density

The track counting of radon exposure detectors were performed by using Optical microscope (10X magnification).The number of tracks were counted view by view changing vertical and horizontal position of detector under the microscope. Then average track density was calculated from the equation:

$$\text{Alpha Average Track Density} = \frac{\text{Average alpha Tracts}}{\text{Microscopic View Area} \times \text{Exposure Time}}$$

Calculation of Radon Concentration and Annual Effective Dose

The radon concentration and annual effective dose can be calculated from the data of average alpha track counts. The calculations are based on the following conversion factor:

$$1\text{Bq/m}^3 = 0.05016\ \text{track/cm}^2\text{/day}$$

$$1\text{Bq/m}^3 = 0.0172\ \text{mSv/yr} \qquad \text{(ICRP, 2007)}$$

Results and Discussion

The alpha tracks photograph of LR 115 type II detector which were placed in the basement of selected building for rainy season, winter and summer were shown in Figure 2 (a), (b) and (c).Table 1 illustrated the average alpha tracks, track density, radon concentration and annual effective dose in the basement of tower for rainy season, winter and summer. The average track density produced by radon, average radon concentration and average annual effective dose in basement were plotted in Figure 3 to Figure 6. It was found that the average alpha track varied from 6.12 ± 0.38 to 12.96 ± 0.71 in rainy season, 4.3 ± 0.26 to 6.9 ± 0.42 in winter and 5.4 ± 0.33 to 11.56 ± 0.58 in summer. Track density of samples ranged from 7.80 ±0.49 to 16.51 ± 0.91 C/cm^2 day in rainy season, 5.48 ± 0.33 to 8.79 ± 0.54 C/cm^2 day in winter and 6.88 ± 0.41to 14.73 ± 0.74 C/cm^2 day in summer. Radon concentration values were found to vary from 155 ± 9.73 to 329 ± 18.14 Bqm^{-3} with a mean value of 239.4 ± 12.35 Bqm^{-3} in rainy season, 109 ± 6.51 to 175 ± 10.71 Bqm^{-3} with a mean value of 139.6 ± 8.79 Bqm^{-3} in winter and 137 ± 8.25 to 294 ± 14.72 Bqm^{-3} with a mean value of 181.8 ± 10.60 Bqm^{-3} in summer. The radon concentration of samples in rainy season were greater than that in other two seasons except sample 2 because there was humidity in basement environment of selected building. The radon concentration in winter was lower than that in summer because of ventilation rate in basement. It was clearly seen that the value of average alpha track, track density due to radon, radon concentration and annual effective dose were changed with season because of daily temperature, humidity, poor ventilation, darkness, and pressure values during the measurements in basements of building.

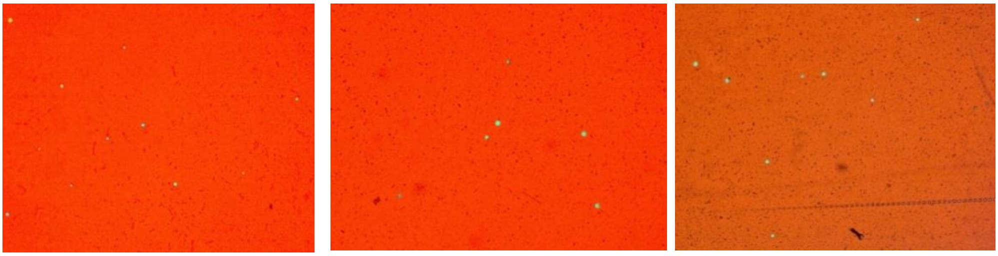

(a) (b) (c)

Figure 2: The photograph of alpha tracks in Samples for the basement of building for (a) rainy season (b) winter and (c) summer

Table 1: Average alpha tracks, track density, radon concentration and annual effective dose of LR 115 from the basement of building for rainy season, winter and summer

		Sample 1	**Sample 2**	**Sample 3**	**Sample 4**	**Sample 5**	**Average**
Average Alpha Tracks	rainy season	12.96 ± 0.17	6.58 ±0.30	11.64 ± 0.56	6.12 ±0.38	9.84 ±0.47	9.43 ±0.38
	winter	4.30 ± 0.26	6.90 ± 0.42	5.20 ± 0.40	5.58 ±0.36	5.52 ± 0.29	5.50 ±0.35
	summer	11.56 ± 0.58	6.96 ± 0.41	5.40 ± 0.33	5.72 ±0.27	6.14 ± 0.40	7.16 ±0.40
Track Density (C/cm^2 day)	rainy season	16.51 ± 0.91	8.38 ± 0.38	14.83 ±0.71	7.80 ±0.49	12.54 ±0.60	12.01 ±0.62
	winter	5.48 ±0.33	8.79 ±0.54	6.62 ±0.51	7.11 ±0.46	7.03 ±0.36	7.01 ±0.44
	summer	14.73 ±0.74	8.87 ±0.52	6.88 ±0.41	7.29 ±0.48	7.82 ±0.50	9.12 ±0.53
Radon Concentration (Bqm^{-3})	rainy season	329 ±18.14	167 ±7.61	296 ±14.22	155 ±9.73	250 ±12.05	239 ±12.35
	winter	109 ±6.51	175 ±10.71	132 ±10.26	142 ±9.26	140 ±7.30	139.6 ±8.81
	summer	294 ±14.72	177 ±10.33	137 ±8.25	145 ±9.61	156 ±10.11	181.80 ±10.60
Annual Effective Dose (mSv/yr)	rainy season	5.66 ±0.31	2.87 ±0.13	5.08 ±0.25	2.67 ±0.17	4.30 ±0.21	4.12 ±0.21
	winter	1.88 ±0.11	3.01 ±0.18	2.27 ±0.18	2.44 ±0.16	2.41 ±0.12	2.40 ±0.15
	summer	5.05 ±0.25	3.04 ±0.18	2.36 ±0.14	2.50 ±0.17	2.68 ±0.17	3.13 ±0.18

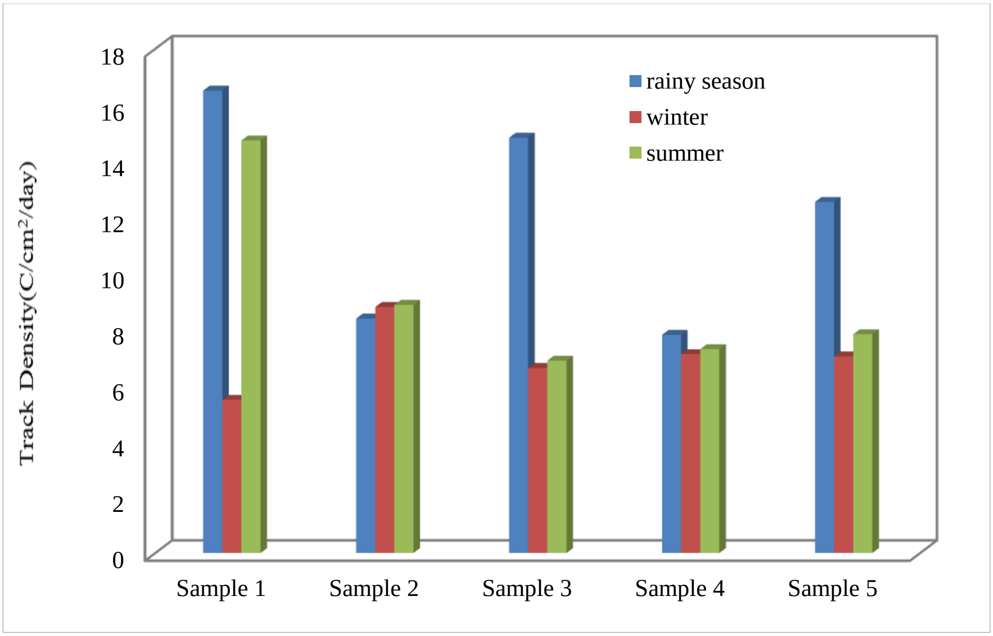

Figure 3: Track density in basement of building with three seasons

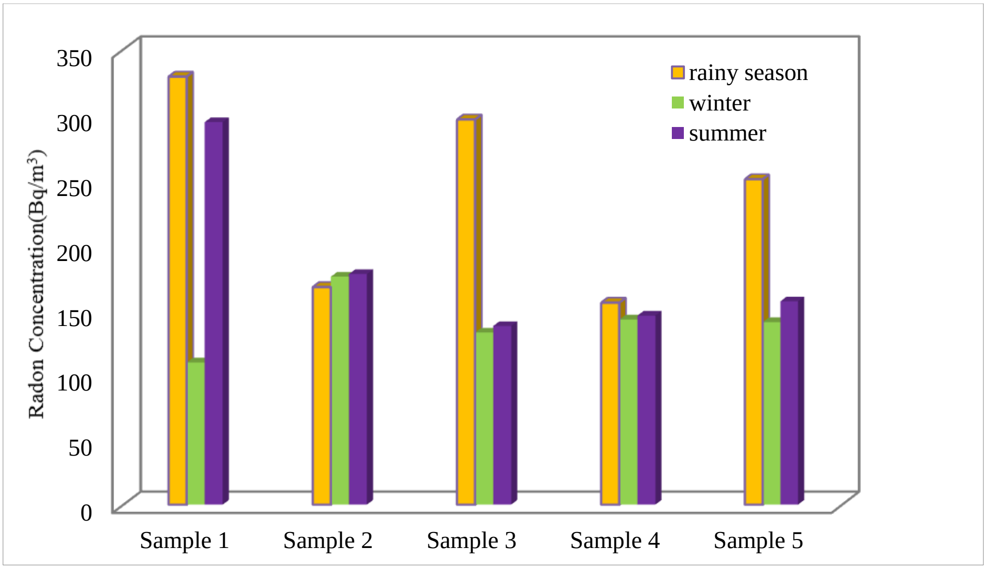

Figure 4: Radon concentration in basement of building with three seasons

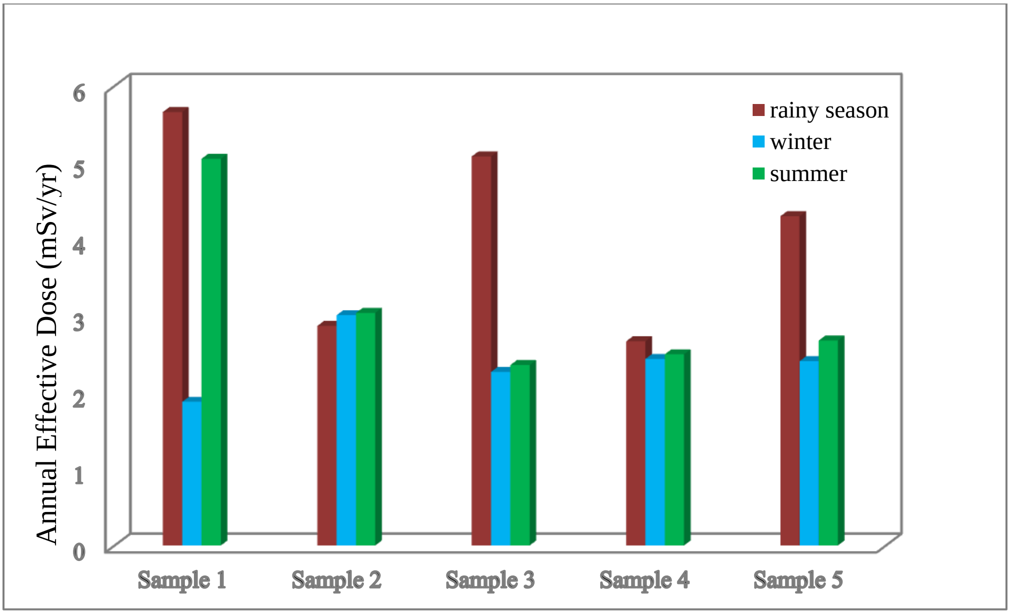

Figure 5: Annual effective dose in basement of building with three seasons

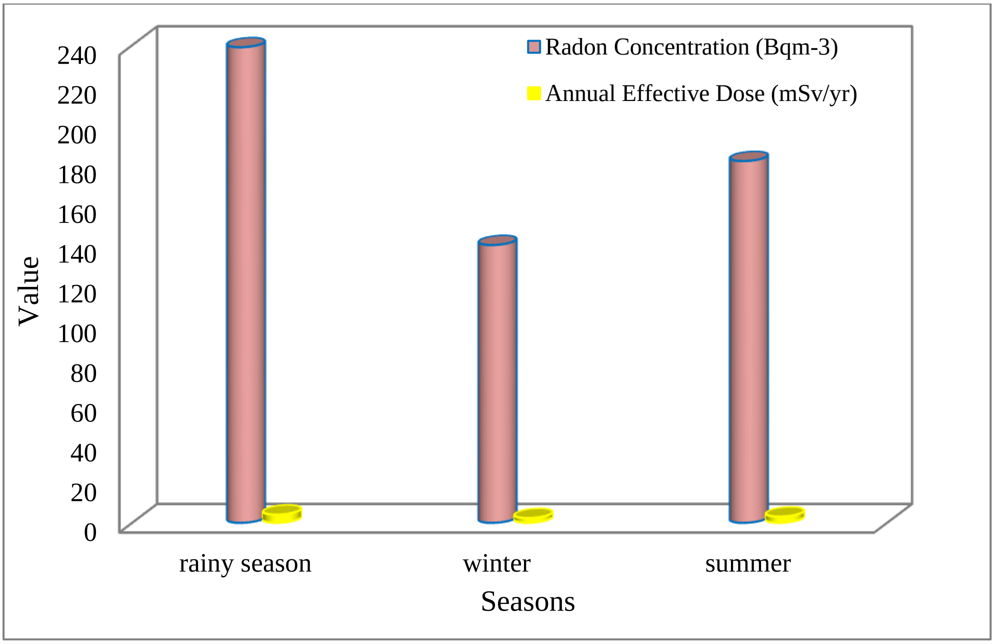

Figure 6: Average radon concentration and Average annual effective dose in basement of building with three seasons

Conclusion

Radon (^{222}Rn) concentrations was measured in basement of building by using solid state nuclear track detectors with exposure period of 100 days in rainy season, winter and summer. The overall radon concentration varied from 109 ± 6.51 to 329 ± 18.14 Bqm^{-3} with an average of 186.80 ± 10.58 Bqm^{-3} and the annual effective dose varied from 1.88 ± 0.11 to 5.66 ± 0.31 mSv/yr with the average value of 3.22 ± 0.18 mSv/yr in basement of selected tower for rainy, winter and summer. Radon levels were found to be seasonal dependent. The average values of concentration of radon and average annual effective dose of radon in basement of tower were within the reference levels (200–600 Bq/m^3 and 3 – 10 mSv/y) of International Commission of Radiological Protection (ICRP). The average value of overall radon concentration and the annual effective dose were lower than the reference levels (200 – 600 Bq/m^3 and 3 – 10 mSv/y) of International Commission of Radiological Protection (ICRP). Thus, seasonal variation was affected radon level in basement of the building but there was no radiological hazards for human beings.

Acknowledgements

I am highly grateful thanks to Professor Dr Khin Khin Win, Head of Department of Physics, University of Yangon for her permission to do and her encouragement throughout this paper.

I also would like to thank Professor Dr Aye Aye Thant, Department of Physics, University of Yangon for her valuable suggestions.

References

BEIR IV *Health Risks of Radon and other Internally Deposited Alpha-Emitters.* National Academy Press, Washington D.C., 1988, pp 602.

E. Dorn, *Über die von radioaktiven substanzen ausgesandte emanation.* Abhandlungen der Naturforschenden Gesellschaft zu Halle (Stuttgart) 22, 155, (1900).

Haque, A.K.M.M. and A.J.L. Collinson, 1967, "Radiation dose to the respiratory system due to radon and its daughter products," Health Phys. 13:431-443.

I. Othman and M. Mahroma, Radionuclides content in some building materials in Syria. Radiation Protection Dosimetry 55/4, 299-304 (1994).

International Agency for Research on Cancer. *Man-made mineral fibres and radon.* IARC Monographs on the Evaluation of Carcinogenic Risks to Humans, 43, IARC, Lyon (1988).

J. Myanmar Acad. Arts Sci. 2019 **Vol. XVII. No.2A**

AUTOMATIC SOLAR TRACKING SYSTEM USING PILOT PANEL

Khaing May Win[1], Than Htike Win[2], and Aye Aye Thant[3]

Abstract

Solar tracker is an automated solar panel that can effectively improve energy efficiency of a solar photovoltaic (PV) panel. The solar panel are intended to follow and track the direction of the highest light intensity from the sun. Development of dual axis solar tracker involves design implementation and software description for the control program. Arduino UNO, DC gear motors and light dependent resistors (LDRs) have been mainly used in the system. The L298N driver has been used to drive DC motors for making the direction and speed decisions of motors. The tracker's control algorithm has been implemented via A Tmega 328p microcontroller on a simple and cheap mechanical structure. The hardware design has been implemented in order to provide high efficiency from the solar PV panel in this work. The movement of dual axis solar panel has been controlled by using the difference of light intensity values from four sensors. The test result has confirmed that the solar panel is controlled by the program to be normal to the sun all the day time in order to provide the maximum energy efficiency. The system can be applicable to receive the maximum energy efficiency from the solar panel all the year around.

Keywords: Arduino, LDR, photovoltaic, solar tracker, microcontroller

Introduction

Global energy consumption is dramatically increasing due to higher standard of living and the increasing world population. The world has limited fossil and oil resources. Solar tracking system is the most immediate and technologically attractive use of solar energy. Solar energy is one of the primary sources of clean, abundant and inexhaustible energy that not only provides alternative energy resources, but also improves environmental pollution. Solar energy is the potential source to be the major energy supply for the future. The sun's position in the sky varies with equipment over any fixed position. If PV systems are built at fixed position, they cannot track the sun. Solar tracker is an automated solar panel that follows the Sun to increase the generated maximum power.

---

[1] Demonstrator, Department of Physics, Sagaing University

[2] Assistant Lecturer, Department of Physics, University of Yangon

[3] Prof., Department of Physics, University of Yangon

Different mechanisms are applied to increase the efficiency of the solar cell to reduce the cost. Solar tracking is the most appropriate technology to enhance the electricity production of a PV system. The orientation of the solar panels may increase the efficiency of the conversion system from 20% up to 50%.

Mechanism of Solar Tracking System

The sun tracking solar power system is a mechatronic system that integrates electrical and mechanical systems, and computer hardware and software. Generally, solar tracking system can be classified as either open-loop tracking types based on solar movement mathematical models or closed-loop tracking types using sensor-based feedback controllers. In the open-loop tracking approach, a tracking formula or control algorithm is used. The control algorithms are executed in a microprocessor controller. This system always involves complex tracking strategies using microprocessor chips as a control platform. In the closed-loop tracking approach, various active sensor devices, such as charge-coupled devices (CCDs) or light dependent resistors (LDRs) have been utilized to sense the Sun's position and a feedback error signal can be generated to the control system to continuously receive the maximum solar radiation on the PV panel.

Design implementation is essential in dual-axis solar tracker. It needs more complex technology and necessary moving parts than single axis solar tracker and fixed panel. By utilizing dual-axis solar tracker, the energy manufacturing is at an optimum and energy output is enhanced year round as the sun's position in the sky will alter gradually during a day and over the seasons throughout the year. Based on this background, solar tracking system has been implemented with the major components of Arduino Uno, DC motors and light dependent resistors (LDRs) in this research.

Development of Automatic Dual Axis Solar Tracker

The developed dual-axis solar tracker consists of 20W solar panel, two DC gear motors, Arduino UNO board as the main components. Arduino UNO microcontroller board and Arduino programming language are mainly used to control the whole circuit. Each of four sensors is connected to the input pins of Arduino UNO board; A0, A1, A2 and A3 respectively. The different values of input data from the sensor are read and calculated by Arduino microcontroller. By comparing these results, the microcontroller determines the highest intensity value and then controls the direction, position and speed of two DC gear motors for altitude and azimuth angles by using a L298N motor driver. A 12 V battery is used to charge the whole circuit (microcontroller and motors). But Arduino UNO can work with 5 V that is output power of L298N motor driver. Liquid crystal display (LCD) displays the direction of solar PV panel by the program. Block diagram of automatic solar tracking system is shown in Figure 1.

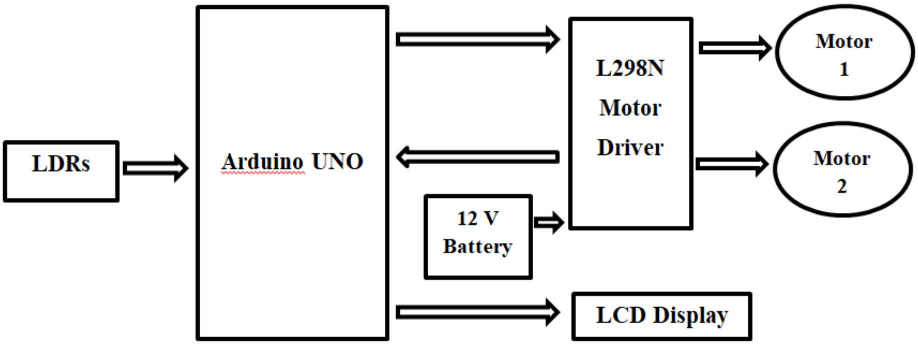

Figure 1: Block diagram of automatic solar tracking system

Function of Light Sensing Circuit

The light sensing circuit uses four LDRs for measuring the light intensity from the sun. Light intensity values from light sensing circuit have been read by the microcontroller and The LDR gives out an analog signal, which is directly proportional to the input light intensity on it. That is, the greater the intensity of light from the LDR, the greater the corresponding voltage will be. Since the LDR gives out an analog voltage, it is connected to the analog input pin of the Arduino. The Arduino, with its built-in ADC (Analog to Digital Converter), then converts the analog voltage (from 0-5 V) into a digital value in the range of (0-1023). Light sensing circuit is assembled as shown in Figure 2.

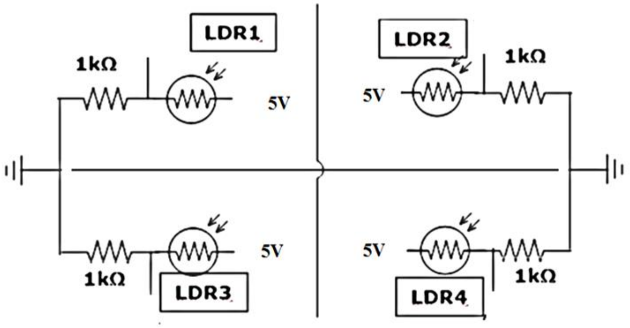

Figure 2: Light sensing circuit diagram

Reading Light Intensities from Light Dependent Resistors

It is investigated that the light intensity values are slightly different under the same light condition although almost the same size LDRs and same resistance valued resistor are used in the light sensing circuit. The different values of light intensity from each LDR in the circuit are read by the Arduino Microcontroller and these data are displayed on the "Serial monitor" of Arduino IDE as seen in Figure 3 by the following program.

```
void setup( ) {    Serial.begin(9600);   }
Void loop ( ){
int Val = analogRead(LDR1); // reading inputs
int Val = analogRead(LDR2);
int Val = analogRead(LDR3);
int Val = analogRead(LDR4);
Serial.print(Val1); //print the light intensities on serial monitor of Arduino
Serial.print(Val2);
Serial.print(Val3 );
Serial.print(Val4);
Delay(100);
 }
```

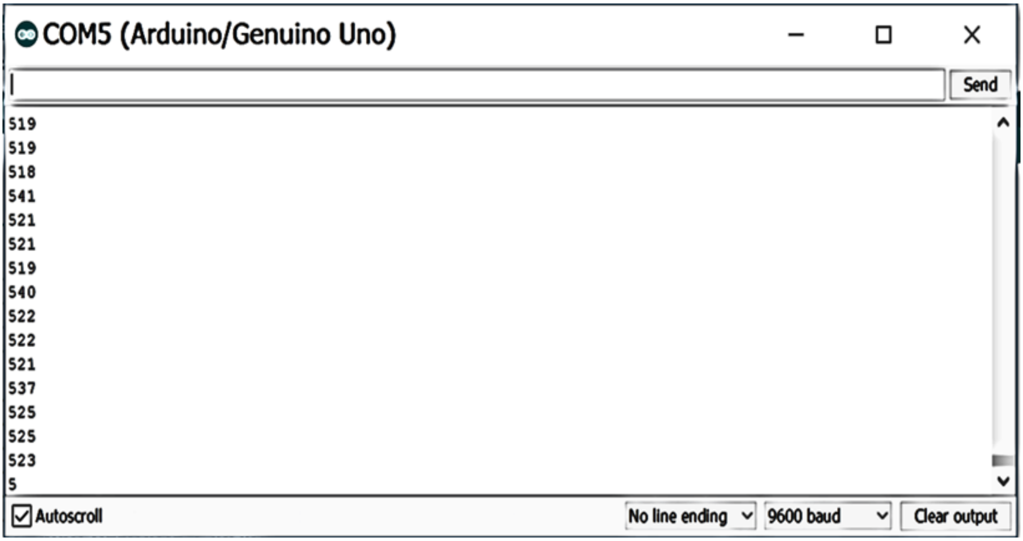

```
519
519
518
541
521
521
519
540
522
522
521
537
525
525
523
5
```

Figure 3: Different values of light intensity on the serial monitor

Building the Control Circuit

Arduino UNO microcontroller board and programming language based on Arduino platform are mainly used to control the operation of the whole circuit. Light dependent resistors are connected to the analog pins of Arduino UNO; A0, A1, A2 and A3, as the input data. The digital pins of Arduino UNO; D4, D5, D6 and D7 are connected to In1, In2, In3 and In4 pins of L298N dual H-bridge motor driver respectively and EnA and EnB pins of the motor driver are connected to D9 and D10 of Arduino respectively. EnA and EnB pins of the driver are attached to the Pulse Width Modulation (PWM) pins of Arduino; D9 and D10 respectively. The output pins of the motor driver are connected with two DC motors for the pitch and azimuth angle of solar panel respectively. The pins of liquid crystal display are connected to the digital pins, power supply and ground. The whole circuit diagram is shown in Figure 4 and connection in control circuit of the automatic dual axis solar tracker in Figure 5.

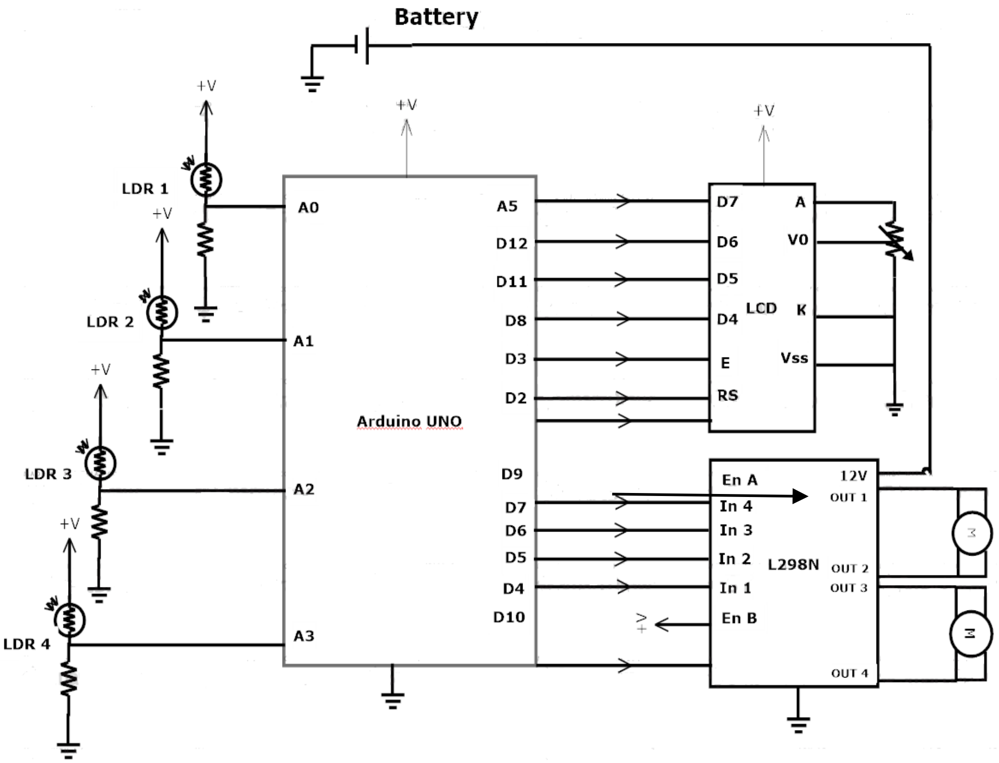

Figure 4: The whole circuit diagram of the dual axis solar tracking system

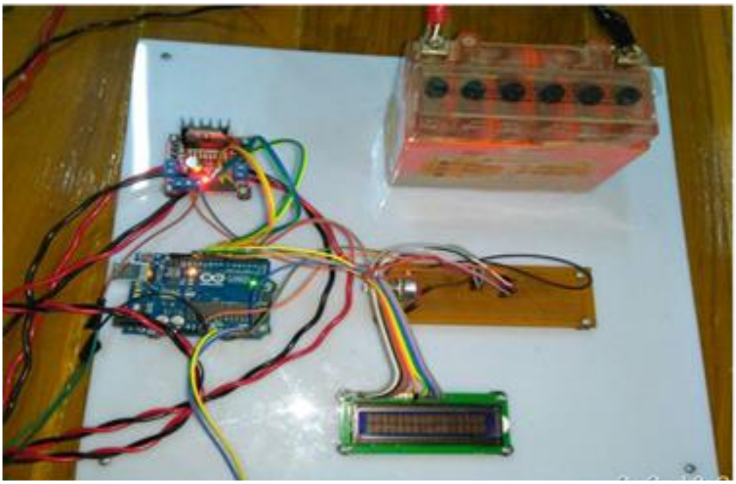

Figure 5: Connection in control circuit of automatic dual axis solar tracker

Operation of the control circuit

The calibration of four sensors under the same light source is very important to get nearly equal resistances. The difference light intensities from four sensor inputs are used to control the direction, position and speed of two DC motors for pitch and azimuth angle tracking of solar panel. According to the control program, Motor1 has been used for the pitch angle tracking and Motor2 has been used for the azimuth angle tracking of solar panel. The difference values of light intensities from LDR1 and LDR2 have been used to determine the direction and speed of Motor 1. The difference value of light intensity (I) from LDR3 and LDR4 have been used to determine the direction and speed of Motor 2. How the tracking system operates after receiving the input signals in order to be normal the solar panel toward the sun is depicted in Table 1.

The speed of Motor 1 and Motor 2 also vary with the difference light intensity values from LDRs by the control program. Therefore, the solar panel follows and tracks the direction of the highest light intensity of the sun to be normal to the sun all the day time because it is attached to pitch and azimuth angle tracking of motors. Liquid crystal display (LCD) displays the directions of solar PV panel as output on the display screen. The flow chart of operation of the control circuit for automatic dual axis solar tracker is shown in Figure 6.

Table 1: Operation of the control circuit with the difference value of light intensity (I) from LDRs

Condition	Responsible motor	Type of movement	Rotated direction
$I_{LDR1} > I_{LDR2}$	Motor 1	pitch angle	counter clockwise
$I_{LDR2} > I_{LDR1}$	Motor 1	pitch angle	clockwise
$I_{LDR3} > I_{LDR4}$	Motor 2	azimuth angle	counter clockwise
$I_{LDR4} > I_{LDR3}$	Motor 2	azimuth angle	clockwise

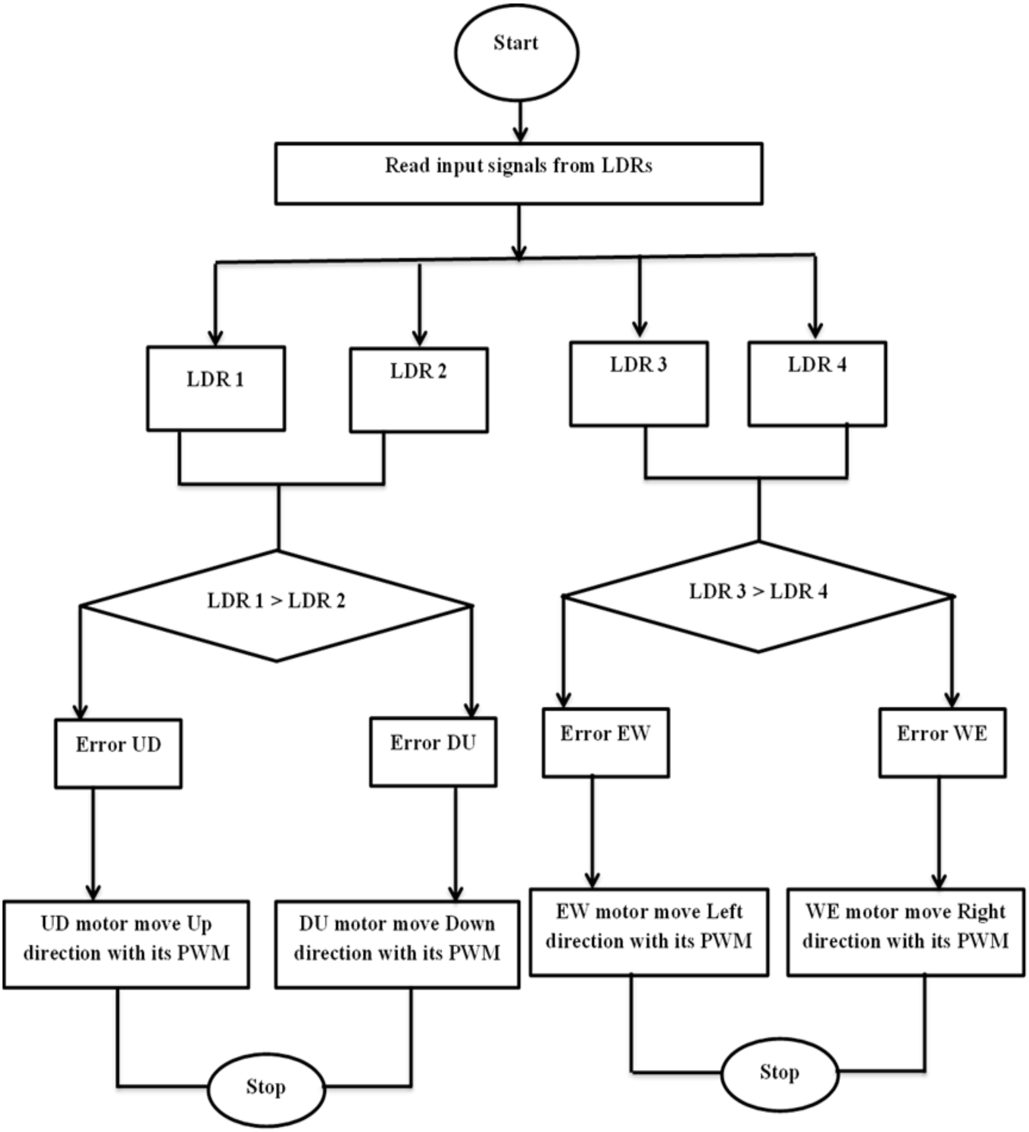

Figure 8: Flow chart of operation of the control circuit for automatic dual axis solar tracker

Designing the Mechanical Structure

The mechanical structure of the automatic dual axis solar tracker has been designed and implemented to hold up the weight of PV panel. In the mechanical structure, two similar DC gear motors are used to obtain the required torque to move the PV panel in pitch and azimuth angle tracking. Light sensing circuits are placed on one side of the PV panel.

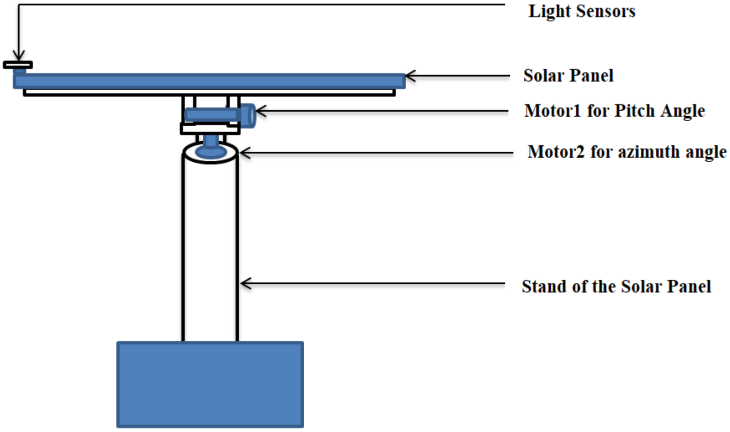

Figure 6: Designed mechanical structure of automatic dual axis solar tracker

Testing Automatic Solar Tracking System

The complete dual-axis automatic solar tracker is illustrated in Figure 7. The maximum solar tracking has been experimentally tested and the data obtained for the orientation of the panel with maximum intensity tracking are presented in Table 2. It has been found that the solar panel follows and tracks the direction of the highest intensity of the sun to be normal to the panel at each interval during testing. It is worth to note that although there is slight variation in intensity, the orientation of the solar panel has changed distinctly.

Figure 7: Complete dual-axis automatic solar tracker

Table 2: The data of the orientation of the dual-axis automatic solar tracker with maximum intensity

Time	Volt (V)	South-West	North-West
12:00 NOON	19.89	207°	313°
12:30 PM	19.64	207°	313°
1:00 PM	19.53	212°	320°
1:30 PM	19.73	213°	320°
2:00 PM	19.81	217°	323°
2:30 PM	19.75	218°	323°
3:00 PM	19.86	218°	326°
3:30 PM	19.87	218°	326°
4:00 PM	19.73	223°	326°

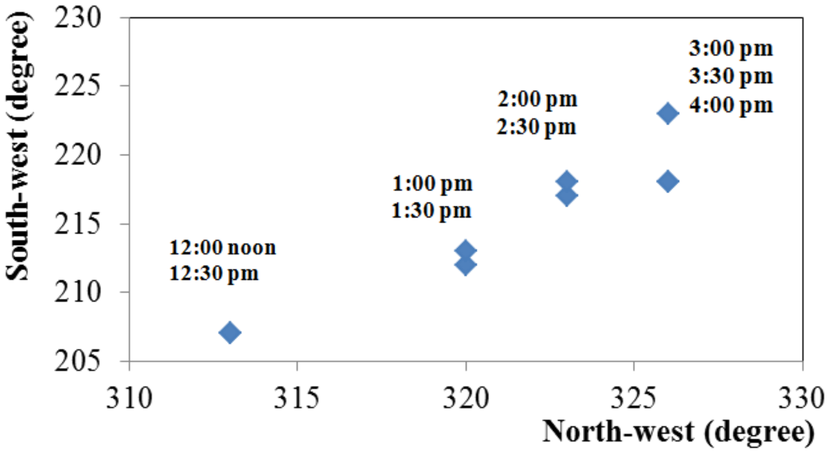

Figure 8: The variation of orientation of the dual-axis automatic solar tracker with maximum intensity

Conclusion

This dual-axis automatic solar tracker has been developed by design implementation and software description for controlling the tracker. The improvement in the hardware design of this solar tracker has also been implemented in order to provide high efficiency from a solar PV panel. The data obtained from the test has confirmed that the dual-axis automatic solar tracker could follow and track the direction of the highest light intensity from the sun. Based on the data obtained, it is concluded that the response of orientation of the solar panel to the light intensity is plausible to be applicable for the solar tracking in the year round.

Acknowledgements

The authors are grateful to Dr. Zaw Win, Rector of Sagaing University and Dr. Thazin, Pro-Rector of Sagaing University, for allowing me to submit this research paper and Professor Dr Khin Khin Win, Head of Department of Physics, University of Yangon for her kind permission to carry out this work.

References

Dinesh Bista. "Understanding and Design of an Arduino-based PID Controller". Virginia Commonwealth University

Dr. Liping Guo (2013). "Design and Simulation of a Sun Tracking Solar Power System". Northern Illinois University.

Durfee, W., (2011). "Arduino Microcontroller Guide, University of Minnesota and www.me.umn.edu/courses/me2011/arduino/".

Masum Bella, M.D., Chayan Biswas, Pallob Das (2016). "Solar Energy Optimization using Arduino based maximum power point tracking system". Department of Electrical and Electronic Engineering Northern University Bangladesh.

Md. Tanvir Arafat Khan et al, "Design and Construction of an Automatic Solar Tracking System", Department of Electrical and Electronic Engineering, Bangladesh University of Engineering and Technology, Dhaka, Bangladesh, 2010

Robert Weissbach, Isaac Aunkst, (2007). "A Microcontroller-Based Solar Panel Tracking System" Pennsylvania State University-Erie.

Salih Fadil1, Ahmet Can ÇAPAR2, Kerim ÇAĞLAR3. "Two Axis Solar Tracker Design and Implementation". ESOGU, Eskisehir, Turkey, sfadil@ogu.edu.tr.

Tejasbhai R. P. et al, "Automatic Solar Tracking System Using Pilot Panel", Dept. of Electrical Engineering, U. V. Patel College of Engineering India, 2015

Qi-Xun Zhang, Hai-Ye Yu, Qiu-Yuan Zhang, Zhong-Yuan Zhang, Cheng-Hui Shao, Di Yang. (2015) "A Solar Automatic System that Generates Power for Lighting Greenhouses". ISSN 1996-1073

J. Myanmar Acad. Arts Sci. 2019 **Vol. XVII. No.2A**

THERMAL AND MORPHOLOGICAL ANALYSES OF HAP/β-TCP BIPHASIC BIOMATERIALS

Nay Win Tun[1], Aye Aye Thant[2] and Win Kyaw[3]

Abstract

This research has been embarked to prepare hydroxyapatite by co-precipitation method to provide an accurate understanding of the behavior of biphasic biomaterials with HAP and β-TCP. Raw materials of calcium sulphate dihydrate ($CaSO_4.2H_2O$, or Gypsum) and di-ammonium hydrogen phosphate ($(NH_4)_2HPO_4$) solution have been used as the starting materials to synthesize high purity hydroxyapatite in the first step. The effect of reaction temperature on conversion efficiencies of gypsum to HAP and reaction kinetics has been reported in the previous work. At heat-treatment of 1100℃, HAP has converted partially into beta-tricalcium phosphate (β -TCP, $Ca_3(PO_4)_2$). The phase formations of these samples have been confirmed by using X-ray Diffraction (XRD) technique. Surface morphology and particle size of HAP and HAP/β-TCP samples have been studied by Scanning Electron Microscope (SEM). The effect of the reaction temperature on the morphology of biomaterials has been investigated. The thermal stability studies of the co-precipitated dry powder have been conducted by using Thermo-gravimetric and Differential Thermal analysis (TG/DTA).

Keywords: calcium sulphate, hydroxyapatite, β -TCP, XRD, SEM, TG/DTA,

Introduction

Among all biomaterials, hydroxyapatite: the mineral component of hard tissues in vertebrates is the most biocompatible material. Hydroxyapatite shows excellent biocompatibility not only with hard tissue but also with soft tissue. This material is capable of integrating biologically when directly implanted into a bone defect. Furthermore, it is not toxic and produces no harmful effect on the immune system with excellent osteoconductive behavior. Tricalcium phosphate is also one of the most important biomaterials based on phosphates, currently recognized as ceramic material that significantly simulates the mineralogical structure of bone. Theoretically, the resorbable β -TCP is an ideal implant material.

---

[1] Demonstrator, Department of Physics, Dagon University

[2] Professor, Department of Physics, University of Yangon

[3] Associated Professor, Department of Physics, Pyay University

The mineral gypsum precipitated in the evaporation of sea water since 100 to 200 million years ago. From a chemical point of view it is calcium sulphate dihydrate ($CaSO_4.2H_2O$) deposited in sedimentary layers on the sea bed. Under high pressure and temperature gypsum turns into anhydrite $CaSO_4$. When gypsum ($CaSO_4.2H_2O$) is ground to form a powder and heated at 150°C to 165°C, three-quarters of its combined water is removed producing hemi-hydrate plaster ($CaSO_4.0.5H_2O$), commonly known as the ‘Plaster of Paris’ (PoP). When this PoP powder is mixed with water, the resulting paste sets hard as the water recombines with anhydrite $CaSO_4$ to produce gypsum again. This process can be repeated almost indefinitely, with important implications for recycling.

In this work, the phase formations of these samples have been confirmed by using X-ray Diffraction (XRD) technique and the synthesized HAP and HAP/β-TCP samples have been characterized by Scanning Electron Microscope (SEM) to observe their surface morphology and particle size. Thermo-gravimetric and Differential Thermal analysis (TG/DTA) has been used to study thermal stability of the co-precipitated dry powder. The effect of calcination temperature on the morphology and thermal properties has been discussed.

Materials and Method

Experimental Procedure

Laboratory grade gypsum ($CaSO_4.2H_2O$) has been used for starting material to synthesize hydroxyapatite (HAP) in the first stage. HAP synthesized from gypsum powder has been achieved by co-precipitation method at 90°C. Figure 1 shows HAP and HAP/β-TCP pellets before sintering. The flow chart in Figure 2 shows the details for conversion of gypsum powder to HAP. This reaction conversion has been achieved according to the reaction below.

$$\mathbf{10CaSO_4.2H_2O + 6(NH_4)_2\,HPO_4 \rightarrow Ca_{10}(PO_4)_6(OH)_2 + 6(NH_4)_2SO_4 + 4H_2SO_4 + 18H_2O}$$

1.6 M of gypsum solution has been prepared with 11.5 g of gypsum and 40 ml of deionized water. Then the gypsum solution has been mixed with 40 ml of 1 M - $(NH_4)_2HPO_4$ solution in conical flask with water bath at the reaction temperature of 90° with magnetic stirring. The reaction time is for 4 hours. At the end of the reaction period, the solid products have been washed with DI-water for 5 times and filtered to eliminate any water soluble remains. After washing, the solid residue has been put in drying oven operating at 75^{o}C for 24 hours. Again, the dry powder has been heat-treated at 500 ^{o}C, 800 ^{o}C, 1100 ^{o}C and 1150 ^{o}C for 2 hours each in a furnace. The HAP phase has been formed at 500 ^{o}C and 800 ^{o}C for 2 hours. However, HAP converts into β-tricalcium phosphate (β-TCP) at 1100 ^{o}C and beyond. After sintering 1200 ^{o}C of HAP/β-TCP pellet partially converts into biphasic HAP/α-TCP. The α-TCP is brittle and more soluble than HAP and β-TCP. Therefore, this research focus on biphasic HAP/β-TCP. The process of sample preparation of HAP is presented. Morphology study has been conducted using JEOL-JSM 5610LV scanning electron microscope. The thermal behavior of the sample has been investigated by using Thermo-gravimetry and Differential Thermal Analysis (TG/DTA).

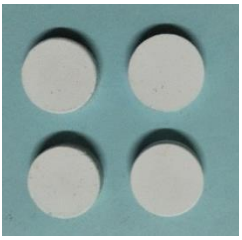

Figure 1: HAP/β-TCP pellets before sintering temperature

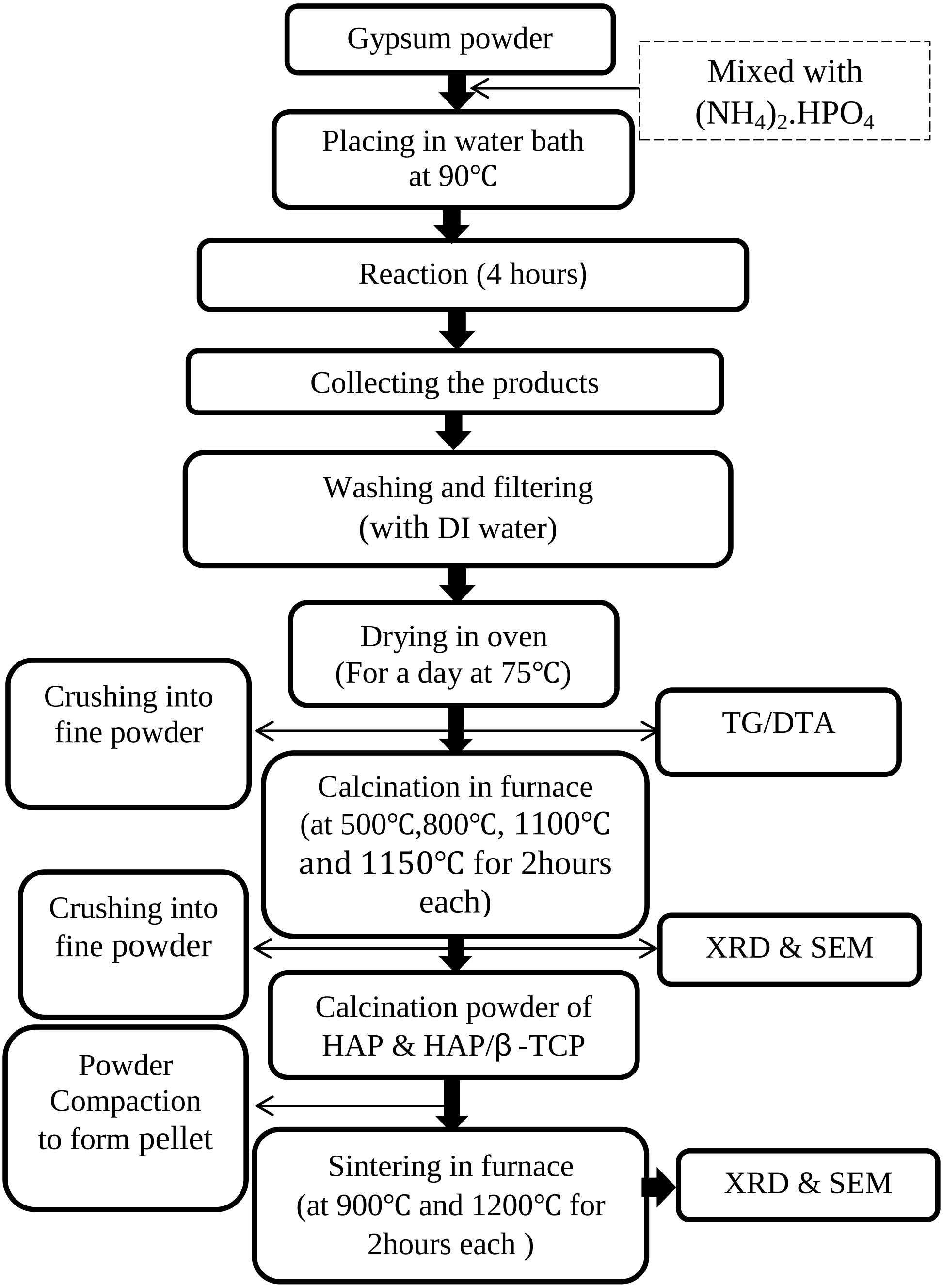

Figure 2: Flowchart of HAP and HAP/β -TCP sample

Results and Discussion

Thermal analysis

Thermal Analysis (TA) is a group of analytical techniques that measures properties or property changes of materials as a function of temperature. But Thermogravimetry (TG) is mainly used to examine the decomposition of materials by monitoring mass change with temperature. In this research, the thermal properties of co-precipitated compound of gypsum and di-ammonium hydrogen phosphate are investigated. A sample of 51.72 mg was placed in a semi-hermetically aluminum sealed container with a pinhole in the lid. The flow rate was 50 ml/min of nitrogen and the heating rate was 15°C/min.

Figure 3 shows the TG/DTA plots for the co-precipitated gypsum and di-ammonium hydrogen phosphate compound. In this semi-hermetic state, the TG curve showed a two-stage weight decrease corresponding to the evaporation of water. The weight loss starts from 34.36°C to 601.58 °C and it is about 35.336% over heating time. From the DTA curve, the decomposition has been investigated at about 122.52°C and 169.68°C to be endothermic reaction. It is important information for the transformation temperature of HAP to β-TCP. From TG curve, the final weight is 33.44 mg and so weight loss is 18.28 mg from an ambient temperature up to 250°C. Beyond that temperature, the synthesized co-precipitated gypsum and di-ammonium hydrogen phosphate compound are stable in thermal analysis.

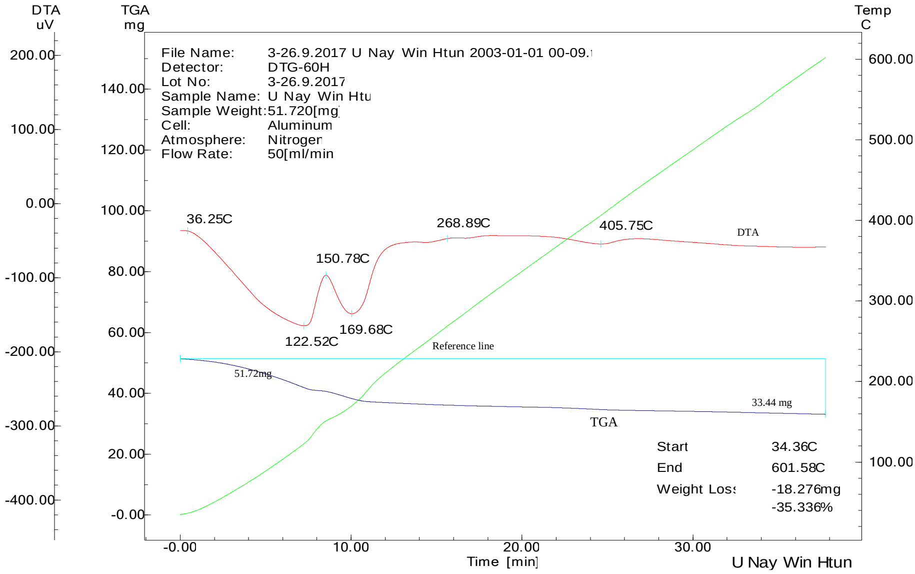

Figure 3: A plot of TG/DTA for the thermal behavior of the co-precipitated gypsum and di-ammonium hydrogen phosphate compound

Phase Formation by XRD analysis

HAP powder has been synthesized from gypsum powder by co-precipitation method at 90°C. After heat-treatment of powder at 500°C and 800°C and that of pellet after sintering at 900°C, HAP phase formed. After heat-treatment of powder at 1100°C and 1150°C, HAP/β-TCP biphasic formed. At 1200°C, the pellet shows the formation of HAP,β-TCP and α-TCP. The XRD diffractograms of powder and pellets samples at different temperatures are shown in Figures 4 to Figures 6.

The pattern in Figures 4 to Figures 6 reveals that the phase precipitated out in the sample is hexagonal structure. There is no trace of starting materials. Therefore, it has been identified that a single phase structure of HAP from gypsum has been formed via the co-precipitation method.

After heat-treatment 1100°C, some of the HAP converts into β-TCP. The lattice parameters ‘a’ and ‘c’ have been calculated by using ‘d’ value of the diffraction peaks. These lattice constants well agree with the typical values for HAP and β-TCP structures.

The crystallite size has also been estimated from FWHM values and it is found that the HAP and β-TCP crystallites have been formed in the nanometer scale. For HAP, the typical standard value of lattice parameter a, b is 9.432 Å and that of lattice parameter c is 6.8814 Å. For β-TCP, the typical standard value of lattice parameter a, b is 10.439 Å and that of lattice parameter c is 37.375 Å. The average lattice vales and crystallite sizes of HAP and β-TCP are shown in Table 1 and Table 2. From all XRD diffractograms, the lattice parameters values well agree with the typical values.

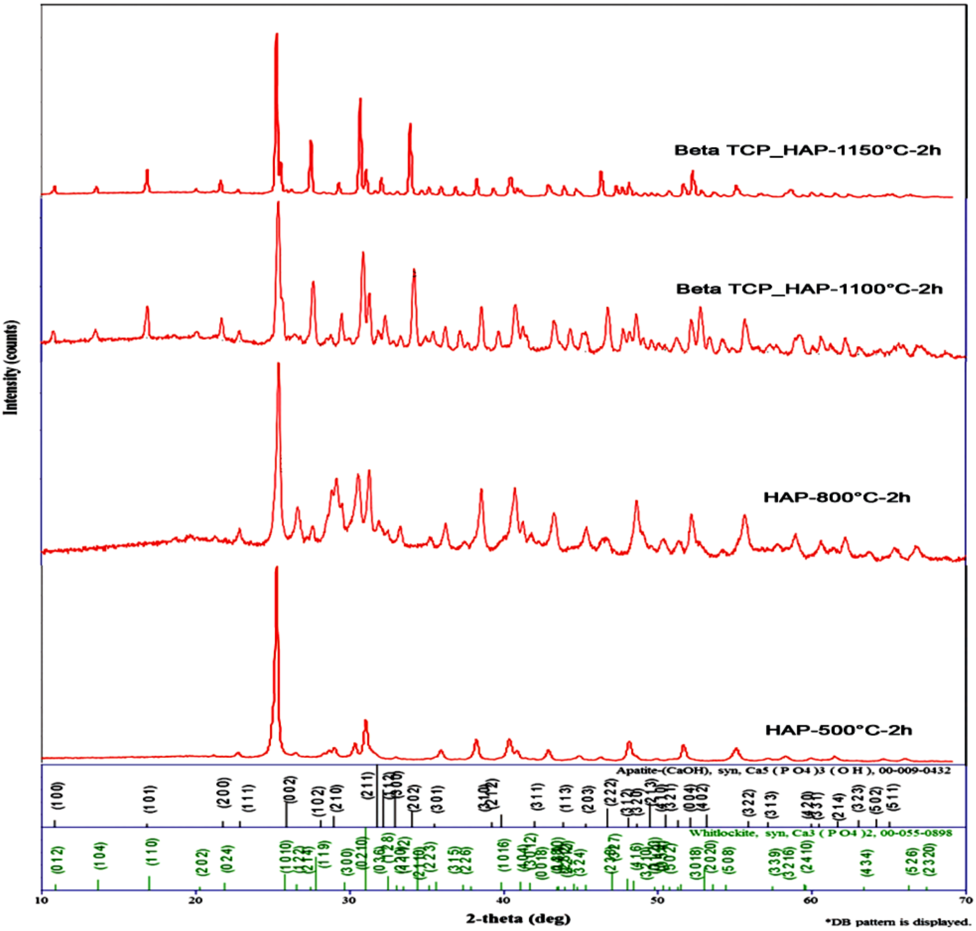

Figure 4: XRD diffractograms of HAP and β-TCP powder for different temperatures

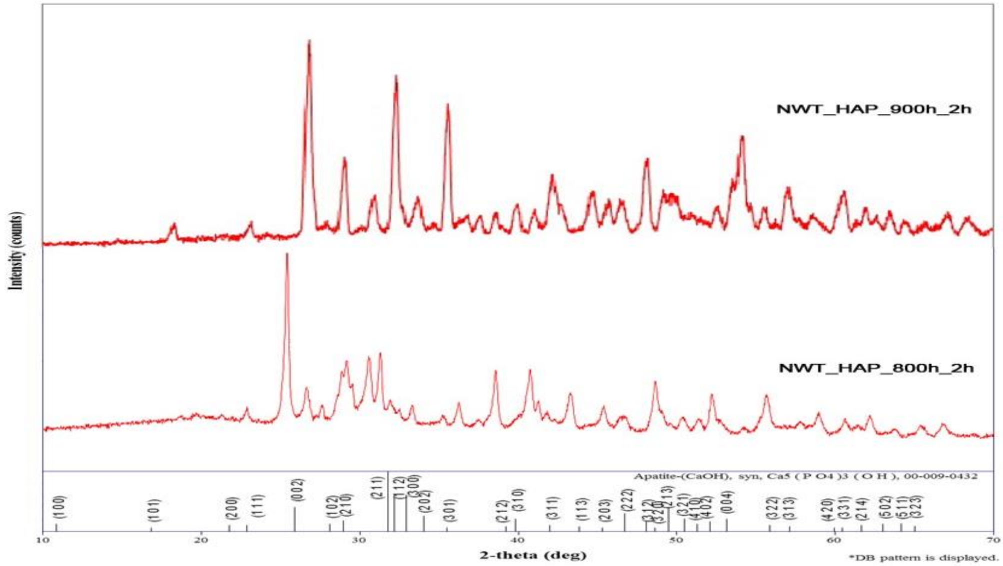

Figure 5: XRD diffractograms of HAP compare with calcination temperature (800℃) and sintering temperature (900℃)

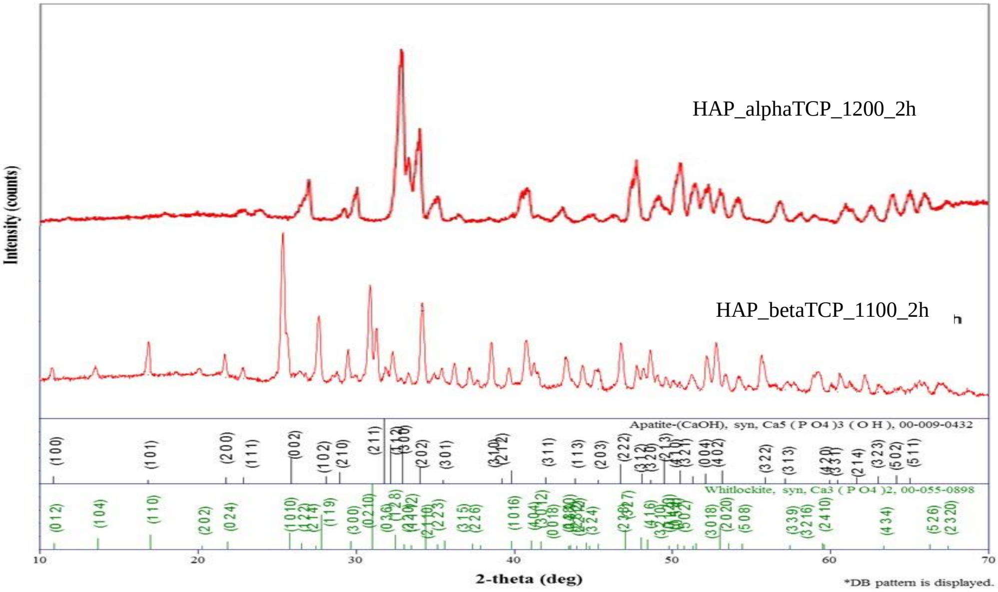

Figure 6: XRD diffractograms of HAP, β-TCP and α-TCP compare with calcination temperature (1100℃) and sintering temperature (1200℃)

Table 1: The lattice parameters (a, b and c) and crystallite size (D) of heat-treatment HAP powder and pellet

Sr. No.	Sample	Heat-treatment temperature (°C)	a (Å)	b (Å)	c (Å)	D (nm)
1	HAP	500(Calcination)	9.409	9.409	7.023	31.48
2	HAP	800(Calcination)	9.251	9.251	6.707	26.56
3	HAP	900(Sintering)	9.220	9.220	6.699	24.01

Table 2: The Lattice parameters (a, b and c) and crystallite size (D) of heat-treatment HAP/ □-TCP powder and pellet

Sr. No.	Sample	Heat-treatment temperature(°C)		a (Å)	b (Å)	c (Å)	D (nm)
1	HAP/ β - TCP	1100 (Calcination)	HAP	9.317	9.317	7.026	41.47
			β -TCP	10.486	10.486	37.561	46.98
2	HAP/ β - TCP	1150 (Calcination)	HAP	9.412	9.412	6.839	66.09
			β -TCP	10.471	10.471	37.469	66.95
3	HAP/ β - TCP	1200 (Sintering)	HAP	9.138	9.138	6.658	19.92
			β -TCP	10.123	10.123	37.761	20.60

Morphological Analysis by SEM Technique

The SEM micrographs of powder and pellets samples at different temperature are shown Figures 7 and Figures 8.

According to the SEM micrograph, the grain sizes of HAP after heat-treatment at 500°C are found to be in the range of 0.50 μm to 1.00 μm. It is observed that the small grains are being agglomerated with the small crystallites which are in nanometer range. The homogeneity of the topography exhibits the formation of pure HAP powder which agrees well with the XRD analysis.

From the SEM micrograph of HAP after heat-treatment at 800°C for 2 hours in a furnace, the grain sizes are estimated by using Line Intercept

Method and found to be 1.22μm. According to the microstructure of the sample heat-treated at 1100°C, it is found that some parts of the HAP has transformed into β-TCP. Therefore, the smaller grains of HAP are more numerical than the larger grains of β-TCP. However, after heat-treatment at 1150°C, most of the HAP has transformed into β-TCP and so the larger grains of β-TCP are more numerical than the smaller grains of HAP. From the SEM micrograph of HAP after sintering 900°C, the average grain size is about 1.45μm and that of HAP/ β-TCP pellet after sintering 1200°C, the average grain size of HAP is about 2.01μm and that of β-TCP is about 6.55 μm. It is worth to note that the grain sizes in biphasic pellets are about two and half times larger than those in biphasic powder. The comparison on grain sizes of HAP powder and pellet and that of HAP/β-TCP powder and pellets are shown in Tables 3 and 4.

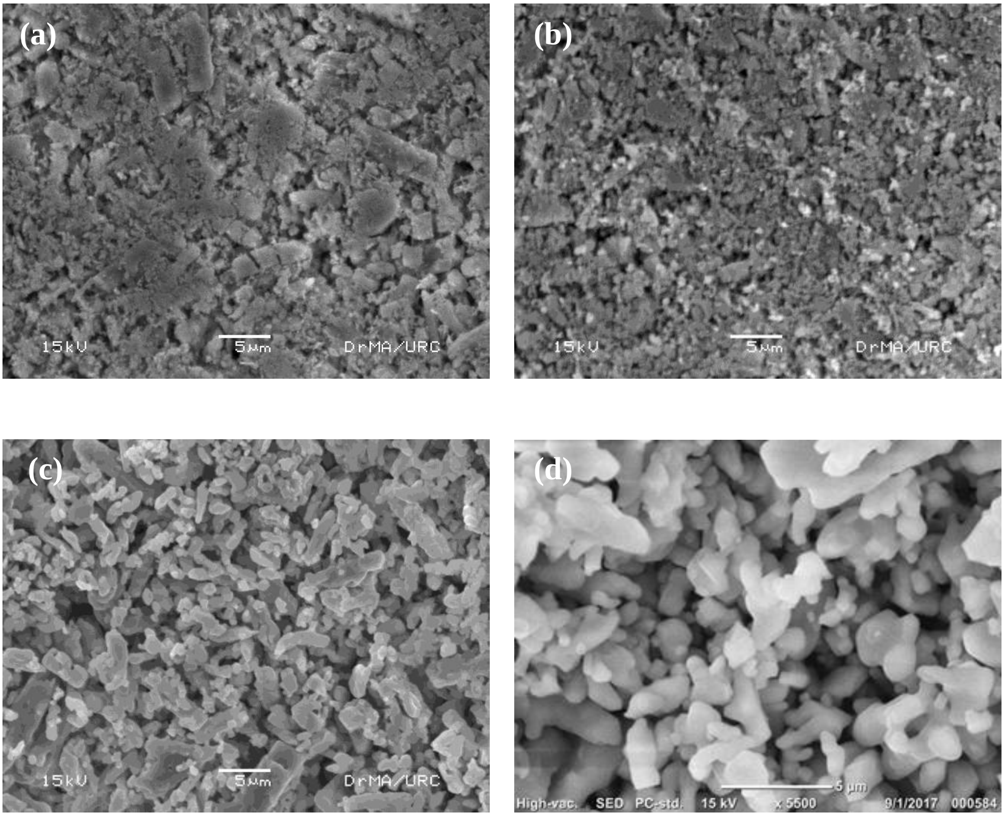

Figure 7: The SEM micrographs of the HAP powder at (a) 500°C, (b) 800°C and that of HAP/β-TCP powder at (c) 1100°C, (d) 1150°C for 2hours

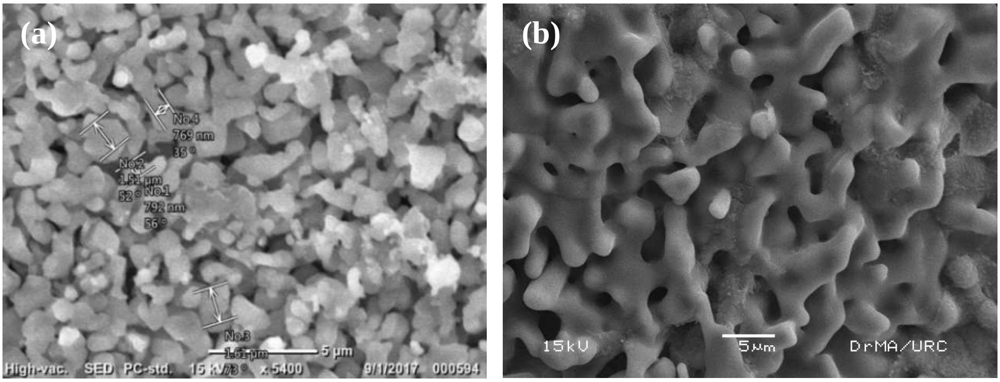

Figure 8: The SEM micrographs of the HAP pellet at (a) 900°C and that of HAP/β-TCP pellet at (b) 1200°C for 2 hours

Table 3: The average grain sizes of heat-treatment HAP powder and pellet

Sr. No.	Sample	Heat-treatment Temperature(°C)	Grain Size (μm)
1	HAP	500(Calcination)	0.50-1.00
2	HAP	800(Calcination)	1.22
3	HAP	900(Sintering)	1.45

Table 4: The average grain sizes of heat-treatment HAP /β-TCP powder and pellet

Sr. No.	Sample	Heat-treatment Temperature(°C)	Grain Size (μm)	
			HAP	β-TCP
1	HAP/β -TCP	1100(Calcination)	0.84	2.51
2	HAP/β -TCP	1150(Calcination)	0.74	1.75
3	HAP/β -TCP	1200(Sintering)	2.01	6.55

Conclusion

Hydroxyapatite, $Ca_{10}(PO_4)_6(OH)_2$ has been prepared from gypsum by co-precipitation method. The raw materials have been well characterized prior to the preparation of HAP. A single phase structure of HAP from gypsum has been successfully formed via the co-precipitation method after heat-treated at 500°C and 800°C for 2 hours. The average lattice constants well agree with the typical values for HAP structure. It is worth to note that some parts of HAP converts to β-TCP phases after heat-treated at 1100°C for 2 hours. These average lattice constants well also agree with the typical values for β-TCP structure. It is interesting to note that transformation to β-TCP has started by the heat treatment at 1100°C and the transformation rate has increased with increase in temperature. From the TG/DTA curves, the decomposition temperature has been found about 122.52°C and 169.68°C in endothermic reactions. The synthesized co-precipitated gypsum and di-ammonium hydrogen phosphate compound are found to be stable beyond 250°C.

Acknowledgements

I would like to express my sincere thanks to Professor Dr Khin Khin Win, Head of Department of Physics, University of Yangon, for her kind permission to carry out this work. I am also greatly indebted to my supervisor Professor Dr Aye Aye Thant, Department of Physics, University of Yangon, for her guidance, helpful advice and valuable Supervision. I am also grateful to my Co-supervisor Dr Win Kyaw, Associate Professor, Department of Physics, Pyay University, for his valuable suggestion.

References

Angelescu, N., Ungureanu, D.N. and Anghelina F.V. (2011). Synthesis and Characteristic of Hydroxyapatite Obtained in Different Experimental Conditions, Valahia University of Targoviste, Romania.

Bahman Mirhadi, Bahman Mehdikhani and Nayereh Askari, (2012). Sintering effects on the hardness of β -TCP, Journal of Ceramic Processing Research, Vol. 13, No.4.

Hitachi High-Tech Science Corporation, (1985). Thermal Analysis of Gypsum, TA No.22, Tokyo.

Kim, S.R., Lee, J.H., Riu, D.H., Jung, S.J., Lee, Y.J., Chung, S.C., Kim, Y.H., (2003).Synthesis of Si, Mg substituted hydroxyapatite and their sintering behaviors. Biomaterials, 24, 1389-1398.

Kannan, S., Lemos, I.A.F., Rocha, J.H.G., Ferreira, J.M.F. (2005). Synthesis and characterization of magnesium substituted biphasic mixtures of controlled hydroxyapatite/beta-tricalcium phosphate ratios, Department of Ceramics and Glass Engineering, University of Aveiro, Portugal.

Living with Gypsum: From Raw Material to Finished Products. (n.d.). Retrieved July 7, 2017 from http://www.eurogypsum.org .

Onur Rauf Bingöl and Caner Durucan (2011). Hydrothermal Synthesis of Hydroxyapatite from Calcium Sulfate Hemihydrate, Department of Metallurgical and Materials Engineering, Middle East Technical University, Ankara, Turkey.

Orlovskii, V.P.et al., (2002). Hydroxyapatite and Hydroxyapatite-Based Ceramics, Inorganic Materials, Vol.38

J. Myanmar Acad. Arts Sci. 2019 **Vol. XVII. No.2A**

CHARACTERIZATION BY XRD ANALYSIS, MOLECULAR VIBRATION AND ELECTRICAL ROPERTIES OF ALUMINIUM DOPED NICKEL-FERRITES PARTICLES

Ye Wint Htun[1], Sandar Oo[2], Soe Soe Han[3], Aye Aye Thant[4]

Abstract

Aluminium doped Nickel-ferrite nanoparticles of general formula: $NiAl_xFe_{2-x}O_4$ (x = 0.0, 0.2, 0.4, 0.6, 0.8 and 1.0) have been synthesized by sol-gel auto combustion method involving final sintering at 900°C with a heating rate of 5 hours. The phase formations of the sintered samples were characterized by X-ray Diffraction analysis. The X-ray diffraction patterns confirmed formation of ferrite with single phase cubic spinel structure with the appearance of small peaks representing secondary phases. The electrical properties of samples have been measured using Fluke- 189 LCR meter in the low frequency range (1-1000) kHz and higher frequency range (1 kHz to 10GHz).

Keywords: Ni-ferrite, sol-gel auto combustion technique, XRD, electrical properties.

Introduction

Ferrites particles have improved catalytic, dielectric and magnetic properties, as they possess high resistivity and negligible eddy current losses [Cullity, B.D. (1989)]. Magnetic particles promise some interesting applications, such as in high frequency devices, magnetic fluids, high density magnetic recording. In the present investigation we have employed sol-gel auto-combustion method to synthesize Al doped nickel ferrite nano-particles [Ghasemi, A., Ekhlasi, (2014)]. The sol-gel auto-combustion method is used to speed up the synthesis of complex materials. It is a simple process, which offers a significant saving in time and energy consumption over the traditional methods, and requires less sintering temperature. This method is employed to obtain improved powder characteristics, better homogeneity and narrow particle size distribution, thereby influencing structural, electrical, and magnetic properties of spinel ferrites [Auzans, E., Zins, D., Blums, E., & Massart, R. (1999)].

---

[1] Assistant Lecture, Department of Physics, Ma U Bin University

[2] Dr, Lecture, Department of Physics, University of Yangon

[3] Dr, Lecture, Department of Physics, University of Yangon

[4] Dr, Professor, Department of Physics, University of Yangon

In the inverse spinel structure of $NiFe_2O_4$ the tetrahedral sites are occupied by ferric ions and octahedral sites by ferric and nickel ions. The investigation of aluminum substituted nickel ferrite $NiAl_xFe_{2-x}O_4$ was not well documented and we present here the synthesis, structural characterization and also the basic magnetic properties of $NiAl_xFe_{2-x}O_4$ nanoparticles.

Experiment

Nano-crystalline powders of $NiAl_xFe_{2-x}O_4$ (x = 0.0, 0.2, 0.4, 0.6, 0.8, 1.0) were prepared by sol-gel auto-ignition method. The Citric acid ($C_6H_8O_7.H_2O$), Nickel Nitrate ($Ni(NO_3)_2.6H_2O$), Ferric Nitrate ($Fe(NO_3)_3.9H_2O$), Aluminium Nitrate ($Al(NO_3)_3$. $9H_2O$). Nano-crystalline powders of $NiAl_x Fe_{2-x}O_4$ (x = 0.0, 0.2, 0.4, 0.6, 0.8 and 1.0) have been prepared by have been used as starting materials. The molar ratio of metal nitrates to citric acid has been taken as 1:3. The metal nitrates have been dissolved together in 100 ml of de-ionized water to get a clear solution. An aqueous solution of citric acid has been mixed with metal nitrates solution, then ammonia hydroxide solution has been slowly added to adjust the pH at 7. The mixed solution has been moved on to a hot plate with continuous stirring at 90ºC - 100ºC. During evaporation, the solution became viscous and finally formed a very viscous brown gel. When finally all remaining water was released from the mixture, the sticky mass began to bubble. After several minutes the gel automatically ignited and burnt with glowing flints. The decomposition reaction would not stop before the whole citrate complex was consumed. The auto ignition was completed within a minute, yielding the brown-colored ashes termed as a precursor. The as-prepared powder has been annealed at 700ºC for 3 hrs to get single phase spinel product and used for further characterization. Then, the powder has been pressed into pellets by hydraulic press at a pressure of 5 tons. The final sintering has been performed at 900°C for 5hrs.The phase formations of the sintered samples have been characterized by X-ray Diffraction (XRD) analysis and the electrical properties.

Figure 1: The starting solutions in the preparation of Aluminium doped Nickel-ferrite particles by sol-gel auto-combustion method

Figure 2: The starting solutions in the preparation of Aluminium doped Nickel-ferrite particles by sol-gel auto-combustion method

Results and Discussion

Phase formation

Aluminium doped Nickel-ferrite nanoparticles, $NiAl_xFe_{2-x}O_4$ (x = 0.0, 0.2, 0.4, 0.6, 0.8 and 1.0) have been synthesized by sol-gel auto combustion method and characterized using X-ray diffraction (XRD). X-ray diffractograms of $NiAl_xFe_{2-x}O_4$ (x = 0.0, 0.2, 0.4, 0.6, 0.8 and 1.0) samples. This XRD diffractograms display formation of well nano-crystalline undoped and alumina doped $NiFe_2O_4$ to be single cubic spinel phase with reflection planes of (2 2 0), (3 1 1), (4 0 0), (4 2 2), (5 1 1) and (4 4 0). The XRD patterns clearly indicate that the prepared samples contain cubic spinel structure only. The strongest reflection peak has resulted from the (3 1 1) plane that indicates the spinel phase. An increase of the aluminium content resulted in a measurable decrease in the degree of crystallinity of spinel nickel ferrite phase with subsequent a decrease in the intensity of its diffraction peaks. Some diffraction planes such as (2 2 0) and (4 4 0) planes are more sensitive to the cations distribution on tetrahedral and octahedral sites, respectively. [10] The sizes of crystallites in the sample have been evaluated by using the FWHM of the most intense peak (220) (311) (400) (511) (440). The results are shown in Table 1. Further, it is observed that particle size decreases with an increase in nonmagnetic Al substitution.

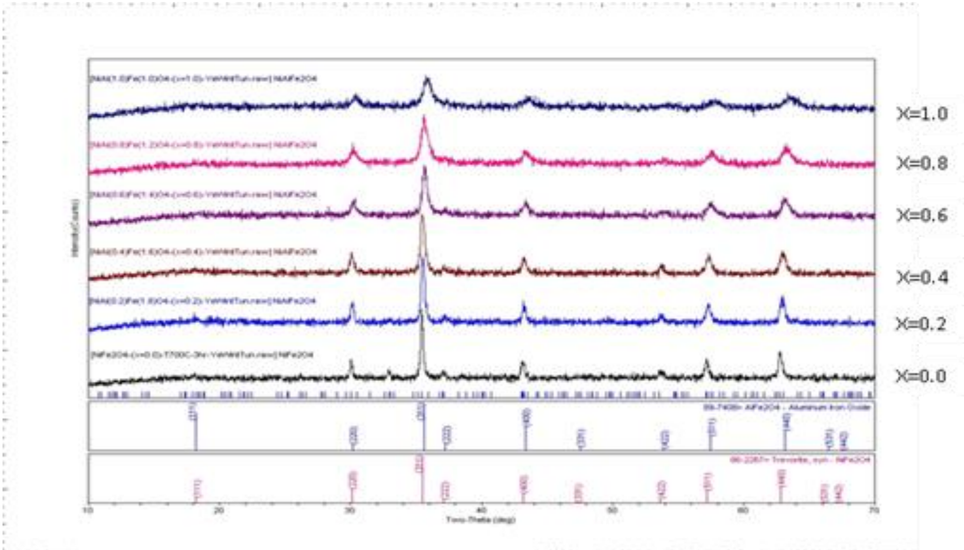

Figure 3: XRD spectra for of $NiAl_xFe_{2-x}O_4$ particles at 900℃ for 5 hours (The inset shows the peak-shift in 311plane.)

Table 1: Comparison of crystallite size for different compositions

Composition (x)	**Lattice parameter (a=b=c) Å**	**Crystallize size D (nm)**
0.0	8.31	57.05
0.2	8.29	46.07
0.4	8.28	54.68
0.6	8.23	34.58
0.8	8.20	31.26
1.0	8.19	30.1

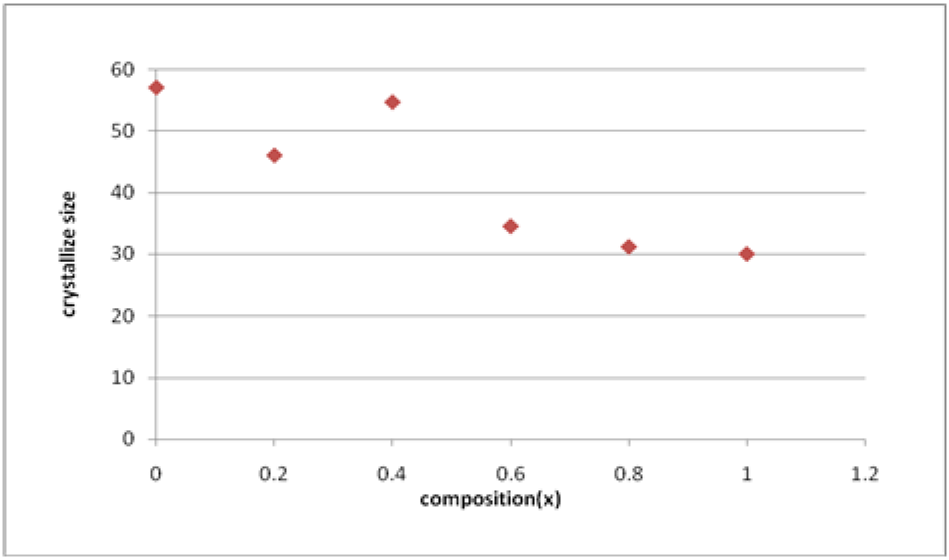

Figure 4: Variation of Crystallite size with chemical composition x

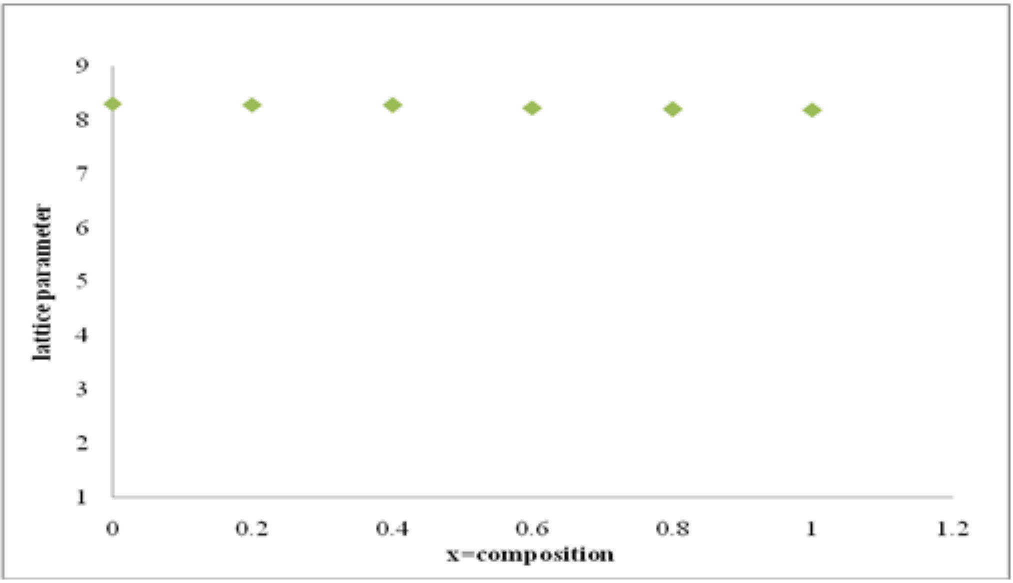

Figure 5: Variation of lattice parameter with chemical composition x

Study on Frequency Dependent Resistivity

Aluminium doped in Nickel ferrite nano-particles have also been synthesized by sol-gel auto combustion method. The measurements on electrical resistance and capacitance were performed on the final sintered pellet at 900□ C. The resistances were measured using Fluke- 189 LCR meter. The resistivity of each sample was calculated by measuring the dimensions and resistance of the sample. Firstly, the cross sectional area (A) and the thickness(t) of each sample were measured accurately. The resistivity of each sample was calculated by using the following relation:

$$\rho = \frac{RA}{t} \tag{1}$$

where R is the resistance of the sample, A is the area of the electrode in contact with the sample (πr^2) and t is the thickness of the sample.

The conductivity σ of the sample ($NiAl_xFe_{2-x}O_4$) was determined from the measure resistance value and sample dimension by using the relation:

$$\sigma = \frac{1}{\rho} \tag{2}$$

The frequency dependent DC resistivity (the inverse of conductivity) and dielectric constant for all sample which are final-sintered at 900°C at lower frequency range 1kHz-1000kHz (1kHz-1MHz) and 1kHz to 10GHz. These grain boundaries are more active at lower frequencies; hence, the hopping frequency of electrons between Fe^{3+} and Fe^{2+} ions have less at lower frequencies. [6] The resistivity shows fluctuation in the lower frequency region and there is almost no variation in the higher frequency region. This is normal behavior of ferrite as grain boundary hinders the conduction mechanism and this effect disappears in the higher frequency region.

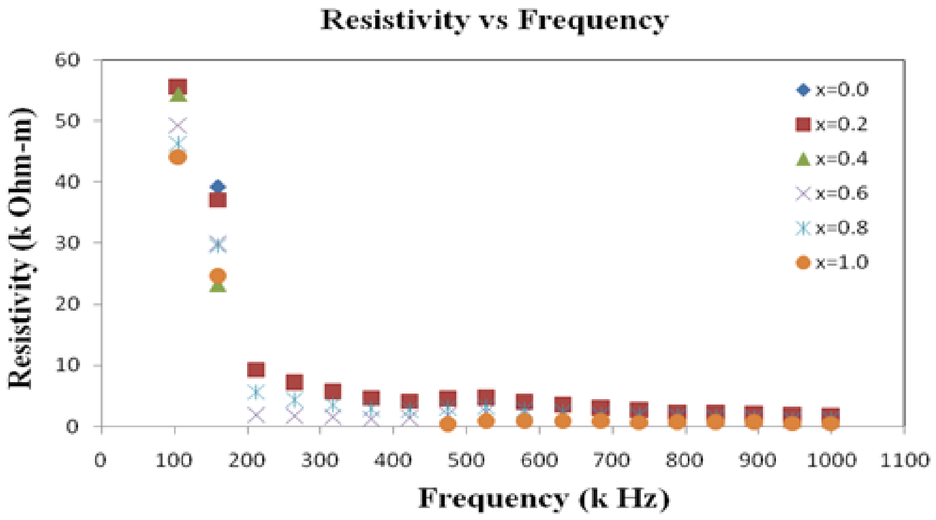

Figure 6: The variation of resistivity with lower frequency range (1kHz to 1000kHz) for (x=0.0 to 1.0)

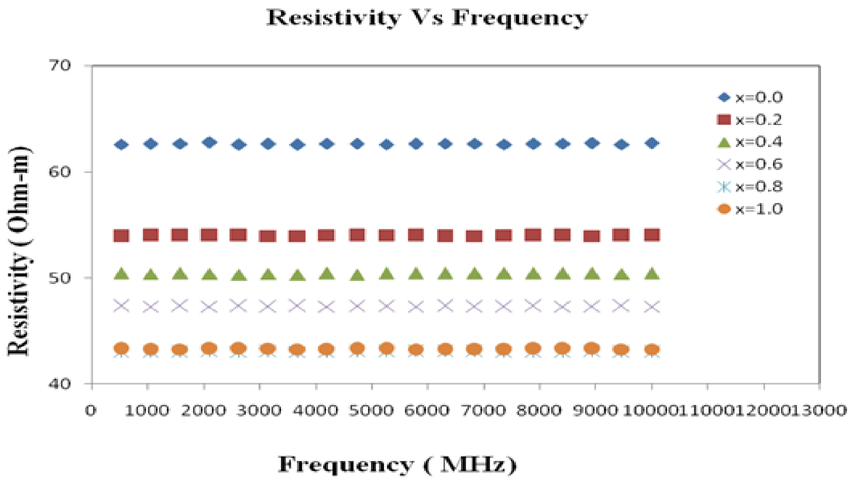

Figure 7: The variation of resistivity with higher frequency range (1kHz to 10GHz) for (x=0.0 to 1.0)

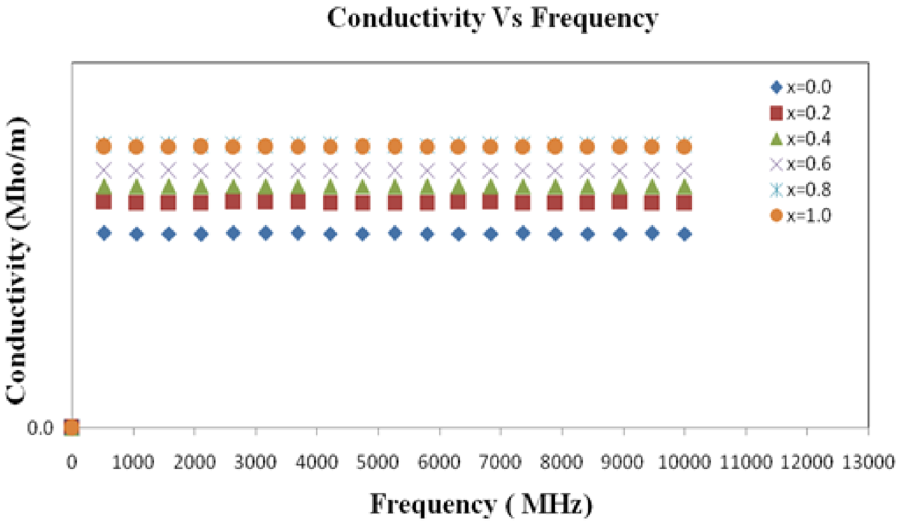

Figure 8: The variation of Conductivity with higher frequency range (1kHz to 10GHz) for (x=0.0 to 1.0)

Conclusion

The XRD patterns clearly indicate that the prepared samples contain cubic spinel structure only. The obtained average crystallite sizes decreases with increase in nonmagnetic Al substitution. An increase of the aluminium content resulted in a measurable decrease in the degree of crystallinity of spinel nickel ferrite phase with subsequent decrease in the intensity of its diffraction peaks. The resistivity shows fluctuation in the lower frequency region and there is almost no variation in the higher frequency region. This is normal behavior of ceramics as grain boundary hinders the conduction mechanism and this effect disappears in the higher frequency region.

Acknowledgements

I would like to express my sincere thanks to Professor Dr Khin Khin Win, Head of Department of Physics, University of Yangon, for her kind permission to carry out this work.

Also, I am thankful to Professor Dr Aye Aye Thant, Department of Physics, University of Yangon, for her suggestion and comment on this work.

I am greatly indebted to my Supervisor Dr Sandar Oo, Lecturer, Department of Physics, University of Yangon, for her help Supervision and guidance on this work.

Also, I would like to thank my Co-supervisor Dr Soe Soe Han, Lecturer, Department of Physics, University of Yangon, for her guidance and discussion on this work.

References

Auzans, E., Zins, D., Blums, E., & Massart, R. (1999). Synthesis and Properties of Ferrite. *Journal of Materials Science,* 34(6), 1253-1260.

Cullity, B.D. (1989). *"Elements of X-ray Diffraction*. Addison-Wesly Publishing Co. Inc.

Ghasemi, A., Ekhlasi, S. and Mousavinia, M. (2014). Structural and Magnetic Properties of Nickel Ferrite Synthesized by Using the sol-gel Auto-Combustion Method. *Journal of Magnetism and Magnetic Materials*, 354, 136-145.

H.P.Klug, L.E.Alexander, 1997, X-Ray Diffraction procedures for Polycrystalline and Amorphous materials, Wiley, New York, NY, **P.637**.

J.Smit & H.P.J.Wijn, (1959). "Ferrites" Physical Properties of Ferrimagnetic Oxides in

KOOPS C.G., Phys. Rev. Lett., 83 (1951), 121.

Mathew, G., Asha, M.J., S.Nair, Joy, P.A., Anantharaman, M.R. & Magn.Magn.Mater. J. (2006). 302**,** 190.

Niu, Z. P., Wang, Y. & Li, F. S. (2006). Magnetic Properties of Nano Crystalline Co-Ni Ferrite. *Journal of Materials Science*, 41(17), 5726-5730.

J. Myanmar Acad. Arts Sci. 2019 **Vol. XVII. No.2A**

PHOTOVOLTAIC PERFORMANCE OF Ag@TiO$_2$ CORE SHELL

Ye Hlyan Win[1], Yin Maung Maung[2] and Than Than Win[3]

Abstract

Silver particles were synthesized by using an aqueous-based reduction method. Silver thin film (core) was synthesized in form of finely silver films. The ITO coated glass was used as substrate for chemical bath deposition (CBD) at 120˚ C for 2 h. Shell material (TiO$_2$ solution) was coated onto Ag thin film by spin coating technique. The grain size of the Ag particles, Ag thin film and Ag-TiO$_2$ thin film were studied by scanning electron microscope (SEM). Optical properties of silver thin film were determined from transmittance spectrum with SHIMADZU UV-1800 spectrophotometer. Ag-TiO$_2$ thin film was prepared by spin coating method. The electrical properties were investigated by leakage current versus voltage (I–V) measurements. The reverse bias characteristics and the forward bias characteristics of the Schottky barrier of the Ag-TiO$_2$ thin film were also determined. Photovoltaic parameters: conversion efficiency (η_{con}) 4.83 % and fill factor (FF) 0.27 are also determined.

Introduction

The second-generation solar cell, which has been under intense development for the 90s and early 2000s, are low-cost thin-film solar cells. These cells use minimal materials and cheap manufacturing processes. [M.A.Green, et al(2010)] These thin materials are usually produced by physical or chemical deposition techniques, which can be applied to large areas and fast throughout. The term "thin film" refers more to the solar cell technologies with mass-production possibilities rather than the film thickness. The main advantage of thin-film solar cells is low cost due to low cost of processing and materials.[E.S.Aydil(2007)]

Polycrystalline and amorphous semiconductors contain intrinsic defects, which increase the density of traps and recombination centers, and reduce diffusion lengths. Therefore, an extended built-in electric field in low-doped absorber layer is used to aid carrier collection. The voltage dependent

---

[1] Dr, Lecturer, Department of Physics, Dagon University

[2] Department of Physics, University of Yangon

[3] Department of Physics, Pinlong University

charge collection in the depleted absorber layer is the dominant charge collection mechanisms in thin film solar cells.[S.M.Sze(1981)]

Thin film technologies have gained much interest because of their potential for low cost, large area fabrication. However, this lack of long range atomic order also results in high defect densities, limiting the film thickness to values ~ 300-500 nm for efficient charge collection. Optical absorption in thin layers is generally weak at infrared wavelengths and therefore requires a light trapping mechanism to increase the path of light travel within the film. Therefore, there is an ongoing interest in improving cell efficiencies while maintaining the low-cost large area advantage of thin film technology. [P.Bermel, et al(2007)]

Thin film solar cells are what many have resorted in order to tackle this issue. This makes it feasible for large-scale production. The deposition techniques involved allow the making of certain novel compound semiconductors which otherwise wouldn't be possible. The deposition techniques are flexible enough for the deposition to be on substrates such as glass, flexible substrates, polymer substrates etc. Certain electrical and optical properties that would not have existed in case of a same single crystal structure deposition becomes available. A few of the very important deposition techniques for thin film includes thermal evaporation, sputtering, CBD (Chemical Bath Deposition), ALD (Atomic Layer Deposition) etc. However the major disadvantage of a thin film solar cell being the high density of defects in their lattices compared to a single crystal structure. [H.J.Moller (1993)]

Recently, core-shell nanowires have brought much attention because of the possibility to tune the properties of core nanocrystal with addition of the shell. By choosing appropriate core and shell materials, the emission wavelength can be tuned in a larger range than both of materials alone. [P.Shimpi, et al(2009)] Based on different band structure alignment at core and shell materials interface, there are three different systems, type I, type II, and type III. At Type I, band gap of shell materials is larger than that of core materials, in which electrons and holes will be confined within core materials. At type II, band gap of shell materials is smaller than that of core materials, in which electrons and holes will be partially or completely confined within shell depending on how thick shell materials is. At type III, either the valence-band edge or the conduction band edge of the shell material islocated in the band gap of the core. [P.Reiss, et al(2009)] Several different technology approaches have been used to build the solar devices, such as thin film solar cells, and dye-sensitized solar cells.

Low dimensional nanostructure have brought up much attention to fabricate photovoltaic devices. [T.J.Hsueh, et al(2007)] Using nanostructure materials can improve not only efficiency but reduce the cost and size. Among all the available nanostructure, recently, core-shell semiconductor nanowires have gained a lot of interests. Comparing to conventional solar cells, core-shell structure solar cells have several advantages. For example, for conventional solar cells, electrons and holes stay in same region after photoexcitation, so electrons and holes have larger chance to recombine again, which will decrease electronic transport efficiency.[Y.Zhang, et al(2007)]

Core-shell structure photovoltaic devices have greater carrier collection and overall efficiency because each core-shell nanostructure might have high aspect ratio which allows optimal light absorption and carrier extraction into orthogonal spatial directions.[B.M.Kayes, et al(2005)]

Experimental

Silver nanoparticles were synthesized by an aqueous-based method. Silver nitrate was taken as the metal precursor. For the synthesis of silver particles, silver nitrate ($AgNO_3$) and deionized water were used as metal precursors. In a synthesis, 10mmol of sliver nitrate was dissolved in 10ml of deionized water. The pH of the solution was adjusted to about 9 by adding drop by drop solution of sodium hydroxide (NaOH). Ascorbic acid ($C_6H_8O_6$) was also used as a stabilizing agent. Then the solution was heated with water bath at 80˚ C until the solution evaporated. The co-precipitated precursor required a calcination at 600˚ C for 1:30 h, in order to be developed into a high purity silver particles.

Core material (Ag thin film) was prepared by mixing 0.0764 g of silver nitrate ($AgNO_3$) and 0.1 g of (NaCl) with 50 ml of dehydrates iodine water (DIW). First solution was stirred by magnetic stirrer to dissolve completely. And then, 10 ml of Ethylene glycol (EG) and 50 ml of DIW were added into 0.564 g of polyvinylpyrrolidone (PVP). Second solution was stirred by magnetic stirrer to dissolve completely. After they dissolved completely, first and second solutions were mixed. The ITO glass substrate was deposited in that mixture solution by chemical bath deposition(CBD) at 120 ° C for 2 h. To form the fine Ag films, Ag glass substrates were annealed at 400 ° C for 1h.

TiO_2 used as a shell material to fabricate core-shell thin film. TiO_2 sol-gel solution was formed from mixture solution of TiO_2 and methanol by stirring with magnetic stirrer for 1.5 h with 600 rpm. Finally, the Ag-TiO_2 core-shell thin film was done by coating TiO_2 sol-gel solution on Ag thin film.

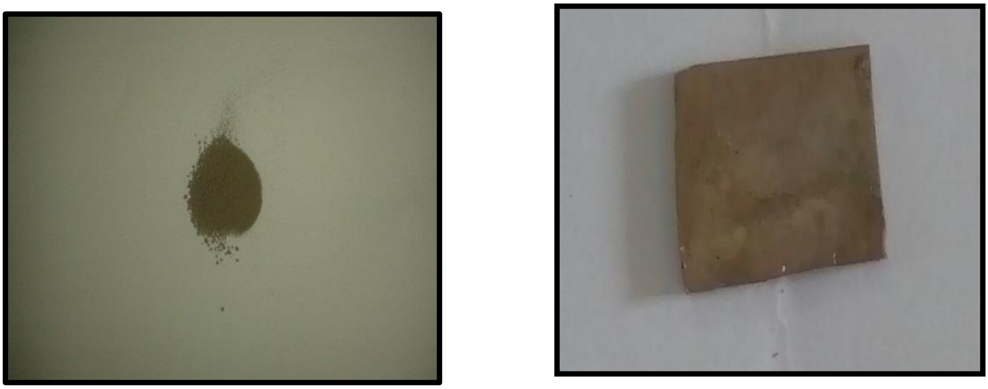

(a) Silver (Ag) nano particles (b) Ag thin film annealed at 400° C

(c) Ag-TiO_2 thin film annealed at

Figure 1: Sample preparation procedure

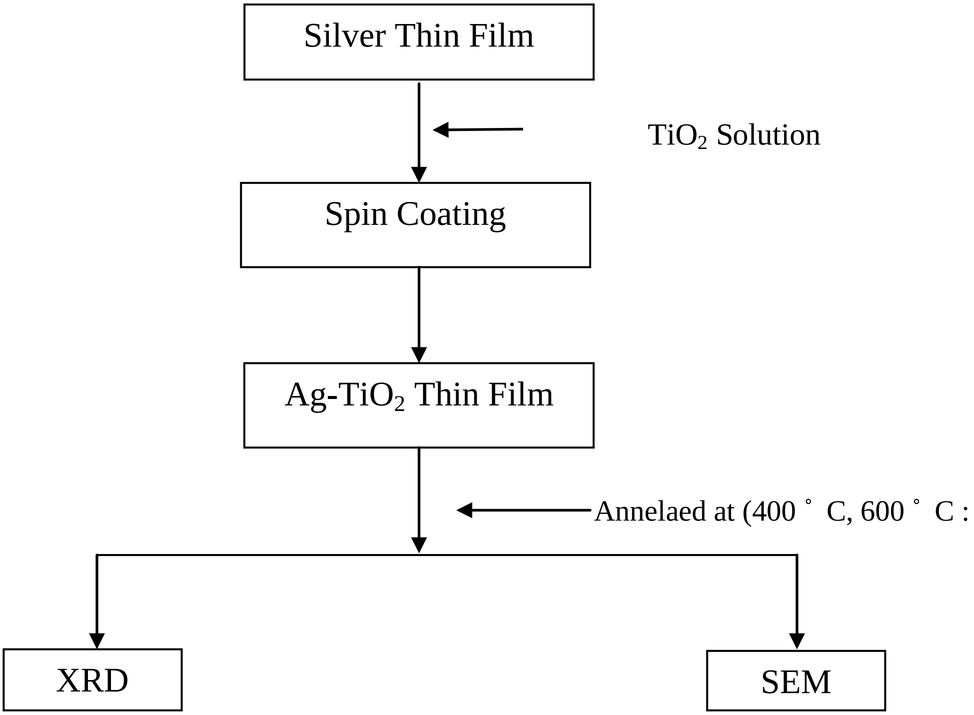

Figure 2: Block diagram for preparation of silver particles

Results and Discussion

Ag film was thus formed onto glass substrate by chemical bath deposition method. XRD analysis was undertaken to examine the crystal structure and phase formation of Ag film. According to the XRD pattern of Ag film at 400˚ C, (111) and (200) diffracted peaks represented the Ag film and some extra peaks were AgCl peaks. Thus, Ag film was formed onto glass substrate at 400□C.

According to the XRD pattern of Ag-TiO_2 film at 600 ˚ C, the intensity of TiO_2 peak (101) was increased and (004) peak was formed. It can be said that Ag-TiO_2 thin film was formed at 600˚ C. The diffraction angle (Bragg angle) (2θ) of observed and standard, lattice parameter, crystal structure of Ag-TiO_2 film at 600 ˚ C were shown in Table 1.

The microstructure of Ag-TiO_2 samples at the annealing temperatures of 400° C and 600° C for 1 h were examined by SEM. The recorded images of those films are shown in Fig 4. The micrograph of Ag-TiO_2 become rough after annealing 400° C. Fig 5 showed the microstructure of Ag-TiO_2 film at 600° C. The grain size of TiO_2 obtained as about Ag was 0.12 μm. It was observed that there was grain size become smaller and crack free. Among these recorded images, the film at 600 ° C was found in the most homogeneous layer. These facts are indicated the grain size and homogeneity of the films depend on the process temperature.

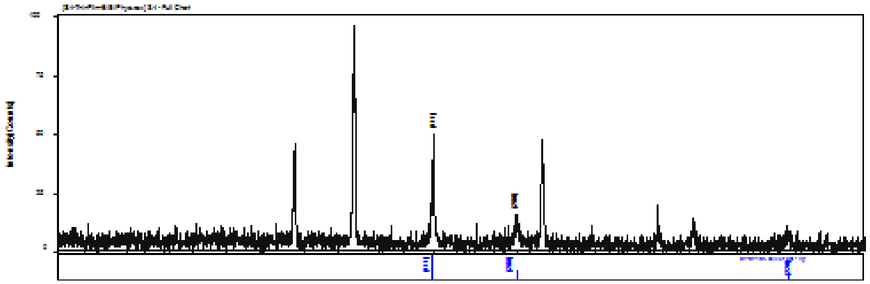

Figure 2: XRD spectrum of Ag thin film at 400 ° C

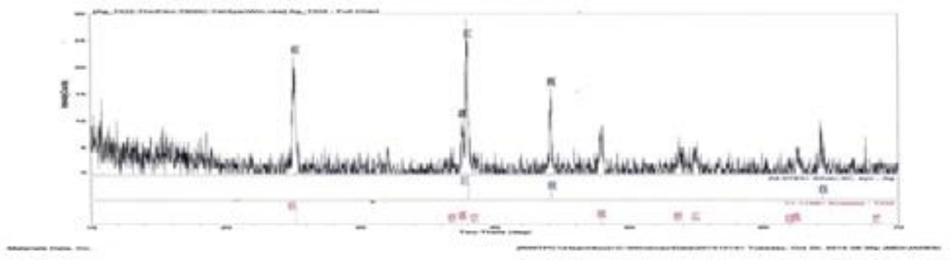

Figure 3: XRD pattern of Ag-TiO_2 thin film at 600 ° C

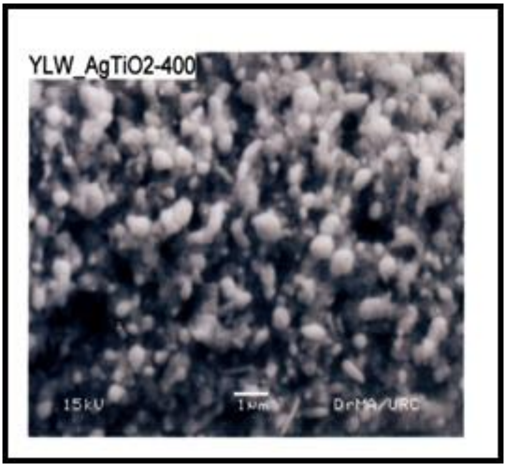

Figure 4: SEM image of Ag-TiO$_2$ film at 400 ° C

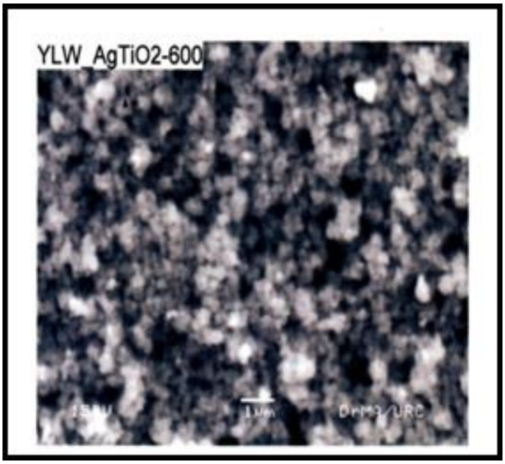

Figure 5: SEM image of Ag-TiO$_2$ film at 600 ° C

Table 1: Lattice parameters of Ag-TiO$_2$ thin films at 600 °C

Ag	**Lattice parameter (Å)**
Peaks	a
101	4.9969
004	4.1421
200	4.0961
Average lattice constant	4.3336

TiO$_2$	**Lattice parameter (Å)**	
Peaks	a	c
101	3.8023	9.4777
004	3.7658	9.4973
200	4.0961	9.4777
Average lattice constant	3.8844	9.4842

Table 2: Observed and standard lattice parameters of Ag-TiO_2 thin film at 600 □C

	Lattice parameter (Å)		Crystal Structure
	Standard	**Observed**	
Ag	4.0853	4.3336	Cubic
TiO_2	3.74	3.8884	Tetragonal
	9.4842	9.502	

J-V Characteristics under Illumination

The performance of Ag-TiO_2 thin film defined by several parameters such as short-circuit current I_{sc} and open-circuit voltage V_{oc} obtained under illumination conditions. The output power was calculated as P=JV from the J-V curves shown in Figure8. The maximum power (Pm) of cell is then obtained. The current (I_m) and the voltage (V_m) corresponding to the maximum power point are then obtained. The photoelectrochemical parameters of Ag-TiO_2 thin film are listed in the Table 3. Fill factor (FF) under illumination condition is a measure of a diode behavior of the cell. It is obtained using a current-voltage characterization as follows

$$FF = \frac{J_m \times V_m}{V_{OC} \times J_{SC}} = \frac{P_m}{V_{OC} \times J_{SC}}$$

The efficiency η describes the overall performance of the thing film solar cell. It is defined as the ratio of P_m to the power of incident radiation (P_{in}). The maximum output power was to be found 0.103 mW/cm^2 for Ag-TiO_2 thin film.

The power conversion efficiency of energy to electricity conversion efficiency (η) of the cell with P_{out} electrical power under illumination condition is given by:

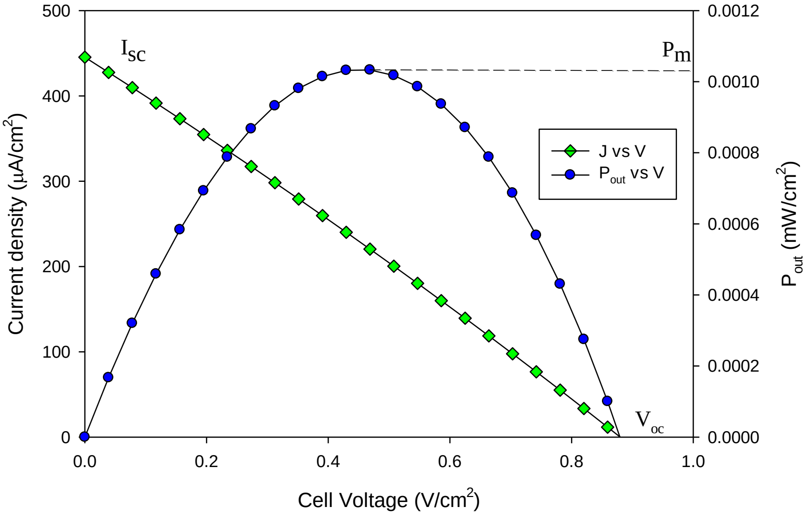

Figure 6: Current density Vs cell voltage curves for Ag-TiO_2 thin film

Table 3: Photovoltaic parameters of Ag-TiO_2 thin film

Thin film	I_m(A)	V_m(mV)	J_{sc}(μA)	V_{oc}(mV)	P_m(mW/cm^2)
Ag-TiO_2	2.20E-04	468.8	4.45E-04	859.4	0.103

Table 4: Efficiency and fill factor of Ag-TiO_2 thin film

Thin film	η_{con}(%)	FF
Ag-TiO_2	4.83	0.27

I-V measurement (under dark condition)

Dark current-voltage (dark I-V) measurements are commonly used to analyze the electrical characteristics of solar cells, providing an effective way to determine fundamental performance parameters without the need for a solar simulator. I-V characteristics of Ag-TiO_2 thin film are measured within the bias voltages. I-V characteristics of Ag-TiO_2 thin film is measured in the region of -5 V to +5 V by using Cu-electrode. Ln I-V characteristics obey the linear relationship and I_s was obtained by extrapolating the variation line in which I_s = exp (intercept) relation is used. The forward applied voltage ranges, the ideality factor (η), zero bias barrier height (□$_{bo}$) are measured by the following equations:

$$I_s = AR^*T^2 \exp\left(\frac{-q\Phi_{bo}}{kT}\right)$$

$$\frac{1}{\eta} = (\frac{1-\eta\Phi_{bo}}{\eta V_f})$$

The zero bias barrier height and ideality factor of the Ag-TiO_2 film are listed in Table 5.

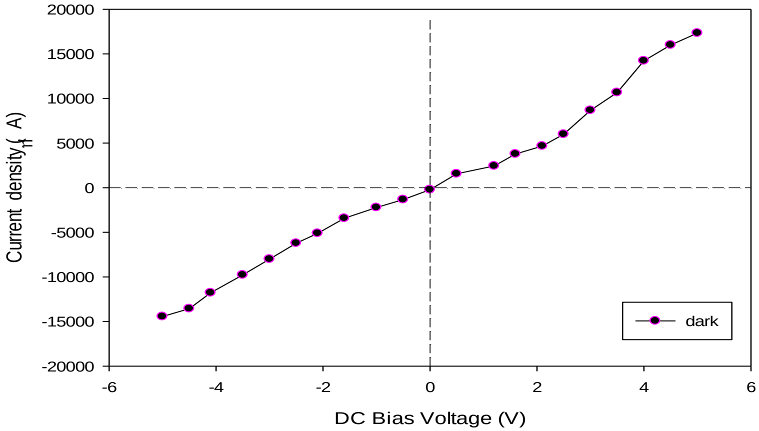

Figure7: I-V characteristics of Ag-TiO_2 thin film (under dark condition)

Table 5: Saturation current (I_s), zero bias barrier height (□$_{bo}$) and ideality factor (*η*) of Ag-TiO_2 thin film

Thin film	**I_s(□A)**	**□$_{bo}$ (mV)**	***η***
Ag-TiO_2	4.26	0.2834	1.2843

Conclusion

Ultrafine silver particles in cubic form have been successfully prepared by aqueous-based reduction method. The Ag film was formed onto glass substrate at 400 ˚ C. It is confirmed that the temperature treated at 400˚ C is more suitable for silver fabrication mechanism. Growth of Ag films and their characterizations (SEM & UV-Vis) have been implemented. Moreover, it was obvious that Ag film was clearly formed onto glass substrate at temperatures 400˚ C. From the optical properties (UV- Vis) spectroscopic measurement, the absorption edge (major peak) position was 471 nm for Ag film at 400˚ C. This value was found to be within the range of acceptable value for visible light. Nevertheless, all optical band gaps in this study are ranged between the standard value of silver (1.3-2.4 eV). According to (SEM) analysis, the grain size and homogeneity of Ag-TiO_2 thin film varied with annealing temperature. Minimum grain size, homogeneous layer and uniform pores are observed at a process temperature 600˚ C. I-V characteristics of Ag-TiO_2 thin film are measured in the region of -5V to +5V. In the dark condition, thin film displays regular diode like characteristics with the curve passing through the origin. According to ln I-V characteristics, the measurements of saturation current, zero-bias barrier height and ideality factor are also studied. I-V curve of fabricated Ag-TiO_2 thin film are found to be p-n contact between metallic (Cu) electrode and film. Photovoltaic parameters: conversion efficiency (η_{con}) 4.83 % and fill factor (Ff) 0.27 are also determined. The growth chemistry of Ag-TiO_2 film preparation are quite acceptable for thin film fabrication manufacture although the methods employed in this work are non-expensive, non-modernized and non-complicated methods. According to experimental results, the fabricated Ag-TiO_2 (core-shell) thin film is quite suitable for photovoltaic applications.

Acknowledgements

This research was totally done at Department of Physics, University of Yangon in Myanmar (2016-2017).

References

B. M. Kayes, H. A. Atwater and N. S. Lewis, (2005), “Comparison of the device physics principles of planar and radial p-n junction nanorod solar cells”, Journal of Applied Physics, 97

Bermel, P., Luo, C., Zeng, L., Kimerling, L.C., Joannopoulos and J.D,(2007) “Improving thin-film crystalline silicon solar cell efficiencies with photonic crystals”, Optics Express 15 (25), 16986-17000.

Eray S. Aydil,(2007)“Nanomaterials for Solar Cells”, Nanotechnology Law & Business, 4 ,275-291

H. J. Moller, Book: Semiconductors for solar cells, Artech house Inc, 1993

M. A. Green, K. Emery, Y. Hishikawa, and W. Warta, (2010), “Progress In Photovoltaics: Research And Applications”, 19, 84-92

P. Shimpi, P. -X Gao, D. G. Goberman and Y. Ding, (2009), “Low temperature synthesis and characterization of MgO/Zn Onanocomposite wire arrays”, Nanotechnology, 20, 125-608

P. Reiss, M. Protière and L. Li, (2009), “Core/shell Semiconductor Nanocrystals”, Small 5, 154 -168

S.M. Sze, “Physics of Semiconductor Devices”, 3rd ed., (Wiley, New York, 2007)

T. -J Hsueh, C. -L Hsu, S. -J Chang, P. -W Guo, J. -H Hsieh and I. -C Chen, Scr. Mater. 57, 53 (2007).

J. Myanmar Acad. Arts Sci. 2019 **Vol. XVII. No.2A**

CHARACTERIZATION OF METHYL AMMONIUM LEAD IODIDE PEROVSKITE FILM BY TWO-STEP DEPOSITION METHOD

Aye Aye Kay Kyi[1], Soe Soe Han[2], May Myint Si[3]

Abstract

Methyl ammonium lead iodide perovskite films were fabricated by using two-step deposition method. PbI_2 film was coated by using spin coating method. Making a high quality PbI_2 film was easier and better to fabricate a good perovskite film.The spin coating rate, the concentration of the solution and the dipping time was varied to analyze the properties of the perovskite films. The structure of the methyl ammonium lead iodide perovskite films was analyzed by using XRD characterization. The color change of the films at different stages and the mesoporous structure of the film in two-step deposition method were evaluated. The morphology of the perovskite film was characterized by scanning electron microscopy (SEM). The band-gap of the film was analyzed to determine the parameter of the photovoltaic performance of the solar cell by using UV measurement. Finally, the combination of light harvesting layer methyl ammonium lead iodide perovskite film and electron transporting layer TiO_2 film was summarized for perovskite solar cell performance.

Keywords: Methyl ammonium lead iodide, X-ray diffraction (XRD), Scanning electron microscopy (SEM) and UV-VIS

Introduction

Organic-inorganic lead halide-based hybrid perovskites have recently emerged as a promising photo-absorber material for efficient and low-cost solar cells. Solar cells with a perovskite structure have high conversion efficiencies and stability as the organic solar cells. The first perovskite solar cell was demonstrated by Miyasaka et al., in 2009. The perovskite solar cells were based on the structure of the solid state dye sensitized solar cell by using perovskite instead of dye as light absorber. Perovskites are absorber materials that have the ABX_3 crystal structure. The most commonly studied perovskite absorber is methyl ammonium lead trihalide ($CH_3NH_3PbX_3$, where X is a halogen atom such as iodine, bromine or chlorine), with an optical bandgap

---

[1] Assistant Lecturer, Department of Physics, Dagon University

[2] Dr, Lecturer, Department of Physics, University of Yangon

[3] Dr, Professor and Head, Department of Physics, Dagon University

between 1.5 and 2.3 eV. The PCE for perovskite solar cells have increased from 3.8% in 2009 to 22.1% in early 2016. The photovoltaic properties of these solar cells are strongly dependent on the crystal structure of the perovskite compound, the fabrication process, the hole transport layer, the electron transport layer, the nanoporous layer and interfacial microstructure. Especially, the crystal structures of the perovskite-type compounds, strongly affect the electronic structures such as energy band gaps and carrier transport, and a detailed analysis of them is mandatory. In this paper, solar cell was investigated by using nanoparticles of TiO_2 and light absorbing perovskite material. Several preparation steps are needed to make perovskite material such as spin coating of TiO_2, deposition the perovskite by spin coating, thermal evaporation and dip coating. The crystal structures of perovskite type compounds $CH_3NH_3PbI_3$ was analyzed by using X-ray diffraction (XRD). Surface morphology and energy band gaps of the perovskite layer were investigated using scanning electron microscopy (SEM) and UV measurements.

Experimental Procedure

Perovskite solar cell was manufactured by going through several processes such as cutting, washing, stirring, spinning, dipping and annealing of under layer.

TiO_2 Film Deposition by Spin Coating

Titanium dioxide (TiO_2) was deposited on glass substrate by spin coating method. To prepare the TiO_2 pastes by mixing 1g of TiO_2, 2 g of terpineol and 2 g of ethanol. Then the mixture was stirred for 30 min to get homogeneous solution. The TiO_2 paste was deposited on glass substrates by spin coating at room temperature with a rate of 1500 rpm for 20 s, 2500 rpm for 30 s and 3500 rpm for 30 s. After each spin coating step, the films were annealed at 80˚ C for 15 min. The procedure from coating to annealing was repeated three times. The flow chat of TiO_2 deposition by spin coating is shown in Figure 1 (a).

PbI_2 Solution for Spin Coating

Prepare the PbI_2 pastes by mixing 1 g of lead (II) iodide powder and 3 ml of dimethyl formamide (DMF) solution. Then the solution was stirred at the temperature of 60° C about 1 hour. When the stirring time was 40 min, TiO_2 glass layers were annealed on the hot plate at 100° C for 15 min. After stirring the solution, the precipitate was filtered and PbI_2 solution was come out. The PbI_2 paste was spin coated on the TiO_2 glass layer at a rate of 3500 rpm for 30 s. All the pastes were come out as light yellow color. And then PbI_2 glass layers were annealed on the hot plate at 70° C for 30 min. After the glass layers were annealed, they changed from light yellow to bright yellow color. The flow chat of spin coating for PbI_2 layer is shown in Figure 1 (b).

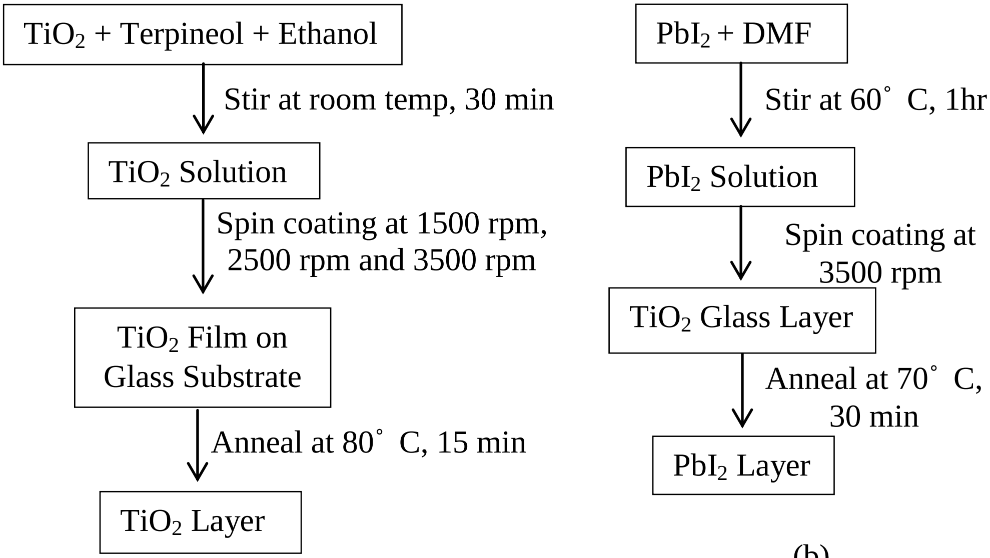

(a) (b)

Figure 1: Spin coating for (a) TiO_2 Layer (b) PbI_2 Layer

Dip Coating Procedure

For dipping process, 0.1 g of MAI powder was dissolved in 10 ml of isopropanol and stirred at room temperature about 10 min to get the homogeneous MAI solution. The PbI_2 layers were pre annealed at 70° C about 30 min before dipping. All the PbI_2 layers were dipped into the MAI solution for 1 hour. While the films were dipping, the color was slightly changed to light brown. Then $CH_3NH_3PbI_3$ perovskite layers were placed on the hot plate at 70° C for 15 min. After annealing, the film's color was changed to dark brown. The flow chat of dip coating process is shown in Figure 2.

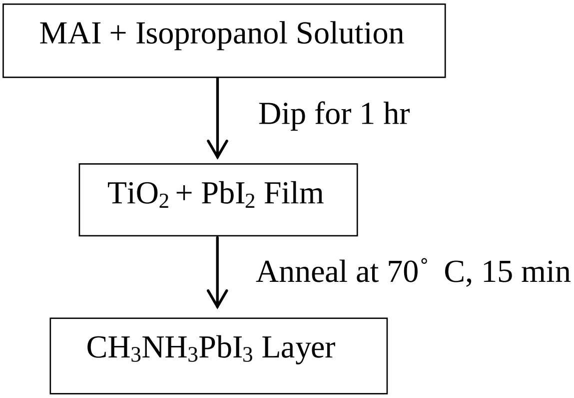

Figure 2: Preparation of perovskite layer by dip coating process

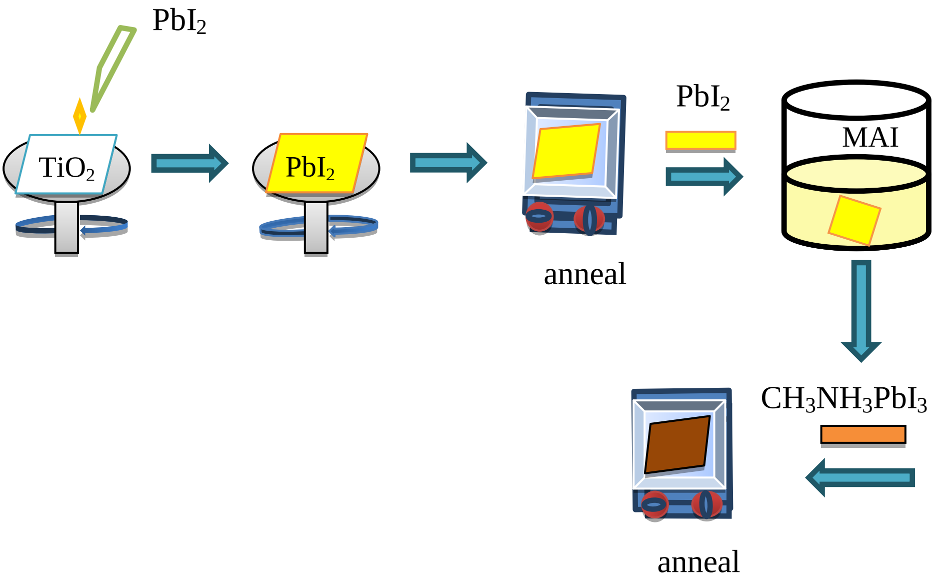

Figure 3: Preparation of methyl ammonium lead iodide layer from PbI_2 spin coating to dip coating

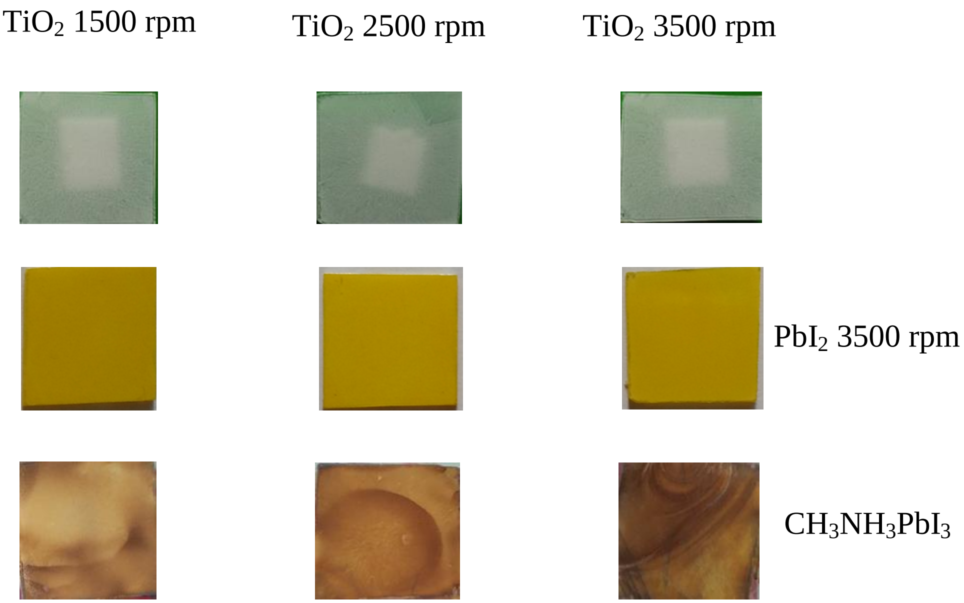

Figure 4: The color changing from TiO_2 spin coating to dip coating

Results and Discussion

XRD Analysis

The crystal structure of methyl ammonium lead iodide perovskite layers was analyzed by using X-ray diffraction technique. For TiO_2 layer coating, the spin coating rate was varied 1500 rpm, 2500 rpm and 3500 rpm for three samples (1), (2) and (3). The crystallite sizes of TiO_2 layers are 58 nm (sample-1), 54 nm (sample-2) and 17 nm (sample-3). By increasing the spin coating rate of TiO_2, the crystallite sizes were gradually decreased. The smallest crystallite size 17 nm is collected the better condition of TiO_2 to fabricate the complete perovskite solar cell. After TiO_2 layer coating, the PbI_2 layer was continued to fabricate by using spin coating rate 3500 rpm for sample 1, 2 and 3. The crystallite sizes of PbI_2 layers are 118 nm, 95 nm and 46 nm for three samples.

Finally, dip coating process of methyl ammonium iodide is continued to fabricate complete ($CH_3NH_3PbI_3$) perovskite layer. After dipping process, the crystallite sizes of PbI_2 are uniformly decreased to 85 nm, 83 nm and 81 nm. The average crystallite sizes of methyl ammonium iodide (MAI) are decreased 59 nm, 26 nm and 22 nm by varying the spinning rate. The XRD spectra of PbI_2 and MAI are illustrated in Figures 5, 6 and 7. The crystallite sizes of TiO_2, MAI and the comparative result of PbI_2 before dipping and after dipping process are shown in Table 1. The humidity and moisture sensitive properties of methyl ammonium lead iodide perovskite layers were studied by observing the changing of the color. The films color was changed from bright yellow to dark brown due to the chemical reaction.

Table 1: The average crystallite size for TiO_2, PbI_2 and MAI

TiO_2 Spin Coating Rate	**Average Crystallite Size (nm)**			
	Before dipping		**After dipping**	
	TiO_2	**PbI_2**	**PbI_2**	**MAI**
1500 rpm	58	118	85	59
2500 rpm	54	95	83	26
3500 rpm	17	46	81	22

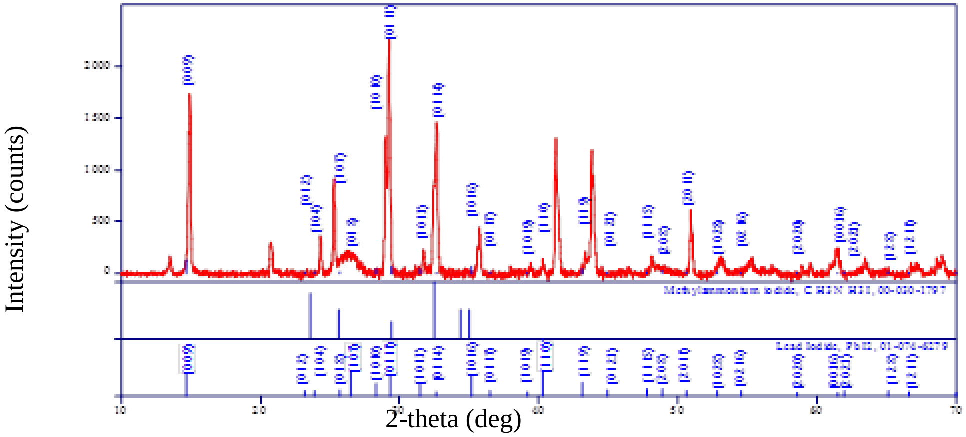

Figure 5: The XRD pattern of crystallite size for PbI_2-3500 rpm at TiO_2 -1500 rpm after dipping

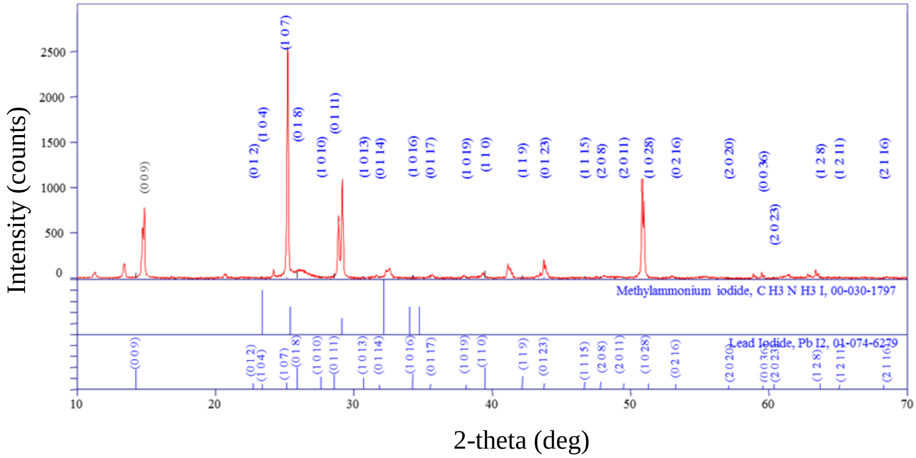

Figure 6: The XRD pattern of crystallite size for PbI_2-3500 rpm at TiO_2 -2500 rpm after dipping

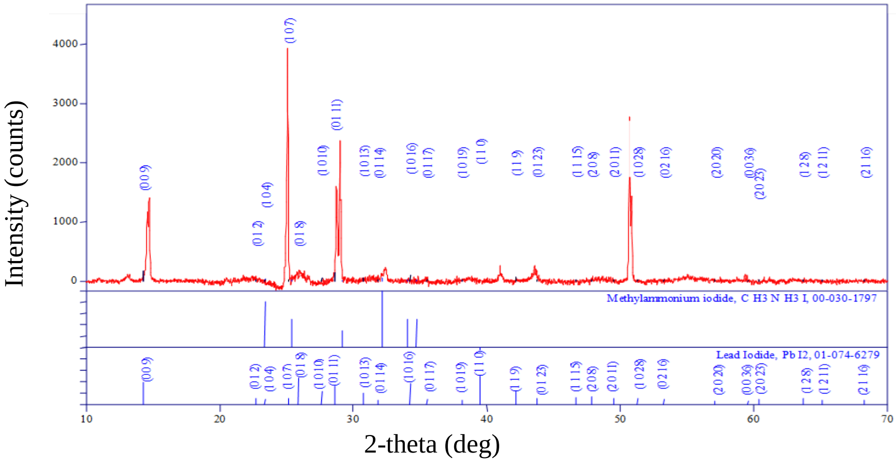

Figure 7: The XRD pattern of crystallite size for PbI_2-3500 rpm at TiO_2 -3500 rpm after dipping

SEM Analysis

Scanning electron microscopy (SEM) is a type of electrons microscope that produces images of a sample by scanning the surface with a focused beam of electrons. The grain size and surface morphology of the methyl ammonium lead iodide ($CH_3NH_3PbI_3$) perovskite layers were analyzed by Scanning Electron Microscope JEOL-JSM 5610 LV (SEM). The grain size was calculated by line interception technique. The average grain sizes of methyl ammonium lead iodide perovskite layers are 3.106 µm (sample-1), 2.329 µm (sample-2) and 2.299 µm (sample-3). By increasing the spin coating rate of TiO_2, the grain sizes were gradually decreased. The decreasing of grain size is getting the better condition of surface morphology. This is the one good reason to fabricate the solar cell. The SEM images of perovskite layers are shown in Figures 8 (a), (b) and (c).

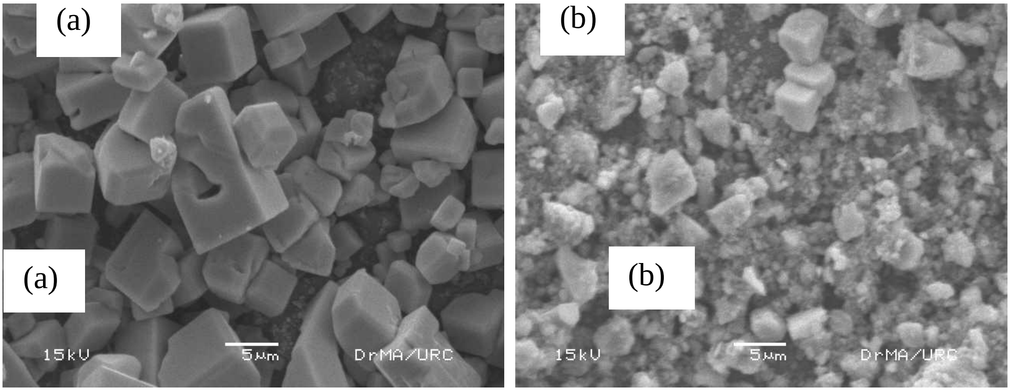

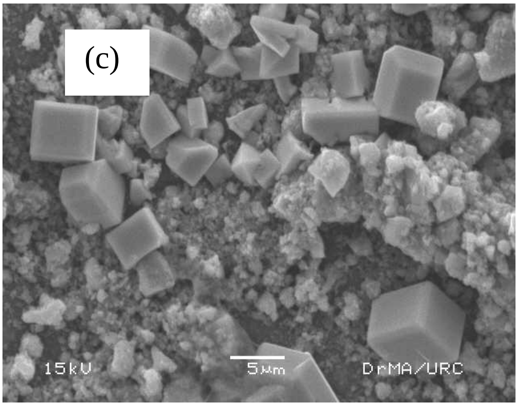

Figure 8: The SEM images of perovskite film for (a) TiO_2 1500 rpm, (b) TiO_2 2500 rpm and (c) TiO_2 3500 rpm

UV Measurement

The energy band gap of the methyl ammonium lead iodide ($CH_3NH_3PbI_3$) perovskite layers were analyzed by UV measurement. The maximum absorbance is observed for TiO_2 spin coated at 1500 rpm with the bigger grain size in the wavelength region from 300 nm to 600 nm. The wavelength is gradually tuned to the red shift from 750 nm to 810 nm. Changes of spin coating rate can tune the wavelength from lower range to higher range. The transmittance is drastically decreased around 800 nm .The transmittance is dropped and closed to 1% in the wavelength range from 400 nm to 315 nm. The highest transmission is at the spin coating rate of TiO_2 3500 rpm. The absorption and transmision spectra of UV measurements for perovskite layers are illustrated in Figures 9 (a) and (b).

The energy gaps of the methyl ammonium lead iodide perovskite layers are 1.475 eV, 1.480 eV and 1.485 eV. By increasing the grain size, the energy gap is tuned to lower range. The energy band gaps of perovskite layers are shown in Figures 10 (a), (b) and (c). The band gap of methyl ammonium lead iodide perovskite layer is typically around 1.5 eV. So the results of the band gap ranges are reliable to fabricate the perovskite solar cell.

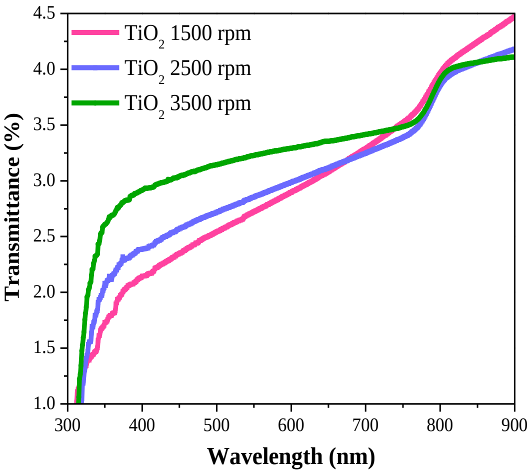

(a) (b)

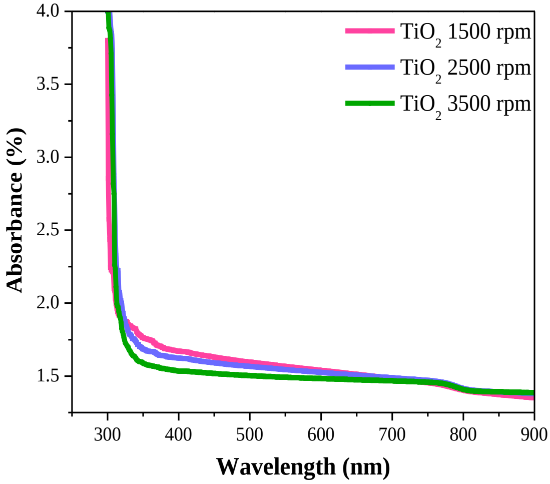

Figure 9: Comparison of UV-Vis spectra at different spin coatin g rates of TiO_2 layers (a) Absorption Vs Wavelength (b) Transmission Vs Wavelength

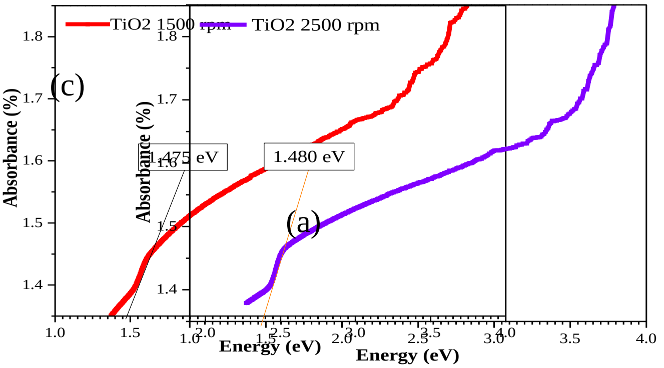

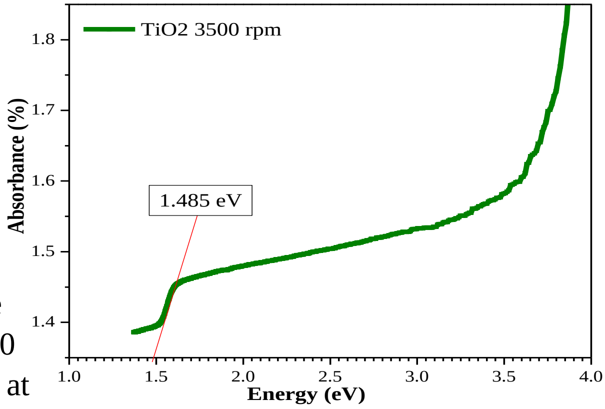

Figure 10: Energy band gap of methyl ammonium lead iodide perovskite layers (a) at TiO_2 1500 rpm, (b) at TiO_2 2500rpm, (c) at TiO_2 3500 rpm

Conclusion

The perovskite layers were prepared by using low cost spin coating method and dip coating method. The XRD studies indicate the hexagonal structure of lead (II) iodide with preferred orientation along the (0 0 9), (1 0 7), (0 1 11) after dipping. Crystallite size has been estimated by using Scherrer equation. The crystallite sizes of PbI_2 and MAI was varied by increasing the spin coating rate of TiO_2. Band gaps have been estimated by using UV measurement. It has been found that the grain sizes of perovskite layers are decreased by increasing the spin coating rate of TiO_2 layer. The average grain size is decreased from 3.106 µm to 2.299 µm. The best surface morphology is observed at spin coating rate 3500 rpm. The wavelengths have been tuned to the higher wave number from 750 nm to 810 nm. By increasing the grain size, the energy gap is shifted to lower range. The results of the energy band gap ranges are around 1.5 eV.

Acknowledgements

This research was totally done at Department of Physics, University of Yangon in Myanmar. I would like to thank Professor Dr Khin Khin Win, Head of Department of Physics, University of Yangon for her kind permission to carry out of this study. I would like to express my sincere thanks to Professor Dr Aye Aye Thant, Department of Physics, University of Yangon for her valuable suggestion and comments for this work.

References

Boopathi, K.M., Ramesh, M., Perumal, P., Huang, Y.C., Tsao, C.S., Chen, Y.F., Lee, C.H., & Chu, C.W. (2015). Preparation of metal halide perovskite solar cells through a liquid droplet assisted method. *J. Mater. Chem. A*, 3, 9257-9263.

Chang, C.Y., Chu, C.Y., Haung, Y.C., Haung, C.W., Chang, S.Y., Chen, C.A., Chao, C.Y., & Su, W.F. (2015). Tuning Perovskite Morphology by Polymer Additive for High Efficiency Solar Cell. *ACS Appl. Mater. Interfaces*, 7, 4955-4961

Chhetri, A.R., Dayal, S., Stephan & J.A., Nanlini, R.P. (2018). A Study on Mixed Halide Perovskites. *IJSER*. 9, 104-106.

Danilchuk, D., Nour, B., & Dahal, L. (2016). Development of Low-cost Hybrid Perovskite Solar Cells. *NCUR Conf. Proc*, 30, 1857-1863.

Oku, T. (2015). *Crystal Structures of $CH_3NH_3PbI_3$ and Related Perovskite Compounds Used for Solar Cells*. Hikone: Shiga Prefecture.

Oku, T., Matsumoto, T., Suzuki, A., & Suzuki, K. (2015). Fabrication and Characterization of a Perovskite-Type Solar Cell with a Substrate Size of 70 mm. *Coatings*, 5, 646-655.

Wu, C.G., Chiang, C.H., Tseng, Z.L., Nazeeruddin, M.K., Hagfeldt, A., & Gratzel, M. (2015). High efficiency stable inverted perovskite solar cells without current hysteresis. *Energy Environ. Sci*, 8, 2725-2733.

Zuo, C., Bolink, H.J., Han, H., Haung, J., Cahen, D., & Ding, L. (2016). Advances in Perovskite Solar Cells. *Adv. Sci*. 1500324,1-16.

J. Myanmar Acad. Arts Sci. 2019 **Vol. XVII. No.2A**

STRUCTURE AND OPTICAL CHARACTERIZATION OF ORGANIC-INORGANIC METHYL AMMONIUM LEAD BROMIDE FILM FOR SOLAR CELLS

Tin Nyein Nyein Khaing[1], Soe Soe Han[2], May Myint Si[3]

Abstract

Structure and optical characterization of organic-inorganic methyl ammonium lead bromide film was fabricated by using spin coating and dipping two-step deposition method. The humidity and temperature effect were characterized to improve the morphology of the perovskite film. To verify the thickness of the film and properties, the spin coating rate, dipping solution concentration and annealing temperature were varied. The consistency with mesoporous structure and the color changes of the film at different stages were initialized. The structure of organic- inorganic lead bromide film was analyzed by using XRD characterization. The nano-range grain size and morphology of the perovskite film were characterized by measuring scanning electron microscopy (SEM). The UV measurement was performed to determine the band-gap of the film to justify the parameter of the photovoltaic performance of the solar cell. Finally, the properties of methyl ammonium lead bromide perovskite film and TiO2 film were optimized by varying the thickness of the TiO2 film for high efficiency solar cell performance.

Keywords: Methyl ammonium leads bromide, X-Ray Diffraction (XRD), Scanning Electron Microscopy (SEM) and Ultraviolet- Visible (UV- VIS).

Introduction

Photovoltaic devices which convert solar energy to electricity are one of the most important technologies for renewable energy. As a photo absorber and carrier transporter, photovoltaic cells using perovskite. Since perovskite based solar cells not only have high power conversion efficiency but also can be fabricated by a solution processed using cheap materials. Organic-inorganic hybrid solar cells with perovskite-type pigments have been widely fabricated and rapidly studied. Solution-processed hybrid organolead trihalide perovskite solar cells (PSCs) have now achieved 21% certified power

---

[1] Assistant Lecturer, Department of Physics, Dagon University
[2] Department of Physics, University of Yangon
[3] Department of Physics, Dagon University

conversion efficiencies . One of the most important properties of the organic-inorganic perovskite for their use in photovoltaic cells is the possibility to tune their optical properties (e.g band gap). The band gap of CH3NH3PbI2Br perovskite is 1.5 eV and it is used as the light- absorbing material in bilayer solar cells architecture. These perovskite-type materials often have nanostructure in the solar cell devices and it is useful for structure analysis on the perovskite-type crystal. One of the most popular methods is the spin-coating technique for applying thin films onto flat surface. In photovoltaic research, it is used frequently due to its ease of use and relatively low cost. By using SEM characterization and UV measurement, methyl ammonium lead bromide film is analyzed. These are powerful tools for surface morphology and energy band gap of perovskite-type solar cells.

Materials and Methods

Preparation of TiO_2 powder

Starting materials TTIP (Titanium tetra isopropoxide), Ethanol and distilled water were used for TiO_2 powder preparation process. Firstly, 50 ml Ethanol and 50 ml distilled water were mixed and stirred at 60 ºC for 30 mins. And then 15 ml TTIP was added to this solution and stirred at 50 ºC for 10 hrs. As soon as adding process, TTIP becomes small pieces. After 10 minutes later, the solution turned to dark milk color solution. Then, this solution was dried at 60ºC for 2 days and pulverized to get TiO_2 powder. Finally, fine and dry nanostructure TiO_2 powder was successfully prepared. The phase formation of the raw and cleaned TiO_2 powder was identified by XRD diffractometer.

Preparation of TiO_2 solution and Film

Titanium dioxide 1g and ethanol 2 g were mixed and stirred by magnetic stirred at room temperature for one hour. After that this solution was pasted on the glass substrates at 2500 rpm for 30 s by using spin coating method. This solution process was performed two times. After the two-circles layer coating process, the substrate was annealed at 80 ºC for 15 mins.

Methyl Ammonium Iodide (MAI) Solution for Dip Coating

Methyl ammonium iodide was formed by doing several steps. CH3NH3I was synthesized by reacting methylamine (33wt% in ethanol) and hydroiodic acid (57wt% in water). Firstly, 7 ml of methylamine was put into the beaker. Then the temperature 3 was adjusted to stabilize at 0 ºC. Then 7.5 ml of hydroiodic acid (HI) was drop wised into the methylamine solution at 0 ºC for 10 min. The solution was slightly changed to light yellow while the dropping time. That solution was stirred at 0ºC for 2 hrs. After stirring 30 mins, the solution was changed to dark yellow color. When the stirring time was finished, the precipitate was collected by removing the solvents at 60 ºC for 2 hrs. The solution was changed to dark brown color after heating 30 mins. When the evaporation time was nearly finished, the solution was getting boiled and changes from solution to semi MAI solid. Then the obtained precipitate was filtered and washed diethyl ether for several times to remove any impurities. The light brown MAI was resulted and called methyl ammonium iodide. Then CH3NH3I was put into the vacuum oven at 100 ºC about one day to get the MAI powder. Lead II bromide (PbBr2) and dimethylformamide (DMF) solution pasted on the three glass substrates and MAI with isopropanol have been used for dipping. Firstly, 3 substrates were heated at 70 ºC for 30 mins. Then these three samples were dipped in the MAI solution for an hour. As soon as dipping, the glass substrate are turned to light brown. Due to humidity, the color of the substrates were changed when they were heated at 70 ºC for 30 min. Finally, CH3NH3PbI2Br perovskite coated layer were completely fabricated.

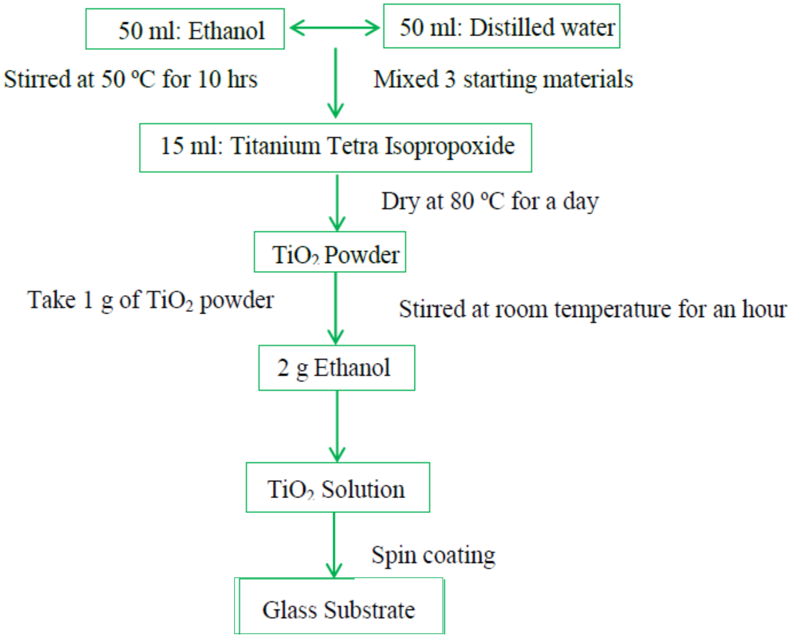

Figure1: Preparation of TiO_2 electron collection layer

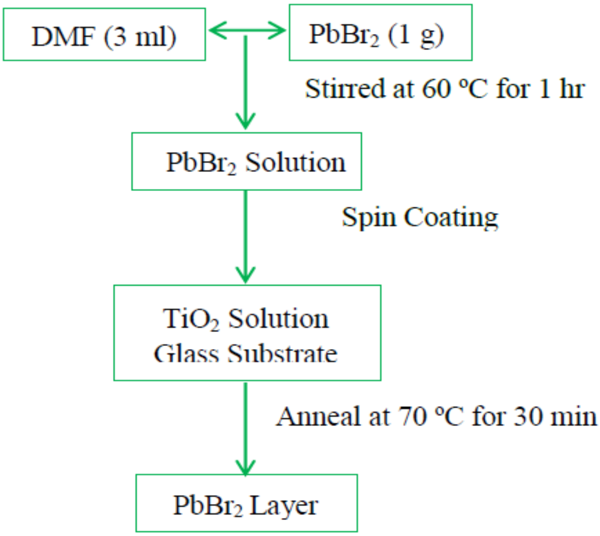

Figure 2: Preparation of spin coating for $PbBr_2$ layer

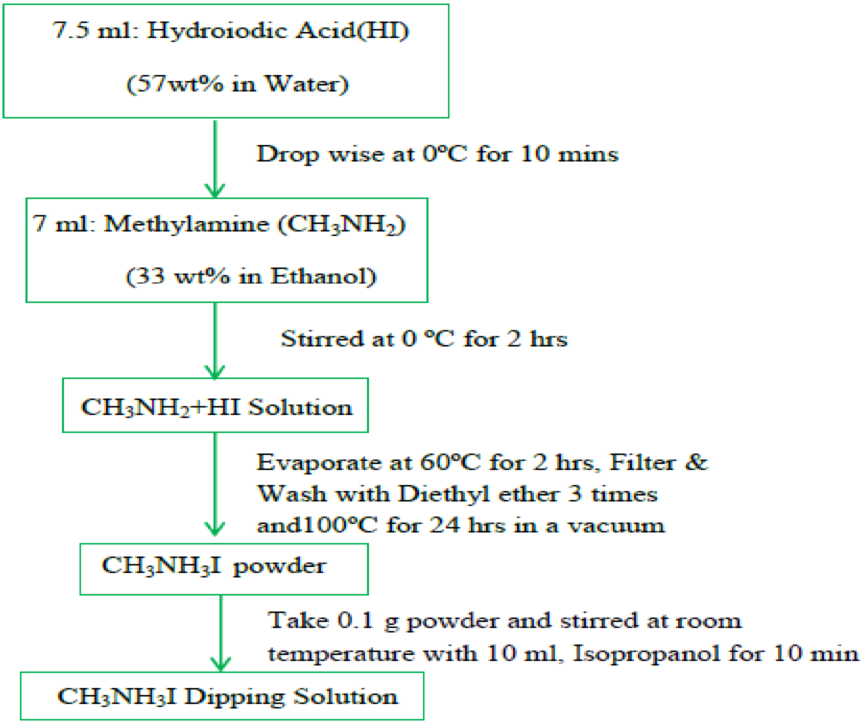

Figure 3: Preparation of methyl ammonium iodide CH_3NH_3I solutions for dipping process

Results and Discussion

XRD Method

For determining the crystal structure of materials, X-Ray Diffraction methods are the most effective methods. By Bragg's law, the relationship is satisfied.

$$n\lambda = 2d\sin\theta$$

λ = the wavelength of the incident X-ray beam

The path difference depends on the incident angle and the spacing between the parallel crystal planes (d). The plane spacing of cubic crystal relates to the lattice parameter (a) by the following equation

$$d = \frac{a}{h^2+k^2+l^2}$$

The crystallite size can be estimated using the Scherrer equation

$$D = \frac{ky}{B\cos\theta}$$

Table 1: The crystallite size of electrons collection layers for TiO_2 at 2500 rpm

No	2-Theta	(hkl)	FWHM	Crystallite size
1	25.9413	(1 0 1)	1.6111	48 nm
2	37.9255	(1 0 3)	1.6111	48 nm
3	39.5673	(1 1 2)	1.6111	48 nm
Average				48 nm

Table 2: XRD parameters of $PbBr_2$ crystallite size at different spinning rate

No	Spinning rate	2-Theta	(hkl)	FWHM	Crystallite size
1	3000 rpm	14.4243	(0 1 1)	0.2054	38.3 nm
2	3500 rpm	14.3831	(0 1 1)	0.2208	35.5 nm
3	4000 rpm	30.1803	(0 1 3)	0.5759	34.3 nm
Average					36.03 nm

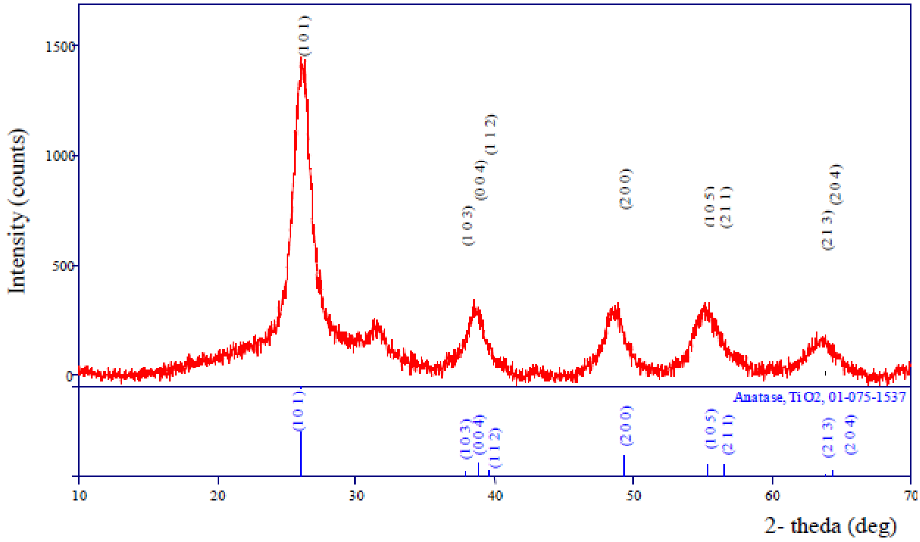

Figure 4: XRD spectrum of TiO2 powder at spinning rate 2500 rpm

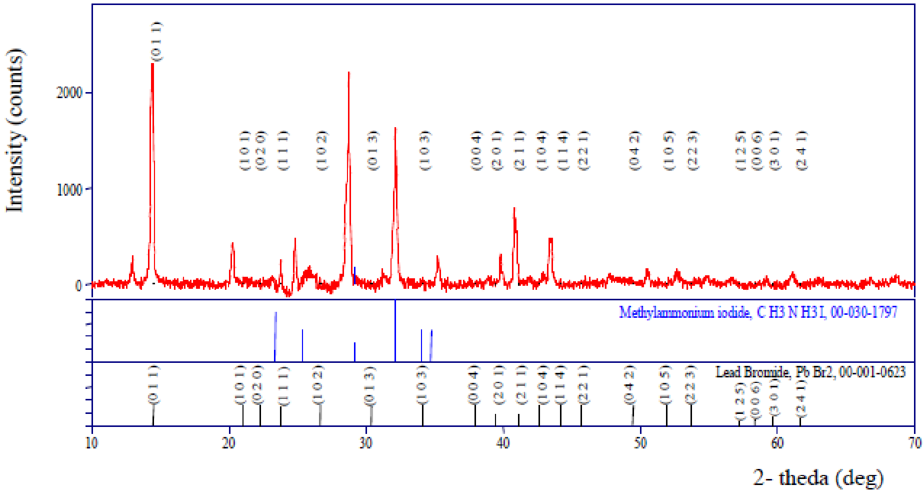

Figure 5: XRD spectrum of CH3NH3PbI2Br perovskite layer at spinning rate 3000 rpm

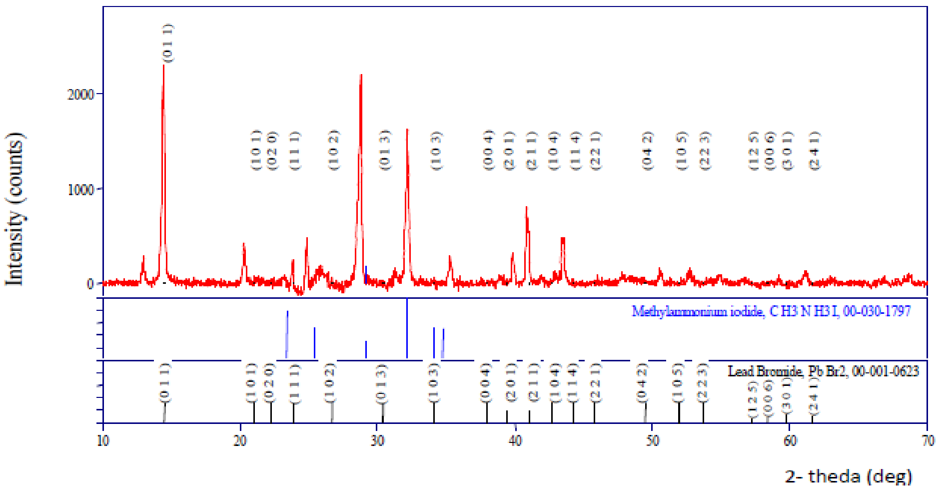

Figure 6: XRD spectrum of CH3NH3PbI2Br perovskite layer at spinning rate 3500 rpm

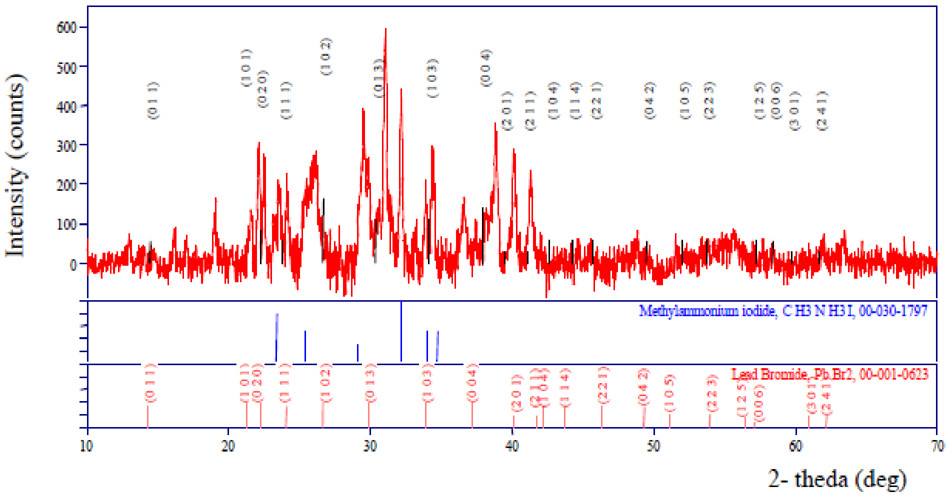

Figure 7: XRD spectrum of CH3NH3PbI2Br perovskite layer at spinning rate 4000 rpm

Scanning electron microscopy (SEM)

Scanning electron microscopy (SEM) is a type of electrons microscope that produces images of a sample by scanning the surface with a focused beam of electrons. The electrons interact with atoms in the sample, producing various signals that contain characteristic information of the samples surface topography, morphology and chemical composition. The electron beam is scanned in a raster scan pattern and the beam position is combined with the detected signal to produce an image. SEM can achieve resolution better than 1 nanometer. Specimens can be observed in high vacuum chamber. The most common SEM mode is detection of secondary electrons emitted by atoms excited by electrons beam. The number of secondary electrons that can be detected depends on the specimen topography. By scanning the sample and collecting the secondary electrons that are emitted using a special detector, an image displaying the topography of the surface is created. The micrographs of thin films were obtained using JEOL Scanning Electron Microscope model JSM – 5610 LV.

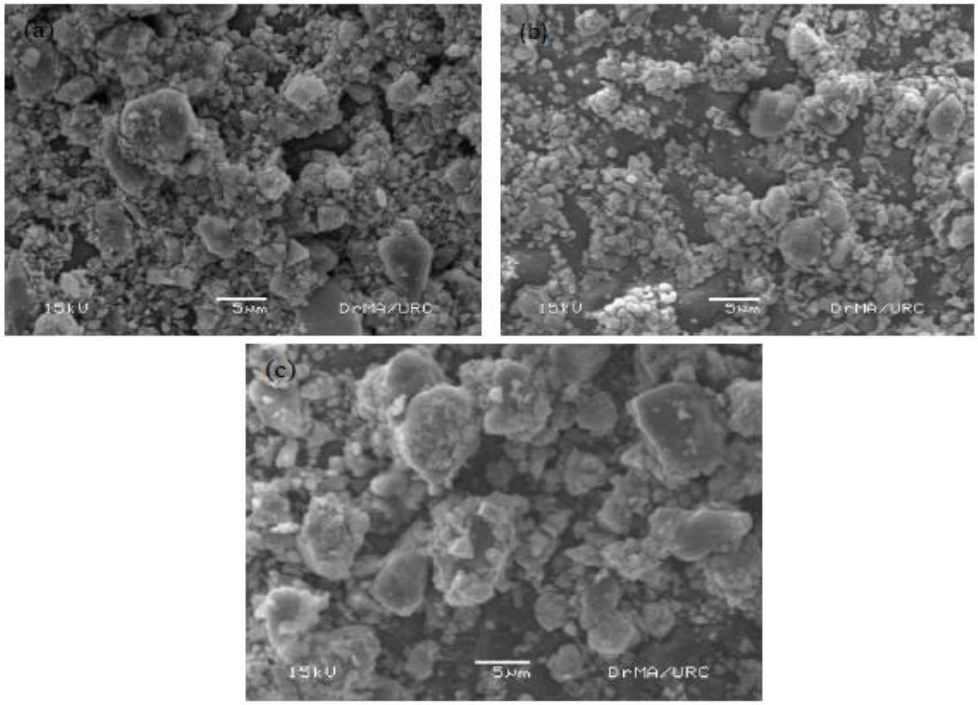

Figure 8: SEM images of PbBr2 perovskite layer spinning rate (a) at 3000 rpm (b) at 3500 rpm and (c) at 4000 rpm

Ultraviolet- Visible (UV- VIS)

UV – VIS refers to absorption spectroscopy or reflectance spectroscopy in the ultraviolet visible spectral region. It uses in the light visible and adjacent range. The absorption or reflectance in the visible range directly affects the color of the chemicals involved. In this region of the electromagnetic spectrum, atoms and molecules undergo electronic transitions. Absorption spectroscopy is complementary to fluorescence spectroscopy, in that fluorescence deals with transitions from the excited state to the ground state while the absorption measures transitions from ground state to the excited state.

For the optical characterization of CH3NH3PbI2Br perovskite, optical absorption spectra of the perovskite layers were investigated with SHIMADZU UV- 1800 Spectrophotometer in the wavelength range of 300 nm to 900 nm. The optical energy band gap, Eg of the perovskite was measured from the absorption spectrum. The band gap is important to enhance the efficiency of photovoltaic cells as it determines the absorbing portion of the solar spectrum.

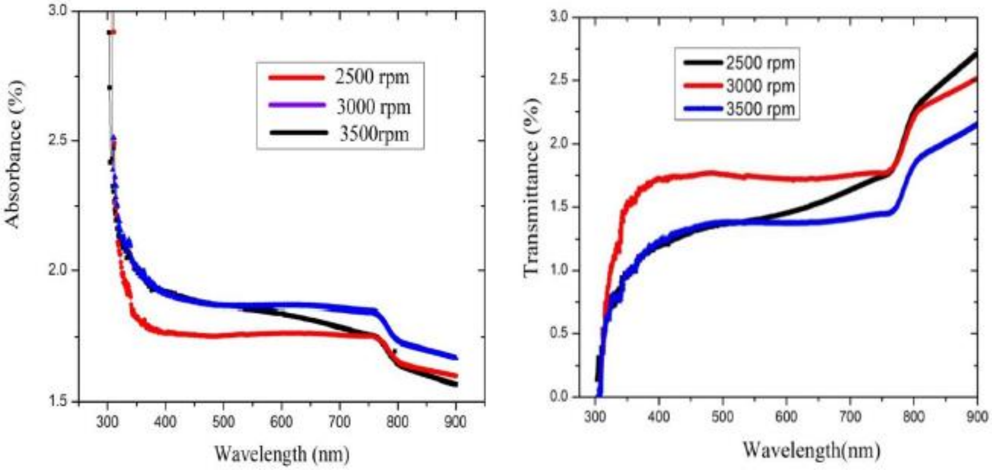

Figure 9: Comparison of UV- Vis spectra at different spin coating rates of PbBr2

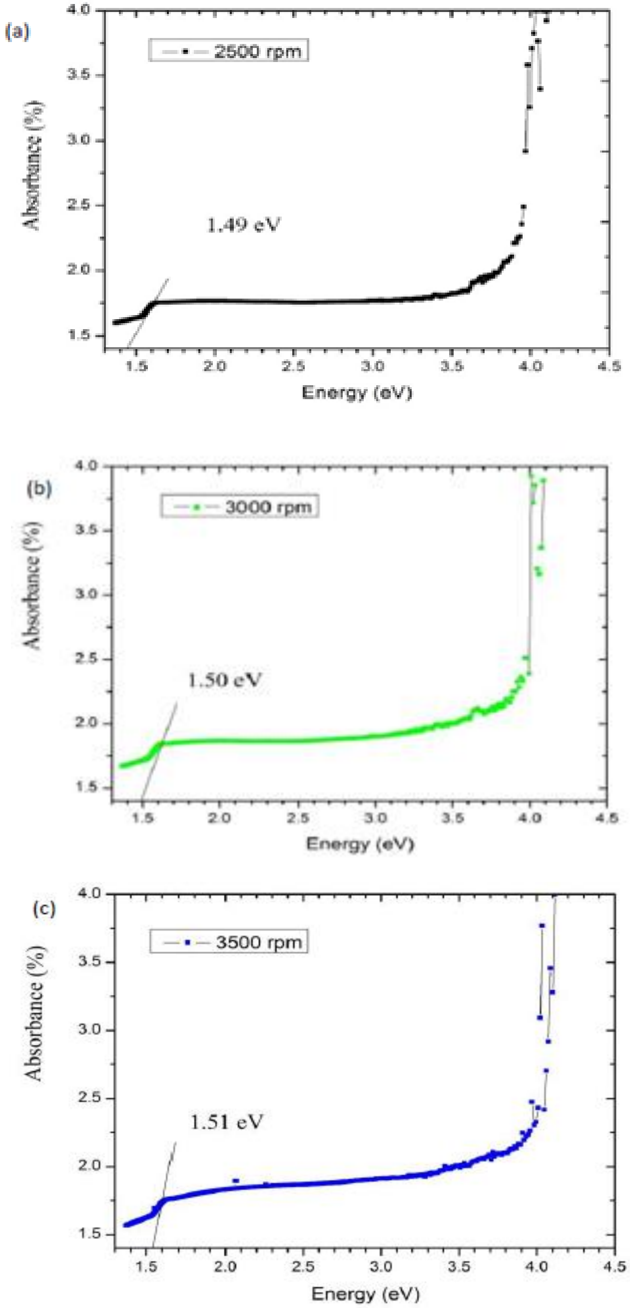

Figure 10: Energy band gap of $CH_3NH_3PbI_2Br$ perovskite layer (a) at 2500 rpm $PbBr_2$ (b) at 3000 rpm $PbBr_2$ (c) at 3500 rpm $PbBr_2$

Structure and optical characterization of organic- inorganic methyl ammonium lead bromide film was prepared by using spin coating and dipping two-step deposition method. Table 1 shows the XRD patterns of TiO_2 powder at spinning rate 2500 rpm for 30 s, the powder was performed at pure anatase phase of tetragonal structure. For XRD characterization, both TiO_2 and $CH_3NH_3PbI_2Br$ are coated by using spin coating and dipping technique as two- step deposition method on glass substrate. The spin coating rates were increased for three samples and the dipping rate was fixed at 1 hr. The spin coating rate is increased, the smaller crystallite size has been characterized from XRD pattern of $CH_3NH_3PbI_2Br$ layer. $CH_3NH_3PbI_2Br$ perovskite coating process, the color rapidly changes from light yellow to light brown color. This effect mentions sensitive to humidity of $CH_3NH_3PbI_2Br$ organometal halide material.

SEM images of perovskite solar cells are shown in figure 8.The surface morphology of perovskite are imaged by using scanning electron microscopy. The average grain sizes of the $CH_3NH_3PbI_2Br$ layer are 1.74 μm at 3000 rpm, 2.12 μm at 3500 rpm and 1.77 μm at 4000 rpm. The bigger grain size is observed in $PbBr_2$ spinning rate at 3500 rpm. The best surface morphology of perovskite layer is 1.74 μm at 3000 rpm. This is one of the important properties of perovskite layer to fabricate perovskite solar cell. To check the variation of the optical properties in the hybrid perovskite, the UV absorption spectra are measured as shown in figure 9. The energy band gap and absorption peaks are characterized from these absorption spectra. The absorbance spectra are shifted from 817.55 nm to 828.53 nm. So the wavelength tuning is observed by varying the spin coating rates. This is the good results for the actual applications. Figure 10 shows the energy band gap of perovskite layers. The results of the energy band gap are 1.49 eV at 2500 rpm, 1.50 eV at 3000 rpm and 1.51 eV at 3500 rpm for perovskite layers. The band gaps of $CH_3NH_3PbI_2Br$ perovskite are reliable range compare with the band gap of typical perovskite film 1.5 eV in all spinning rates.

Conclusion

Structure and optical characterization of organic- inorganic methyl ammonium lead bromide film was fabricated by using spin coating and dipping two-step deposition method. Methyl ammonium lead bromide perovskite layer was fabricated on TiO_2 electron collection layer and glass substrate. The dipping time and annealing temperature are fixed and the variation of spinning rate was characterized. The 12 crystallite size of TiO_2 layer was characterized 48 nm. From the first step spin coating and second step dipping $CH_3NH_3PbI_2Br$ layer, the crystallite size was characterized 38.3 nm, 35.5 nm and 34.3 nm for three samples. The better spinning rate was configured at 4000 rpm for perovskite layer. The dependence of crystallite size of perovskite on spinning rate and influence of humidity was characterized. The average grain sizes of the $CH_3NH_3PbI_2Br$ perovskite are slightly changed and the best surface morphology of the perovskite layer is 1.74 μm at 3000 rpm. The results of the energy band gap are 1.49 eV at 2500 rpm, 1.50 eV at 3000 rpm and 1.51 eV at 3500 rpm for perovskite layers. The band gaps of $CH_3NH_3PbI_2Br$ perovskite are reliable range compare with the band gap of typical perovskite film 1.5 eV in all spinning rates.

Acknowledgements

This research has been supported by University of Yangon, Myanmar and Dagon University, Yangon, Myanmar.

I would like to thank Professor Dr Khin Khin Win, Head of Department of Physics, University of Yangon, for her kind permission and encouragements to carry out of this work.

I would also like to acknowledge Professor Dr Aye Aye Thant, Department of Physics, University of Yangon, for her valuable suggestion and comments for this work.

References

Boopathi, K. M., Ramesh, M., Perumal, P., Huang, Y. C., Tsao, C. S., Chen, Y. F., Lee, C.H and Chu, C. W. (2015), Preparation of metal halide perovskite solar cells through a liquid droplet assisted method: J. Mater. Chem. A, pp. 9257- 9263.

Chang, C. U., Chu, C. Y., Huang, Y.C., Huang, C. W., Chang, S. Y., Chen, C. A., Chao, C. Y., and Su, W. F. (2015), Tuning Perovskite Morphology by Polymer Additive for High Efficiency Solar Cells: *ACS Appl. Mater. Interfaces* pp 4955_ 4961.

Lungu, J., Stefan, N., Prodan, G., Geogrescu, A., Mandes, A., Ciupina, V., Mihsilescu, I. N., Girtu, M. A. (2015), Characterization of Spin- Coated TiO2 Buffer Layers for Dye- Sensitized Solar Cells: Digest Digest Journal of Nanomaterials and Biostructures, Vol. 10, No. (3), pp. 967- 976.

Oku, T., (2015), Chapter 3*: Crystal Structures of CH3NH3PbI3 and Related Perovskite Compounds Used for Solar Cells*. Hikone: Shiga Prefecture.

Wang, H. H., Chen, Q., Zhou, H., Song, L., Louis, Z. S., Marco, N. D., Fang, P., Sun, P., Song, T. B., Chen, H. and Yang, Y. (2015), ImprovingthevTiO2 electron transport layer in perovskite solar cells using acetylacetone- based additives: J. Mater. Chem. A.

Wu, C. G., Chiang, C. H., Tseng, Z. L., Nazeeruddin, Md. K., Hagfeldt, A. and Gratzel, M. (2015), High efficiency stable inverted perovskite solar cells without current hysteresis: The journal of The Society of Chemistry, pp.2725- 2733.

J. Myanmar Acad. Arts Sci. 2019 **Vol. XVII. No.2A**

MICROCONTROLLER BASED GAME TIME CLOCK

Kyaw Hlaing[*]

Abstract

Microcontroller based game time clock was constructed for three games. The first one is chess game, the second one is crossword game and the last on is stopwatch (game of go). There are two types in chess game. The first chess game time clock is a "sudden-death" contest with five minutes for each size. The second chess game time clock is a dual counter mode. In dual counter mode, the chess game time intervals can be chosen by the player. In crossword mode, game time clock shows the over time condition by blanking on the appropriate players LED. In the stopwatch mode, the exact time of event especially sports event can be measured. In game time clock the main controlled device is PIC16F887 microcontroller and its software is written in assembly language. The other devices are 7-segment LED, transistor and counter.

Keywords-Microcontroller, preset time control, assembly language

Introduction

Game time clock can be applied in chess game, crossword game and game of go. There are two modes in chess game, speed chess game and dual counter mode. The time in speed chess game is 5 minutes for each side. This time control is officially called "Game in 5 minutes". The time interval for each side in dual counter mode is set by the player.

A chess game consists of two adjacent clocks with buttons to stop one clock while starting the other, so that the two clocks never run simultaneously. Chess game clocks are used in chess and other two-player games where the players move in turn. The purpose is to keep track of the total time each player takes for their own moves, and ensure that neither player delays the game.

The players may take more or less time over any individual move. The opening moves in chess are often played quickly due to their familiarity, which leaves the players more time to consider more complex and unfamiliar positions later. The time of game may be unlimited. Therefore chess clock is used to limit the time of game.

---

[*]. Dr, Lecturer, Department of Physics, Taungoo University

In crossword game mode, the time interval for each player is 25 minutes. The game time clock shows the over time condition by blanking on the LED. In go time mode, it records the exact time of events whose spends the game.

In this paper, PIC16F887 microcontroller based game time clock is construed. In this game time clock, the display unit is 7-segments LEDs and ULN2803APG Darlington transistor array is used as current sink driver. PIC 16F887 microcontroller is used as control device. The block diagram of game time clock is shown in Figure 1.

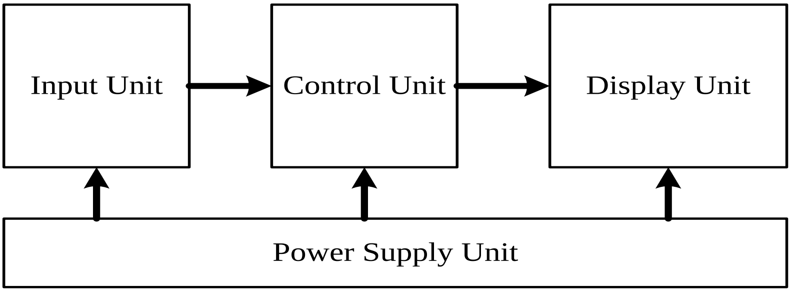

Figure 1: Block diagram of game time clock.

Hardware Design

The constructed system is divided into three units, the input unit, the control unit and the display unit.

The Input Unit

The input unit is a keypad with four buttons namely 'SELECT/ RESET', 'START/PAUSE', 'LEFT' and 'RIGHT' key. In order to determine the state of each button either as a HIGH (pulled to the V_{CC}) or a LOW (pulled to the ground) on the microcontroller, pull-down resistors connected to the input pin of microcontroller or else the input pin will be in a floating state. With a pull-down resistor, the input pin will read a LOW state when the button is not pressed. When the button is pressed, it connects V_{CC} to both the input pin and through the resistor to the ground; thus the input pin reads close to V_{CC}.

Display Unit

The visual display has four digits for each side of game time clock, two digits for minutes and two digits for seconds. Each digit is made up of 7-segments whose configuration is common cathode. These segments are turned on by applying logic ‘1’ to the required segment LEDs via current limiting resistors.

Each 7-segments LED is connected to the microcontroller via a Darlington transistor array driver in current draining mode. ULN2803 APG Darlington transistor array was chosen as the LED segment driver.

Control Unit

The main device of this system is control unit, PIC 16F887 microcontroller. It receives the input data of the keypad and scanning the corresponding pattern on the 7-segments LEDs display. The input method of PIC 16F887 microcontroller is portB change interrupt. Therefore, if two keys are pressed simultaneously microcontroller determines which key is first press. PIC 16F887 microcontroller is scanning the 7-segments LEDs display according to the input key.

Software Implementation

There are five programs in the software implementation. They are main program, PortB change interrupt subroutine, speed chess program, dual counter mode chess program, crossword mode program and game of go program.

The main program selects the types of game and counting the time of the game. The flowchart of main program is shown in Figure 2.

In PortB change interrupt subroutine, it selects which switch of PortB is pressed. Figure 3 shows the flowchart of PortB change interrupt.

In speed chess program mode, the time of game is already set 5 minutes for each side. When the ‘LEFT’ key button is pressed the right side of the time of 7-segment will decrease. Also the ‘RIGHT’ key button is pressed the left side of the time of 7-segments will decrease. If the

‘STOP/PAUSE’ key button is pressed the time of every side will pause. The flowchart of speed chess game is shown in Figure 4.

In dual counter chess program mode, the time of game can be set by using ‘LEFT’ and ‘RIGHT’ key button. The ‘SELECT/RESET’ key button is pressed to start the game. When the ‘LEFT’ key button is pressed the right side of the time of 7-segment will decrease. Also the ‘RIGHT’ key button is pressed the left side of the time of 7-sements will decrease. If the ‘START/PAUSE’ key button is pressed the time of every side will pause. The flowchart of dual counter chess program mode is shown in Figure 5.

In crossword game mode, the time of game is already set 25 minutes for each player. Before switch ‘SELECT/RESET’ is pressed, the time of player is reduced. When switch ‘START/PAUSE’ is pressed, the time of game is set 25 minutes for the next player. Figure 6 shows the flowchart of crossword game mode.

In game of go mode, the time is reset. When the ‘RIGHT’ key button is pressed, it counts the time of game. When the ‘START/PAUSE’ key button is pressed the time of game will be paused. When the ‘SELECT/RESET’ key button is pressed, the time is ready for the next game. The flowchart of game of go is shown in Figure 7.

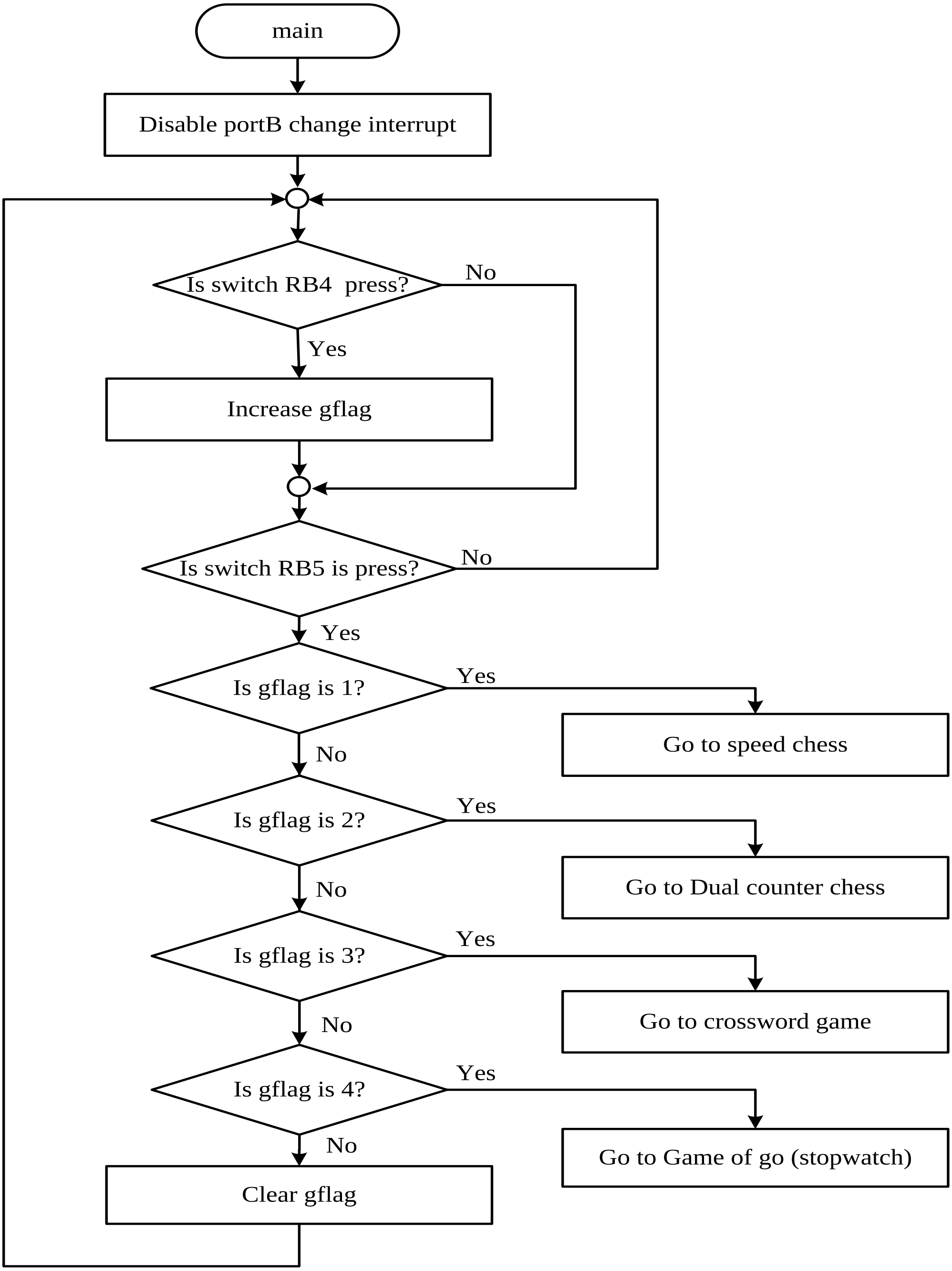

Figure 2: Flowchart of main program.

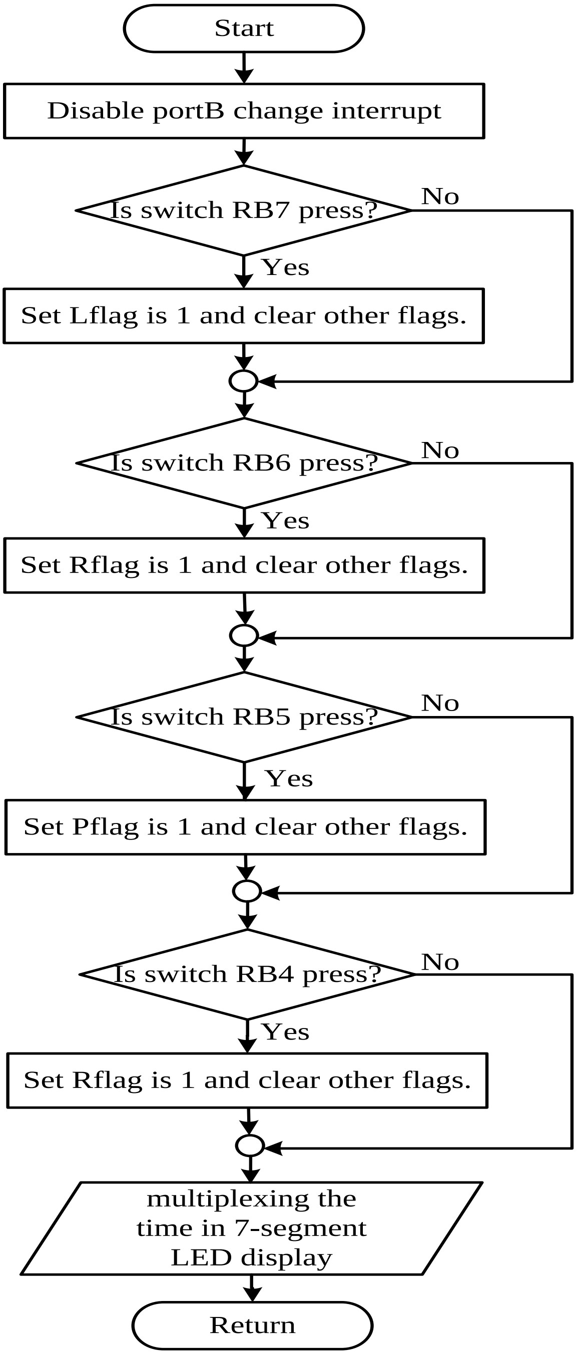

Figure 3: Flowchart of PortB change interrupt subroutine.

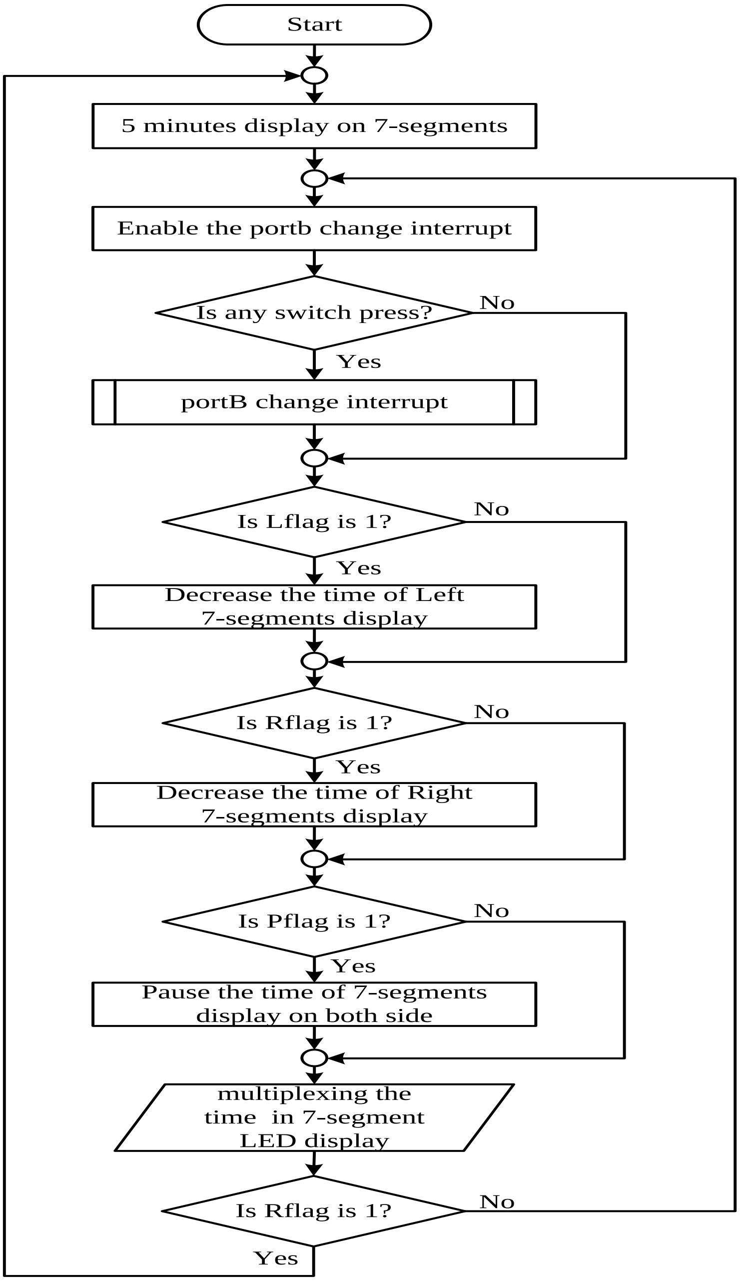

Figure 4: Flowchart of speed chess game.

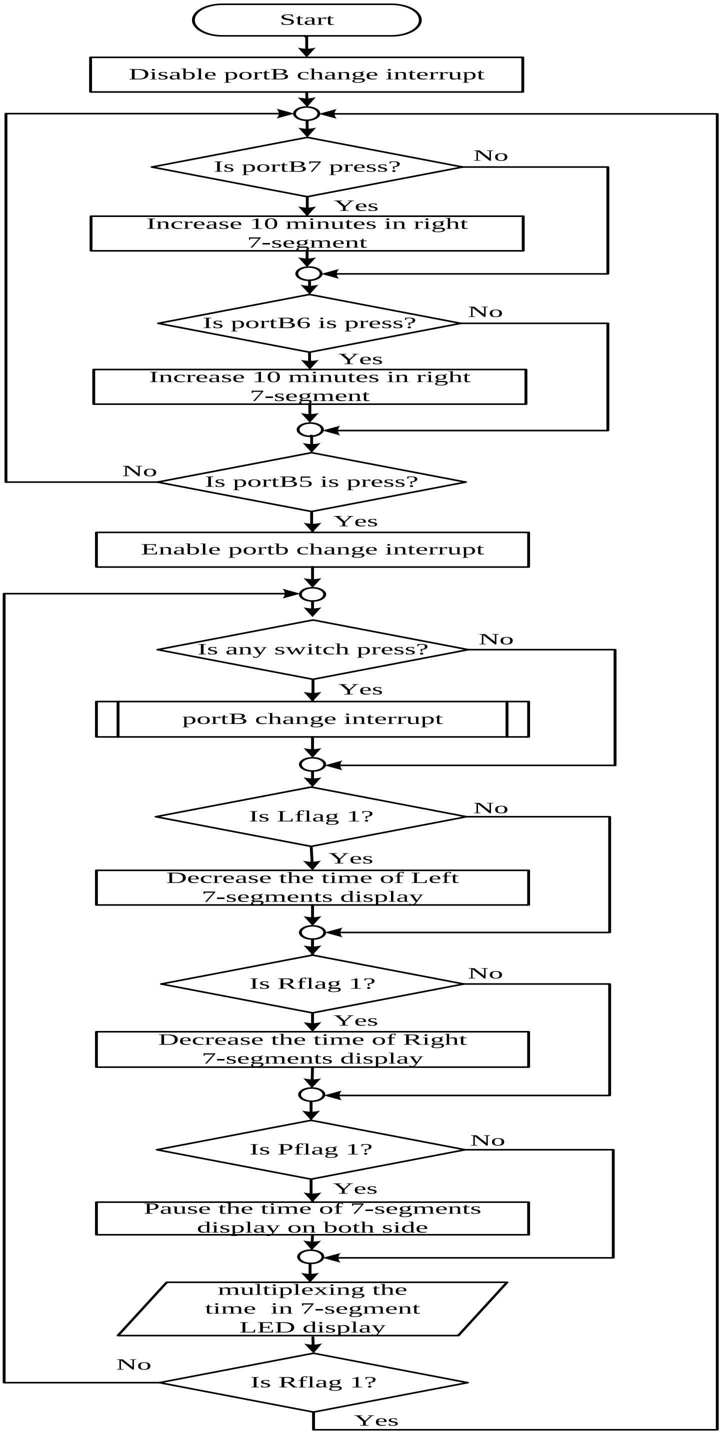

Figure 5: Flowchart of dual counter chess game.

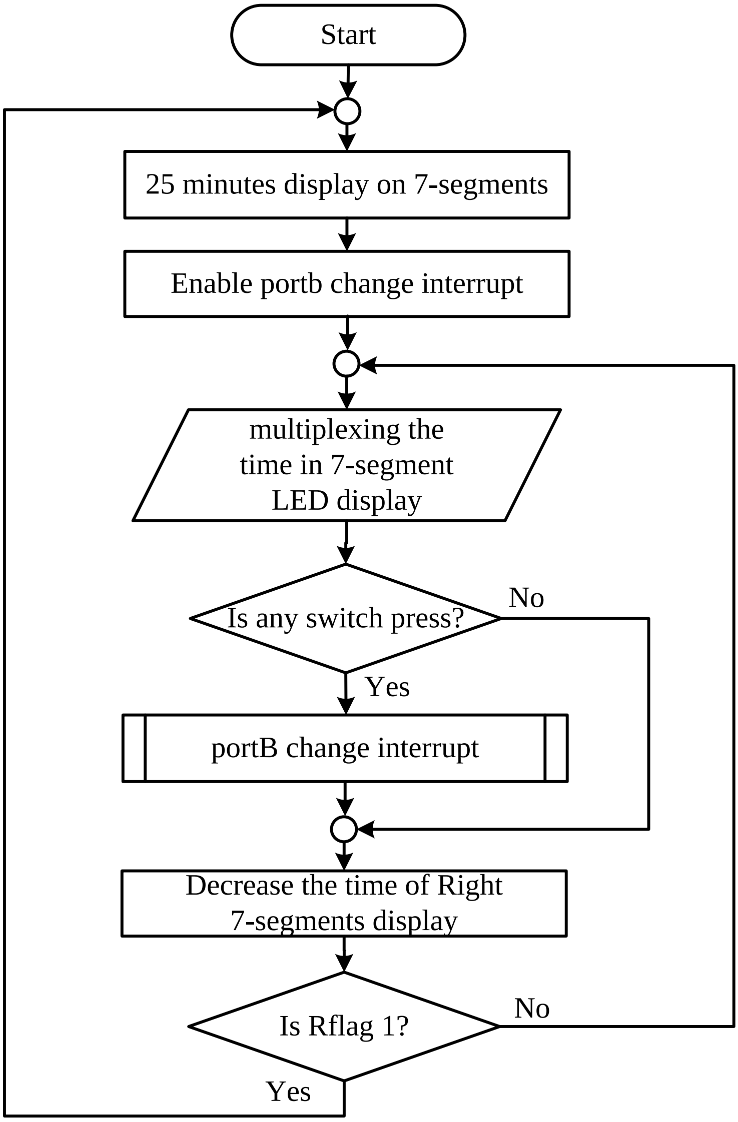

Figure 6: Flowchart of crossword game.

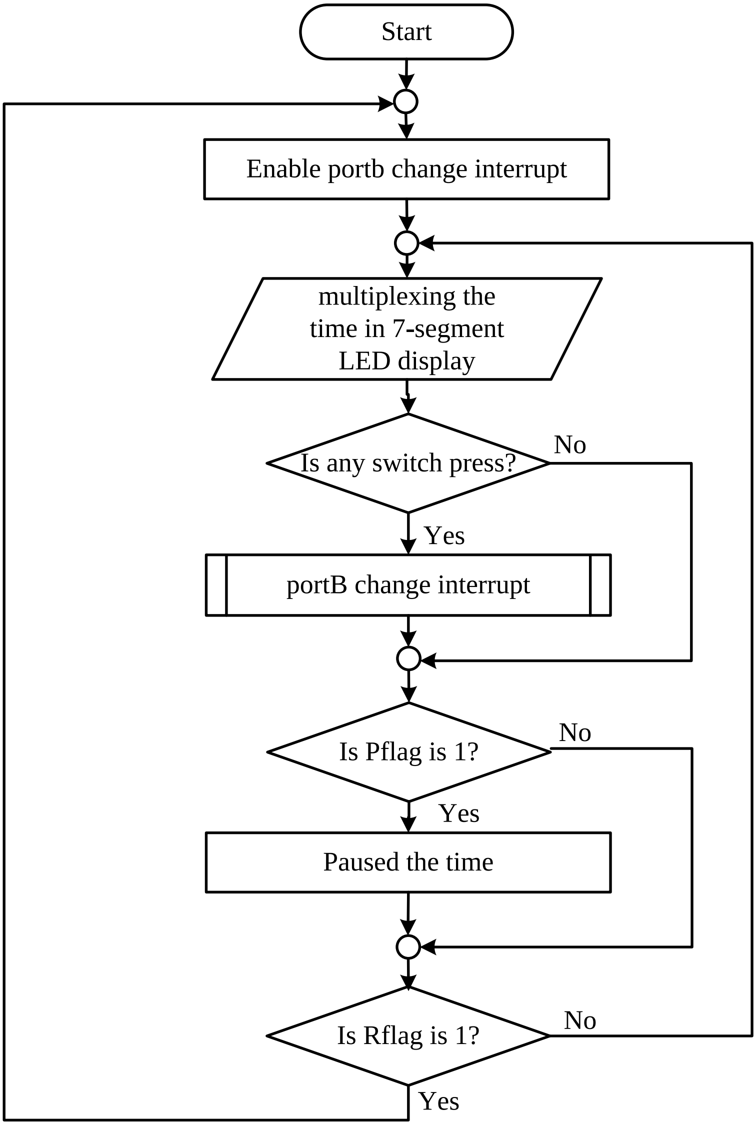

Figure 7: Flow chart of Game of Go.

Construction and Operation

In this system, the main control device is PIC16F887 microcontroller. Common cathode 7-segments LEDs are also used to display the time. PortC of PIC microcontroller is connected to anodes of left side of 7-segments LEDs and portD is connected to anodes of right side of 7-segments LEDs. PortA and portE are connected with the input pin of ULN2803APG Darlington transistor array IC. The output pin of Darlington transistor array is connected with the common cathode pins of 7-segments LEDs. Darlington transistor array IC acts as a switch to multiplex the 7segments LEDs. The PCB layout of this system is shown in Figure 8. The complete circuit diagram of the constructed system is shown in Figure 9.

In this system, PIC16F887 microcontroller is used as a control device. There are four switches in this circuit. The photograph of initial state of game time clock is shown in Figure 10. At first, select the type of games using ‘SELECT/RESET’ key button (yellow colour). Figure 11 to Figure 14 shows types of games. If the type of games is selected, press the ‘START/PAUSE’ (green colour) button to start the game. The Figure 15 shows the photograph of speed chess game can be started.

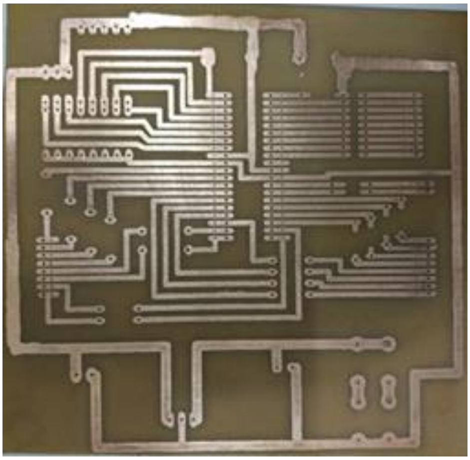

(a)

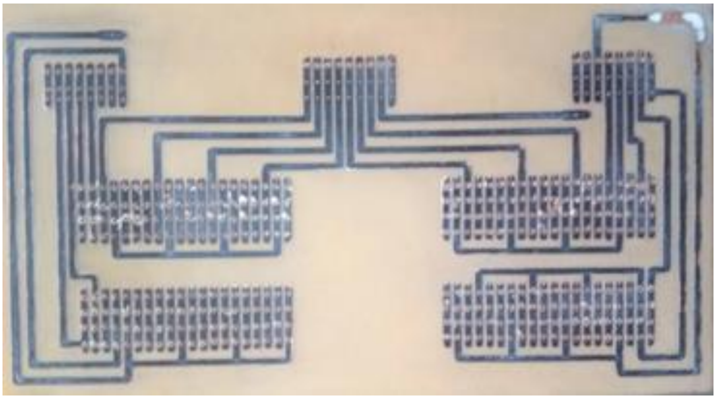

(b)

Figure 8 (a) Photograph of control unit PCB design.
(b) Photograph of display unit PCB design.

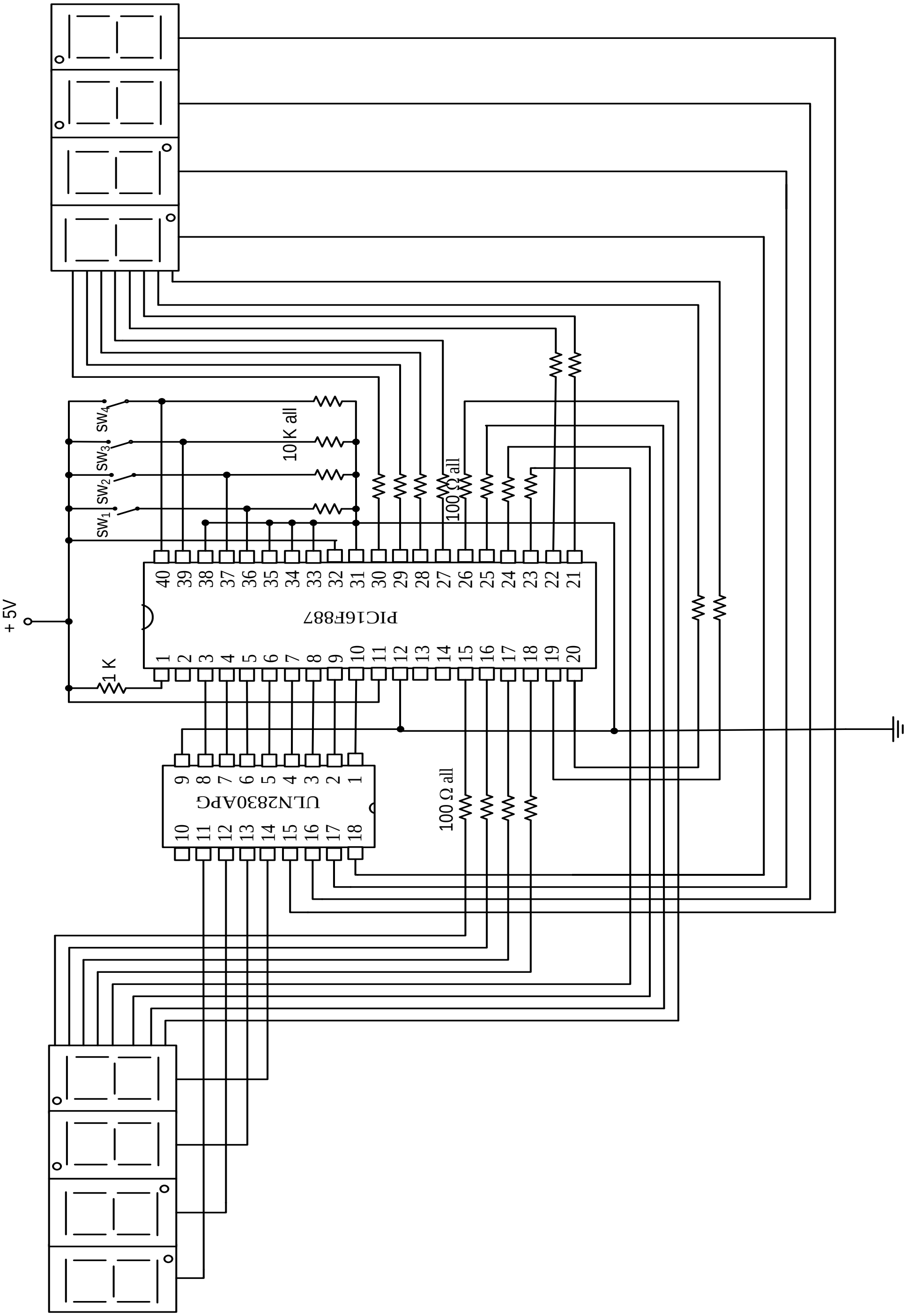

Figure 9: The complete circuits diagram of the constructed system.

Figure 10: Photograph of initial state of game time clock.

Figure 11: Photograph of speed chess game mode.

Figure 12: Photograph of dual chess game mode.

Figure 13: Photograph of cross word game mode.

Figure 14: Photograph of game of go mode.

Figure 15: Photograph shows speed chess game can be started.

Conclusion

Microcontroller based game time clock was constructed. In the clock display system, two groups of 7-segment LEDs are used. Microcontroller controls these two groups in separate bus. Therefore the duty cycle of on time of 7-segment LEDs is twice the same bus. The brightness of 7-segments LEDs is higher than that of the same bus. The program is written in assembly language in this system. PIC 16F887 microcontroller use internal clock of 4MHz. Thus most of the instruction is complete in 1 μs. The input switches of the game time clock is used as portB change interrupt. There is no waste of time when the switch is pressed. Therefore the clock time of this game time clock is adequate.

In this paper, two types of chess game can be played. By modifying software program, other types of chess game can be played.

Acknowledgements

I would like to express my gratitude and sincere thanks to Dr Khin Khin Win, Professor and Head, Department of Physics, University of Yangon, for her kind permission to perform this research work.

I would like to express my gratitude and sincere thanks to Dr Myat Htut, Professor and Head, Department of Physics, Taungoo University, for his kind permission to perform this research work.

I also would like to express my gratitude and sincere thanks to Dr Nge Nge Khaing, Professor, Department of Physics, Taungoo University, for her kind permission to conduct this research work.

References

Floyd T.L., (2012), “Electronics Devices”, Ninth Edition, Prentice-Hall, Inc., New York.

Microchip Technology Inc., (2006), “Microcontroller selection for applications”, New York.

Microchip Technology Inc., (2006) ,“PIC16F887 Data Sheet”, New York.

htpp://www.chesshouse.com. (Retrieved on January 3, 2017)

htpp://www.chesspraga.cz.com. (Retrieved on February 3, 2017)

J. Myanmar Acad. Arts Sci. 2019 **Vol. XVII. No.2A**

FORMATION OF BIPHASIC BIOMATERIALS FROM WHITE CORAL (*ANTHOZOA CNIDRIA*) AND ITS CHARACTERISTICS

Khin Myat Thu[1], Aye Aye Thant[2] and Than Htike Win[3]

Abstract

Bioceramics made of hydroxyapatite [$Ca_{10}(PO_4)_6(OH)_2$: HAP] would be good example of bioactive materials. In the other hand, bones graft made of Beta-Tricalcium Phosphate [$Ca_3(PO_4)_2$: β-TCP] appears to be an example of bioresorbable materials. Based on this background, biphasic calcium phosphate comprising of Hydroxyapatite and Beta-Tricalcium Phosphate (HAP- β-TCP) has been prepared in this work. White Coral (*Anthozoa Cnidria*) has been used to produce biphasic calcium phosphates by mechano-chemical method. X-Ray Diffraction (XRD) analysis has confirmed the presence of HAP and β-TCP in major proportions along with Calcium Carbonate ($CaCO_3$) and Calcium Oxide (CaO) in traces revealing the biphasic calcium phosphate nature of synthetic powders. Crystallite size and lattice parameters at different calcination temperatures of 900°C, 1000°C and 1100°C have been calculated and compared. Fourier Transform Infrared (FTIR) spectroscopy has also been confirmed the presence of various chemical ions groups. The surface topography, morphology and agglomerated distribution of the biphasic particles have been characterized by using Scanning Electron Microscopy (SEM). Importantly, the hardness of the biphasic calcium phosphate at different calcination temperatures has been determined for future application as bone replacement.

Keywords: hydroxyapatite, beta-tricalcium phosphate, white coral, biphasic

Introduction

Biphasic biomaterials, hydroxyapatite and beta-tricalcium phosphate are chemically similar to the inorganic component of bone matrix. It is a class of calcium phosphate-based bioceramic. HAP products are poorly resorbable, which retain for years after the implantation. β-TCP has much faster resorption rate. However, it has been investigating to control the resorption rate of biphasic calcium phosphates (BCP) with HAP and β-TCP. Generally,

---

[1] Demonstrator, Department of Physics, Hinthada University

[2] Dr, Professor, Department of Physics, University of Yangon

[3] Dr, Assistance Lecturer, Department of Physics, University of Yangon

the resorption rate of BCP depends on the molar ratio of β-TCP/HAP in the mixture. The ratio of HAP and β-TCP is higher, the resorption is faster.

Biphasic calcium phosphate, HAP and β-TCP in powder form is frequently used in biomedical applications such as prosthetic implants and coating implants. This is due to its excellent biocompatibility (ability of material to perform with an appropriate host response under specific condition), bioactivity (ability of material to provide an appropriate scaffold for bone formation) and osteoconductivity (formation of bone-like apatite on their surface with a strong bone-calcium phosphate biomaterial interface) and its chemical and structural similarity with natural bone mineral.

Mechano-chemical reaction is a process that is strong mechanical force proceeds materials destruction and causes a formation of a different structure. Mechano-chemical method can be employed in the synthesis of materials and replaced the solid state reaction at high temperature· It is a simple, environmental and low-cost technology and has been widely used in synthesis of advanced materials, covered almost all aspects of material science.

In order to achieve biphasic calcium phosphate, mechano-chemical method is used in the process and the calcium carbonate skeleton of marine coral is converted into HAP and β-TCP. After the preparation process, characterization of biphasic biomaterials with HAP/β-TCP prepared from white coral (*Anthozoa Cnidaria*) has been performed.

Materials and Method

Calcium Source; White Corals

Coral is a living animal which is similar to all living things. It suffers from many environmental factors and fossilizes as inorganic component. In this research, non-living corals obtained from the Chaung Thar Beach, Ayeyarwady Division, lower part of Myanmar have been used (Figure 1). Prior to the preparation of biphasic biomaterials, the content of calcium in the white coral has been investigated.

Figure 1: The fossilize of white coral *Anthozoa Cnidaria* obtained from Chaung Thar Beach, Ayeyarwady Division, lower part of Myanmar

Sample Preparation

Conversion of coral to calcium phosphate biphasic biomaterials was conducted by using mechano-chemical method. Stoichiometric amount of 3.3 g of $(NH_4)_2HPO_4$ has been dissolved in 25 ml of distilled water. Then, required amount of coral powder has also been dissolved in 300 ml of distilled water. Then, the ammonium solution has been added and gradually dropped at a rate of 2 ml min^{-1} into coral solution while heating at (80±5)°C on a hot plate with magnetic stirring. The reaction vessel has been covered with rubber cork to prevent evaporation and kept under stirring (800 rpm) for 24 hours. The pH of reaction mixture has been monitored at the end of the experiment. After that solids have been separated by centrifuging with Gallenkamp Junior Centrifuge for 1 min at 3660 rpm. The solid have been washed for three times with distilled water and separated by centrifuge for 5 min, followed by drying overnight in an oven at 80°C. Finally, the sample has been grounded with agate motor and heat-treated at 900°C, 1000°C and 1100 °C for 2 hours in each temperature. The structural analysis has been carried out by XRD analysis. The molecular vibrations have been examined by Fourier Transform Infrared Spectroscopy (FTIR). The surface morphology has been studied by Scanning Electron Microscopy (SEM). The hardness of the BCP pellets has been measured by using Hardness Tester (Mecmesin BFG-500N, Basic Force Guage). Figure 2 presents flowchart for the sample preparation and characterization of biphasic biomaterials.

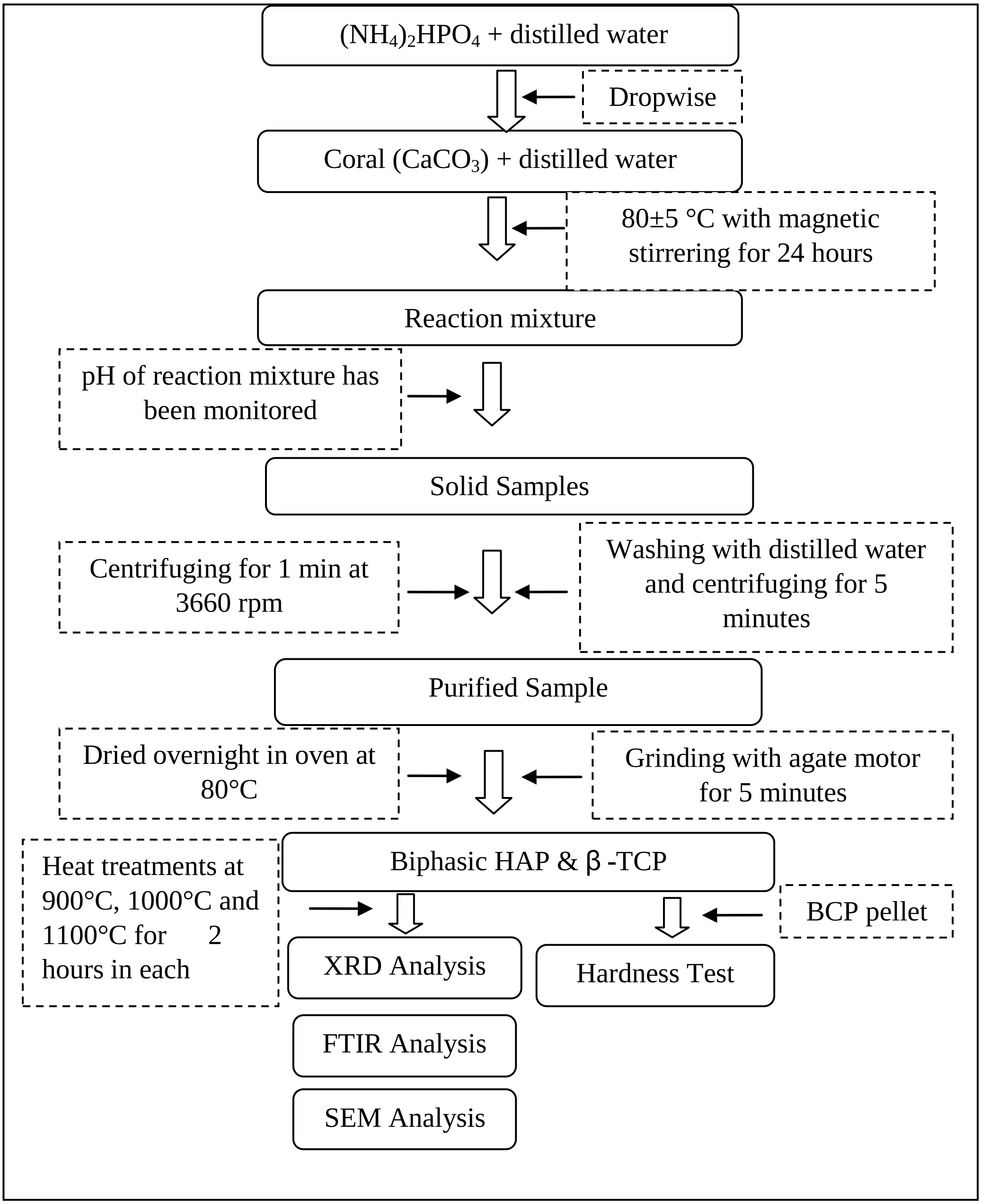

Figure 2: Flow chart of the sample preparation and characterization of biphasic calcium phosphate from white coral

Results and Discussion

Phase formation

XRD Analysis of Biphasic Biomaterials

The X-ray Diffraction has been applied to monitor the phase composition feature of the sample before and after the calcination at different temperatures of 900°C, 1000°C and 1100°C. The powder has been ground and pressed into homogeneous compacted layer in samples holder. The XRD patterns were scanned between 2θ value of 10° to 70° by using the RIGAKU, MINIFLEX600 powder X-ray Diffratometer.

Biphasic Hydroxyapatite and Beta-Tricalcium Phosphate are prepared at an aging time of 24 hours, aging temperature of 80°C followed by calcination at temperatures of 900°C, 1000°C and 1100°C. The XRD patterns of the sample without heat-treatment and those calcined at 900°C, 1000°C and 1100°C are shown in Figure 3. From the XRD analysis, diffraction peaks have been identified as the hexagonal phase of the HAP and β-TCP (ICDD- PDF Release 2015 RD). From the XRD data, weight percentages of HAP and β-TCP, lattice parameters and mean crystallite size has been calculated. The sample without heat treatment exhibits the presence of $CaCO_3$ in the spectrum. Starting from the calcination temperature of 900°C, biphasic biomaterial of HAP/β-TCP has been formed involving CaO peaks in the spectrum. However, the number of CaO peaks is gradually increased at the calcination temperatures of 1000°C and 1100°C.

From the XRD data, lattice parameters and mean crystallite size have been calculated and tabulated in Table 1 and Table 2. Crystallite size has been found to be 21.52 nm for HAP and 29.52 nm for β-TCP with poor crystallinity before calcination. After calcination at 900°C, the crystallite size of HAP and β-TCP has been increased to 56.74 nm and 44.95 nm. Again, the crystallite size of HAP and β-TCP has been gradually decreased with the higher calcination temperatures to 35.06 nm and 23.21 nm respectively at 1100°C as shown in Figure 4. The relative intensity ratio (RIR) of HAP/β-TCP in the biphasic calcium phosphate has been calculated by using the formula, $RIR= I_{\beta\text{-TCP}} /(I_{\beta\text{-TCP}}+I_{HAP})$. The obtained RIR follow the same trend as the decreasing value of crystallite size with increasing calcination temperature. Based on the XRD analysis, it has been confirmed that white coral can be utilized for preparing biphasic biomaterials, HAP/β -TCP

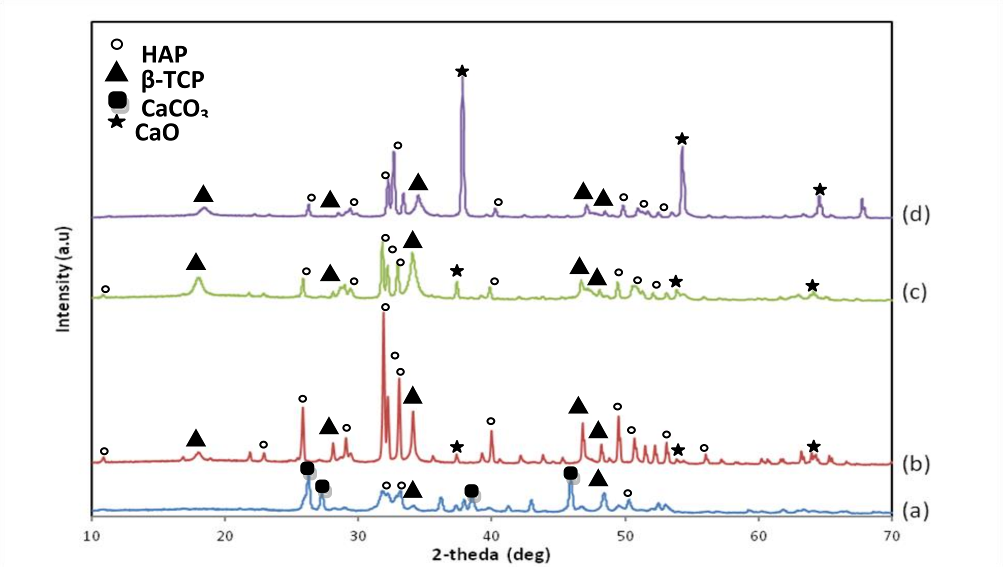

Figure 3: XRD spectra of biphasic calcium phosphate (HAP and β -TCP) with different calcination temperatures (a) before calcination, calcination at (b) 900°C, (c) 1000°C and (d) 1100°C

Table 1: Lattice constant of biphasic calcium phosphate before and after calcination

Type	Lattice Parameter	Before calcination	900°C	1000°C	1100°C
Hydroxyapatite $(Ca)_{10}(PO_4)_6(OH)_2$	a (Å)	9.413	9.384	9.405	9.321
	b (Å)	9.413	9.384	9.405	9.321
	c (Å)	6.807	6.893	6.897	6.780
β -Tricalcium Phosphate $(Ca_3)(PO_4)_2$	a (Å)	10.428	10.180	10.150	10.413
	b (Å)	10.428	10.180	10.150	10.413
	c (Å)	36.647	36.912	37.570	36.552
Aragonite ($CaCO_3$)	a (Å)	5.735	-	-	-
	b (Å)	4.948	-	-	-
	c (Å)	7.974	-	-	-

Table 2: Crystallite size of biphasic calcium phosphate before and after calcination

Type	Before calcination	900°C	1000°C	1100°C
Hydroxyapatite $(Ca)_{10}(PO_4)_6(OH)_2$	21.518 nm	56.735 nm	52.021 nm	35.056 nm
β -Tricalcium Phosphate $(Ca_3)(PO_4)_2$	29.516 nm	44.944 nm	41.944 nm	23.206 nm

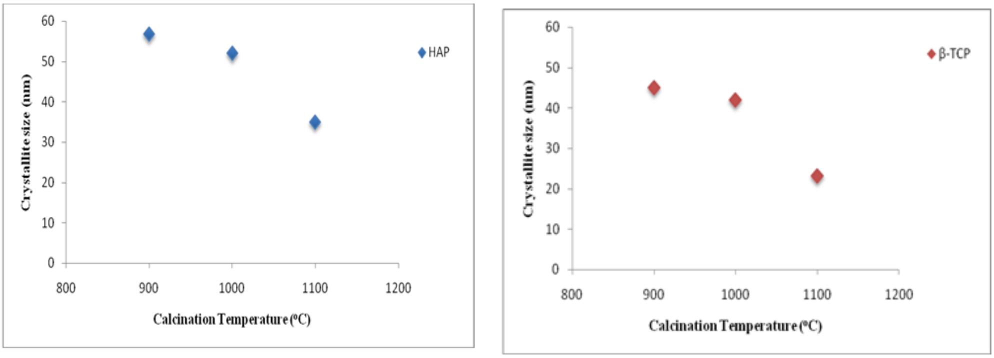

Figure 4: The Variation of crystallite size of HAP and β -TCP in biphasic calcium phosphate with different calcination temperatures

Table 3: Relative intensity ratio of biphasic biomaterials before and after calcination

Condition	Relative Intensity Ratio
Before calcination	22% HAP : 18% β -TCP: 60% CaCO3
Calcination at 900°C	70% HAP : 20% β -TCP: 10% CaO
Calcination at 1000°C	65% HAP : 13% β -TCP: 23% CaO
Calcination at 1100°C	59% HAP : 9% β -TCP: 32% CaO

Table 4: Comparison of phase analysis of white coral and biphasic calcium phosphate

Condition	Sample	Phase	Phase ID	Crystal Structure
Raw	White Coral powder	Single phase	-Aragonite ($CaCO_3$)	Ortho- rhombic
After preparation	Calcium phosphate biomaterials	Bi-phase	-Hydroxyapatite ($Ca_{10}(PO_4)_6(OH)_2$) -Beta-tricalcium phosphate ($Ca_3(PO_4)_2$)	Hexagonal

FTIR Analysis of Biphasic Calcium Phosphate

The FTIR spectra of biphasic calcium phosphate has been recorded in the wave number region 2000-400 cm^{-1} by using Fourier Transform Infrared spectrometer (FTIR-8400 Shimadzu) and shown in Figure 5. It is found that FTIR analysis strongly supported the XRD result. The most characteristic vibrational chemical groups in the FTIR spectrum of synthesized biphasic biomaterials are found to be PO_4^{3-}, OH^-, CO_3^{2-} and HPO_4^{2-}. The absorption peak of O-H bending mode is evidence of the presence of absorbed water that appeared after the calcinations temperature of 900°C, 1000°C and 1100°C. The other vibration modes of structural OH^- group indicate the existence of a Ca-O phase in the structure. In the FTIR analysis, it has been confirmed that phosphate groups represent biphasic biomaterials, HAP/β -TCP. The bending vibration of PO_4^{3-} has been formed at 560-610 cm^{-1} for all the calcination temperatures. According to the FTIR analysis, PO_4^{3-}group of HAP and β -TCP at calcination temperature of 900°C is stronger than those in the other calcination temperatures. This finding again confirmed the formation of biphasic calcium phosphate from white coral by using mechano-chemical method. The type of molecules and vibration mode of biphasic HAP/β -TCP with different calcination temperature have been described in Table 5.

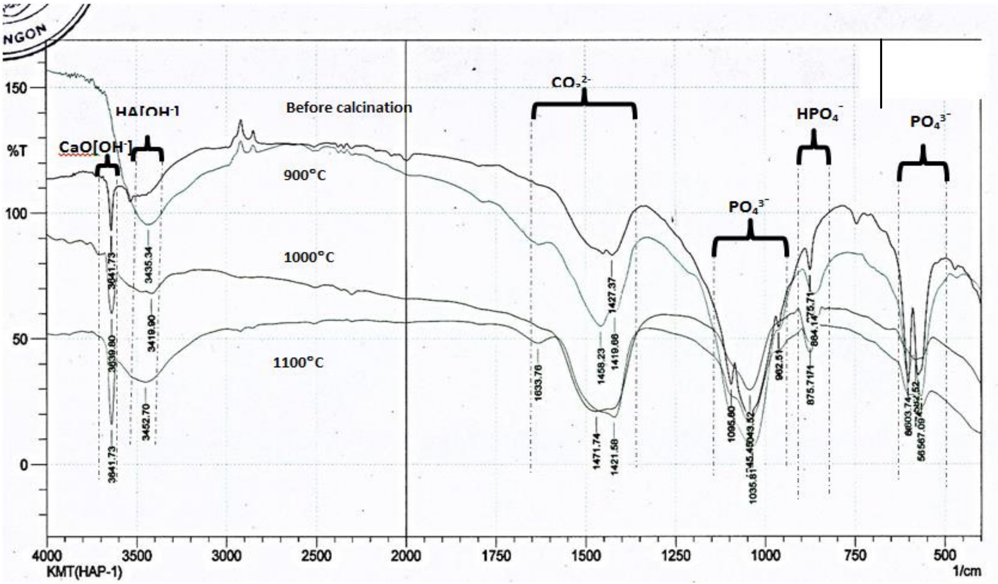

Figure 5: FTIR spectra of biphasic HAP/ β-TCP with different calcination temperatures (a) before calcination, (b) 900°C, (c) 1000°C and (d) 1100°C

Table 5:The type of molecules and vibration mode of biphasic HAP/□-TCP with different calcination temperatures

Functional Groups	**Before Calcination**	**900°C**	**1000°C**	**1100°C**
	Absorption band, cm^{-1}			
CO_3^{2-} (O-C-O)	1419.66, 1458.23	1427.37	1471.74	1421.58, 1633.76
HPO_4^-	864.14	875.71	875.71	875.71
OH^-(HAP)	-	3485.49	3419.90	3462.70
OH^- (Ca-O)	-	-	3639.80	3641.73
PO_4^{3-}	1035.81	1043.52, 1095.60	1043.52	1045.45
PO_4^{3-} (HAP)	567.09, 603.76	574.81, 601.81, 962.51	582.52	567.09

SEM Analysis of Biphasic Calcium Phosphate

Morphological properties of biphasic biphasic calcium phosphate has been determined by using SEM (model: JEOL-JSM 5610LV) in this work. The SEM micrographs of biphasic HAP/β-TCP at different calcination temperatures are as shown in Figure 6. The SEM images of all powders exhibit agglomerated nature with irregular grains. It has observed that, the grain size of the sample is gradually increased from 1.7 μm to 3.7 μm for HAP and 1.1 μm to 2.4 μm for β-TCP with increasing calcination temperature. It is essential to investigate the porosity of the sample and determine for the circulation of the physiological fluid in biomedical purpose. The grain size of the sample at different calcination temperatures is shown in Table 6.

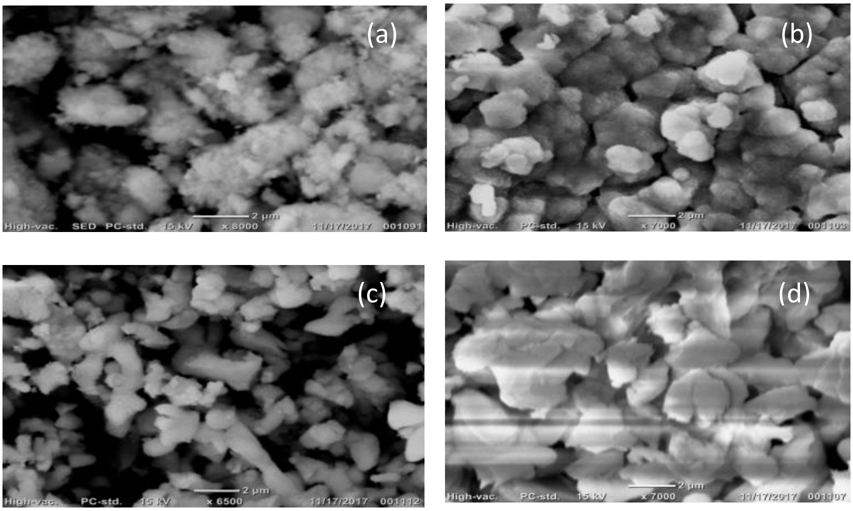

Figure 6: The SEM micrographs of HAP and β-TCP with different calcination temperatures (a) before calcination, (b) 900°C, (c) 1000°C and (d) 1100°C

Table 6: The average grain size of the Biphasic Calcium Phosphate of HAP and □-TCP

Condition	Grain size of HAP (□m)	Grain size of □-TCP (□m)
Before calcination	1.70	1.11
Calcination at 900°C	2.06	1.20
Calcination at1000°C	3.00	2.22
Calcination at 1100°C	3.70	2.35

Hardness of Biphasic Calcium Phosphate

Hardness test has been performed by Hardness Tester (Mecmesin BFG-500N, Basic Force Guage) in Department of medical research, Innsein, Myanmar. The maximum applied force of the Hardness Tester is 51 kg (1 kg = 9.80665 N). Figure 7 shows the variation of hardness with calcination temperature

It has been investigated that biphasic HAP/β -TCP pellets calcined at temperature 1100^{o}C has very low hardness than compared to those calcined at 900 ^{o}C and 1000 ^{o}C. During pelletization process, biphasic HAP/β -TCP powder calcined at temperature 1100^{o}C are difficult to make pellet as it has non-interconnected grains which is observed in SEM image. Therefore, it is worth to note that calcination temperatures of 900 ^{o}C and 1000 ^{o}C can be utilized to form dense BCP structure where the calcination temperature of 1000 ^{o}C can produce BCP with the high hardness value of 41.23 N.

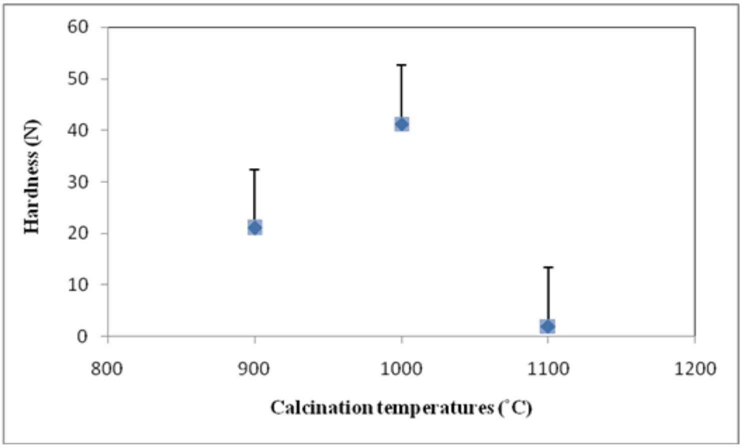

Figure 7: The variation of Hardness with calcination temperature

Conclusion

Biphasic calcium phosphate (BCP) has been prepared from white coral and diammonium hydrogen phosphate using mechano-chemical method. In present study, biphasic calcium phosphate has been crystallized at the calcination temperatures of 900°C, 1000°C and 1100°C. X-Ray Diffraction (XRD) has been confirmed the presence of HAP and β-TCP in major proportions along with Calcium Carbonate ($CaCO_3$) and Calcium Oxide (CaO) in traces revealing the biphasic calcium phosphate nature of synthetic powders. The FTIR result of BCP shows the presence of PO_4^{3-}group in HAP and β-TCP. The SEM micrographs proved the formation of grains in the non-uniform circular grain shape and grain size are increased with calcination temperature and some pore has been formed in the sample. Importantly, this work pointed out that dense BCP structure could unified at calcination temperatures of 900 °C and 1000 °C and the BCP with relatively higher hardness can be obtained at the calcination temperature of 1100 °C.

Based on the results obtained, it has suggested that white coral can be successfully converted to biphasic calcium phosphate (HAP/β-TCP) with optimized synthesis parameters and interesting characterizes.

Acknowledgements

The authors are grateful to Dr. Tin Htwe, Rector of Hinthada University and Dr. Marlar, Pro-Rector of Hinthada University, for allowing us to submit this research paper and We are also greatly indebted to Professor Dr Win Win Thein, Head of Department of Physics, Hinthada University, for her continual supports. Professor Dr Khin Khin Win, Head of Department of Physics, University of Yangon for her kind permission to carry out this work.

References

Berzina-Cimdina, L. and Borodajenko, N. (2012) "Infrared Spectroscopy", Material Science, Engineering and Technology, Intech publisher, Croatia.

CarolineVitoria, E. and Gnanan, F. D. (2002). "Synthesis and Characterization of Biphasic calcium phosphate", Center of Ceramic Technology, Department of Physics, Anna University.

Hao WU and Qiang Li (2012). " Journal Advanced ceramic", Department of Chemistry, East China National University, Shanghai 200062, China.

Hanno Zur Loye (2001). "X-Ray Diffraction, How it works what it can and what it cannot tell us", University of South Carolina.

Innocent Meachal, J., Upsorn Booyang, Sophie Cazalbou, Besim Ben-Nissan, Cedric Charvillat, Faik N Oktar and David Grossin (2015). "Comparative study of Coral Conversion, Part 2:Micro structural evolution of calcium phosphate", Department of Chemistry and Forensic Science, University of Technology Sydney.

Liga Berzina-Cimdina and Natalija Borodajenko (2012)."Research of Calcium Phosphates Using Fourier Transform Infrared Spectroscopy", Riga Technical University, Institute of General Chemical Engineering, Latvia.

Maninder Singh Mehta and Ravinder Pal Singh (2014). " Effect of Aging Time and Sintering temperatures on the Structral, Morphological and Thermal properties of Coralline Hydroxyapatite", Sri Guru Granth Sahib World University, Fatehgarh Sahib, Punjab, India.

Rebea-Naemi Rosa Cegla, Innocent MeachaJ., Besim Ben-Nissan, David Grossin, Greg Heness and Ren-Jei Chung (2014). "Comparative Study of Conversion of Coral with Ammonium Dihydrogen Phosphate and Orthophosphoric Acid to Produce Calcium Phosphates", Department of Materials Engineering Glass and Ceramics, Westerwald Campus, University of applied science, Koblenz, German.

Teerawat Laonapakul (2015). "Synthesis of hydroxyapatite from biogenic wastes", Department of Industrial Engineering, Faculty of Engineering, Khon Kaen University, Khon Kaen 40002, Thailand.

Zhang Xing (2007). "Preparation and characterization of Calcium Phosphate Ceramics and Composite as bone substitutes", Electronic Thesis and Dissertation, UC San Diego.

J. Myanmar Acad. Arts Sci. 2019 **Vol. XVII. No.2A**

CONSTRUCTION OF HEN EGG INCUBATOR CONTROLLED CIRCUIT USING PIC16F877A

Thet Lwin Oo[1], Hla Htay[2], Aye Min Oo[3]

Abstract

The hen egg incubator model is constructed using composite aluminum plate to enable reproduction process with the developing embryo. Light sources (40W, two bulbs) are used to maintain the require temperature. Two fans (5VDC) are also used to provide oxygen and to remove waste carbon dioxide. These are controlled by the circuit constructed using PIC16F877A microcontroller and other electronic devices. The program is written by using Basic Pro Language and it is compiled by Micro Studio Plus Software. The hexafile is downloaded by Win PIC 800. The temperature sensor, LM35DZ IC is used to detect the surrounding temperature. LCD module, TS1620L is used to display the present temperature in the hen egg incubator model from outside it. The chickens can be incubated from hen eggs by using Hen Egg Incubator Controlled Circuit.

Introduction

The hen egg incubator model which can be hatched eight eggs is constructed with aluminium and composite aluminium plate. This model is constructed with five components. They are the temperature controlled circuit, two light sources of bulbs (40W), two fans, egg tray and water container.

The controlled circuit is constructed with PIC16F877A microcontroller and other electronic components. Microcontrollers are intelligent electronic devices used to control and monitor devices in the real world. Microcontrollers are programmed devices. Pic Basic Pro Languages are used to program PIC microcontrollers. The two bulbs (40W) are used as light sources to get the available temperature. The two fans control the available temperature in the incubator. The egg tray is used for rolling eggs to obtain the same temperature on the eggs. The egg must be frequently turned and carefully positioned so that the embryo passes through fresh nutrients in the white of the egg, while forming in the correct position hatching. In the

---

[1] Demonstrator, Department of Physics, Kalay University
[2] Dr, Associate Professor, Department of Physics, Kalay University
[3] Assistant Lecturer, Department of Physics, University of Yangon

incubation period, the egg loses water by passing through pore in the shell. The humidity of the air in the incubator must be controlled by the water container. Four holes on one side, four holes on other side and eight holes on above side of the incubator are drilled to provide ventilation automatically. The egg breathes so there must be a supply of fresh air to provide oxygen and to remove waste carbon dioxide. Eggs are susceptible to infection so the incubator must provide a clean, disinfected environment.

Theoretical Background

Microcontroller Systems

A microcontroller is a single chip computer. Micro suggests that the device is small, and controller suggests that the device can be used in control applications. Another term used for microcontrollers is embedded controller, since most of the microcontrollers are built into (or embedded in) the devices they control. The simplest microcontroller architecture consists of a microprocessor, memory, and I/O. The microprocessor consists of a central processing unit (CPU) and the control unit (CU). The CPU is the brain of the microcontroller and this is where all of the arithmetic and logic operations are performed. The CU controls the internal operations of the microprocessor and sends out control signals to other parts of the microcontroller to carry out the required instructions. Memory is an important part of a microcontroller system. Depending upon the type used memories can classified into two groups: program memory and data memory. Program memory stores the program written by the programmer and this memory is usually non-volatile, i.e. data is not lost after the removal of power. Data memory is where the temporary data used in a program are stored and this memory is usually volatile, i.e. data is lost after the removal of power.

There are basically five types of memories. They are RAM, ROM, EPROM, EEPROM and Flash EEPROM. RAM means Random Access Memory. It is a general-purpose memory which usually stores the user data used in a program. RAM is volatile, i.e. data is lost after the removal of power. ROM is Read Only Memory. This type of memory usually holds program or fixed user data. EPROM is Erasable Programmable Read Only Memory. This is similar to ROM, but the EPROM can be programmed using a suitable programming device. EEPROM is Electrically Erasable Programmable Read Only Memory, which is a non-volatile memory. These memories can be erased and also be programmed under program control. EEPROMs are used to save configuration information, maximum and minimum values, identification data, etc. Flash EEPROM is non-volatile and is usually very fast. The data is erased and then re-programmed using a programming device.

The Hardware Features of Microcontroller

Supply Voltage

Most microcontrollers operate with the standard logic voltage of +5V. Some microcontrollers can operate at as low as +2.7 V and some will tolerate +6 V without any problems. A voltage regulator circuit is usually used to obtain the required power supply voltage when the device is to be operated from a mains adaptor or batteries.

The Clock

The microcontroller requires a clock (or an oscillator) to operate. The clock is usually provided by connecting external timing devices to the microcontroller. Most microcontrollers will generate clock signals when a crystal and two small capacitors are connected. Some will operate with resonators or external resistor–capacitor pair. Some microcontrollers have built-in timing circuits and they do not require any external timing components. The microcontroller is actually operated at a clock rate which is a quarter of the actual oscillator frequency.

Timer

Timers are important parts of any microcontroller. A timer is basically a counter which is driven either from an external clock pulse or from the internal oscillator of the microcontroller. It is typical to have at least one timer in every microcontroller. Some microcontrollers may have two, three, or even more timers where some of the timers can be cascaded for longer counts.

Watchdog

Most microcontrollers have at least one watchdog facility. The watchdog is basically a timer which is refreshed by the user program and a reset occurs if the program fails to refresh the watchdog.

Reset Input

A reset input is used to reset a microcontroller. An external reset action is usually achieved by connecting a push-button switch to the reset input such that the microcontroller can be reset when the switch is pressed.

Interrupts

Interrupts are very important concepts in microcontrollers. An interrupt causes the microcontroller to respond to external and internal (e.g. a timer) events very quickly.

Brown-out Detector

Brown-out detector reset a microcontroller if the supply voltage falls below a nominal value.

Analogue-to-digital Converter

An analogue-to-digital converter (A/D) is used to convert an analogue signal such as voltage to a digital form so that it can be read by a microcontroller. Some microcontrollers have built-in A/D converters.

EEPROM Data Memory

EEPROM type data memory is also very common in many microcontrollers. The advantage of an EEPROM memory is that the programmer can store non-volatile data in such a memory, and can also change this data whenever required.

Analogue Comparator

Analogue comparators are used where it is required to compare two analogue voltages. Although these circuits are implemented in most high-end PIC microcontrollers they are not common in other microcontrollers.

PIC16F877A Microcontroller

In the constructed system, PIC16F877A microcontroller is used as one digit score board which is manufactured by the Microchip Technology Inc. It is a 40-pin device with 8 Kbytes of flash program memory. The PIC16F877A has five I/O ports, PortA, PortB, PortC, PortD and PortE. Some pins for these I/O ports are multiplexed with an alternate function for the peripheral features on the device. In general, when a peripheral is enabled, that pin may not be used as a general purpose I/O pin .The pin diagram of the PIC16F877A microcontroller are shown in figure1.

Introduction to Bipolar Junction Transistor

Two basic types of transistor are the bipolar junction transistor (BJT) and the field-effect transistor (FET). The BJT is used in two broad areas such as linear amplifier and as an electronic switch.

In the bipolar junction transistor (BJT), three doped semiconductor regions are formed as two back to back connected p-n junctions consists of two n regions separated by a p region, and the other consists of two p regions separated by an n region.

The p-n junction joining the base region and the emitter region is called the base emitter junction. The junction joining the base region and the collector region is called the base collector junction. These leads are labeled E, B, and C for emitter, base, and collector, respectively.

The base region is lightly doped and very thin compared to the heavily doped emitter and the moderately doped collector regions. Figure 2 shows the schematic symbols for the n-p-n and p-n-p bipolar transistors. The term bipolar refers to the use of both holes and electrons as carriers in the transistor structure.

Embryo Development (based on hen egg)

The yolk is dropped from the ovary into the unfundibilum where it is fertilised by the male sperm if present. The embryo commences development while the yolk travels down the egg canal. Here it receives coatings of white. The egg progresses to the shell gland where it receives membranes and forms the shell itself. This process takes approximately 20 hours, in which time the embryo grows to about 4mm in diameter. The egg is laid.

After the egg is laid it cools and growth slows or stops. Many birds (but not all) accumulate a ‘clutch’ of eggs before commencing incubation. During this ‘storage’ time temperature is preferably between 0 and 20°C but some species tolerate more extreme temperatures. However, embryonic death is a risk if extremes are maintained. In the first day of incubation a line called the primitive streak appears. This allows the formation of a third layer of cells. From these new cells the organs of the body will form. The cells are made up in three layers called ectoderm, mesoderm and endoderm. Ectoderm forms the skin, feathers, beak, nervous system, claws eyes and mouth. Mesoderm forms the skeleton, muscle, blood and reproductive organs. Endoderm forms the respiratory organs, secretary system and digestive system. By the end of the first day’s incubation, the head, eyes, nervous system and blood island have started to form. The heart is formed on the second day and is functioning by 44 hours.

On the fourth day the heart changes from its simple form and becomes a fully formed beating heart. During this time extra membranes are formed to produce the amniotic sack. The embryo will now float in the amniotic fluid for the rest of incubation. The amniotic fluid and turning of the egg ensure the embryo orientsitself correctly for hatching. By the fourth day, legs and wing buds begin to form and the heart is still positioned outside the body.

By six days the legs and wings are almost complete, and by eight days feathers are appearing. On the 9th day the embryo starts to look like a chick. The heart is now within the body with blood circulation to the outside via the umbilicus. By ten days the bones are now being formed.

Thirteen days into incubation and the down is apparent and is coloured. By sixteen days the beak, leg scales and claws are almost complete. The albumen is used up with just the yolk remaining. The amniotic fluid decreases and the yolk then acts as a food source. By the nineteenth day the yolk is incorporated into the body. The ability of the embryo or now ‘chick’, to get oxygen through the shell and into the blood system is now limited. The carbon dioxide levels in the blood therefore rise dramatically, which causes twitches in the chick’s neck muscle. The beak then forces its way into the air cell at the large end of the egg. The beak now opens for the first time and the lungs inflate. This causes the blood system to circulate within the lungs. This is time of great stress for the chick, where any deficiencies become apparent. The stress is so much that it will kill chicks that are not strong enough, usually those who have a lack of group B vitamins. The chick continues to try to breath in earnest, which causes more twitching and hopefully a breakout through the shell. This process forces the beak out and chips a small hole in the shell. The legs push the chick slightly to the side so next time there is a twitch the next piece of shell will fall off. This continues all the way round the shell until the end of the shell falls off. The chick has an egg tooth, which helps with this hatching process. The tooth falls off soon after hatching. After the end falls off the chick kicks itself out of the shell. The old blood vessels and membranes in the cell. Embryo development of hen egg from first day to 21days is shown in Figure 3.

Temperature

Accurate incubation temperature is by far the most important requirement for successful hatching of chicks. Even marginal temperature differences can affect hatch rates, although these differences seem to have less effect on eggs in contact incubators. The growth processes in the development of the embryo are very temperature sensitive and small deviation can cause development to progress out of sequence resulting in losses or deformities. The design basis for Brinsea incubators is a maximum ±0.25C across the egg tray and ±0.25C over a period of time.

It is the egg centre or embryo temperature that is most critical. To ensure this is correct it is of highest importance that the incubator is set up correctly, particularly for still air machines. Still air incubators have temperature variations from top to bottom, therefore the sensor of the temperature controller and the thermometer bulb need to be positioned as close as possible to the top of the eggs. Here the temperature needs to be slightly higher than the mean temperature used in forced draft incubators and accounts for the important difference found in the instructions. It is therefore vital to follow the manufacturer’s recommendations for the incubator used.

Humidity

Constant accuracy of humidity is less critical than that of temperature. Ideally, the egg needs to lose 13 – 15% of its weight between the time of laying and pipping, (more for some altricial species). Fairly wide tolerances in humidity are bearable although not ideal, as long as the chick ends up having lost the correct amount of weight by the time of hatching. Correction can be made in later stages for errors earlier.

Experience has shown Contact Incubation to be less critical of exact humidity control, perhaps due to the egg being in a more natural air-flow environment. Never the less, digital humidity control is available for all Brinsea Contact and Forced Air incubators.

The weight loss rate will vary according the type of egg, the amount of ventilation, the handling of the egg, the breeder diet and the time in the season in which it was hatched. There are two guides that help indicate correct humidity.

Firstly, the air cell. The air cell increases as the incubation proceeds. In order to see this at first sight, the eggs need to be candled.

The other indicator is weight loss. If you weigh eggs before setting and weigh them as incubation progresses, the weight loss can be plotted on a graph (example below) to determine if the average weight loss has been correct.

Humidity can be adjusted during the incubation period according to the graph reading at that particular time in the incubation process. As a general rule, if actual weights are lower than ideal, then humidity needs to be increased. If actual weights are higher than ideal, then humidity needs to be decreased.

All incubators should have the facility to adjust humidity levels. There are two controllable factors that influence humidity levels. These are the amount of water surface area, and the amount of fresh air that the incubator draws in. The greater the water surface area, and the less fresh air being drawn in, the higher the humidity levels inside the incubator will be. One method to increase water surface area is to use evaporating pads or blotting paper. Finally, the environment in which the incubator is set up in can have an effect on accurate humidity control. If the ambient humidity in the air outside the incubator is very dry, then incubation humidity levels will be lower than if the air is very humid (wet). Also, cold air cannot retain much water vapour, so when cold winter air is warmed the RH level will be very low. This happens in heated houses in winter, and also inside incubators. The result of this in general is that humidity levels tend to be lower in the winter than in summer and so humidity levels should be adjusted with this in mind.

Some breeders go to great lengths to control the incubation room environment and overcome seasonal variations in ambient humidity. In extreme cases, sections of the egg’s shell are removed to allow extra water loss, or covered with tape to reduce water loss. This should be regarded as strictly for the experts though and a high risk method. The humidity levels required when a chick is hatching need to be higher than previously in the incubation period. For the last day or so, high humidity levels are required to prevent the membranes of the egg drying too fast as the chick hatches and becoming tough and difficult to tear. The humidity level when hatching should therefore be at least 60%RH.

Turning and Rolling

As the egg is turned the embryo is swept into fresh nutrients, allowing the embryo to develop. This is critical for the first week when the embryo has no circulation system. After the first week, eggs still need to be turned but not as often. The turning regime is often different between species and altricial birds tend to need more frequent turning than precocial birds. Whereas fowl are turned through 80 degrees every hour or so, parrots are often turned through 180 degrees many times an hour in the early stage.

Rollers work by being rotated by a moving floor. Eggs sit on rollers that in turn sit on the moving floor. Ribs on the rollers help reduce the tendency for an egg to ‘walk’ along the roller length.

Candling

Candling lamps are lights with a concentrated beam that may be shone through the shell of the egg to illuminate the egg contents. This allows the size of the airspace to be determined which offers a guide to the weight loss rate. If the air space is larger than expected too much water is being lost and the humidity in the incubator should be increased to reduce the rate of water loss. If the air space is smaller than expected then the opposite applies. Diagram for extent of airspace development throughout incubation (in days) is shown in Figure 4.

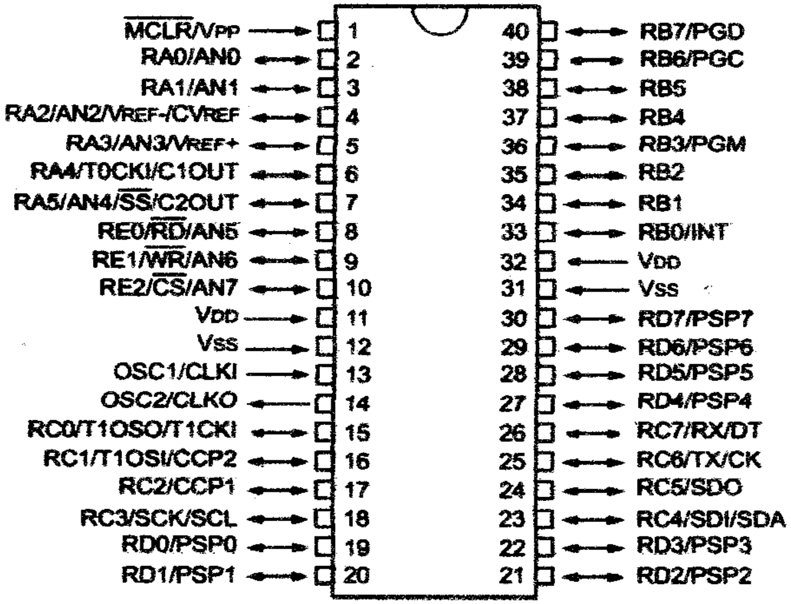

Figure 1: Pin diagram of PIC16F877A microcontroller

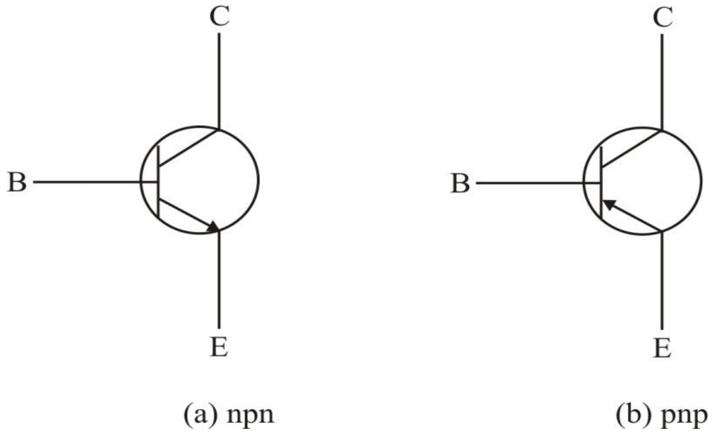

(a) npn

(b) pnp

Figure 2: Standard bipolar junction transisor (BJT) symbols

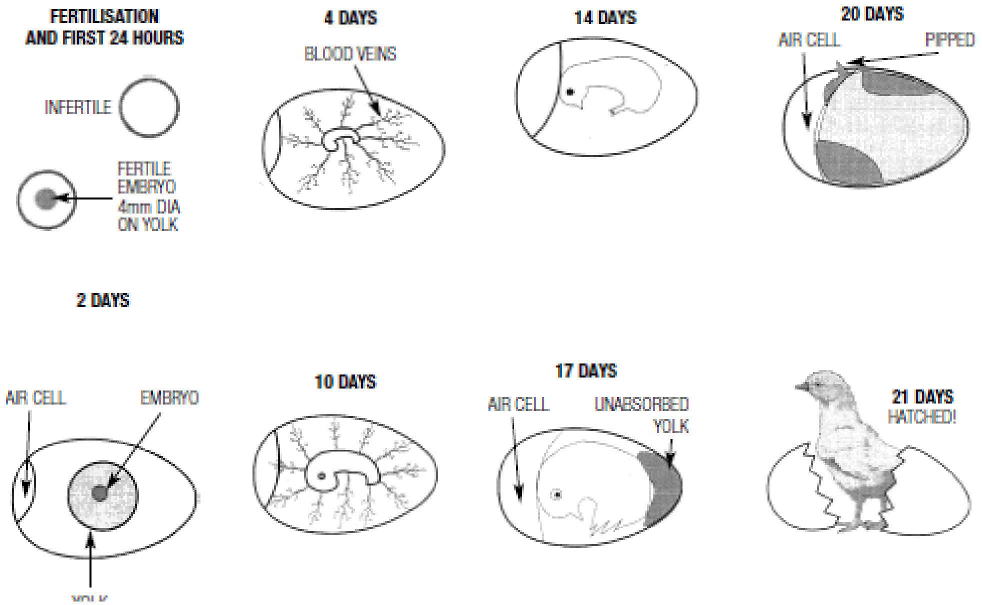

Figure 3: Embryo development of hen egg from first day to 21days

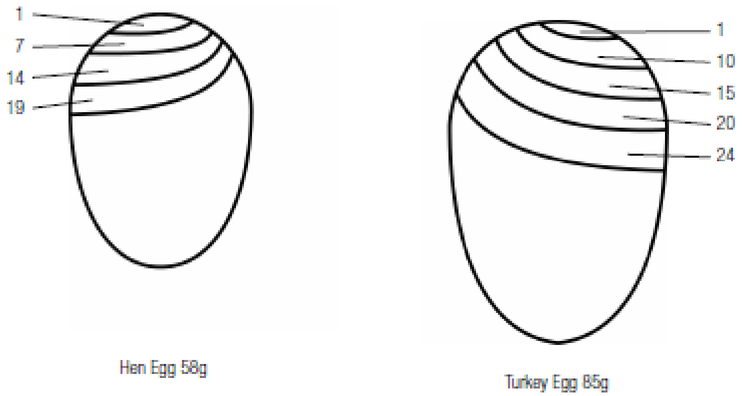

Figure 4: Diagram for extent of airspace development throughout incubation(in days)

Construction and Operation of the Whole system

Constructed hen egg incubator

The incubator can take up to 8 eggs. It is 30cm length, 30cm breadth and 45cm long . It can be made composite aluminium plate. The aluminium plate of the front side of the incubator is used as the window to open by pulling upward and to close by pushing downward. The lamp 1 controlled by dimmer is set up on the back side of the incubator. The lamp 2 controlled by the setting temperature is set up on the top side of the incubator. The two fans are also set up in topside of the incubator. The eight holes are drilled on the right side and left side. The four holes in the center of each fan are also drilled on the top of the incubator. The water container $(25cm \times 15cm \times 2cm)$ costructed by using zinc plate is taken place on the bottom side of the incubator. The dimension of constructed is shown in Figure 5.

Power Supply Circuit

A positive 5V regulated power supply has been constructed. A 7805 IC, a step-down transformer, two 1N4007 p-n junction diodes and a capacitor are used. The voltage regulator give positive 5V. IC7805 is a three terminal voltage regulator . Pin 3 of IC gives the output. An input voltage is given to pin 1 and Pin 2 must be grounded. The input voltage must be DC voltage higher than the desired output voltage. To obtain two 5V DC inputs, a full-wave rectifier converts AC to DC and a 9V step-down transformer is also used. The circuit diagram of the constructed +5V regulated power supply is shown in Figure 6.

Controlled circuit of constructed hen egg incubator

The controlled circuit of hen egg incubator is constructed by using PIC 16F877A, LM35, LCD display, two relays, two fans, two bulbs, AC220V, dimmer, two transistors (BD139 and C945), capacitors and resistors. The pin 1 of pic is used as master clear that is joined to the 4.7kΩresistor applied by the +5VDC.The pin 2 of pic is connected to the pin1 of LM35 and the pin2 of LM35 is applied by+5VDC and pin3 is grounded. The pin 3 of pic is connected to the variable resistor (10k) applied by +5VDC. The pin11 of pic is applied by +5VDC and the pin 12 of pic is grounded. The pin 13 of pic is as the RC network (4.7k and 22pF) that is generated to the clock pulse. The pin

15, 16 of pic is connected to the base of BD139 and C945 transistor with 1k resistor respectively. The pin 21, 22, 27, 28, 29, 30 of pic is connected to the pin 4, 6, 11, 12, 13, 14 of LCD module respectively. The pin1 of LCD is connected to the pin3 of LCD with 4.7k resistor and is grounded. The pin2 of LCD is applied by +5VDC and the pin 5 of LCD is grounded. The collector of C945 transistor and BD139 transistor is connected to relay 1 and relay 2 respectively. The relay 1 is connected to the bulb 1 applied by AC220V but the bulb 2 is connected to AC220V with dimmer. The relay 2 is connected to fan1 and used as a switch for fan2 applied by +5VDC.The constructed controlled circuit of hen incubator is shown in Figure 7.

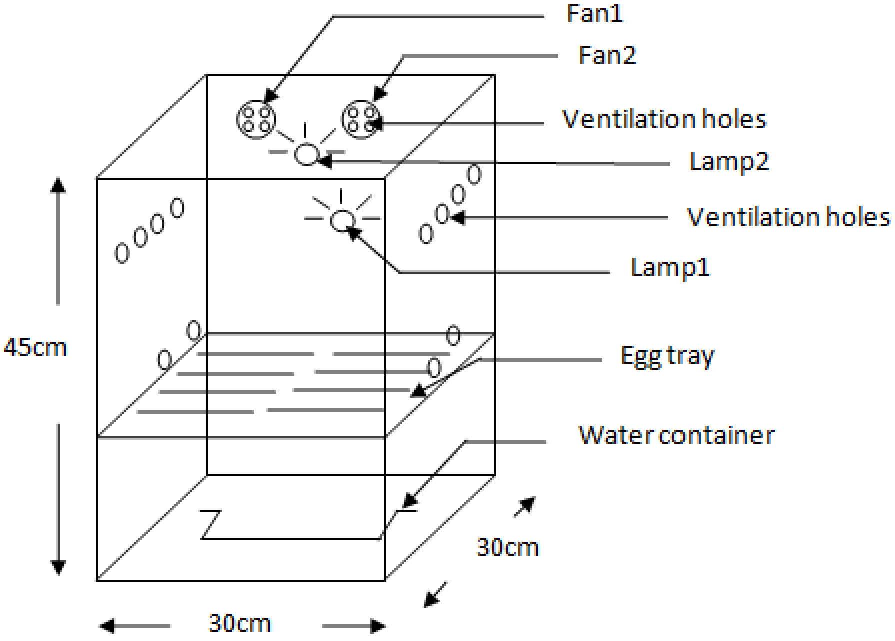

Figure 5: Dimension of constructed hen incubator model

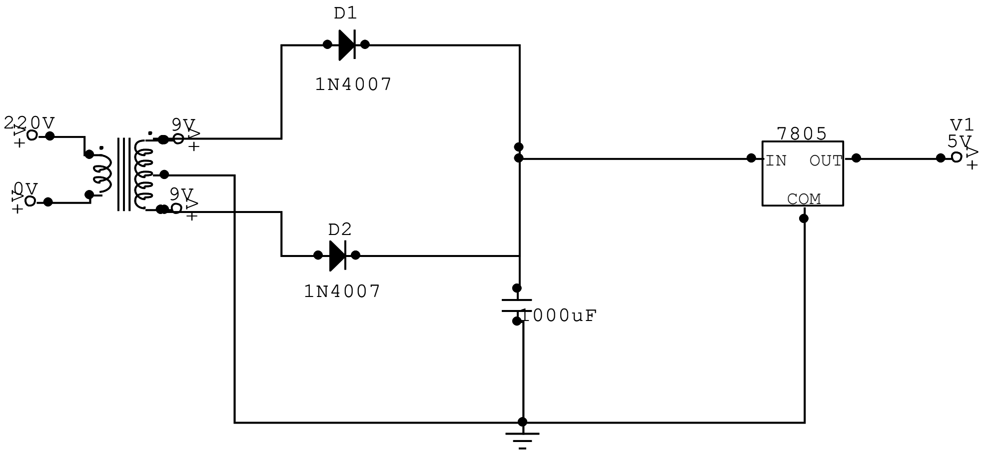

Figure 6: Constructed circuit diagram of +5V regulated power supplies

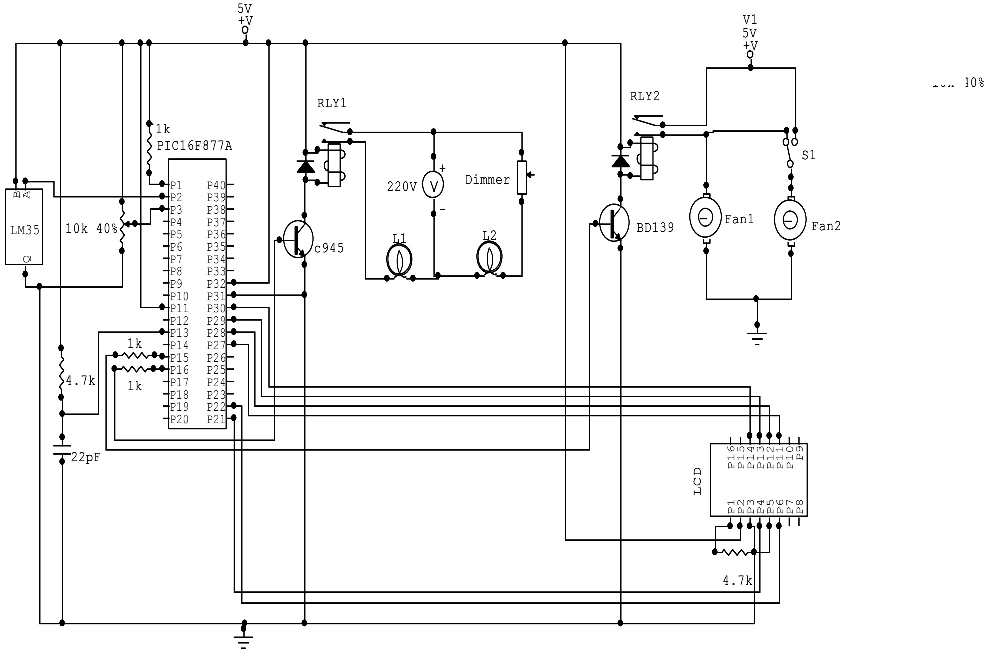

Figure 7: The constructed controlled circuit of hen egg incubator model

Results and Discussion

Results

The controlled circuit by using PIC16F877A microcontroller for hen egg incubator has been constructed as shown in Figure 8. The hen egg incubator model as shown in Figure 9 has also been constructed to investigate the growth of the embryo. The incubator is set up correctly, particularly for still air machines to have temperature variation from top to bottom. The right side of incubator as shown in Figure 10 exists the ventilation holes and the rope tied the rod for rolling eggs. The light sources, fans and temperature sensor as shown in Figure 11 are set up in the incubator model. Before hatching the position of the eggs on the trays, water container and thermometer for measuring the surrounding temperature are shown in Figure12.

To investigate the growth of embryo for the first time we choose the five eggs which each have weight of 36 gram. They are placed into the egg tray as shown in figure 12. The total time taken for the eggs is 21days from 1.11.15 to 22.11.15. The incubator without controlled circuit and the light source controlled by the dimmer are provided on the eggs, therefore the temperature stored by the eggs is from minimum temperature 32^0C to maximum temperature 40^0C. The surrounding temperature is nearly from 19^0C to 28^0C during the incubation period. After 7days, we observed dead embryo due to the lack of electricity. This situation is shown in Figure 14.

For the second time we choose the eight eggs which each has weight of 45 gram. The total time taken for the eggs is 26days from 14.12.15 to 9.1.16. The incubator with controlled circuit, fans, light source controlled by the dimmer are provided on the eggs, therefore the temperature stored by the eggs is from minimum temperature 35^0C to maximum temperature 40^0C. The surrounding temperature is nearly from 9^0C to 25^0C during incubation period.

After 21days, when the one of the eggs is cracked, we observed that the alives in the shell. The front and back view of chick are shown in Figure 14 and 15. So the seven eggs were still-born in the incubator. After 24days, the three egg were successfully cracked and hatched out. The next day, the one egg is also cracked and hatched out. The photograph of the chicks breaking out of the four eggs after 25days is shown in Figure 16.

After 26days, the two eggs do not hatch out and do not alive in the shell. The two dead chicks without hatching out of the eggs as shown in Figure 17. Since the last one egg does not crack, when it is cracked by hand, we observed that the chick alives in the shell. The living chick without cracking of the egg after 26days is shown in Figure 18.

Discussion

Our constructed model is a small incubator capable of holding eight eggs by using the cheapest local materials. It is weak embryos so that chicks hatch late for 4-days. Because the window of incubator is after opened or closed, it is low incubation temperature and humidity in storage. So the two chicks stuck in shell and dead without breaking out of the eggs.

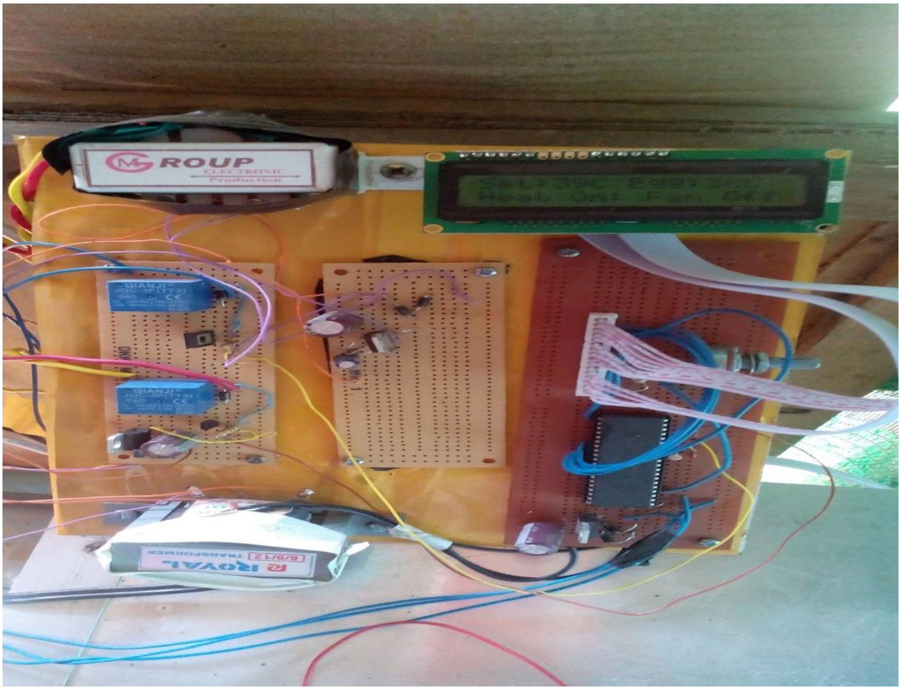

Figure 8: Photograph of the controlled circuit for hen egg incubator.

Figure 9: Photograph of hen egg incubator model.

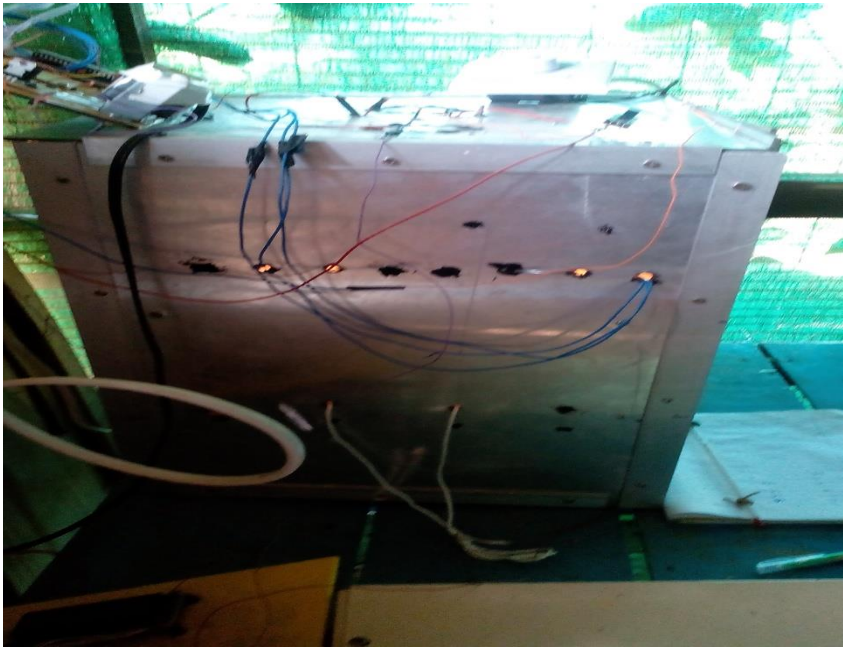

Figure 10: Photograph of the right side of incubator model**.**

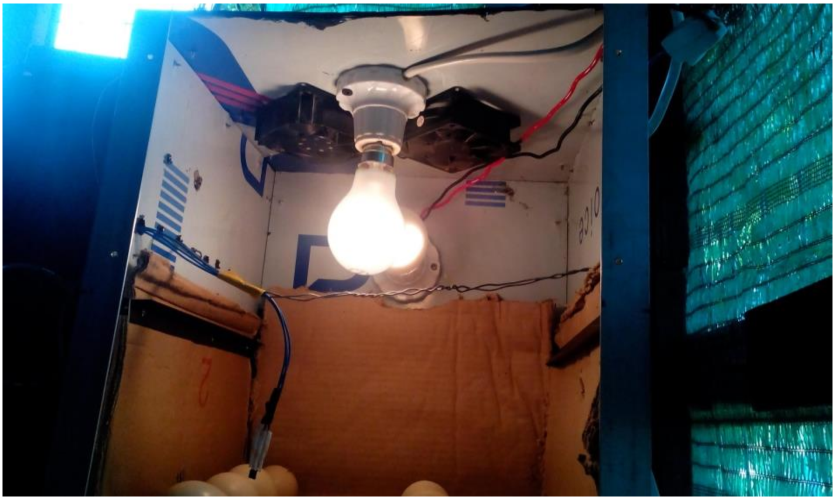

Figure 11: Photograph of setting bulbs and fans in the incubator model.

Figure 12: Photograph of the eggs on the tray before hatching.

Figure 13: Photograph of the condition to develop the embryo.

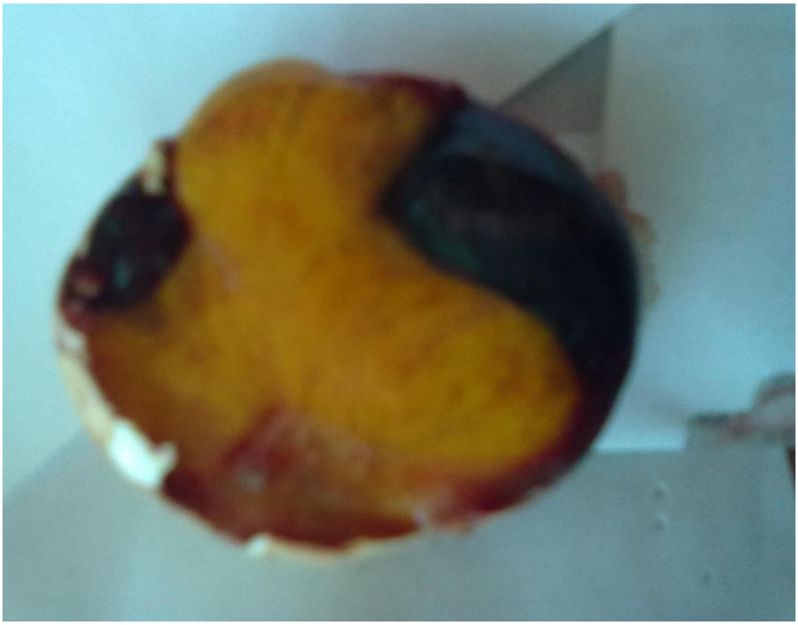

Figure 14: Photograph of the front view of chick after 21days.

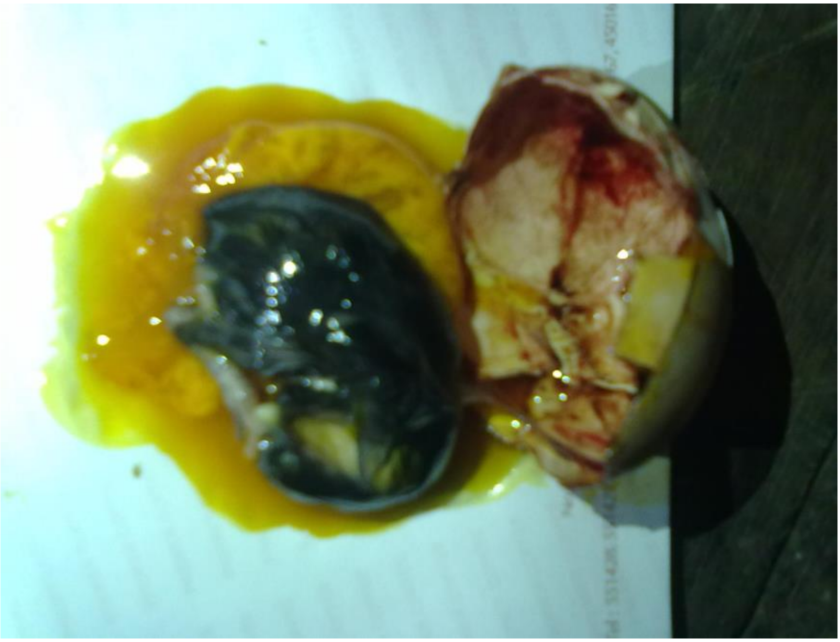

Figure 15: Photograph of the back view of chick after 21days .

Figure16: Photograph of the chicks hatching out of the four eggs after 25days.

Figure17: Photograph of the two dead chicks without hatching after 26days.

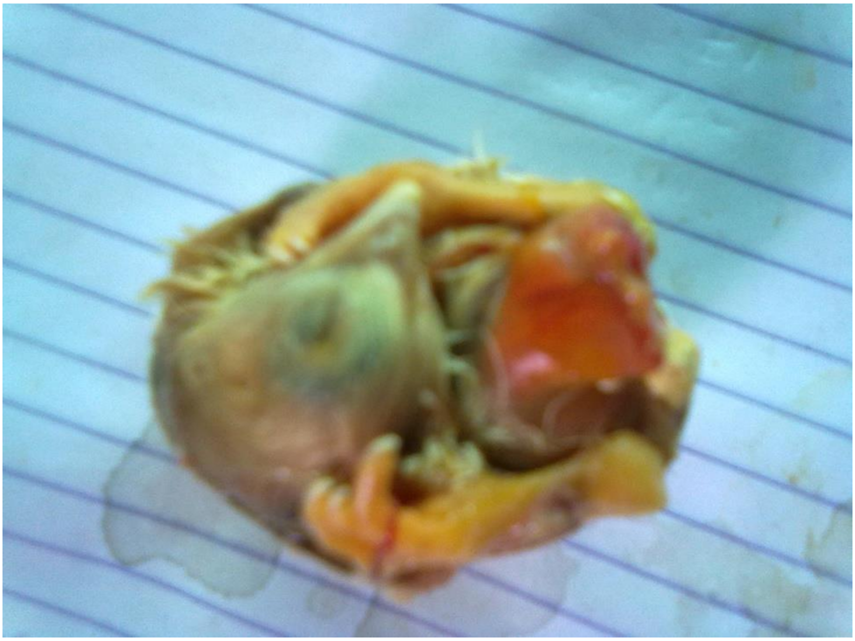

Figure 18: Photograph of the living chick without cracking after 26days

Acknowledgements

I am very grateful to Professor Dr Ah Mar Kywe, Head of Department of Physics, Kalay University, for her kind permission to this work.

I wish to thank Dr Thein Zaw, Lecturer, Department of Physics, Shwe Bo University, and U Aye Min Oo, Assistant Lecturer, Department of Physics, University of Yangon, for their encouragement to this work.

References

http://www.brinsea.co.uk, “Incubation Handbook”.

N.van Wageningen, J.Meinderts, P.Bonnier,H.Kasper, “Hatching Eggs by Hens or in an Incubator”, Agromisa Foundation, Wageningen (2004).

P.Horowitz and W.Hill, “The Art of Electronics”, (Second Edition), Cambridge University Press, United Kingdom, New York, (1995).

R.L.Geiger; “VLSI Design Techniques for Analog and Digital Circuit”, McGraw- Hill, Book Co., Singapore, (1990).

T.L.Floyd; “Digital Fundamentals”, (Eight Edition), Pearson Education, Inc., upper saddle River, New Jersey, (2003).